UNIVERSITY OF CALIFORNIA SAN DIEGO

Seismic Performance of Existing and New Bridge Substructures

A Dissertation submitted in partial satisfaction of the requirements
for the degree Doctor of Philosophy

in

Structural Engineering

by

Lucas Claude Deyglun

Committee in charge:

Professor P. Benson Shing, Chair
Professor Janet Becker
Professor Machel Morrison
Professor Gilberto Mosqueda

2024

The Dissertation of Lucas Claude Deyglun is approved, and it is acceptable in quality and form for publication on microfilm and electronically.

University of California San Diego

2024

DEDICATION

To my parents and loved ones

TABLE OF CONTENTS

LIST OF NOTATIONS

CHAPTER 4

A	modelling parameter
B	modelling parameter
C	modelling parameter
D	modelling parameter
d_i	undeformed length of diagonal linear potentiometers in pile segment *i*
f_c'	concrete compressive strength
f_p	stress in prestressing strands
f_{pu}	tensile strength of prestressing strands
h_L	height at which lateral displacement is considered measured with respect to the soffit of the pile cap
l	undeformed horizontal distance between pairs of linear potentiometers
u_f	lateral displacement due to flexure
u_{si}	shear deformation in pile segment *i*
u_θ	lateral displacement due to rotation at the end of the pile
y_i	distance of the top of the pile segment with respect to the soffit of the pile cap

α dimensionless parameter

δ_N average displacement measured by linear potentiometers on north side of pile

δ_S average displacement measured by linear potentiometers on south side of pile

ε_p strain in prestressing strands

$\Delta\theta$ relative rotation in pile segment

θ_p rotation at the end of the pile measured relative to the pile cap

ϕ curvature of pile segment

CHAPTER 5

d_b bar diameter

D_1 inner diameter of precast shell

l_1 vertical distance between horizontal crack in precast shell and core bar termination point

l_2 retrofit length beyond termination of core bars

P axial tensile force

τ_D interface shear demand

CHAPTER 9

$A_{loop(i)}$	area of hysteretic cycle
k	elastic column stiffness
F_f	friction force
F_{max}	maximum experimental force
F_{min}	minimum experimental force
t^i	time at data point *i*
t^{i-1}	time at data point *i-1*
u_i	displacement amplitude of i^{th} cycle
u_{i+1}	displacement amplitude of $(i+1)^{th}$ cycle
$\Delta_{max(i)}$	maximum displacement in i^{th} hysteretic loop
$\Delta_{min(i)}$	minimum displacement in i^{th} hysteretic loop
θ^i	angle of rotation at data point *i*
θ^{i-1}	angle of rotation at data point *i-1*
$\dot{\theta}^i$	rotational velocity

CHAPTER 10

A (grout) modelling parameter for parabolic transition curve in concrete model

A (prestressing strands) modelling parameter

A_e cross-sectional area of elastic bar

A_f cross-sectional area of fuse bar

A_i cross-sectional area of fiber *i*

A_{pl} cross-sectional area of steel rocking plate

a dimensionless parameter

B modelling parameter

b dimensionless parameter

C modelling parameter

c (grout) modeling parameter for cyclic stress-strain curve

c (longitudinal reinforcement) modeling parameter for fracture

D (longitudinal reinforcement) total accumulated damage in longitudinal reinforcing bar

D (prestressing strands) modelling parameter

D_i damage in longitudinal reinforcement during i^{th} cycle

E linear-elastic stiffness of prestressing strands

E_c linear-elastic stiffness of concrete

E_{pl} linear-elastic stiffness of steel plate

E_{plr} post-yield modulus of steel plate

E_r modulus of concrete on reloading reversal

E_{re} common return point tangent modulus

E_s linear-elastic stiffness of longitudinal reinforcement

E_{sec} secant modulus of confined concrete at peak stress

E_{sr} post-yield modulus of longitudinal reinforcement

E_u initial concrete modulus of elasticity at onset of unloading

F lateral resistance

F_1 yield force of longitudinal reinforcement in series

F_2 ultimate force of longitudinal reinforcement in series

F_a total applied axial force

dF_f full differential maximum friction force that can develop on top and bottom face of outer grout fiber

ΔF_f finite discretized maximum friction force that can develop on top and bottom face of outer grout fiber

F_{po} initial prestressing force

F_s force in longitudinal reinforcement in series

f_c concrete stress

f'_{co} unconfined concrete compressive strength

f'_{cc} confined concrete compressive strength

f'_l effective lateral confining stress

f_{new} new concrete stress on reloading at strain of ε_{un}

f_{ps} stress in prestressing strands

f_{py} yield stress of prestressing strands

f_{pu} tensile strength of prestressing strands

f_{so} (prestressing strands) modelling parameter

f_{re} return point stress on monotonic stress-strain curve

f_{ro} concrete stress at reloading reversal

f_{un} reversal (unloading) stress in concrete model

f_{yh} yield strength of transverse reinforcement

H_c column height

H_h height of hinge

i analysis step counter

$\widetilde{K_1}$ linear-elastic stiffness of longitudinal reinforcement in series

$\widetilde{K_2}$ post-yield stiffness of longitudinal reinforcement in series

K_e linear-elastic stiffness of elastic bar

K_f linear-elastic stiffness of fuse bar

k iteration step counter

k_e confinement effectiveness coefficient

L_p unbonded prestressing strand length

L_u unbonded length of reinforcing bars

L_{ue} unbonded length of elastic bars

L_{uf} unbonded length of fuse bars

l_{io}	effective fiber length
M	moment resistance
M_i	moment resistance during i^{th} analysis step
N	axial resistance
N^k	axial resistance during k^{th} iteration
N_i^k	axial resistance during k^{th} iteration of analysis step i
N_f	number of half-cycles until longitudinal reinforcement fractures
P	applied axial load
P'	total force in post-tensioned rods
R^k	residual error during k^{th} iteration
R_o	radius of outer grout that has not been crushed
r	dimensionless parameter
r_e^{fib}	outer radius of individual grout fiber
t	thickness of sacrificial zone
u_1	yield displacement of longitudinal reinforcement in series
u_2	displacement of longitudinal reinforcement in series at which ultimate force is achieved

u_1^0 initial trial axial deformation after converged axial deformation u_o

u_{fy} axial displacement at which fuse bar yields

u_{fu} axial displacement at which fuse bar achieves ultimate force

$u_{o,i}$ converged axial deformation during analysis step *i*

$u_{o,i-1}$ converged axial deformation during previous analysis step *i-1*

u_o' axial deformation at column centroid

$u_o'^k$ trial axial deformation at column centroid during k^{th} iteration at initial analysis step

$u_{o,i}^k$ trial axial deformation at column centroid during k^{th} iteration at analysis step *i*

Δu^k axial deformation increment/decrement during k^{th} iteration

Δu^o initial axial deformation increment value

u_T total axial deformation in a given line of longitudinal reinforcement

W_c self-weight of the column above the hinge

x dimensionless parameter

x_i perpendicular distance of fiber from centroid axis about which rotation occurs

α_1 modeling parameter

Δ lateral displacement at top of column

$\Delta\varepsilon$ total strain range in a cycle of longitudinal reinforcement cycle

ε_a common strain at intersection of initial tangent and plastic unloading slopes

ε_c concrete strain

ε_{cc} strain at maximum concrete stress f'_{cc}

ε_{co} strain at maximum stress f'_c of unconfined concrete

ε_e strain in an elastic bar

ε_f strain in a fuse bar

ε'_f modeling parameter for longitudinal reinforcement fracture

$\varepsilon_{failure}$ strain at which outer grout fiber crushes

ε_i strain in fiber *i*

$\Delta\varepsilon_i$ total strain range in i^{th} cycle of longitudinal reinforcement cycle

$\varepsilon_{i,shrink}$ shrinkage strain in grout fiber *i*

$\varepsilon_{max,i}$ maximum longitudinal reinforcement strain in i^{th} cycle

$\varepsilon_{min,i}$ minimum longitudinal reinforcement strain in i^{th} cycle

ε_{pl} plastic strain in concrete model

ε_{ply} yield strain of steel plate model

ε_{plu} strain at which ultimate stress is achieved in steel plate model

ε_{po} strain corresponding to initial prestress in strands

ε_{ps} strain in prestressing strands

ε_{pu} ultimate strain of prestressing strands

ε_{re} return point strain on monotonic stress-strain curve

ε_{ro} concrete strain at reloading reversal

ε_{sp} strain at which cover concrete is considered to have completely spalled and ceases to carry any stress

ε_{sy} yield strain of longitudinal reinforcement

ε_{su} strain at which longitudinal reinforcement achieves ultimate stress

ε_{un} reversal (unloading) strain in concrete model

$d\phi$ arc angle of grout discretization

μ coefficient of friction between grout and steel plates

θ rotation at column hinge

θ_i rotation at column hinge at analysis step i

ρ_s ratio of volume to transverse confining steel to volume of confined concrete core

σ_i stress in fiber i

σ_{ply} yield stress of steel plate

σ_{plu} ultimate stress of steel plate

σ_{sy} yield stress of longitudinal reinforcement

σ_{su} ultimate stress of longitudinal reinforcement

CHAPTER 11

A_d cross-sectional area of bridge deck

$A_{g,col}$ cross-sectional area of a single column

C_{pi}^{eq} equivalent viscous damping coefficient of bridge pier

C^* equivalent viscous damping of SDOF structure in Rayleigh-Ritz analysis

E_{pi}^H total hysteretic energy dissipated in pier i during one cycle of displacement response with an amplitude of $\pm u_{pi,\max}$

$EI(x)$ bending stiffness of bridge superstructure

F ground motion scaling factor

$F_{c,bar}$ yield force of a single column

$F_{pi,bar}$ lateral resistance of a pier with reinforcing bars only

$F_{pi,\max}$ total strength of bridge pier

g acceleration due to gravity

H_c column height

K_{pi}^{eq} equivalent stiffness of bridge pier

K^* equivalent stiffness of SDOF structure in Rayleigh-Ritz analysis

L length of bridge superstructure

L_1 distance between left bridge abutment and first deck hinge

L_2 distance between two deck hinges

L_d length of bridge deck

L^* $\int_0^L m(x)\psi(x)dx + \sum_i M_{pi}\psi(x_i)$

M^* equivalent mass of SDOF structure in Rayleigh-Ritz analysis

M_{pi} tributary seismic mass of pier *i*

$m(x)$ mass per unit length of bridge superstructure

N_{col} number of columns per pier

PSa pseudo-spectral acceleration

PSa_{AASHTO} design pseudo-spectral acceleration from AASHTO

PSa_{gm} pseudo-spectral acceleration of unscaled ground motion

$S_d(T,\xi)$ spectral displacement as a function of period T and damping ratio ξ

S_d^* maximum allowed spectral displacement

S_{D1} spectral displacement for a structure with a period of 1 second

S_{DS} spectral displacement for structures with short periods

T period

T_{eq} equivalent period of bridge structure

T_n natural period of bridge structure

t time

u displacement

$u(x,t)$ lateral displacement of a bridge superstructure as a function of distance x and time t

$u_{c,bar\ yield}$ nominal yield displacement of a single column

$u_{pi,bar\ yield}$ nominal yield displacement of pier

$u_{pi,\lim}$ maximum allowable displacement for each pier

$u_{pi,\max}$ maximum lateral displacement to be induced on bridge pier

$\ddot{u}_g$ ground acceleration

x distance relative to end point of bridge superstructure

x_i location of pier *i* relative to end point of bridge superstructure

$z(t)$ generalized coordinate of SDOF system as a function of time *t*

z displacement of SDOF structure in Rayleigh-Ritz analysis

$\dot{z}$ velocity of SDOF structure in Rayleigh-Ritz analysis

$\ddot{z}$ acceleration of SDOF structure in Rayleigh-Ritz analysis

$z_{\max}$ maximum displacement response of SDOF system

α reduction factor

γ_c unit weight of concrete

ω_{eq} equivalent natural frequency of bridge structure

ξ^* equivalent damping ratio of SDOF structure in Rayleigh-Ritz analysis

$\psi(x)$ shape function describing bridge superstructure lateral displacement

APPENDIX B

A_c concrete shell cross-sectional area

A_p total strand cross-sectional area

d_b nominal strand diameter

E_{ci} modulus of elasticity of concrete at stress transfer

E_p modulus of elasticity of prestressing strands

f_{pi} initial prestress immediately after stress transfer

f_{pj} jacking stress

l_t stress transfer length

α dimensionless parameter

APPENDIX C

A_c cross-sectional area of concrete

$A_{c,t}$ age adjusted transformed cross-sectional area of concrete

A_p cross-sectional area of prestressing strands

A_s cross-sectional area of longitudinal reinforcing steel

E_{ci} modulus of elasticity of concrete at stress transfer

$E_{c.t}$ age adjusted modulus of elasticity of concrete

E_p modulus of elasticity of prestressing strands

E_s modulus of elasticity of longitudinal reinforcing steel

f'_{ci} compressive strength of concrete at stress transfer

Δf_{pC} prestress loss due to creep

f_{pe} effective prestress on the pile test day

Δf_{pS} prestress loss due to shrinkage

H humidity in %

k_A age adjusted factor for calculating prestress loss

k_{cs} factor for the effect of the volume-to-surface ratio for creep

k_f factor for the effect of concrete strength

k_{hc} humidity factor for creep

k_{hs} humidity factor for shrinkage

k_s factor for the effect of the volume-to-surface ratio of the component

k_{td} time development factor

r_o outer radius of precast shell

r_i inner radius of precast shell

S exposed surface area of concrete

t age of concrete in days measured from the end of the curing period

t_i age of concrete in days at time of stress transfer

V volume of concrete

ε_0 $\frac{A_p f_{pi}}{A_c E_{ci}}$

ε_{sh} shrinkage strain

Ψ creep coefficient

APPENDIX E

A_n net cross-sectional area of column

clear colum height height of column during period of interest

E_c modulus of elasticity of concrete

ΔF change in applied axial force

F_p prestressing force

$H_{c,free}$ free-standing length of column

$H_{c,fixed}$ clear height of column after being secured in foundation slab

L_{ub} unbonded length of prestressing strands

$\Delta\varepsilon_c$ change in concrete strain measured from vibrating wire gauges

$\Delta\varepsilon_{c,sh+cr}$ change in column strain measured from vibrating wire gauges

$\Delta\varepsilon_{p,sh+cr}$ change in strain in prestressing strands due to creep and shrinkage

$\Delta\varepsilon_{p,sh+cr,1}$ change in strain in prestressing strands due to creep and shrinkage during period 1

$\Delta\varepsilon_{p,sh+cr,2}$ change in strain in prestressing strands due to creep and shrinkage during period 2

$\varepsilon_{p,ug}$ average tensile strain in prestressing strands at beginning of ungrouted test

$\varepsilon_{p,gr}$ average tensile strain in prestressing strands at beginning of grouted test

$\Delta\varepsilon_{ug}$ change in strain in prestressing strands between the beginning of the ungrouted test and the beginning of the grouted test

APPENDIX F

α dimensionless parameter

LIST OF FIGURES

LIST OF TABLES

ACKNOWLEDGEMENTS

The research presented in this dissertation was conducted under the supervision of Professor P. Benson Shing and alongside Professor Dimitrios Kalliontzis, who is now at the University of Houston. The work conducted on the seismic assessment and retrofit of the Coronado Bridge piles was carried out and funded as part of Contract No. 65A0722 for the California Department of Transportation. The work conducted on the Recovery Columns for seismically resistant bridge structures was carried out and funded as part of Contract No. 65A0638 for the California Department of Transportation.

I would like to thank the members of my committee, Professors P. Benson Shing, Janet Becker, Machelle Morrison, and Gilberto Mosqueda for their suggestions and aid in my research, feedback on my writing and modeling, and offering courses, all of which were vital to my work.

I would like to express my profound appreciation to my advisor, Professor P. Benson Shing, for his guidance, patience and tutelage for these years spent at UC San Diego, not just with research, but during the more difficult times of my life as well. I have benefitted greatly from his knowledge in structural engineering, concrete design, and advice on my research. He has provided me with a great opportunity to study under and work with an individual at the top of his field.

I would like to express my gratitude for Professor Dimitrios Kalliontzis who performed a significant amount of design, planning, and pre-test analysis for the projects discussed in this dissertation. His guidance and work served as a great aid to my experimental work and post-test analysis.

I would like to express my sincere gratitude to the technical staff at Powell Structural Laboratories of UC San Diego for their professionalism and taking the time to teach me everything

I needed to know for conducting the experimental work for my research, and for constructing the tests specimens, and setting up and carrying out the tests.

I would like to express my deepest appreciation to Dr. Karan Taneja, Dr. Benjamin Katko, and all other graduate students within the Structural Engineering department of UC San Diego for always allowing me to discuss my research with them and the feedback they offered over the years.

Finally, I would like to thank my parents, Rémy and Nina Deyglun, as well as Jessica Freeman and Arlo, for the love and encouragement they showed me over the years. I dedicate this dissertation to them.

Chapters 2, 3, 4, and 5 are, in part, a reprint of the material in a California Department of Transportation report entitled "Assessment of Seismic Performance of Coronado Bay Bridge Piles with and without Simulated Damage and the Effectiveness of a Retrofit Method." The authors of the report are: P. Benson Shing, Dimitrios Kalliontzis, and the author of the dissertation. Professor Dimitrios Kalliontzis provided the pre-test analysis, and much of the design of the test specimens and was extensively involved in the tests of the first two specimens. The author of the dissertation provided the design of several testing components and the post-test analysis of all test specimens, and was responsible for the design and testing of the third specimen.

Chapters 7, 8, 9, 10, and 11 are, in part, a reprint of the material in a California Department of Transportation report entitled "Experimental Investigation of a Self-Centering RC Column Design and a Displacement-Based Design Method for Highway Bridge Applications." The authors of the report are: the author of the dissertation, Dimitrios Kalliontzis, and P. Benson Shing. Professor Dimitrios Kalliontzis worked on much of the construction of the first test specimen. The author of the dissertation provided input for the design of the second specimen, and was

responsible for overseeing the construction and experimental work, post-test analysis of the two specimens, modeling and worked with Professor P. Benson Shing on the development of the displacement-based design methodology.

VITA

2011-2016 Bachelor of Science in Civil Engineering, Rensselaer Polytechnic Institute

2014-2016 Master of Engineering in Structural Engineering, Rensselaer Polytechnic Institute

2018-2024 Doctor of Philosophy in Structural Engineering, University of California San Diego

ABSTRACT OF THE DISSERTATION

Seismic Performance of Existing and New Bridge Substructures

by

Lucas Claude Deyglun

Doctor of Philosophy in Structural Engineering

University of California San Diego, 2024

Professor P. Benson Shing, Chair

The two studies within this dissertation aim to assess the seismic performance of both existing and new reinforced concrete (RC) bridge substructures, and to develop modeling tools and design procedures for new self-centering column systems for bridges.

The first section of this dissertation outlines a recent study conducted to assess the seismic performance of piles in the Coronado Bay Bridge in San Diego. Three 7/9-scale pile specimens were tested, representing a prototypical Type-II pile in Pier 22. All bridge piles were constructed with precast, prestressed shells filled with cast-in-place concrete, sharing similar reinforcement details and diameter. Specimen 1 represented an as-built pile, Specimen 2 had unbonded strands in the shell over a length of 31.5 in. to simulate construction-induced damage, and Specimen 3, retrofitted with a high-strength bar, aimed to evaluate a seismic retrofit method. The study aimed to determine whether a pile with or without simulated damage could perform satisfactorily in a design earthquake event and to develop an effective seismic retrofit method if needed. Testing involved fully-reversed lateral displacement cycles up to a maximum drift ratio of 2.5%, while the drift ratio corresponding to the design earthquake response was 1.8%. The maximum net axial tension and compression applied to the piles was 575 kips during positive displacement and 910 kips during negative displacement respectively. These forces correspond to 11% and 48% of the uniaxial compressive and tensile capacity, respectively, of Specimen 1. These values were based on seismic analysis of the bridge structure performed by Caltrans. Specimen 2 revealed tension failure due to prestressing strand loss, while Specimen 3 demonstrated the effectiveness of the retrofit method in restoring performance and enhancing ductility. Recommendations for retrofit evaluations and design in the bridge are provided based on experimental data. Additionally, interaction diagrams were created to aid in the evaluation of the capacity of the piles, and understanding of how the materials within the piles behave under combined axial load and bending moment.

The second section of this dissertation focuses on the design, and modeling of a novel self-centering column design for use in seismically resistant bridge structures. Two specimens were

tested. The first represented an initial design created by a team at Caltrans while the second was a modified design aimed at reducing early damage induced by cyclic loading, and allowing for potential rehabilitation without the need for complete column replacement. Both specimens were constructed with cast-in-place, post-tensioned concrete, sharing similar reinforcement and column geometries. The study aimed to achieve a design for self-centering columns which would allow drifts up to 10% during a seismic event with minimal column damage. Testing involved fully-reversed lateral displacement cycles up to 10% drift, with Specimen 1 showing rebar fracture at low drift levels, whereas Specimen 2 showed that the modifications to the design allowed for the longitudinal reinforcement to assist in lateral load resistance and energy dissipation through the ±10% drift cycles. Furthermore, a fiber-section model was developed to simulate the behavior of these self-centering column designs during a seismic event, and a displacement-based design methodology was developed for industry engineers to use in the design and implementation of these self-centering columns for seismically resistant bridge structures.

Chapter 1 Introduction

1.1 Background

In the state of California, one major seismic event initiated the need to reevaluate bridge design and motivated a seismic retrofit program that continues to this day: the 1971 San Fernando earthquake (Yashinsky et. al, 2022). On February 9th, 1971, Caltrans was nearing the completion of the State Highway System (SHS) when the San Fernando earthquake occurred, resulting in five collapsed bridges and interchanges. While Caltrans proceeded to swiftly act in order to make changes to bridges that were in their design and construction phases, this did not help the approximately 8,500 bridges built before California developed and adopted seismic design standards for bridges in approximately 1973 (Yashinsky et. al, 2022). Because of the San Fernando earthquake, Caltrans initiated a seismic retrofit program to improve the strength and performance of bridges in California. As major seismic events occurred in the 1970s, 80s, and 90s, inspection and retrofit programs remained a priority for Caltrans.

Based on observations from past earthquakes and research findings, Caltrans has developed the Seismic Design Criteria (SDC) for the design and construction of new bridge structures, that continues to be updated and improved with new research studies. In spite of this, the current design philosophy of Caltrans still focuses on life-safety and collapse prevention. According to current design standards, bridge structures can sustain severe and irreparable damage in the event of a major earthquake but shall not collapse. This can result in a significant economic loss in a major seismic event. As a result, a number of researchers are looking towards innovative design concepts that can lead to damage resilient structures (Ladjinovic and Folic, 2004; Chouw, 2017; Wang and Zhao, 2018), i.e. RC bridges that not only remain standing after a major seismic event, but can be

immediately functional after a major seismic event. This can lead to significant savings in repair costs and uninterrupted traffic flow that is important for post-earthquake recovery.

Seismic retrofit of older bridges presents a major challenge for engineers as the use of current code specifications is often is not feasible. This dissertation presents two studies. One is on the seismic retrofit of submerged piles in a bridge built in the 1960s. The study was to determine if and how the pile foundation of the Coronado Bay Bridge may be retrofitted to allow it to withstand projected future seismic events. The bridge was designed to code standards of the 1960s, and has been part of the retrofit considerations for Caltrans for the past several decades. This study discusses three specimens that were designed based on the original construction drawings and a site inspection carried out by Caltrans, and tested in Powell Laboratories at UC San Diego, in order to determine if the original design of the pile foundations is adequate. The study also aims to determine a retrofit plan for piles that have been damaged over the past several decades to recover their structural performance and ductility. This study is presented in the first section of this dissertation.

The second section of this dissertation examines a novel design of a self-centering bridge column aimed at providing damage resilience for RC bridges. This section discusses the design and testing of two self-centering column specimens. Furthermore, this study examines the formulation of a fiber section model that can be used to analyze these columns, as well as the formulation of a displacement-based design procedure to make these types of columns available for engineers in industry.

1.2 Outline of Dissertation

This dissertation has two distinct sections. Each section is dedicated to a single project that was undertaken by the author of this dissertation with Professor P. Benson Shing, and Dr. Dimitrios Kalliontzis, who is now a professor at the University of Houston, Texas.

Section 1 discusses the seismic performance assessment and retrofit of the Coronado Bay Bridge piles. This section discusses the background, testing, post-test analysis, modeling, assessment and retrofit recommendations for the Coronado Bay Bridge Pile project.

Section 2 discusses the self-centering columns for seismically resistant bridge structures. This section discusses the background, design, testing, post-test analysis, and modeling of the self-centering column project, as well as a displacement-based design methodology proposed for the design and implementation of these types of columns.

Chapter 2 Introduction

2.1 Background

Section 1 of this dissertation details a research project conducted at the Powell Structural Laboratories at UC San Diego, focusing on the seismic performance assessment of piles in the Coronado Bay Bridge, located in San Diego, California, which was constructed in the 1960s. All bridge piles were constructed with precast, prestressed shells filled with cast-in-place concrete, sharing similar reinforcement details and diameter. The piles were categorized as Type I or Type II, with Type-II piles having higher prestressing force and higher-strength concrete.

During construction, a number of piles suffered damage to the top region of the precast shell due to pile driving forces, potentially compromising the bond between prestressing strands and concrete. An underwater inspection in the mid-1990s revealed cracks in piles near pile caps, allowing seawater penetration and causing corrosion of transverse reinforcement. To investigate the impact of debonding and corrosion on pile structural performance, Silva et al. (1997) conducted tests on three 2/3-scale pile specimens, including pile caps, at UC San Diego. In that study, the pile specimens had two different height-to-diameter ratios, with one specimen having simulated damage via cutting of prestressing strands and transverse reinforcement, as well as cracks introduced in the precast shell. The study indicated that, despite imposed damage, all three specimens met performance criteria, leading to no retrofit measures for the piles.

In 2013, an extensive underwater inspection by the Office of Structure Maintenance and Investigations (OSM&I) of Caltrans revealed more extensive crack problems than in the mid-1990s, averaging 1.5 cracks per pile. Concerns about structural integrity led to evaluations by the Office of Earthquake Engineering Analysis and Research (OEEAR) in 2014 and 2018. The latter

study, using numerical simulations, highlighted potential vulnerabilities to shear failures during a 1000-year return-period earthquake. Specifically, some piles could experience high tensile forces when subjected to severe lateral seismic forces, significantly reducing shear capacity. The tensile forces observed were several times higher than in the 1990s study. Consequently, a decision was made to investigate pile structural integrity, considering the high axial tension, and to develop and evaluate effective retrofit measures if deemed necessary based on the performance assessment.

2.2 Research Objectives and Scope

The primary objective of the research conducted in Section 1 of this dissertation was to address concerns highlighted in a recent OEEAR investigation. The specific aims of the study included assessing the seismic performance of a representative pile identified as vulnerable in the OEEAR investigation, particularly in the context of a major earthquake with a 1000-year return period. Additionally, the research aimed to investigate the impact of strand debonding in the precast shell near the pile cap on the overall performance of the pile. The study also sought to develop and assess retrofit measures if the pile's performance indicated the need. Furthermore, a key goal was to establish a methodology for evaluating the moment capacity of the piles, serving as an analytical tool to determine the necessity of retrofits.

The research involved the experimental examination of three pile specimens, each representing a 7/9-scale model of a Type-II pile in Pier 22 of the Coronado Bay Bridge. The first specimen replicated an as-built pile without any damage, the second simulated a pile with partially unbonded strands to mimic construction-induced damage, and the third represented a pile with similar damage as the second specimen but underwent retrofitting with a high-strength steel bar to restore its capacity. Additionally, the study included the development of interaction diagrams and

material models to accurately assess the moment capacity of the piles under both tensile and compressive axial loads.

2.3 Outline of Section 1 of Dissertation

Chapter 3 presents the experimental program including the specimen design, test setup, instrumentation of the pile specimens, and the loading protocol.

Chapter 4 presents the test observations, experimental results, and the analysis of the test data.

Chapter 5 presents recommendations for the evaluation of the retrofit need of the piles and for the retrofit design based on the method investigated in this study.

Chapter 6 discusses the summary and conclusions of this study.

Chapter 2 is, in part, a reprint of the material in a California Department of Transportation report entitled "Assessment of Seismic Performance of Coronado Bay Bridge Piles with and without Simulated Damage and the Effectiveness of a Retrofit Method." The authors of the report are: P. Benson Shing, Dimitrios Kalliontzis, and the author of the dissertation. Professor Dimitrios Kalliontzis provided the pre-test analysis, and much of the design of the test specimens and was extensively involved in the tests of the first two specimens. The author of the dissertation provided the design of several testing components and the post-test analysis of all test specimens, and was responsible for the design and testing of the third specimen.

Chapter 3 Description of Experimental Program

3.1 Introduction

A total of three pile specimens were tested. They were 7/9-scale models of a prototypical Type-II pile in Pier 22 of the Coronado Bridge. The pile has a precast prestressed concrete shell filled with cast-in-place concrete. Specimen 1 represented an as-designed pile. The pile in Specimen 2 had all the prestressing strands in the precast shell unbonded near the pile cap to simulate a worst-case scenario that the strands have lost all the prestressing force in that region due to the cracking and damage of the concrete incurred during pile driving. The pile in Specimen 3 also had unbonded strands near the pile cap, and had a high-strength DYWIDAG bar placed at the center of the concrete core as a retrofit method. The specimen design, test setup, instrumentation, and loading protocol are described in this chapter.

To mimic the as-built pile, the precast shell of each specimen had a specified minimum 28th-day compressive strength of 7,000 psi, while the concrete core had a specified compressive strength of 3,000 psi. The pile cap had 4,000-psi concrete. All the reinforcing bars in the pile were Grade 40. Since the performance of the cap pile was not the focus of this investigation, it was reinforced with Grade-60 bars. The prestressing strands were Grade 270.

3.2 Design of Test Specimens

The specimens were tested in an upside-down position with the pile cap secured to the strong floor of the laboratory with post-tensioned bars. All three specimens had the same dimensions and reinforcement details, which complied with the length scale of 7/9 and the scale factor of one for the stress. However, the size and spacing of the reinforcing steel and prestressing strands could not be scaled exactly due to the availability of the bar and wire sizes. Instead, they

were scaled as close as possible with the total cross-sectional area or volumetric ratio of the respective steel satisfying the scaling law. Detailed design drawings for the three specimens can be found in Report No. SSRP-21/02 entitled "Assessment of Seismic Performance of Coronado Bay Bridge Piles with and without Simulated Damage and the Effectiveness of a Retrofit."

The dimensions of a test specimen in elevation view are shown in Figure 3.1. The elevation of the mid-height point of the load stub at the top of the pile specimen represents the inflection point between the pile cap and the mudline when the pile is subjected to lateral seismic loading. Two horizontal actuators were attached to the load stub to control the lateral displacement of the pile specimen, which represented the relative displacement of the pile cap with respect to the inflection point. A loading beam was secured on top of the load stub for connecting to two vertical actuators to exert an axial force on the pile specimen. The loading beam consisted of two side-by-side post-tensioned reinforced concrete beams, which were placed on the load stub one at a time by an overhead crane and then connected to each other by ten high-strength steel rods.

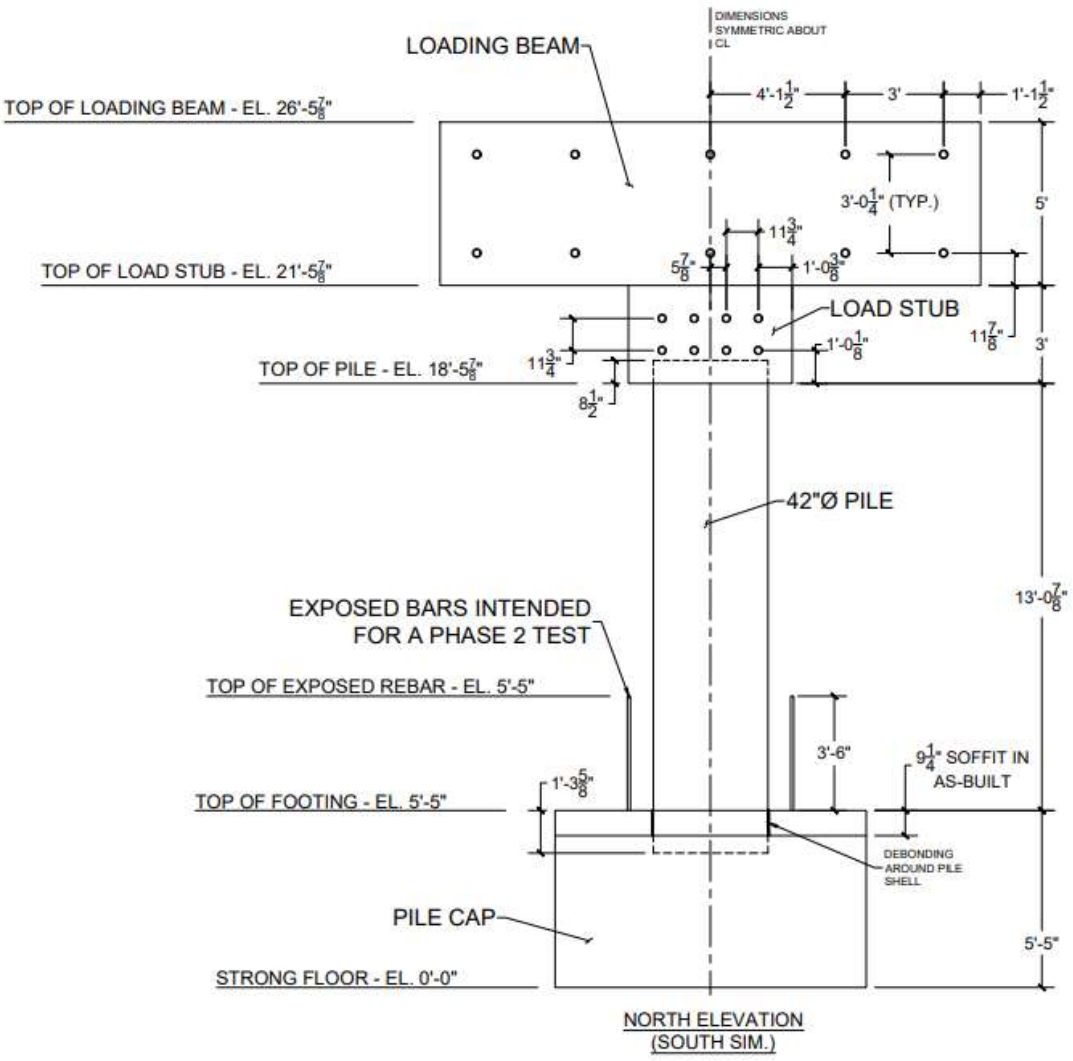

Figure 3.1: North elevation view of a specimen

The reinforcement within the core of the pile specimens is shown in Figures 3.2 and 3.3. As will be discussed later, Specimen 3 had a DYWIDAG bar at the center.

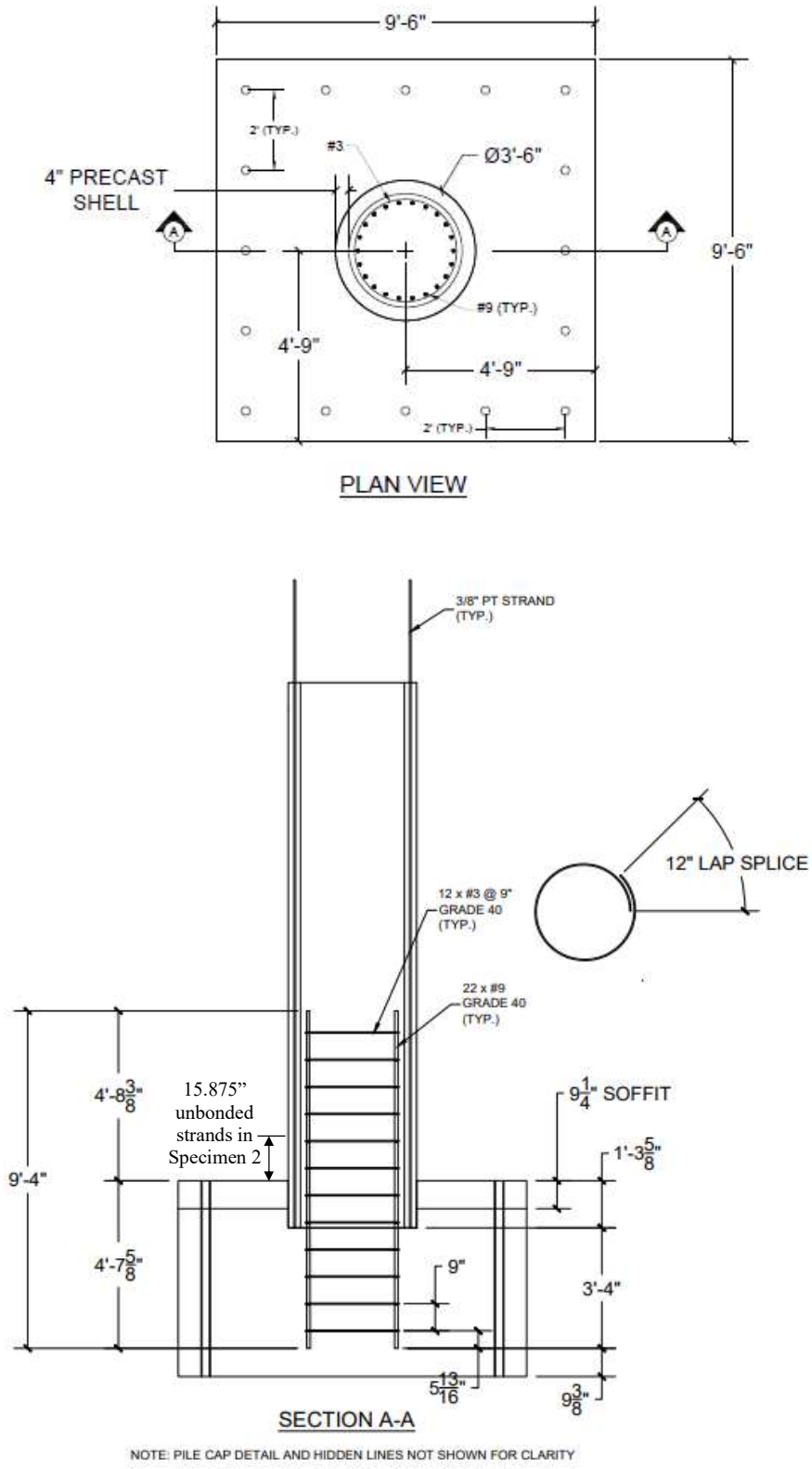

Figure 3.2: Pile core reinforcement for Specimens 1 and 2

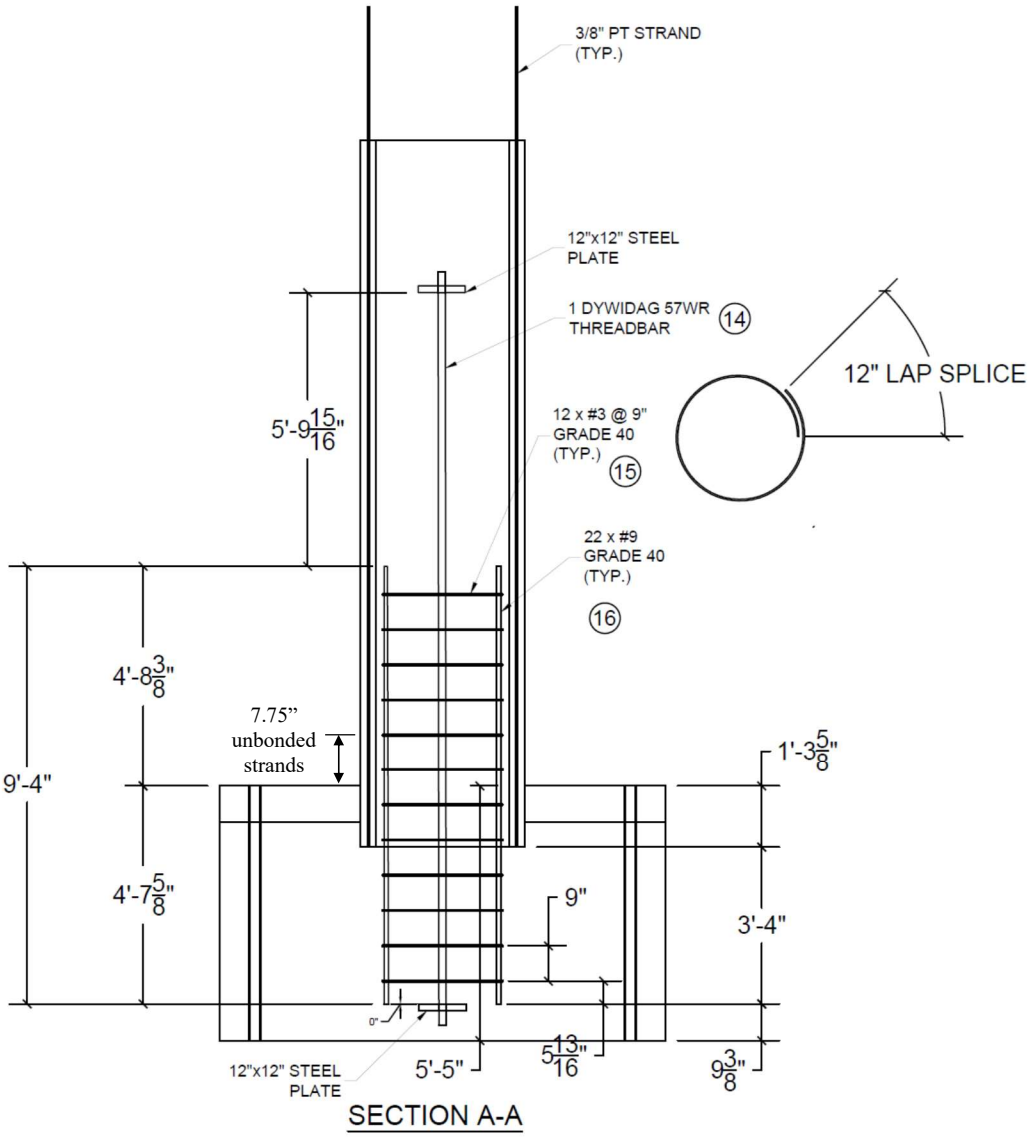

Figure 3.3: Pile core reinforcement for Specimen 3

As shown in Figures 3.2 and 3.3, each pile specimen was connected to the pile cap with 22 Grade-40 #9 bars, which are equivalent to 24 #11 bars, which are in the as-built pile. Since Grade-40 bars with sizes greater than #3 were not commercially available, Grade-60 QST bars that met the ASTM A615/A706-60 standard were acquired and heat treated to obtain the strength properties of Grade-40 bars. The #9 bars were placed in the pile cap with an embedment length of 40 in., which is equivalent to an embedment length of 48 in. for the #11 bars placed in the as-built pile.

These bars were intended to transfer the tensile forces induced by axial loading and bending near the pile cap to the prestressing strands in the pile. To satisfy the similitude of the stress transfer distance, the embedment length of these bars in the concrete core of the pile was scaled according to the diameters of the strands in the pile specimen and as-built pile. This resulted in an embedment length of 72 in. for the pile specimen, which had 3/8-in. seven-wire strands, to match the 96-in. length for the as-built pile, which has ½-in. strands. The pile specimens was connected to the load stub with 18 Grade-60 double-headed #9 bars, which were only for carrying tension and were not part of the as-built pile.

The reinforcement details of the precast concrete shells are shown in Figure 3.4. Each precast shell had an outside diameter of 42 in. and a 4-in. thick wall, and was 15 ft.-1 in. tall. The shell was prestressed with 50 Grade-270, 3/8-in. seven-wire strands. This is equivalent to 46 ½-in. strands, which are used in an as-built pile. The effective prestress after all losses was targeted at 153 ksi, as specified in the construction plan for the as-built piles. As shown in Figure 3.4, the strands protruded from top end of the shell specimen with a length of 3 ft.-5 in. They were later bent and anchored in the load stub. The strands in Specimen 1 were bonded to the concrete along the entire length. The strands in Specimen 2 were unbonded over a distance of 2 ft.-7 1/2 in. (0.75 x pile diameter) from the end of the shell that was connected to the pile cap to simulate the total loss of the prestressing force in the region due to damage in the concrete caused by pile driving. Specimen 3 had the strands unbonded for a distance of 1 ft.-9 in. (0.5 x pile diameter). These distances more or less correspond to the extent of concrete damage observed by the inspection crew of Caltrans. Specimen 2 failed early. Test results from Specimen 2 suggested that the performance of Specimen 3 would be the same if no retrofit measures were introduced. Hence, a retrofit scheme was developed and evaluated with Specimen 3. As shown in Figure 3.3, Specimen

3 had a 2-1/4-in. (57-mm) diameter Grade-150 DYWIDAG Threadbar® at the center of the concrete core. The bar was bonded with the concrete and had a 12 x 12 x 3 – in. steel anchor plate at each end. This was to compensate for the loss of the effectiveness of the prestressing strands near the pile cap, preserve the ability of the concrete core to transmit tension, and, thereby, restore the performance of an intact pile as observed from Specimen 1. This retrofit scheme will be explained in more detail in Chapters 4 and 5, where the test results are presented and discussed.

The transverse reinforcement in the shell near the pile cap consisted of Grade 40 #3 spirals, which were acquired from a steel supplier, while the rest of the shell had Grade-70 W3 wire spirals. The pitch of the spirals was so determined that the volumetric ratios of the spirals matched those in the as-built pile.

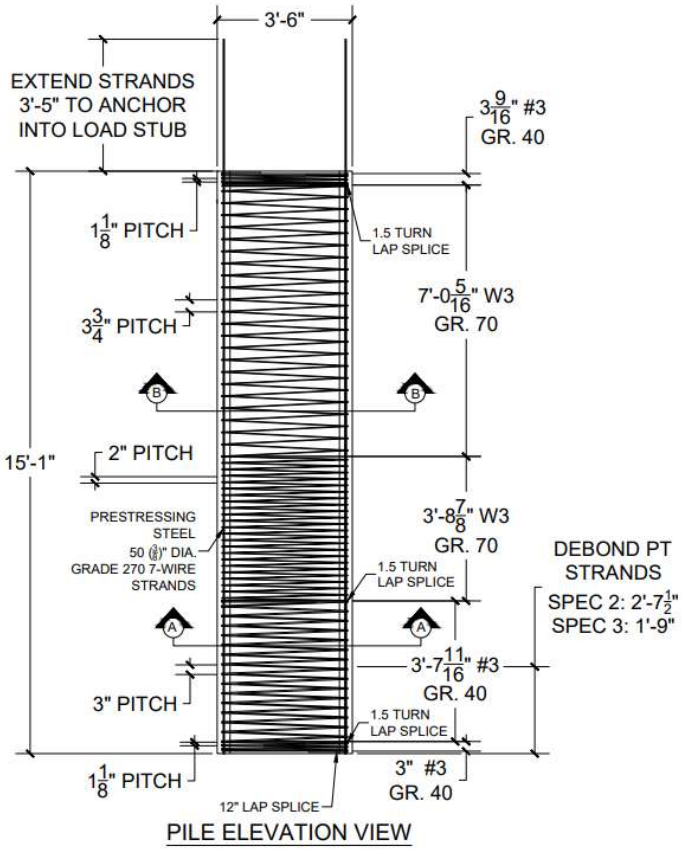

Figure 3.4: Pile shell reinforcement

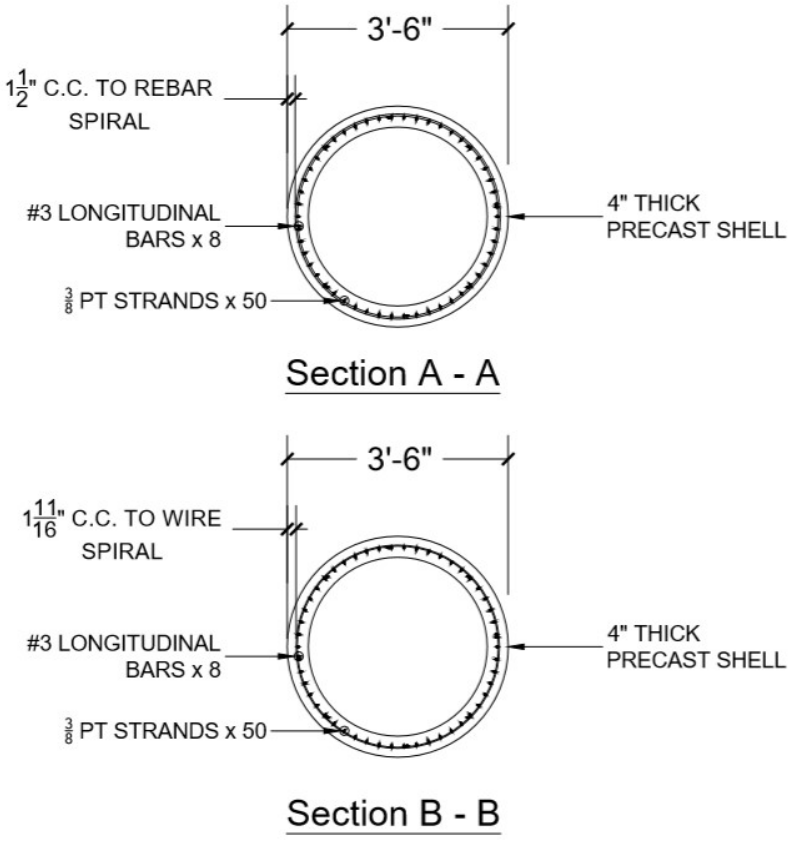

Figure 3.4 (continued): Pile shell reinforcement

3.3 Construction of Test Specimens

The shells of the pile specimens were fabricated in a precast plant, Oldcastle, in Perris, California, while the rest of the specimens was constructed in the Powell Laboratory at UC San Diego. Each specimen was cast in five phases as shown in Figure 3.5.

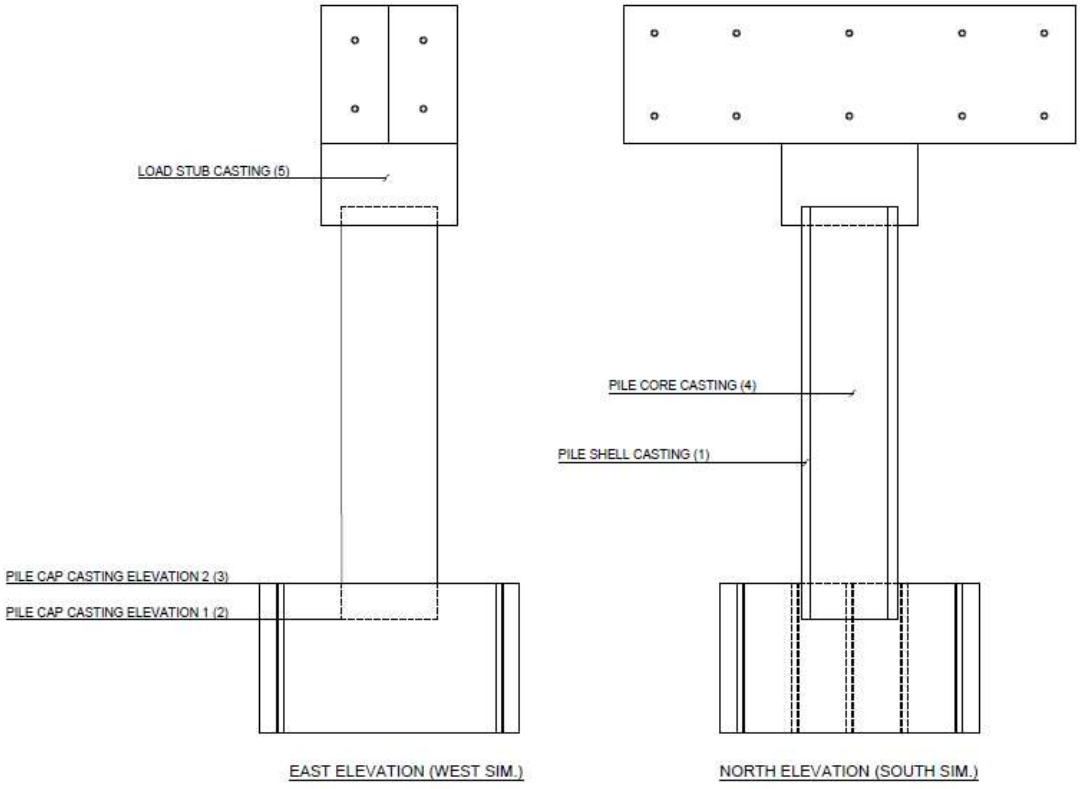

Figure 3.5: Casting phases for each specimen

3.3.1 Fabrication of Precast Shells

The reinforcement steel cages for the precast shells were provided by a supplier in San Diego and the prestressing strands were provided by Oldcastle. The steel cages were first delivered to the Powell Laboratory at UC San Diego, where final adjustments were made to, and strain gauges were installed on, the longitudinal and transverse reinforcement. Prestressing strands that needed to be instrumented were delivered to the laboratory for installing strain gauges. The instrumentation scheme for the specimens are presented in Appendix A. Once all the gauges were placed and checked, the steel cages and strands were delivered to Oldcastle for shell fabrication.

The shells were cast sequentially one at a time in a steel form placed in a long casting bed. The fabrication of each shell took several days. A cylindrical Styrofoam form made to the size of

the inside diameter of the shell was placed inside the steel cage and was removed after the shell was cast. The jacking stress of the prestressing strands was specified to be 189 ksi with the effective prestress targeted at 153 ksi for the time the specimen was expected to be tested. Once the pre-tensioning was completed, concrete was poured into the form through an opening in the cover. The concrete had a specified minimum strength of 7,000 psi. The specimen was heat-cured for one day. Stress transfer took place on the following day when the concrete strength reached 4,500 psi. Strain gauge and vibrating-wire gauge data were collected during the pre-tensioning of the strands, casting, and stress transfer. Data from the pre-tensioning and stress transfer can be found in Appendix B.

The inside diameter of the shells was specified to be 34 in. However, because of the use of Styrofoam forms, the inside surface was not perfectly smooth. After delivery to the laboratory, the inside diameter of the shells was measured at locations shown in Figure 3.6 to determine the roughness of the pile shell's inner surface, which influenced the shear transfer length between the shell and the core. Multiple measurements were taken at each location. Table 3.1 summarizes the values obtained from the shell of Specimen 1. The minimum inside diameter was measured at the middle section with values ranging from 33.50 to 33.75 inches. Similar values were obtained for the other two shells.

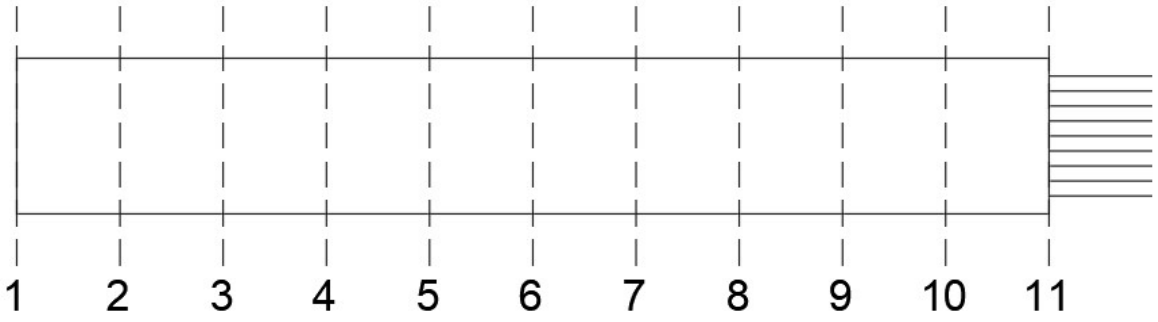

Figure 3.6: Locations at which the inside diameter of each shell was measured (at every 18 in.); length of the shells was measured to be around 180.5 inches

Table 3.1: Measured inside diameter of the shell of Specimen 1

Point	Inside Diameter (inches)
1	33.75
2	33.75 – 34
3	33.75 – 34
4	33.75 – 34
5	33.75 – 34
6	33.50 – 33.75
7	33.75 – 34
8	33.75 – 34
9	33.75 – 34
10	33.75 – 34
11	34

3.3.2 Construction of Cast-in-Place Parts of the Specimens

In the laboratory, the pile cap was constructed first on the strong floor. As shown in Figure 3.5, the pile cap was cast in two phases. In the first phase, concrete was poured to an elevation of 4 ft. – 1 3/8 in. above the strong floor in the laboratory. After the concrete had set, the shell of the pile was placed on the top. The shell sat on a smooth concrete surface, which was created by a plywood ring, which had a surface slightly larger than the cross-section of the shell. The ring was removed before the placement of the shell. The concrete surface outside the ring was not smoothened to create a good bonding with the concrete in the second pour. Once the shell was in place, the rest of the pile cap and the soffit layer was cast. To mimic the as-built condition, a dry joint was created between the pile shell and the soffit. To create this, a 9 ¼ -in. wide strip of cardboard was cut and attached to the surface of the shell at 6 3/8 in. away from the end of the pile before the second cast. After the placement of the shell, the top core bar cage was secured in place, and the shell was filled with 3,000-psi concrete. The load stub was constructed last. The prestressing strands from the shell were bent and tied down to the top rebars in the load stub. The load stub was cast with 8,000 psi concrete so that the desired strength would be developed in less than two weeks for the pile test to be carried out without a long wait.

3.4 Material Properties

Tests were conducted on material samples for all the materials used to construct the specimens. Table 3.2 summarizes the yield and tensile strengths of the reinforcing steel. They are the average values obtained from three samples. The Grade-60 #9 headed bars (placed at the top of the pile specimens) were not tested because they were expected to remain within the elastic regime during the pile tests. Except for the Grade-40 #9 bars, the rebars and the steel wire used in all three specimens were from the same batch. The Grade-40 #9 bars were obtained by heat treating

Grade-60 QST bars (ASTM A615/A706). The bars for Specimens 1 and 2 were heat treated in the same batch, while those for Specimen 3 were treated in a separate batch. After heat-treatment, the bars were sand-blasted to remove the heat treat scale from the surface. In Figure 3.7, the stress-strain curves for the heat-treated bars in the two batches are compare to those for two Grade-40 bars reclaimed from an old bridge which had been demolished.

Table 3.2: Average yield and tensile strengths of reinforcing steel

Steel	Pile Specimen	Grade	Yield Strength f_y (ksi)	Tensile Strength f_u (ksi)
W3 Wire	1, 2, 3	70	94	105
#3	1, 2, 3	40	50	70
#3	1, 2, 3	60	70	102
#9	1, 2 (Batch 1)	40	47	77
#9	3 (Batch 2)	40	49	81

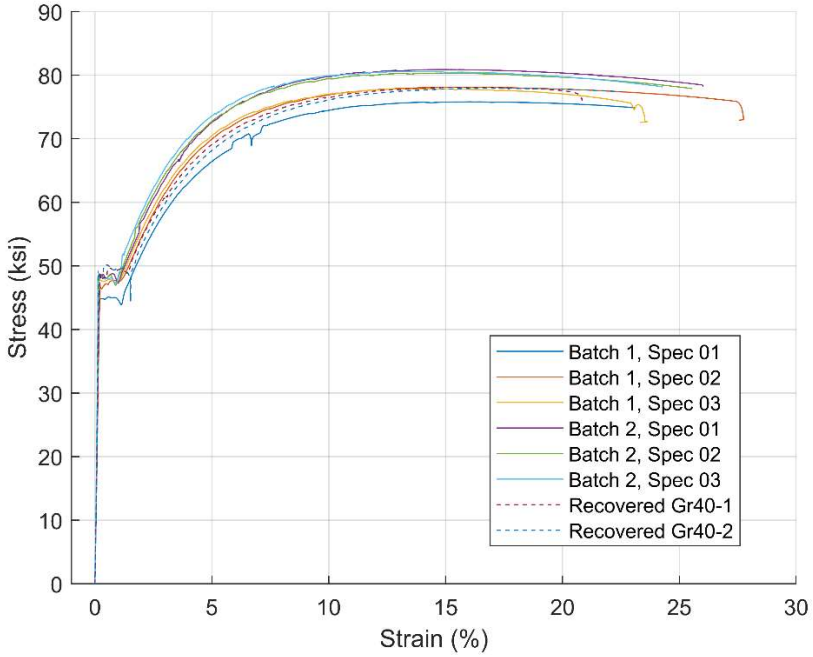

Figure 3.7: Stress-strain curves for heat-treated #9 bars

Figure 3.8 shows the tensile stress-strain curves obtained from samples of Grade-270 seven-wire strands provided by the precast plant. Three strand samples were provided, and two pieces from each sample were tested. The curves show an average modulus of elasticity of 30,800 ksi and an average yield strength (stress at 1% extension) of 271 ksi. One sample (SP3-2) shows an ultimate tensile stress of 283 ksi. The yield and ultimate tensile stresses determined during material testing were later used to calibrate material models for the prestressing strands. Figure 3.9 shows the tensile stress-strain curve for a Grade-150 DYWIDAG Threadbar® similar to the one used in Specimen 3. It is based on the data reported in a study by Anderson et al. (2017).

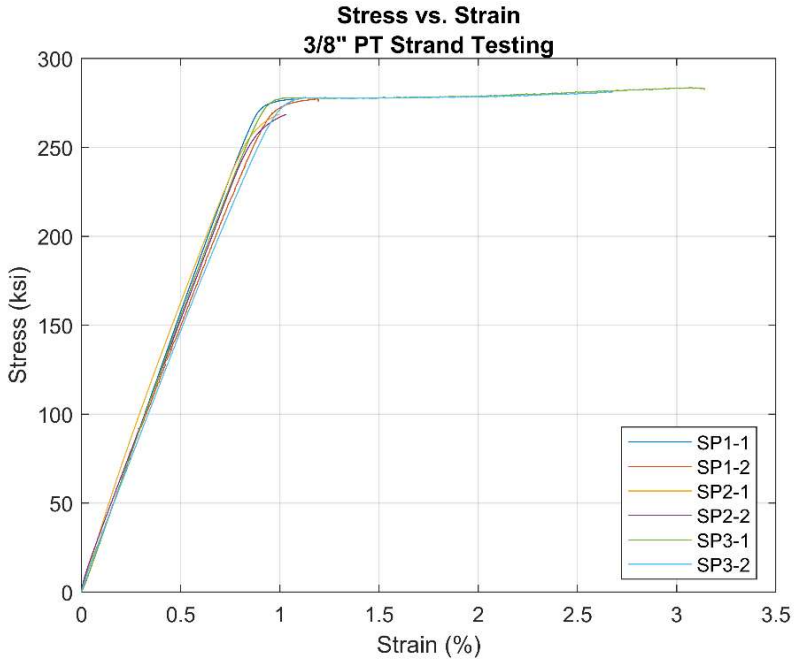

Figure 3.8: Tensile stress-strain curves for the 3/8-in. seven-wire strands

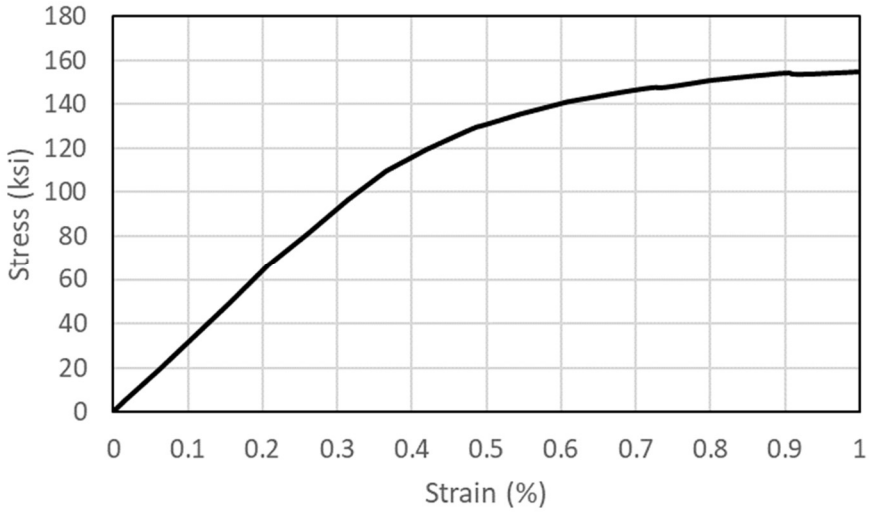

Figure 3.9: Stress-strain curve for Grade-150 DYWIDAG Threadbar® (data from Anderson et al., 2017)

Table 3.3 summarizes the compressive strengths of the concrete poured in different phases with different specified strengths. They are average values obtained from two or three 6 x 12 – in. cylinders

Table 3.3: Average concrete compressive strengths (in ksi)

Concrete	Specified	Specimen 1		Specimen 2		Specimen 3	
		28 Day	Pile Test Day	28 Day	Pile Test Day	28 Day	Pile Test Day
Pile Cap (1st Pour)	4	4.6	4.6	4.3	5.8	4.5	-
Pile Cap (2nd Pour)	4	5.1	5.1	5.1	6.0	5.1	-
Pile Shell	7	-	10.3	-	10.7	-	11.7
Pile Core	3	4.1	4.1	4.6	4.8	4.0	4.0
Load Stub	8	-	8.7	-	7.75	5.2	-

3.5 Test Setup

The pile specimens were tested in an upside-down position with the pile cap tied down to the strong floor of the laboratory with 10 post-tensioned, high-strength, 2 ½-in.-diameter steel rods. Figure 3.10 shows a schematic of the test setup. A picture of the test setup is shown in Figure 3.11. Two 220-kip horizontal actuators were used to exert a lateral force at the top of the pile specimen. The horizonal center line of the actuators represents the location of the inflection point that can develop between the pile cap and the mudline when the pile is subjected to lateral seismic loading, as shown by the schematic in Figure 3.12. The location of the inflection point shown in Figure 3.12 was identified in Caltrans' analysis using p-y springs to model the soil-pile interactions

(OEEAR, 2018). Hence, the lateral displacement imposed by the actuators represents the displacement of the pile cap with respect to the inflection point. The location of the inflection point was identified from a computer model of the bridge structure developed by Caltrans. Two 500-kip actuators were attached to the loading beam to exert an axial tension or compression on the pile.

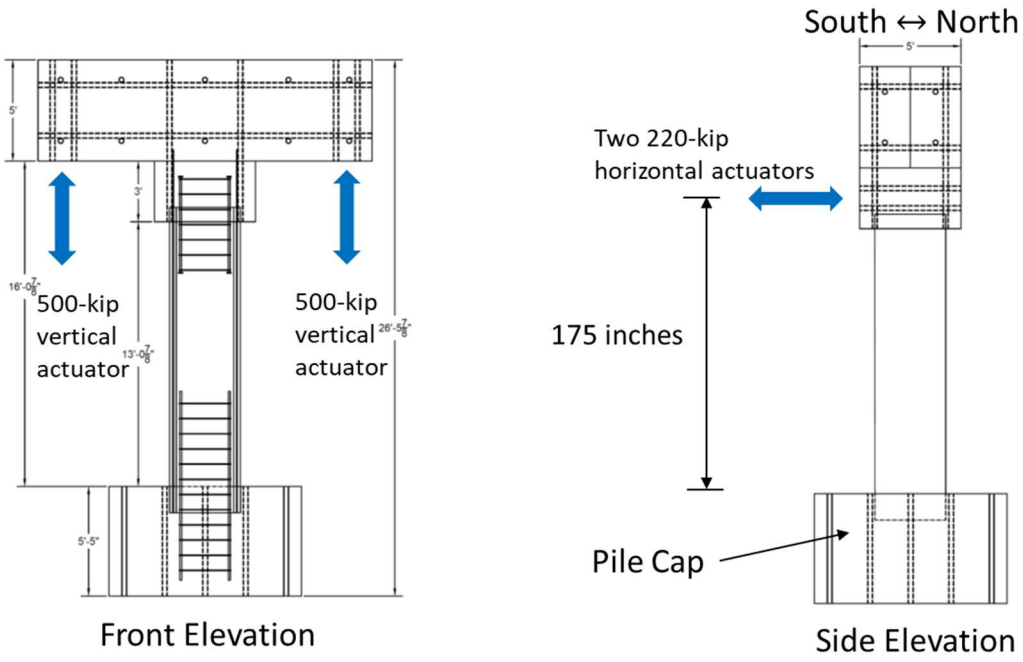

Figure 3.10: Schematic of test setup

Figure 3.11: Picture of test setup

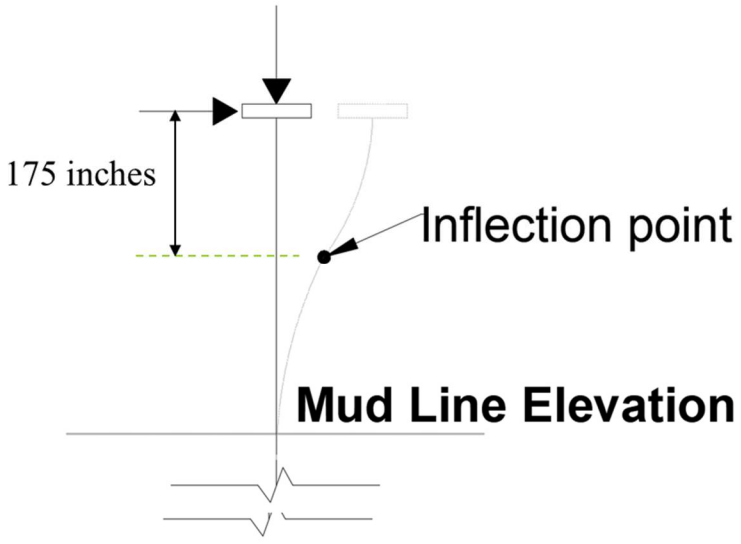

Figure 3.12: Schematic of pile deformation under lateral loading

3.6 Instrumentation

Strain gauges and vibrating-wire gauges were placed in the precast shell of each specimen to monitor strains developed in the steel and concrete during the precast process and the pile test. Strain gauges were also placed on the core bars that connected the pile to the pile cap, the DYWIDAG bar in Specimen 3, and on select bars in the pile cap of Specimen 1. The plan for these gauges varied slightly from one specimen to the other due to the change in the unbonded strand length for each specimen or other factors. External displacement transducers were mounted on each specimen to measure the flexural and shear deformations and the rotation of the pile along its height during the test. Detailed instrumentation drawings for each of the three specimens can be found in Appendix A.

3.6.1 Instrumentation Plan for Specimen 1

A total of 88 strain gauges, 8 vibrating-wire gauges, 59 linear displacement transducers, 4 string potentiometers, and 6 inclinometers were used installed in Specimen 1. In Appendix A, Figures A.1 through A.4 show the locations and identification numbers of the strain gauges and vibrating-wire gauges placed in the precast shell of Specimen 1. These gauges provided strain data within and outside the stress transfer and development length regions near the pile end, which are estimated to be 19 and 63 in., respectively, for the 3/8-in. strands according to the formula in ACI 318.

As shown in Appendix A, Figure A.5, the pile cap had 4 strain gauges placed on two headed bars in the middle reinforcement layer. These gauges were oriented in the north-south direction, which was the loading direction. The gauges were intended to determine the level of engagement of the bars during the test.

Figure A.6 in Appendix A shows the locations of the strain gauges on the core bars. Strain gauges were placed on 8 core bars, 3 on the south side (S-1, S-2, S-3), 3 on the north side (N-1, N-2, N-3), 1 on the west side (W-1), and one on the east side (E-1). Gauges were placed at different levels on each bar.

Figures A.7 and A.8 in Appendix A show the positions of linear displacement potentiometers placed to measure the flexural and shear deformations of the pile along its height. Measurements were taken in 6 segments, and each segment had one pair of potentiometers placed in a diagonal orientation on each of the east and west sides. The potentiometers were secured with rectangular aluminum tubes clamped to the surface of the pile with rods, springs and pointed screws, as shown in Figure 3.13. A picture of a mounting bracket is shown in Figure 3.14. The linear potentiometers in the top and bottom segments had the load stub and pile-cap surfaces as the reference positions, respectively.

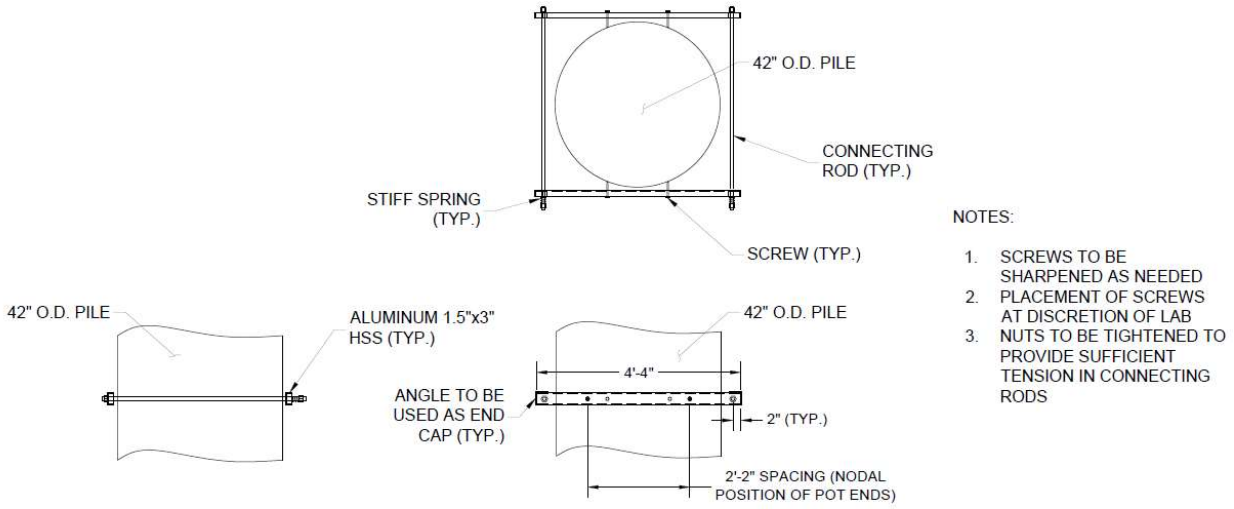

Figure 3.13: Aluminum mounting brackets for the linear displacement potentiometers to measure flexural and shear deformations

Figure 3.14: Picture of aluminum mounting brackets for the linear displacement potentiometers to measure flexural and shear deformations

Three linear displacement transducers were placed at the pile-pile cap interface on each of the north and south faces to measure rocking of the pile with respect to the pile cap. Figure A.10 in Appendix A shows linear potentiometers installed to measure the lateral displacements of the pile in the direction of loading at five elevations. Two string potentiometers were used to measure the lateral displacement of the pile at the centerline level of the horizontal actuators. All these potentiometers had a steel column secured to the strong floor of the laboratory as the reference frame. The out-of-place displacement (normal to the direction of loading) of the pile, if any, was also monitored with two string potentiometers. Six inclinometers mounted on the west face of the specimen to measure the rotations of the pile at different elevations. Five were located at the center of each segment that was instrumented with diagonal linear potentiometers, and one was on the load stub. Rotations measured by the inclinometers can be compared to the rotations calculated from the measurements obtained by the linear potentiometers.

3.6.2 Instrumentation Plan for Specimen 2

The external instrumentation for Specimen 2 was practically identical to that for Specimen 1, except for the linear transducers placed at the pile-pile cap interface. The latter transducers were replaced with longer stroke ones in Specimens 2 and 3 as some of them went out of their range in the Specimen 1 test. Many of the strain gauge locations in Specimen 2 were changed with respect to Specimen 1 because the strands in Specimen 2 were unbonded near the pile cap. These changes are primarily seen in the strain gauges and vibrating-wire gauges placed in the precast shell. Furthermore, strain gauges were added to the core bars in the pile-cap region in Specimen 2. Strain gauges on horizontal rebars in the pile cap were eliminated. The complete set of instrumentation drawings for Specimen 2 can be found in Appendix A.

3.6.3 Instrumentation Plan for Specimen 3

The external instrumentation for Specimen 3 was identical to that for Specimens 1 and 2. The complete set of instrumentation drawings for Specimen 3 can be found in Appendix A.

3.7 Loading Protocol and Pre-test Analysis

A model for the bridge structure was developed and analyzed by Caltrans, including the piles and soil-structure interaction effect. The loading protocol applied in the tests was based on the results of the time-history analyses performed by Caltrans and the nonlinear static analysis performed on a single bridge pier by the project team at UC San Diego. Based on Caltrans' analysis, the maximum drift ratio that could be experienced by a pile during a design-level earthquake was $\pm$1.8%, which was the drift level of interest in the tests.

The gravity load carried by each as-built pile was calculated to be 413 kips. This corresponds to 250 kips for the 7/9-scale pile specimens. The overturning moment induced by the

lateral seismic forces on a bridge pier could subject the piles to increased axial compression when the pile cap moves towards one direction and tension when the pile cap moves in the opposite direction. The piles at the corners of a pile cap will experience the most severe axial load variation. In Caltrans' analysis, a corner pile in Pier 22, which was considered here, could experience a maximum net tension of 950 kips and a net compression of 1,500 kips during a design level earthquake. For the 7/9-scale pile specimens, these correspond to 575 kips and 910 kips, respectively. These forces correspond to 11% and 48% of the uniaxial compressive and tensile capacity, respectively, of Specimen 1.

All three pile specimens were subjected to the same loading protocol. Each specimen was subjected to a sequence of lateral displacement cycles with gradually increasing amplitudes up to a maximum drift ratio of $\pm$2.5%. The drift ratio is defined as the displacement at the actuator level divided by the elevation of the actuators with respect to the surface of the soffit of the pile cap. The lateral displacement was imposed by two 220-kip servo-controlled hydraulic actuators, which were under displacement control.

The relation between the axial load and lateral displacement applied to each pile specimen was determined with a nonlinear static analysis of the pier including the entire pile group. The analysis accounted for horizontal seismic forces applied in two orthogonal directions. The maximum net tension to be applied was 575 kips, while the target net compression was 910 kips. The total weight of the load stub, the loading beam, and the horizontal actuator carried by the pile specimen was estimated to be 73 kips. This was taken into account in determining the axial force to be exerted by the vertical actuators. Two 500-kip servo-controlled hydraulic actuators were used to exert the axial force. The relation between the axial load and lateral displacement applied to each specimen is shown in Figure 3.16. The actuators first applied an axial compression of 177

kips at zero lateral displacement to result in a net compression of 250 kips. The pile was subjected to tension when it was displaced towards north (which is defined as the positive direction), and was subjected to compression when it was displaced toward south. The maximum tension and compression exerted by the actuators were 648 kips and 837 kips, respectively, to achieve the targeted maximums. The loading protocol is shown in Table 3.4.

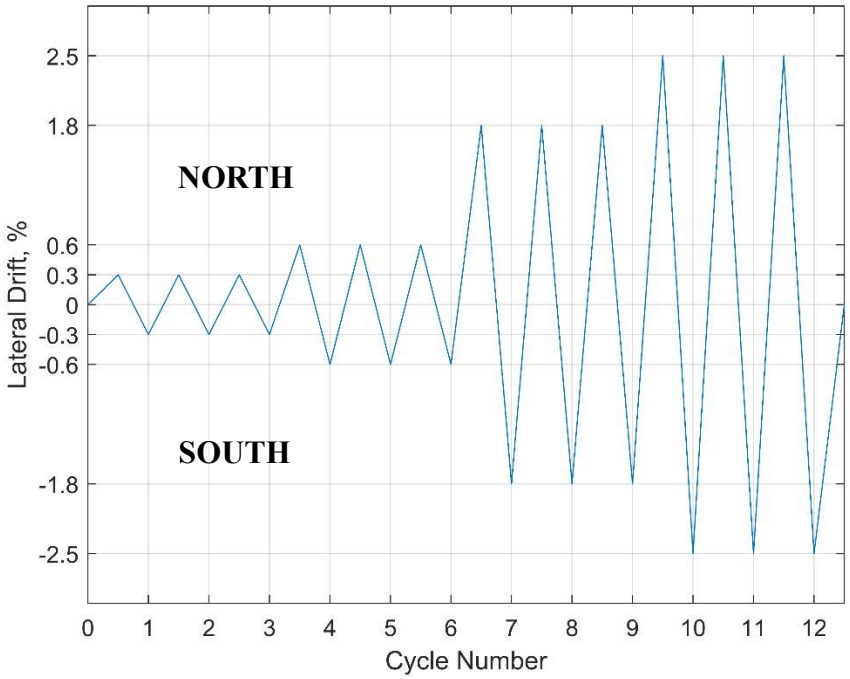

Figure 3.15: Horizontal drift history for each test

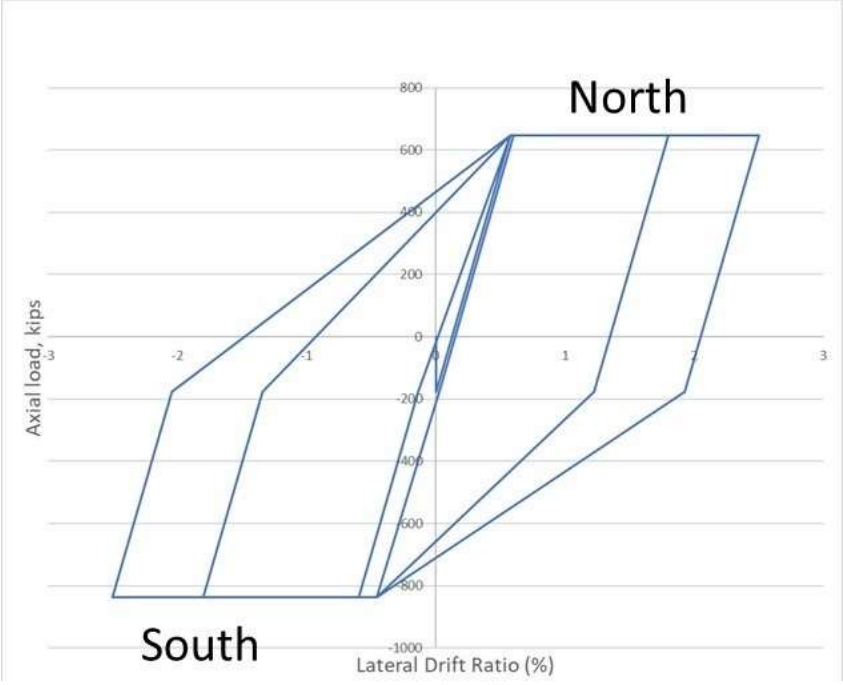

Figure 3.16: Axial force - vs. – lateral drift relation

Table 3.4: Loading Protocol

Drift Ratio (%)	**Axial Load Applied by Actuators (kips)**	**Net Axial Load Including Dead Load Above Pile (kips)**
0	-177	-250
0.3	253.5	180.5
-0.3	-607.5	-680.5
0.6	648	575
-0.6	-837	-910
1.8	648	575
-1.8	-837	-910
2.5	648	575
-2.5	-837	-910

Chapter 3 is, in part, a reprint of the material in a California Department of Transportation report entitled "Assessment of Seismic Performance of Coronado Bay Bridge Piles with and without Simulated Damage and the Effectiveness of a Retrofit Method." The authors of the report are: P. Benson Shing, Dimitrios Kalliontzis, and the author of the dissertation. Professor Dimitrios Kalliontzis provided the pre-test analysis, and much of the design of the test specimens and was extensively involved in the tests of the first two specimens. The author of the dissertation provided the design of several testing components and the post-test analysis of all test specimens, and was responsible for the design and testing of the third specimen.

Chapter 4 Experimental Results

4.1 Introduction

Test results from the three pile specimens are presented in this chapter. The specimens represented 7/9-scale models of a prototypical Type-II pile in the Coronado Bay Bridge. Specimen 1 represented an undamaged as-built pile, Specimen 2 had the same design as Specimen 1 except that it had the strands unbonded over a length adjacent to the pile cap. Specimen 3 was similar to Specimen 2 but had a shorter unbonded strand length, and it was retrofitted with a high-strength bar placed in the center. The instrumentation schemes and loading protocol for the tests are presented in Appendix A and Section 3.7 respectively. Each specimen was subjected to three cycles of lateral displacements at each of the targeted drift levels of ±0.3, 0.6, 1.8, and 2.5%, respectively, while the total axial load applied by the vertical actuators varied between tension and compression according to the drift level and direction. The maximum axial compression applied by the actuators was 837 kips and the maximum applied tension was 648 kips, which resulted in a net compression and tension of 910 kips and 575 kips, respectively, after including all the dead weight supported by the pile. For the data presented here, positive displacement is in the north direction, in which the pile was subjected to tension, and the negative displacement is in the south direction, in which the pile was subjected to compression. Unless otherwise stated, the lateral displacement of a pile specimen refers to the average of the displacements measured by the two external string potentiometers positioned at the level of the centerline of the horizontal actuators, while the lateral drift ratio is calculated as that displacement divided by 175 inches, which was the distance of the horizontal actuators to the soffit of the pile cap.

4.2 Pile Specimen 1

Specimen 1 represented a 7/9-scale model of an undamaged as-built Type-II pile. The load-displacement hysteresis curves and general test observations are presented in the following section. Data from the external transducers and strain gauges are analyzed and discussed in subsequent sections.

4.2.1 Experimental Observations

Figure 4.1 shows the hysteresis curves of the lateral load vs. the lateral displacement measured at the top of the pile specimen, and Figure 4.2 shows the plots of the applied axial load and the resulting vertical displacement at the top of the pile against the lateral displacement. As Figure 4.1 shows, the lateral resistance of the pile remained stable up to the drift level of 1.8%. When the pile was loaded to negative 1.8% drift for the 2nd time (with the pile in compression), the hysteresis curve shows some pinching and a 5% drop in the peak lateral resistance. However, the hysteresis loop remained more or less the same in the 3rd cycle at that level. When loaded to positive 1.8% drift for the 2nd time (with the pile in tension), the drop in the lateral resistance was about 20% of the maximum reached in the 1st cycle at that level. As Figure 4.2 shows, there was a marked increase of the upward vertical displacement in each loading cycle, indicating a progressive decrease of the axial stiffness in tension. This could be attributed to horizontal cracking in the precast shell and concrete core, the slip of the reinforcing bars connecting the core to the pile cap, the slip of the prestressing strands, and the slip of the precast shell with respect to the concrete core after horizontal cracks had developed in the core and the shell.

The pile exhibited significant load degradation once the lateral displacement had passed the drift ratio of 1.8%, and a sudden load drop was observed for the negative loading direction due to severe concrete crushing at the elevation where the core bars were terminated in the pile. The

concrete crushing and load degradation became significantly more severe in the 2nd cycle at 2.5% drift. Because of this, the test was terminated once the pile was unloaded in the 2nd cycle. As it will be further discussed in this section, the formation of a plastic hinge near the core bar termination region was probably caused by the plying action of the core against the precast shell after a horizontal cracked had developed in the core at the core bar termination point and the precast shell started to slip. The plying action weakened the compressive resistance of the precast shell and, thereby, the moment capacity of the pile section near the core bar termination point.

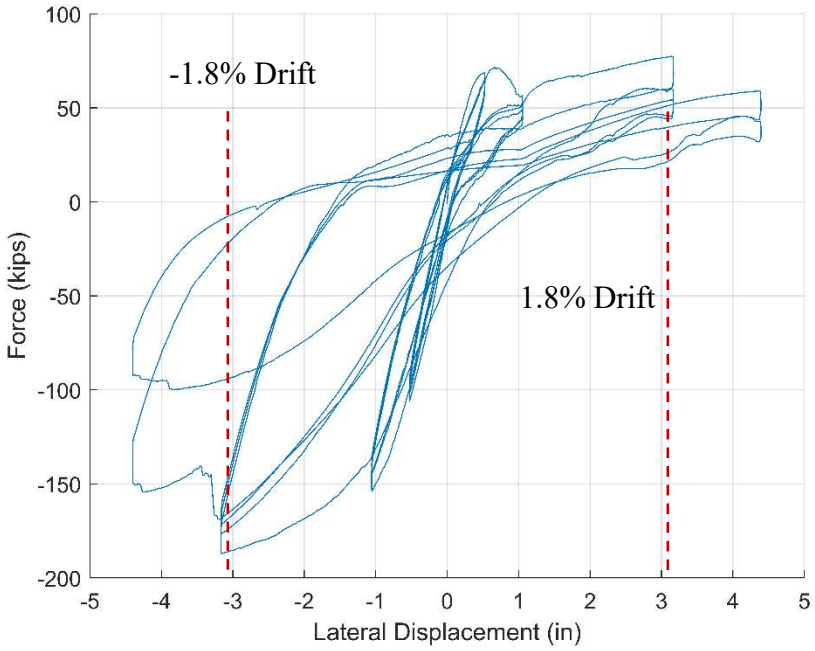

Figure 4.1: Lateral load-vs.-lateral displacement hysteresis curves for Specimen 1

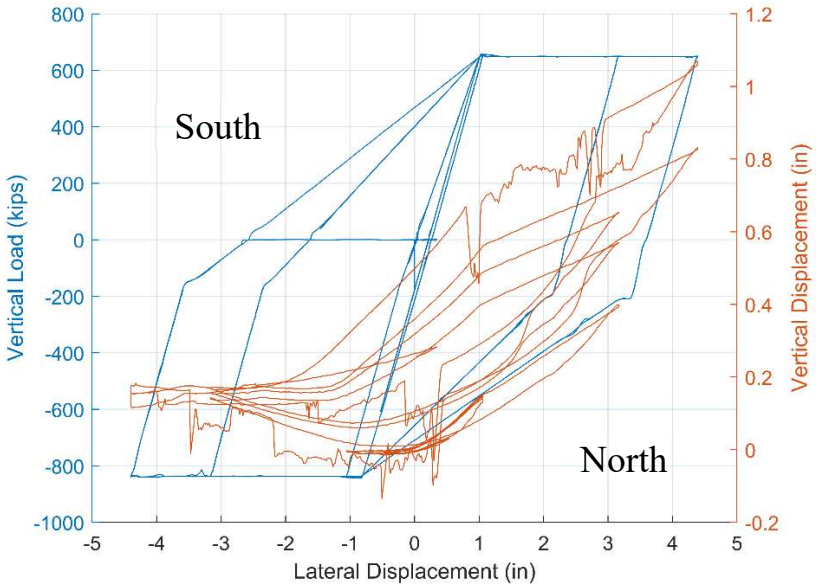

Figure 4.2: Plots of applied vertical load and vertical displacement against lateral displacement for Specimen 1

Pictures of Specimen 1 at different stages of testing are shown in Figures 4.3 through 4.8. Cracking was first observed in the 1st cycle at 0.6% drift level. As shown in Figure 4.3, there were a lot more cracks on the south side than on the north side, which is consistent with the fact that the pile was subjected to tension when being displaced towards north and the maximum tensile force of 650 kips was reached at that drift level.

South

North

Figure 4.3: Pictures of Specimen 1 after 3rd cycle at drift ratio of 0.6%

In the cycles at the drift level of 1.8%, new cracks occurred and the existing cracks propagated further, as shown in Figure 4.4. Concrete crushing was first observed on the south side in the 1st cycle at 2.5% drift level, as shown in Figure 4.5. This was accompanied by a sudden drop of the lateral load resistance in the negative direction as shown in Figure 4.1. As shown in Figure 4.5, the crushing occurred in the region between the two bottom horizontal aluminum bars, which were used for mounting displacement transducers. The upper bar is at the elevation of the core bar termination point. In the second cycle at 2.5% drift, severe concrete spalling occurred on the south

side and spread to the east and west sides as shown in Figure 4.6. This was accompanied by a significant drop of the lateral resistance by about 45% in the negative direction compared to the peak reached at 1.8% drift. Pictures taken after the test are shown in Figure 4.7.

South-East North

Figure 4.4: Pictures of Specimen 1 after 3rd cycle at drift ratio of 1.8%

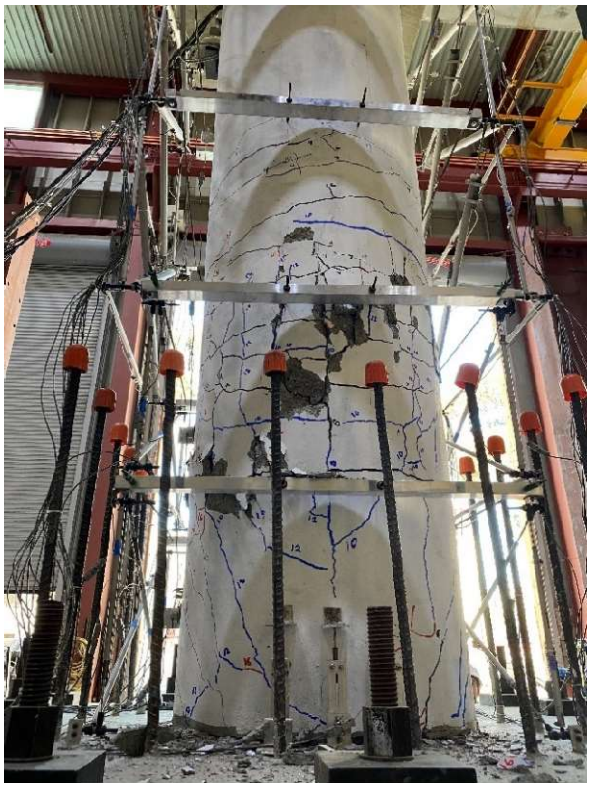

South

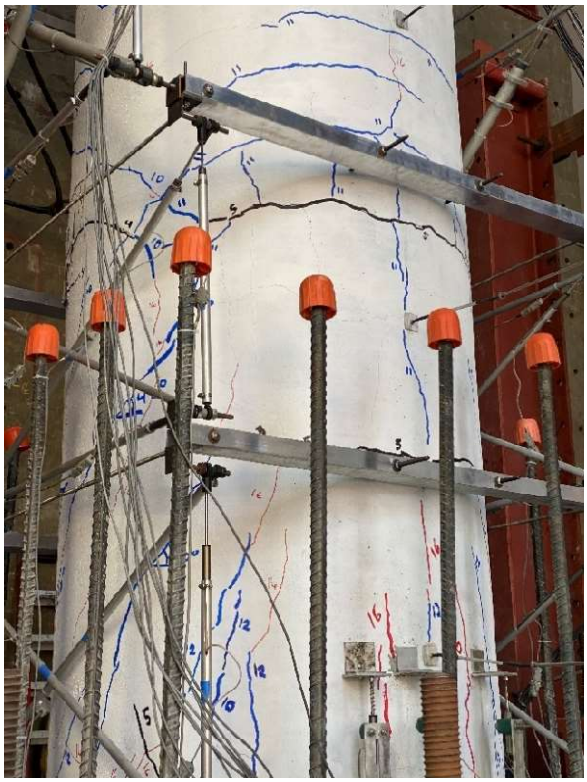

North-East

Figure 4.5: Pictures of Specimen 1 after 1st cycle at drift ratio of 2.5%

South

North-West

Figure 4.6: Pictures of Specimen 1 after 2nd cycle at drift ratio of 2.5%

North-East

North-West

South-West

South-East

Figure 4.7: Pictures of Specimen 1 after test

Figure 4.8 shows close-up views of damage in the pile specimen. The left picture shows diagonal cracks propagating from the bottom towards north. It was noted that these cracks developed when the pile was being displaced towards north, inconsistent with the direction of the diagonal tension that could be induced by the shear force acting towards north. This is an indication that slip occurred between the precast shell and the core in that region, after a horizontal crack had developed in the core right above the core bar termination point. The slip led to a plying action against the shell as illustrated in Figure 4.9. The direction of the diagonal cracks is consistent with the shear induced by the plying force as shown in the same figure.

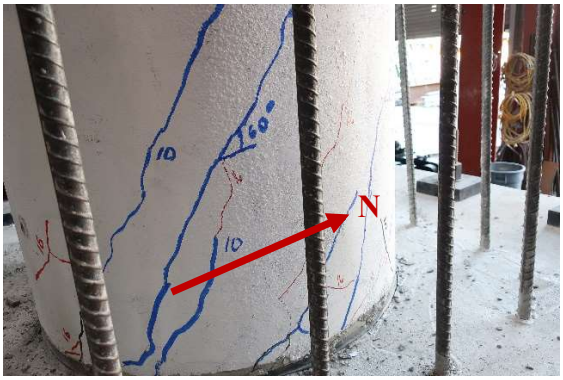

Diagonal cracks developed at 1.8% drift towards north

Fracture of wire spiral at 2.5% drift

Figure 4.8: Pictures of close-up views of damage in Specimen 1

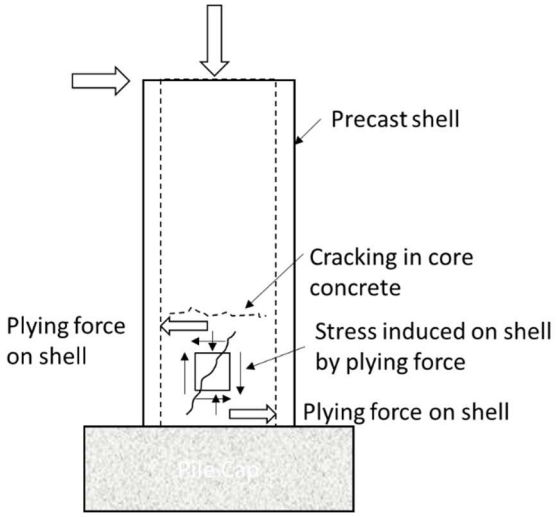

Figure 4.9: Schematic of interaction between precast shell and core

The right picture in Figure 4.8 shows that the wire spiral in the precast shell fractured in the region where severe concrete spalling occurred. Figure 4.10 shows sections of the pile cut during the demolition of the specimen after testing. As shown in the left picture, the separation of the precast shell from the core is quite obvious on the south side of the pile in the region close to the core bar termination point. This is another evidence of the plying action mentioned above, which resulted in extensive cracking of the shell concrete as shown in Figure 4.5. The section right above the soffit of the pile cap also had slight separation between the shell and the core (as shown in the right picture).

Section right above core bars

Section right above pile cap soffit

Figure 4.10: Pictures of Specimen 1 pile sections cut during demolition

4.2.2 Data from External Transducers

The instrumentation plan for the specimen is presented in Appendix A. Figure 4.11 shows the lateral displacement profiles of the pile at the peaks of each displacement cycle. The elevations at which the displacements were measured are with respect to the soffit of the pile cap. It can be observed that the deflected shapes were quite linear up to the drift level of 0.6%. At 1.8% drift ratio, a mild kink can be observed at the elevation of 42 in., and it became more severe in the 2nd cycle at negative 2.5% drift, which is consistent with the severe concrete crushing (the formation of a plastic hinge) observed in the region between 30 and 60 in. from the soffit.

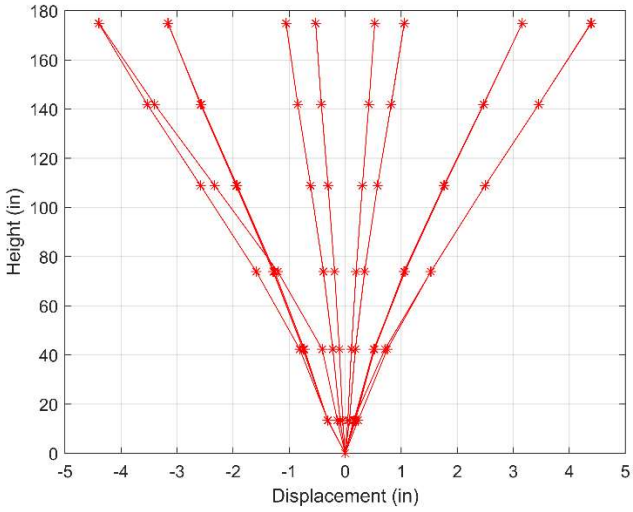

Figure 4.11: Lateral displacements along the height of Specimen 1

The flexural and shear deformations of the pile specimen were measured in five continuous segments at different elevations along the pile, as shown in Figures A.7 and A.8. For each segment, there were six linear potentiometers mounted in the vertical, horizontal, and diagonal directions on each of the east face and west face of the pile. For the purpose of later discussion, the segments are numbered as shown in Figure 4.12. From the measurements obtained with the vertical

potentiometers, the relative rotation between the top and bottom sections of each segment was calculated as follows.

$$\Delta\theta = \tan^{-1}\left(\frac{\delta_S - \delta_N}{l}\right) \approx \frac{\delta_S - \delta_N}{l} \tag{4.1}$$

in which δ_N and δ_S are the average displacements measured by the pair of potentiometers on the north side and the pair on the south side, respectively, and l is the undeformed horizontal distance between the two pairs of potentiometers, which is 45.4 inches. The total rotation at the top section of each segment was obtained by adding the relative rotation to the total rotation at the section below. Pile rotation was also measured by the inclinometer mounted at the center of each segment. To compare with the total section rotations obtained from the linear potentiometer data, linear interpolation was performed on the inclinometer data to estimate the rotation at each section between two adjacent segments. Figure 4.13 compares the total rotations obtained with the inclinometers with those with the linear potentiometers at the last cycle of each drift level. Positive rotation indicates the pile leaning towards north. It can be observed that the rotation values obtained from the two sets of instruments are very close until the drift ratio of 2.5%, at which the spalling of concrete affected the instruments in the first two segments next to the pile cap.

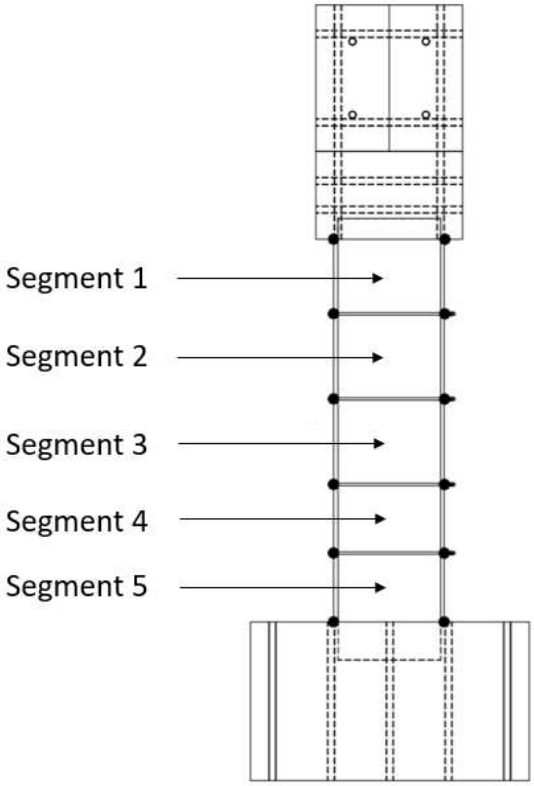

Figure 4.12: Numbering of segments where deformations were measured with linear potentiometers (potentiometer and inclinometer locations are shown in Figures A.7, A.8, and A.14)

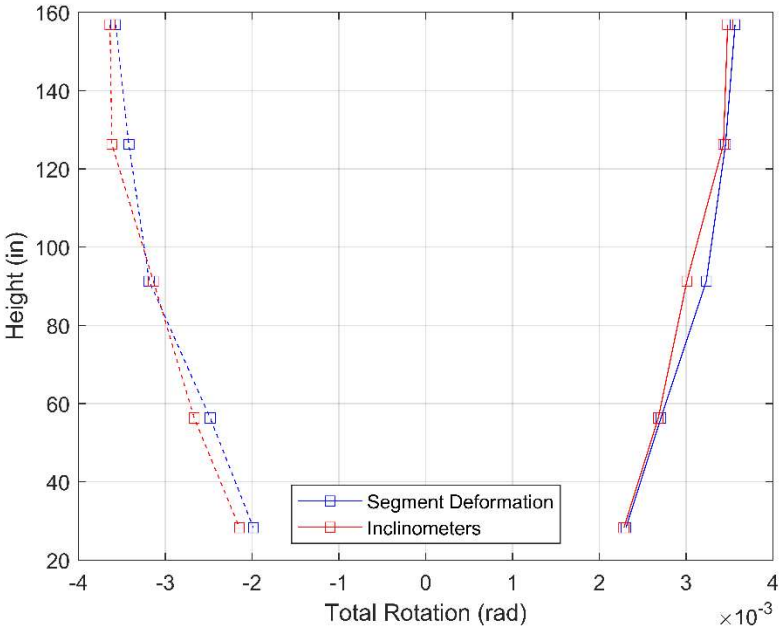

(a) 0.3% drift

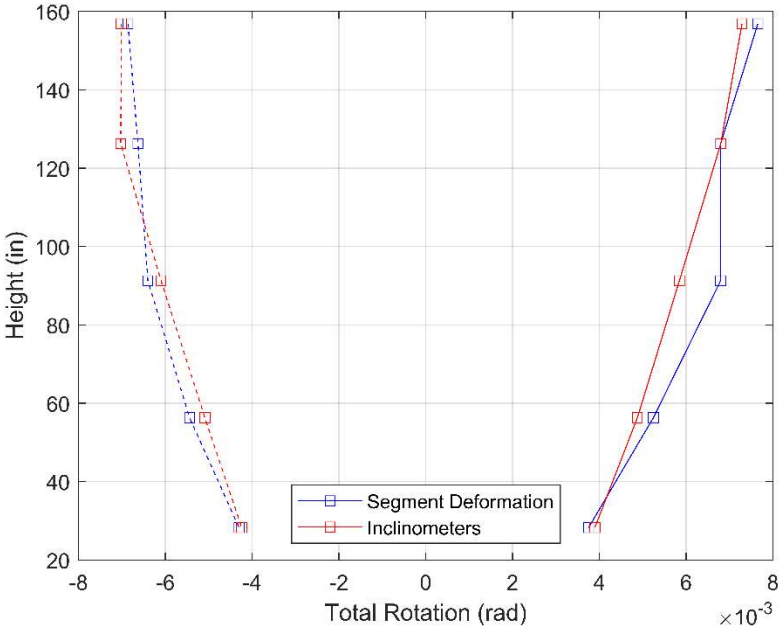

(b) 0.6% drift

Figure 4.13: Pile rotations at different elevations along Specimen 1 measured by inclinometers and linear potentiometers

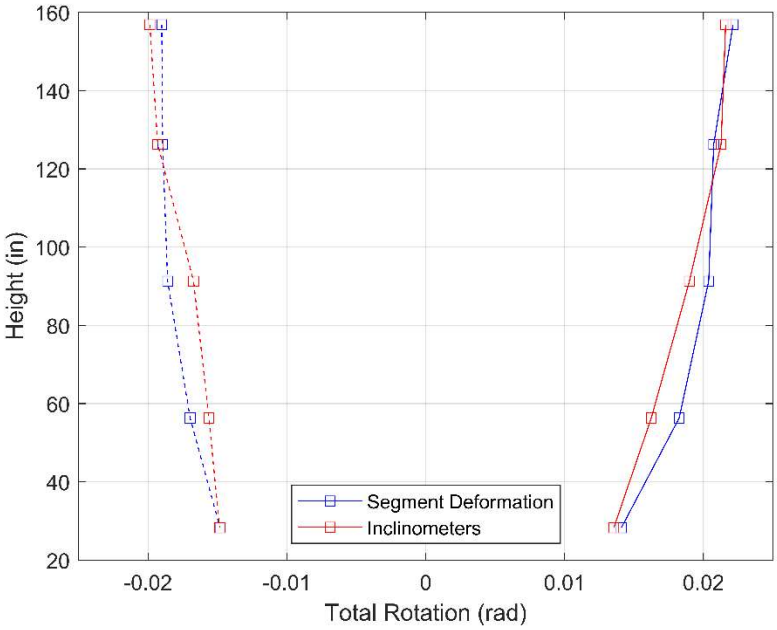

(c) 1.8% drift

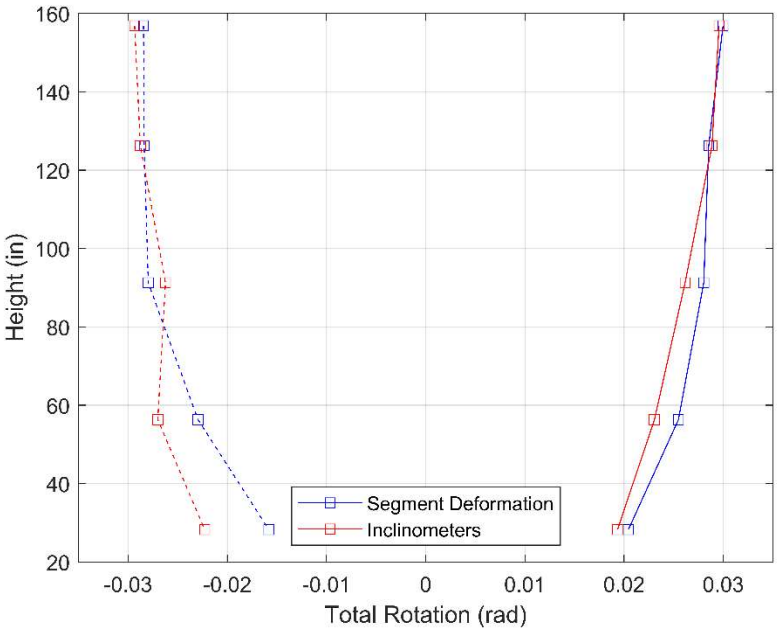

(d) 2.5% drift

Figure 4.13 (continued): Pile rotations at different elevations along Specimen 1 measured by inclinometers and linear potentiometers

The curvature of each segment was calculated by dividing the relative rotation, $\Delta\theta$, between the top and bottom sections of the segment (calculated with Equation (4.1)) by the segment height. The moment at each segment was calculated as the product of the lateral load applied by the horizontal actuators and the distance from the centerline of the actuators to the center of the segment. The moment is plotted against the curvature for each segment in Figure 4.14. These plots are used to identify the plastic hinge locations. Similar to the sign convention for the pile rotation, positive curvature corresponds to the pile bending towards north. It can be observed that the curvatures developed in Segments 1 and 2 are very small compared to those in other segments. The negative curvatures of Segments 3 and 4 remained small until the last displacement cycle, in which severe concrete spalling occurred when the pile was displaced towards south. The magnitudes of the calculated curvatures in Segments 3 and 4, relative to the other segments, are consistent with the observed location of the plastic hinge formation in the pile specimen. Segment 5 developed the largest curvatures in both the positive and negative directions, starting at the drift level of 1.8%. However, this does not reflect the true curvature of the segment because a large portion of the curvature shown was actually contributed by the rotation between the pile end and the pile cap due to the penetration of plastic strains in the core bars connecting the two into the pile and pile cap. Figure 4.14(e) also shows a moment-curvature plot with the pile end rotation taken out from the curvature calculation. The pile end rotation was calculated with the data from the linear transducers mounted right above the pile cap as shown in Figures A.9 and A.10. With the rotation taken out, it can be observed that the actual curvature developed along Segment 5 was very small.

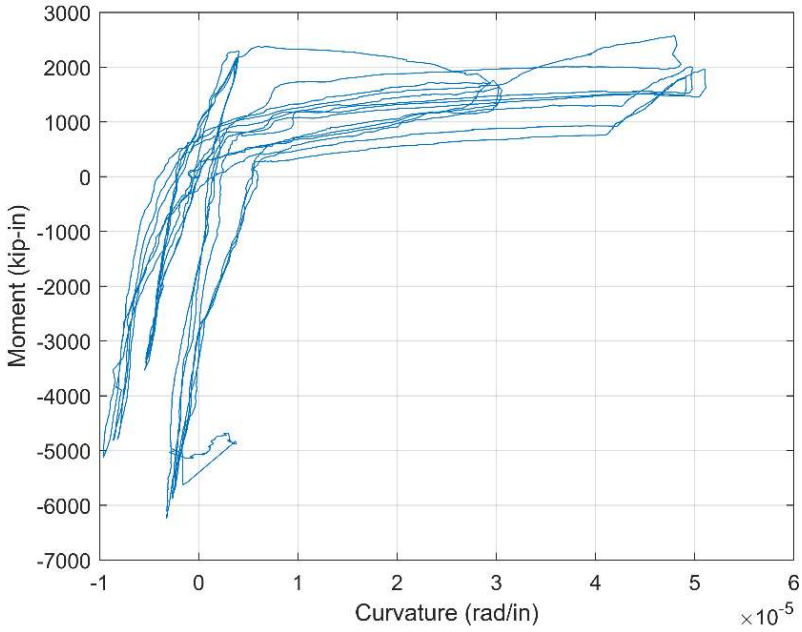

(a) Segment 1

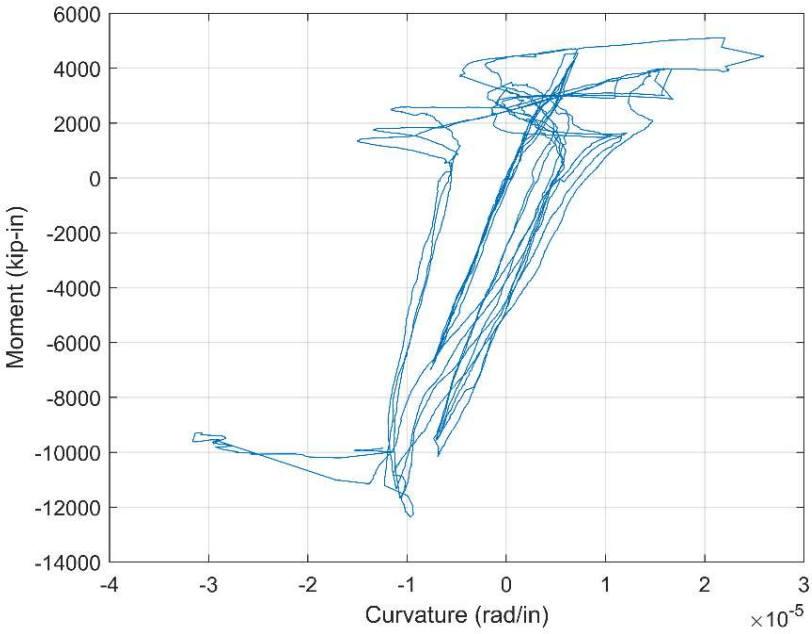

(b) Segment 2

Figure 4.14: Moment-vs.-curvature plots for Specimen 1

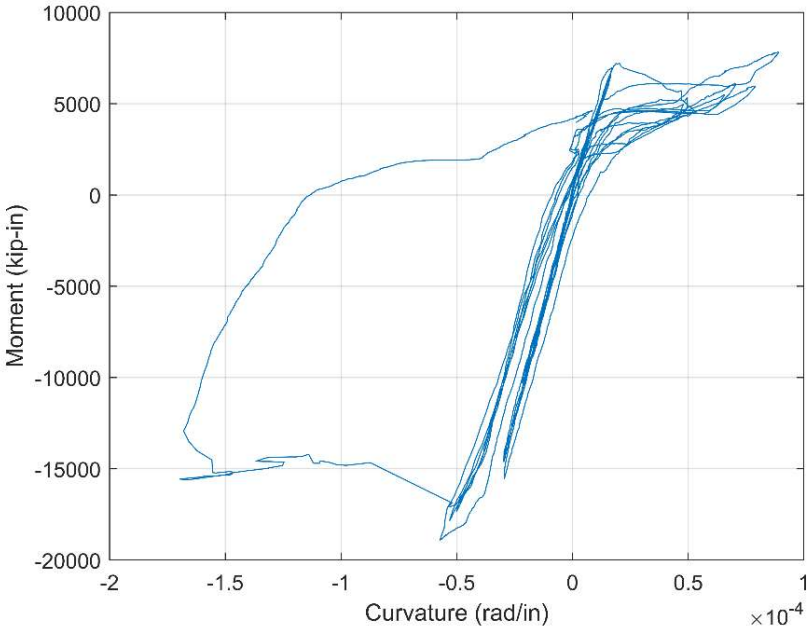

(c) Segment 3

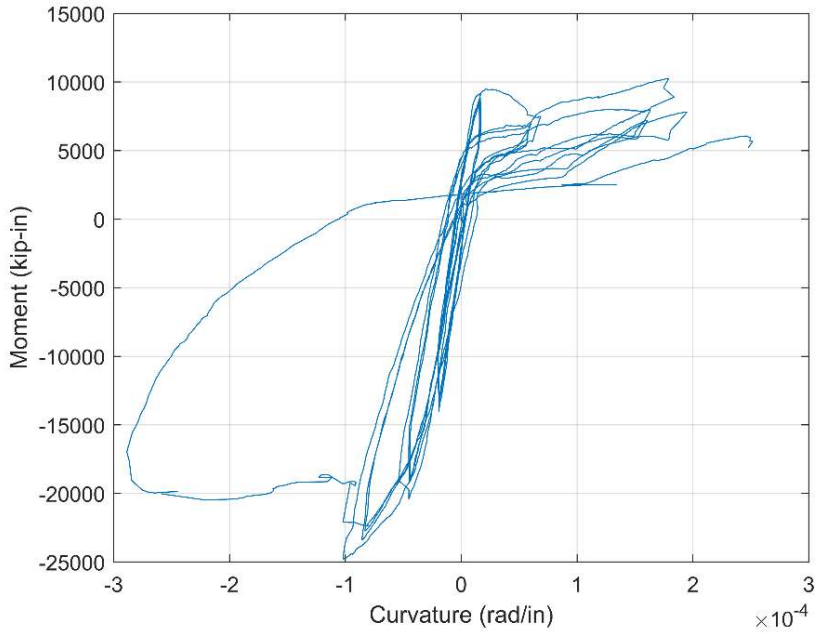

(d) Segment 4

Figure 4.14 (continued): Moment-vs.-curvature plots for Specimen 1

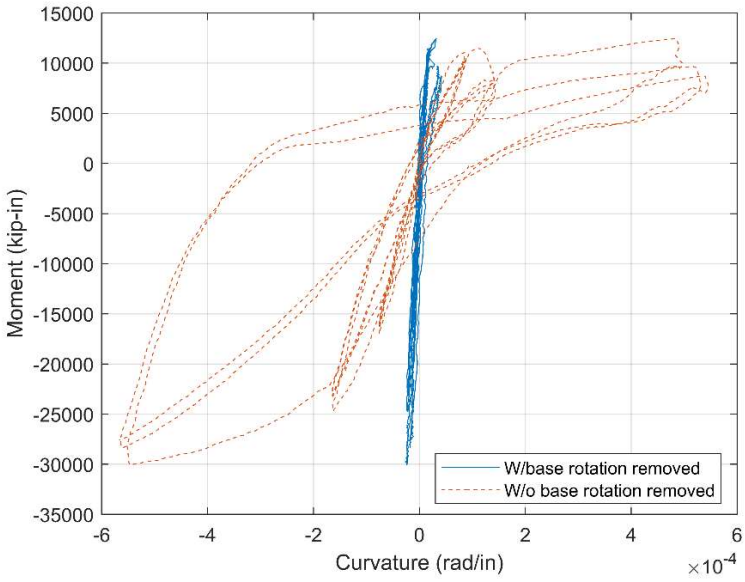

(e) Segment 5

Figure 4.14 (continued): Moment-vs.-curvature plots for Specimen 1

The respective contributions of the rotation of the pile end with respect to the pile cap, and of the flexural deformation and shear deformation of the pile specimen to the total lateral displacement measured were estimated. With the method explained in Hiraishi (1984), the lateral displacements contributed by the flexure and shear deformations were calculated with data from the linear potentiometers mounted in each segment of the pile specimen as follows. The exact locations of the linear potentiometers are shown in Figure 3.26.

The lateral displacement, u_f, due to flexure was calculated from the measured segment rotations with the following equation.

$$u_f = \int_0^{h_L} (h_L - y)\phi dy \approx \sum_{i=1}^{5} (h_L - y_i)\Delta\theta_i \tag{4.2}$$

in which h_L is the height at which the lateral displacement is considered, with respect to the soffit of the pile cap, which is 175 in., ϕ is the curvature of the pile section, y_i is the distance of the top of pile segment *i* (as numbered in Figure 4.12) from the soffit of the pile cap, and $\Delta\theta_i$ is the incremental rotation along segment *i* as calculated with Equation (4.1).

The shear deformation u_{si} in each segment *i* was calculated with Equation (4.3).

$$u_{si} = \frac{d_i}{2l}(\delta_1 - \delta_2)_i - \frac{h_i}{l}\left(\alpha - \frac{1}{2}\right)\left(\delta_S - \delta_N\right)_i \tag{4.3}$$

in which δ_1 and δ_2 are the displacements measured by the two diagonal linear potentiometers in the segment, with δ_1 in the direction from bottom south to top north and δ_2 from top south to bottom north; l is the undeformed horizontal distance between the two vertical linear potentiometers; h_i is the undeformed length of the vertical potentiometers; d_i is the undeformed length the diagonal potentiometers; and δ_S and δ_N are average displacements measured by the two south and two north vertical potentiometers, respectively. The value of α was assumed to be 0.5. The displacement value is positive when the potentiometer is extended. With Equation (4.3), the total shear displacement u_S was calculated as the sum of the shear deformations of the five segments:

$$u_s = \sum_{i=1}^{5} u_{si} \tag{4.4}$$

The lateral displacement, u_θ, due to rotation at the pile end was calculated as follows.

$$u_\theta = \theta_p h_L \tag{4.5}$$

in which θ_p is the rotation of the pile end with respect to the pile cap measured by the linear transducers mounted right above the pile cap, and is entirely due to the propagation of the plastic strains in the core bars into the pile cap and the pile.

The three displacement components computed are compared to the directly measured total in-plane lateral displacement in Figure 4.15. For comparison, the displacement due to shear was also computed indirectly by subtracting the calculated rotational and flexural components from the total lateral displacement measured. It can be seen that the contribution of the shear deformation to the lateral displacement is very small, while the base rotation constitutes a significant portion of the lateral displacement.

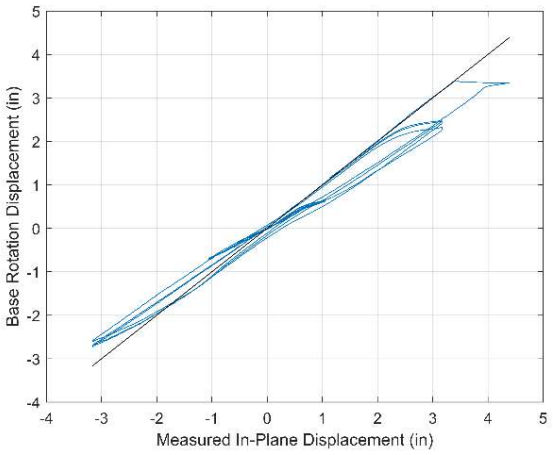

(a) Pile End Rotation

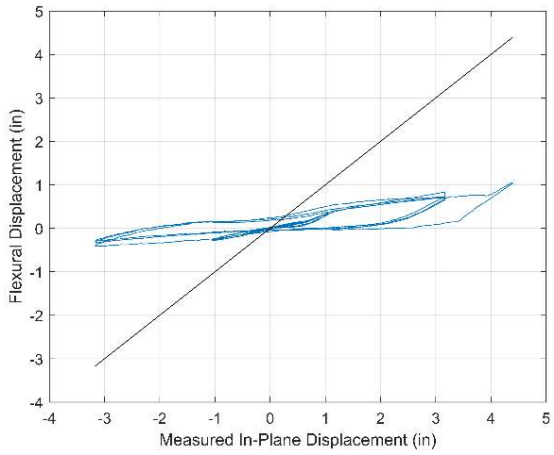

(b) Flexural Deformation

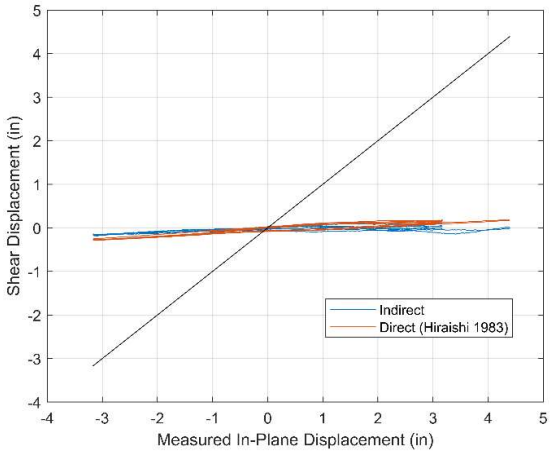

(c) Shear Deformation

Figure 4.15: Lateral displacements contributed by different mechanisms in Specimen 1

4.2.3 Data from Strain Gauges

Figure 4.16 shows the distribution of the strains in the extreme north and south core bars at the peaks of the first cycle at each drift level. The core bars had an average yield stress of 46 ksi, resulting in a yield strain of 0.0016. These bars had the highest strains near the soffit of the pile cap. The extreme north bar had tensile yielding first occurring at -0.63% drift in the cycle towards -1.8% drift, while the extreme south bar had yielding first occurring at +0.64% drift in the

cycle towards 1.8% drift. Severe tensile yielding occurred in both bars at 1.8% drift, but the north bar had a higher tensile strain at that drift level, even though the pile was subjected to compression when the north bar developed flexural tensile stress. The south bar developed a higher compressive strain than the north bar. The higher tensile strain in the north bar can be explained with the strain-displacement plots in Figure 4.17 as will be discussed below. The tensile strains in both bars decreased a little bit when the drift ratio increased from 1.8 to 2.5%. This could be partly caused by the increased slip of the bars and partly by the formation of a plastic hinge in the pile near the termination point of the core bars, which reduced the moment demand near the pile cap. In the region near the bar termination point, there was not sufficient bond length to develop high tensile strains in the core bars.

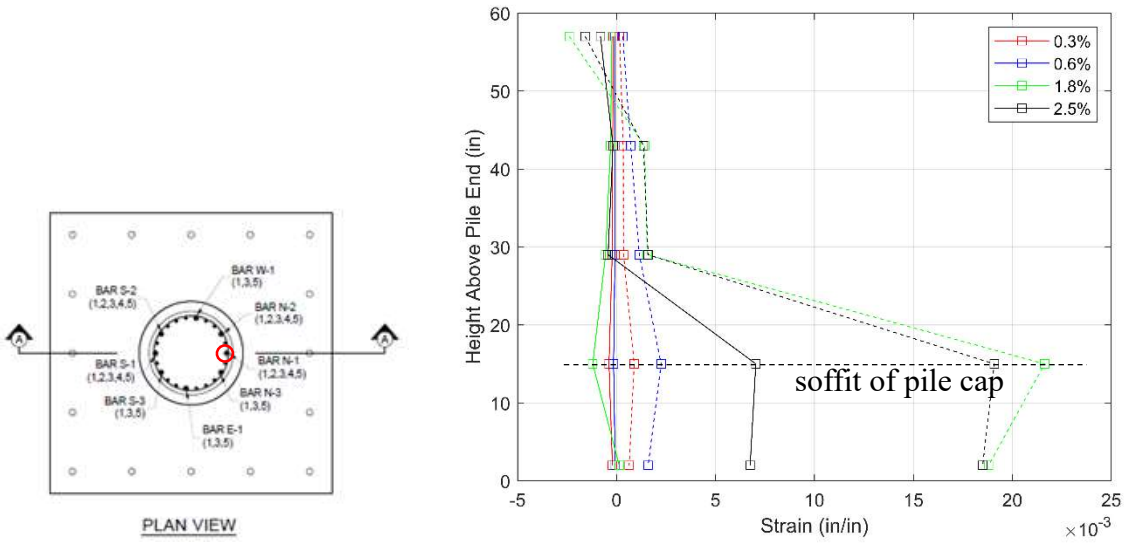

(a) Core bar at extreme north (Bar N-1)

Figure 4.16: Strain profiles of core bars in Specimen 1 at different drift levels (dashed lines are for drifts towards south and the solid lines for drifts towards north)

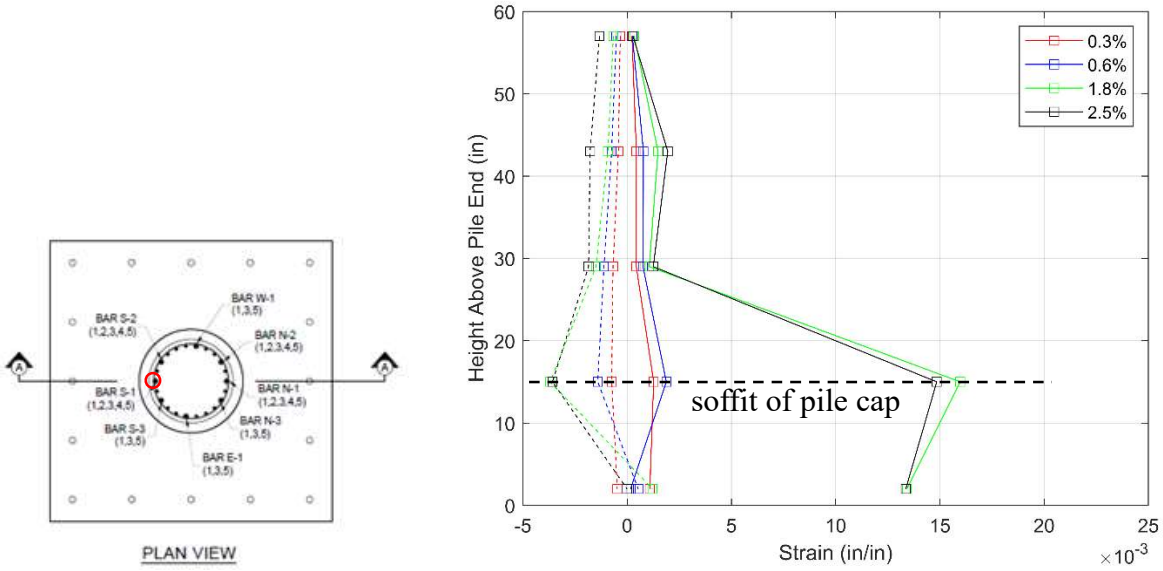

(b) Core bar at extreme south (Bar S-1)

Figure 4.16 (continued): Strain profiles of core bars in Specimen 1 at different drift levels (dashed lines are for drifts towards south and the solid lines for drifts towards north)

Figure 4.17 shows the plots of the strains in the extreme north and south core bars against the lateral displacement of the pile specimen. It can be observed that the tensile strains measured by gauges SG21 and SH25 on the north bar jumped suddenly when the pile was displaced more than 1 in. (0.6% drift) towards the negative (south) direction, while the tensile strains at the same elevations in the south bar varied more gradually. This sudden jump in tensile strains in the north bar could be caused by the sudden development of flexural cracks on the north side of the core near the gauge locations. The south side of the core cracked early on in the test due to the high axial tension applied, which induced higher tensile strains in the south bar at low drift levels. The sudden transfer of high tensile stress to the north bar due to flexural cracking did not provide sufficient time for the bar to slip and resulted in tensile strain concentration near the cracks. The rapid drop of the tensile strain measured by gauge SH23 on the south bar during unloading from

the first positive peak of 1.8% drift could be caused by the rapid unloading of the tensile force applied to the pile, which resulted in the closing of the flexural cracks by the prestressing strands near that location.

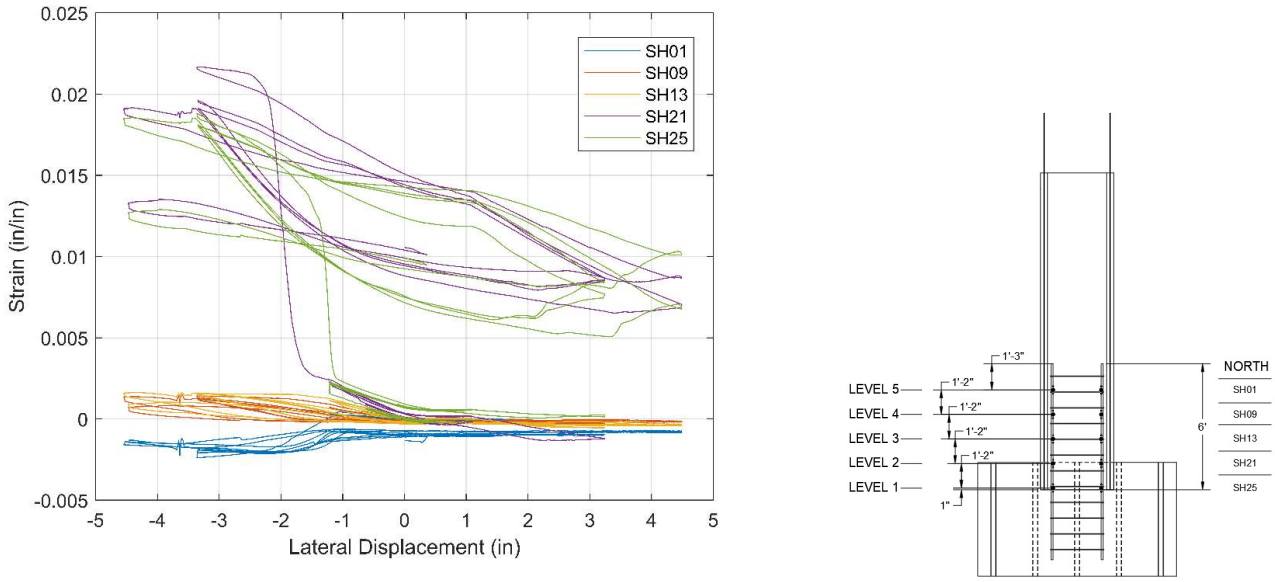

(a) Core bar N-1

Figure 4.17: Strain-vs.-displacement plots for strains measured at different elevations along (a) extreme north and (b) south core bars in Specimen 1

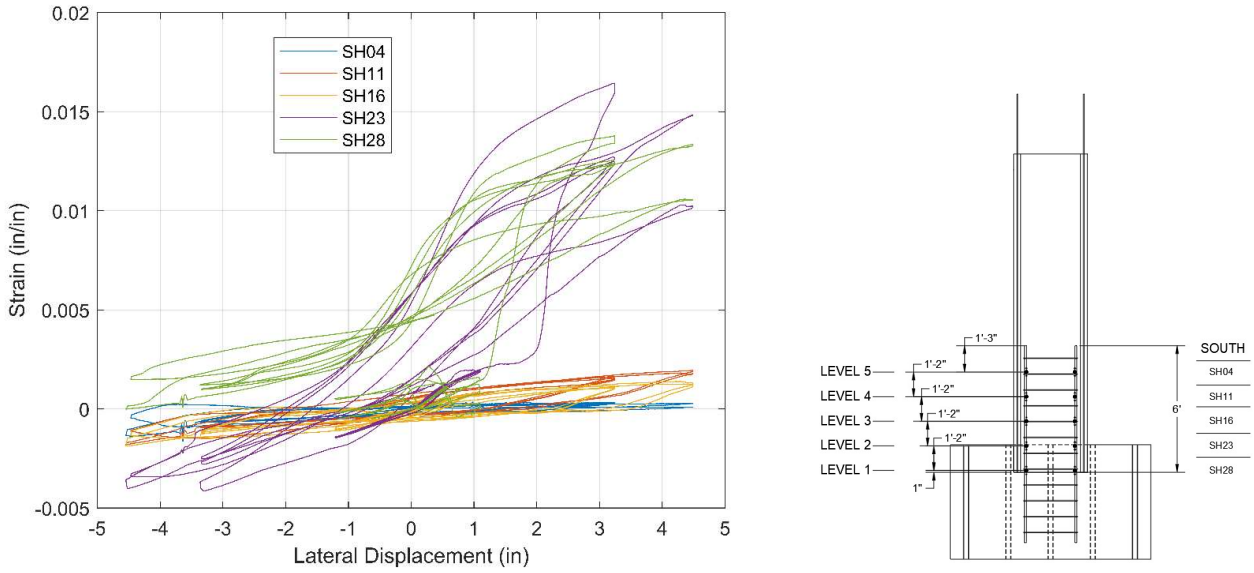

(b) Core bar S-1

Figure 4.17 (continued): Strain-vs.-displacement plots for strains measured at different elevations along (a) extreme north and (b) south core bars in Specimen 1

Figures 4.18 and 4.19 show the plots of the strains measured on the extreme north prestressing strand against the lateral displacement of the pile specimen. The effective prestress in the strand at the beginning of the test without considering the vertical load from the load stub, load beam, and the vertical actuators was estimated to be 145 ksi (as shown in Appendix C), which corresponds to an initial strain of 0.0048 based on the stress-strain plot for the strand shown in Figure 3.8. The elastic shortening loss caused by the application of the gravity load from the load stub and load beam, and the initial compression exerted by the vertical actuators was estimated to be 0.45 ksi. This was calculated with the composite modulus of elasticity of 4,715 ksi for the shell and core concrete, estimated from the strain measured during the application of the vertical actuator load. Hence, the initial strain in the strands is set to be 0.0048 in Figures 4.18 and 4.19.

Figure 4.18 shows a sudden jump in tensile strain measured by gauge S11 at a displacement level of about -2 in. (-1.14% drift), which is similar to the strain jump observed at a similar elevation on the north core bar (see Figure 4.17). The maximum tensile strain reached slightly exceeds 0.055, which corresponds to a tensile stress exceeding 275 ksi (close to the measured tensile strength of the strand). It is a bit surprising that the strand was able to develop such a large stress at a point that had such a short development length of 15 in. As discussed in Section 3.6.1, the required development calculated according to the ACI 318 formula is 63 in. After the jump, the strain appears to remain in tension regardless of the displacement direction. This indicates that the gauge was probably damaged and the maximum strain actually developed was much lower than what is shown in the plot. Figure 4.19 shows that the strains measured by the two gauges above S11 were much lower, with the maximum strain measured by gauge S15 barely reaching the yield strain.

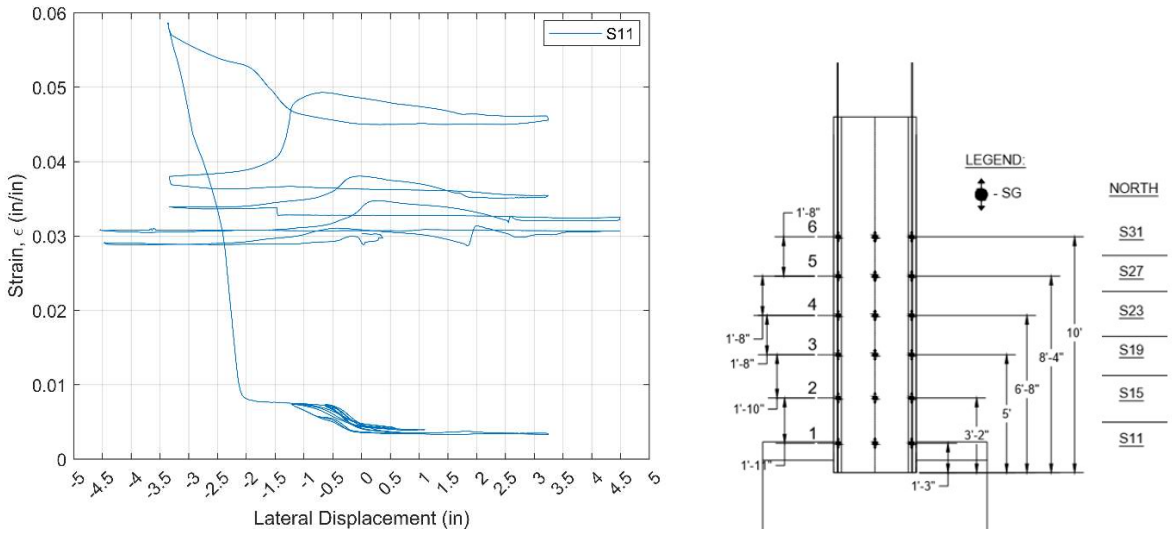

Figure 4.18: Strain-vs.-displacement plot measured by gauge S11 on the north strand in Specimen 1

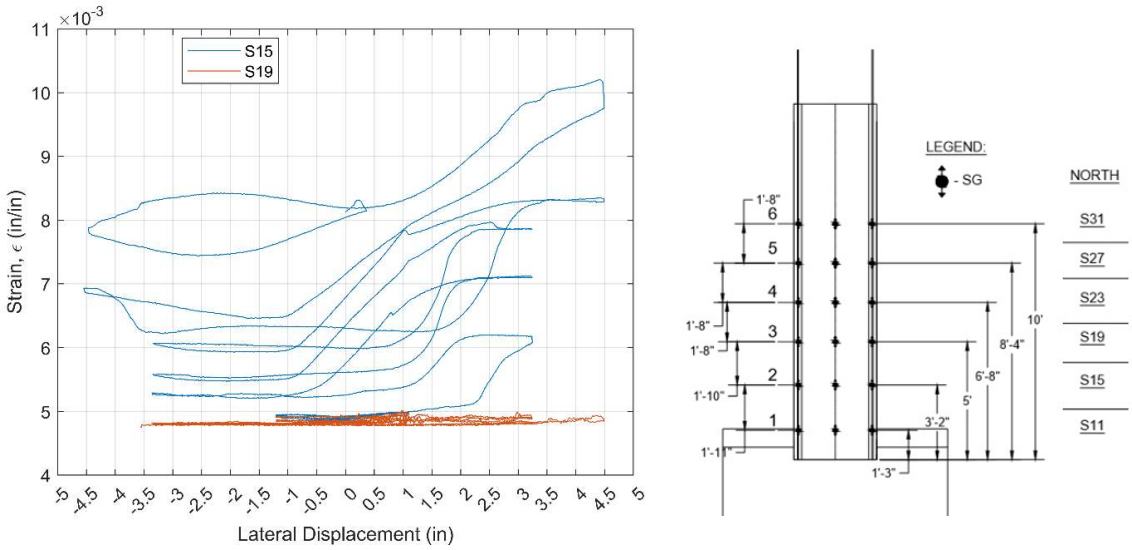

Figure 4.19: Strain-vs.-displacement plots measured by gauges S15 and S19 on the north strand in Specimen 1

Figure 4.20 shows the strains measured in the transverse reinforcement in the precast shell. The highest strain was measured by gauge S33, which was closest to the pile cap. The second highest strains were measured by gauges S40 and S41, which were in the region where severe concrete crushing occurred. However, these gauges were lost before reaching the concrete crushing point. In fact, some of the transverse reinforcement in that region fractured when crushing occurred. The strains measured by all these gauges at drift levels beyond 0.6% exceeded the yield strains of the steel.

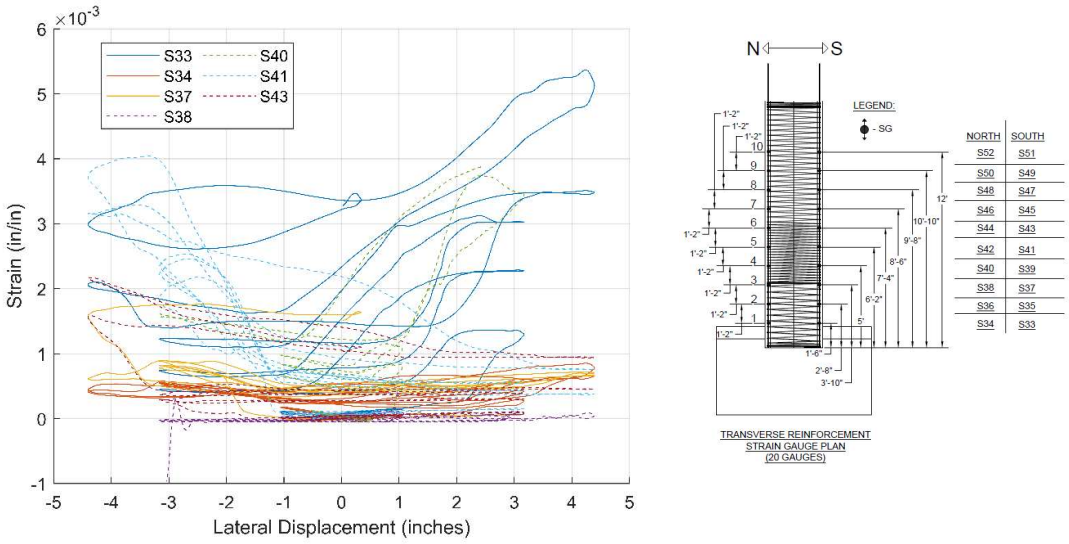

Figure 4.20: Strains in transverse reinforcement in Specimen 1

4.2.4 Concluding Remarks

Specimen 1 represented an undamaged as-built pile. Its performance was satisfactory up to 1.8% drift ratio, which is the maximum drift demand expected of the piles under the 1000-year earthquake, according to the analyses performed by the Office of Earthquake Engineering Analysis and Research (OEEAR 2018) of Caltrans. The pile specimen was able to resist the maximum tensile force of 575 kips (equivalent to 950 kips for the full-scale pile) expected from the earthquake, and was able to regain the moment capacity under compression upon displacement reversal to negative 1.8% drift. It exhibited only mild load degradation in the two subsequent displacement cycles at negative 1.8% drift. Major load degradation occurred when the drift ratio passed 1.8%, with the eventual formation of a plastic hinge that exhibited severe concrete crushing near the core bar termination point. This can also be attributed to the plying action of the core against the precast shell. As explained in Section 4.2.1 and Figure 4.9, the plying action was caused by the formation of a through crack across the core near the core bar termination point and the slip of the precast shell.

4.3 Pile Specimen 2

Specimen 2 had the same design as Specimen 1, except that all the prestressing strands in the precast shell were unbonded for a length of 2 ft. and 7-1/2 in. from the end of the shell that was connected to the pile cap. From the soffit of the pile cap, the unbonded distance was 15.875 in., as shown in Figure 3.2. This was to simulate the loss of bonding due to the cracking of the concrete near the pile end caused by pile driving. It was considered as the worst-case scenario based on underwater inspection performed by Caltrans.

4.3.1 Experimental Observations

Figure 4.21 shows the lateral load-vs.-lateral displacement hysteresis curves for Specimen 2. The pile showed a sudden loss of lateral resistance at the displacement of about 0.7 in. (0.4% drift). This was due to the slip of the precast shell with respect to the core after a horizontal through crack had developed in the shell near the pile cap. As shown in Figure 4.22, the slip started at the lateral displacement of 0.7 in. and increased rapidly as the lateral displacement approached 1 in., after which the resistance to axial tension dropped to zero quickly. The maximum vertical actuator force reached was 600 kips. This corresponds to a maximum tensile force of 525 kips, after subtracting the weight of the load stub and loading beam from the actuator force. As will be discussed later, the slip was triggered by the development of a horizontal through crack in the core right above the core bar termination point. Figure 4.23 compares the lateral load-lateral displacement hysteresis curves for Specimens 1 and 2. Specimen 2 had a lower strength and more brittle behavior. It failed prematurely.

Figure 4.24 shows pictures of the pile specimen taken at the drift ratio of 0.6% (1.1 in. lateral displacement) towards north (when the pile was subjected to tension), showing a widely opened horizontal crack. This crack was first observed as a fine crack at the drift ratio of 0.3%.

The crack was not level. Its distance varied around the circumference of the pile from 6 to 16 in. from the soffit of the pile cap, as shown in the two bottom pictures.

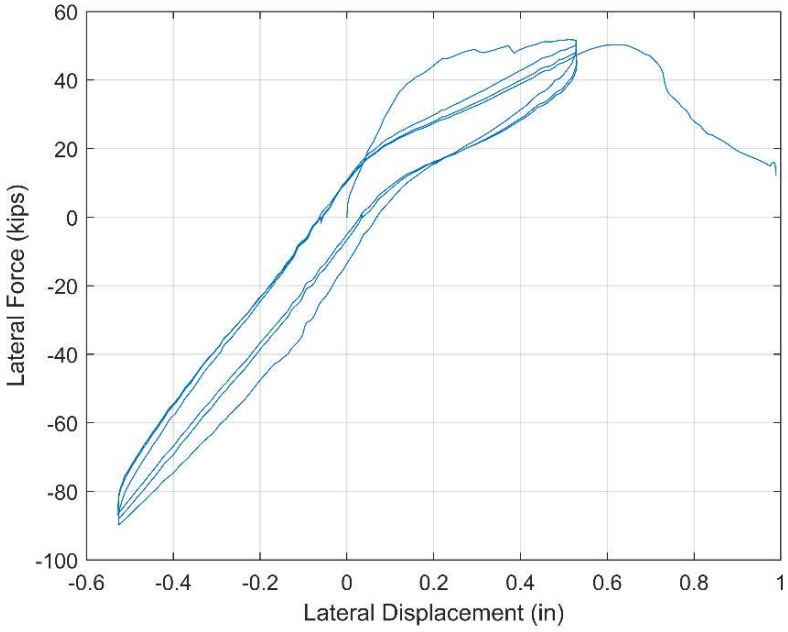

Figure 4.21: Lateral load-vs.-lateral displacement hysteresis curves for Specimen 2

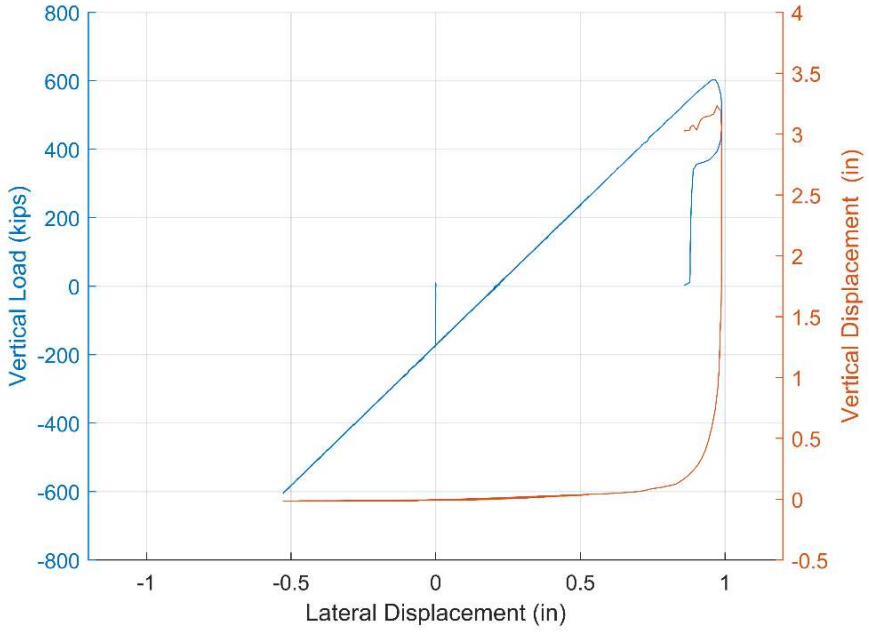

Figure 4.22: Plots of vertical load and vertical displacement against lateral displacement for Specimen 2

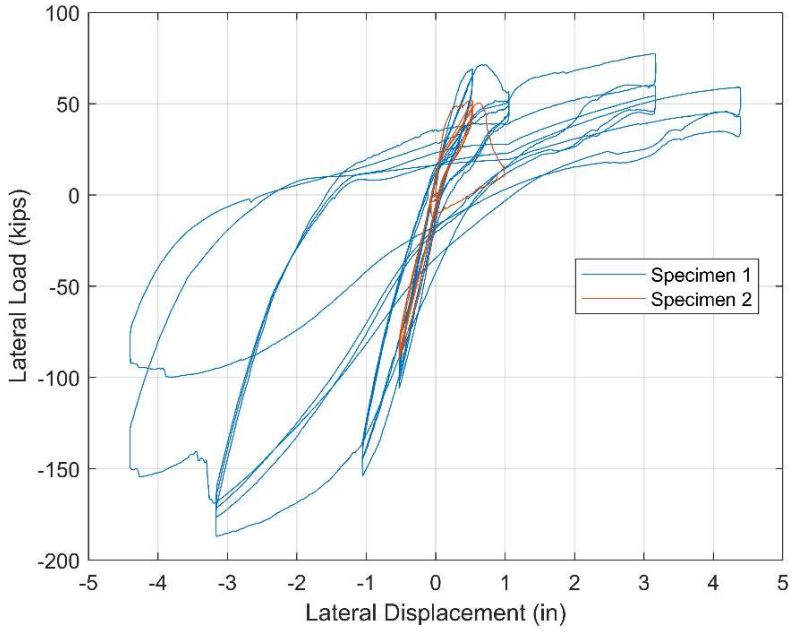

Figure 4.23: Comparison of load-displacement curves for Specimens 1 and 2

North-West

South

South-East

South

Figure 4.24: Pictures of Specimen 2 after reaching a drift ratio of 0.6% towards north (the horizontal crack in the shell initiated near pile cap at 0.3% drift)

When the specimen was demolished after the test, a portion of the precast shell was cut and removed from a segment of the pile above the pile cap. The cut segment is shown in Figure 4.25. It shows a through crack developed across the core during the test right above the core bar

termination point. Once this crack occurred in the test, the tensile force at that section was entirely carried by the precast shell and was gradually transferred to the core below that was connected to the pile cap through the interface shear between the shell and the core. However, since the strands in the shell were unbonded over a distance of 15.875 in. from the soffit of the pile cap, the shell cracked in that region before the tensile force was completely transferred to the core, as shown in Figure 4.24. After that, the shell started to slip because of the short distance for shear transfer. It is very likely that the interior crack in the core occurred prior to the exterior crack in the shell in the cycle at 0.3% drift. However, slip did not occur till the drift ratio of 0.4% (0.7 in.) was reached and it accelerated when the drift ratio reached 0.57%, at which the axial tension reached 525 kips.

Figure 4.25: Exposed core after the shell was partially removed from Specimen 2 showing a through crack in the core near the termination point of the core bars

4.3.2 Data from External Transducers

Figure 4.26 shows the lateral displacement profiles of the pile at the peaks of each cycle at 0.3% drift ratio. The shapes are quite linear except for a slight kink at the elevation of 42 in. It

could be related to the horizontal through crack developed in the core above that location. Figure 4.27 compares the rotation measured at the top section of each instrumented segment of the pile (as identified in Figure 4.12) by the linear potentiometers with that measured by the inclinometers. Positive rotations correspond to the bending of the pile towards north. While the positive rotations measured by the two types of devices have very close values, the negative rotations measured by the inclinometers are a bit higher that those by the linear potentiometers at several locations. However, the rotations measured are close to those measured in Specimen 1 at the same drift ratio.

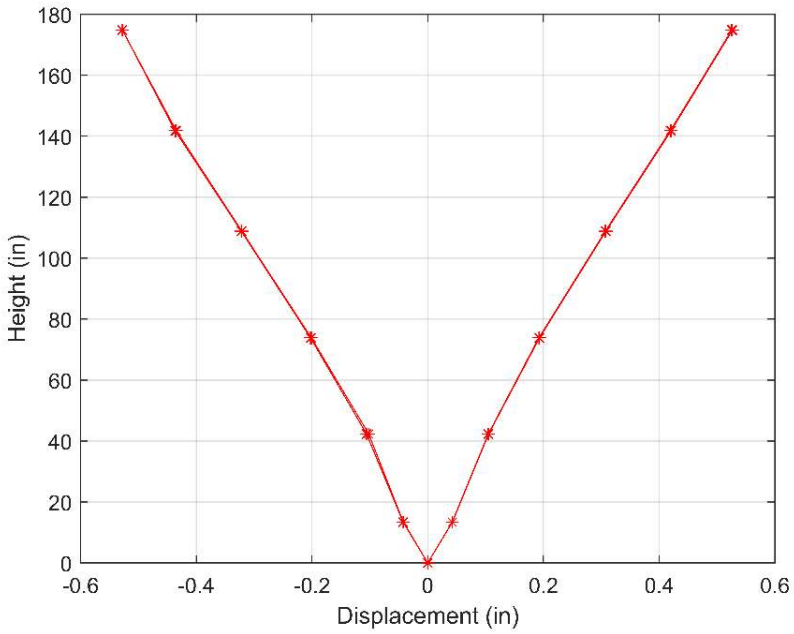

Figure 4.26: Lateral displacements along the height of Specimen 2

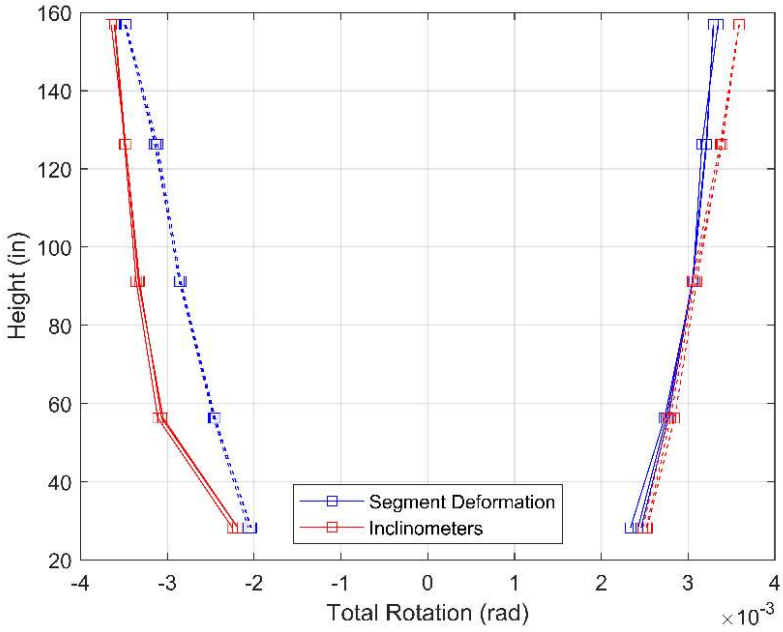

Figure 4.27: Pile rotations at different elevations along Specimen 2 measured by inclinometers and vertical linear potentiometers in pile segments at drift ratio of 0.30%

Figure 4.28 shows the moment-curvature plot for each instrumented segment along the pile specimen. However, results beyond 0.3% drift are not shown because of the failure of the instruments in segment 5 as the shell slipped excessively.

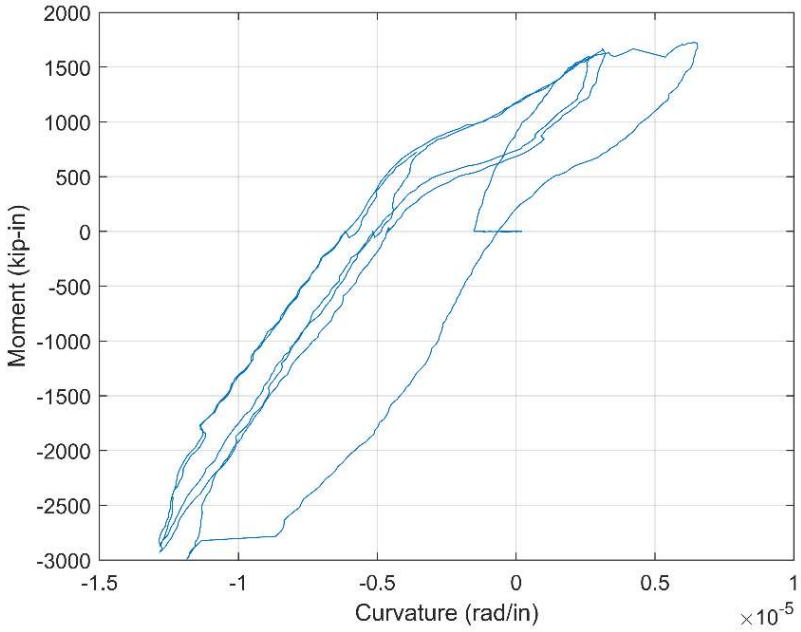

(a) Segment 1

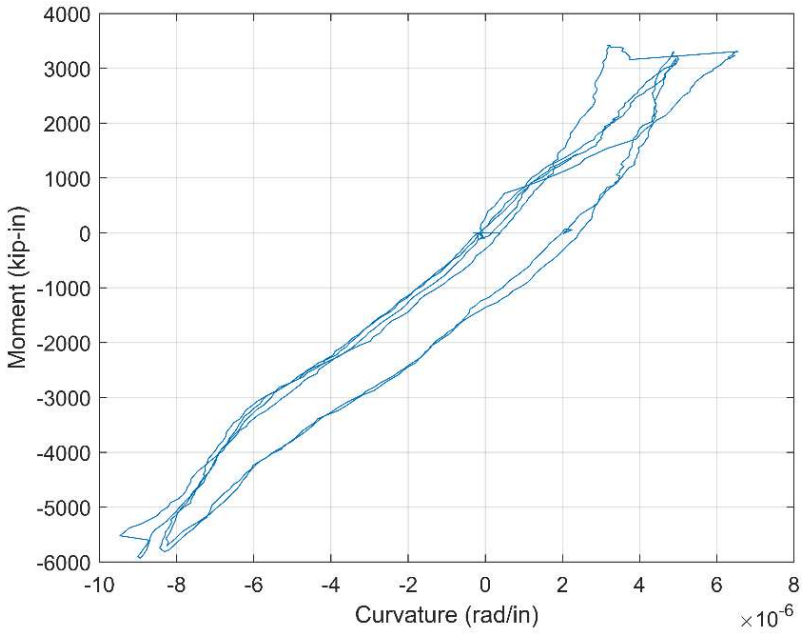

(b) Segment 2

Figure 4.28: Moment-vs.-curvature plots for Specimen 2 (segment locations shown in Figure 4.12; data up to 0.3% drift)

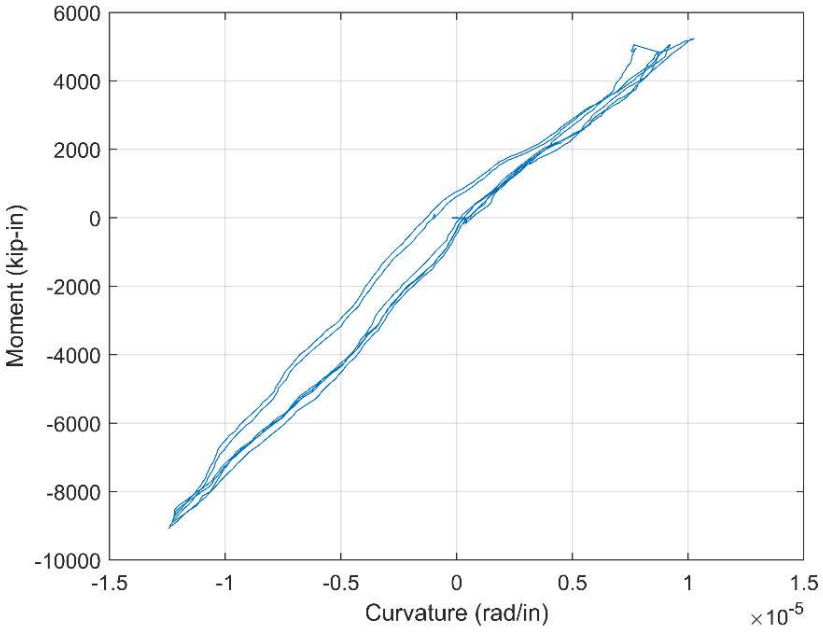

(c) Segment 3

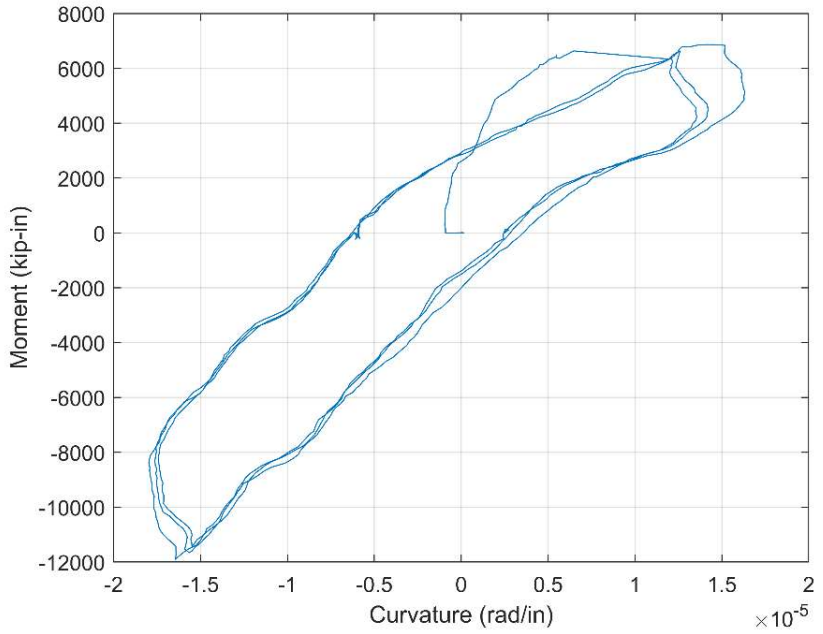

(d) Segment 4

Figure 4.28 (continued): Moment-vs.-curvature plots for Specimen 2 (segment locations shown in Figure 4.12; data up to 0.3% drift)

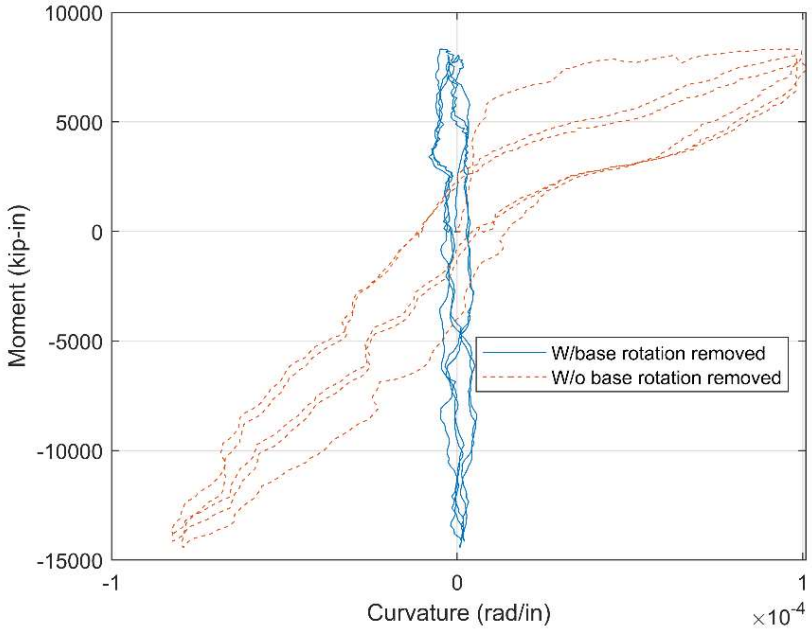

(e) Segment 5

Figure 4.28 (continued): Moment-vs.-curvature plots for Specimen 2 (segment locations shown in Figure 4.12; data up to 0.3% drift)

4.3.3 Data from Strain Gauges

Figure 4.29 shows the distribution of the strains in the extreme north and south core bars at the peaks of each displacement cycle. The core bars had an average yield stress of 46 ksi, resulting in a yield strain of 0.0016. As shown in Appendix A, this specimen had strain gauges attached to core bars down into the region inside in the pile cap. The zero elevation in the graphs corresponds to the pile end. As expected, the south bar shows a higher maximum tensile strain because the pile was in axial tension when this bar developed tensile flexural strain. At the 0.3% drift ratio, the strains in the north and south bars are comparable to those developed in Specimen 1 at the same drift ratio (see Figure 4.16). Nevertheless, at the positive drift of about 0.6%, the strain in the south bar dropped instead of increasing as in Specimen 1. This is attributed to the slip

of the precast shell, which prevented the axial tension from being transmitted to the core. None of the core bars reached the yield strain.

Figure 4.30 shows the plots of the strains in the extreme north and south core bars against the lateral displacement of the pile specimen. Strains in the south bar show sudden jumps at several locations at lateral displacements between 0.2 and 0.3 in. This could be caused by the cracking of the precast shell near the pile cap, transmitting additional axial tension to the core. The strains then started to drop after the lateral displacement passing 0.7 in., at which significant slip of the precast shell occurred.

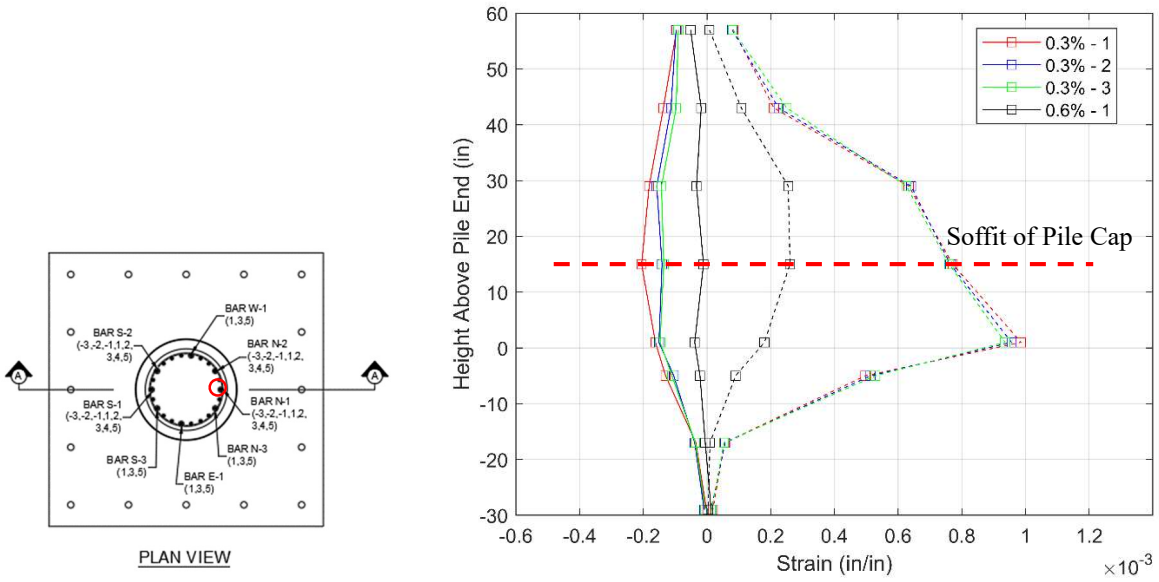

(a) Core bar at extreme north (Bar N-1)

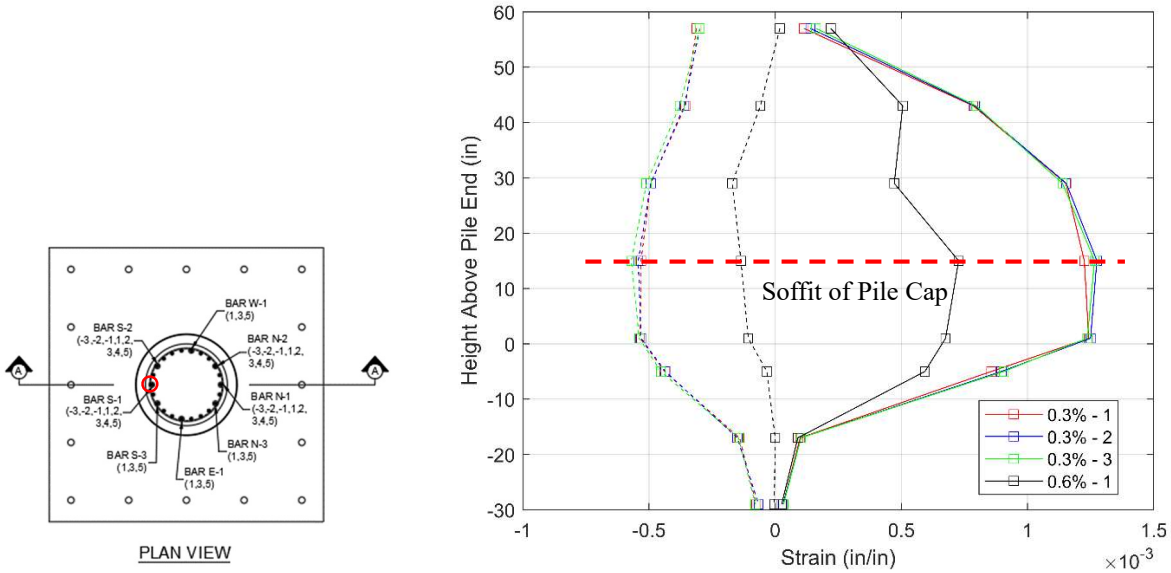

(b) Core bar at extreme south (Bar S-1)

Figure 4.29: Strain profiles of core bars in Specimen 2 at different drift levels (dashed lines are for drifts towards south and the solid lines for drifts towards north)

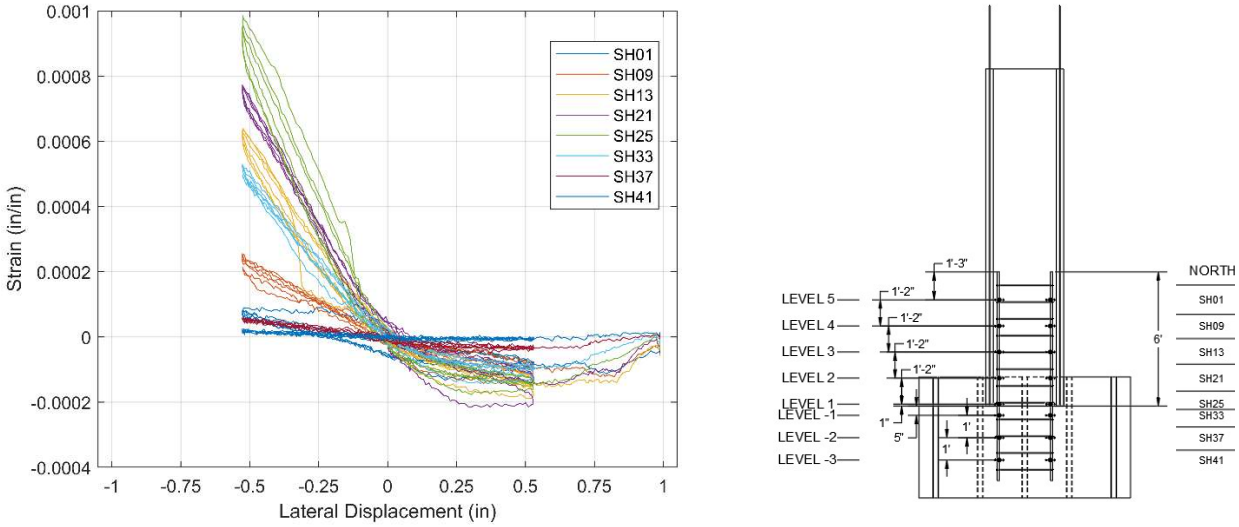

(a) Core bar N-1

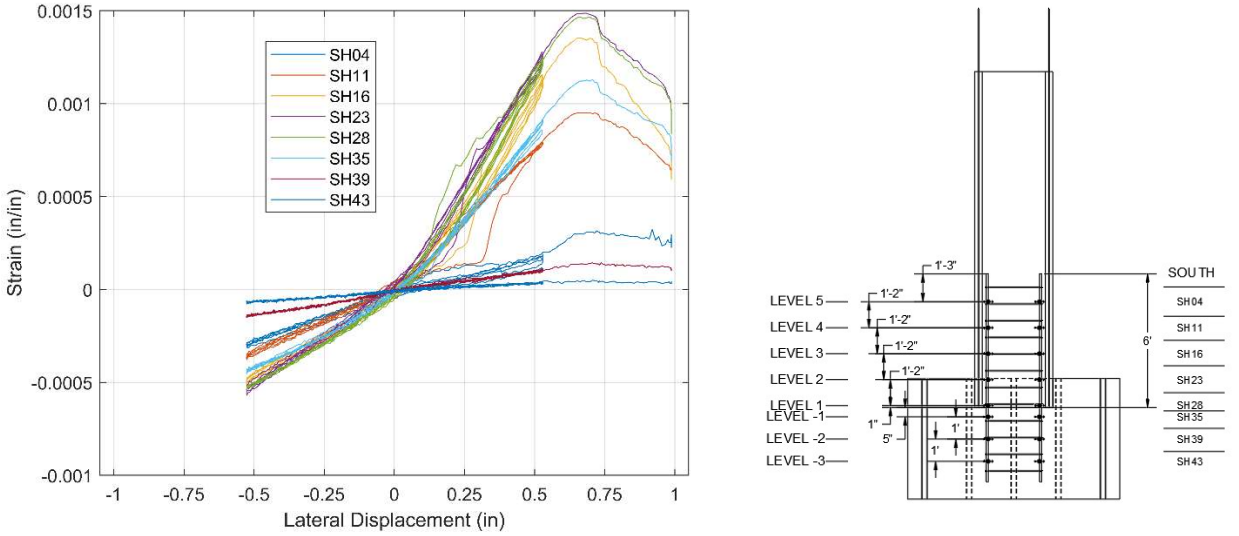

(b) Core bar S-1

Figure 4.30: Strain-vs.-displacement plots for strains measured at different elevations along (a) extreme north and (b) south core bars in Specimen 2

The strain gauges on the prestressing strands showed very small strain variations, indicating that the precast shell did not take much tension due to the slip of the shell with respect to the core, which occurred early in the test.

4.3.4 Estimation of Shear Transfer between Precast Shell and Concrete Core

As discussed in the previous sections, the slip of the precast shell in the pile specimen was triggered by the development of two cracks at a drift ratio close to 0.3%. One was a horizontal through crack developed in the core right above the core bars and the other was a horizonal through crack in the shell developed near the pile cap. The slip of the shell initiated at 0.4% drift (0.7-in. displacement) and accelerated at 0.57% drift, at which the tensile force applied to the pile specimen reached 525 kips. The elevation of horizontal crack in the shell varied around the circumference of the pile from the lowest point of 6 in. to the highest point of 16 in. from the soffit of the pile cap. Hence, the average elevation of the crack is assumed to be 11 in. Based on this information, a segment of the pile between the two cracks is extracted as a free body, as shown in Figure 4.31. The forces on the segment reflect those occurring at 0.57% drift ratio. At the top of this segment, the core had cracked, and therefore, the entire tensile force of 525 kips had to be carried by the precast shell. At the bottom of the segment, the shell had cracked and the tensile force was thus carried by the concrete core and the 22 #9 core bars. In fact, based on the data shown in Figure 4.30, the average strain measured in the north and south core bars right before reaching 1.0 in. displacement (0.57% drift) is 0.00063, which corresponds to an average stress 18 ksi. If this represents the average stress in all 22 bars, then the total axial tension carried by these bars is estimated to be 396 kips. The remaining tensile force of 129 kips had to be carried by the concrete core, whose section might not have been completely cracked. This corresponds to an average tensile stress of 0.142 ksi in the core. Based on the free body shown in Figure 4.31, the average shear stress developed between the shell and the core right before slip occurred would be 0.108 ksi.

After the test, a segment of the pile was cut out (about 12 in. above the core bar termination point as shown in Fig. 4.31) and subjected to a push test as shown in Figure 4.32. The segment was supported at the shell and the core was pushed down with a hydraulic jack. When the push force reached 79 kips, the core started to slip and the shell fractured with a vertical splitting crack, as shown in the picture, due to the internal pressure exerted at the interface as a result of the wedging action along the rough sliding surface. It should be mentioned that this segment had lighter transverse reinforcement (W3 spiral) than the region next to the pile cap, which had #3 spiral. The maximum interface shear stress reached is calculated to be 0.048 ksi, which is much lower than the 0.108 ksi estimated from the free-body diagram in Figure 4.31. This difference is largely attributed to the lighter transverse reinforcement in the shear-test segment.

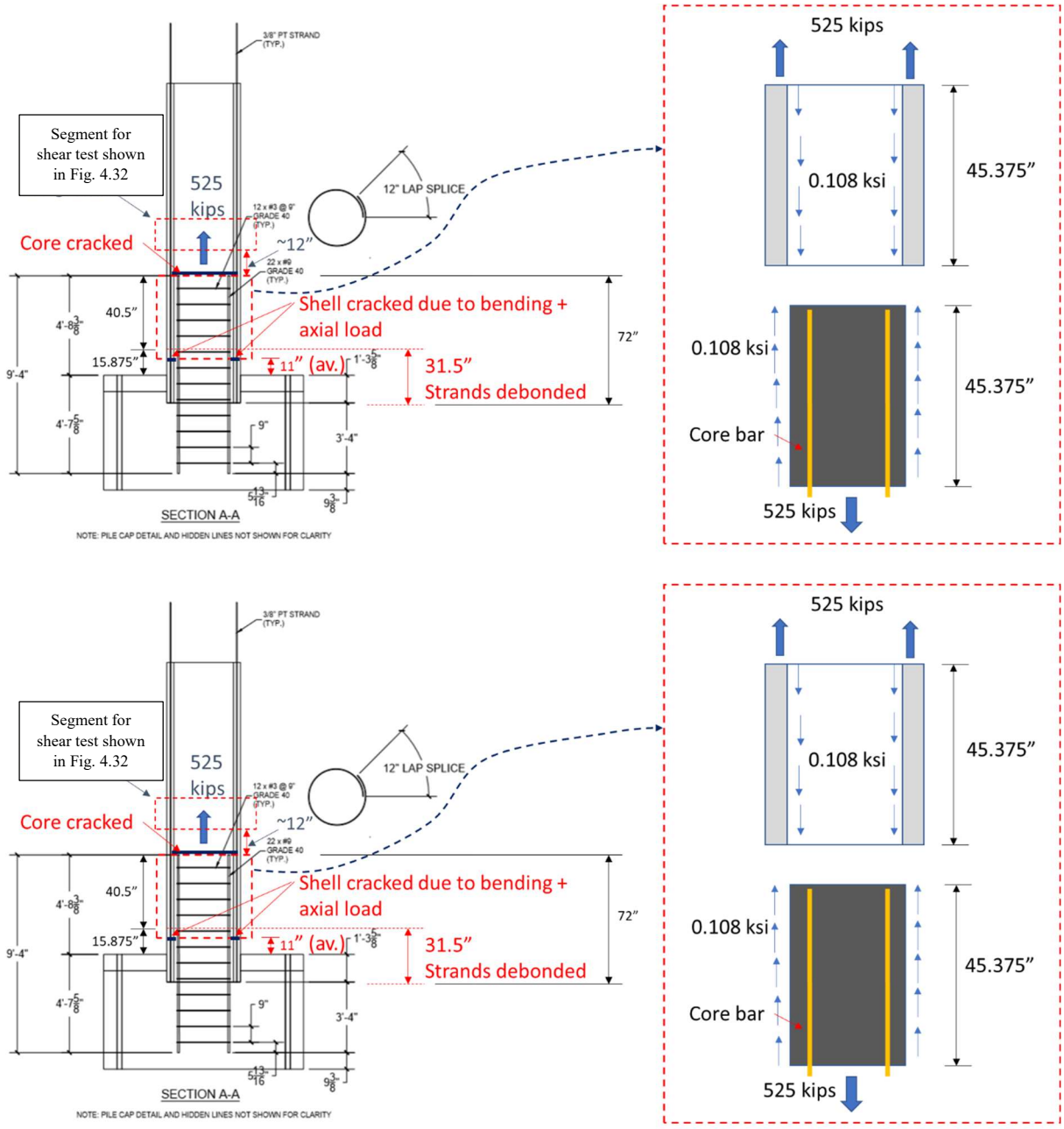

Figure 4.31: Estimation of shear transfer between precast shell and concrete core

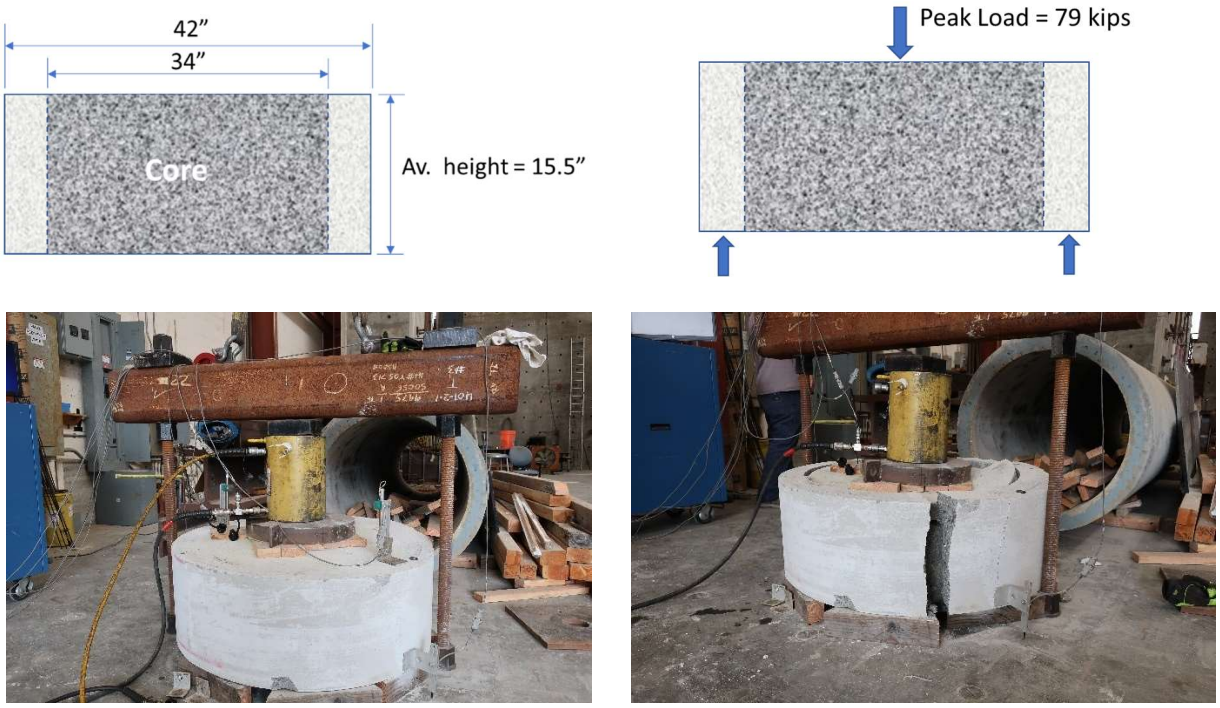

Figure 4.32: Shear transfer test on a pile segment cut from Specimen 2 (shell had W3 wire spiral)

However, the shear transfer strength between the precast shell and the core in an actual pile could be different from what was observed in the laboratory as the roughness of the inner surface of the precast shell in an actual pile could be different. Another factor to consider is the respective drying shrinkage of the inner core and the precast shell of a pile. However, since the piles in the bridge are submerged in water and the core concrete is concealed within the precast shell, the shrinkage of the core is expected to be negligible and will not jeopardize the bond between the shell and the core. A study by Gebman et al. (2006) has shown that the drying shrinkage of concrete within cast-in-steel-shell piles is negligible.

4.4 Pile Specimen 3

Specimen 3 had the same design as the other two specimens except that the pile was retrofitted with a DYWIDAG bar, as shown in Figure 4.34 and discussed in Section 3.2. The DYWIDAG bar extended all the way in the pile specimen to the elevation at which the core bars

connecting the pile to the load stub were terminated. Since the elevation of the horizontal actuators represented the inflection point of the prototype pile, which is about midway between the pile cap and the mudline, the DYWIDAG bar can go further in an actual pile. Another difference between this specimen and Specimen 2 is that the strands in the precast shell had an unbounded length of 1 ft.-9 in., compared to 2 ft.-7 ½ in. in Specimen 2, from the pile end, as shown in Figure 3.4 and Figure 4.33. Furthermore, the reinforcement details in the pile cap of Specimen 3 were changed a little bit; but it was not expected to affect the specimen behavior. If this pile specimen were not retrofitted, it would have behaved in a way similar to Specimen 2 with a premature failure due to the slip of the shell.

As shown in Figure 4.33, the distance from the bottom surface of the top anchor plate of the DYWIDAG bar to the soffit of the pile cap was 126.3 in. By assuming that a horizontal crack might develop through the core at the elevation of the bottom surface of the top anchor plate and a horizontal crack might develop in the shell at the end of the unbonded strand region in the pile, the shear transfer between the shell and core would occur over a distance of 121 in. This would result in a shear stress of 0.045 ksi when the maximum axial tension of 575 kips was reached. This is far lower than the shear strength of 0.108 ksi deduced from the results of Specimen 2, and is comparable to the shear strength of 0.048 ksi obtained from the push test conducted on a pile segment cut from the least confined portion of Specimen 2.

The DYWIDAG bar had a cross-sectional area of 4.08 in. and a minimum tensile load capacity of 612 kips, which was sufficient to carry the maximum tension of 575 kips applied to the pile for the worst-case scenario that a through crack occurred in the pile near the pile cap.

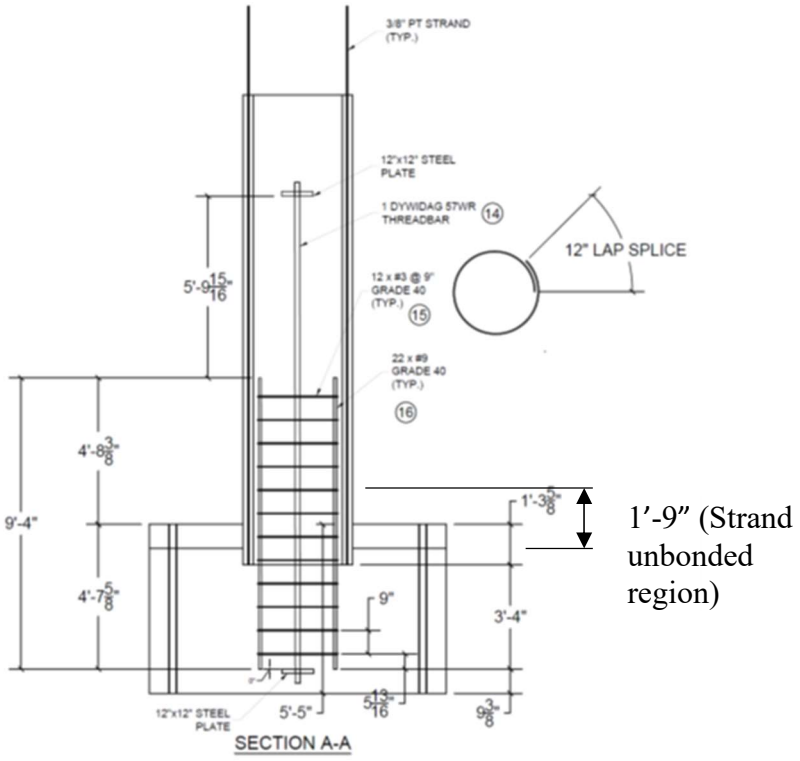

Figure 4.33: Retrofit design of Specimen 3

4.4.1 Experimental Observations

Figure 4.34 shows the hysteresis curves of the lateral load vs. the lateral displacement at the top of the pile specimen, and Figure 4.35 shows the plots of the applied axial load and the resulting vertical displacement at the top of the pile against the lateral displacement. It shows that the vertical uplift of the pile in the last cycle of loading was about 30% less than that in Specimen 1 (which is shown in Figure 4.2), indicating the effectiveness of the DYWIDAG bar in improving the tensile resistance of the pile. The lower axial elongation also implies less slip between the precast shell and the pile when compared to Specimen 1. The premature failure observed in Specimen 2 was completely prevented.

Figure 4.36 compares the load-displacement hysteresis curves for Specimens 1 and 3. It can be seen that Specimen 3 was a little softer at the beginning and had a lower resistance in both loading directions in all cycles except the very last cycle at 2.5% drift ratio, in which Specimen 3 showed a much lower strength degradation in the negative direction and a little higher strength in the positive direction. The lower stiffness and strength of Specimen 3 can be attributed to the unbonding of the strands near the pile end, and as a consequence, the strands were not able to provide moment resistance in the region near the pile cap. The DYWIDAG bar was located at the center of the pile and was therefore not as effective in resisting moment. Figure 4.37 compares the load-displacement hysteresis curves for Specimens 2 and 3. As shown, Specimen 3 had significantly better performance, but its stiffness and strength in the positive loading direction at low drift levels were slightly lower than those of Specimen 2. This indicates that the DYWIDAG bar was probably not engaged in flexural resistance at these drift levels. The above comparisons show that Specimen 3 would have developed the same failure as Specimen 2 if the former was not retrofitted with the DYWIDAG bar.

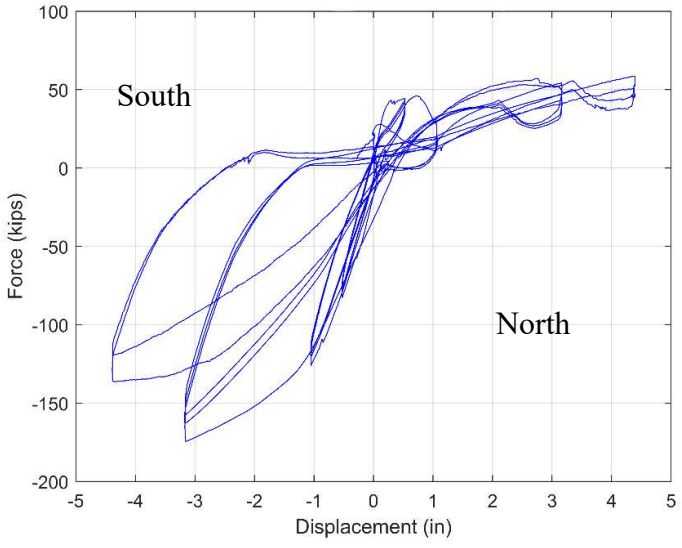

Figure 4.34: Lateral load-vs.-lateral displacement hysteresis curves for Specimen 3

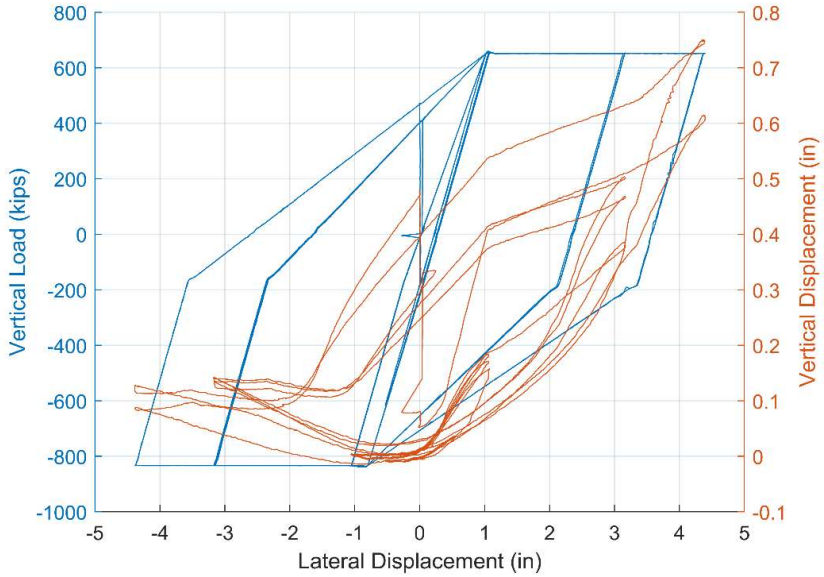

Figure 4.35: Plots of applied vertical load and vertical displacement against lateral displacement for Specimen 3

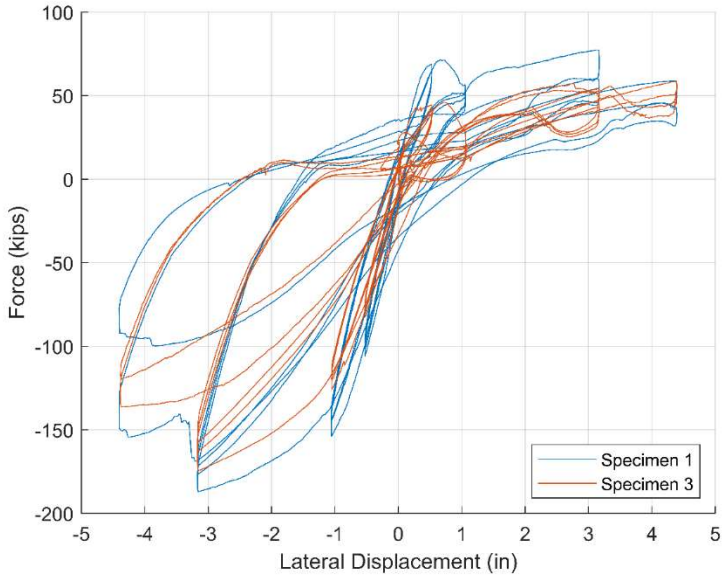

Figure 4.36: Comparison of lateral force-vs.-displacement curves for Specimens 1 and 3

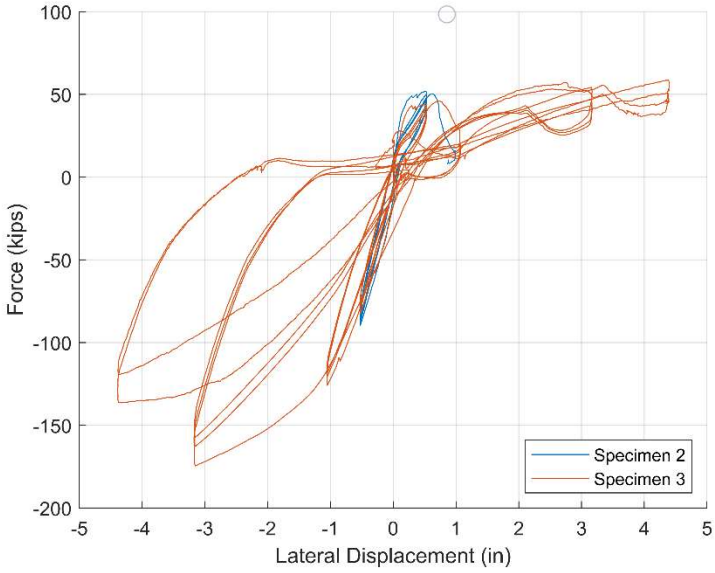

Figure 4.37: Comparison of lateral force-vs.-displacement curves for Specimens 2 and 3

The damage observed from the pile specimen at different drift levels is shown in the pictures in Figures 4.38 through 4.41. Figure 4.38 shows the cracks in the pile specimen at the end of the 3rd load cycle at 0.6% drift ratio. The horizontal crack on the south side near the pile cap occurred in the cycle at 0.3% drift. This was due to the fact that the strands in the shell were unbonded in that region and were thus ineffective in resisting tension. The maximum tensile force of 575 kips was reached in the pile at positive 0.6% drift (towards north). Numerous cracks occurred in the cycles at 1.8% drift, including many vertical cracks, as shown in Figure 4.39. The vertical cracks were probably caused by the slip of the precast shell with respect to the core and the resulting wedging action of the rough interface. However, the slip was small, and was due to the lack of the tensile resistance of the shell near the pile cap because the strands there were unbonded. Some very minor concrete crushing was also observed on the south side at 1.8% drift ratio. Figure 4.40 shows that the horizontal crack on the south side near the pile cap became more severe in the 1st cycle at 2.5% drift, accompanied by some concrete crushing and spalling. Severe

concrete spalling occurred on the south side in the 2nd cycle at 2.5% drift, as shown in Figure 4.41. For this specimen, concrete spalling occurred near the pile cap, while for Specimen 1, it occurred in the region in which the core bars were terminated.

Figure 4.42 shows pictures of close views of the pile specimen near the pile cap. No fracture was observed in the spiral transverse reinforcement. During the demolition of the specimen, a strip of the precast shell was cut and removed to expose the concrete core, as shown in the pictures in Figure 4.43. The pictures show that the only crack in the core was at a location 13 in. away from the soffit of the pile cap, while the crack in the precast shell was 3 in. away from the soffit. The crack in the core was caused by the combined actions of tension and flexure. No crack was observed in the core at the core bar termination point and beyond. This shows that the DYWIDAG bar was effective in preserving the integrity of the concrete core beyond the core bar termination point and thus prohibiting the plying action observed in Specimen 1. As explained in Section 4.2.5, the plying contributed to the formation of a plastic hinge in Specimen 1 near the core bar termination point, which did not occur in Specimen 3.

South

North-East

Figure 4.38: Pictures of Specimen 3 after 3rd cycle at drift ratio of 0.6%

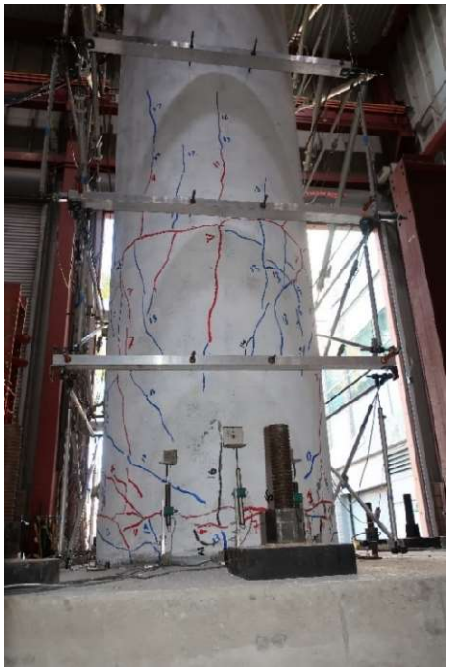

South

North-West

Figure 4.39: Pictures of Specimen 3 after 3rd cycle at drift ratio of 1.80%

South

North-West

Figure 4.40: Pictures of Specimen 3 after 1st cycle at drift ratio of 2.5%

South

North-West

Figure 4.41: Pictures of Specimen 3 after 2nd cycle at drift ratio of 2.5%

South

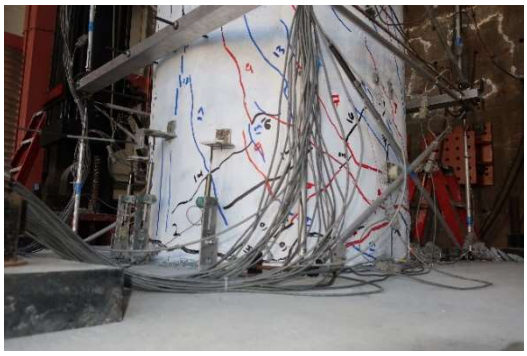

North-West

Figure 4.42: Pictures of close views of Specimen 3 after test

Figure 4.43: Pictures of exposed concrete core of Specimen 3 showing a crack at 13 inches from the soffit of the pile cap (shell removed during demolition)

4.4.2 Data from External Transducers

Figure 4.44 shows the lateral displacement profiles of the pile at the peaks of each displacement cycle. The elevations shown are with respect to the soffit of the pile cap. It can be observed that the deflected shapes were quite linear up to the drift level of 0.6%. Like Specimen

1, at 1.8% drift ratio, a mild kink can be observed at the elevation of 42 in. However, in the cycles at 2.5% drift, the kink does not appear to be as severe as in Specimen 1. The kink can be attributed to the fact that the core was stiffer in the region that had core bars.

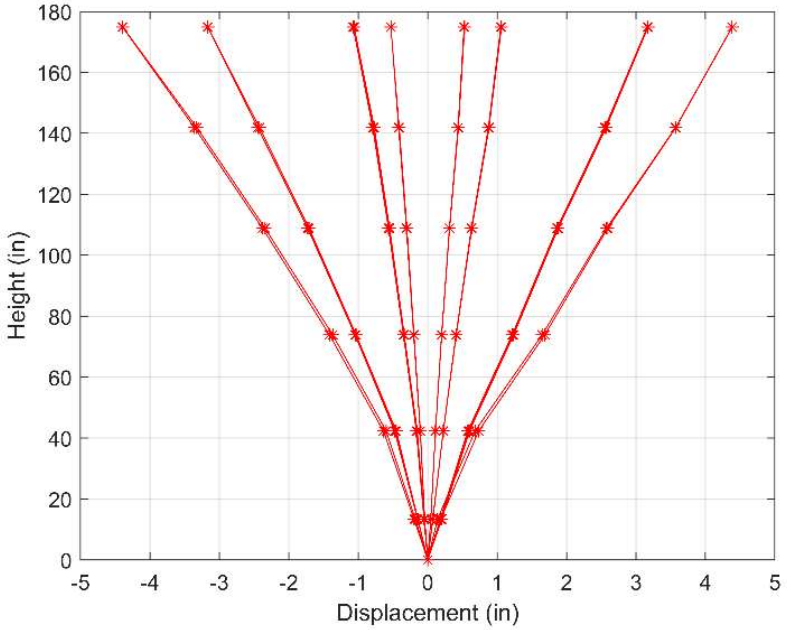

Figure 4.44: Lateral displacements along the height of Specimen 3

Figure 4.45 compares the total rotations measured by the inclinometers with those calculated from the linear potentiometer readings in the last cycle of each drift level. How these values were obtained or calculated is explained in Section 4.2.2. Positive rotation indicates the pile leaning towards north. It can be observed that the rotation values obtained from the two sets of instruments are very consistent. The rotation increased slightly with height in cycles at 0.3% and 0.6% drift levels, showing that the pile had some slight flexural deformation along the height. However, at 1.8 and 2.5% drift levels, the rotation became uniform, showing that the pile began to develop rigid-body rotations near the pile cap. This is attributed to the plastic strain penetration of the core bars as well as the formation of a plastic hinge near the pile cap. In fact, the rotation at the

base of the pile (near the pile cap) contributed to most of the lateral displacement of the pile at all drift levels. The base rotation and the resulting lateral displacement are calculated from linear potentiometers readings obtained at the base in the same way as for Specimen 1 (which is explained in Section 4.2.2). The calculated displacement is plotted against the total lateral displacement directly measured by string potentiometers in Figure 4.46. The figure shows the predominance of base rotation even at low displacement levels.

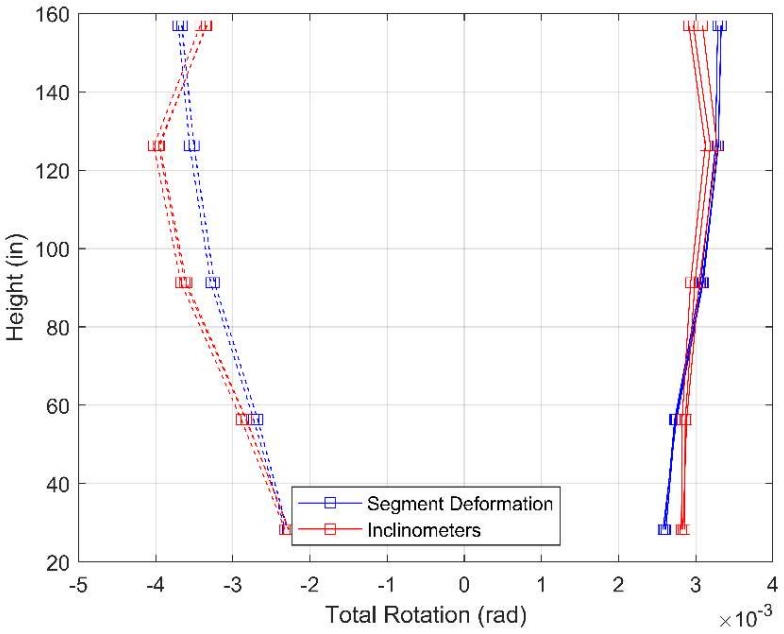

(a) 0.3% drift

Figure 4.45: Pile rotations at different elevations along Specimen 3 measured by inclinometers and linear potentiometers

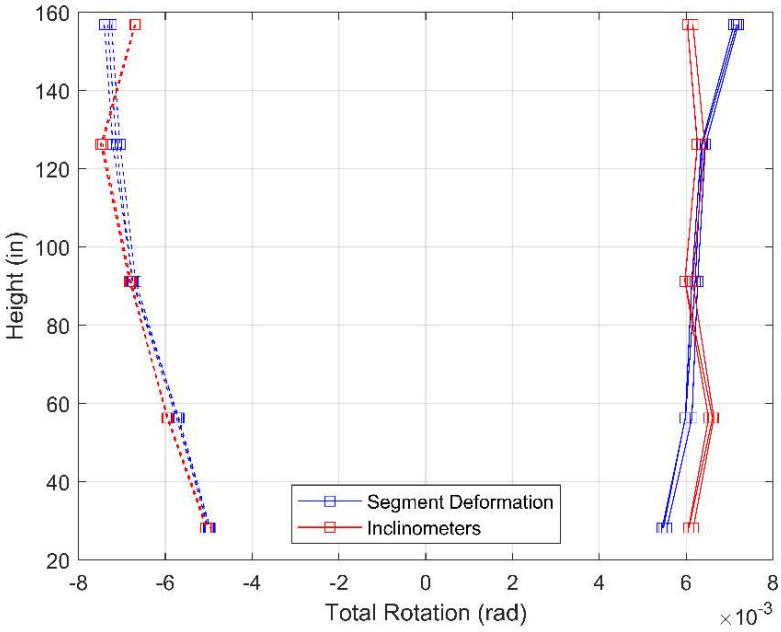

(b) 0.6%

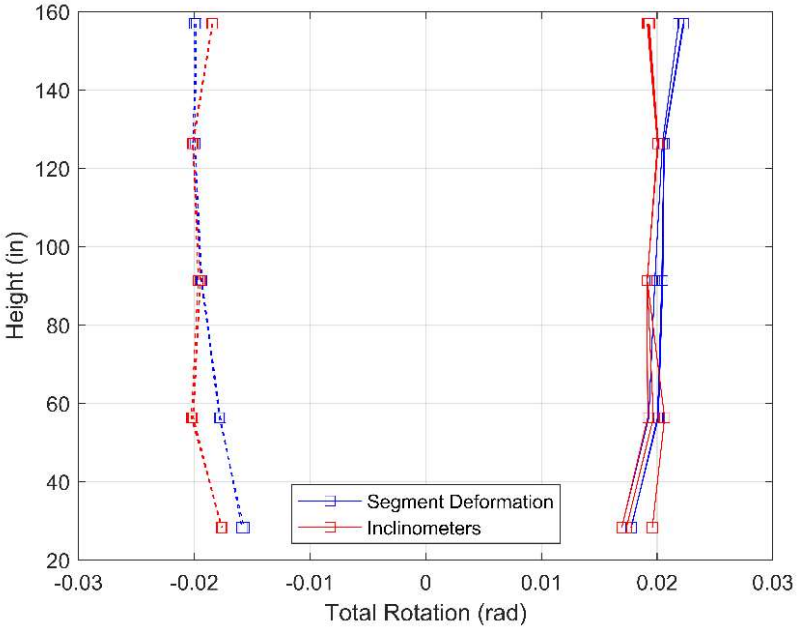

(c) 1.8% drift

Figure 4.45 (continued): Pile rotations at different elevations along Specimen 3 measured by inclinometers and linear potentiometers

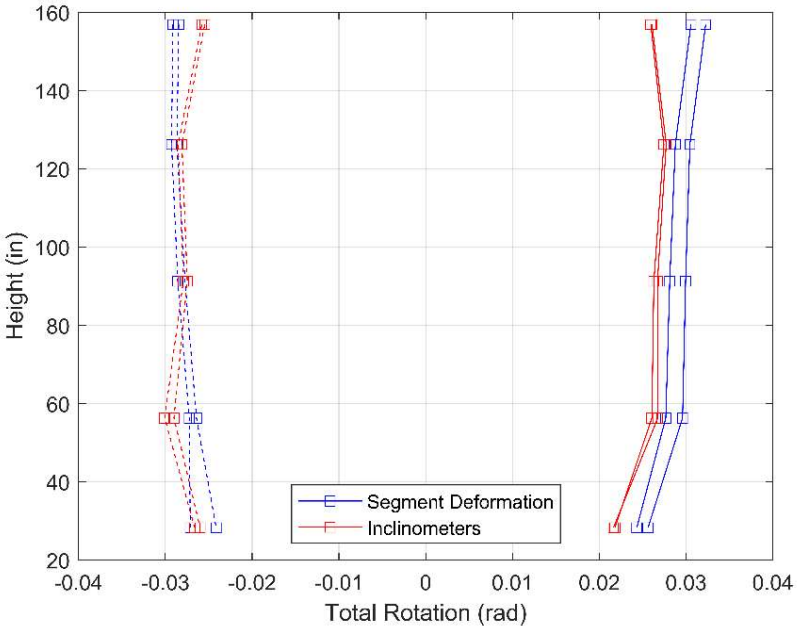

(d) 2.5% drift

Figure 4.45 (continued): Pile rotations at different elevations along Specimen 3 measured by inclinometers and linear potentiometers

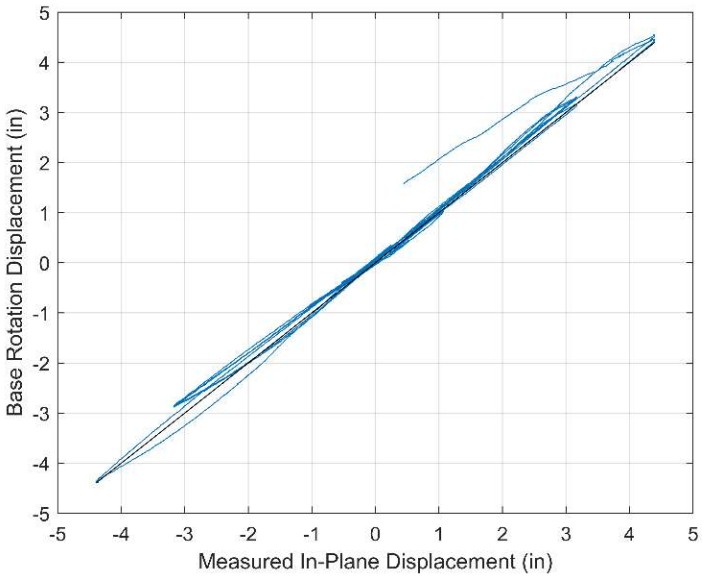

Figure 4.46: Plot of lateral displacement contributed by base rotation against the directly measured total displacement for Specimen 3

Figure 4.47 shows the moment plotted against the curvature for each segment of the pile specimen. Results for Specimen 1 are also shown for comparison. The calculation of the moment and curvature values from the measured data is explained in Section 4.2.2. Similar to the sign convention for the pile rotation, positive curvature corresponds to the pile bending towards north. It can be seen that the curvatures developed in Segments 3 and 4 of Specimen 3 in the cycles at 2.5% drift are much lower than what was observed in Specimen 1 at the same drift level. This can be attributed to the localization of concrete crushing (plastic hinge formation) in that region of Specimen 1, while concrete crushing was observed only near the pile cap for Specimen 3. In Segment 5 (near the pile cap), Specimen 3 had larger curvature developed in the second cycle at 2.5% drift, which was associated with the spalling of concrete in that region. However, the curvature was mainly contributed by the rotation at the pile end as in Specimen 1.

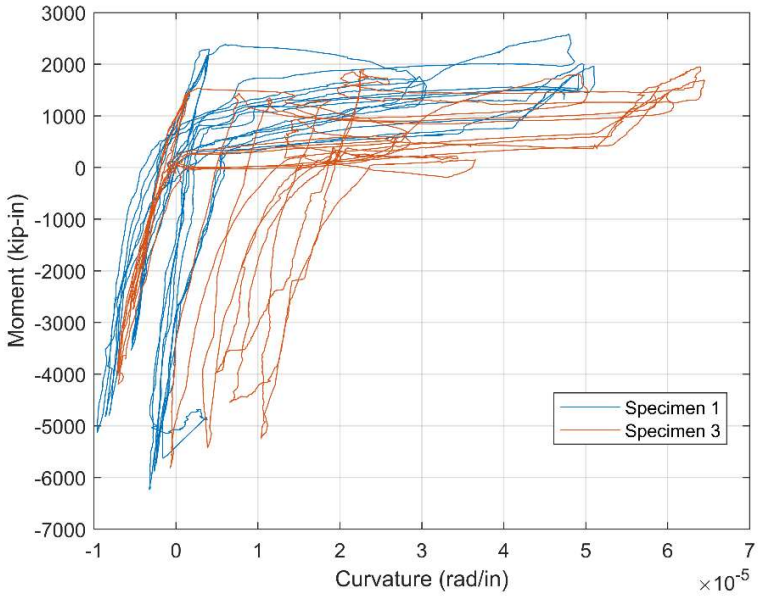

(a) Segment 1

Figure 4.47: Moment-vs.-curvature plots for Specimen 3 (segment locations shown in Figure 4.11)

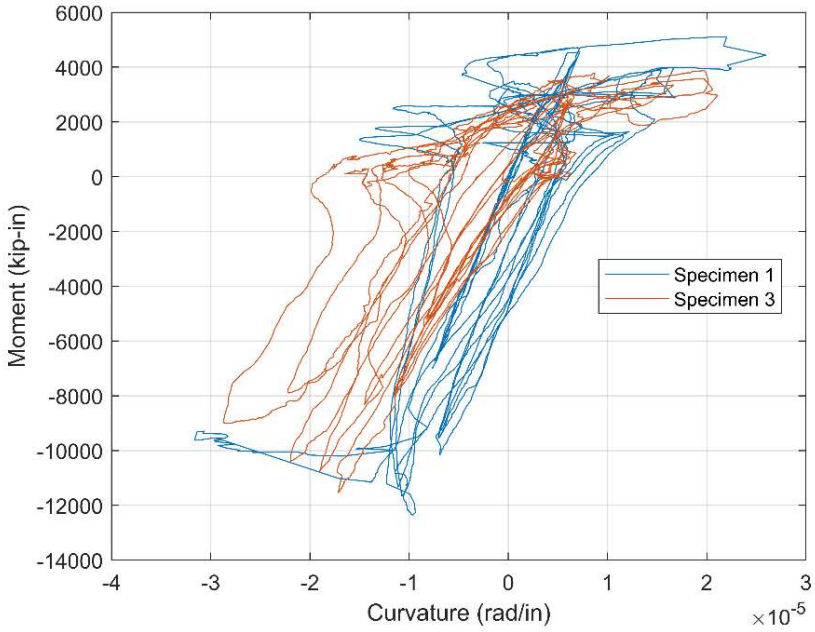

(b) Segment 2

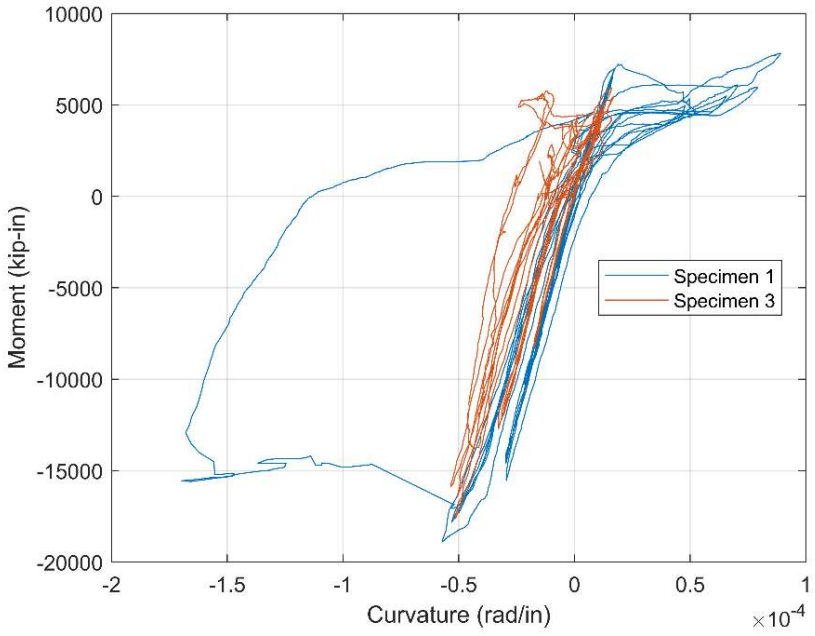

(c) Segment 3

Figure 4.47 (continued): Moment-vs.-curvature plots for Specimen 3 (segment locations shown in Figure 4.11)

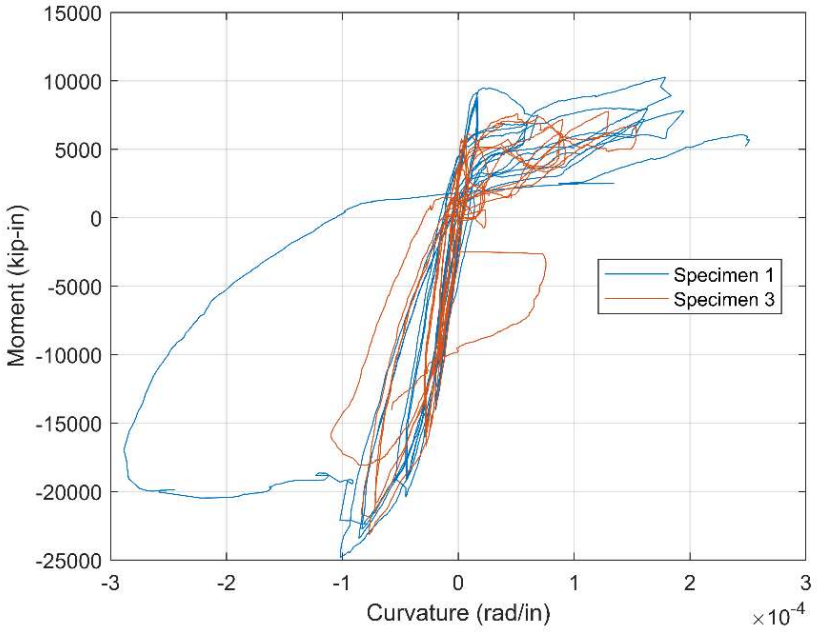

(d) Segment 4

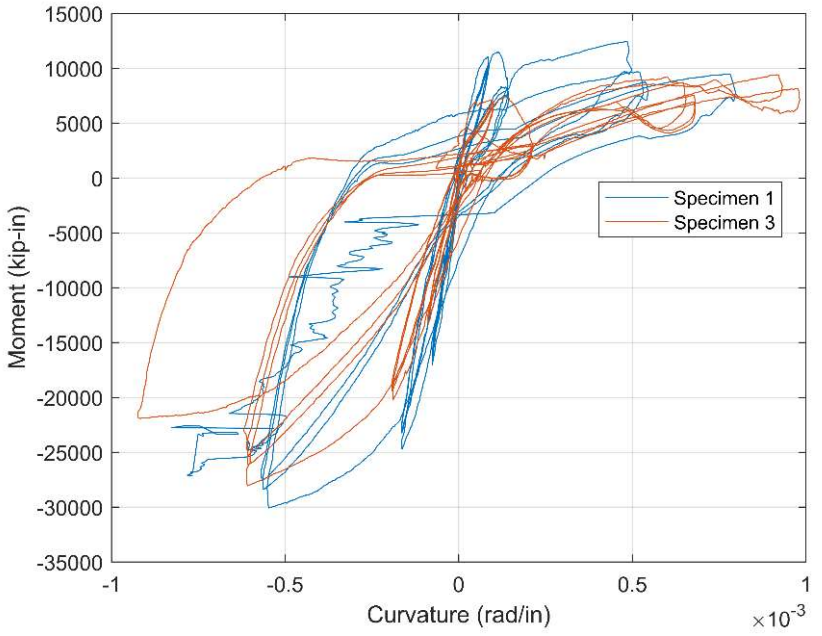

(e) Segment 5 (with pile end rotation included)

Figure 4.47 (continued): Moment-vs.-curvature plots for Specimen 3 (segment locations shown in Figure 4.11)

4.4.3 Data from Strain Gauges

Figure 4.48 shows the distribution of the strains in the extreme north and south core bars at the peaks of each cycle. The core bars in Specimen 3 also had strain gauges installed in the region within the pile cap (as shown in Figure A.22). The zero elevation in vertical axes of the graphs is at the pile end. The core bars had an average yield stress of 46 ksi, corresponding to a yield strain of 0.0016. Both the north and south bars had tensile yielding first occurring at 0.6% drift. Severe tensile yielding started in both bars in the 2nd cycle at 1.8% drift, with the north bar developing a higher tensile strain than the south bar, which was also observed in Specimen 1. The tensile strains were highest at the pile end for both bars. There was no increase in tensile strain as the drift ratio increased from 1.8 to 2.5%. The observation that the north bar developed a higher tensile strain than the south bar even though the pile was subjected to compression when the north bar experienced flexural tension is due to the phenomenon explained in Section 4.2.3 for Specimen 1. This is attributed to the fact that the north bar had a higher tensile strain concentration at the pile end because the south bar was subjected to higher tension early in the test and therefore experienced more severe bond deterioration and slip, resulting in more spread plastic deformation. This is supported by the degrees of plastic strain penetration shown by the strain profiles of the two bars in Figure 4.48.

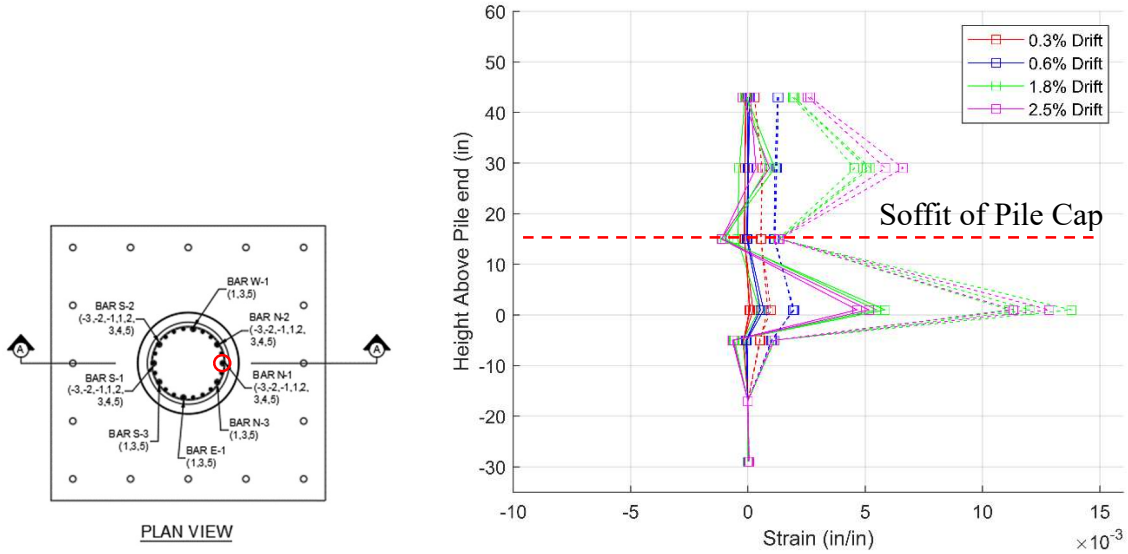

(a) Core bar at extreme north (Bar N-1)

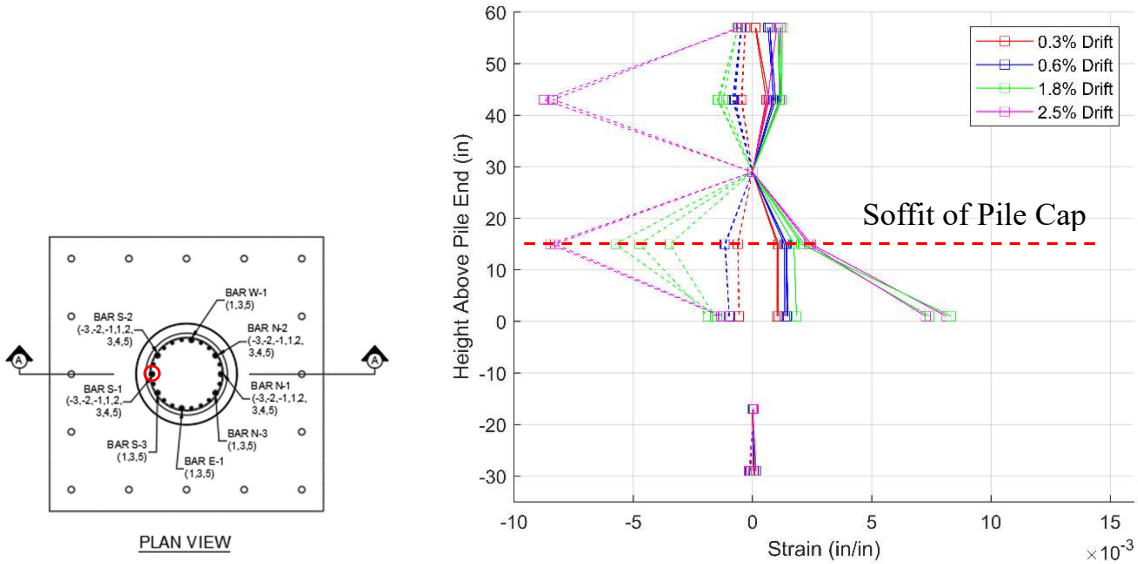

(b) Core bar at extreme south (Bar S-1)

Figure 4.48: Strain profiles of core bars in Specimen 3 at different drift levels (dashed lines are for drifts towards south and the solid lines for drifts towards north; some data points missing for the south bar because of strain gauge malfunctioning)

Figure 4.49 shows the plots of the strains in the extreme north and south core bars against the lateral displacement of the pile specimen. It can be observed that the tensile strains measured by gauge SH25 on the north bar jumped suddenly when the pile was displaced more than 1 in. towards the negative (south) direction, while the tensile strain at the same elevation in the south bar varied more gradually. Before this jump, the tensile strain in the north bar was very small.

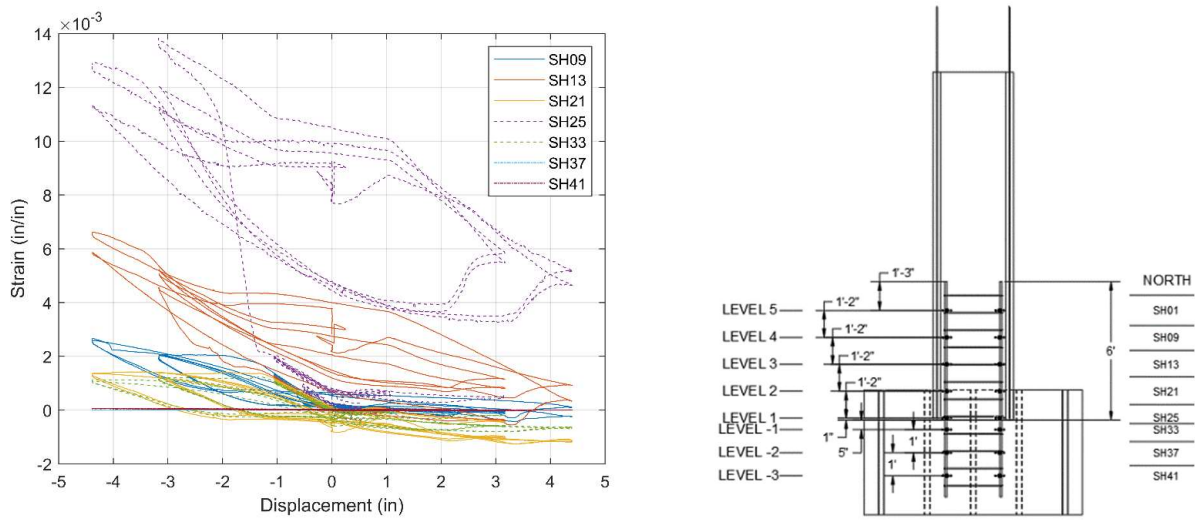

(a) Core bar N-1

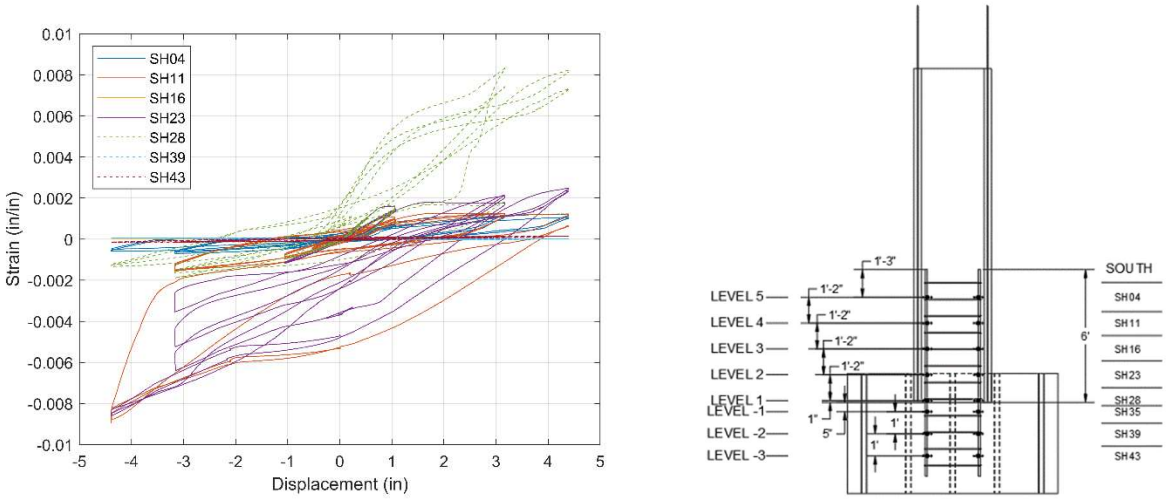

(b) Core bar S-1

Figure 4.49: Strain-vs.-displacement plots for strains measured at different elevations along (a) extreme north and (b) south core bars in Specimen 3

The sudden jump in the tensile strain of the north bar can be attributed to the sudden opening of the construction joint on the north side of the pile end due to flexure, which allowed little time to redistribute the tensile strain in the north bar through slip and resulted in strain concentration at that location. On the south side, joint opening started at low drift levels when the

pile was subjected to high tension. This resulted in a more uniform strain distribution in the south bar through bond slip, as explained before.

Figures 4.50 and 4.51 show the plots of the strains measured on the extreme north and south prestressing strands against the lateral displacement of the pile specimen. Gauge S09 on the extreme south strand is assumed to have zero initial strain because it was in the region the strands were unbonded. For the other gauge locations, the initial strain right before the test and the application of the vertical load from the load stub, load beam, and vertical actuators was estimated to be 0.0039 (based on the effective prestress calculated in Appendix C). The strain due to the application of the vertical load from the load stub, load beam, and vertical actuators was estimated to be 0.45 ksi based on the measured modulus of elasticity of 4,700 ksi for the composite pile section. Hence, the initial strain in the strands is set to be 0.0039 in Figures 4.50 and 4.51.

The strain variation occurred during the test is within ±0.0015, which is much smaller than that occurring in Specimen 1. The strands in Specimen 1 developed very high tensile strains. This difference is attributed to the presence of the DYWIDAG bar in Specimen 3, which carried a significant portion of the axial tension.

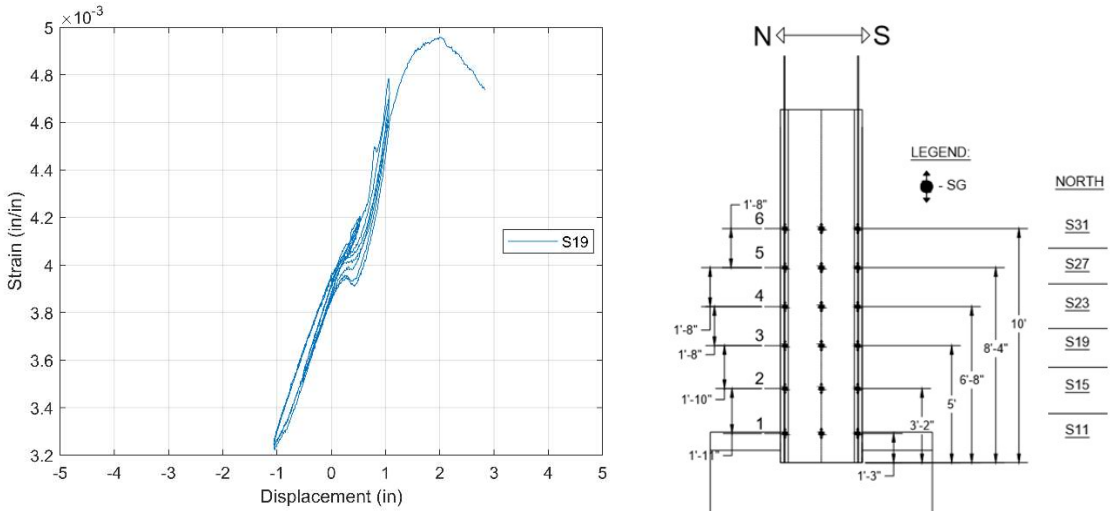

Figure 4.50: Strain-vs.-displacement plots for the north strand in Specimen 3

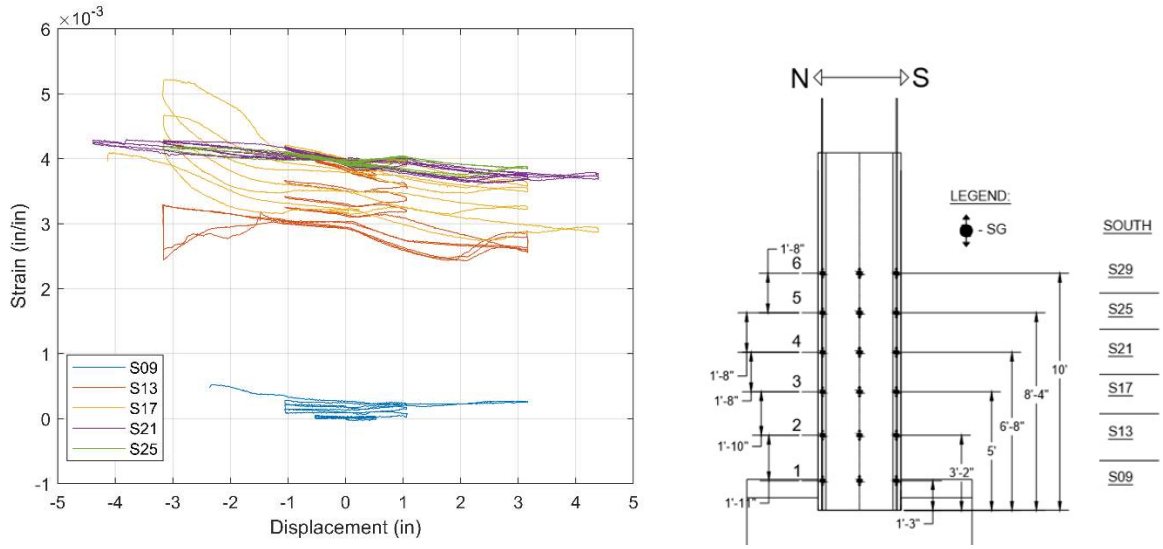

Figure 4.51: Strain-vs.-displacement plots for the south strand in Specimen 3

Figures 4.52 and 4.53 show the strains measured in the transverse reinforcement in the precast shell. The strain gauges were located on the north and south sides of the pile. The level of tensile strains recorded is comparable to that for Specimen 1, with high tensile strains recorded near the soffit of the pile cap and around the core bar termination point.

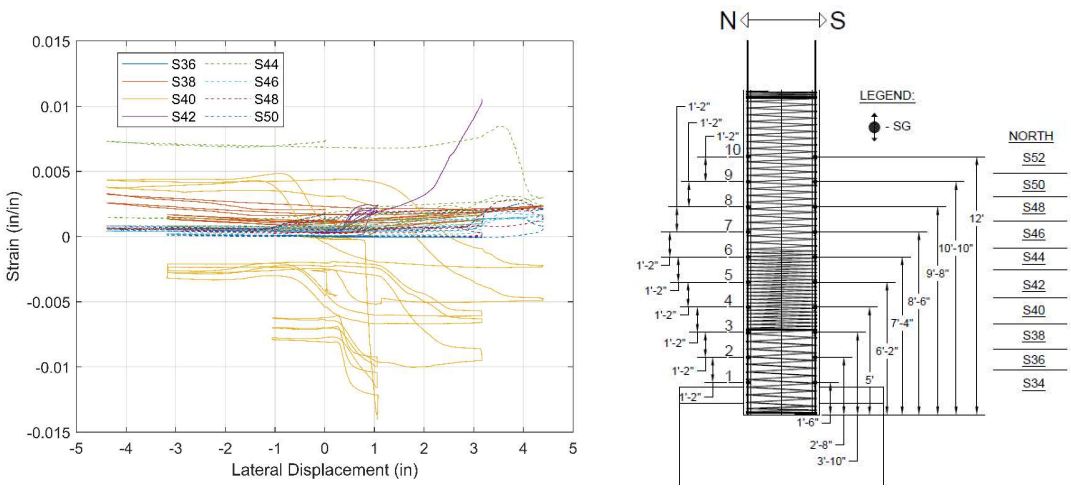

Figure 4.52: Strains in the transverse reinforcement in Specimen 3 (north side)

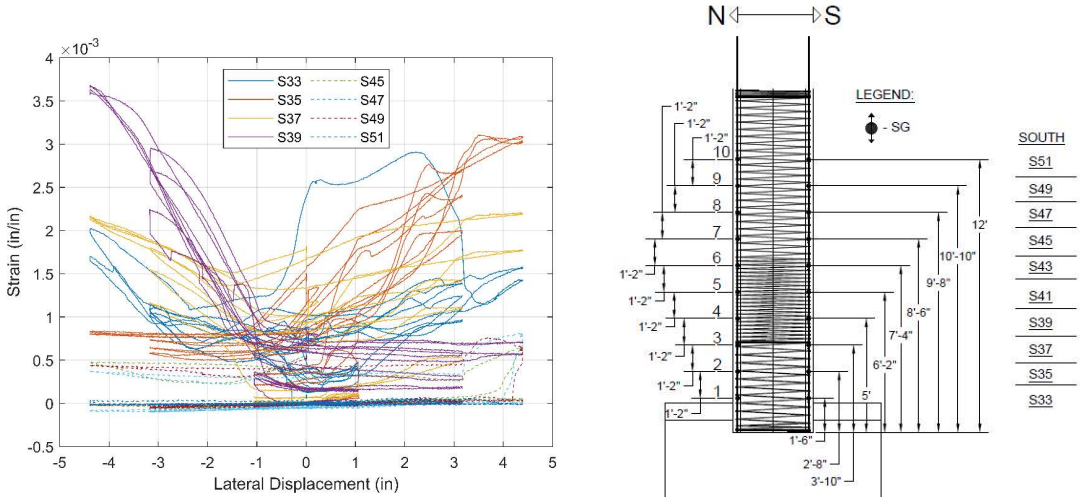

Figure 4.53: Strains in the transverse reinforcement in Specimen 3 (south side)

Figure 4.54 shows the strain profiles of the DYWIDAG bar in Specimen 3 at different drift levels. The strain values are the average of the readings from two strain gauges on opposite sides at each elevation. The zero elevation is at the pile end. At 0.6% drift ratio, the highest tensile strain was measured at the core bar termination point. This strain is about 0.0015. According to the stress-strain plot shown in Figure 3.9, the tensile stress in the bar would be 50 ksi. The cross-sectional area of the bar is 4.08 in. (57-mm diameter). Hence, the bar force developed at that elevation would

be 200 kips, which is far below the guaranteed minimum tension strength of 612 kips. At 2.5% drift ratio, the tensile strain reached in the DYWIDAG bar at the core bar termination point is about 0.002, which corresponds to a bar force of 265 kips. The bar resisted part of the moment developed at that section and part of the net tension of 575 kips exerted on the pile. The precast shell resisted the rest of the moment as well as most of the remaining tensile force on the pile. The concrete core might have provided a small portion of the tensile resistance. Based on the tensile strain of 0.002 measured in the DYWIDAG bar and the fact that the only crack observed in the core was 13 in. from the soffit of the pile cap (see Figure 4.43), away from the core bar termination point, the DYWIDAG bar must have slipped. Otherwise, the core concrete would have cracked at the core bar termination point based on the tensile strain measured in the bar. The slip of the DYWIDAG bar allowed the tensile strain to be accommodated by the opening of the crack in the core 13 in. from the soffit. Furthermore, Figure 4.55 shows that the strain readings from the bar at the pile-tip and the soffit elevations are very close to each other, indicating possible slip of the bar in that region.

At 1.8 and 2.5% drift levels, the DYWIDAG bar had the highest tensile strain occurring at the pile end, and, at 2.5% drift, this strain reached 0.0025, which corresponds to a tensile force of 326 kips. However, at 0.6% drift ratio, the bar strain near the pile end was substantially lower than that at the core bar termination point. The jump in strain at that end when the pile was displaced from 0.6 to 1.8% drift was most likely caused by the cracking of the core. The maximum average tensile strain of 0.0025 measured in the DYWIDAG bar is at the proportional limit of the bar stress-strain curve shown in Figure 3.9.

The strains measured right below the anchor plate at the top end of the bar (the bottom end in an actual pile) are very small, indicating negligible bar slip occurring in the top region.

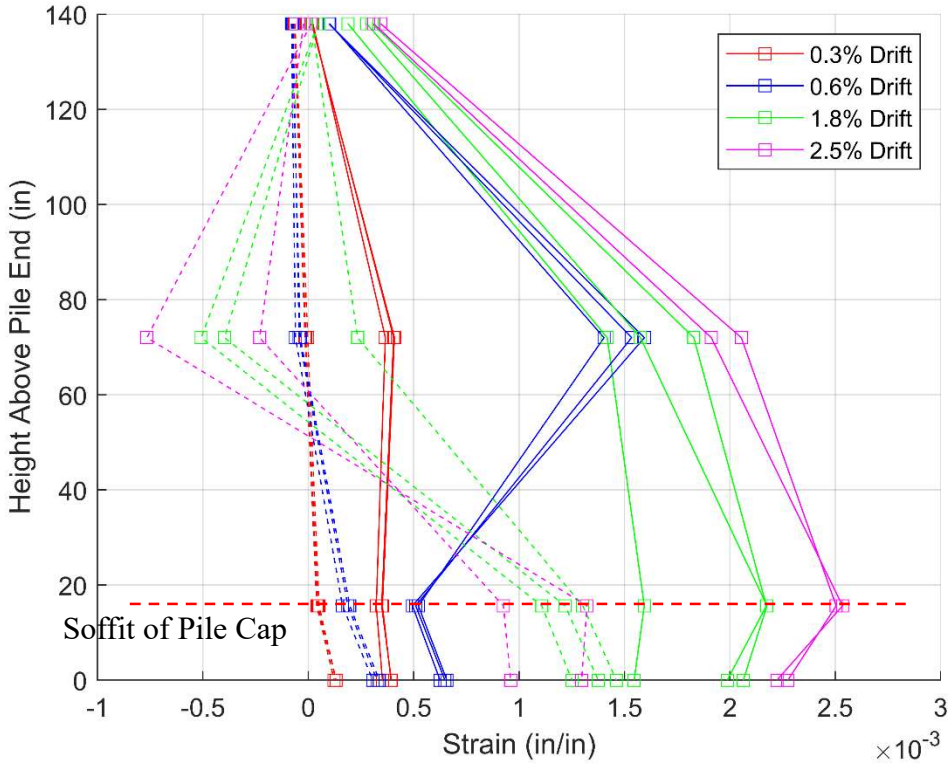

Figure 4.54: Strain profiles of DYWIDAG bar in Specimen 3 (dashed lines are for drifts towards south and the solid lines for drifts towards north)

Figure 4.55 shows plots of the strains measured in the DYWIDAG bar by individual gauges against the lateral drift ratio. It shows that the localized strain measured by gauge SD03 in the bar reached 0.004, which is in a mildly nonlinear regime of the stress-strain curve for the bar.

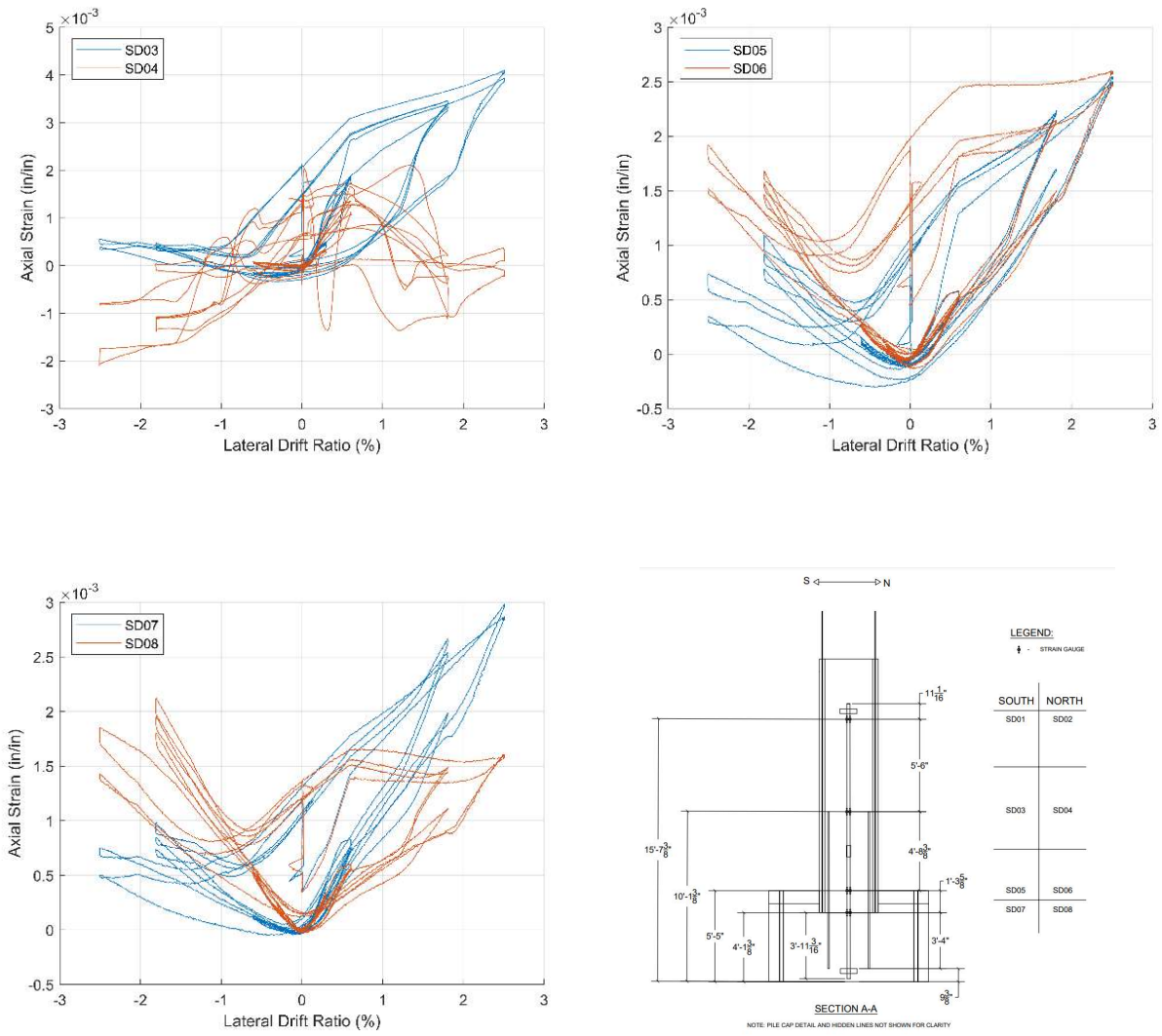

Figure 4.55: Strain–vs.–drift ratio plots for DYWIDAG bar in Specimen 3

4.4.4 Concluding Remarks

Results from the Specimen 3 test have shown that the DYWIDAG bar was effective in preserving the structural integrity of the concrete core, which could otherwise have cracked at the section where the core bars connecting the pile to the pile cap were terminated when the pile was subjected to high tension. Specimen 2 had shown that the cracking of the core at that location would immediately pass all the axial tension to the precast shell, causing the slip of the shell and the subsequent tensile failure of the pile because the unbonded strands near the pile cap were

unable to carry tension. This could also result in severe plying action between the shell and the core segment between the crack and the pile cap, causing a bursting failure of the shell and the subsequent loss of the moment capacity of the pile near the pile cap. Prohibiting the cracking of the concrete core at the core bar termination point allowed a longer distance to transfer the axial tension from the core to the shell and thus prevented the slip of the shell. The maximum tensile force experienced by the bar was 326 kips, while the bar had a minimum guaranteed tensile strength of 612 kips. The bar barely reached the proportional limit of its stress-strain relation.

In Specimen 3, the DYWIDAG bar had one end anchored in the pile cap and the other end anchored in the pile at 70 in. (31 x bar diameter) beyond the core bar termination point, with an anchor plate at each end. The diameter (d_b) of the bar was 2.25 in. The maximum tensile strain measured near the end anchored in the pile was very small (about 0.0004). Hence, extending the DYWIDAG bar beyond the core bar termination point for a length of 31 d_b is deemed sufficient as long as the state of deterioration or damage in the pile is comparable to that of Specimen 3. In Specimen 3, the unbonding of the prestressing strands (simulated strand damage) was limited to the region near the pile cap where core bars were present, and there was no damage induced on the transverse reinforcement or prestressing strands beyond the core bar termination point prior to the test. To determine an adequate termination point for the DYWIDAG bar used to retrofit an actual bridge pile, the state of damage of the precast shell and the extent of corrosion of the steel within the shell should be considered. Regardless, the use of an anchor plate at each end is recommended for added safety.

It should also be noted that in spite of the presence of the DYWIDAG bar, the lateral load capacities of Specimen 3 were a little lower than the capacities of Specimen 1 in both loading directions (whether the pile was in tension or compression). Hence, the increase in flexural strength

provided by the bar was not sufficient to offset the loss of the strength caused by the unbonding of the strands in the plastic-hinge region. This was partly because of the location of the bar and partly due to the bond-slip developed in the bar. However, compared to Specimen 1, Specimen 3 retained higher lateral strength on the compression side and comparable strength on the tension side in the final displacement cycle at 2.5% drift ratio.

4.5 Moment Capacity Assessment of Pile Specimens

Axial load – moment (P-M) interaction diagrams have been developed to examine if the moment capacities of Specimens 1 and 3 observed in the tests can be predicted analytically. Specimen 1 represented an undamaged as-built pile while the other a damaged pile with retrofit. Since Specimen 2 failed prematurely in axial tension due to the slip of the precast shell before reaching its moment capacity under compression, it is excluded from consideration. Pile sections at two locations, as shown in Figure 4.56, are considered for the P-M curves. One is the section at the soffit of the pile cap, and the other is the section at the core bar termination point. The properties of the concretes and reinforcing steel used to generate the P-M curves are based on the measured properties presented in Section 3.4. As shown in Figure 4.56, each pile cross-section consists of areas with different concrete properties due to the different concretes used and the presence or absence of confinement.

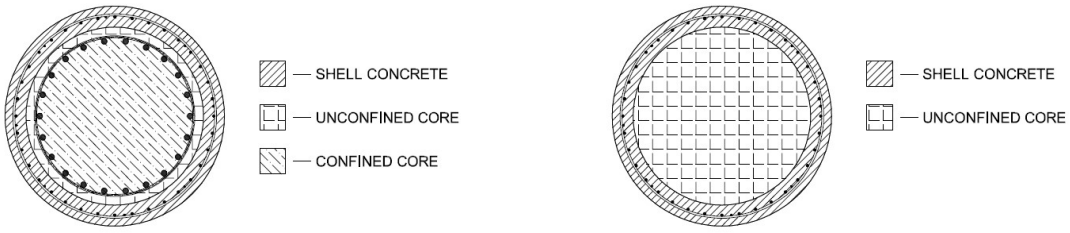

(a) Section at soffit of pile cap (b) Section at core bar termination

Figure 4.56: Pile sections analyzed

In the analysis, the confinement provided by the spirals within the precast shell is ignored. This stems from the consideration that the shell was relatively thin and its confinement would be rendered ineffective once the concrete started to spall. Hence, the shell concrete is assumed to be unconfined with the compressive strength equal to 11 ksi, which is the average strength of the shell concretes in Specimens 1 and 3 from cylinder tests. At the section at the pile cap, where #9 longitudinal bars and #3 hoops are present in the core, the core concrete outside the perimetrical centerline of the horizontal hoops is considered as unconfined and that within is confined, with an unconfined compressive strength of 4 ksi, which is the average from cylinder tests. For the confined core, the confinement consists of #3 hoops spaced at 9 in. on center. For the section at the core bar termination point, both the shell and core are considered as unconfined. The compressive stress-strain relation of the confined concrete is simulated with the model of Mander et al. (1988). The compressive stress-strain relations of the unconfined concretes are simulated with Mander et al.'s model up to the peak stress, and are represented by a straight declining line from the peak to zero stress. The slope of the declining line is based on the data presented in Papadopoulos and Shing (2015). The compressive stress-strain relations of the concretes are shown

in Figure 4.57. The tensile strength of the concretes is assumed to be $7.5\sqrt{f_c'}$, with the stress in psi, which has a negligible influence on the moment capacity.

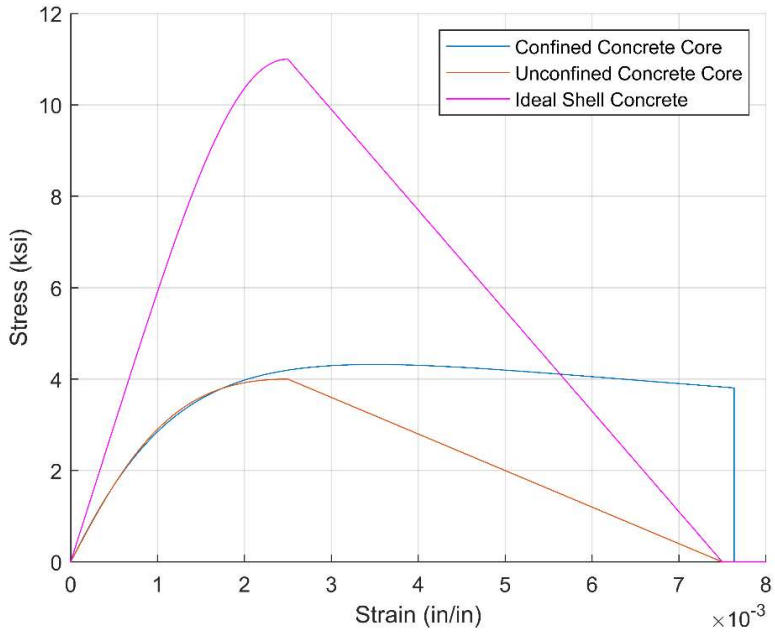

Figure 4.57: Compressive stress-strain relations of concretes

As discussed in Sections 4.2.1 and 4.2.4, in Specimen 1, the plying action of the cracked concrete core against the precast shell caused severe cracking in the shell in the region near the core bar termination point, and thus weakened the concrete in compression and reduced the moment capacity, leading to the formation of a plastic hinge in that region. To account for this phenomenon in the analysis, a concrete model with reduced strength and ductility is also considered for the shell. The stress-strain relation for this model is labeled as "weakened shell concrete" and is compared to that for the "ideal shell concrete" in Figure 4.58. The latter represents the behavior of the shell concrete without the plying action. The former relation is determined empirically by trial and error until the moment capacity measured from Specimen 1 at the core bar termination point at 910-kip compression can be matched by the P-M curve. This exercise is to

demonstrate that the weakening of the shell concrete due to the plying action could indeed contribute to the reduction of the moment capacity of Specimen 1 at the core bar termination point, in the absence of other verifiable reasons.

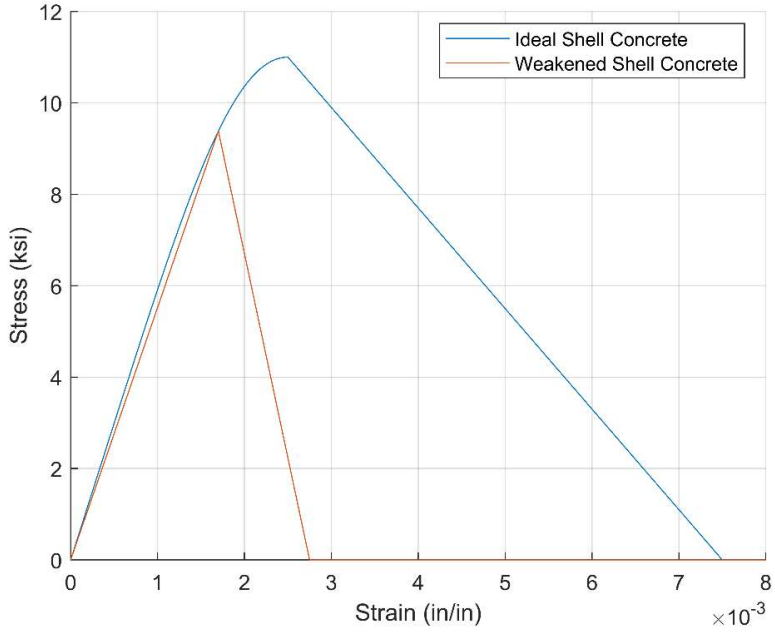

Figure 4.58: Compressive stress-strain relation of concrete weakened by plying action

The stress-strain relations adopted for the reinforcing steel are shown in Figure 4.59. They are the same for tension and compression. In the figures, the relations are compared to data from tension tests. The stress-strain relation adopted for the core bars is a tri-linear curve, and so is that for the DYWIDAG bar, for which the stress remains constant when the strain is between 0.01 and 0.065 and drops to zero when the strain is beyond 0.065. The stress-strain relation for the prestressing strands is calculated with the following equation proposed by Devalapura and Tadros (1992).

$$f_p = \varepsilon_p \left[A + \frac{B}{\left(1 + \left(C\varepsilon_p\right)^D\right)^{1/D}} \right] \leq f_{pu} \tag{4.6}$$

in which ε_p is the strain in the strand, f_p is the corresponding stress in ksi, f_{pu} is the tensile strength, and A, B, C, and D are modeling parameters whose values are to be determined from tensile test data. Based on the results of the tensile tests presented in Section 3.4, f_{pu} = 292 ksi, A = 18.5, B = 30,803, C = 109, and D = 9.35.

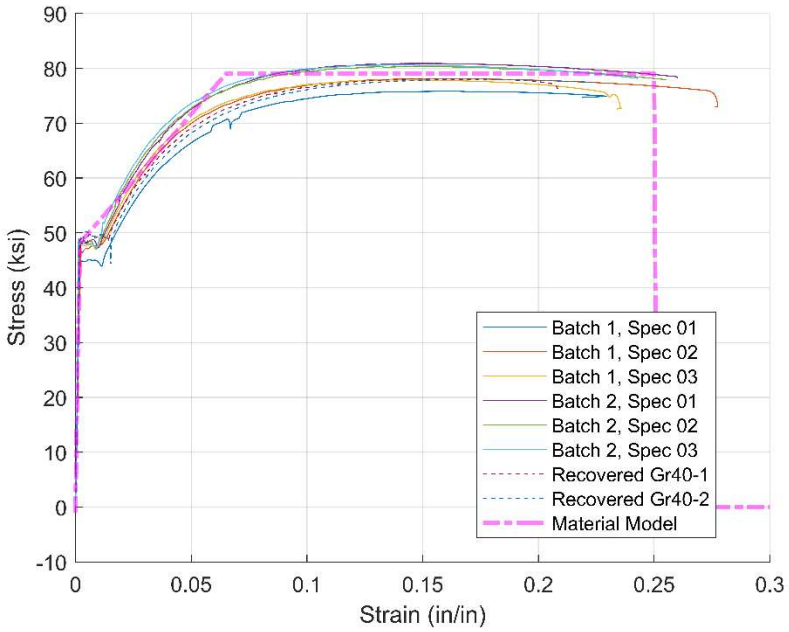

(a) #9 core bars

Figure 4.59: Steel models

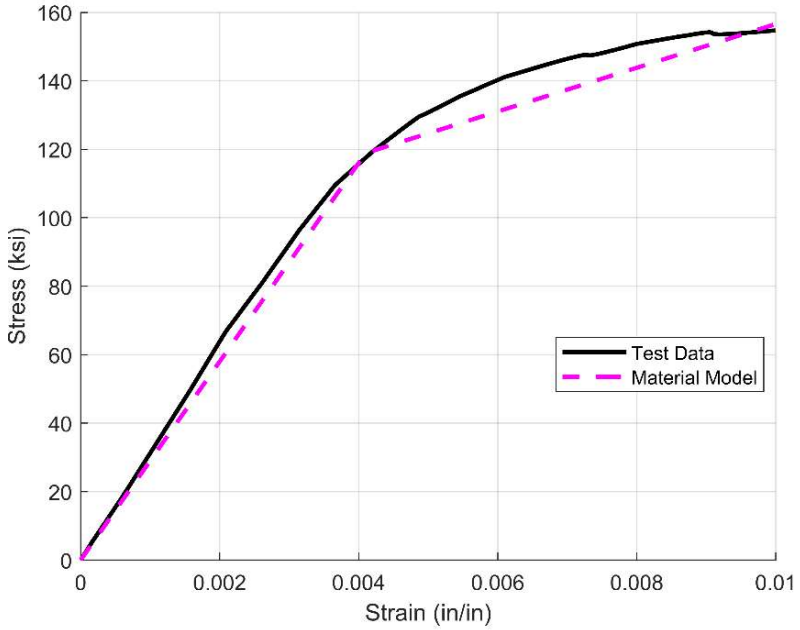

(b) DYWIDAG bar

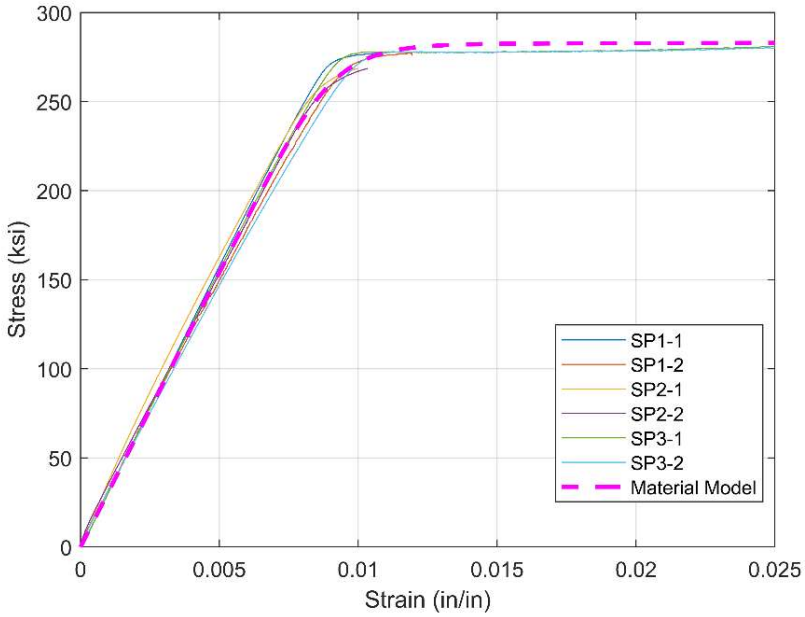

(c) Prestressing strands

Figure 4.59 (continued): Steel models

To generate the P-M curves, it is assumed that the strain at the extreme compression fiber of the pile section is equal to 0.003 when the moment capacity is reached. The stresses in the reinforcing bars and prestressing strands are determined with the strain compatibility assumption, assuming zero bond-slip. The effective prestress in the strands before the application of the axial load and moment is taken to be 132 ksi, which is the average of the effective prestresses estimated for Specimens 1 and 3 as presented in Appendix C. The core concrete and bars have zero initial strains, while the precast shell has an initial strain of -0.0002 induced by the effective prestress.

The P-M curves for the pile section at the soffit of the pile cap are shown in Figure 4.60, with the positive axial load representing compression. As shown, three reinforcement scenarios are considered. One represents an ideal condition that the strands and core bars are fully effective without any debonding of the strands. The second has only core bars, representing the condition that all the strands are unbonded and are thus ineffective in resisting loads. The third scenario has core bars as well as a DYWIDAG bar at the center, representing the condition of Specimen 3. The concretes have the stress-strain relations shown in Figure 4.57. Figure 4.60 shows that the strands have a major contribution to the moment capacity of the pile for the tension-controlled region of the P-M curve, while the influence of the DYWIDAG bar is small, which is due to the bar location. In the compression-controlled region, the presence of the strands leads to a lower moment capacity as expected.

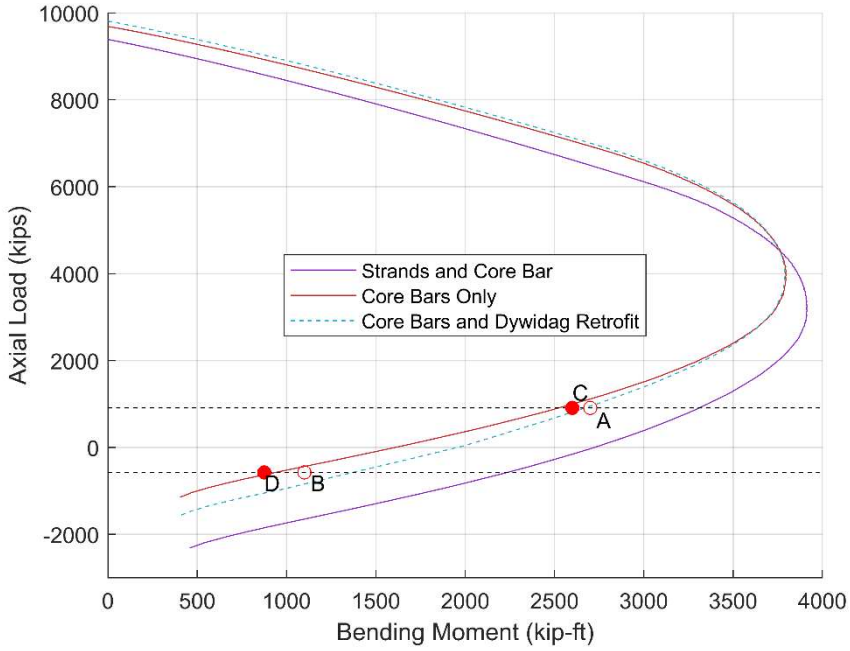

Figure 4.60: Pile section at the soffit of pile cap

The P-M curves for the section at the core bar termination point are shown in Figure 4.61. There are three scenarios. One has only strands with the shell concrete and unconfined core having the stress-strain relations shown in Figure 4.57. This represents an ideal condition. The second has the same reinforcement condition as the first, but it has the shell concrete assuming the more brittle behavior shown in Figure 4.58 to reflect damage introduced by the plying action of the core against the precast shell (as observed in Specimen 1). The third scenario represents Specimen 3, which was retrofitted with a DYWIDAG bar, and it has the same material properties as the first scenario. The figure shows that the influence of the DYWIDAG bar on the P-M curve is small. However, the behavior of the shell concrete has a very significant influence on the P-M curve, except when the section is subjected to a very high axial tension.

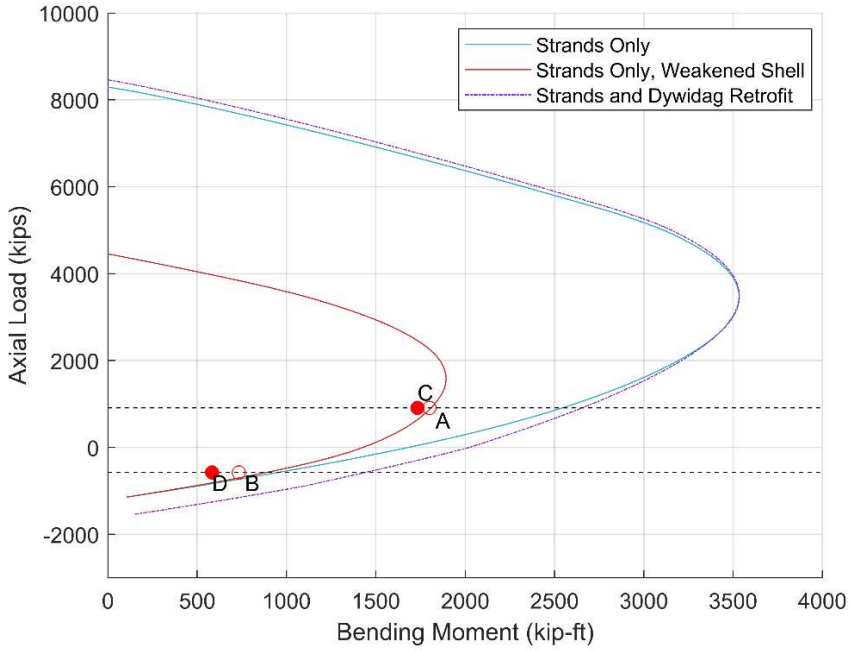

Figure 4.61: Pile section at core bar termination point

Figures 4.60 and 4.61 also show the maximum moments reached at the respective sections of Specimens 1 and 3 in the tests under the maximum tension and compression. Points A and B in the figures are data from Specimen 1 for the axial compression of 910 kips and the axial tension of 575 kips, respectively, while C and D are data from Specimen 3 for the same axial load conditions. It should be noted that the maximum moments attained in the tests may not necessarily represent the moment capacities at the sections because the moment capacity was only reached in one critical section of each specimen. Specimen 1 had the plastic hinge developed near the core bar termination point. This is consistent with the comparison shown in Figure 4.60 that the maximum moments attained in Specimen 1 at the soffit level (indicated by points A and B) are way below the moment capacities given by the P-M curve that considers both the strands and the core bars. Figure 4.61 shows that the formation of the plastic hinge at the core bar termination point of Specimen 1 under the axial compression of 910 kips (point A) can only be confirmed by

the P-M curve considering the weakened shell, and the curve with ideal shell concrete (the "strands only" case) way over-predicts the capacity.

Specimen 3, which was retrofitted with a DYWIDAG bar, had the plastic hinge developed near the soffit. As shown in Figure 4.60, for the section at the soffit of Specimen 3, the maximum moment attained in the test at the compressive load of 910 kips (point C) is very close to but slightly less than that predicted by the P-M curve that considers the DYWIDAG bar, while the maximum moment attained at the tensile force of 575 kips (point D) is significantly less than that from the P-M curve. As the data have shown, these discrepancies can be attributed to the slip of the DYWIDAG bar and core bars in the test, which resulted in bar strains and stresses much lower than those attained in the P-M curve, which does not account for bar slip. The DYWIDAG bar prohibited the development of the plying action, which occurred in Specimen 1, by preventing the cracking of the core at the core bar termination point. Hence, in Figure 4.61, for the section at the core bar termination point, the P-M curve that considers both the strands and the DYWIDAG bar is based on the ideal shell concrete property. As shown in the figure, the maximum moments (points C and D) reached in the test are way lower than those given by the P-M curve, which is consistent with the fact that the section did not develop a plastic hinge in the test.

The results presented here have shown that the weakening of the shell concrete in the region near the core bar termination point due to the aforementioned plying action should be considered in calculating the moment capacity of an un-retrofitted pile. Furthermore, it has been shown that the influence of bar slip on the moment capacity of a pile section near the soffit of the pile cap is very significant. Data from the tests and P-M interaction analyses show that ignoring bar slip can over-estimate the bar tensile strain by a factor of three. For all practical purposes, the contribution

of a DYWIDAG bar to the moment capacity of a retrofitted pile can be ignored. The small increase in moment capacity from the bar can be entirely offset by bar slip.

Chapter 4 is, in part, a reprint of the material in a California Department of Transportation report entitled "Assessment of Seismic Performance of Coronado Bay Bridge Piles with and without Simulated Damage and the Effectiveness of a Retrofit Method." The authors of the report are: P. Benson Shing, Dimitrios Kalliontzis, and the author of the dissertation. Professor Dimitrios Kalliontzis provided the pre-test analysis, and much of the design of the test specimens and was extensively involved in the tests of the first two specimens. The author of the dissertation provided the design of several testing components and the post-test analysis of all test specimens, and was responsible for the design and testing of the third specimen.

Chapter 5 Recommendations for Pile Evaluation and Retrofit

5.1 Introduction

This chapter provides recommendations on criteria that can be used for the seismic safety assessment and retrofit of piles in the Coronado Bay Bridge. The recommendations are based on the experimental results obtained in this study, as presented in Chapter 4.

5.2 Retrofit Need Assessment

If the prestressing strands in the precast shell have lost bonding in the region near the pile cap, due to damage caused by pile driving, the shell will lose its tension capacity and may develop a horizontal crack in that region when the pile experiences a large tensile force during an earthquake. The concrete core may also crack at the core bar termination point. Once these cracks occur, tension will be transmitted to the rest of the pile through interface shear between the precast shell and the core over a length l_1, which is the vertical distance between the horizontal crack in the shell and the crack at the core bar termination point, as shown in Figure 5.1. The location of the crack in the shell can be conservatively estimated to be at the end of the strand debonded region. The interface shear demand in the stress transfer region can be calculated as:

$$\tau_D = \frac{P}{\pi D_I l_1} \tag{5.1}$$

in which P is the axial tensile force exerted on the pile and D_I is the inner diameter of the precast shell. For the design earthquake, if τ_D will exceed the shear transfer resistance at the interface, then retrofit is needed to prevent the tension failure of the pile. Tension failure is undesirable in that it could be followed by the bursting failure of the shell near the pile cap due to the plying acting between the precast shell and the core.

Results from the test of Specimen 2, as discussed in Chapter 4, indicate that the shear transfer resistance between the shell and the core was about 0.10 ksi. However, this shear resistance depends on the roughness of the inner surface of the shell. For the test specimens, the inner surface of the shells was not perfectly smooth as the hollow core was formed by Styrofoam during casting. Hence, it will be helpful to identify the type of precast forms used for the actual piles in the bridge, and thereby the condition of the inner surface. If such information is not available, the shear transfer resistance may be assumed to be 0.05 ksi, provided that there is no separation between the core and the shell due to the drying shrinkage of the core concrete, which was placed after the shell had been installed. This criterion is believed to be conservative considering that not all the strands in the pile have the complete loss of bonding near the pile cap.

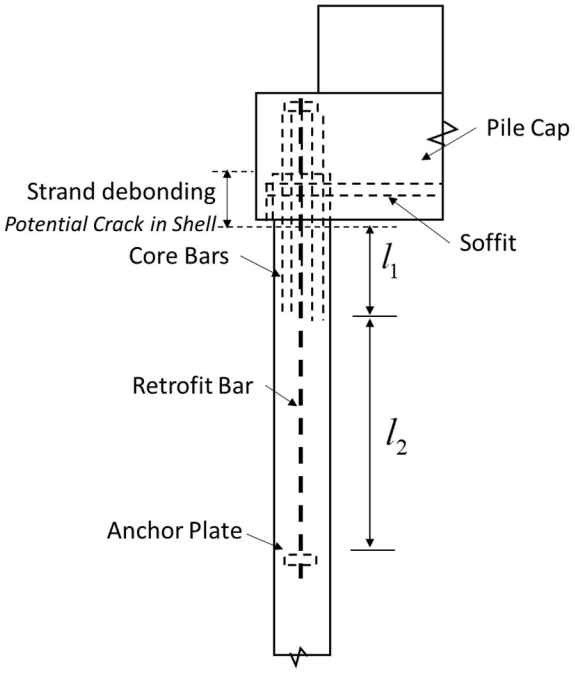

Figure 5.1: Pile retrofit scheme

5.3 Retrofit Method

The retrofit method using a DYWIDAG bar was proven to effective in this study. In the 7/9-scale pile specimen studied here, a W57 (57-mm diameter) Grade 150 Threadbar® was used. It had a minimum tensile capacity of 612 kips, which was about 70% of the total nominal tensile capacity of the 22 Grade 40 #9 core bars in the specimen. For a full-scale pile, a W75 Grade 150 Threadbar® or equivalent will be adequate. The bar should have an anchor plate at each end. In Specimen 3, the distance l_2, shown in Figure 5.1, was equal to $31\,d_b$, where d_b is the diameter of the bar. This distance appeared to be adequate in that the tensile stress developed in the bar near the anchor plate was very small. Beyond that point, the axial tension in the pile was practically carried by the precast shell. For added factor of safety, it is recommended that l_2 be no less than $60\,d_b$ and preferably extend beyond the expected flexural inflection point in the pile.

To install the retrofit bar in a pile, a hole needs to be drilled in the center of the core. After the placement of the bar inside the hole, the hole can be filled with high-strength, low-shrinkage concrete. The wall of the drilled hole has to be roughened to ensure good bonding between the old and the new concretes so that the tensile force in the bar can be effectively transmitted to the shell.

Before real pile retrofit is going to be performed on the bridge, it is highly recommended that the retrofit procedure be tried in one or more piles in a non-critical pier to ensure that the procedure is practical and doable in the field. Furthermore, in the trials, tension tests should be performed on the bars installed to make sure that the bonding between the old and the new concretes is adequate.

Chapter 5 is, in part, a reprint of the material in a California Department of Transportation report entitled “Assessment of Seismic Performance of Coronado Bay Bridge Piles with and

without Simulated Damage and the Effectiveness of a Retrofit Method." The authors of the report are: P. Benson Shing, Dimitrios Kalliontzis, and the author of the dissertation. Professor Dimitrios Kalliontzis provided the pre-test analysis, and much of the design of the test specimens and was extensively involved in the tests of the first two specimens. The author of the dissertation provided the design of several testing components and the post-test analysis of all test specimens, and was responsible for the design and testing of the third specimen.

Chapter 6 Summary and Conclusions

6.1 Introduction

This dissertation presents two studies aimed at assessing the seismic performance of existing and new bridge structures. The first study had the goal of determining a retrofit methodology that would restore the performance, and increase the ductility, of damaged piles in the Coronado Bay Bridge, as well as providing assessment tools to determine how the piles would behave under combined axial load and bending moment.

6.2 Summary, Main Observations and Conclusions of Study 1

6.2.1 Testing of Coronado Bay Bridge Piles

In this study, and as explained in Chapter 3, three 7/9-scale specimens were tested to investigate how the inspected damage affected the performance of the foundation piles, and a retrofit was designed and tested in the third pile Specimen. The pile specimens that were tested represented a prototypical Type-II pile in Pier 22 of the bridge. The piles were composed of prestressed, precast concrete shells with cast-in-place concrete cores. Specimen 1 represented an undamaged, as-built pile, whereas Specimens 2 and 3 had prestressing strands in the shell debonded over specific lengths to simulate damage due to pile driving. The specimens were subjected to fully-reversed lateral displacement cycles up to 2.5% drift, except for Specimen 2 which prematurely failed. During the displacement cycles, the piles were also subjected to axial load, reaching peak loads of 575 kips of tension in the positive displacement region, and 910 kips of compression in the negative displacement region. After testing, section fiber models were developed to assess the axial load-moment capacity of the pile specimens. The models were calibrated using the experimental data from testing.

6.2.2 Conclusions

As shown in Chapter 4, testing of Specimen 1 proved that an as-built pile can sustain a lateral drift ratio of 1.8%, corresponding to the design earthquake with a 1000-year return period, with only moderate damage and mild strength degradation. Upon testing to 2.5% drift, which corresponds to the Caltrans analysis of the maximum considered earthquake, severe load degradation occurred. Specimen 2 experienced sudden loss of its axial tensile capacity when the net axial tension reached 525 kips upon reaching a drift ratio of +0.6% for the first time. A through crack formed near the termination point of the core bars and in the shell near the pile cap. These cracks transferred the axial force to the surface boundary between the cast-in-place concrete core and the precast shell. When the shear force exceeded the capacity of the boundary, the pile shell slipped resulting in complete uplift. Specimen 3 showed that the addition of a single high-strength steel bar in the pile's core as a retrofit is effective in increasing the performance and ductility of a damaged pile. The specimen had slightly lower lateral resistance compared to Specimen 1, but it had significantly less load degradation at -2.5% drift when subjected to the maximum 910 kip axial compression. Based on this study, the retrofit method recommended in Chapter 5 is found to be effective in restoring the performance of damaged piles without increasing the lateral resistance.

Interaction diagrams were created using fiber section models at two distinct cross-sections of the pile specimens. The materials properties used in the fiber section models are calibrated using the experimental data. It was determined from testing that in the piles without the retrofit, the bars that tie the pile cap to the cast-in-place concrete core cause plying action when the piles are subjected to lateral displacement. This plying action caused a significant weakening of the shell concrete's strength and ductility. It was found during testing of the retrofitted specimen that the

addition of the high-strength steel bar alleviated the plying action, leading to an increase in ductility.

Chapter 7 Introduction

7.1 Background

Prestressed concrete columns featuring unbonded tendons exhibit remarkable resilience to lateral displacements without enduring severe damage or significant residual deformations upon unloading. Commonly known as self-centering or rocking columns, they offer the added benefit of being precast and erected onsite to expedite bridge construction. The self-centering principle has been harnessed to develop diverse seismic load-resisting systems, including precast-prestressed concrete frames (Priestley and Tao 1993, Priestley and MacRae 1996) and reinforced concrete (RC) shear walls (Kurama 2005, Belleri, et al. 2014, Sritharan et al. 2015). Various design concepts for self-centering RC columns have been proposed by researchers such as Cheng (2007, 2008), Lee et al. (2007), Davis et al. (2012), Schaefer et al. (2013), Guerrini et al. (2015), Tronol et al. (2015), Mantawy et al. (2016), Thonstad et al. (2016), Nema and Restrepo (2020), Kalliontzis et al. (2022), to name a few. Analytical studies by Makris and Vassiliou (2013, 2015), among others, have delved into the seismic response and stability of free-standing and vertically restrained rocking columns, providing valuable insights into the dynamics of self-centering systems.

Under intense seismic loading, rocking columns leverage unbonded post-tensioning tendons to generate a re-centering moment, designed to respond elastically up to the designated drift level. These columns are typically reinforced with partially debonded mild steel bars near the column-to-foundation interface to facilitate hysteretic energy dissipation during seismic events. Research indicates that rocking columns equipped with supplemental energy-dissipation elements can achieve maximum drift levels comparable to or slightly greater than conventional columns (Lee et al. 2007). Additional energy dissipation arises from radiation damping due to column impacts on the foundation surface (Housner 1963).

In previous research investigations focusing on self-centering columns, various design configurations and details were examined concerning the type and cross-sectional locations of prestressing tendons, protective measures to prevent or mitigate concrete crushing near the rocking interface, and the inclusion of supplemental energy-dissipation mechanisms. Typically, the prestressing tendons were based on high-strength bars or 7-wire strands, which were unbonded throughout the entire column height. In many of the design scenarios, these tendons were concentrated at or in close proximity to the column centroid, while mild steel bars were embedded near the perimeter of the column (Lee et al. 2007, Davis et al. 2012, Schaefer et al. 2013, Tronol et al. 2015, Mantawy et al. 2016, Thonstad et al. 2016, Nema and Restrepo 2020). These bars were deliberately debonded over a specified length. Some design variations explored the integration of external energy-dissipation devices, as demonstrated in Guerrini et al. (2015). Guerrini et al. (2015) also investigated a design featuring a steel casing covering the entire column height, while others explored the application of steel casing near the rocking interface (e.g., Davis et al. 2012, Schaefer et al. 2013, Mantawy et al. 2016).

Section 2 of this dissertation presents a research study that evaluated a self-centering column design developed by Caltrans engineers (Bromenschenkel and Mahan 2014; Yoon et al. 2015). The design, which will be discussed in Chapter 8, was aimed to achieve the following performance objectives:

- Provide adequate resistance to service-level forces, which could be induced by wind, the creep and shrinkage of concrete, the braking actions of vehicles, and the ability to resist extreme seismic forces without significant damage or residual displacements.
- Allow pre-fabrication and easy onsite erection for accelerated bridge construction.

- Prevent the buckling of longitudinal reinforcing bars introduced to provide supplemental hysteretic energy dissipation.
- Have rocking hinges that can be easily repaired after a major earthquake.
- Allow efficient replacement of reinforcing bars.

7.2 Research Objectives and Scope

The primary goals of this study were twofold: (1) conduct laboratory testing to assess the efficacy of self-centering columns using the design framework developed by Caltrans (Bromenschenkel and Mahan 2014; Yoon et al. 2015), and (2) enhance the original design, if necessary, based on findings from the initial testing phase. To this end, the Caltrans-proposed design concept underwent refinement by incorporating practical details that met both construction feasibility and performance objectives. Two full-scale column specimens were constructed and subjected to testing. The tests were performed with quasi-static cyclic lateral loading. The first specimen, referred to as the baseline specimen, had the basic features of the original design. The second specimen incorporated improvements aimed at addressing performance issues identified during the testing of the first specimen. After the test, a fiber-section model was developed and refined, introducing additional features to enhance its correlation with the experimental data. This refined model provided insights into local mechanisms influencing the response of the column specimens. Parametric studies were conducted using the analytical model to explore the impact of various design parameters on column performance. Finally, a comprehensive design methodology, based on Rayleigh's method, was developed for the displacement-based design of bridge structures featuring self-centering columns. This section includes design examples to illustrate the application of the methodology.

7.3 Outline of Section 2 of Dissertation

Chapter 8 presents the experimental program, including the specimen design and construction, the material properties of the specimens, test setup, instrumentation, and loading protocol.

Chapter 9 presents the experimental observations and data obtained from the quasi-static cyclic loading tests, and the free-vibration tests conducted on the first column specimen after the quasi-static test.

Chapter 10 presents the development of the fiber-section model used to simulate the experimental results. Design assumptions, material models and the nonlinear solution scheme are discussed.

Chapter 11 presents a general design methodology based on Rayleigh's method for the displacement-based design of bridge structures with self-centering columns. Design examples are provided.

Chapter 12 presents the summary and conclusions of the study.

Chapter 7 is, in part, a reprint of the material in a California Department of Transportation report entitled "Experimental Investigation of a Self-Centering RC Column Design and a Displacement-Based Design Method for Highway Bridge Applications." The authors of the report are: the author of the dissertation, Dimitrios Kalliontzis, and P. Benson Shing. Professor Dimitrios Kalliontzis worked on much of the construction of the first test specimen. The author of the dissertation provided input for the design of the second specimen, and was responsible for overseeing the construction and experimental work, post-test analysis of the two specimens,

modeling and worked with Professor P. Benson Shing on the development of the displacement-based design methodology.

Chapter 8 Experimental Program

8.1 Introduction

Two self-centering column specimens were tested. The design of the specimens was based on the self-centering mechanism conceived by Caltrans. Each specimen represented one-half of a full-height column that has a hinge at the top and a hinge at the bottom for the column to rock as a rigid body. The specimens were tested as cantilever columns, with the top end representing the mid-height of a full column. The effect height of the specimens, measured from the surface of the footing to the elevation of the applied horizontal load is 120 in. Each specimen had a 48-in.-diameter, circular, reinforced concrete, section and a rocker hinge at the base. The rocker hinge consisted of two unconnected steel rocker plates with a shear pin at the center to prevent sliding. The self-centering mechanism was provided by a set of unbonded, post-tensioned, seven-wire strands, while longitudinal, mild steel, reinforcing bars were incorporated to provide additional hysteretic energy dissipation. The main difference between the two specimens was in the size and detailing of the longitudinal reinforcing bars. The reinforcing bars in the second specimen were configured to avoid bar buckling and fracture, and for easy replacement after experiencing excessive plastic deformation. The specimen design, test setup, instrumentations, and loading protocols for the two specimens are described in this chapter. Results from the tests are presented and analyzed in Chapters 9 and 10.

8.2 Design of Test Specimens

8.2.1 Design of Specimen 1

The elevation of Specimen 1 showing dimensions and design details are shown in Figure 8.1. As shown in Figure 8.1, the specimen had a loading block above the column and a pedestal at

the bottom. The loading block measured 8’-0” by 7’-10” and was for transmitting the vertical and horizontal loads applied to the column. The axial compressive load was exerted on the column by four post-tensioned high-strength bars, which passed through holes in the loading block and the footing, and were anchored above the loading block and beneath the strong floor of the laboratory. Two horizontal actuators were attached to the loading block to impose lateral displacement on the column.

Right above the pedestal was a rocker hinge assembly that consisted of two 2-in.-thick steel plates and an 8-in.-diameter steel pin, which will be described later in more detail. The pedestal was designed to fit into a hole with a slightly larger diameter in the footing. The footing slab was precast as two separate pieces, which were identical to each other and were later post-tensioned together with 12 threaded bars to form the footing slab. Each footing piece had 2 tapered vertical ducts to accommodate the vertical post-tensioned bars. The angle of the taper was determined so that it would accommodate the sway of the vertical bars as the column was displaced laterally. After the placement of the pedestal in the footing hole, the remaining void in the hole was filled with a quick-set high-strength concrete. The outer face of the pedestal and the wall of the footing hole were lined with corrugated steel pipes to securely anchor the column in the footing. The pipes also served as stay-in-place form for the concrete. The footing was designed to be reusable for other specimens. To prevent the separation of the corrugated pipe from the concrete when the footing pieces were disassembled after the test, the outer wall of the pipe had steel studs welded to it and embedded in the footing concrete. The full set of reinforcement and construction drawings can be found in Report No. SSRP-24-01 entitled “Experimental Investigation of a Self-Centering RC Column Design and a Displacement-Based Design Method for Highway Bridge Applications.”

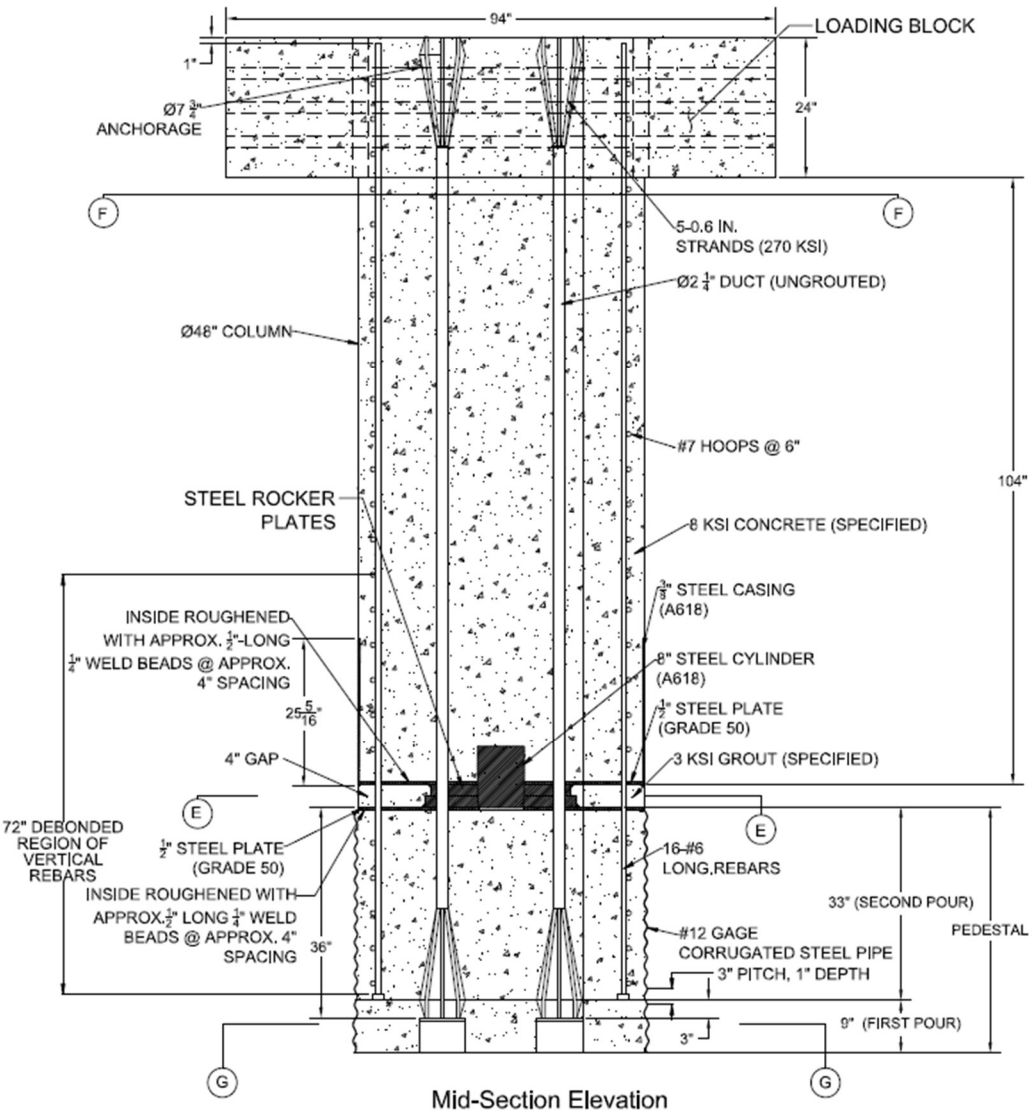

Figure 8.1: Elevation view of Specimen 1 with reinforcement details

The column was reinforced with sixteen Grade-60, No. 6, longitudinal bars running from the bottom of the pedestal into the top of the loading block. As shown in Figure 8.1, each bar was debonded from concrete over a length of 72 in. from the lower end of the bar, while the remaining length of the bar was bonded. Debonding was achieved by wrapping around each bar with many rounds of plastic wrap. It was intended to reduce plastic strain concentration so that the maximum compressive strain reached at the targeted maximum column drift ratio of 10% would not exceed

-0.015 while the maximum tensile strain would be less than 0.045. The bars were anchored in the pedestal with welded 1 3/8” heads . Steel hoops were provided along the column height to serve as transverse reinforcement. They were Grade-60, No. 7, hoops spaced at 6-in. on center. The column had twenty 0.6-in.-diameter, Grade-270, unbonded, seven-wire strands to provide the self-centering mechanism. The strands were grouped in four PVC ducts, with five strands in each duct. Each group of strands was anchored at the top of the loading block and the bottom of the pedestal with DYWIDAG MA-Anchorages. The unbonded strand length between the top and bottom anchorages was 162 in. The strands were expected to develop mild inelastic deformation with a maximum tensile strain of 0.0095 when the lateral drift of the column reached 10%. To this end, the target prestress level of the strands were 60 ksi.

As shown in Figure 8.1, the rocker hinge consisted of a steel casing secured around the bottom 25-5/16-in. of the column. There was a ½-in. steel plate at the column base, which was welded to the casing. The underside of the plate was welded to a 2-in.-thick steel plate that sat on another 2-in.-thick steel plate that was welded to a ½-in. plate on top of the pedestal. The design details of the steel assembly are shown in Report No. SSRP-24-01. The 2-in. plate at the top could rock on the bottom plate. An 8-in.-diameter steel pin was used to serve as a shear key that prevented sliding. It passed through the holes in the 2-in. steel plates with a tight fit. The two ½-in. plates were secured to the concrete column and pedestal with 7/8-in. x 6-in. headed studs. The inner face of the steel casing and the ½-in. plates were roughened with weld beads to prevent slippage between the steel assembly and the concrete.

The gap in the rocker hinge was filled with a fast-setting grout, which was expected to reach a compressive strength of 3 ksi within a week (by the time the specimen would be tested) to serve as a sacrificial material.

8.2.2 Design of Specimen 2

An elevation view showing the design details for Specimen 2 are shown in Figures 8.2 They were similar to those for Specimen 1 except for several changes, which were intended to prevent the buckling of the longitudinal bars in the rocker hinge region, and delay or prevent the fracture of the bars due to cyclic bending. First, the longitudinal bars of Specimen 2 were unbonded to concrete over the entire length by wrapping many rounds of plastic wrap around each bar. Second, the top heads of the longitudinal reinforcing bars were outside the loading block on top of the column so that the bars could develop only tension. These changes aimed to prevent the longitudinal bars from developing compression. To minimize any bending of the longitudinal bars in the rocker hinge region as the column rocked, ½-in.-thick foam padding was placed around the longitudinal bar for a length of 1 ft. above and 1 ft. below the rocker hinge to introduce a gap between the bar and the concrete. Third, each longitudinal bar consisted of two segments of different sizes connected to each other with a mechanical coupler. The lower segment was a Grade-60 No. 10 bar, while the upper segment was a Grade-60 No. 8 bar, which served as a replaceable fuse where plastic deformation was expected to concentrate. The length of the No. 8 bars was approximately 33½" in. and that of the No. 10 bars was approximately 119¼" in. These lengths were determined with a target that the maximum tensile strain developed in the fuse bar would not exceed 0.07 when the column drift reached 10%. The bars were coupled with mechanical transition couplers right below the loading block where the column had a reduced section. In an actual full-height bridge column, there can be one rocker hinge at the top and one at the bottom, and the couplers need not be exposed in that it can be places in a duct surrounded by concrete. The fuse bar can be located a short distance below the top rocker hinge and connected to a larger bar above and a larger bar below. Two other minor design changes were the reduced height of the steel casing

at the bottom of the column because little strain was observed in the casing of Specimen 1, and the use of an 8-in. double extra-strong steel pipe instead of a solid steel cylinder for the shear pin.

Additional reinforcement was provided in the region with reduced section. They consisted of No. 8 longitudinal bars and No. 7 hoops spaced at 6 in. on center. The longitudinal bars extended 41in. below the reduced section to provide the full development length of the bars. These changes are shown in Figures 8.6. The length of the loading block was slightly reduced in order to reduce the total weight of the test specimen. The full set of reinforcement and construction drawings can be found in Report No. SSRP-24-01 entitled "Experimental Investigation of a Self-Centering RC Column Design and a Displacement-Based Design Method for Highway Bridge Applications."

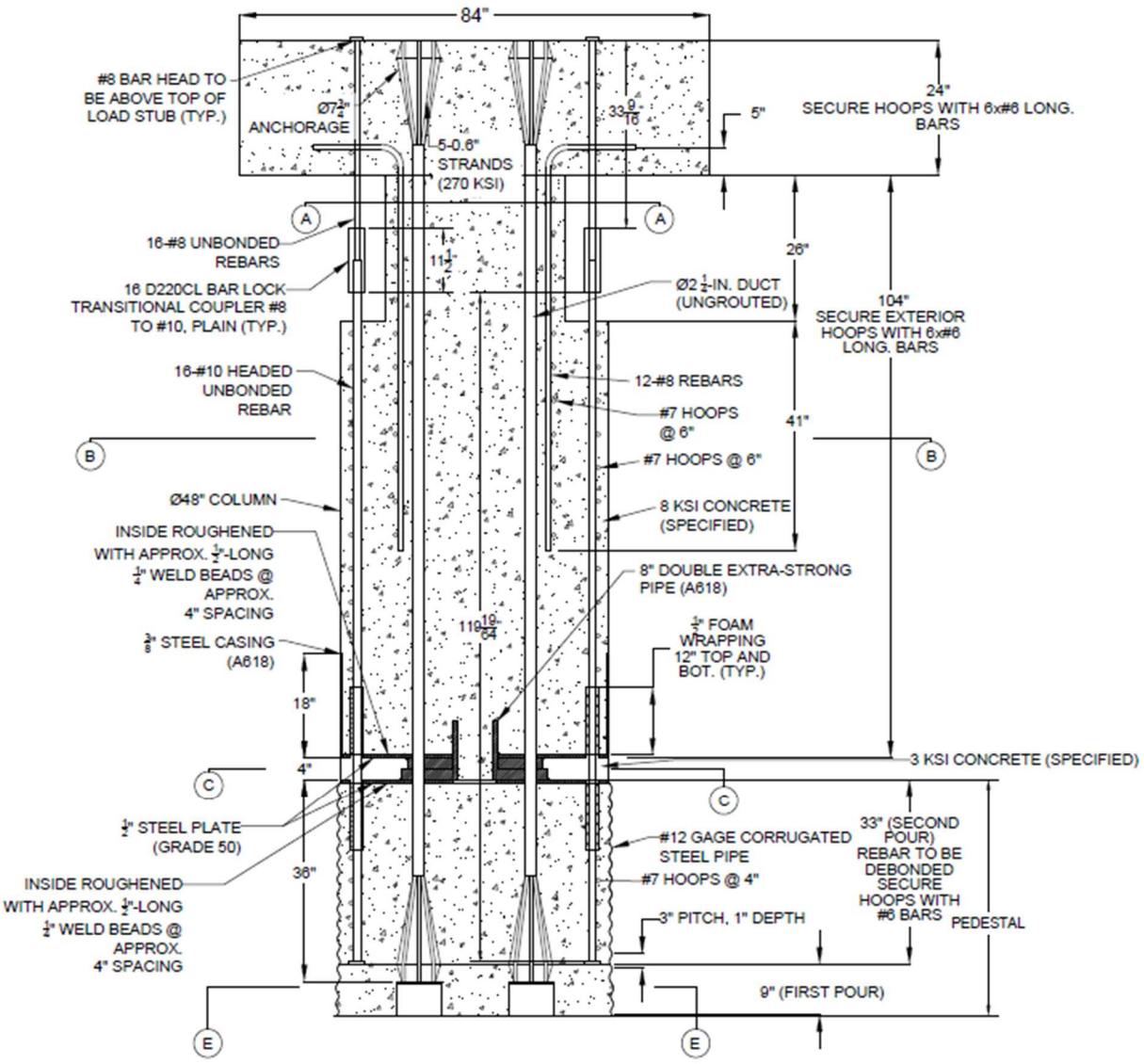

Figure 8.2: Elevation view of specimen 2

8.3 Construction of Test Specimens

All concrete components of the test specimens were constructed and assembled in the Powell Labs at UC San Diego. The rocker-hinge assembly for each specimen was fabricated in a machine shop. The assembly for Specimen 2 was similar with a couple of minor changes as described in the previous section.

The order of casting the concrete components of each specimen is shown in Figure 8.3. The pedestal was constructed first in an up-right position. Each pedestal was cast in two stages for the convenience of placing the post-tensioning anchorages and the column reinforcing bars. The corrugated steel pipe, which served as a stay-in-place form, was placed on top of a flat wood platen, which was raised several feet from the strong floor of the laboratory with support. Four post-tensioning anchorages were set in place, each supported by a Sonotube, at the bottom of the steel form, six inches above the wood platen surface. The steel reinforcement cage for the pedestal was placed inside the steel form. Then, a 9-in. layer of concrete was cast. After the concrete hardened, lower segments of the four PVC ducts for the prestressing strands were placed on top of the post-tensioning anchorages, and the sixteen reinforcing bars for the columns were placed. The bar heads sat on the concrete surface. The rocker-hinge assembly was suspended over the pedestal form with chains tied to the outrigger, and the reinforcing bars were threaded through the holes in the base plate of the casing. Then, the rest of the pedestal was cast, and the top plate of the pedestal was lowered and placed on top of the steel form while the concrete was still wet. After the concrete in the pedestal set, the steel casing assembly for the rocker hinge was lowered and placed on the pedestal. The transverse reinforcement and the upper segments of the PVC tubes were tied in place, and the Sonotube form for the column was placed. The bars were held in the position with a wood template at the top of the column form. The wood form for the loading block was placed on top of the column form. The pre-stressing strands were threaded through the PVC ducts and the bottom anchorages. The column was then cast.

After casting the column, the steel cage for the loading block was placed in the wood form, and the strands were threaded through four post-tensioning anchorages, which were positioned flush with the top face of the loading block. The loading block was then cast. After the concrete in

the loading block reached a compressive strength of at least 5,000 psi, the support below the pedestal was removed, and the whole specimen was hung on the steel outrigger that was secured on the strong wall in the lab. The steel grips in the post-tensioning anchorages at the bottom of the pedestal were pushed in to have an initial firm grip on the strands. The strands were then tensioned one-by-one using a hand-held pneumatic jack at the top of the loading block. The target prestress level for the strands was 60 ksi. In order to account for the stress loss caused by the settling of the conical grips as the jacking force was released and the elastic shortening loss, each strand was jacked to 115 ksi, which corresponds to a jacking force of 25 kips. Data on the anchorage loss was provided by the anchorage supplier. Jacking was done in an order that would balance the prestressing force in the column as much as possible. The strands were tensioned in two stages. First, they were jacked to approximately 20% of the target force, and then to the full force.

For Specimen 1, the strands were prestressed on May 29th, 2019. During jacking, the elongation of the strands was measured to estimate the modulus of elasticity of the strands. This was determined to be about 29,000 ksi. After the jacking force was relieved, the final strain in the strands was found to be about 0.0022, corresponding to a tensile stress of 64 ksi. For Specimen 2, the strands were prestressed on January 15, 2021. The strain measured in the strands right after the post-tensioning process was 0.0023, corresponding to a stress of 67 ksi.

The two segments of the footing were assembled at the location at which the specimen was to be tested. The segments were leveled on the strong floor with a layer of hydro-stone underneath, and were post-tensioned together with 12 high-strength threaded bars. It was then tied to the strong floor with 14 post-tensioned bars. After the column specimen was constructed, it was lifted and moved by an overhead crane, and lowered into the hole of the footing. After the column was

leveled, the void between the pedestal and the wall of the hole was filled with a quick-set high-strength concrete.

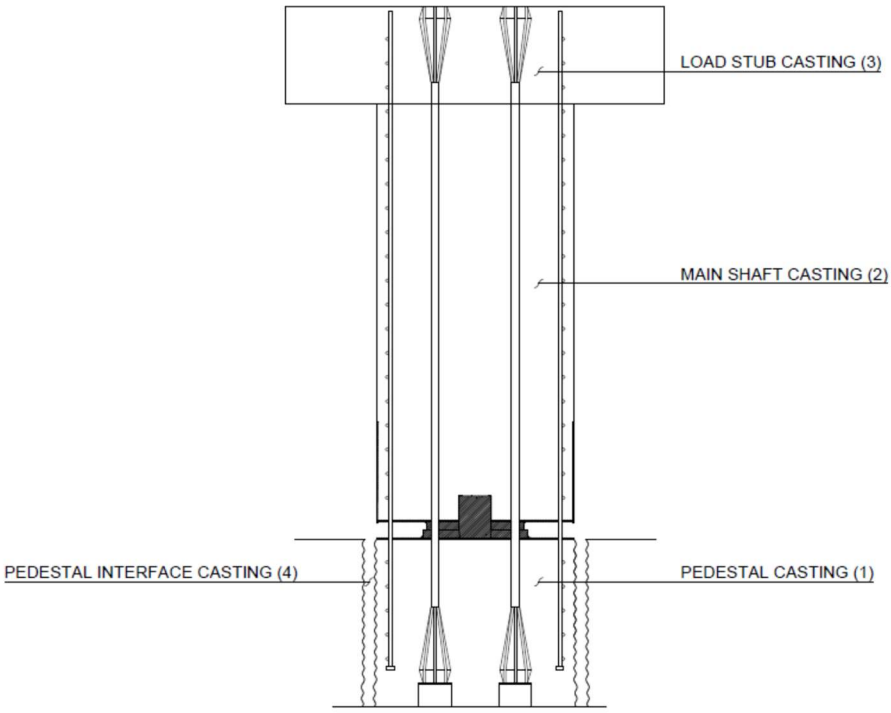

Figure 8.3: Casting order for Specimen 1 (same for Specimen 2)

8.4 Material Properties

Tests were conducted on samples of materials used in the construction of the two specimens. Table 8.1 shows the average yield and tensile strengths of the reinforcing steel and prestressing strands, averaged over three test samples each. The prestressing strands for the two specimens were from the same batch. The yield strength of a strand is defined as the stress at a tensile strain of 0.01. The strand specimens started to slip in the grips of the testing machine as the tensile stress approached the ultimate strength. Hence, the ultimate tensile strength of the strands shown in the table is an estimate based on the minimum specified by ASTM A416/A416M-12 according to the measured yield strength. The tensile stress-strain curves, with loading and

unloading cycles, for the strands are shown in Figure 8.4, where X in the legends SGX-Y is the strain gauge number and Y is the sample number. The modulus of elasticity of the strands determined from the curves is about 29,000 ksi, which is consistent with that estimated from the data obtained in the column post-tensioning process.

Table 8.1: Average yield and tensile strengths of reinforcing steel and prestressing strands

Specimen	**Column Specimen**	**Grade**	**Yield Strength f_y (ksi)**	**Tensile Strength f_u (ksi)**
#6 Rebar	1	60	77	101
#8 Rebar	2	60	70	98
#10 Rebar	2	60	72	104
7-wire Strand	1, 2	270	262	291

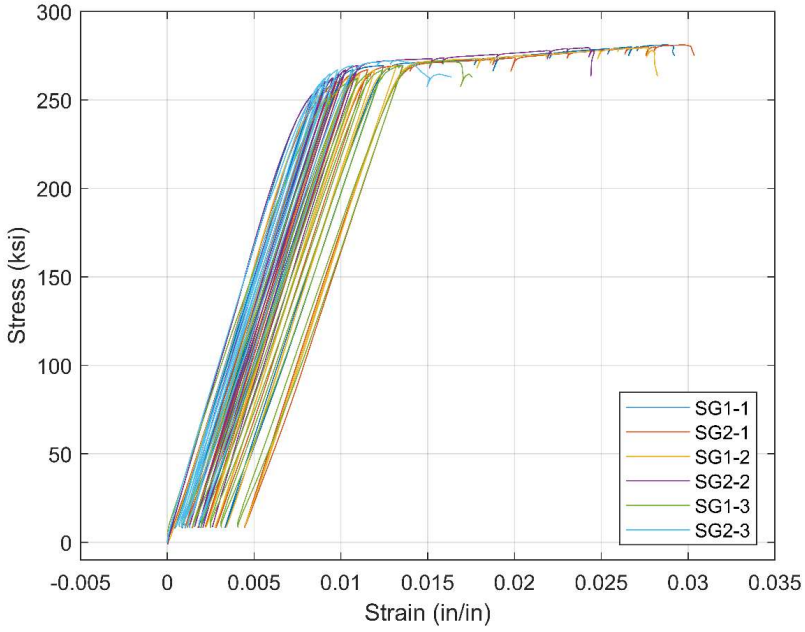

Figure 8.4: Stress-strain curves for 0.6-inch seven-wire strands

The compressive strengths of the concrete were obtained from 6-in.-by-12-in. cylinder samples. For the first column specimen, the concrete samples were tested on the 28th day after casting, but the concrete samples for the loading block were tested on the 14th day, which was close to the day on which the column was first tested. The loading blocks and footing had a specified concrete strength of 8 ksi, which was way above what was actually needed. Since all the samples had strengths that surpassed the target strength, no additional concrete samples were tested. For the second column specimen, only the concrete samples for the column itself were tested on the day the column was tested. Samples of the sacrificial grout that filled the void in the rocker-hinge regions were tested on the days the respective column specimens were tested.

Table 8.2: Average compressive strengths of concrete and grout (in ksi)

Concrete	**Specified**	**Specimen 1**		**Specimen 2**
		28 Day	Test Day	Test Day
Footing[1]	8	9.1	-	NA
Pedestal	8	8.7	-	-
Column	8	8.3	-	9.3
Loading Block	8	5.2[2]	-	-
Sacrificial Grout	3	NA	5.0	5.1

[1]Same footing used for Specimens 1 and 2

[2]14th-day strength

8.5 Test Setup

8.5.1 Quasi-Static Testing Setup

The load application scheme for the quasi-static tests of the two column specimens is shown in Figure 8.5, and a picture of the test setup for Specimen 1 is shown in Figure 8.6. Specimen 2 was tested with the same setup. Four threaded bars were used to apply 900 kips of compressive force on the column specimens. The bar force was exerted and maintained constant throughout each test using center-hole hydraulic jacks, whose pressure was maintained by an electric pump.

Two horizontal 220-kip servo-controlled hydraulic actuators, whose one end was affixed to the loading block on the column and the other end to a strong wall, were used to control the lateral displacements of the column. The loading protocols can be found in Section 8.7.1. The effective height of the columns was 120 in., which was the distance from the top face of the footing to the centerline of the horizontal actuators.

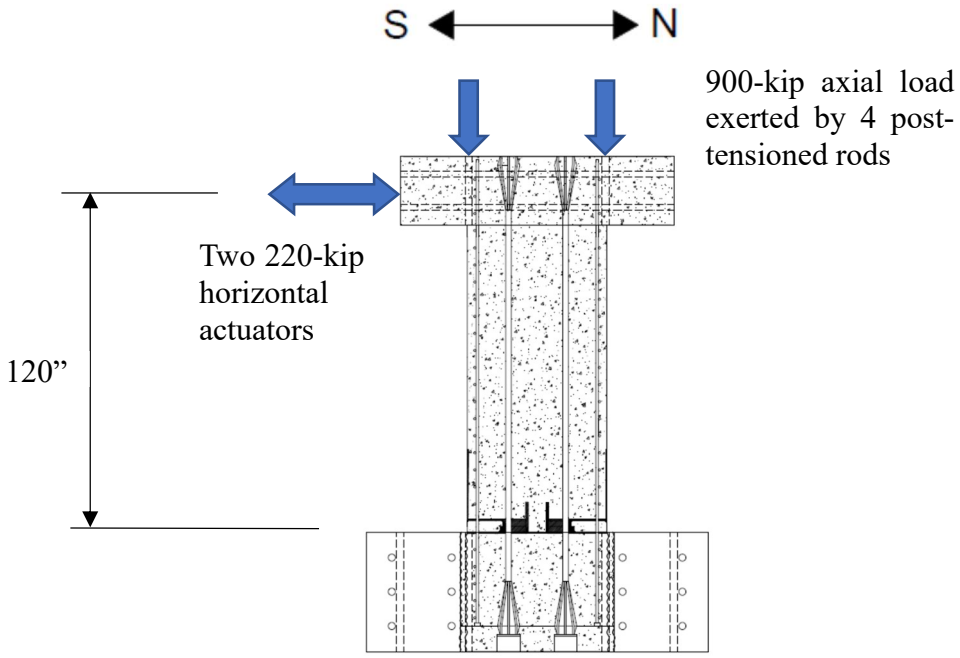

Figure 8.5: Load application during quasi-static tests of Specimens 1 and 2

Figure 8.6: Picture of test setup for Specimen 1

8.5.2 Free-Vibration Testing Setup

After the quasi-static test, Specimen 1 was subjected to free-vibration tests. For the free-vibration tests, all the grout in the rocker-hinge region was removed and the exposed longitudinal rebars was cut and removed by a torch so that they would not play a role in the tests. No axial load was applied in the tests. The initial displacement of the column was imposed by a loading bar that had a built-in fuse and was loaded with a center-hole hydraulic jack, as shown in Figure 8.7. A picture of the test setup is shown in Figure 8.8. It can be seen that the horizontal actuators were disconnected from the specimen. The loading bar consisted of two 1-1/4-in.-diameter high-strength DYWIDAG Threadbars connected by a fuse bar, which was a Grade-60 rebar with its diameter milled down to a specified dimension. The tensile strength of the fuse bars was identified with tensile tests. The fuse-bar diameter was determined based on the tensile force at which the fuse was supposed to break. A stronger fuse would impose a larger initial column displacement. A picture of a fuse connected to the Threadbars is shown in Figure 8.9. A set of fuse bars with different diameters were fabricated so that free-vibration tests with different initial displacements could be performed. As shown in Figure 8.7, the loading bar, which was secured to the strong wall, was threaded through the center duct in the loading block so that it could be loaded with a center-hole jack on the other side of the block. The setup was such that as the hydraulic jack extended, the column would displace. When the jacking force reached the target value, the fuse bar would fracture, sending the column into free vibration. The targeted initial displacements are presented in Section 8.7.2.

The free-vibration tests were followed by quasi-static tests conducted with servo-controlled hydraulic actuators with a range of displacement amplitudes comparable to the initial displacements imposed in the free-vibration tests.

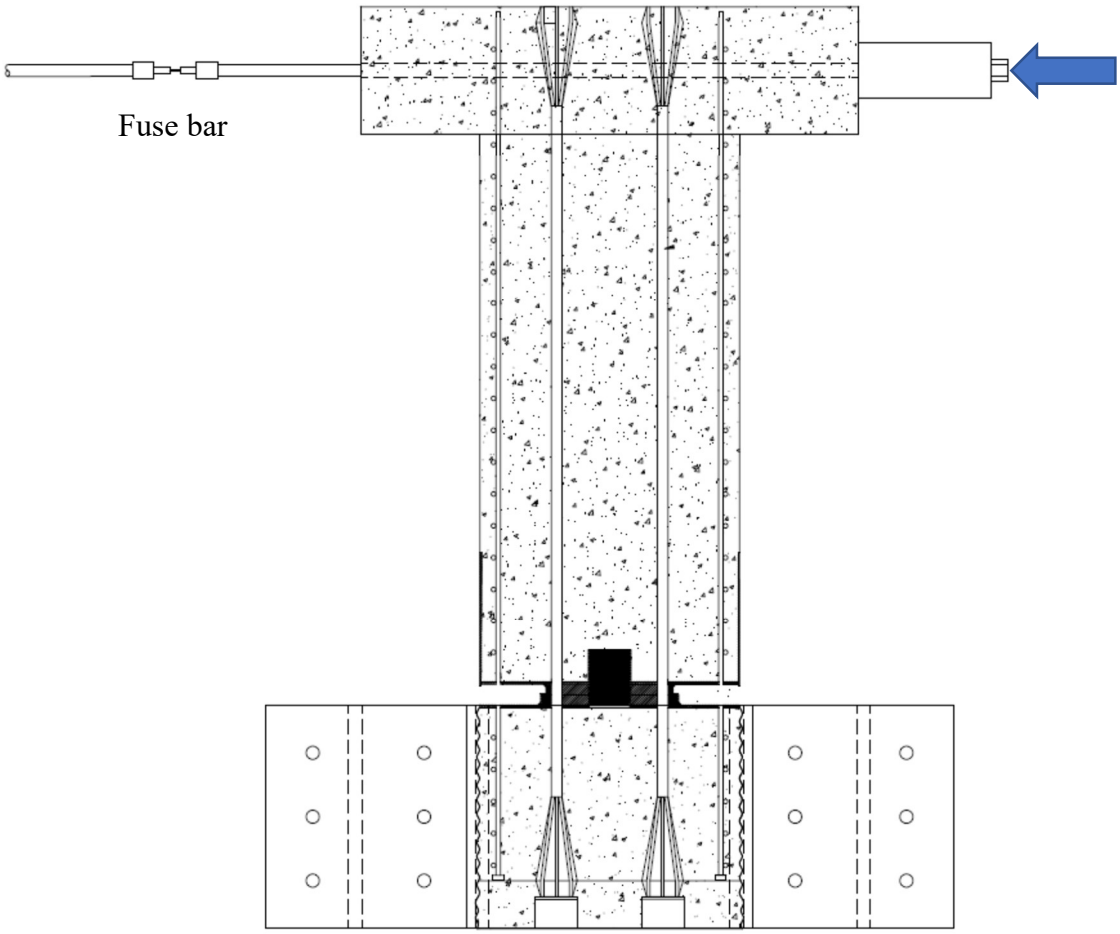

Figure 8.7: Setup for free-vibration tests of Specimen 1

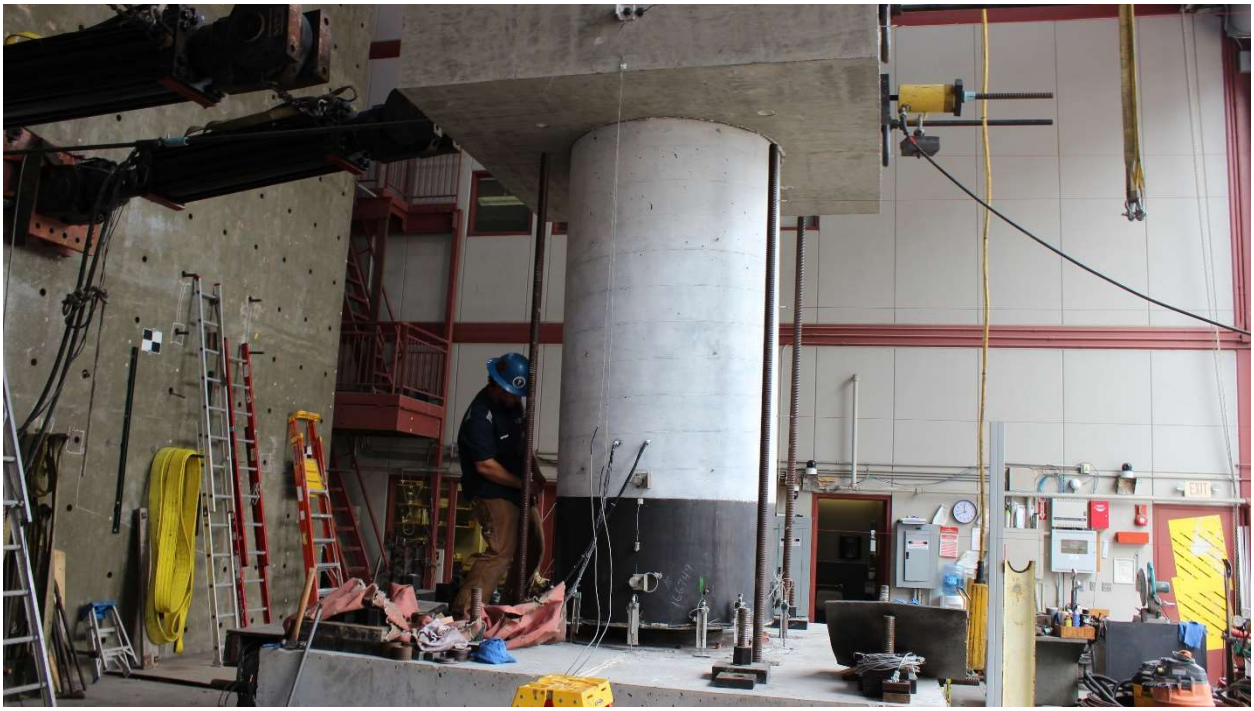

Figure 8.8: Picture of free-vibration tests of Specimen 1

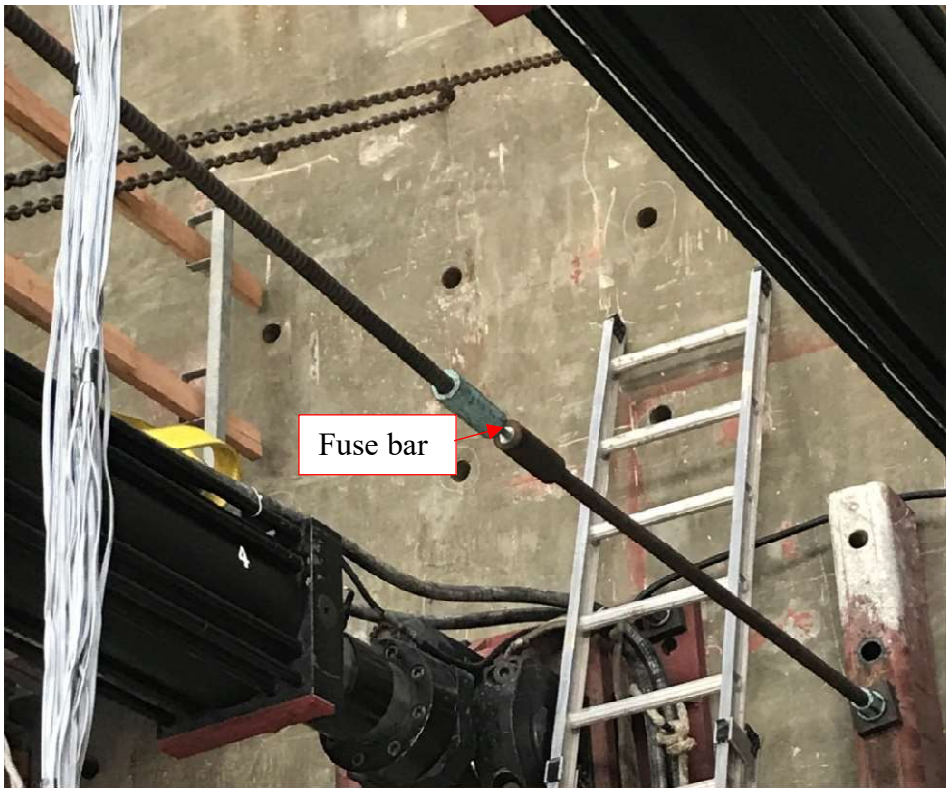

Figure 8.9: Fuse bar for free-vibration tests of Specimen 1

8.6 Instrumentation

Strain gauges were placed on the longitudinal reinforcing bars, transverse reinforcement, and prestressing strands, and vibrating wire gauges were placed within the columns to measure concrete strains in the axial direction. In addition, displacement transducers were installed to measure the deflection, and the flexural and shear deformations of the columns. The instrumentation scheme for Specimen 2 was adjusted based on observations from Specimen 1.

8.6.1 Instrumentation for Column Specimen 1

There were a total of 62 strain gauges, 8 vibrating-wire gauges, 7 string-potentiometers, 46 linear displacement transducers, and 3 inclinometers installed on Specimen 1. The full set of instrumentation figures can be found in Appendix D. Strain gauges were placed on 8 longitudinal rebars, three of which are on the south side and three on the north side of the column, to capture the most severe tensile and compressive strains as the column was loaded in the north-south direction. On each bar, gauges were placed at 5 elevations as shown in the figure. Two of the transverse reinforcement hoops, had strain gauges placed at locations shown in Figure D.2. There were four exterior strain gauges placed on the steel casing above the rocker hinge to measure the axial and hoop strains. Two (vertical and horizontal gauges) were located on the east side and two on the west side of the steel casing. One strand in each of the four groups (ducts) had strain gauges at three elevations. Vibrating wire gauges were located at two elevations each with four gauges to measure the average axial strain in the column right after post-tensioning, and at the beginning and the end of the column test.

There were two string potentiometers used to measure the in-plane lateral displacement of the column at the elevation where the horizontal load was applied, and five string potentiometers to measure the column deflection along its height. An array of 16 linear displacement

potentiometers were mounted on each of the east and west faces of the column to measure the shear and flexural deformations along the column height. The deformation of the rocker-hinge region was measured by 14 linear displacement potentiometers placed around the region. Three inclinometers were placed on the column at different elevations to measure the column rotation.

8.6.2 Instrumentation for Column Specimen 2

Specimen 2 had 52 strain gauges, 8 vibrating-wire gauges, 7 string potentiometers, 12 linear displacement transducers, and 6 inclinometers. The full set of instrumentation drawings can be found in Appendix D. Some of the sensors used on Specimen 1 were not installed because they were not expected to yield new important information. The string potentiometers used to monitor the lateral deflection of the column were placed at the same locations as those for Specimen 1, as shown in Appendix D. Strain gauges on the longitudinal rebars were placed at 6 elevations. Two of the elevations were within the fuse bar. Only one transverse reinforcement hoop had strain gauges. Strain gauges located on the steel casing had the same orientations as those on Specimen 1, and were located on the south and north sides of the column. Similar to Specimen 1, there were 24 strain gauges placed on the prestressing strands. However, instead of instrumenting one strand per duct with 6 gauges each, there were two instrumented strands per duct with 3 gauges each. This change was made with the aim to increase the survival rate of these strain gauges during the installation and post-tensioning of the strands.

The linear displacement transducers used to monitor the shear and flexural deformations of Specimen 1 were not used on Specimen 2 because it was confirmed in Specimen 1 that the column would practically rock as a rigid body. Twelve linear displacement transducers were placed around the rocker-hinge region of Specimen 2. Six inclinometers were placed along the height of the column to measure the rotation of Specimen 2.

8.7 Loading Protocols

Each of Specimens 1 and 2 were tested with quasi-static loading twice, first without grout in the rocker-hinge region and then with grout. The specimens were subjected to a constant axial compressive load of 900 kips, applied by four post-tensioned bars, each of which was controlled by a center-hole jack, throughout the tests, as discussed in Section 8.5.1. This axial load was in addition to the self weight of the load stub and column, which was 35.1 kips for specimen 1, and 30.9 kips for specimen 2. The lateral displacements were applied quasi-statically using two horizontal servo-controlled actuators. After the quasi-static tests, free-vibration tests were conducted on Specimen 1 with the grout and rebars in the rocker-hinge region, as well as the applied axial load, removed to examine the energy dissipation property of a rocking column without rebars. After the free-vibration tests, a quasi-static test was conducted, again without the axial load, with different displacement amplitudes, to examine the contribution of the hysteretic energy dissipation to the total energy dissipation. The dates on which these tests were conducted are shown in Table 8.3.

Table 8.3: Testing dates for Specimens 1 and 2

Specimen	Test Description	Test Date
1	Rocker Hinge Ungrouted	June 11, 2019
	Rocker Hinge Grouted	June 14, 2019
	Free-Vibration Tests	June 20, 2019
	Quasi-Static Tests After Free-Vibration Tests	June 21, 2019
2	Rocker Hinge Ungrouted	February 3, 2021
	Rocker Hinge Grouted	February 9, 2021

8.7.1 Quasi-Static Testing

Quasi-static tests were conducted with a constant axial compressive load of 900 kips applied to the columns. Before the rocker-hinge region was filled with grout, each specimen was subjected to low-amplitude displacement cycles with the maximum drift ratio to be reached targeted at 1%. There was one cycle at each amplitude level. It should be noted that there was a problem in actuator control during the test of Specimen 1, accidentally displacing it to -1.46% (~1.75") drift. It was then decided to complete one full cycle of -/+ 1.46% drift.

In the main tests, the rocker hinges were filled with grout. After the compressive strength of the grout exceeded 3 ksi, each specimen was tested with gradually increasing displacement cycles up to a drift ratio of 10%. The amplitude and number of cycles imposed on the columns at each drift level are shown in Table 8.4.

Table 8.4: Loading Protocol for quasi-static testing of Specimens 1 and 2 with grouted Rocker Hinge

Displacement, in	Drift, %	# of Cycles
0.125*	0.11	1
0.25	0.21	1
0.50	0.42	1
0.75	0.63	1
1.0	0.83	3
2.0	1.67	3
3.0	2.50	3
4.0	3.33	3
6.0	5.00	2
8.0	6.67	2
10.0	8.33	1
12.0	10.00	1

*Only for Specimen 1

8.7.2 Free Vibration Testing

After the quasi-static tests, Specimen 1 was subjected to free-vibration tests. No axial load was applied in these tests. All the grout in the rocker-hinge region was removed, and the rebars in the region were cut and removed. The lateral resistance of the column was provided by the prestressing strands only. Each of these tests was conducted by displacing the column quasi-statically to a target drift level and then setting it to free vibration by suddenly releasing it. As

discussed in Section 8.5.2, this was achieved with a fuse bar that would fracture at the load level developed by the column at the target initial displacement. A total of four tests were conducted with the initial drift levels varying from 0.70 to 4.26%, as shown in Table 8.5. The influence of the displacement amplitude on the energy dissipation in the rocking column was identified from the test results. After the free-vibration tests, the column was subjected to a quasi-static test with cyclic loading. Eight fully-reversed displacement cycles were imposed, with the displacement history resembling that measured in the fourth free-vibration test, as shown in Table 8.6.

Table 8.5: Free-vibration tests for Specimen 1

Test	**Initial Displacement, in**	**Drift, %**
1	0.84	0.70
2	2.28	1.90
3	3.75	3.13
4	5.11	4.26

Table 8.6: Displacement amplitudes for quasi-static tests after free-vibration tests of Specimen 1

Displacement Amplitude, in	**Drift, %**
5.1	4.25
4.3	3.58
3.4	2.83
2.7	2.25
1.9	1.58
1.4	1.17
1.1	0.92
0.7	0.58

Chapter 8 is, in part, a reprint of the material in a California Department of Transportation report entitled "Experimental Investigation of a Self-Centering RC Column Design and a Displacement-Based Design Method for Highway Bridge Applications." The authors of the report are: the author of the dissertation, Dimitrios Kalliontzis, and P. Benson Shing. Professor Dimitrios Kalliontzis worked on much of the construction of the first test specimen. The author of the dissertation provided input for the design of the second specimen, and was responsible for overseeing the construction and experimental work, post-test analysis of the two specimens, modeling and worked with Professor P. Benson Shing on the development of the displacement-based design methodology.

Chapter 9 Testing of Self-Centering Column Specimens

9.1 Introduction

Results from the testing of the two self-centering column specimens are presented in this chapter. As discussed in Chapter 8 the column specimens represented the lower half (from the base to the inflection point) of a prototype rocking column with the upper and lower halves being mirror images of each other. Specimen 1 was based on the initial design derived from the concepts proposed by Caltrans (Bromenschenkel and Mahan 2014; Yoon et al. 2015). Specimen 2 had changes in the reinforcement scheme with the goal to avoid the shortcomings of the initial design as observed in Specimen 1. The design of the specimens and the loading protocols are presented in Chapter 8. Both specimens were subjected to cyclic quasi-static loading tests. Specimen 1 was also subjected to free-vibration tests after the quasi-static test had been completed. During each quasi-static test, an axial compressive load of 900 kips was applied to the column specimen by four post-tensioned, threaded, rods. The force in each rod was maintained by a center-hole hydraulic jack, whose pressure was controlled by a pump. Both specimens were first tested with the sacrificial zone at the base not filled with grout, and then tested with the sacrificial zone filled with grout to a large drift level. During the free-vibration testing of Specimen 1, the 900-kip axial load, and the grout and rebars in the rocking hinge zone were removed. For the data presented in this chapter, positive displacement is towards the north direction. Unless otherwise stated, the lateral displacement of the column specimens is the average displacement measured by the two string potentiometers positioned at the level of the centerline of horizontal actuators. Lateral drift ratios are calculated as the lateral displacement divided by the column height, which was 120 inches, measured from the top of footing (TOF) to the centerline of the horizontal actuators.

9.2 Quasi-Static Testing of Column Specimen 1

The lateral load-vs.-drift ratio hysteresis curves and general test observations are first presented in the following section. Data from displacement transducers and strain gauges will be presented in subsequent sections.

9.2.1 General Test Observations

Figure 9.1 shows the lateral load-vs.-drift ratio hysteresis curves for Specimen 1 with the ungrouted sacrificial zone. The lateral load shown in the figure is total force measured by the load cells in the two horizontal actuators attached to the top of the column specimen subtracted by the horizontal component of the total axial force exerted by the four post-tensioned rods, which was determined from the oil pressure in the hydraulic jacks. This is to account for the fact that the top of the rods moved with the top of the column, while the base of each rod was pinned. As the lateral displacement increased, the P-Δ effect of the vertical load exerted by the rods increased. A second set of hysteresis curves that has the P-Δ effect of the vertical load removed is also shown in Figure 9.1. Figure 9.2 shows a plot of the axial load applied by the rods versus the lateral drift ratio. The specimen was subjected to displacement cycles with gradually increasing amplitudes. However, after the specimen reached the drift amplitude of 0.2% in the positive direction for the second time, it was accidentally displaced to a drift ratio of -1.46% (-1.75-inch displacement) in the negative direction, exceeding the targeted maximum drift limit of 1% for the test, due to equipment malfunctioning. The specimen was then displaced to a positive drift ratio of 1.46%, and the test was terminated after unloading. As shown by the picture in Figure 9.3, the extreme north bar experienced notable bending in the gap region.

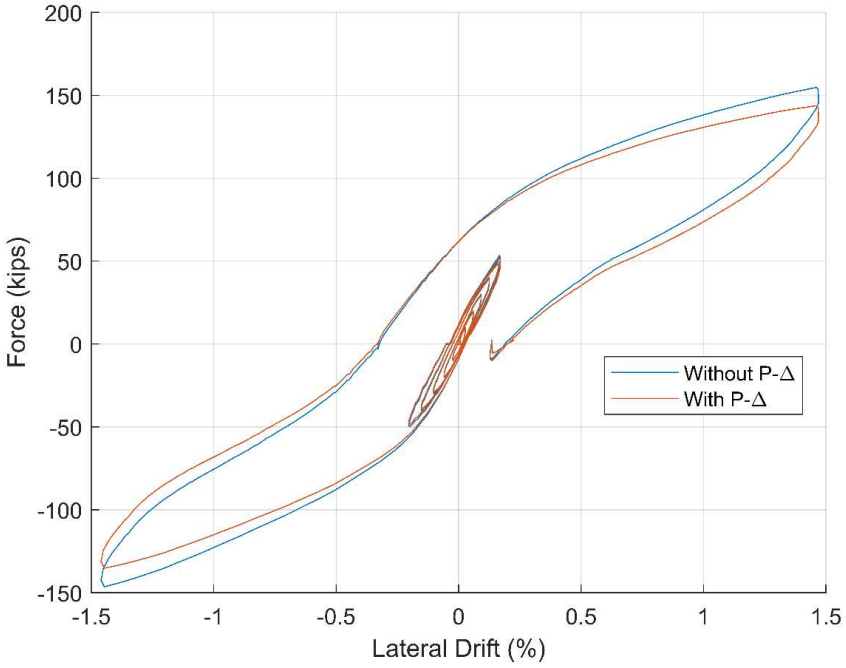

Figure 9.1: Lateral load-vs.- drift ratio hysteresis curves for Specimen 1 with ungrouted sacrificial zone

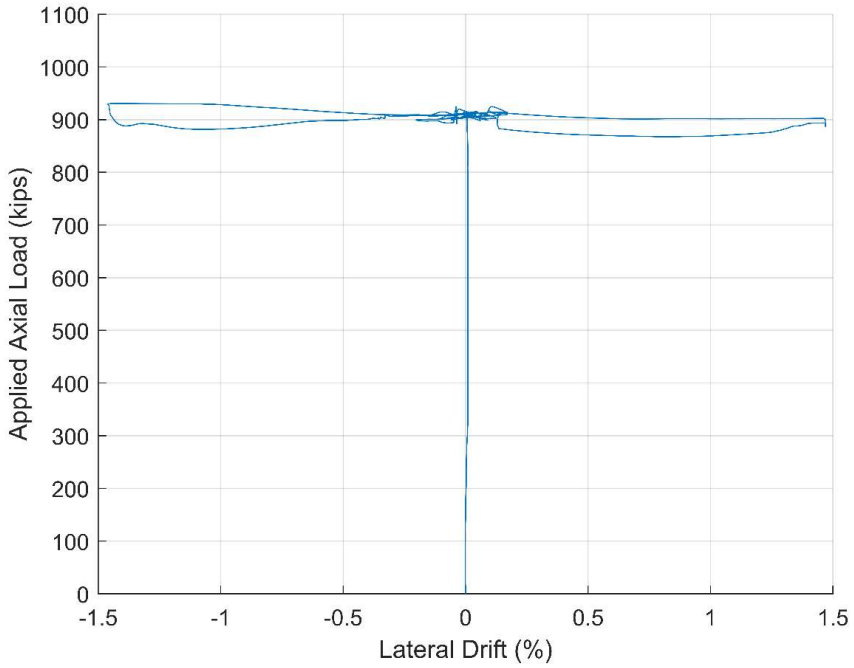

Figure 9.2: Applied axial load vs. lateral drift with ungrouted sacrificial zone

Figure 9.3: Extreme north rebar bent in ungrouted gap of Specimen 1

Figure 9.4 shows the lateral load vs. drift ratio hysteresis curves for Specimen 1 with the sacrificial zone filled with grout. Two sets of curves are shown in the figure. One has the P-Δ effect included and one does not. In both cases, the influence of the horizontal component of the axial force exerted by the post-tensioned rods is removed. Figure 9.5 shows a plot of the axial load applied by the rods versus the lateral drift ratio. Pictures of damage in the grouted sacrificial zone are shown in Figures 9.6 through 9.10. Figure 9.6 shows some mild crushing occurring in the grouted sacrificial zone during the cycle with a drift amplitude of 0.63%. Severe cracking and crushing occurred in the drift cycle of 2.51%, as shown in Figure 9.7. Severe grout spalling occurred in the drift cycle of 5.01%, as shown in Figure 9.8. The grout in the entire sacrificial zone was crushed when the drift ratio reach 10%, as shown in Figure 9.9. Bar fracture occurred at drift levels between 2.5 and 3%, as shown by small sudden load drops in the load – drift hysteresis curve in Figure 9.4. The fractured rebars are shown in Figures 9.9 and 9.10. No damage was observed in the rest of the column, as shown in Figure 9.11.

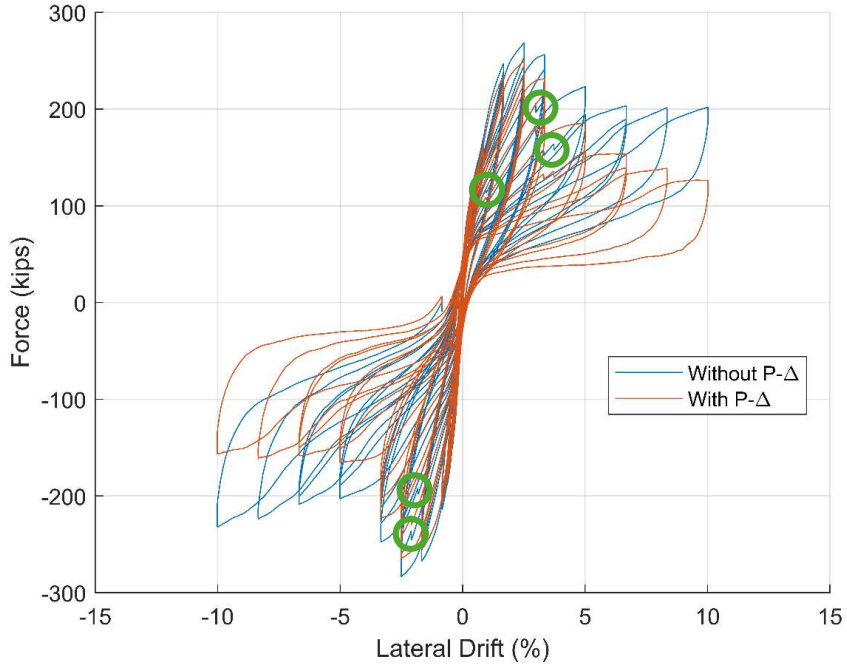

Figure 9.4: Lateral load-vs.-drift ratio hysteresis curves for Specimen 1 with grouted sacrificial zone (circles identify load drops due to rebar facture)

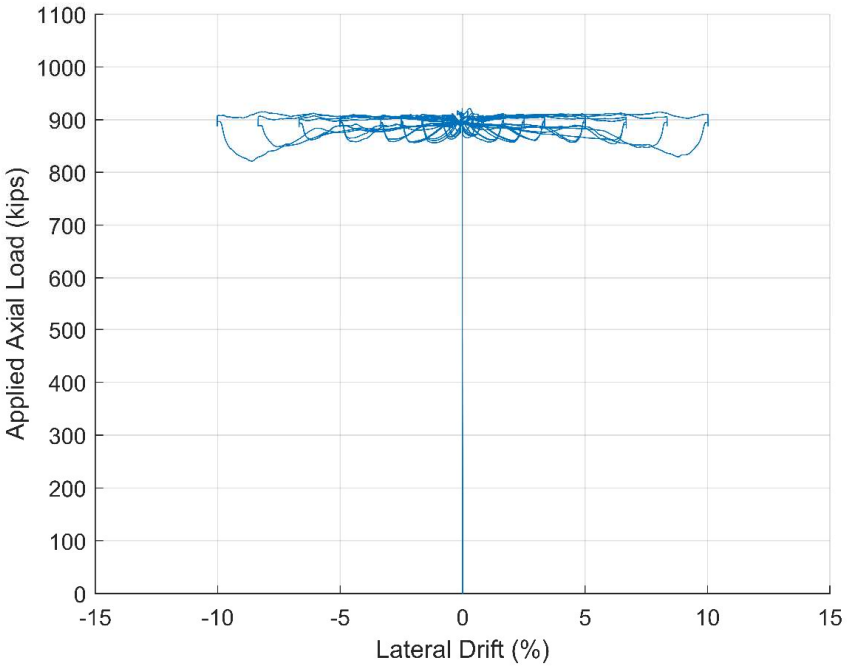

Figure 9.5: Applied axial load vs. lateral drift with grouted sacrificial zone

Figure 9.6: Picture of north-west side of Specimen 1 at peak drift of 0.63%

Figure 9.7: Picture of south side of Specimen 1 after peak drift of 2.51%

Figure 9.8: Picture of south side of Specimen 1 at peak drift of 5.01%

Figure 9.9: Picture of west side of sacrificial region of Specimen 1 at -10% drift ratio

Figure 9.10: Picture showing rebar bending and fracture in sacrificial region of Specimen 1 after the test

Figure 9.11: Picture of Specimen 1 at 10% drift ratio

9.2.2 Data from External Instrumentation

The instrumentation plans for Specimen 1 can be found in Appendix D of this dissertation. Figure 9.12 shows the lateral displacement profiles of the specimen, with the sacrificial region filled with grout, at the peaks of each displacement cycle. In the plots, readings from string potentiometer SP04 (located approximately 75 inches above the top of the footing) were omitted due to a calibration error found in the potentiometer. The plots show that the column practically rocked as a rigid body about the base throughout the test, with deformation concentrated in the sacrificial region. This is consistent with the data obtained from the three inclinometers mounted at different elevations along the column, as shown in Figure 9.13. The angles of inclination measured by the three inclinometers are almost identical, and their values in radians multiplied by the column height yield almost the same lateral displacement directly measured at the top of the column.

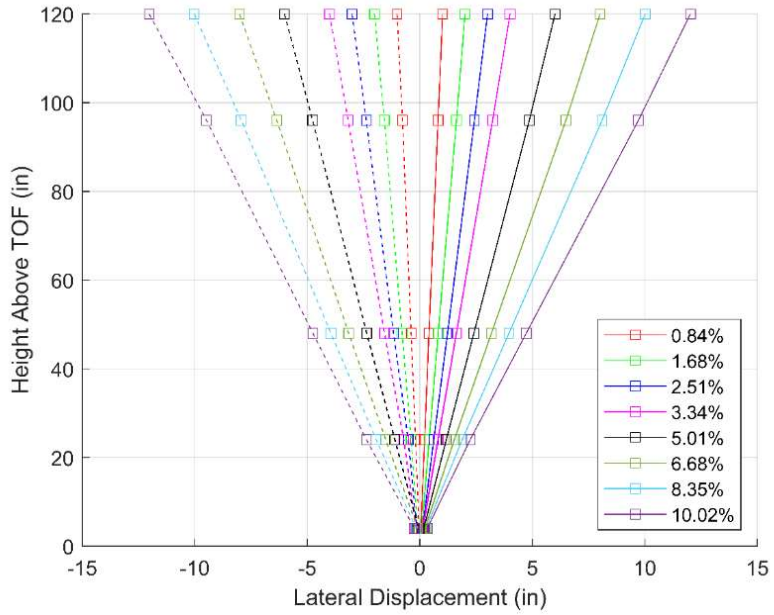

Figure 9.12: Lateral displacements along height of Specimen 1 with grouted sacrificial zone (measured with string potentiometers shown in Figure D.6)

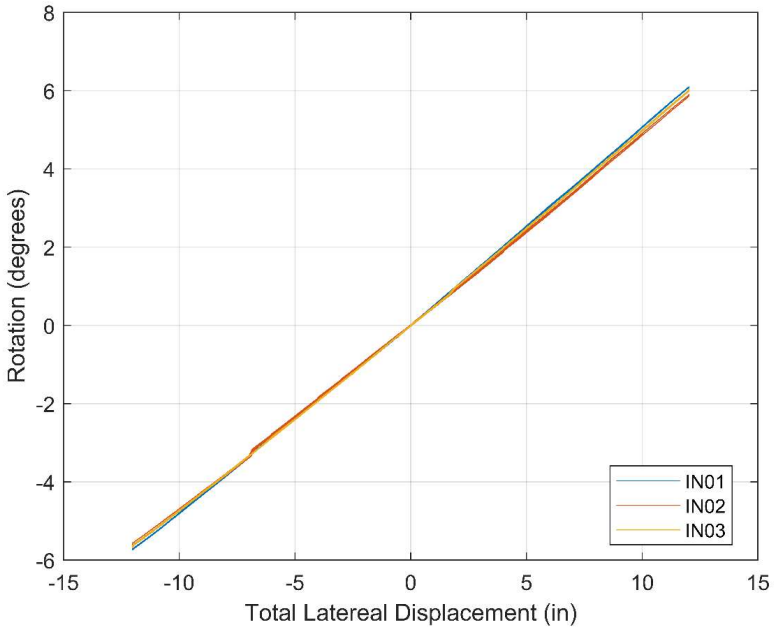

Figure 9.13: Rotation of Specimen 1 measured by inclinometers during test with grouted sacrificial zone (inclinometer locations shown in Figure D.10)

Measurements from the linear potentiometers installed around the sacrificial zone, with their locations shown in Figures D.8 and D.9, are used to calculate the location of the neutral axis of bending in the plane at the mid-height of the sacrificial zone. The neutral axis location was the result of the deformations of different components in the sacrificial zone, including the steel rocking plates, the grout, the reinforcing bars, and the steel plates directly in contact with concrete above and below the rocking plates, as well as the axial load applied to the column and the tensile force exerted by the prestressing strands.

Figure 9.14 shows a plot of the distance of the neutral axis versus the lateral drift of the column for the test without grout in the sacrificial zone. The neutral axis distance is measured from the center of the column, and has the same sign convention as the lateral drift of the column. For a column section under compression, the distance of the neutral axis from the center of the section

is undefined when the column deflection is zero. When the column deflection is positive and very small, the neutral axis distance is negative and very large. When the column deflection is negative, the distance of the neutral axis will be initially positive and very large. This trend is clearly observed in Figure 9.14. Figure 9.15 shows a plot of the neutral axis distance for the test with grout in the sacrificial zone. At small drift levels, the plot shows a similar trend as Figure 9.14. However, at higher positive drift levels, the neutral axis distance became positive; and at higher negative drift levels, the neutral axis distance became negative. The shift of the neutral axis distance from negative to positive and positive to negative in the respective drift directions at higher drift levels is due to the inability of the grout and steel rocking plates to transmit tension. In later cycles, the starting point of the neutral axis distance when column drift was close to zero was flipped, as shown by the small graph inserted in Figure 9.15. This could be due to the residual plastic elongation of the remaining reinforcing bars near the center of the section. At 10% drift in the positive and negative directions, the neutral axis distance was between 8 and 9 inches from the center.

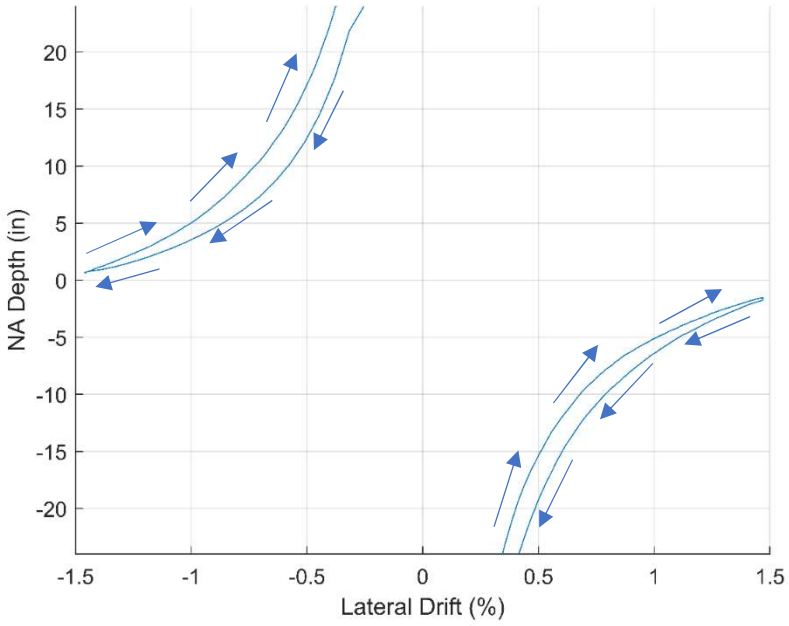

Figure 9.14: Neutral axis distance-vs.-drift ratio curves for Specimen 1 with ungrouted sacrificial zone (with respect to the center of the column section)

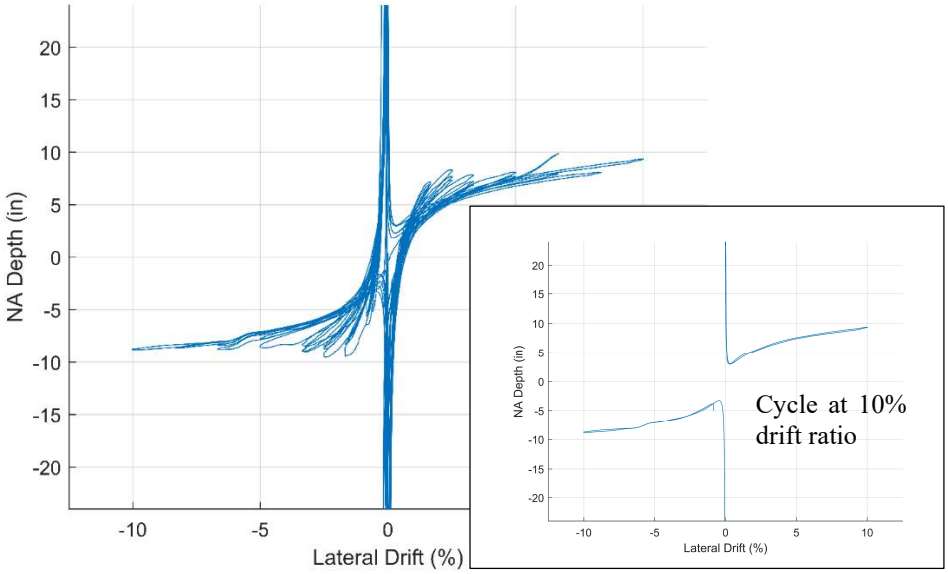

Figure 9.15: Neutral axis distance-vs.-drift ratio curves for Specimen 1 with grouted sacrificial zone (with respect to the center of the column section)

Figure 9.16 shows a plot of the average axial deformation of the sacrificial zone versus the lateral drift. It is calculated by averaging the axial displacements measured by the linear potentiometers around the sacrificial zone, and represents the axial deformation at the center of the cross-section, excluding the initial deformation induced by the axial load and the prestressing strands. The plot has a V shape, which indicates a rocking behavior, and it shows that a small residual compressive deformation developed in later displacement cycles after the lateral drift returned to zero. The residual axial deformation could be caused by the deformation of the steel plates above and below the rocking plates and that of the adjacent concrete.

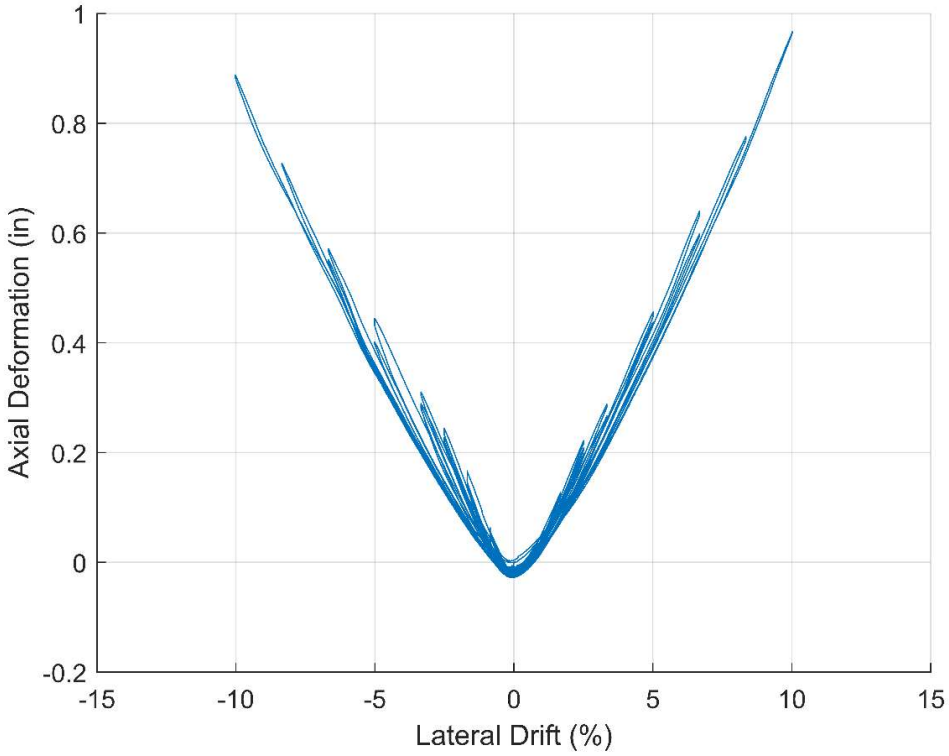

Figure 9.16: Average axial deformation of grouted sacrificial zone of Specimen 1

9.2.3 Data from Strain Gauges

Figure 9.17 shows the plots of strains measured in the rebar (Bar 1) located on the extreme south side of the column at different elevations and column drift levels during the test with the ungrouted sacrificial zone. The elevation is measured from the surface of the footing. The strain-vs.-lateral drift hysteresis curves from gauges at different locations on the bar are shown in Figure 9.18(a). The initial point for the rebar strain gauge data was manually biased. The justification for the bias is discussed in Appendix E. Unfortunately, the rebar on the extreme north side (Bar 4) did not have enough functioning strain gauges to create strain profiles. The strain-vs.-lateral drift hysteresis curves from a pair of functioning gauges at one location on the bar are shown in Figure 9.18(b). The bars were #6 bars. Based on the tensile test data presented in Table 8.1, the yield strain of the bars is estimated to be 0.0027. As shown in Figures 9.17(b) and 9.18(a), the maximum compressive strain reached in Bar 1 was about -0.0063, which is way above the yield strain. This strain value was obtained by one gauge (S29) located in the ungrouted sacrificial zone, and was thus significantly influenced by bar bending. The strain measured by the pair of gauges (S13 and S21) right above S29 registered a much smaller strain, which is close to the yield point. The two upper most gauges on Bar 1 were in the region where the rebar was bonded to the concrete, and they registered much smaller strain values. Figure 9.18(b) shows that Bar 4 reached similar strain levels as Bar 1 but with the sign flipped in the respective drift directions due to the bar location.

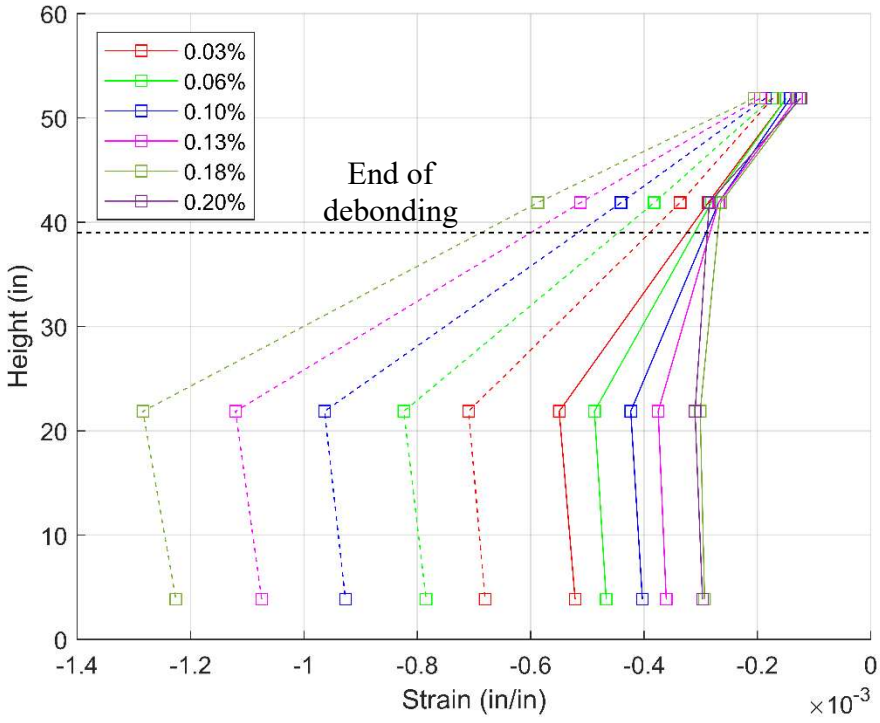

(a) Lower drift levels

Figure 9.17: Strain profiles of Bar 1 (extreme south) in Specimen 1 at different drift levels during test with ungrouted sacrificial zone (dashed lines are for drifts towards the south, and the solid lines for drifts towards the north)

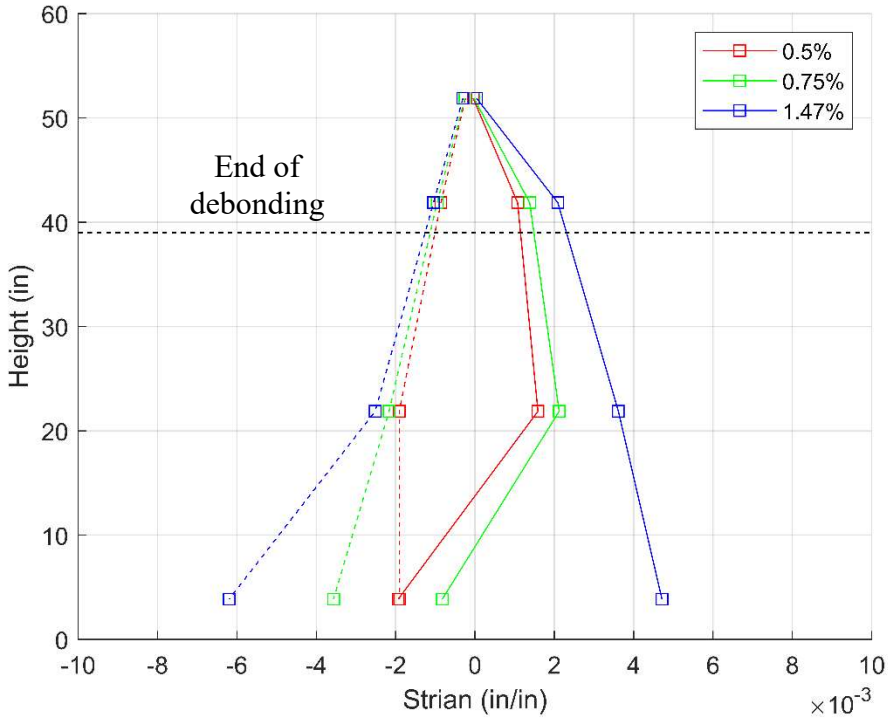

(b) Higher drift levels

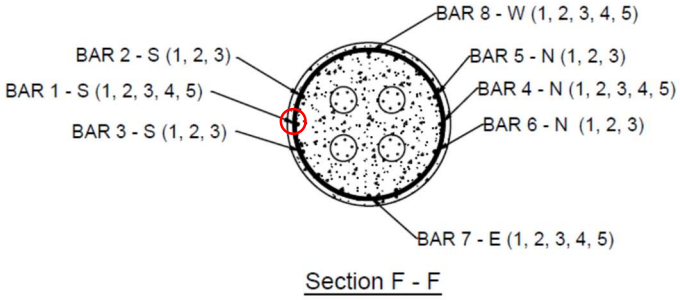

Figure 9.17 (continued): Strain profiles of Bar 1 (extreme south) in Specimen 1 at different drift levels during test with ungrouted sacrificial zone (dashed lines are for drifts towards the south, and the solid lines for drifts towards the north)

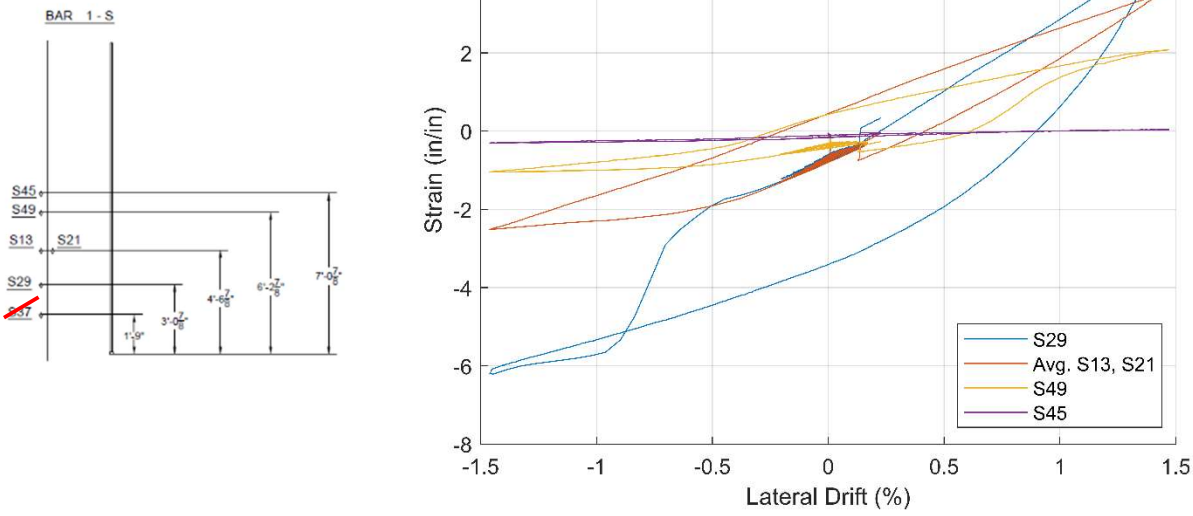

(a) Bar 1 (Extreme South)

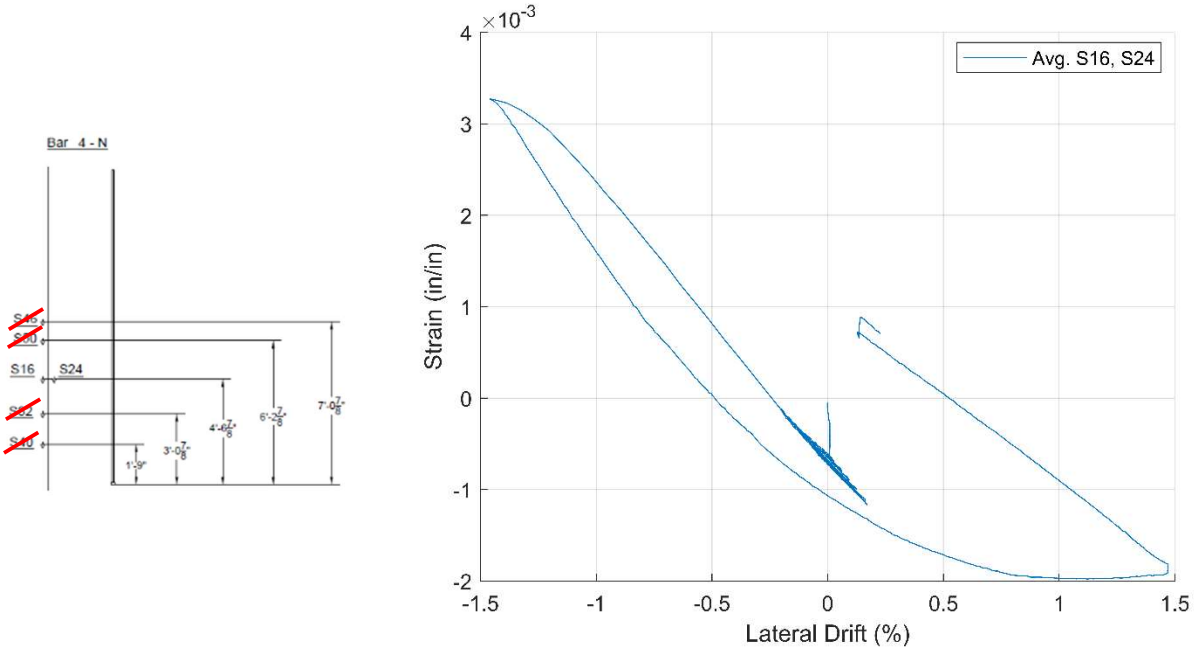

(b) Bar 4 (Extreme North)

Figure 9.18: Strain-vs.-drift ratio curves for extreme north and south bars in Specimen 1 with ungrouted sacrificial zone (the crossed-out gauges did not function)

Figure 9.19 shows the plots of strains measured in Bar 1 (the extreme south bar) at different elevations and column drift levels during the test with the sacrificial zone filled with grout. The strain-vs.-lateral drift hysteresis curves from gauges at different locations on the bar are shown in Figure 9.20(a). Gauge S29, located in the sacrificial zone of the bar, stopped functioning after the lateral drift exceeded 0.84%, probably because the bar was severely bent in that region. The remaining gauges on the bar continued to function till the drift level of about 3% was reached. The maximum average tensile strain registered by S13 and S21 was 0.01 at the positive drift level of about 3%. The bar fractured after that point, which was accompanied by a sudden load drop as shown in the lateral load-vs.-drift curves in Figure 9.4. The strain-vs.-lateral drift hysteresis curves from the pair of functioning gauges at one location on Bar 4 (the extreme north bar) are shown in Figure 9.20(b). The gauges remained functional till the drift level of about -2.5% was reached, after which the strain dropped suddenly due to bar fracture occurring in the sacrificial region, which was accompanied by a sudden drop of the lateral load resistance as shown in Figure 9.4.

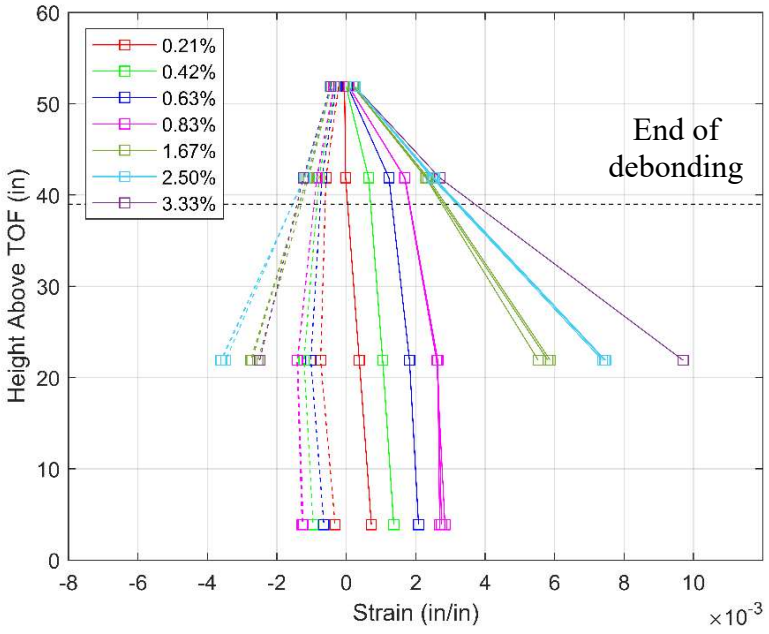

Figure 9.19: Strain profiles of Bar 1 (extreme south) in Specimen 1 at different drift levels during test with grouted sacrificial zone (dashed lines are for drifts towards the south, and the solid lines for drifts towards the north)

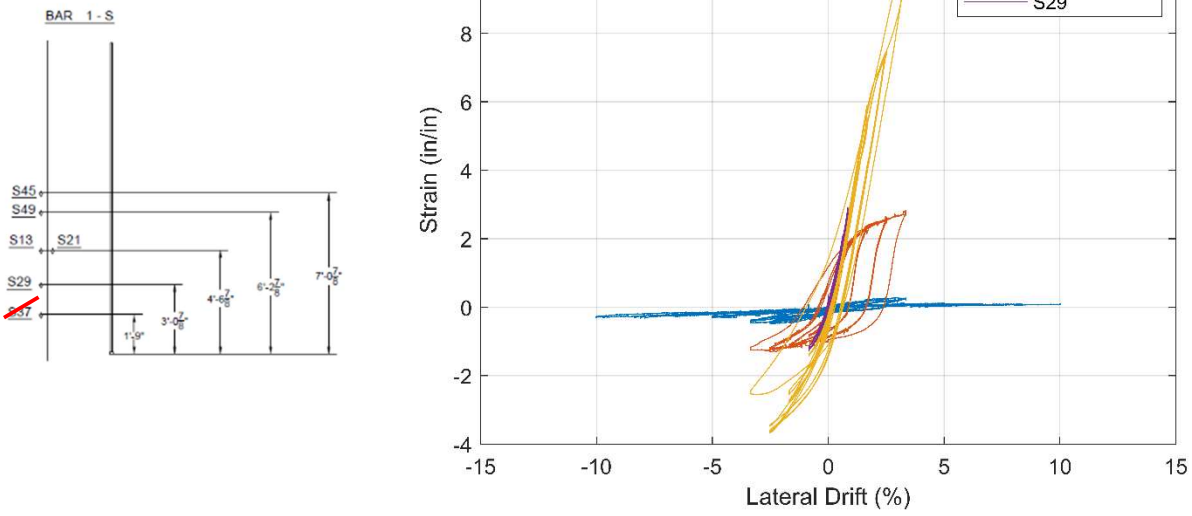

(a) Bar 1 (Extreme South)

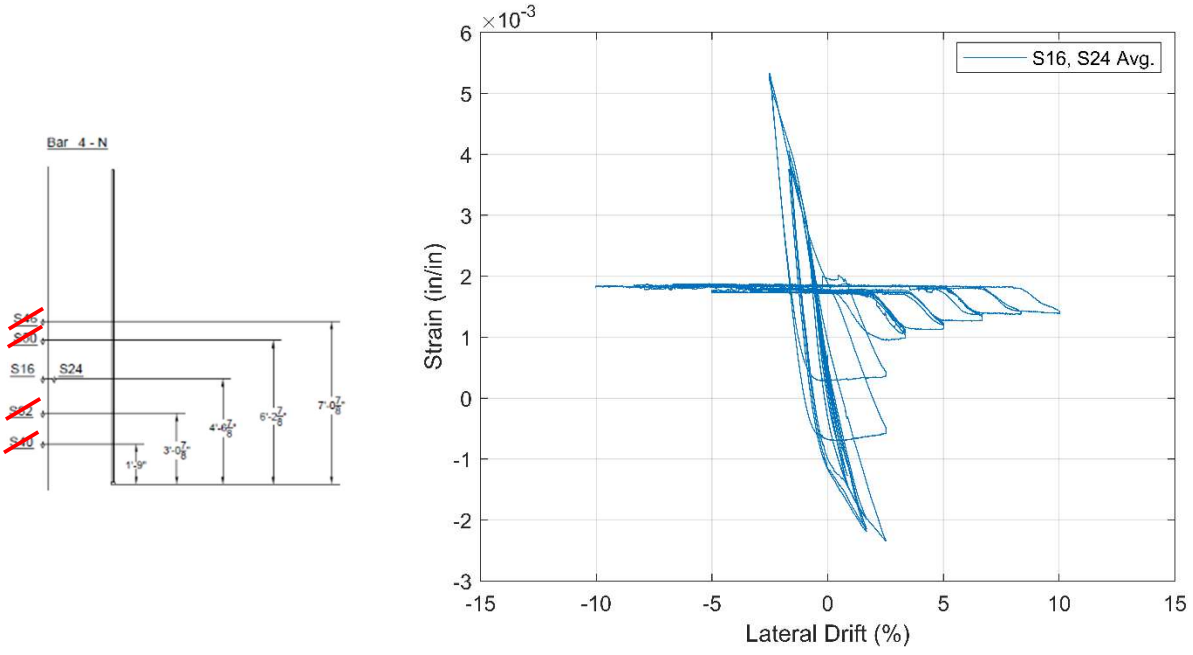

(b) Bar 4 (Extreme North)

Figure 9.20: Strain-vs.-drift ratio curves for extreme north and south bars in Specimen 1 with grouted sacrificial zone (the crossed-out gauges did not function)

Figures 9.21 and 9.22 show the strains in the post-tensioned strands plotted against the lateral drift ratio of the column with the grouted sacrificial zone. The strands were grouped in four post-tensioning ducts, with five strands in each duct. Two of the ducts were on the north side of the column and two were on the south side. Due to an issue with several strain gauges in the strands being mislabeled, it is not possible to determine the specific duct a strand was in, but it is possible to determine whether a gauge was on a strand located in a north or south duct. The initial strain value prior to the first test with an ungrouted sacrificial zone is estimated to be 0.00217. The calculations for this estimate are shown in Appendix E. The initial strain in the strands during the test with the grouted sacrificial zone is set to the final strain registered right after the test with the ungrouted sacrificial zone, which is approximately 0.00216. As can be seen in Figures 9.21 and 9.22, the strain-vs.-lateral drift curves for each set of strands have a V-shape. The slope of the curves for the positive drift direction is different from that for the negative direction because of the shift of the neutral axis location as the column rocked. The curves show a more gentle slope and lower peak strain values for the drift direction in which the strands were closer to the neutral axis. The behavior of the strands on the north side is almost a mirror image of that on the south. The maximum tensile strain reached in the south strands is around 0.009 and that in the north strand is about 0.0094. They correspond to a stress level of 270 ksi, according to Figure 8.4, which is beyond the elastic limit and close to the tensile strength of the strands. The strain plots also show a reduction in the initial tensile strain of about 0.0013 when the lateral drift returned to zero at the end of the test. This can be attributed to the gradual shortening the column due to plastic deformation in the sacrificial zone, as shown in Figure 9.16, as well as the slip of the strands in the anchors.

According to the geometry of the cross-section of the column, as shown in Appendix D, the center of each strand group (which is the center of the post-tensioning duct) is 7 inches from the center of the column. Figure 9.15 shows that the neutral axis of bending in the sacrificial zone was about ±8 inches from the column center when the lateral drift was at ±10%. Hence, the distance of the north strands from the neutral axis was about 1 inch when the lateral drift was 10% towards north, and 15 inches when the drift was 10% towards south. If the column rocked as a rigid body, the maximum elongation developed in the north strands would be 0.1 inch when the column drifted towards north and 1.5 inch when the column drifted toward south. The length of the unbonded strands between the anchors was about 165 inches. These result in tensile strain increases of 0.0006 and 0.009 in the north strands for the two drift directions, respectively. The same can be said for the south strands. These values are slightly higher than the strain increments shown in Figures 9.21 and 9.22 for one drift direction and lower than those shown for the other direction.

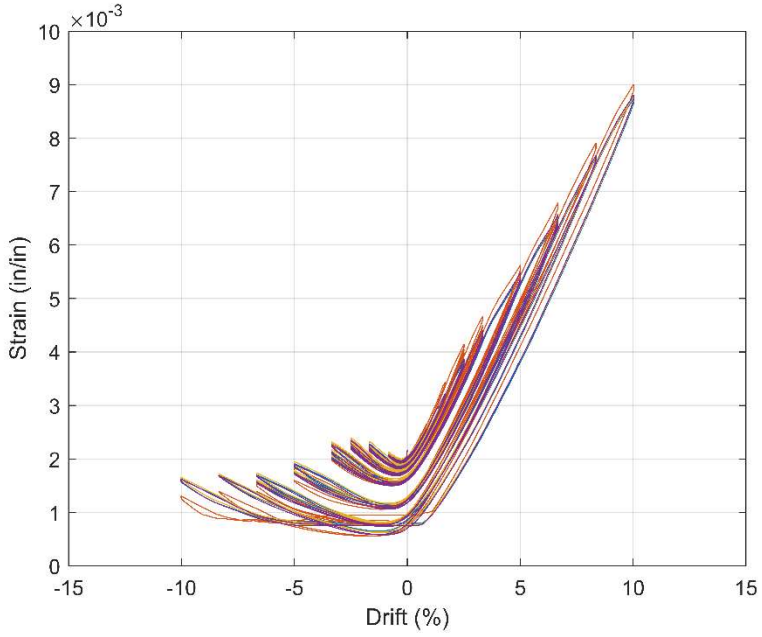

Figure 9.21: Strain-vs.-drift ratio curves for south strands of Specimen 1 with grouted sacrificial zone (strain gauge locations shown in Figure D.4)

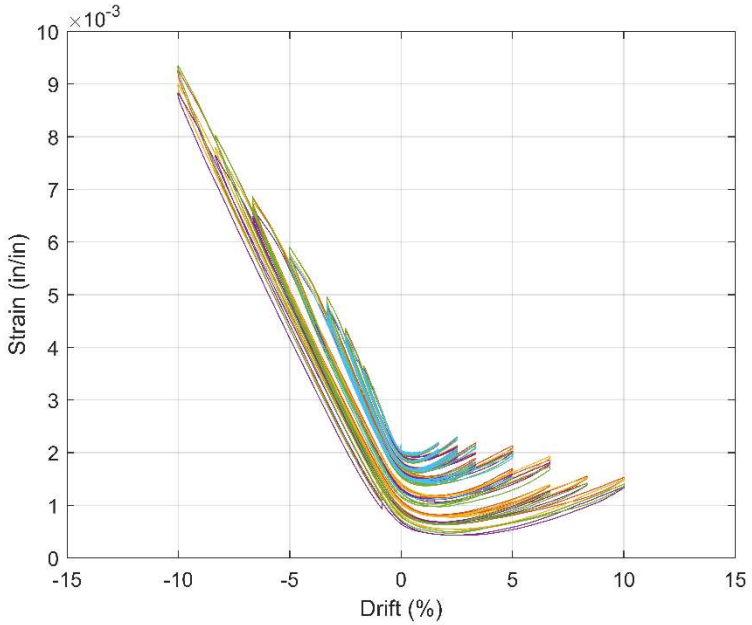

Figure 9.22: Strain-vs.-drift ratio curves for north strands of Specimen 1 with grouted sacrificial zone (strain gauge locations shown in Figure D.4)

9.2.4 Concluding Remarks

Specimen 1 performed according to the expectation in terms of its recovery capability, having a negligible residual drift and a moderate load degradation of about 26% after reaching a lateral drift of 10%. Outside the sacrificial zone, the column remained undamaged and maintained of its axial load capacity. However, the reinforcing bars fractured relatively early at drift levels between 2 and 3% due to the crushing of the grout in the sacrificial zone and the bending of the bars. The energy dissipation exhibited by the hysteresis curves was moderate and stable, and was mainly contributed by the inelastic tensile deformation of the strands and reinforcing bars.

9.3 Free-Vibration Testing of Column Specimen 1

9.3.1 General Test Observations

Figures 9.23 through 9.26 show the displacement time histories from the free-vibration tests of Specimen 1 with different initial displacement amplitudes. In these tests, the reinforcing bars in the rocking hinge were cut and the applied axial load was removed. The response time histories appear to be shifted upward from the zero-displacement line. This could be caused by crushed grout particles scattered on one side of the rocking surface between the steel rocking plates, as shown in Figure 9.27. For the low-amplitude tests (Figures 9.23 and 9.24), the decay of the response amplitude appears to be a little irregular, indicating possible wobbling motion during oscillations. For the higher amplitude tests (Figures 9.25 and 9.26), even though the response is not perfectly symmetric about the zero line, the rate of decrease of the free-vibration amplitude in each cycle of response is more or less uniform till the amplitude became very small. This trend of amplitude decay is consistent with Coulomb damping. Since the strains developed in the prestressing strands during the free-vibration tests were way below the yield level, as it will be shown later, the contribution of the inelastic deformation of the strands to the energy dissipation should be negligible.

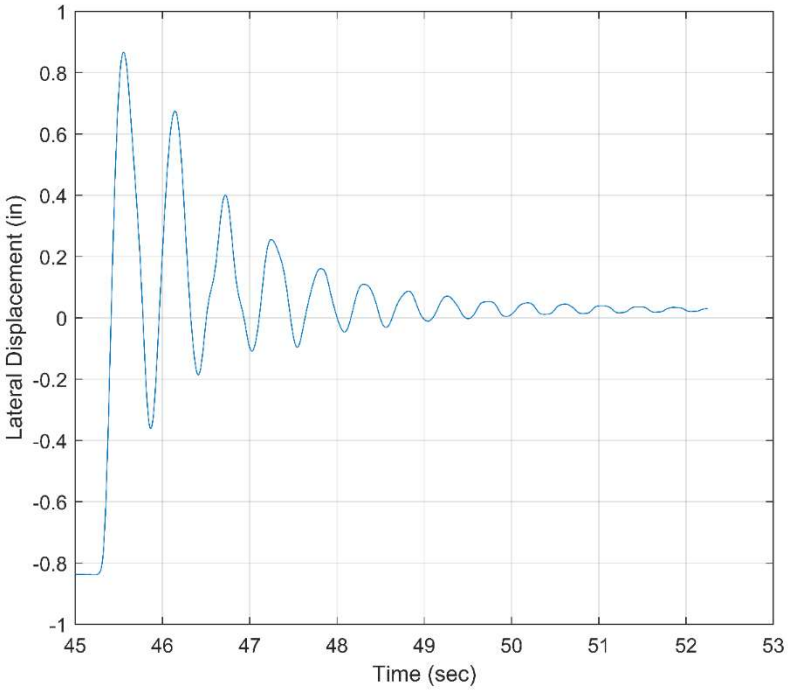

Figure 9.23: Displacement-vs.-time for free vibration test 1

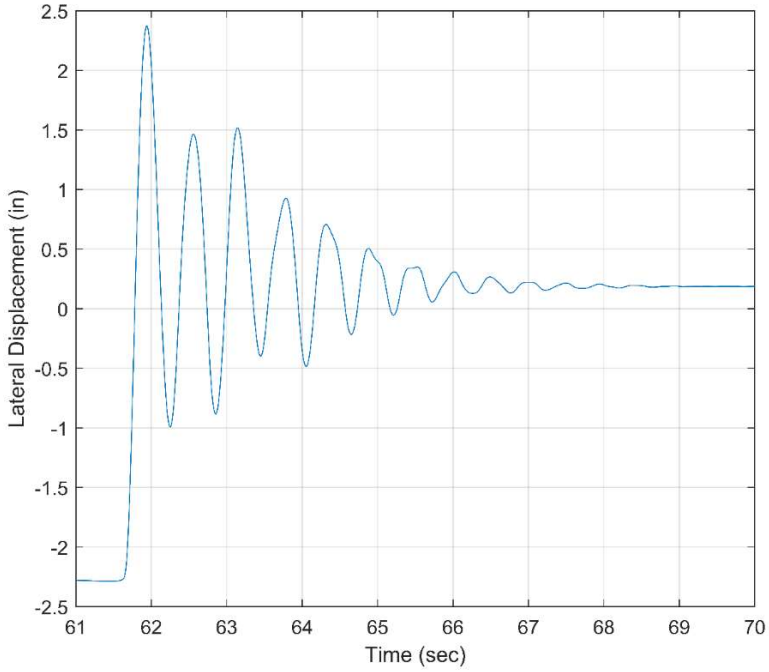

Figure 9.24: Displacement-vs.-time for free vibration test 2

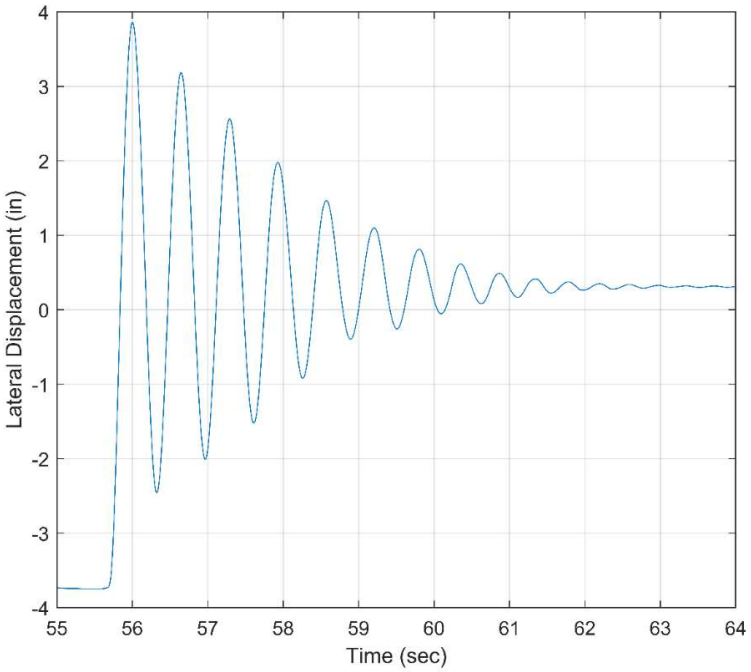

Figure 9.25: Displacement-vs.-time for free vibration test 3

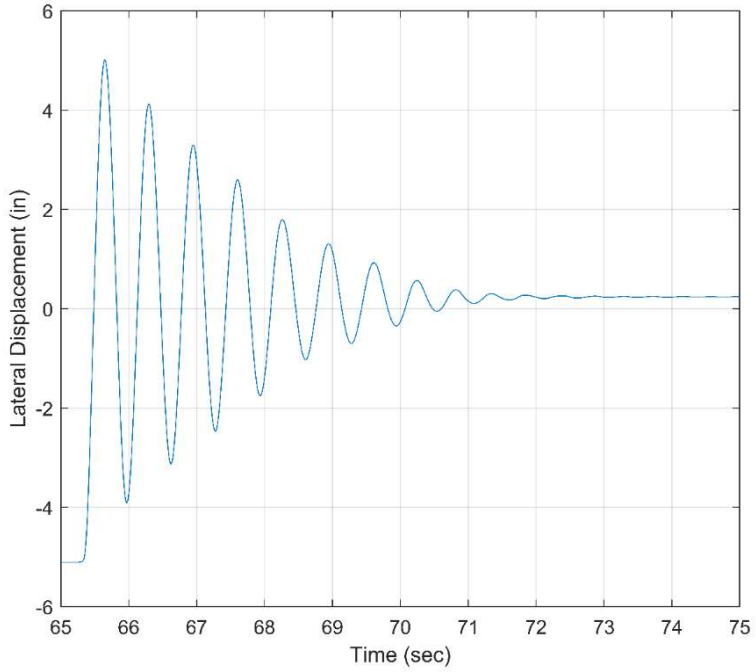

Figure 9.26: Displacement-vs.-time for free vibration test 4

Figure 9.27: Opening of rocker hinge at the beginning of free-vibration test 4

9.3.2 Data from External Instrumentation

Figures 9.28 through 9.31 show the rotational velocity of the column plotted against the drift ratio for each of the free-vibration tests. The rotational velocity was calculated using Equation 9.1:

$$\dot{\theta}^i = \frac{\theta^i - \theta^{i-1}}{t^i - t^{i-1}} \tag{9.1}$$

where t^i and t^{i-1} are two consecutive time instants at which data were collected, and θ^i and θ^{i-1} are the angles of rotation of the column calculated from the readings obtained at these two time instants with the linear potentiometers mounted around the base of the column, and the superposed dot represents differentiation with respect to time. It can be noted from these curves that the rotational velocity varies smoothly and continuously across the zero-drift point. This indicates that there was no loss of kinetic energy that could be caused by impact between the rocking plates when the gap was closed.

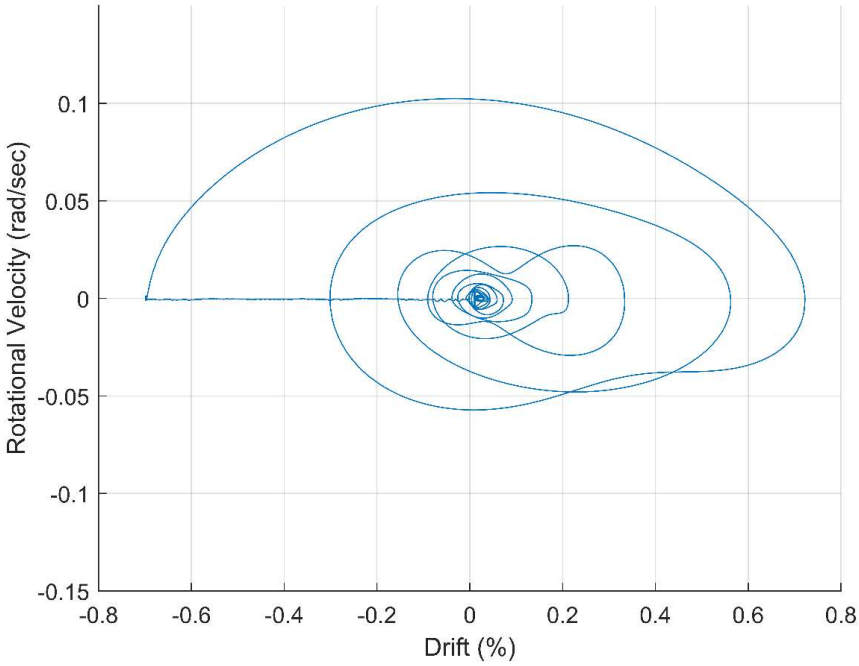

Figure 9.28: Rotational velocity-vs.-drift curves during free-vibration test 1

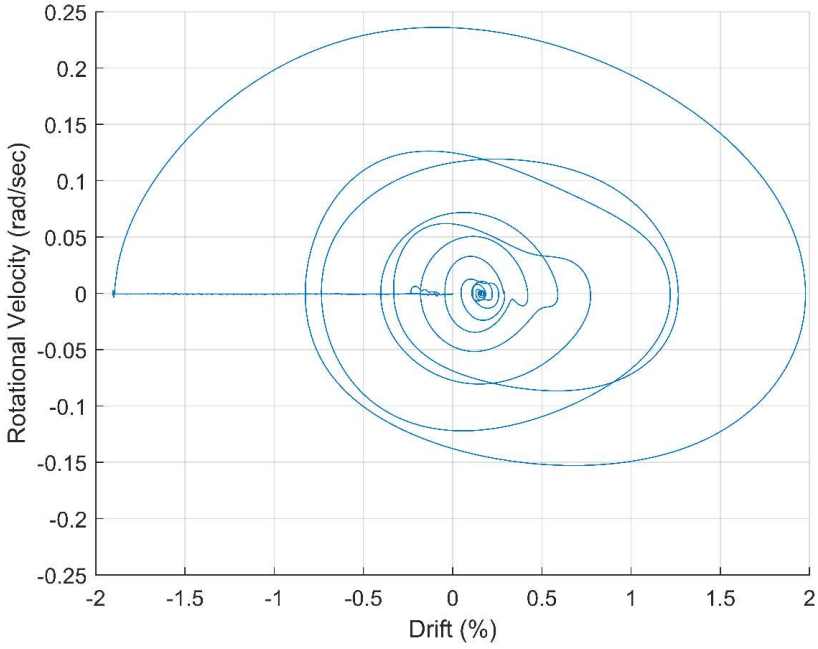

Figure 9.29: Rotational velocity-vs.-drift curves during free-vibration test 2

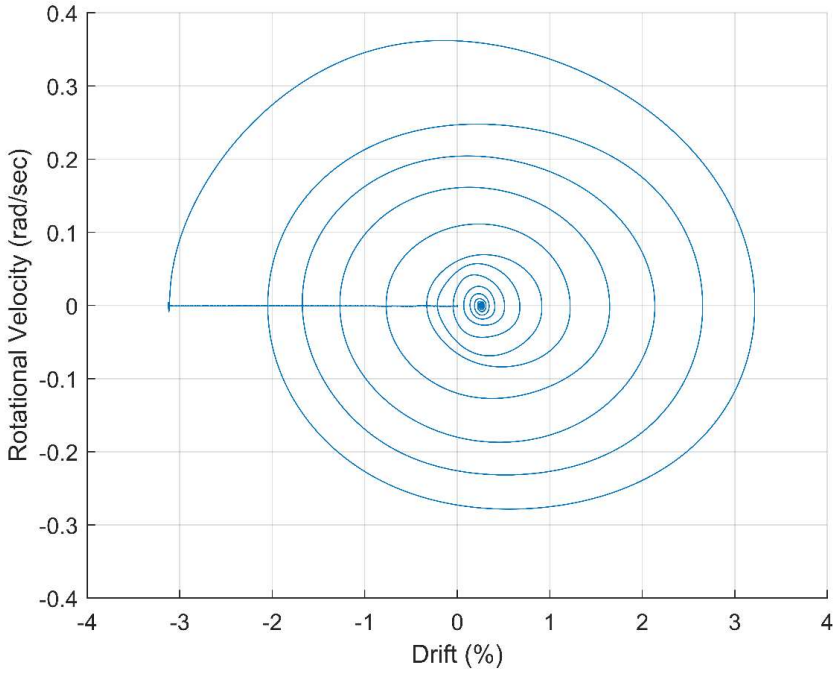

Figure 9.30: Rotational velocity-vs.-drift curves during free-vibration test 3

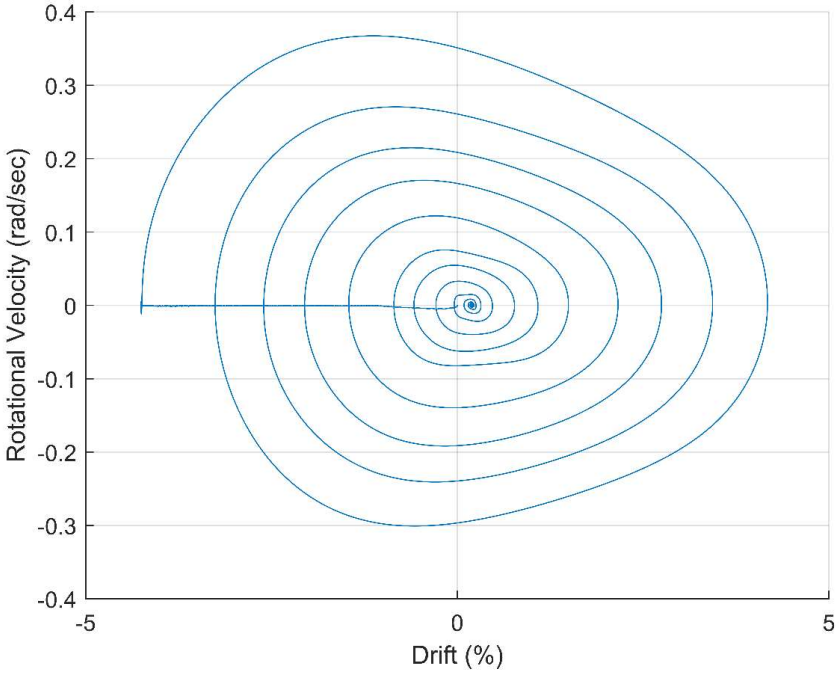

Figure 9.31: Rotational velocity-vs.-drift curves during free-vibration test 4

9.3.3 Data from Strain Gauges

Figures 9.32 and 9.33 show the strains in the prestressing strands plotted against the drift ratio of the column for the fourth free-vibration test including the phase in which the column was loaded to the initial displacement point. The strain-vs.-drift ratio curves show substantially fatter hysteresis loops than those observed in the quasi-static test (see Figures 9.21 and 9.22). The hysteretic behavior was probably caused by the temporary locking and delayed slip of the strands in regions near the two ends of the strands, due to friction in the post-tensioning ducts and anchors, during the dynamic response. In the quasi-static test, the strands had more time to slip and redistribute the strain uniformly over the entire strand length.

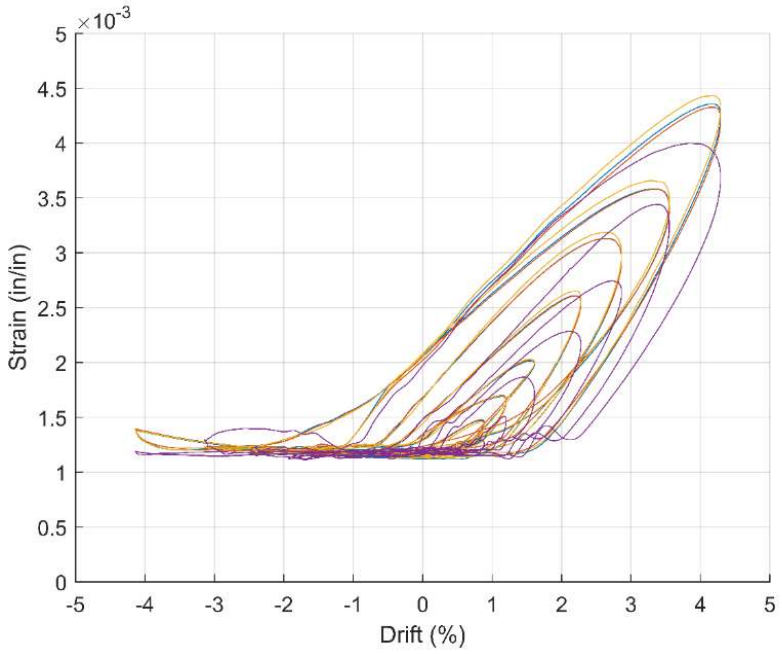

Figure 9.32: Strain-vs.-drift ratio curves for south strands of Specimen 1 during free-vibration test 4 (strain gauge locations shown in Figure D.4)

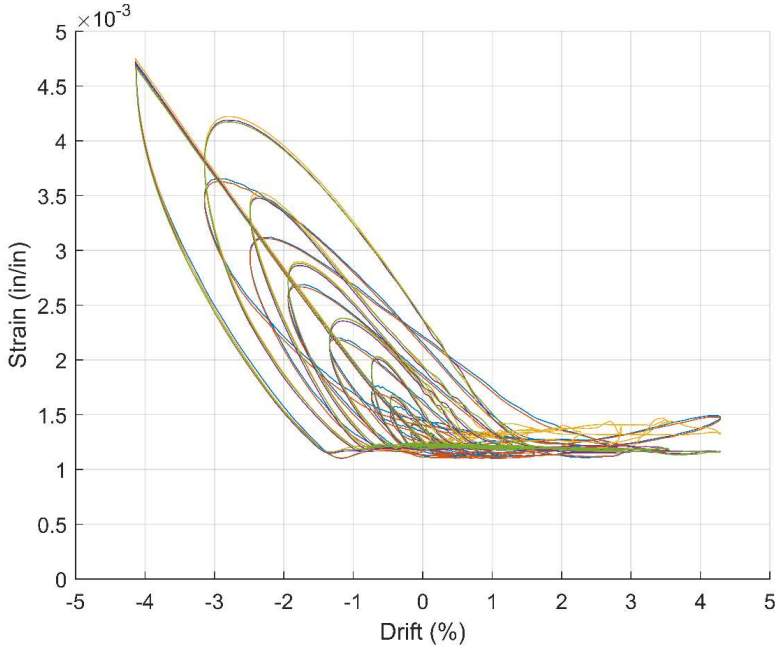

Figure 9.33: Strain-vs.-drift ratio curves for north strands of Specimen 1 during free-vibration test 4 (strain gauge locations shown in Figure D.4)

9.3.4 Simulation of Free-Vibration Test with Quasi-Static Loading

After the completion of the free-vibration tests, a quasi-static loading test was performed on Specimen 1 with a displacement history identical to that for the fourth free-vibration test. The goal of this test was to compare the energy dissipations in the dynamic and quasi-static responses.

Figure 9.34 shows the lateral load-vs.-drift ratio hysteresis curves. It can be seen that the shape and fatness of the hysteresis loops remain the same regardless of the amplitude of the displacement cycles. This is typical for structures with Coulomb damping. If damping is Coulomb, the friction force F_f in the lateral resistance of the column is equal to one-half of the vertical width of the hysteresis curves. The friction force estimated this way for each cycle of the quasi-static test is shown in Table 9.1. From the free-vibration response histories shown in Section 9.3.1, the friction force can also be calculated from the amplitude decay as follows (Chopra 2017):

$$F_f = k\frac{u_{i+1} - u_i}{4} \tag{9.2}$$

where u_i is the displacement amplitude in cycle *i* and *k* is the elastic stiffness of the column. The friction force calculated this way for each response cycle of the fourth free-vibration test is also shown in Table 9.1 for comparison with that calculated from the hysteresis curves.

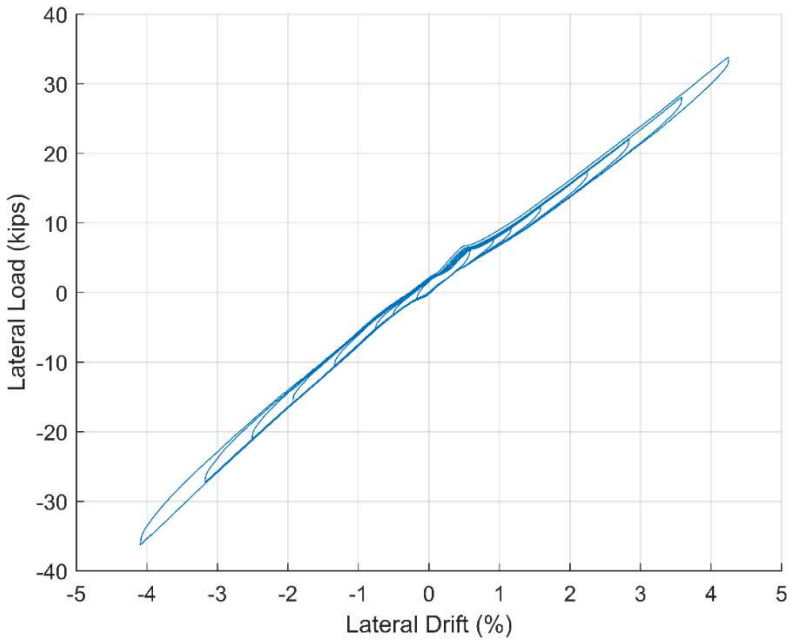

Figure 9.34: Lateral load-vs.-drift ratio hysteresis curves for Specimen 1 during simulated free-vibration test with quasi-static loading

Table 9.1: Average friction force in first 5 cycles of quasi-static simulation

Drift Amplitude (%)	Average Friction Force QS (kips)	Average Friction Force FV (kips)[a]
4.17	1.20	1.68
3.38	0.99	1.58
2.67	0.88	1.35
2.09	0.80	1.45
1.46	0.68	1.12

[a]: Based on analysis of free-vibration data from test 4

Figures 9.35 and 9.36 show the strains in the prestressing strands plotted against the lateral drift ratio for the quasi-static loading test. It is notable that the curves show no fat hysteresis loops, because the strands had sufficient time to slip and redistribute the strain along their length during the slow-motion test.

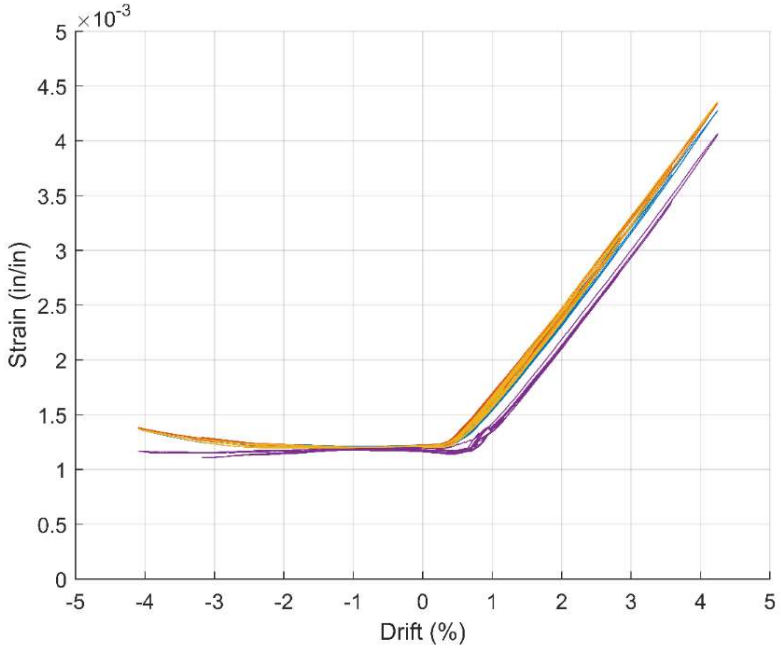

Figure 9.35: Strain-vs.-drift ratio curves for south strands of Specimen 1 during quasi-static simulation of free-vibration (strain gauge locations shown in Figure D.4)

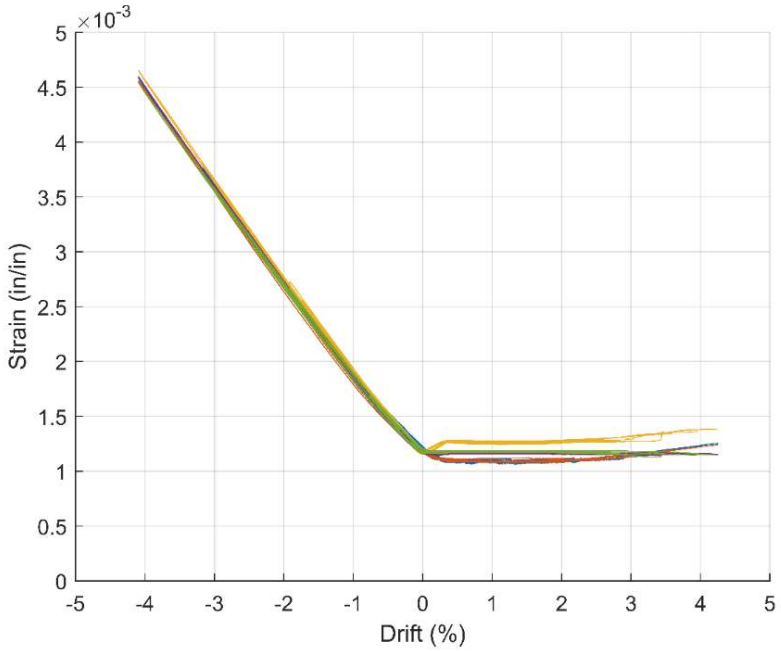

Figure 9.36: Strain-vs.-drift ratio curves for north strands of Specimen 1 during quasi-static simulation of free-vibration (strain gauge locations shown in Figure D.4)

9.3.5 Concluding Remarks

There was little difference in energy dissipation by the column when it was loaded quasi-statically or subjected to dynamic free vibration. The energy dissipation at the drift level considered was mainly contributed by the friction between the prestressing strands and the ducts and anchors.

9.4 Quasi-Static Testing of Column Specimen 2

Based on test data from Specimen 1, several changes were introduced to the design of Specimen 2, as described in Section 8.2.2. The major changes introduced were to prevent the buckling of the longitudinal bars in the sacrificial zone, which was observed in Specimen 1. The longitudinal bars in Specimen 2 were unbonded along the entire length. The bar hats at the upper end were outside the load stub so that the bars would not be subjected to compression. Finally, each longitudinal bar consisted of a #10 bar and a #8 bar spliced together with a mechanical coupler, with the #8 bars located at the upper end to serve as structural fuse where yielding would occur.

The lateral load-vs.-drift ratio hysteresis curves and general test observations are first presented in the following section. Data from displacement transducers and strain gauges will be presented in subsequent sections.

9.4.1 General Test Observations

Figure 9.37 shows the lateral load-vs.-drift ratio hysteresis curves for Specimen 2 (RC2) with the ungrouted sacrificial zone. The data were processed in the same way as for Specimen 1 (RC1), whose hysteresis curves are also shown for comparison. Specimen 2 was subjected to the displacement history presented in Section 8.7. Even though the displacement histories for the two

specimens are different, their hysteresis curves have similar shapes. No bar bending was observed in the sacrificial zone of Specimen 2. Figure 9.38 shows the axial load applied to the column plotted against the column drift ratio. Except for a couple of glitches, the load remained constant at 900 kips.

Figure 9.39 shows the lateral load-vs.-drift ratio hysteresis curves for Specimen 2 with the grouted sacrificial zone. Small sudden load drops can be observed in the hysteresis curves between drift ratios of 5% and 10%. They were caused by the slip of the strands in the anchors at the top end. A loud noise was heard when a wedge in an anchor popped out at the positive drift level of 6.7%. Figure 9.40 shows the axial load plot.

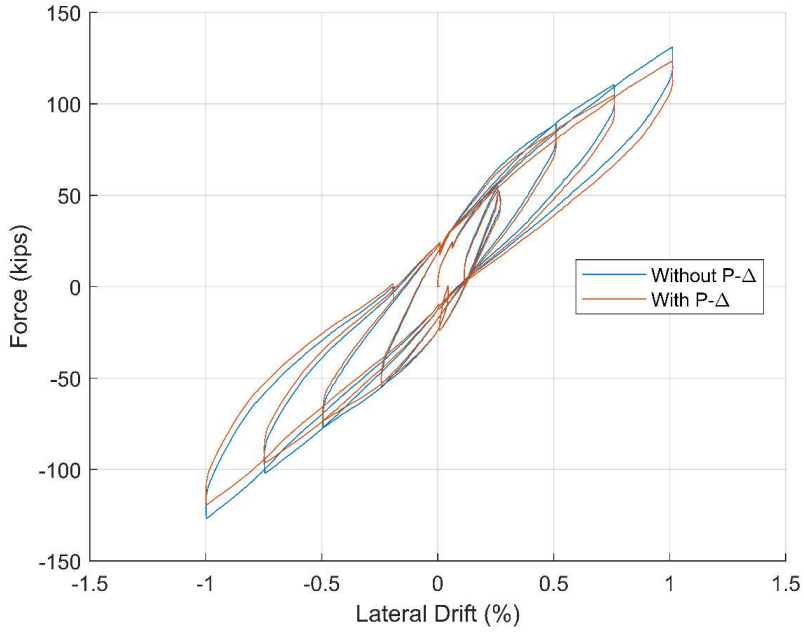

Figure 9.37: Lateral load-vs.-drift ratio hysteresis curves for Specimen 2 with ungrouted sacrificial zone

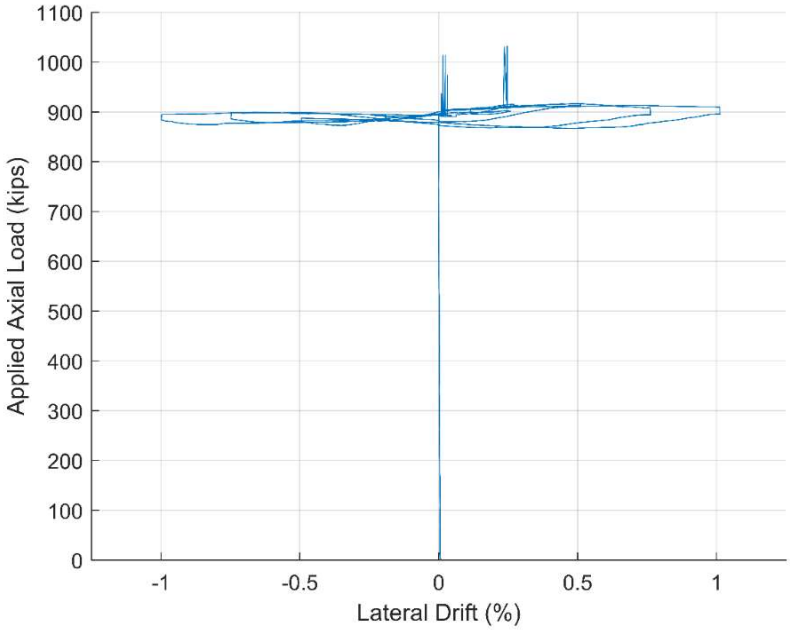

Figure 9.38: Applied axial load vs. lateral drift with ungrouted sacrificial zone

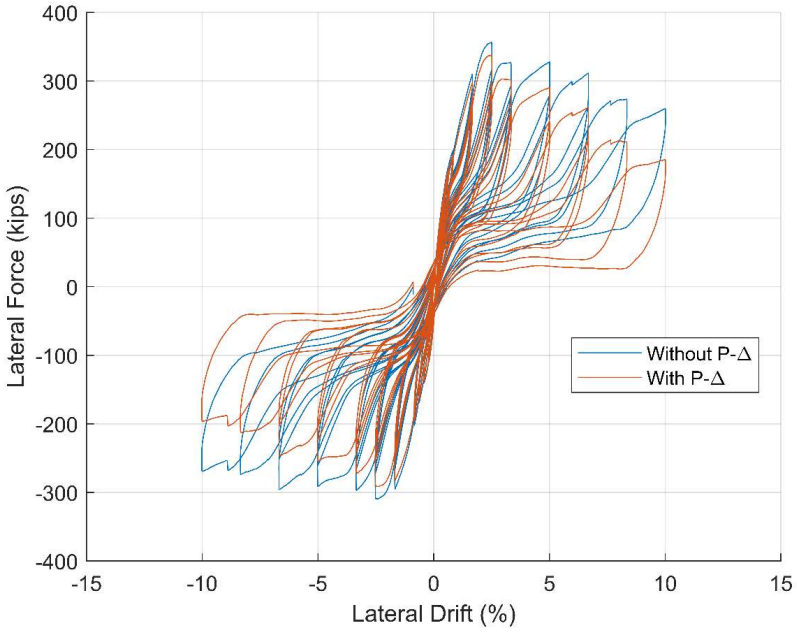

Figure 9.39: Lateral load-vs.-lateral displacement hysteresis curves for Specimen 2 with grouted sacrificial zone

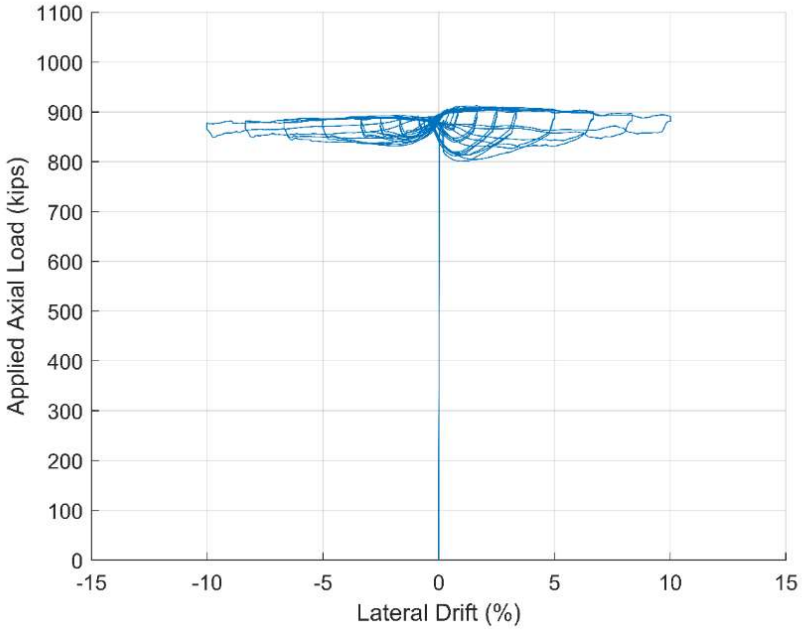

Figure 9.40: Applied axial load vs. lateral drift with grouted sacrificial zone

Pictures of damage in the grouted sacrificial zone and load stub are shown in Figures 9.41 through 9.45. Cracking and mild crushing of the grout were first observed on the south side of the specimen in the cycle that reached a drift amplitude of 0.63%. Crushing on the south side became more significant when the drift ratio reached 0.83%, as shown in Figure 9.41. No obvious damage was observed on the north side at 0.83% drift. Severe crushing and grout spalling occurred on the south side in the first cycle at 1.68% drift. The north side showed significant spalling in the second cycle at 1.68% drift. Grout crushing progressed on both sides, as shown in Figure 9.43, and the uplift of the column base became significant in later cycles with drift ratios exceeding 5%. Figure 9.44 shows the state of the specimen at the end of the test after reaching the maximum drift of 10%. It can be seen that significant portions of the grout were crushed on both the north and the south sides. However, none of the reinforcing bars fractured. The significant uplift of the column base was attributed to the crushing of the load stub concrete underneath the anchor heads of the

vertical reinforcing bars, as shown in Figure 9.45. The crushing under the anchor heads delayed the engagement of the bars in tension when the column was displaced in the other direction, contributing to the pinching of the hysteresis curves shown in Figure 9.39. Figure 9.45 also shows a missing wedge piece in the top anchor. The wedge popped out during the test.

Figure 9.41: Picture of spalling on south side of Specimen 2 after first cycle at 0.83% drift ratio

Figure 9.42: Picture of spalling on south side of Specimen 2 after first cycle at 2.51% drift ratio

Figure 9.43: Picture of south side of Specimen 2 after first cycle at 5.01% drift ratio

Figure 9.44: Picture of east side of Specimen 2 at -10% drift ratio

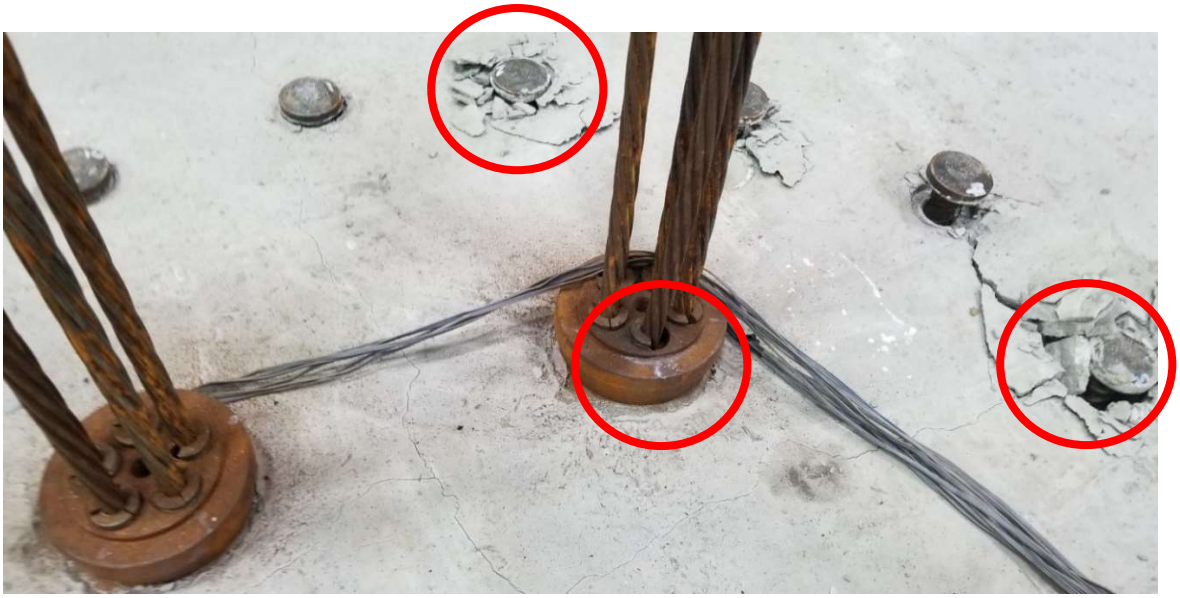

Figure 9.45: Picture of the top of load stub after the test of Specimen 2

9.4.2 Data from External Instrumentation

The instrumentation plans for the specimen can be found in Appendix D. Figure 9.46 shows the lateral displacement profiles of the specimen at the peaks of each displacement cycle, with the sacrificial region filled with grout. Similar to Specimen 1, the plots show that the column practically rocked as a rigid body about the base throughout the test, with deformation concentrated in the sacrificial region. The rotations measured by four inclinometers mounted at different elevations along the column height are almost identical, as shown in Figure 9.47, which is consistent with rigid-body rotation.

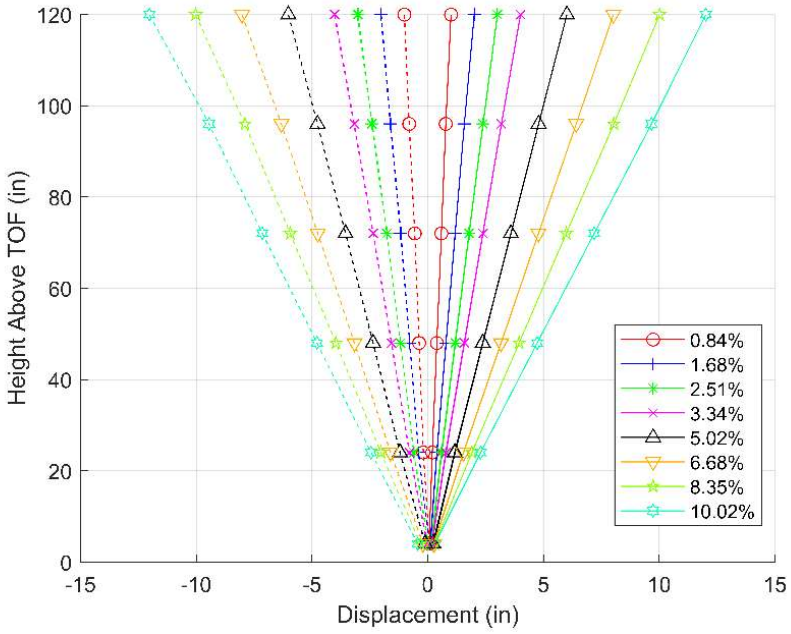

Figure 9.46: Lateral displacements along height of Specimen 2 with grouted sacrificial zone (measured with string potentiometers shown in Figure D.16)

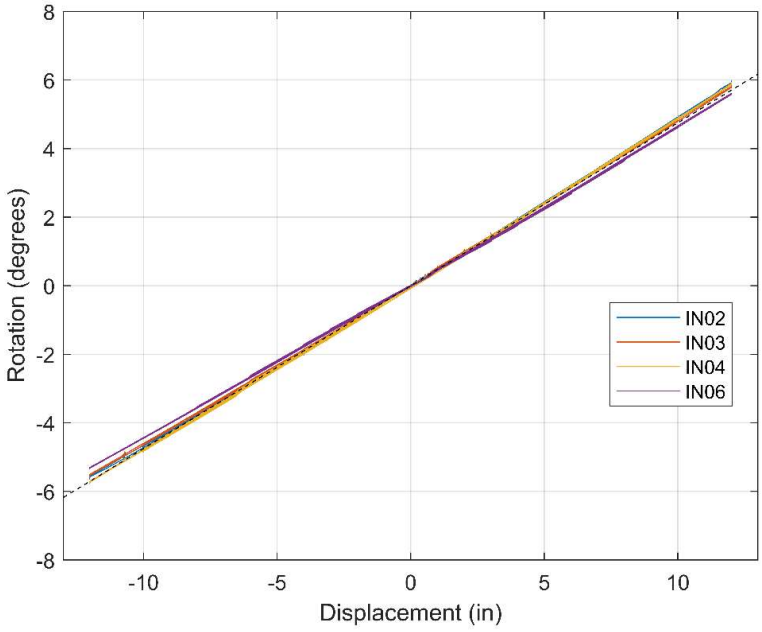

Figure 9.47: Rotation of Specimen 2 measured by inclinometers during test with grouted sacrificial zone (inclinometer locations shown in Figure D.18)

Measurements from the linear potentiometers installed around the sacrificial zone, as shown in Figure D.17, are used to estimate the location of the neutral axis of bending at the mid-plane of the sacrificial zone. Figures 9.48 and 9.49 shows plots of the distance of the neutral axis from the centerline of the column against the lateral drift of the column for the tests with the ungrouted and grouted sacrificial zone, respectively. The trend is similar to that observed for Specimen 1 (as shown in Figures 9.14 and 9.15). However, the data from Specimen 2 show a more consistent trend from the beginning to the end of the test. As the lateral drift increased in the positive direction, the neutral axis shifted from a far negative distance toward the positive side. For the test with the grouted sacrificial zone, the neutral axis distance leveled off at about 7.5 in. from the column center as the drift increased. The same trend is observed when the column was displaced in the negative direction with the direction of shift of the neutral axis reversed. Similar to that in Specimen 1, the neutral axis location is influenced by different deformation mechanisms occurring in the sacrificial zone, including the deformation of the rocker plates, the deformation of the grout, and the deformation of the steel plates directly in contact with concrete above and below the rocker plates.

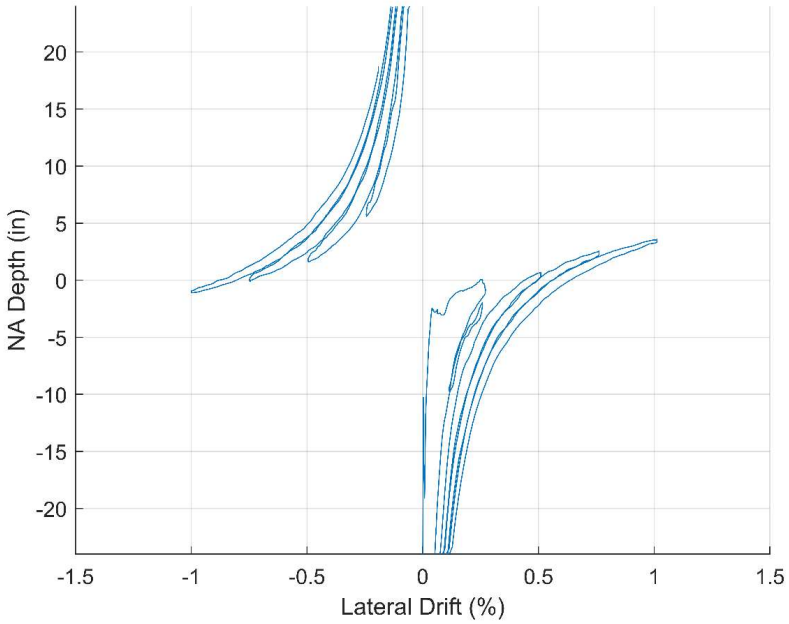

Figure 9.48: Neutral axis distance-vs.-drift ratio curves for ungrouted sacrificial zone of Specimen 2 (with respect to center of the column section)

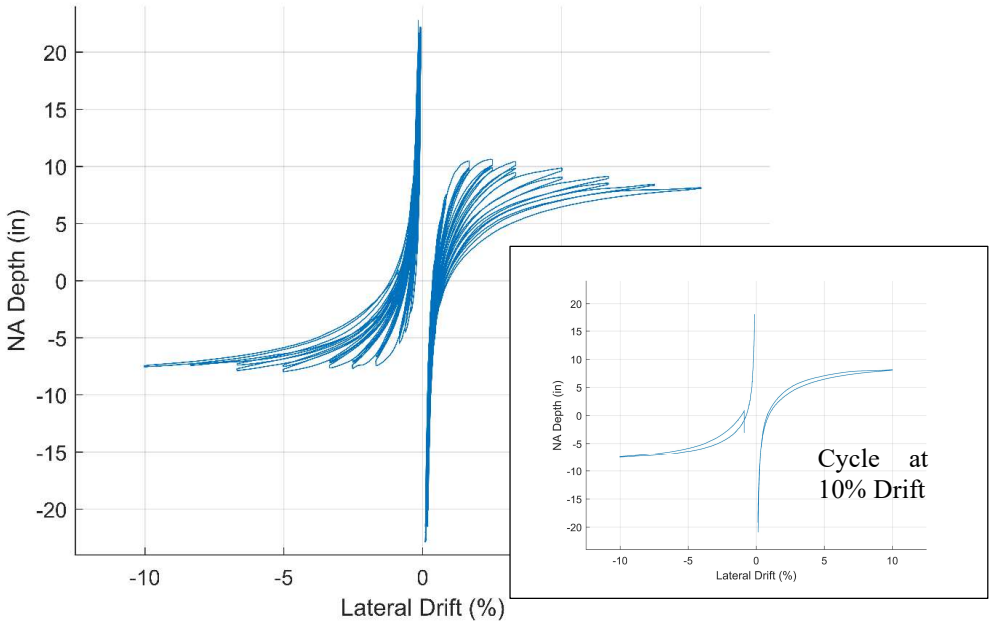

Figure 9.49: Neutral axis distance-vs.-drift ratio curves for grouted sacrificial zone of Specimen 2 (with respect to center of the column section)

Figure 9.50 shows a plot of the average axial deformation of the sacrificial zone against the lateral drift. It is calculated by averaging the axial displacements measured by the linear potentiometers around the sacrificial zone, and therefore, represents the axial deformation at the center of the cross-section. Similar to that for Specimen 1, the plot has a V shape, which indicates a rocking behavior, and it shows that a small residual compressive deformation developed in later load cycles after the lateral drift returned to zero. The residual axial deformation could be caused by the deformation of the steel plates above and below the rocker plates, as well as the deformation of the adjacent concrete.

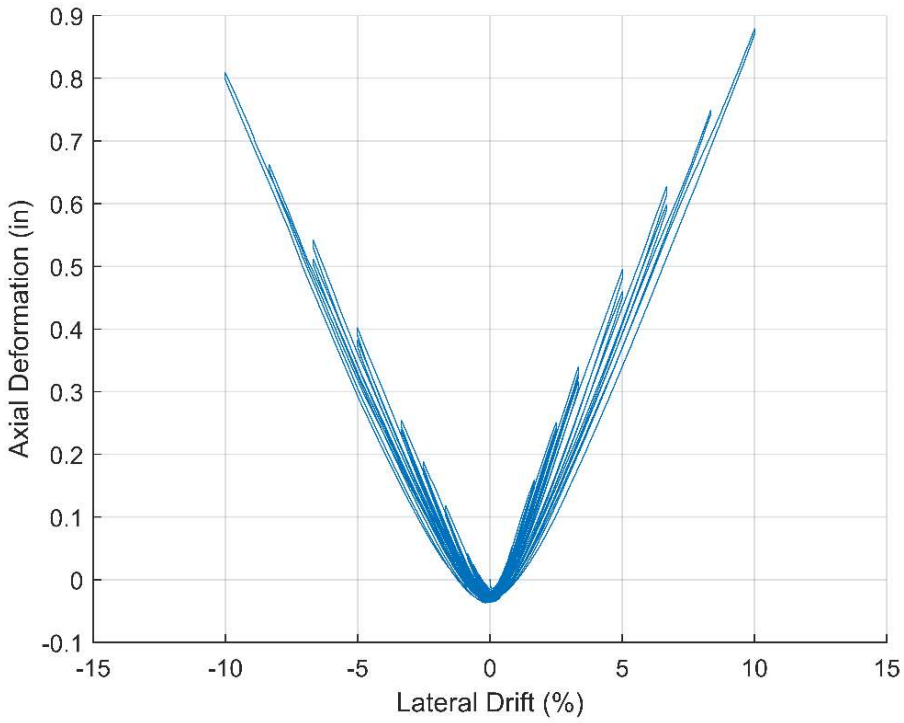

Figure 9.50: Average axial deformation of grouted sacrificial zone of Specimen 2

9.4.3 Data from Strain Gauges

Figures 9.51 and 9.52 show the plots of strains measured in Bar 1 (located on the extreme south side of the column) and Bar 2 (located on the extreme north side), respectively, at different elevations and column drift levels during the test with the ungrouted sacrificial zone. The elevation is measured from the surface of the footing. Unlike the bars in Specimen 1, these bars were unbonded over the entire length and had the top anchor heads unrestrained from upward movement. Therefore, these bars could not develop compression. Each of these bars consisted of two segments of different bar sizes joined by a mechanical connector. The lower segment was a No. 10 bar, while the upper segment was No. 8. The strain readings for the two uppermost elevations are from the No. 8 bar segment, while the rest are from the No. 10 segment, as shown in the instrumentation diagram in Figure D.11. The strain-vs.-lateral drift hysteresis curves for gauges at different locations on Bar 1 are shown in Figure 9.53, while those for gauges on Bar 4 are shown in Figure 9.54. Based on the tensile test data presented in Table 8.1, the yield strains of the No. 8 and 10 bars are around 0.0024 and 0.0025, respectively.

As shown in Figures 9.51 and 9.52, the maximum compressive strain reached in Bars 1 and 4 was about -0.001 (measured at the two lowest gauge locations) and the maximum tensile strain was about 0.0005. The presence of the compressive strains and the variation of the strains along the length of the bars, with higher strains in the bottom segments of Bars 1 and 4, indicate that the bars were not perfectly debonded. The strain readings indicate that the bars remain linearly elastic. The nonlinearity shown in the strain-vs-lateral drift plots in Figures 9.53 and 9.54 was caused by the intermittent slip and locking of the bars due to the partial bonding of the bars to the concrete. The curves also show delayed engagement in bar tension, which occurred early in the test. Bar tension was not developed till a drift of 0.5% for both drift directions. This is probably

caused by a small gap between the bar heads and the top surface of the concrete load stud. Assuming that the neutral axis of bending in the sacrificial zone was close to the column center at that small drift level and the distance of an extreme bar from the neutral axis was 21 in., the gap between the bar heads and concrete surface is estimated to be 0.03 in. This could be partly caused by the creep of the column and partly by the deformation of the column due to the applied axial load.

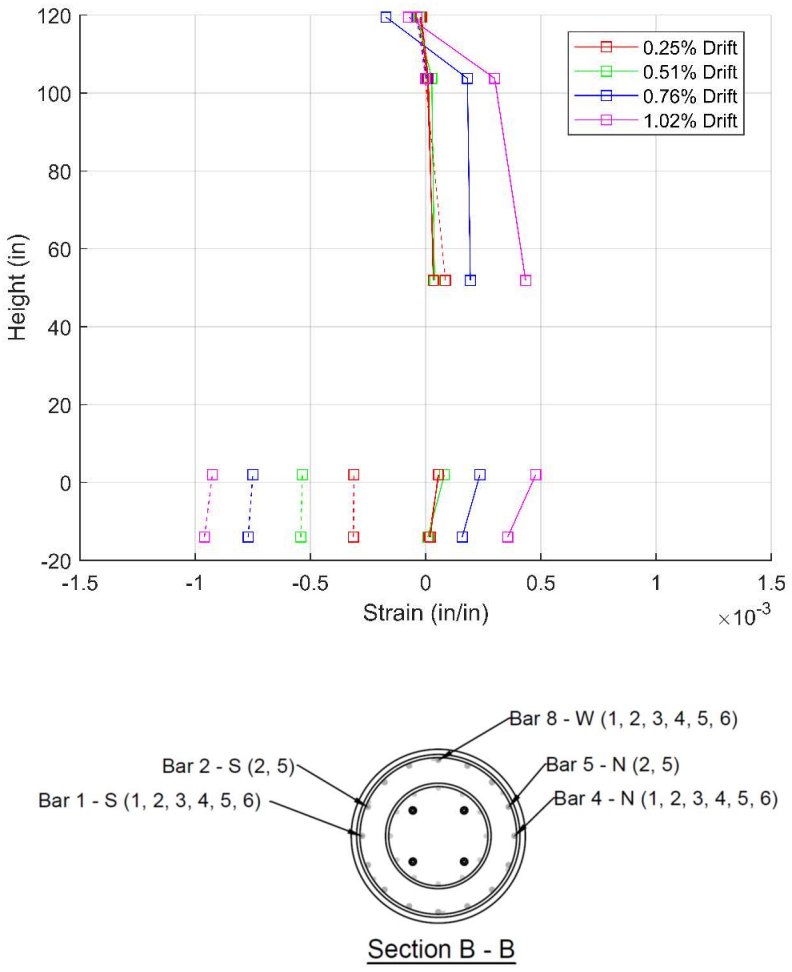

Figure 9.51: Strain profiles of Bar 1 (extreme south) in Specimen 2 at different drift levels during test with ungrouted sacrificial zone (dashed lines are for drifts towards the south, and the solid lines for drifts towards the north; reading at 22-in. elevation is absent due to non-working gauge)

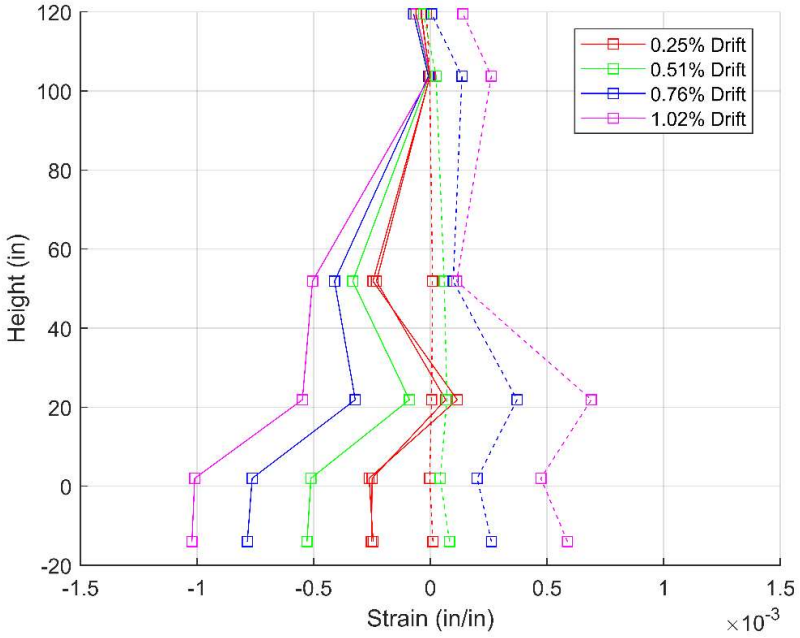

Figure 9.52: Strain profiles of Bar 4 (extreme north) in Specimen 2 at different drift levels during test with ungrouted sacrificial zone (dashed lines are for drifts towards the south, and the solid lines for drifts towards the north)

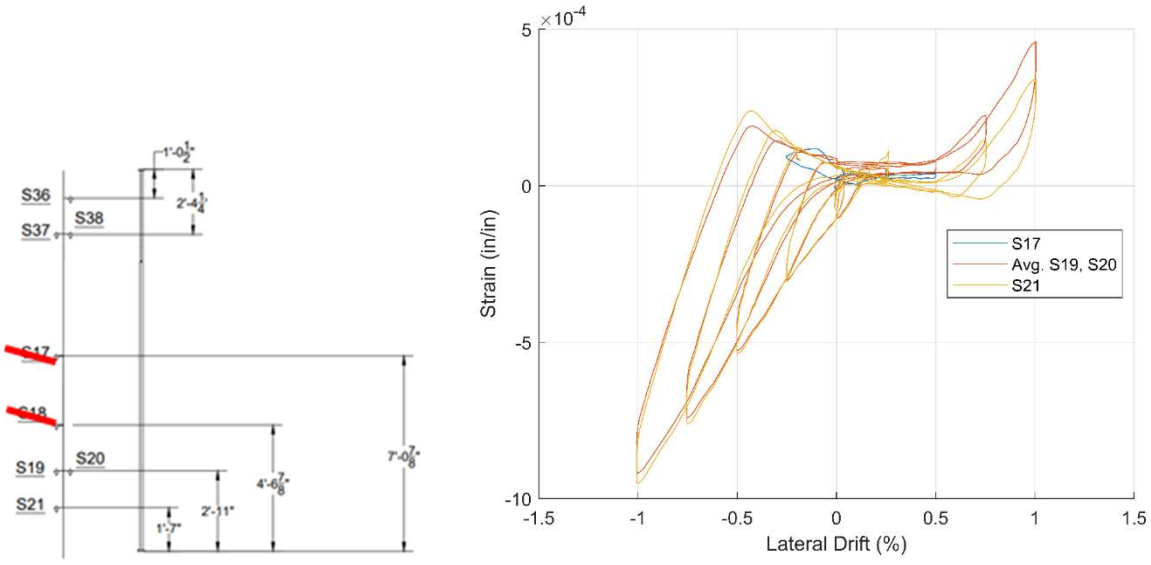

(a) No. 10 Bar (lower segment)

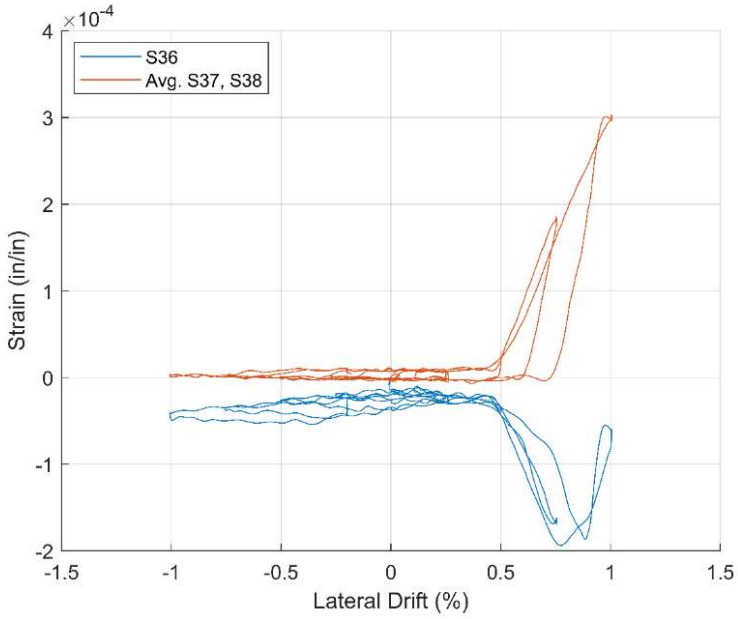

(b) No. 8 Bar (upper segment)

Figure 9.53: Strain-vs.-drift ratio curves for Bar 1 (extreme south) in Specimen 2 with ungrouted sacrificial zone (the crossed-out gauges did not function)

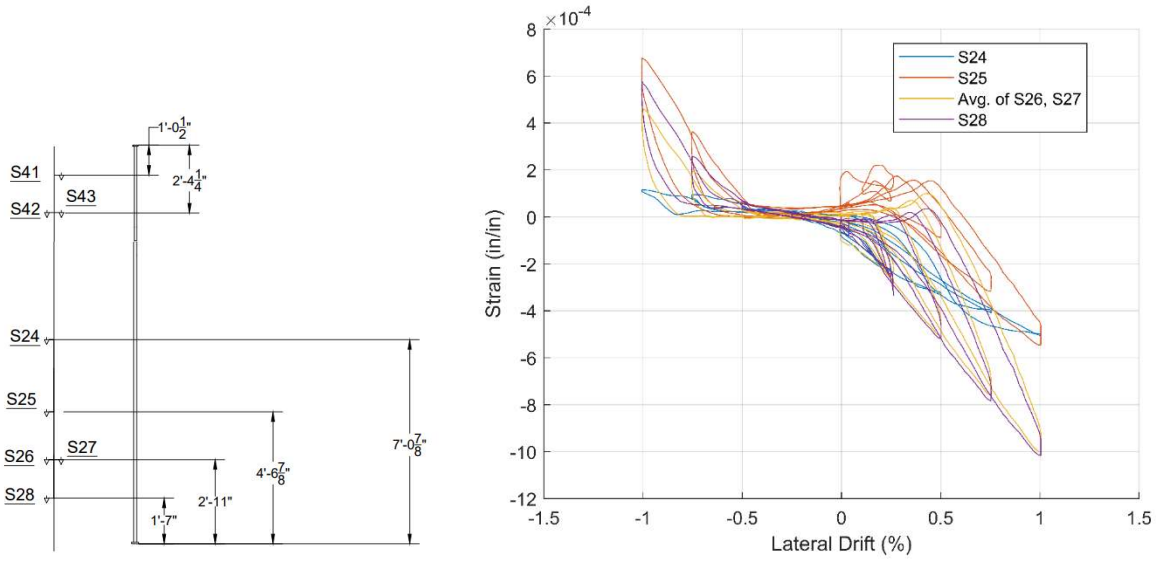

(a) No. 10 Bar (lower segment)

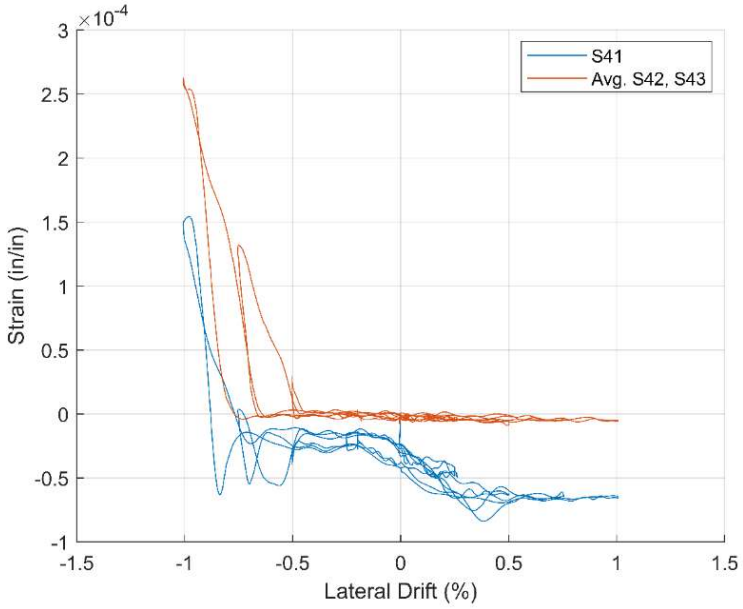

(b) No. 8 Bar (upper segment)

Figure 9.54: Strain-vs.-drift ratio plots for Bar 4 (extreme north) in Specimen 2 with ungrouted sacrificial zone

Figures 9.55 and 9.56 show the plots of strains measured in Bar 1 (the extreme south bar) and Bar 4 (the extreme north bar), respectively, at different elevations and column drift levels during the test with the sacrificial zone filled with grout. The strain-vs.-lateral drift hysteresis curves for strain gauges at different locations on the bars are shown in Figures 9.57 and 9.58. Many of the strain gauges stopped functioning after a few displacement cycles. This could be attributed to the significant amount of slip of the bars, which caused damage to the wires and wire connections for the gauges. The gauges that remained functioning till the end of the test were near the top and bottom of the bars.

The compressive strains registered in the bottom gauges indicate some locking of the bars, preventing free slips, in the lower region of the column. The maximum compressive strains registered in Bars 1 and 4 at 10% drift are slightly short of -0.002. The maximum tensile strains registered in the bars are around 0.003, by the gauges in the sacrificial zone, when the drift reached 10%. They are slightly above the yield strain of 0.0025. In spite of the fact that the top segments of the bars were of smaller diameter (size No. 8), the tensile strains developed in the top segments are slightly less than those in the bottom segments (size No. 10). This is attributed to the locking of the bottom segments in the column above the rocking hinge. The top gauges on Bar 1 stopped functioning after the drift ratio reached 5%. However, as Figure 9.57(b) shows, the strain in the top segment of Bar 1 reached 0.0025 when the drift reached 5%. The hysteresis curves in Figures 9.57(b) and 9.58(b) show that the top bar segments had progressive delays in developing tension as the number of displacement cycles increased. This is largely attributed to the crushing of the concrete underneath the bar heads creating a larger gap between the anchor heads and the concrete surface.

The strains developed in the bars in Specimen 2 are significantly lower than those in Specimen 1. The bars in Specimen 1 were only unbonded over a length of 72 inches in the vicinity of the rocking hinge. No bar fracture was observed in Specimen 2.

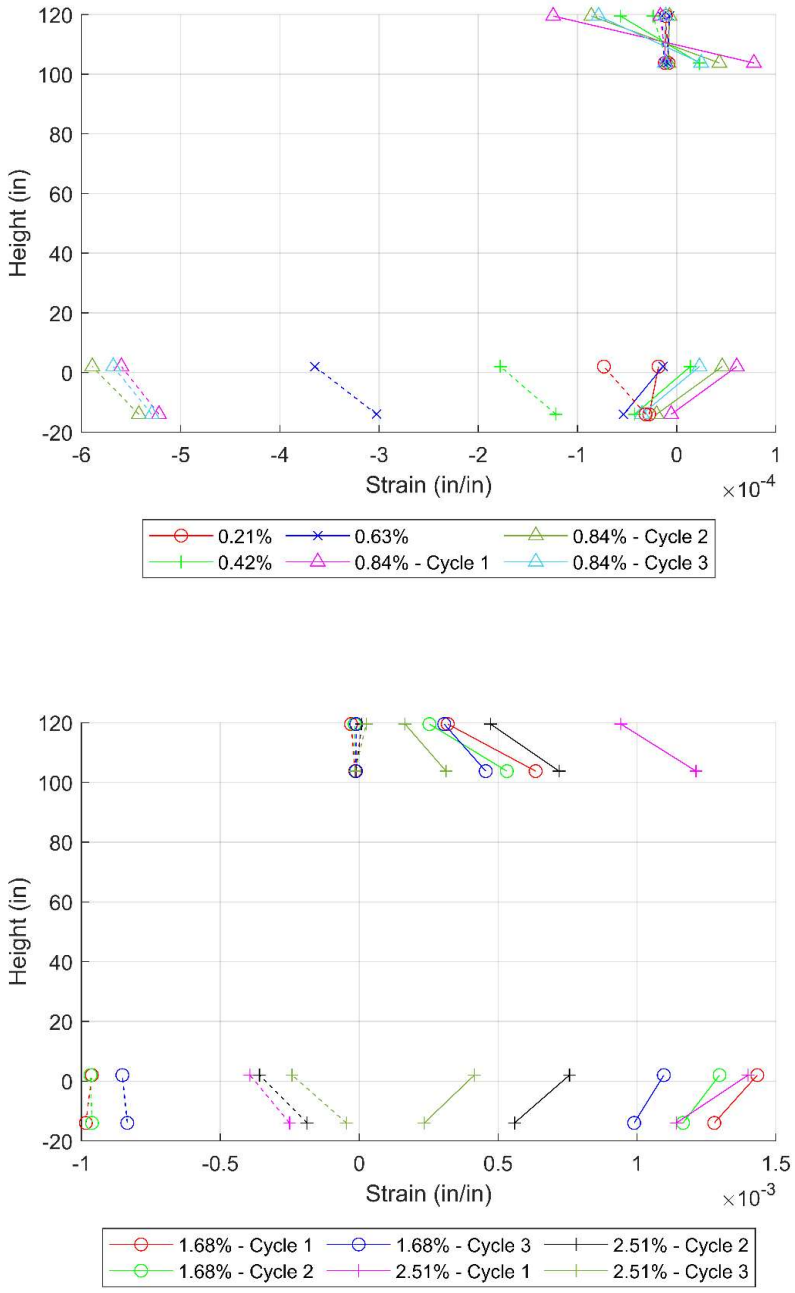

Figure 9.55: Strain profiles of Bar 1 (extreme south) in Specimen 2 at different drift levels during test with grouted sacrificial zone (dashed lines are for drifts towards the south, and the solid lines for drifts towards the north)

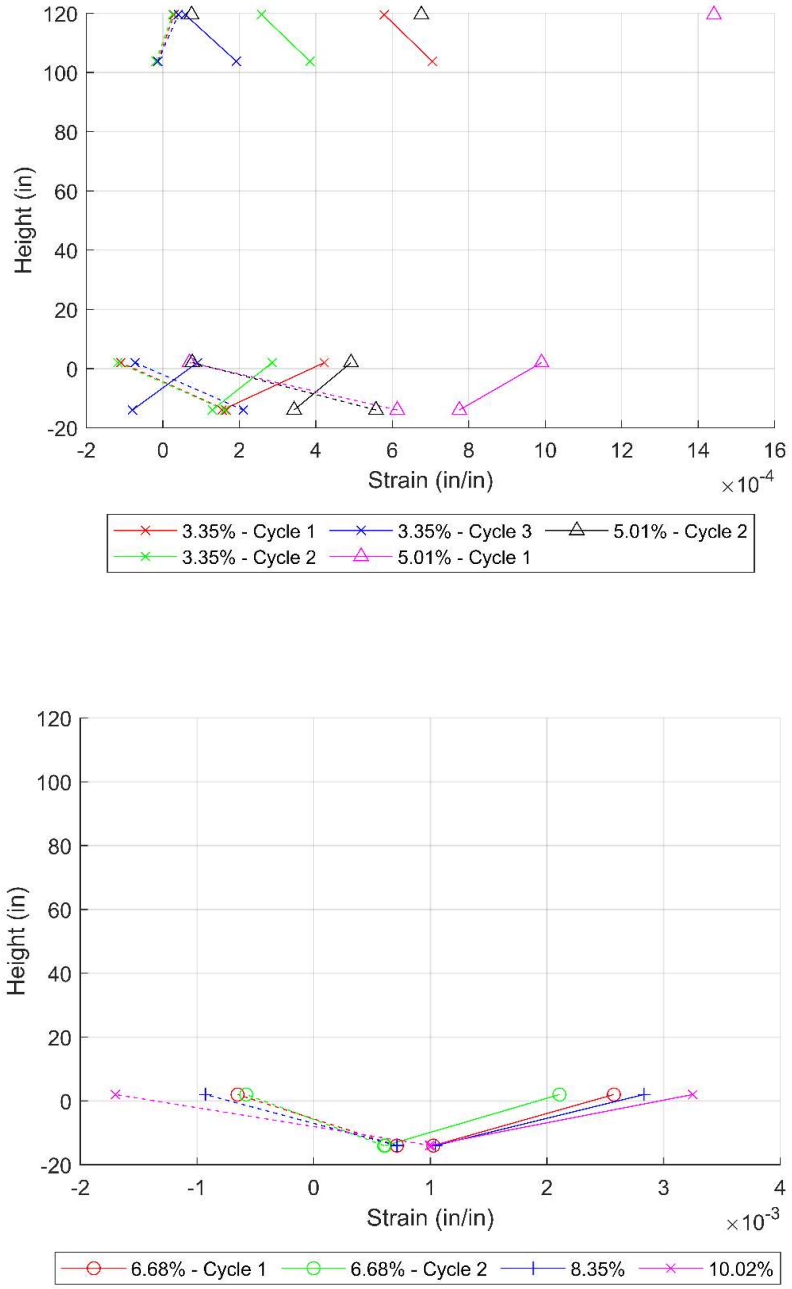

Figure 9.55 (continued): Strain profiles of Bar 1 (extreme south) in Specimen 2 at different drift levels during test with grouted sacrificial zone (dashed lines are for drifts towards the south, and the solid lines for drifts towards the north)

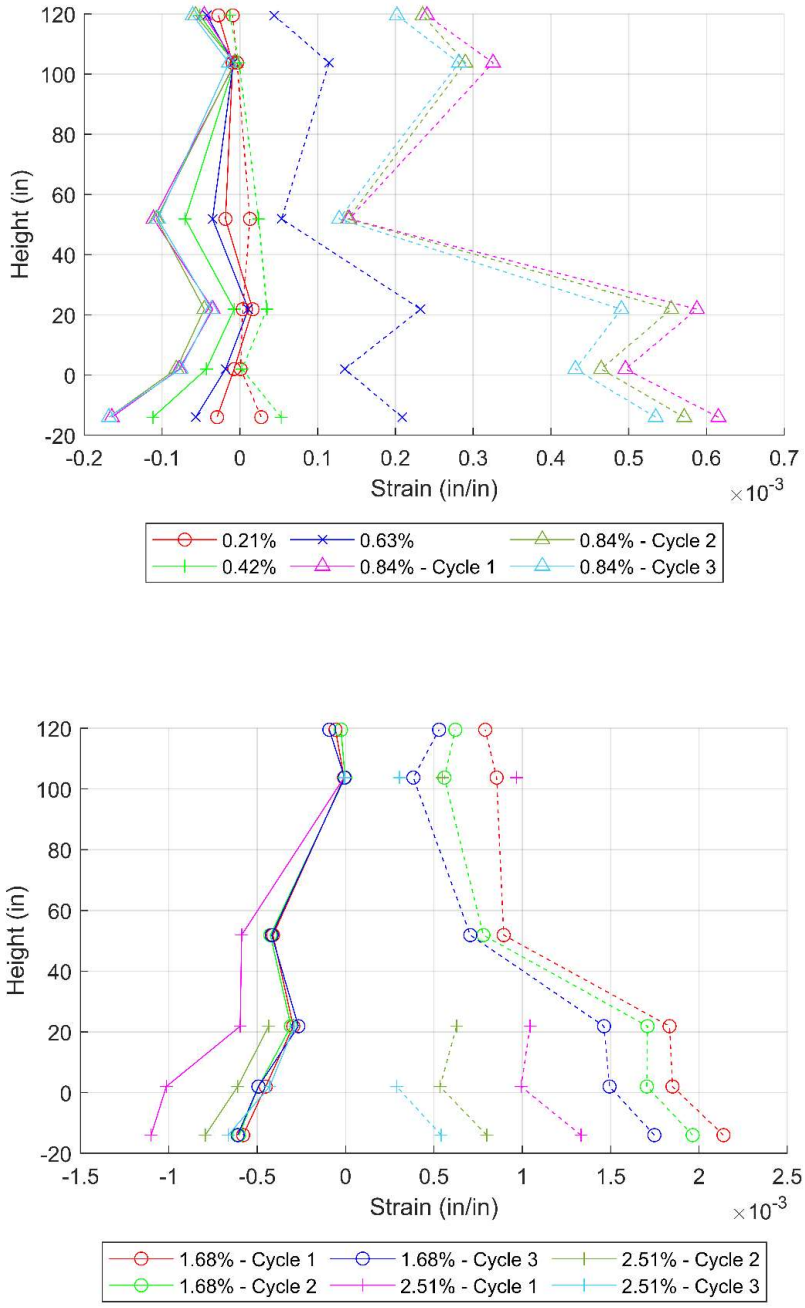

Figure 9.56: Strain profiles of Bar 4 (extreme north) in Specimen 2 at different drift levels during test with grouted sacrificial zone (dashed lines are for drifts towards the south, and the solid lines for drifts towards the north)

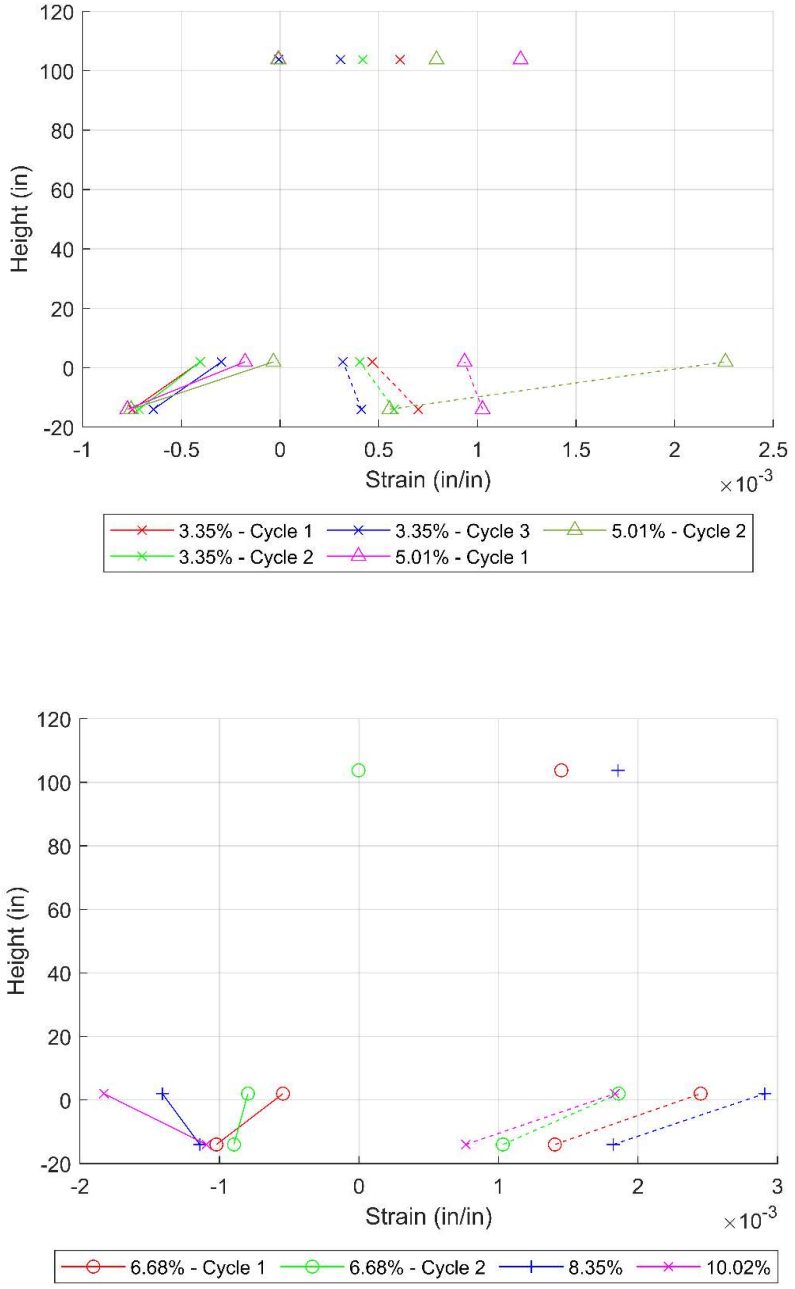

Figure 9.56 (continued): Strain profiles of Bar 4 (extreme north) in Specimen 2 at different drift levels during test with grouted sacrificial zone (dashed lines are for drifts towards the south, and the solid lines for drifts towards the north)

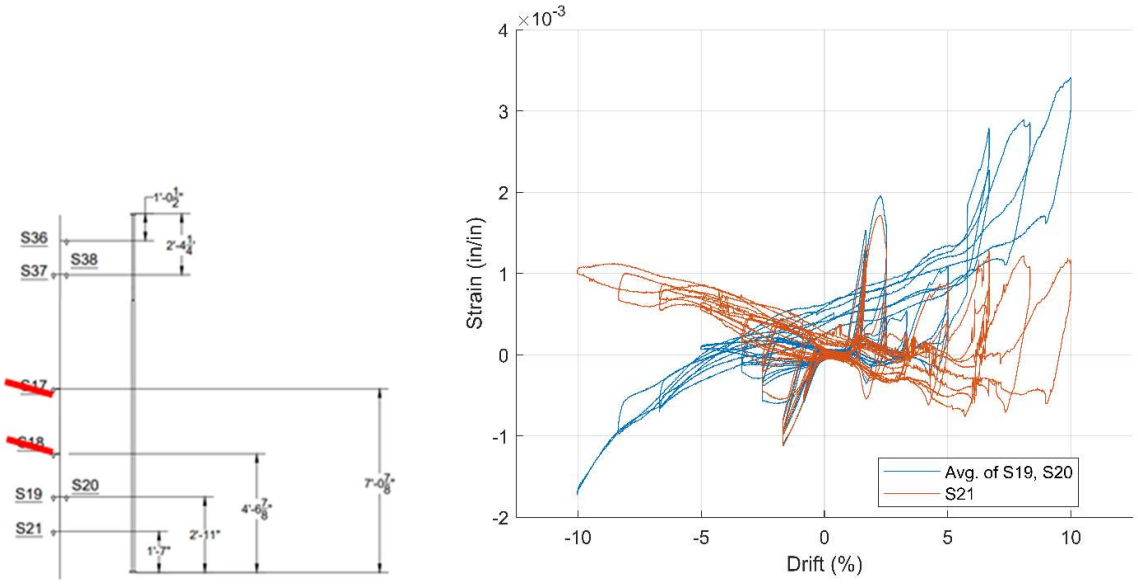

(a) No. 10 Bar (lower segment)

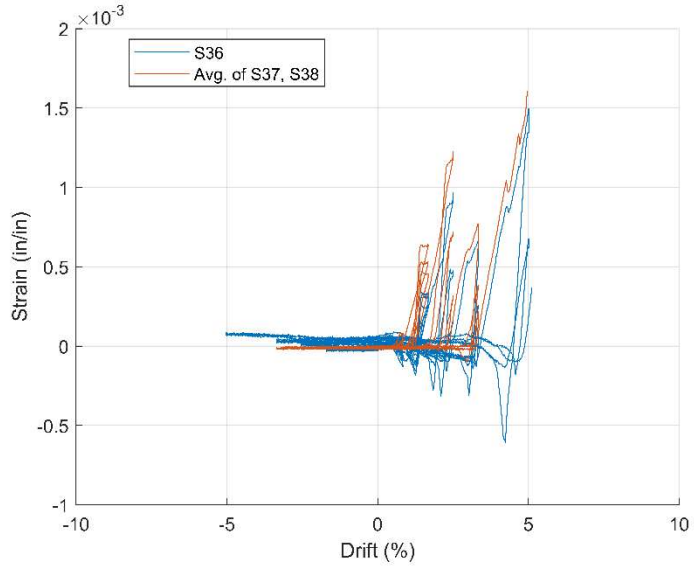

(b) No. 8 Bar (upper segment)

Figure 9.57: Strain-vs.-displacement plots for the strains measured at different elevations along Bar 1 (extreme south) in Specimen 2 with grouted sacrificial zone

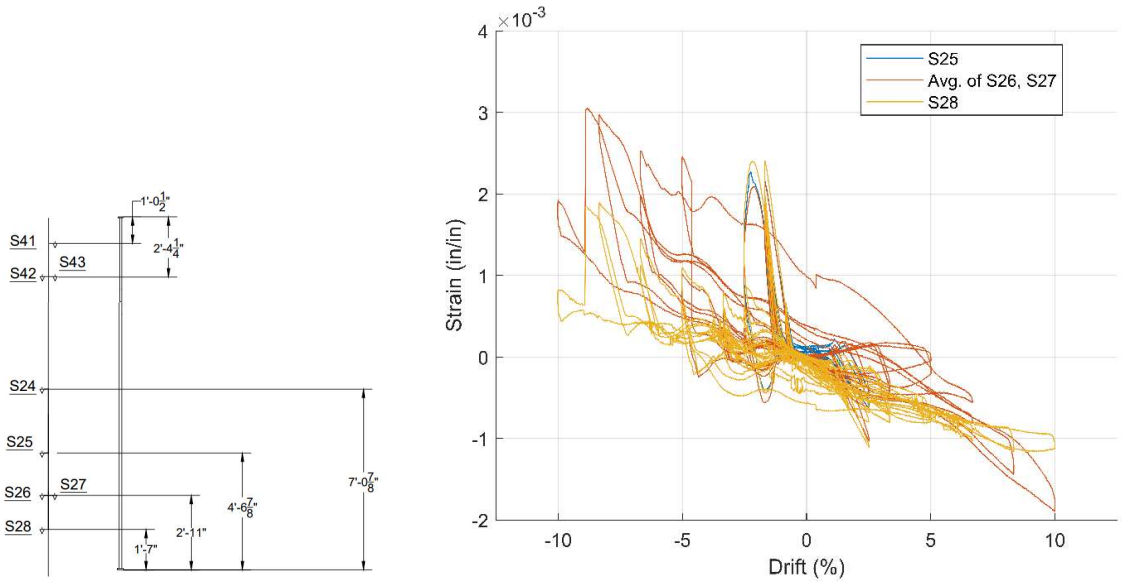

(a) No. 10 Bar (lower segment)

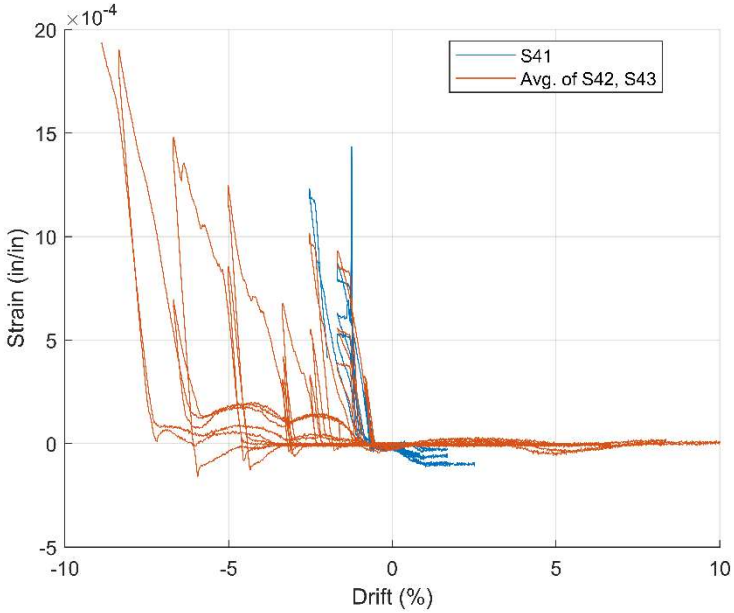

(b) No. 8 Bar (upper segment)

Figure 9.58: Strain-vs.-displacement plots for Bar 4 (extreme north) in Specimen 2 with grouted sacrificial zone

Figures 9.59 and 9.60 show the strains in the post-tensioned strands plotted against the lateral drift ratio of the column with the grouted sacrificial zone. Like those in Specimen 1, the strands were grouped in four post-tensioning ducts, with five strands in each duct. Two of the ducts were on the north side of the column and two were on the south side. The initial strain value prior to the first test with the ungrouted sacrificial zone is estimated to be 0.0023. The calculations for the initial strains are shown in Appendix E. The initial strain in the strands during the test with the grouted sacrificial zone is set equal to the final strain value registered right after the test with the ungrouted sacrificial zone, which is approximately 0.0022. As can be seen in Figures 9.59 and 9.60, similar to that observed for Specimen 1, the plots have a V shape. The slope of the strain-vs.-lateral drift hysteresis loops changes as the lateral drift changes direction due to the change of the distance of the strands from the neutral axis, as explained for Specimen 1 in Section 9.2.3. The behavior of the strands on the north side is almost a mirror image of that on the south side. The maximum tensile strain reached in the south strands is around 0.0085 and that in the north strand is about 0.008. These strains are slightly lower than those observed from Specimen 1, probably due to the fact that the distance of the neutral axis of bending in the sacrificial zone of Specimen 2 from the center of the column section when the drift reached 10% is slightly less than that for Specimen 1. These tensile strains correspond to a stress level of 270 ksi, according to Figure 8.4. The strain plots in the figures also show a reduction of the initial tensile strain by about 0.0014 when the lateral drift returned to zero at the end of the test. This can be attributed to the gradual shortening the column due to the permanent axial deformation in the sacrificial zone, as shown in Figure 9.50, and the slip of the strands in the anchors, similar to those happening in Specimen 1.

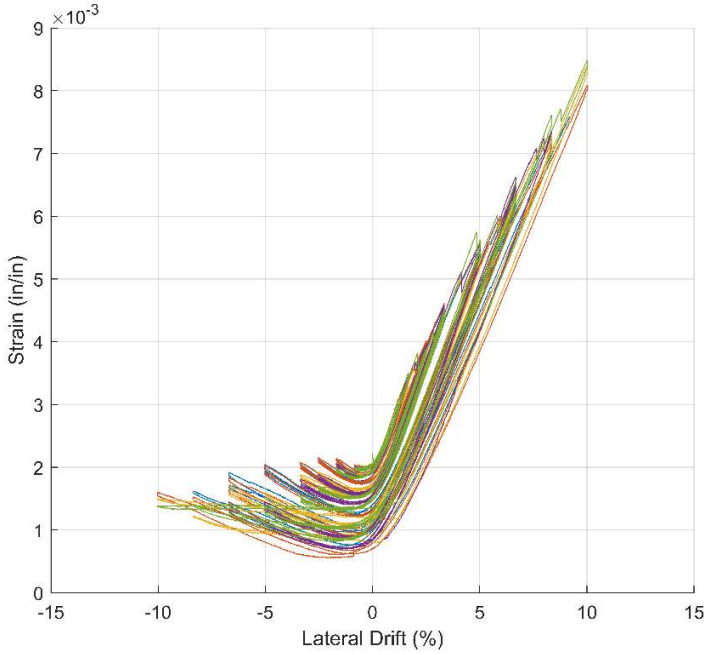

Figure 9.59: Strain-vs.-drift ratio curves for south strands of Specimen 2 with grouted sacrificial zone (strain gauge locations shown in Figure D.14)

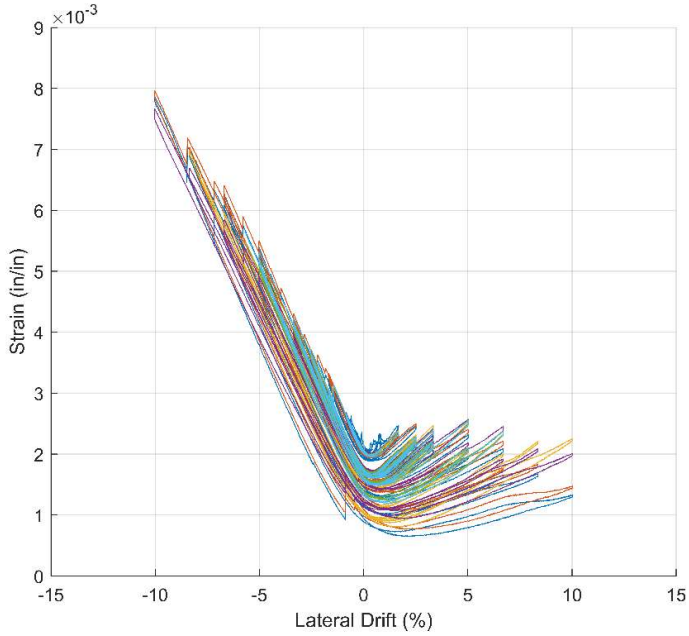

Figure 9.60: Strain-vs.-drift ratio curves for north strands of Specimen 2 with grouted sacrificial zone (strain gauge locations shown in Figure D.14)

9.4.4 Comparison of Specimen 2 with Specimen 1

The load-displacement plots for Specimens 1 and 2 are compared in Figure 9.61. Specimen 2 had a higher lateral load resistance than Specimen 1 because it had a larger amount of longitudinal reinforcing bars. Specimen 1 had 16 No. 6 longitudinal bars, which were bonded to concrete except for a 72-in. unbonded bar length over the region right below and above the rocking hinge. Specimen 2 also had 16 longitudinal bars, but each of the bars consisted of two segments, a No. 10 bar segment and a No. 8 bar segment. The No. 8 segment served as a fuse where plastic deformation was expected to concentrate. The bars in Specimen 1 experienced both tension and compression, while those in in Specimen 2 were allowed to develop tension only. Specimen 1 had severe bar bending and fracture occurring in the sacrificial zone, while Specimen 2 did not have any. The plastic strains developed in the bars in Specimen 2 were significantly lower than those in Specimen 1. Plastic strains were also developed in the No. 10 segments because of imperfect debonding that resulted in bar locking in the bottom region of the column. However, the maximum strains developed in Specimen 2 were only slightly higher than the yield strains of the bars.

As shown in Figure 9.61, the shapes of the load-vs.-drift hysteresis loops for the two specimens resemble each other, with the loops for Specimen 2 appearing to be more pinched because of the progressive delay in the engagement of the longitudinal bars in tension due to the crushing of the concrete underneath the anchor heads of the No. 8 bars. The load degradation in Specimen 1 was mainly caused by bar fracture, while that in Specimen 2 was caused by the crushing of the concrete underneath the anchor heads.

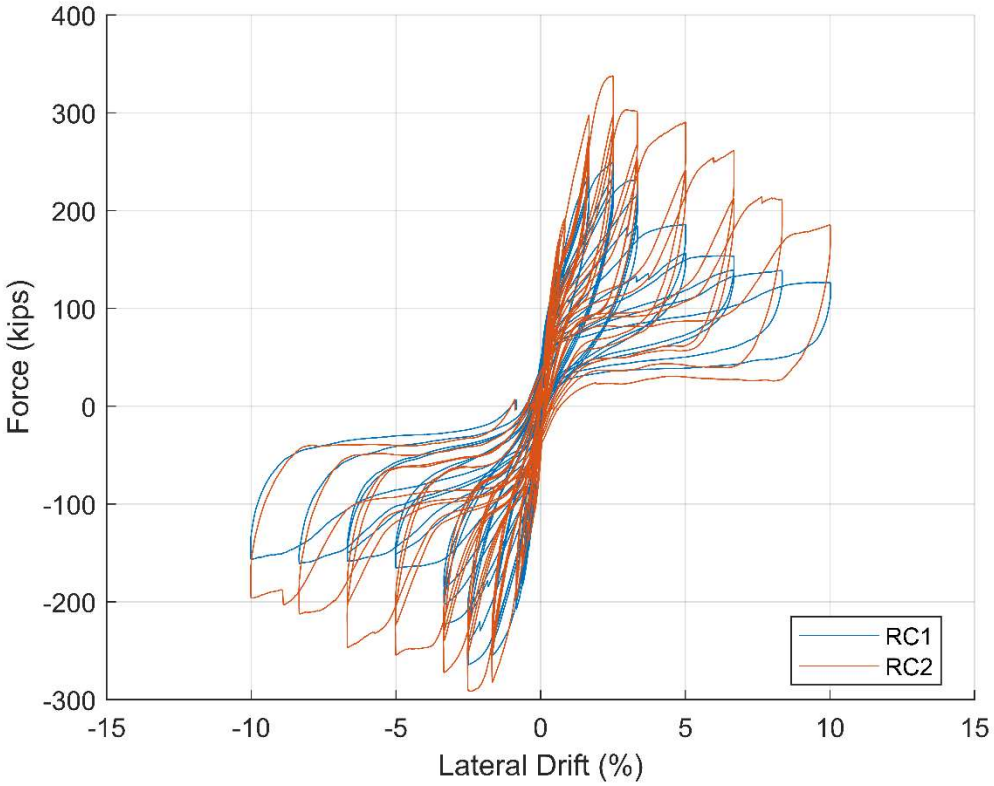

Figure 9.61: Lateral force vs. drift comparison for the grouted tests of specimens 1 and 2

To best compare the energy dissipation between the two columns, the methodology developed by Cohagen et al. (2008) was employed. The peak maximum and minimum forces for each specimen's grouted test were identified and each displacement cycle was isolated. For each cycle, the area of the cycle was determined and then divided by the area of the box shown in Figure 9.62, using the following calculation

$$E_{h(i)}^{norm} = \frac{A_{loop(i)}}{(F_{\max} - F_{\min}) * (\Delta_{\max(i)} - \Delta_{\min(i)})} \tag{9.3}$$

where $A_{loop(i)}$ is the area of the cycle of interest, $F_{\max}$ is the maximum lateral force throughout the experiment, $F_{\min}$ is the minimum lateral force throughout the experiment, $\Delta_{\max(i)}$ is the maximum

displacement in the cycle of interest, and $\Delta_{\min(i)}$ is the minimum displacement in the cycle of interest.

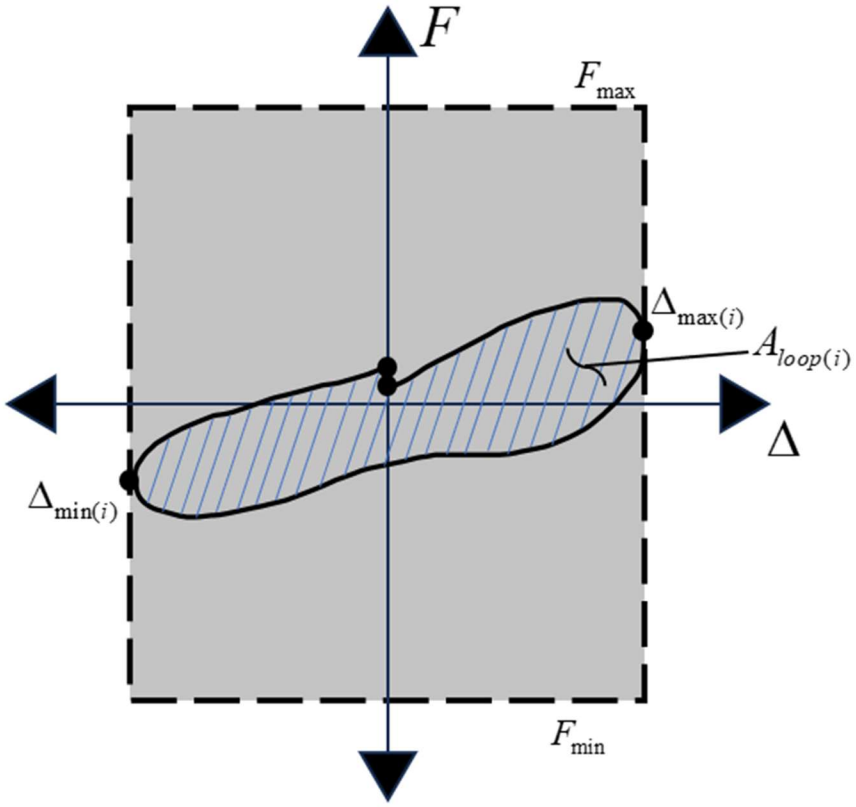

Figure 9.62: Illustration of calculating normalized energy dissipation within one displacement cycle

Figure 9.63 compares the normalized hysteretic energy dissipations exhibited by the two specimens. Early cycles of Specimen 1 exhibited large deformations of the mild longitudinal reinforcement which contributed to larger energy dissipation when compared to Specimen 2. Specimen 1 also experienced fracture of the longitudinal reinforcement between 1.8% and 6% drift which greatly increased the energy dissipation. Specimen 2 did not have similar material failures which is why the total cumulative energy dissipation is smaller than that of Specimen 2.

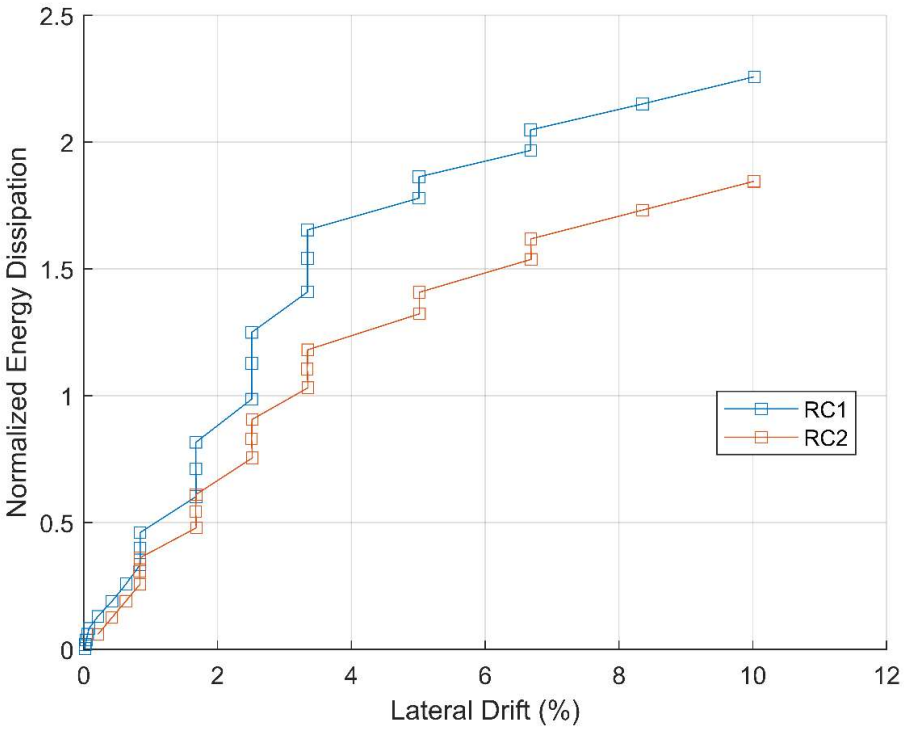

Figure 9.63: Comparison of cumulative energy dissipation-vs.-drift ratio curves for both specimens during tests with grouted sacrificial zone

Chapter 9 is, in part, a reprint of the material in a California Department of Transportation report entitled "Experimental Investigation of a Self-Centering RC Column Design and a Displacement-Based Design Method for Highway Bridge Applications." The authors of the report are: the author of the dissertation, Dimitrios Kalliontzis, and P. Benson Shing. Professor Dimitrios Kalliontzis worked on much of the construction of the first test specimen. The author of the dissertation provided input for the design of the second specimen, and was responsible for overseeing the construction and experimental work, post-test analysis of the two specimens, modeling and worked with Professor P. Benson Shing on the development of the displacement-based design methodology.

Chapter 10 Modeling of Rocking Behavior of Self-Centering Columns

10.1 Introduction

To simulate the response of the self-centering column specimens under lateral loading, a fiber-section model (FM) was developed to model the behavior of the rocking hinge. This chapter presents the formulation of the model, the modeling assumptions, and the material laws used.

10.2 Basic Assumptions in the Model

To model lateral load – vs. – displacement response of the self-centering column specimens, it is assumed that the body of the column behaves as a rigid body with all the deformation concentrated in the rocking hinge region, which is depicted in Figure 10.1(a). With this assumption, the column has two degrees of freedom, one axial and one lateral, associated with the axial and rotational deformations of the hinge. To model these deformations and calculate the resistance developed by the rocking hinge, a fiber-section model is used. The hinge behavior is modeled with a single fiber section, which represents the section between the two rocking plates, identified as Section A-A in Figure 10.1. The plan view of the section is shown in Figure 10.1(b), the discretization of the section into fibers is shown in Figure 10.1(c), in which the hole at the center represents the space occupied by the pin that served as the shear key and had no resistance in tension or compression. It is assumed that the strain in each fiber is uninform over the entire height of the hinge, H_h, but may not necessarily represent the deformation of the material that occurs only in the hinge region as will be discussed later.

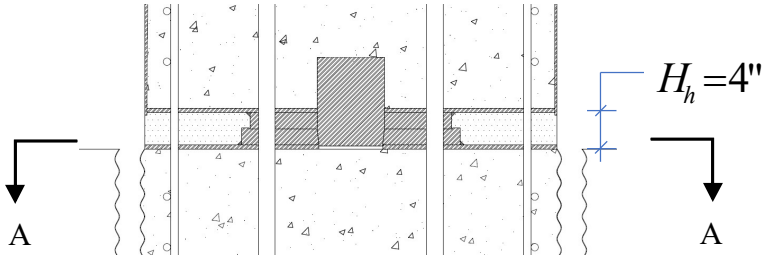

(a)

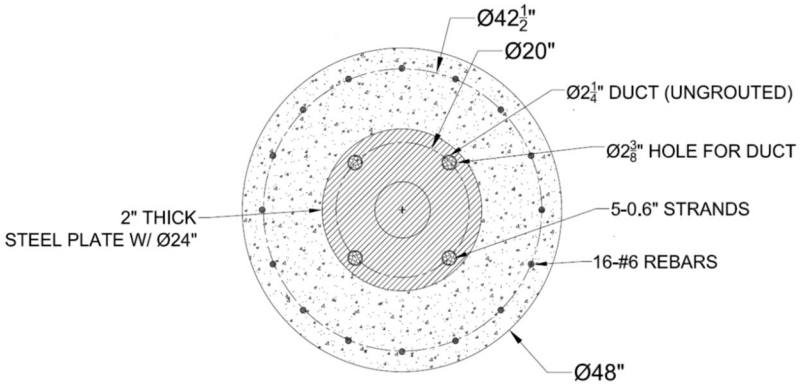

(b)

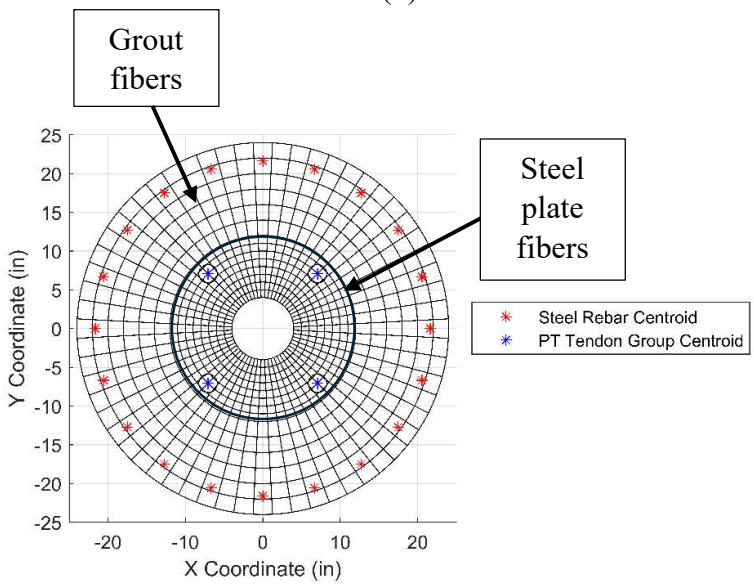

(c)

Figure 10.1: Modeling of the rocking hinge: (a) elevation view of grouted hinge region; (b) Section A-A of the hinge; (c) discretization of Section A-A

The hinge is assumed to have two degrees of freedom, which are the axial deformation at the centroid of the hinge section, denoted by u_o, and the rotation in the hinge, denoted by θ. The strain in each fiber *which*, representing the grout, the rocking plate, or a rebar is calculated as the total deformation of the fiber divided by the respective effective length, as shown in the following equation, assuming a small hinge rotation.

$$\varepsilon_i = \frac{1}{l_{io}}\left(u_o - x_i\theta\right) \tag{10.1a}$$

where ε_i is the strain in fiber *which*, which is positive for tension; the axial deformation u_o is positive when the hinge opens; the hinge rotation θ, in radians, is positive when it is clockwise; x_i is the perpendicular distance of the fiber from the axis passing through the centroid of the section about which the hinge rotates, and l_{io} is the effective length of the fiber. For the grout fibers and the rocking plate fibers, l_{io} is equal to the height of the hinge, H_h. For the rebar fibers, l_{io} is equal to the total unbonded length, L_u, of the rebars, measured from the pedestal below the hinge through the column region above the hinge, as shown in Figure 8.1.

The strain in a prestressing strand fiber is calculated by the following equation.

$$\varepsilon_i = \frac{1}{l_{io}}\left(u_o - u_o' - x_i\theta\right) + \varepsilon_{po} \tag{10.1b}$$

where u_o' is the axial deformation induced by the self-weight of the column and the initial prestressing force exerted by the strands, ε_{po} is the strain corresponding to the initial prestress in the strands, and l_{io} is the total unbonded length, L_p, between the top and bottom anchors of the

strands. The axial deformation u_o' is subtracted from u_o because the effect of u_o' is already accounted for in the value of ε_{po}.

Once the strains in the fiber are determined, the stresses in the fibers are calculated with the respective material laws, which are presented in Section 10.3. The axial resistance, *N*, and the moment resistance, *M*, about the centroidal axis of the hinge section are calculated with the following equations.

$$N = \sum_i \sigma_i A_i \tag{10.2a}$$

$$M = -\sum_i \sigma_i A_i x_i \tag{10.2b}$$

where σ_i is the stress in fiber *which*, A_i is the cross-sectional area of the fiber, x_i distance of the fiber centroid from the centroid axis of the hinge section about which rotation occurs. Here, *M* is positive when it is caused by a clockwise rotation, and *N* is positive when it is a tension force. The lateral resistance of the column, including the *P*-Δ effect, is given by the following equation.

$$F = \frac{M}{H_c} - \frac{P\Delta}{H_c} \tag{10.3a}$$

where *P* is the vertical axial compressive load applied to the column, H_c is the column height, and $\Delta = H_c\theta$, the lateral displacement at the top of the column. The *P*-Δ effect of the self-weight of the column is ignored. In the tests, the axial load was applied with post-tensioned rods, which had the same angle of rotation as the column when a lateral displacement was imposed on the column. If the total force in the post-tensioned rods is *P'*, then the *P*-Δ effect of the vertical

component of *P'* is exactly cancelled out by the horizontal component of *P'*, and the lateral resistance directly measured from the column specimen is given by the following equation.

$$F = \frac{M}{H_c} \tag{10.3b}$$

For the given applied vertical axial compressive load P and hinge rotation θ, the value of the axial displacement u_o is calculated to satisfy the equilibrium condition that $P = N$. With the nonlinear material behavior, this requires an iterative solution using the Newton's method, as discussed in Section 10.4. Once the solution converges, then the moment resistance, M, is computed with Equation (10.2b).

The stress-strain relation for each fiber is modeled with an appropriate material law. There are four types of materials to be modeled. One is the grout filling the gap, which has only compressive resistance, the second is the material representing the behavior of the two steel rocking plates, which can develop only compression during rocking, the third is the reinforcing bars, and the last is the prestressing strands. The material law proposed for each material is presented in Section 10.3.

10.3 Employed Material Models

10.3.1 Grout Material

The grout material in a rocking hinge is assumed to have no tensile strength. The model takes into account of the condition that the grout in the inner region the hinge section is confined by the outer grout. Hence, the confinement effect is zero for the grout at the perimeter of the section and increases toward the interior. Here, the compressive stress-strain relationship for the grout is represented by the model proposed for confined concrete by Mander, Priestley, and Park (1988),

with slight modifications to account for the different confinement mechanism in the rocking hinge. Mander et al.'s model is first summarized below.

10.3.1.1 Mander et al.'s Model

Figure 10.2 shows the stress-strain envelope curves proposed by Mander et al. for unconfined and confined concrete.

In Mander et al.'s model, the effective lateral confining pressure, f_l', on concrete provided by spirals or circular hoops in the column is calculated with Equation (10.4).

$$f_l' = \frac{1}{2} k_e \rho_s f_{yh} \tag{10.4}$$

where k_e is the confinement effectiveness coefficient, ρ_s is the ratio of the volume of the spirals or hoops to the volume of the confined concrete core, and f_{yh} is the yield stress of the transverse reinforcement. With the effective lateral confining pressure calculated, the compressive strength, f_{cc}', of the confined concrete can then be calculated using Equation (10.5).

$$f_{cc}' = f_{co}'(-1.254 + 2.254\sqrt{1 + \frac{7.94 f_l'}{f_{co}'}} - 2\frac{f_l'}{f_{co}'}) \tag{10.5}$$

where f_{co}' is the compressive strength of unconfined concrete.

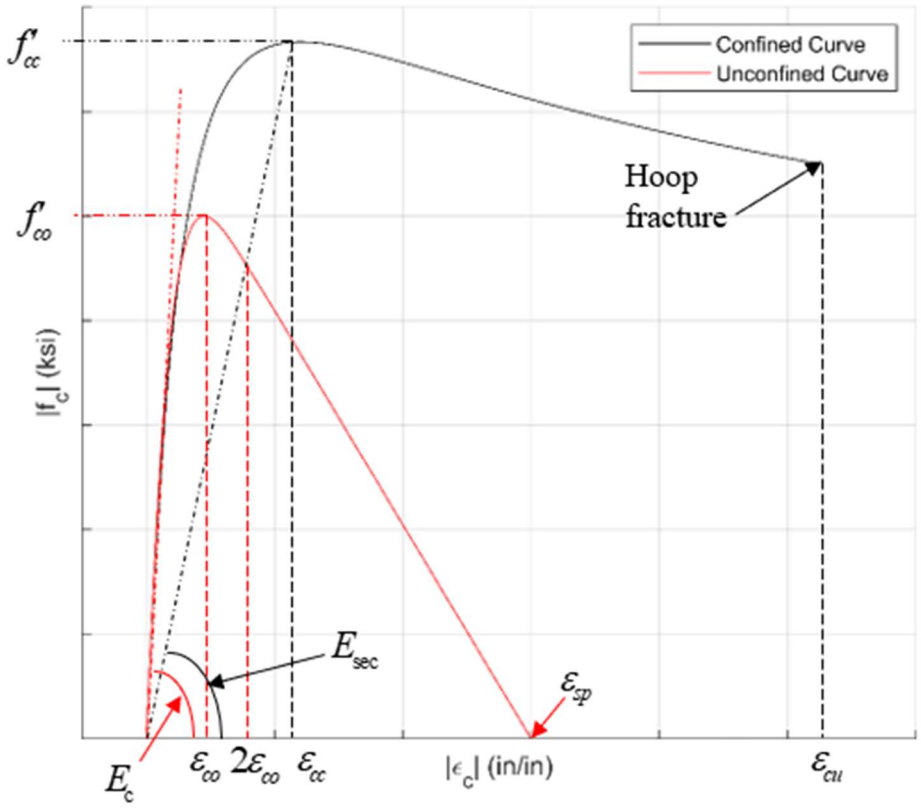

Figure 10.2: Effect of confinement on the stress-strain curve for concrete (Mander et. al 1988)

The stress-strain ($f_c - \varepsilon_c$) relation for confined concrete under monotonic loading is represented by Equation (10.6).

$$f_c = \frac{f'_{cc} x r}{r - 1 + x^r} \tag{10.6a}$$

where

$$x = \frac{\varepsilon_c}{\varepsilon_{cc}} \tag{10.6b}$$

$$\varepsilon_{cc} = \varepsilon_{co}\left[1 + 5\left(\frac{f'_{cc}}{f'_{co}} - 1\right)\right] \tag{10.6c}$$

$$r = \frac{E_c}{E_c - E_{\text{sec}}} \tag{10.6d}$$

$$E_c = 57{,}000\sqrt{f'_{co}} \quad \text{(in psi)} \tag{10.6e}$$

$$E_{sec} = \frac{f'_{cc}}{\varepsilon_{cc}} \tag{10.6f}$$

in which ε_{cc} and ε_{co} are the strains at which the peak compressive stresses in the confined and unconfined concrete are reached, as shown in Figure 10.2. Equations (10.6e) and (10.6f) calculate the modulus of elasticity of unconfined concrete and the secant modulus of confined concrete, respectively.

For cyclic loading, Mander et al. proposed a hysteretic unloading and reloading law that accounts for the degradation of the modulus of elasticity of concrete under cyclic loading. The hysteretic law proposed by Mander et al. is illustrated in Figures 10.3 and 10.4.

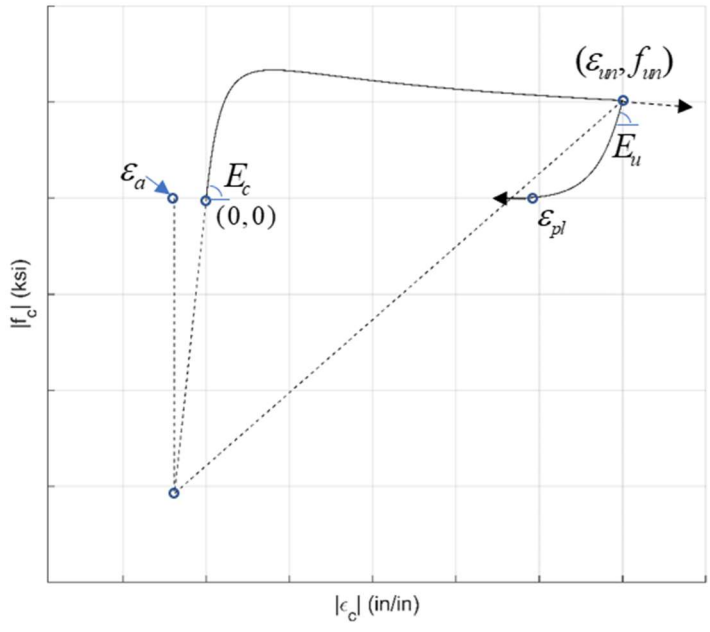

Figure 10.3: Unloading curve for concrete proposed by Mander et. al (1988)

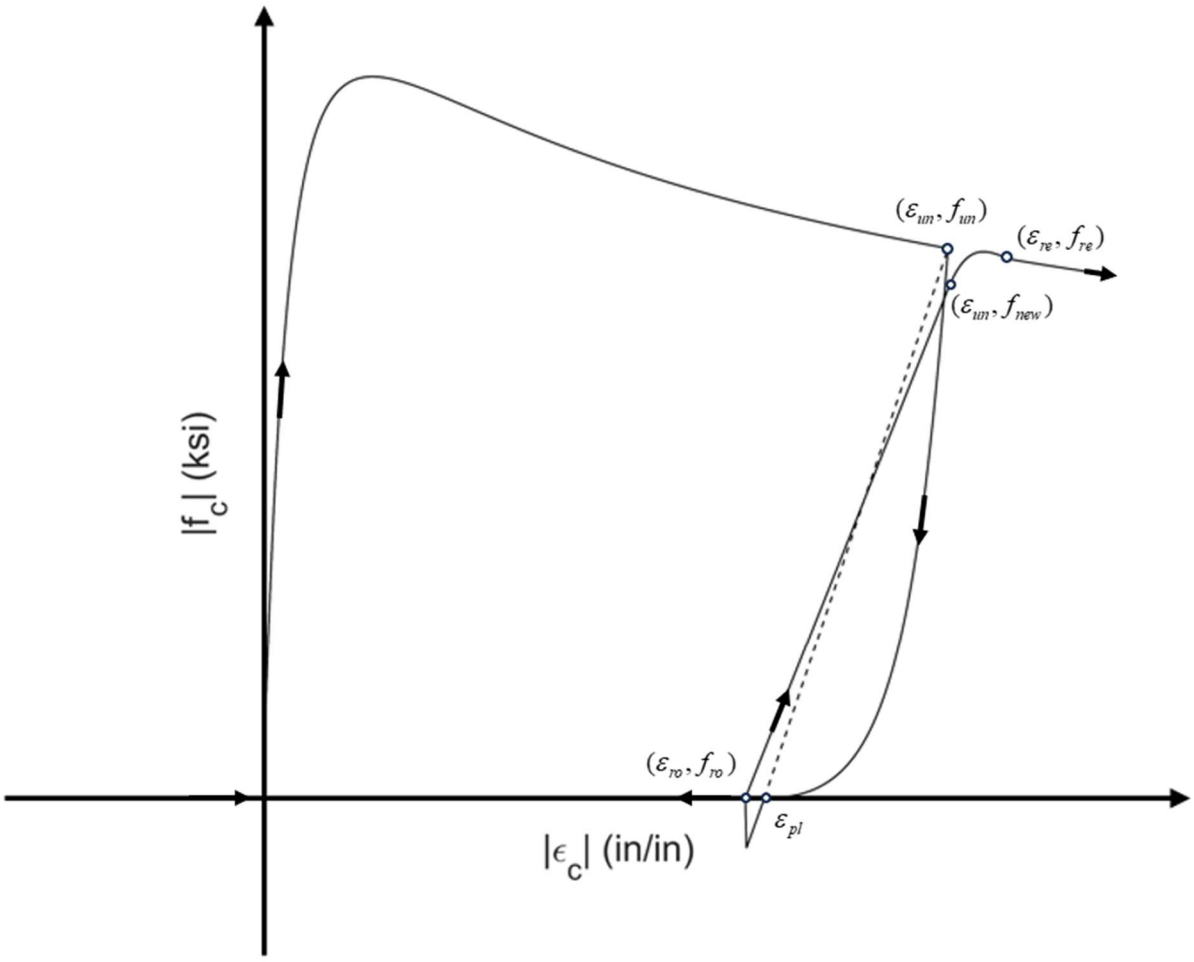

Figure 10.4: Hysteretic concrete model proposed by Mander et. al. (1988)

As shown in Figures 10.3 and 10.4, when unloading occurs, the coordinate $(\varepsilon_{un}, f_{un})$ at which it starts is identified and the unloading stiffness is determined with the secant line joining points $(\varepsilon_{un}, f_{un})$ and $(\varepsilon_{pl}, 0)$, where ε_{pl} is the residual plastic strain, which is to be calculated with the following equation.

$$\varepsilon_{pl} = \varepsilon_{un} - \frac{(\varepsilon_{un} + \varepsilon_a) f_{un}}{(f_{un} + E_c \varepsilon_a)} \tag{10.7a}$$

where

$$\varepsilon_a = a\sqrt{\varepsilon_{un}\varepsilon_{cc}} \tag{10.7b}$$

$$\text{with } a = \max\left(\frac{\varepsilon_{cc}}{\varepsilon_{cc}+\varepsilon_{un}} \quad \text{or} \quad \frac{0.09\varepsilon_{un}}{\varepsilon_{cc}}\right) \tag{10.7c}$$

The stress-strain relation for the unloading path is governed by Equation (10.8).

$$f_c = f_{un} - \frac{f_{un} x r}{r - 1 + x^r} \tag{10.8a}$$

where

$$r = \frac{E_u}{E_u - E_{\text{sec}}} \tag{10.8b}$$

$$E_{\text{sec}} = \frac{f_{un}}{\varepsilon_{un} - \varepsilon_{pl}} \tag{10.8c}$$

$$x = \frac{\varepsilon_c - \varepsilon_{un}}{\varepsilon_{pl} - \varepsilon_{un}} \tag{10.8d}$$

In Equation (10.8b), E_u is the initial modulus of elasticity at the onset of unloading, and is determined as

$$E_u = bcE_c \tag{10.9a}$$

where

$$b = \frac{f_{un}}{f'_{co}} \geq 1 \tag{10.9b}$$

$$c = \left(\frac{\varepsilon_{cc}}{\varepsilon_{un}}\right)^{0.5} \leq 1 \tag{10.9c}$$

The reloading stress-strain curve is linear from the reloading point $(\varepsilon_{ro}, f_{ro})$ to the point $(\varepsilon_{un}, f_{new})$, where f_{new} is defined as

$$f_{new} = 0.92 f_{un} + 0.08 f_{ro} \tag{10.10}$$

The stress along the reloading path is then calculated as

$$f_c = f_{ro} + E_r(\varepsilon_c - \varepsilon_{ro}) \tag{10.11a}$$

where

$$E_r = \frac{f_{ro} - f_{new}}{\varepsilon_{ro} - \varepsilon_{un}} \tag{10.11b}$$

As shown in Figure 10.4, Mander et al. define a parabolic transition curve between $(\varepsilon_{un}, f_{new})$ and $(\varepsilon_{re}, f_{re})$ on the reloading branch. The point $(\varepsilon_{re}, f_{re})$ is the common return point at which the parabolic curve intersects the envelope curve given by Equation (10.6a). The strain ε_{re} at the common return point is calculated by Equation (10.12).

$$\varepsilon_{re} = \varepsilon_{un} + \frac{f_{un} - f_{new}}{E_r\left(2 + \frac{f'_{cc}}{f'_{co}}\right)} \tag{10.12}$$

The corresponding stress, f_{re}, can be calculated with Equation (10.6a) for the given strain ε_{re}. The stress at a given point along the parabolic curve can be calculated with the following equation.

$$f_c = f_{re} + E_{re}x + Ax^2 \tag{10.13a}$$

where

$$x = \varepsilon_c - \varepsilon_{re} \tag{10.13b}$$

$$A = \frac{E_r - E_{re}}{-4\left[\left(f_{new} - f_{re}\right) - E_r\left(\varepsilon_{un} - \varepsilon_{re}\right)\right]} \tag{10.13c}$$

The value of E_r is calculated with Equation (10.11b) and E_{re} is the tangent modulus at the common return point.

10.3.1.2 Modifications to Mander et al.'s Model

The main change to Mander et al.'s model for simulating the behavior of the grout in the rocking hinge is the modeling of the confinement effect. The grout in the hinge was not confined by any transverse reinforcement. However, the grout in the gap was not free to expand laterally when subjected to vertical compression during rocking. The lateral expansion was restrained by the friction forces developed at the interfaces between the grout and the top and bottom steel surfaces, as shown in Figure 10.5. It can be perceived that the interior grout was confined by the exterior grout, which was restrained from lateral movement by the friction forces.

To account for the lateral confining pressure introduced by the friction, the equation for f_l' in Mander et al.'s model is modified as explained in the following discussion. Consider the fiber-section discretization shown in Figure 10.5. The circular section is discretized by dividing it into wedge segments, each of which is defined by an angle $d\phi$. Each segment is subdivided along the radial direction into fibers by circular arcs. To determine the confining pressure on each fiber, consider a fiber whose outer arc has a radial distance r_e^{fib}, as shown in Figure 10.5. The fiber is confined by the uncrushed outer grout in the wedge segment. With the assumption that the maximum compressive stress that can be reached in the outer grout during rocking is equal to the compressive strength, f_{co}', of unconfined grout, the maximum friction force ΔF_f that can develop

on each of the top and bottom faces of the outer grout in the segment is given by the following equation.

$$\Delta F_f = \frac{\left(R_o^{\,2} - (r_e^{fib})^2\right) d\phi}{2} \mu f'_{co} \tag{10.14}$$

where R_o is the radius of the outer grout that has not been crushed, $d\phi$ is the angle in radians, and μ is the coefficient of friction between the grout and the steel plates. The friction coefficient may be assumed to be 0.07 based on calibration with the column test data.

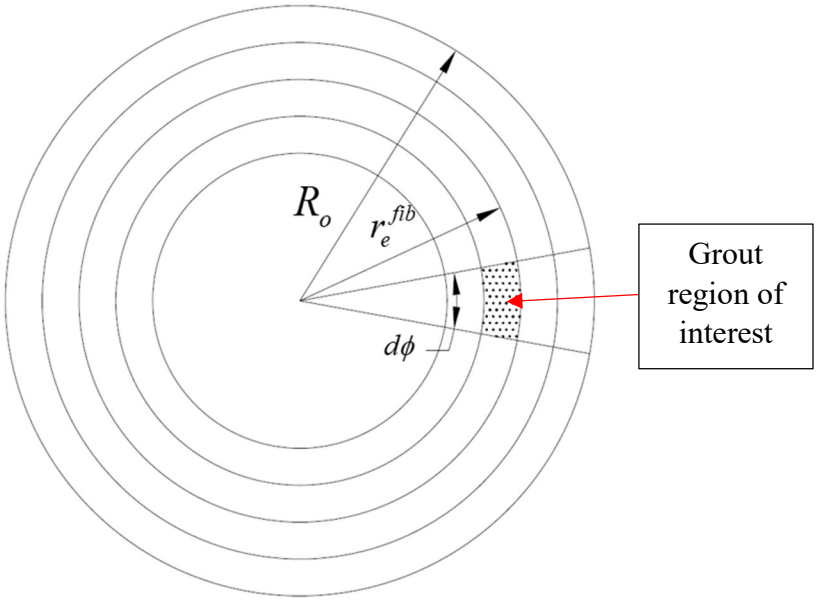

(a)

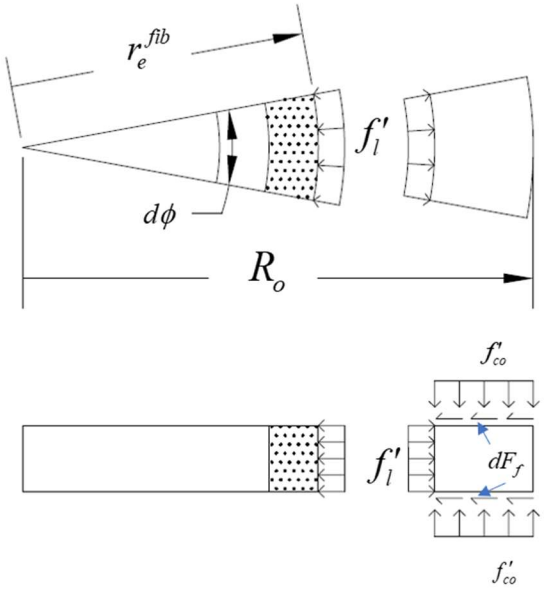

(b)

Figure 10.5: (a) Plan view of grout cross-section with region of interest; (b) *top*: plan view of a wedge segment of the cross-section showing confining pressure, *bottom*: elevation view of a wedge segment showing confining pressure

Crushed outer grout cannot provide any confining pressure to the inner grout. A strain criterion has been adopted here to signify grout crushing, after which the grout is no longer able to resist compression. A grout fiber is considered crushed when its compressive strain reaches a critical value $\varepsilon_{failure}$, which is assumed to be 0.06. The large value of the failure strain assumed here is based on the calibration of the fiber-section model using the column test data presented in Chapter 9, and it can be largely attributed to the fact that the grout was confined between the steel plates. Once the compressive strain in the outer-most uncrushed fiber in a wedge segment reaches the critical strain, the fiber is considered crushed and the value of R_o for that segment is reduced by the radial length of the crushed fiber, and the confined strengths as well as the stress-stress relations of the inner fibers in the segment is recalculated to reflect the reduction of the confining pressure.

It is assumed that the confining pressure f_l' is the stress that will be developed when the friction limit state is reached. Hence, it can be determined from the equilibrium condition for the outer uncrushed grout in the wedge segment, i.e.,

$$f_l' = \frac{2\Delta F_f}{td\phi r_e^{fib}} \tag{10.15}$$

where t is the thickness of the grout in the hinge. Substituting Equation (10.14) into Equation (10.15), we have

$$f_l' = \frac{(R_o^{\,2} - (r_e^{fib})^2)\mu f_{co}'}{t r_e^{fib}} \tag{10.16}$$

Another modification to Mander et al.'s model is the simplification in the reloading curve under cyclic loading. In Mander et al.'s model, there is a parabolic curve from $(\varepsilon_{un}, f_{new})$ to

$(\varepsilon_{re}, f_{re})$, as shown in Figure 10.4. To simplify the calculations, the reloading curve is assumed to be linear till it reaches the monotonic skeleton curve. An example of the modified reloading curve is shown in Figure 10.6.

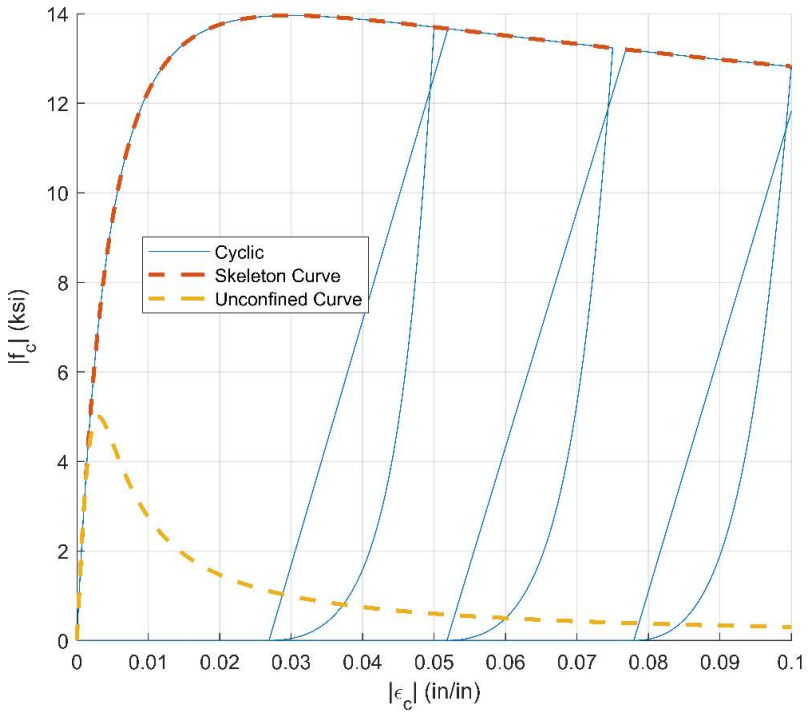

Figure 10.6: Cyclic behavior of Modified Mander's model

The grout in the hinge region may shrink during curing, resulting in a very small shrinkage gap between the grout and the ½ in.-thick steel top plate. This can affect the initial stiffness of the self-centering column. The gap is expected to be wider in the grout closer to the outside surface, where drying is more rapid. To account for this phenomenon, a shrinkage gap is introduced in the grout model. The shrinkage gap is introduced as a shrinkage strain in the grout fibers. Hence, for a grout fiber *which* that has a shrinkage gap, the strain used to calculate the fiber stress at a given hinge rotation θ is given by the following equation, instead of Equation (10.1a).

$$\varepsilon_i = \frac{u_o - x_i\theta}{H_h} + \varepsilon_{i,shrink} \tag{10.17}$$

where u_o is the axial deformation of the hinge, x_i is the distance of the centroid of the grout fiber from the centroidal axis of the fiber section, H_h is the height of the hinge, and $\varepsilon_{i,shrink}$ is the shrinkage strain in the fiber (which is a negative value).

The shrinkage strain is assumed to vary along the radial direction of the section, as shown in Figure 10.7. The shrinkage strain profile shown in the figure is determined through empirical calibration in order to have the initial stiffness given by the model closely match the stiffness measured in the column test.

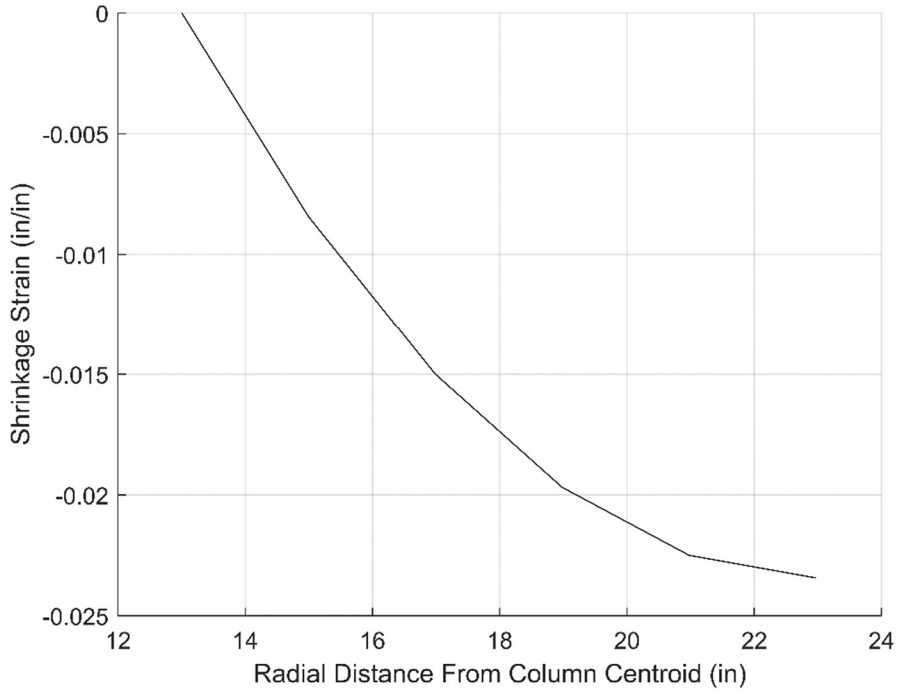

Figure 10.7: Shrinkage strain of grout fibers as a function of radial distance from the centroidal axis of the fiber section

10.3.2 Steel Materials

10.3.2.1 Steel Rocking Plates

The deformation occurring in the rocking hinge can be attributed to several sources. The 2-in.-thick rocking plates were welded to two ½-in.-thick steel plates, which were in contact with concrete at the bottom of the column and at the top of the pedestal, respectively, as shown in Figure 5.1(a). As the hinge rotated, the rocking plates, the grout, the ½-in. plates, and the concrete above and below the ½-in. plates would all deformed, as shown in Figure 5.8. In this model, the bending deformation of the ½-in. plates as well as that of the adjacent concrete is not modeled explicitly, but is accounted for phenomenologically in the material model for the steel rocking plates, as described below.

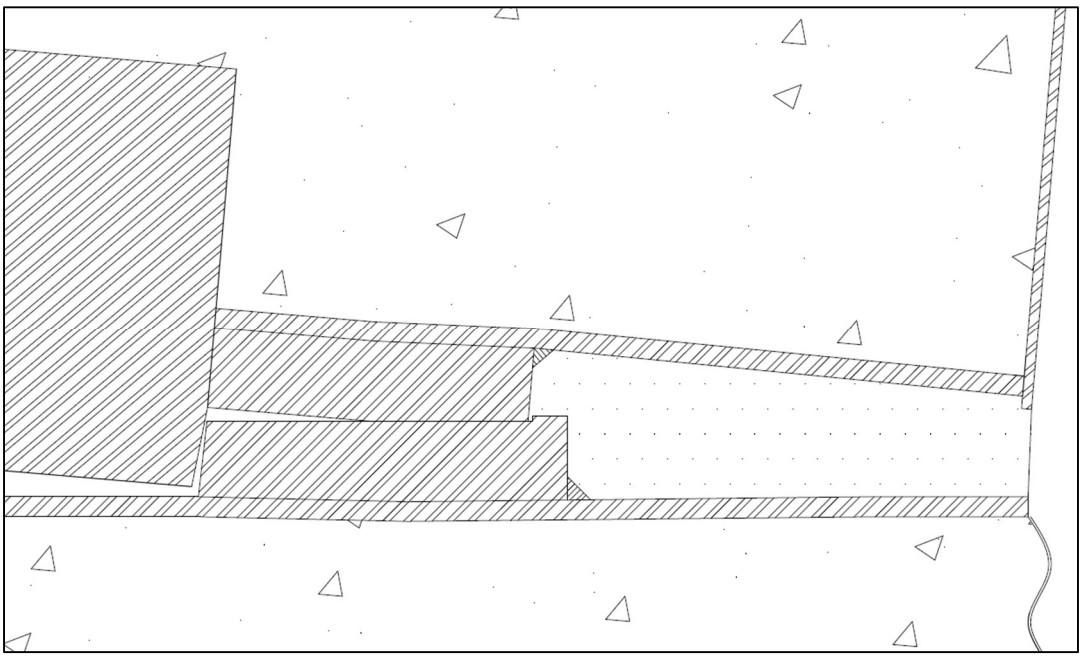

Figure 10.8: Illustration of deformations of various components within the rocking hinge

The material model for the 2-in.-thick steel rocking plates is assumed to have no tensile strength in order to simulate the rocking mechanism. The plates in the column specimens were

made of ASTM A572 Grade-50 steel, which had the yield and ultimate strengths of 50 and 65 ksi, respectively. To account for the effect of the deformation of the ½-in. steel plates and the adjacent concrete, which is not explicitly modeled, on the deformation of the hinge, the stress-strain relationship for the rocking plate material in compression is represented by a tri-linear curve, as shown in Figure 10.9, in which E_{pl} is 29,000 ksi, the stress at which yielding first occurs, σ_{ply}, is assumed to be 2.5 ksi, the post-yield tangent modulus, E_{plr}, is chosen to be 638 ksi, and the ultimate strength, σ_{plu}, is 65 ksi. After reaching the ultimate strength, the compressive stress will remain constant if the compressive strain continues to increase. These parameters are calibrated in an *ad hoc* manner to match the initial stiffness of the first column specimen. Figure 10.10 shows a cyclic stress-strain curve given by the model.

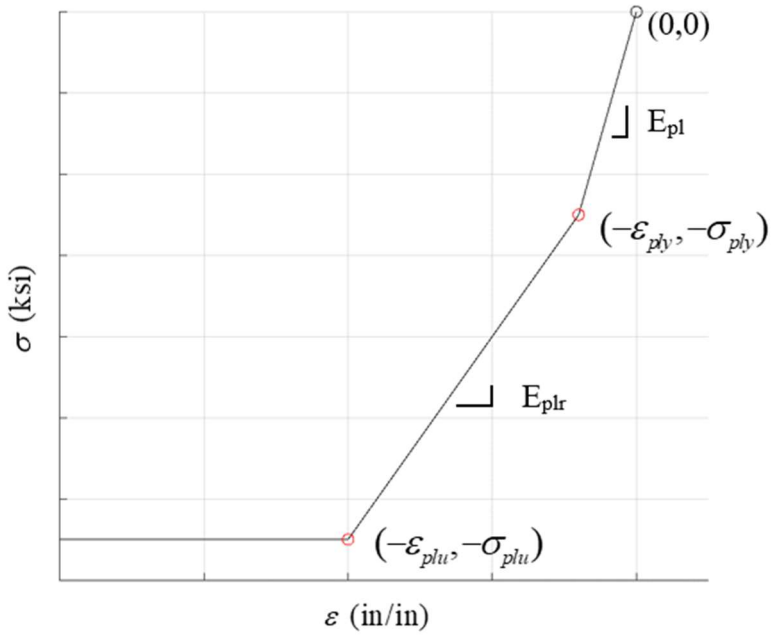

Figure 10.9: Material model for fibers representing steel rocking plates under monotonic loading with user input material parameters

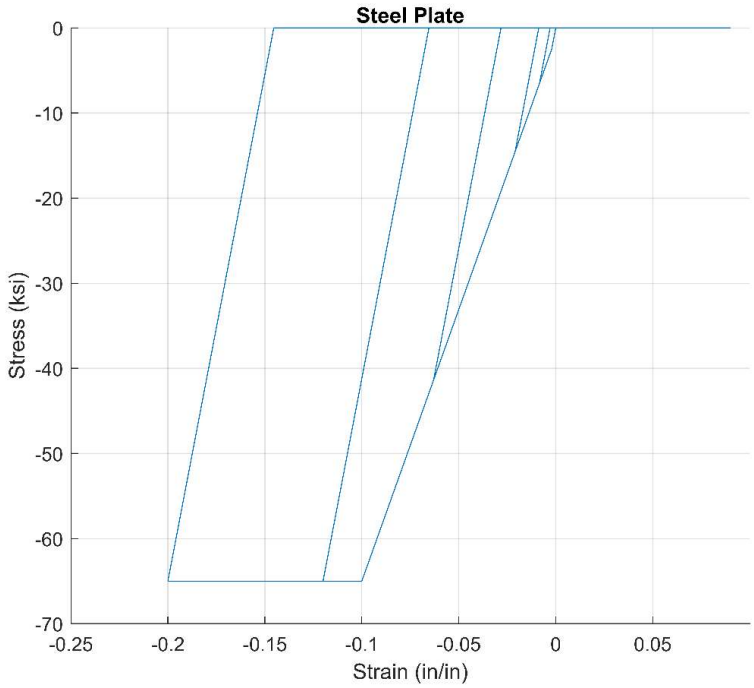

Figure 10.10: Material model for fibers representing steel rocking plates under cyclic loading

10.3.2.2 Mild Steel Rebars

The rebars in the rocking hinge region of Specimen 1 experienced cyclic tension and compression. During the test with the ungrouted hinge, some of the bars bent a little in the hinge region. During the main test with the grouted hinge, some of the bars buckled when the grout was crushed and eventually the bars fractured after a few cycles of bending and straightening as the column rocked back and forth. The fracture was caused by low-cycle fatigue due to large-amplitude cyclic strain reversals experienced by the bars. The material model presented in this section is aimed to capture the aforementioned behavior of the rebars in Specimen 1. In Specimen 2, rebars were not expected to experience compression, and each rebar consisted of two bars of different cross-sectional areas connected by a coupler. To represent the behavior of these coupled bars in the fiber-section model, the material model presented in Section 10.6 is used.

The tensile stress-strain relation for the rebars is represented by a tri-linear curve, while the compressive stress-strain relation is modeled with a bilinear curve that has a negative post-peak slope, as shown in Figure 10.11. The latter is to model the buckling behavior of a bar in a phenomenological manner. Based on the material test data presented in Chapter 8, the #6 rebars in Specimen 1 had a yield strength, σ_{sy}, of 77 ksi and a tensile strength, σ_{su}, of 101 ksi. The initial modulus of elasticity, E_s, is 29,000 ksi, and the post-yield tangent modulus, E_{sr}, is assumed to be 798 ksi. As observed in the test of Specimen 1, bar buckling did not initiate in perfectly straight bars but in bars that had a residual bending developed during hinge rotation in prior load cycles. Because of this, it is not appropriate to use the theoretical critical stress as the buckling criterion. Hence, the stress at which buckling will occur has been determined in an *ad hoc* manner so that the model will capture the rate of load degradation of the column observed in the test. This buckling stress has been determined to be -38.7 ksi (which is 50% of σ_{sy}) and the post-buckling tangent

modulus has been determined to be $-E_{sr}$. For the cyclic response, unloading follows the initial modulus of elasticity. Figure 10.11 shows an example of the cyclic stress-strain response for a bar without low-cycle fatigue. The modeling of the loss of the resistance of a bar due to low-cycle fatigue will be discussed next.

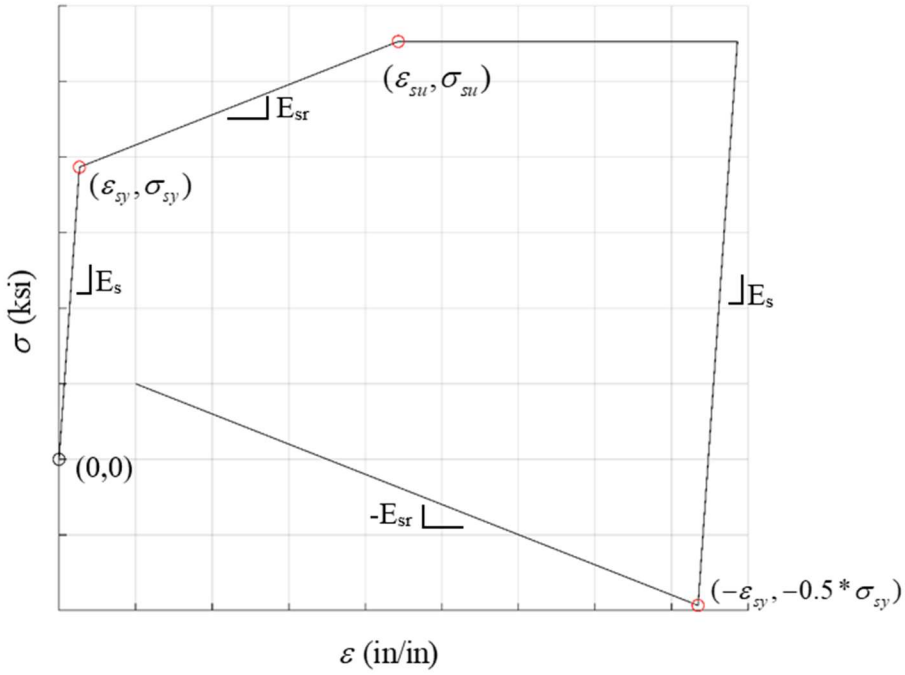

Figure 10.11: Material model for rebar with user input parameters identified

Rebar fracture caused by low-cycle fatigue is modeled with the approach adopted by Papadopoulos and Shing (2015) based on the low-cycle fatigue law proposed by Manson (1953) and Coffin (1954). In this law, the number of half-cycles, N_f, to fracture is given by the following equation.

$$N_f = \left(\frac{\Delta\varepsilon}{2\varepsilon'_f} \right)^{-\frac{1}{c}} \tag{10.18}$$

where ε_f' and c are coefficients to be calibrated with experimental data, and $\Delta\varepsilon$ is strain range in each cycle. For modeling the rebars in Specimen 1, c is set to be 0.455, and ε_f' is assumed to be 0.05 for the five bars on each of the south and north sides of the hinge, and 0.382 for the three bars on each of the east and west sides. These values have been determined in an *ad hoc* manner to capture the loading degradation observed and the column drift ratio at which bar fracture first occurred in the test. The smaller value of ε_f' for the north and south bars is due to the fact that these bars buckled early in the test and were, therefore, subjected to much more severe bending strains that resulted in earlier fracture. The bending of the bars is not modeled here and its effect has to be indirectly accounted for in the material parameter. For random strain histories, Miner's rule (Miner, 1945) is adopted to estimate cumulative damage induced by low-cycle fatigue. For this purpose, the strain range in each half-cycle is calculated as follows.

$$\Delta\varepsilon_i = \varepsilon_{\max,i} - \varepsilon_{\min,i} \tag{10.19}$$

where $\varepsilon_{\max,i}$ and $\varepsilon_{\min,i}$ are the maximum and minimum strains, respectively, experienced by the rebar in any given half-cycle *which*, which may or may not have been completed. Damage incurred in the half-cycle is defined as

$$D_i = \frac{1}{\left(N_f\right)_i} \tag{10.20}$$

where $\left(N_f\right)_i$ is the number of half-cycles to fracture calculated according to Equation (10.18) with $\Delta\varepsilon = 2\Delta\varepsilon_i$. Cumulative damage in the rebar after n half-cycles is then calculated with the following expression.

$$D = \sum_{i=1}^{n} D_i \tag{10.21}$$

As soon as the value of D reaches 1.0, it is assumed that the rebar will fracture, and the compressive and tensile strengths of the bar will drop to zero.

10.3.2.3 Prestressing Tendons

The prestressing tendons used in the column specimens were ASTM A416 Grade 270 low-relaxation strands. The monotonic tensile stress-strain (f_{ps} - ε_{ps}) relation for the strands is represented by the material model proposed by Devalapura and Tadros (1992), which has the following expression.

$$f_{ps} = \varepsilon_{ps} \left[A + \frac{B}{\left\{1 + \left(C\varepsilon_{ps}\right)^{D}\right\}^{\frac{1}{D}}} \right] \leq f_{pu} \tag{10.22}$$

where

$$A = E_p \left(\frac{f_{pu} - f_{so}}{\varepsilon_{pu} E_p - f_{so}} \right) \tag{10.23a}$$

$$B = E_p - A \tag{10.23b}$$

$$C = \frac{E_p}{f_{so}} \tag{10.23c}$$

$$f_{so} = 1.04 f_{py} \tag{10.23d}$$

Some of the material parameters are defined in Figure 10.12. The nominal yield stress, f_{py}, is defined as the stress developed at the tensile strain of 0.01, which is termed the nominal yield strain, ε_{py}. The parameter *D* controls the shape of the nonlinear curve.

Strands have no compressive resistance. Unloading and reloading of the strands are assumed to follow a linearly elastic relation with stiffness E_p. Figure 10.13 shows an example of the cyclic stress-strain behavior obtained with the model. The unloading stress-strain path for the strands follows a linearly elastic relation until the stress reaches zero and the strain reaches a residual plastic strain. The stress will remain zero if the strain decreases further because the strands cannot resist compression. When the strands are reloaded in tension, the stress remains zero until the previously attained residual plastic strain is reached, after which the stress-strain curve follows a linearly elastic ascending path. After the stress during reloading intersects the monotonic curve given by Equation (10.22), the stress-strain path is governed by the nonlinear relation again.

The values of the parameters E_p, *D*, f_{pu}, and f_{py} are to be determined from the stress-strain data for the prestressing strands obtained from tension tests. The values of E_p, f_{pu}, and f_{py} can be determined first, and then the value of *D* is determined so that f_{ps} given by Equation (10.22) is equal to f_{py} when ε_{ps} is equal to 0.01.

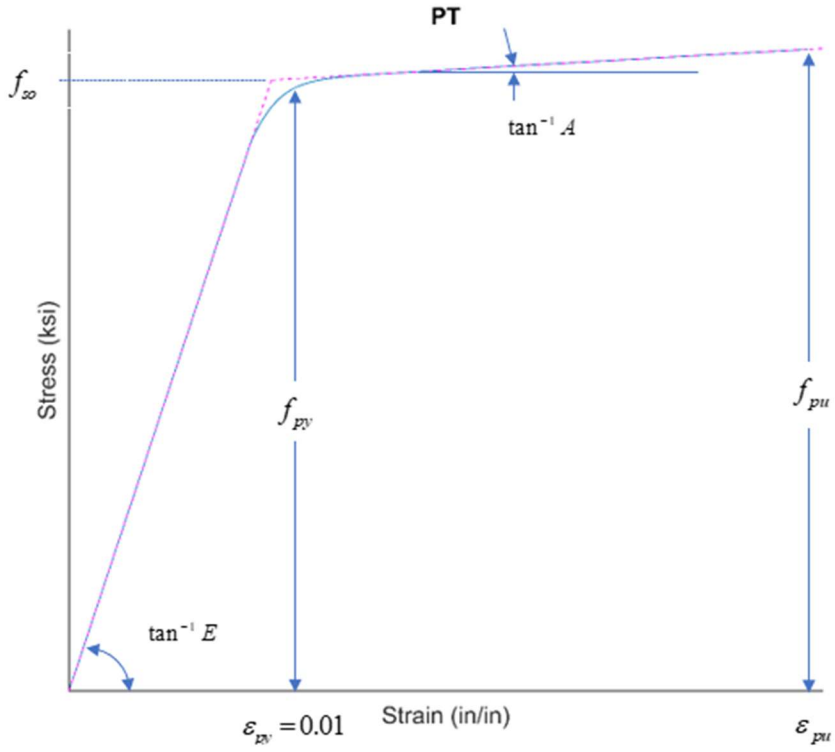

Figure 10.12: Monotonic stress-strain curve for prestressing steel (Devalapura & Tadros 1992)

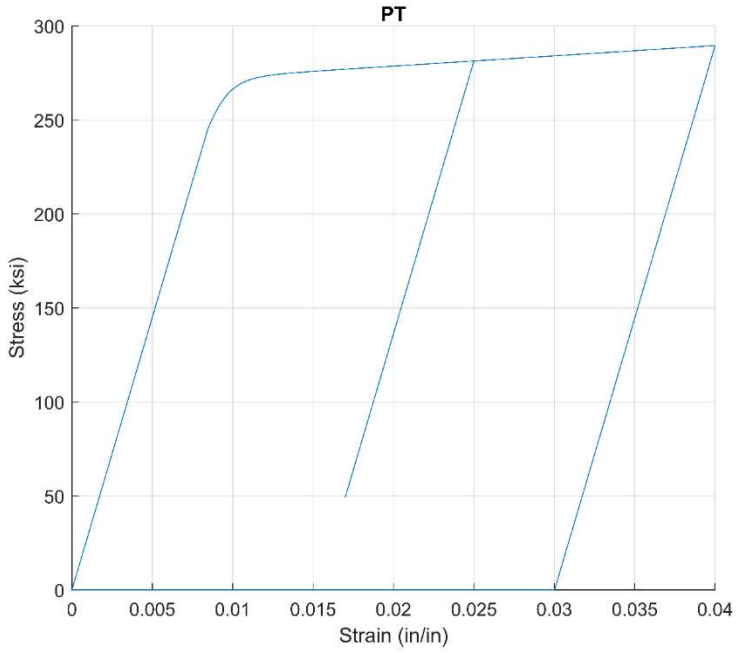

Figure 10.13: Cyclic behavior of prestressing strands in fiber model

10.4 Nonlinear Solution Scheme

To determine the moment resistance developed by the rocking hinge for a given rotational deformation and axial load with the fiber-section model, a nonlinear solution scheme is needed. The nonlinear solution scheme adopted here consists of the following steps.

1. Construct the fiber-section model based on the geometric properties and reinforcement details of the rocking hinge, including the diameter of the rocking plates, the size, number, and locations of the reinforcing bars and prestressing strands, and the unbonded lengths of the bars and strands.
2. Specify the material properties for the reinforcing bars, prestressing strands, and steel rocking plates, and the unconfined compressive stress-strain relation for the grout within the rocking hinge.
3. Specify the applied axial load and the initial strain, ε_{po}, in the prestressing strands.
4. Calculate the effective lateral confining pressures on the grout fibers based on an estimated coefficient of friction of 0.07 and Equation (10.16), when none of the grout fibers have been crushed. Determine the compressive stress-strain relations for the grout fibers using Equations (10.5) and (10.6).
5. Calculate the axial deformation, u_o', of the hinge due to the self-weight, W_c, of the column above the hinge and the initial prestressing force, F_{po}. Because of the possible nonlinear behavior of the concrete and prestressing strands, a bisection method is used to solve the nonlinear problem. The computation algorithm is shown in Figure 10.14. Since the self-weight and the prestressing force are applied to the column prior to filling the hinge with grout, grout fibers are ignored at this stage. For this step, the axial force, F_a, in Figure 10.14

is calculated as $F_a = -W_c - F_{po}$, where F_{po} is calculated with the initial prestress in the strands due to the initial strain, ε_{po}, and the total strand area. The value of F_a is negative if it is a compressive force. Similarly, the internal axial force, *N*, developed in the hinge is negative when it is compression. The solution strategy shown in Figure 10.14 is summarized as follows.

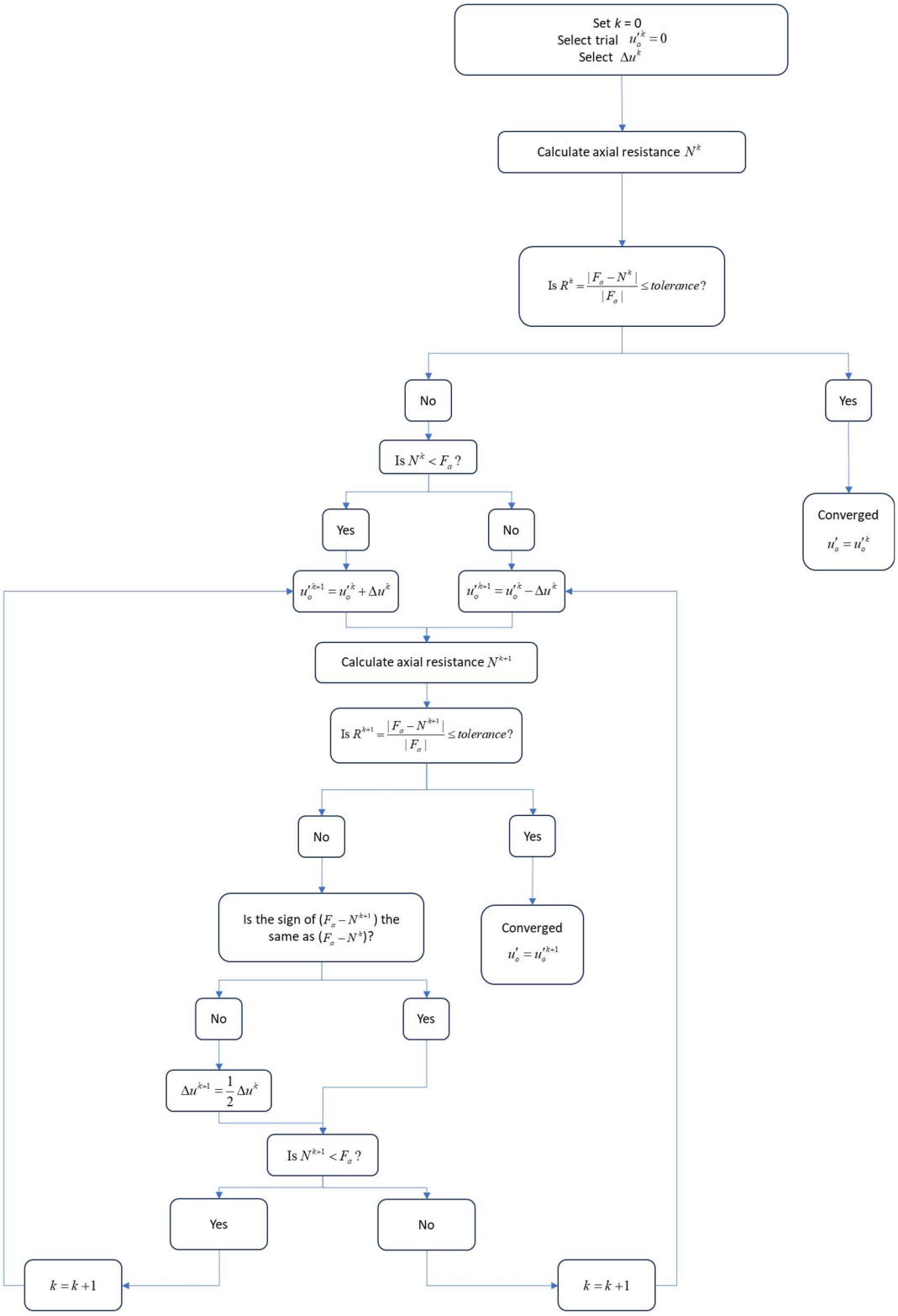

Figure 10.14: Flowchart describing bisection algorithm used to determine initial axial deformation for Step 5

a. Set the iteration number $k = 0$ and trial axial displacement $u_o'^k = 0$.

b. Select a small initial value for the incremental correction of the axial displacement, Δu^k. This can be calculated using an elastic prediction: $\Delta u^k = \frac{H_h \mid F_a \mid}{E_{pl} A_{pl}}$, where A_{pl} is the cross-sectional area of the rocking plates and E_{pl} is the modulus of elasticity of the plates.

c. Calculate the strains in the steel plates and rebars with Equation (10.1a) by having $u_o = u_o'^k$ and $\theta = 0$. Calculate the fiber stresses using the material laws for the steel plates and rebars.

d. Calculate the axial resistance, N^k, developed by the steel plates and rebars by substituting the fiber stresses calculated above into Equation (10.2a), excluding the force from the prestressing strand fibers.

e. If $\left(\left|F_a - N^k\right| / \left|F_a\right|\right)$ is greater than the preset tolerance value, update the value of $u_o'^k$ with Δu^k using the strategy shown in Figure 10.14 until the value of $u_o'^k$ satisfies the equilibrium of the axial forces.

6. Calculate the moment resistance of the grouted hinge for a given hinge rotation, θ_i, and applied axial compressive load, *P*, (in addition to the self-weight of the column and prestressing force) using the algorithm outlined in Figure 10.15. In this step, F_a, is defined as $F_a = -W_c - P$. The solution strategy, which is similar to that in Step 5, is summarized as follows.

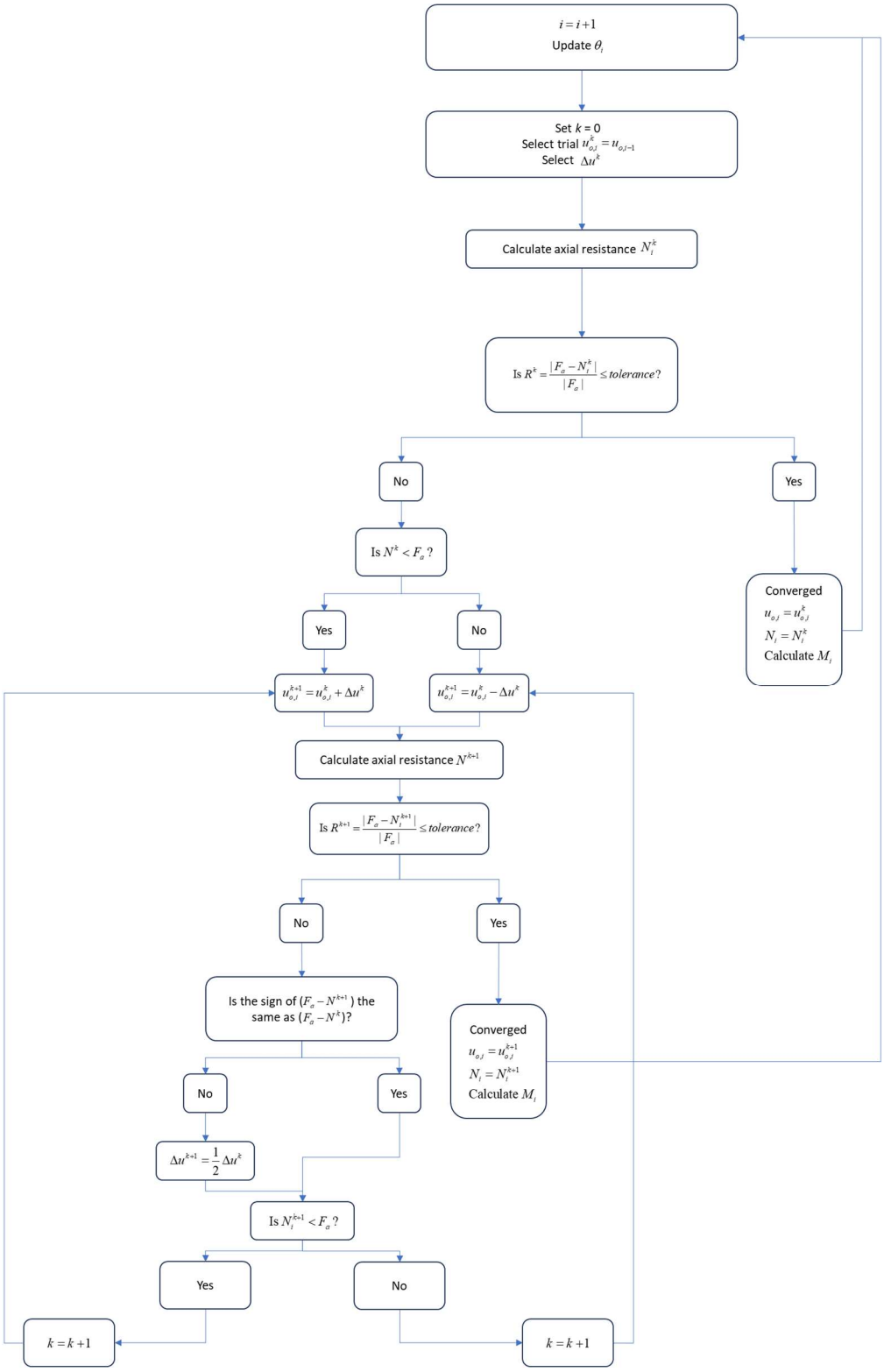

Figure 10.15: Flowchart describing bisection algorithm used to achieve equilibrium of axial forces for Step 6

a. At the beginning of incremental step *which* that has hinge rotation θ_i, set the iteration number $k = 0$ and the initial trial axial displacement $u_{o.i}^k = u_{o,i-1}$, where $u_{o,i-1}$ is the converged axial displacement in the previous step. For the very first step, $u_{o,1}^0 = u_o'$, which is equal to the axial displacement calculated in Step 5.

b. Calculate the strains in the fibers representing the rebars, steel plates, and prestressing strands using Equation (10.1) and the strains in the grout fibers using Equation (10.17). Calculate the stress in each fiber using the respective material law.

c. Calculate axial resistance of the section, N_i^k, using Equation (10.2a), which includes the forces exerted by the prestressing strands.

d. Check the equilibrium of the axial forces and update the value of $u_{o,i}^k$ until equilibrium is reached.

e. Calculate the moment resistance, M_i, developed by the section using Equation (10.2b).

10.5 Modeling of Specimen 1 using the Fiber-Section Model

The fiber-section model presented in Section 10.4 is used to simulate the response of Specimen 1 with the grouted hinge. Figure 10.16 shows the lateral force-vs.-lateral drift curves from the model and the test. As shown in the figure, the model underestimates the peak force developed by the column, but it captures the load degradation and the shape of the hysteresis loops well.

In Figures 10.17 and 10.18, the axial deformations and the locations of the neutral axis in the rocking hinge obtained from the fiber model and the test are plotted against the lateral drift of

the column. The neutral axis distance is measured from the centroid of the section. The numerical results match the experimental data well.

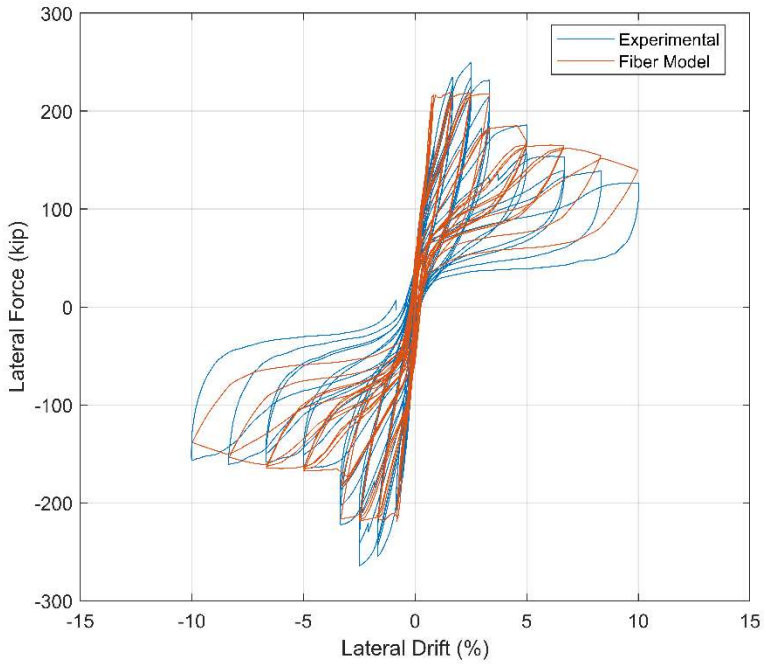

Figure 10.16: Comparison of lateral load-vs.-lateral drift curves obtained from fiber model and test of Specimen 1 with grouted hinge

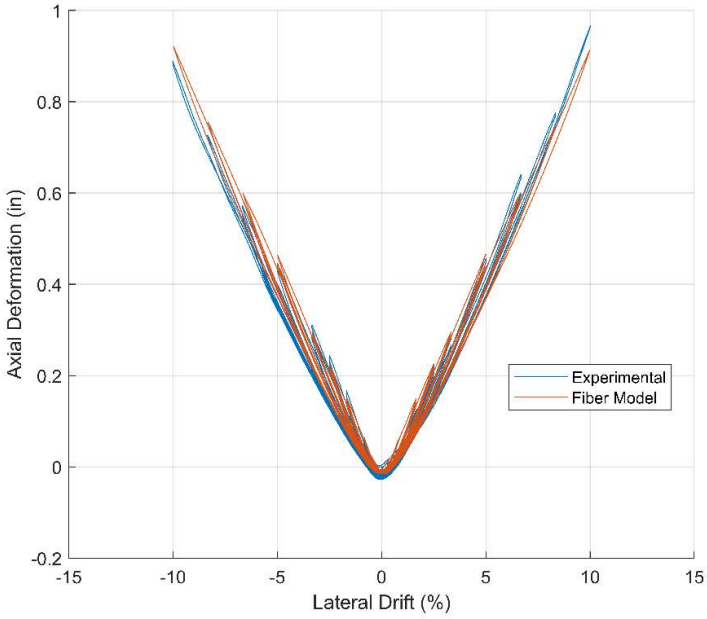

Figure 10.17: Comparison of hinge axial deformation-vs.-lateral drift curves obtained from fiber model and test of Specimen 1 with grouted hinge

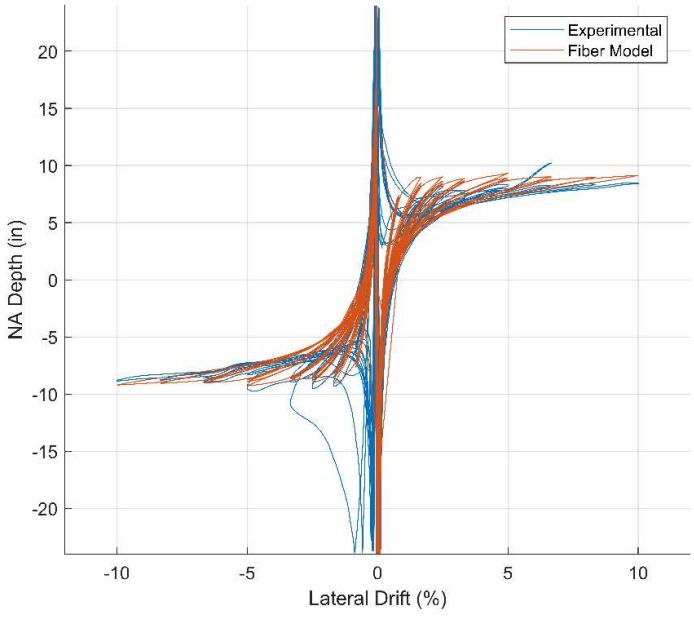

Figure 10.18: Comparison of neutral axis (NA) depth-vs.-lateral drift curves obtained from fiber model and test of Specimen 1 with grouted hinge

Figure 10.19 shows the comparison of the strains in the extreme south rebar in Specimen 1 obtained from the fiber-model analysis and the test, while Figure 10.20 shows the same comparison for the extreme north rebar. In the test, the rebars fractured at a drift ratio between 2.5 and 3%. This is well captured by the fiber model. However, it should be pointed out that the good match can be attributed to the fact that the low-cycle fatigue model for the rebars is calibrated with the data from this test.

Figure 10.21 compares the strains in the prestressing strands on the south side of the column obtained from the analysis and the test, while Figure 10.22 shows the same comparison for the strands on the north. The test results are the average strains measured. While the V-shaped curves are well captured, the numerical results show higher tensile strains. The reason for this discrepancy can be largely attributed to the slip of the strands in the mechanical anchors during the test as well as the progressive shortening of the hinge. The slip is not simulated in the model. However, since the maximum strains attained in the analysis and the test exceed the yield strain (based on the stress-strain relations of the strands shown in Figure 8.4), the difference in the strain levels has little effect on the maximum tensile stress developed by the strands.

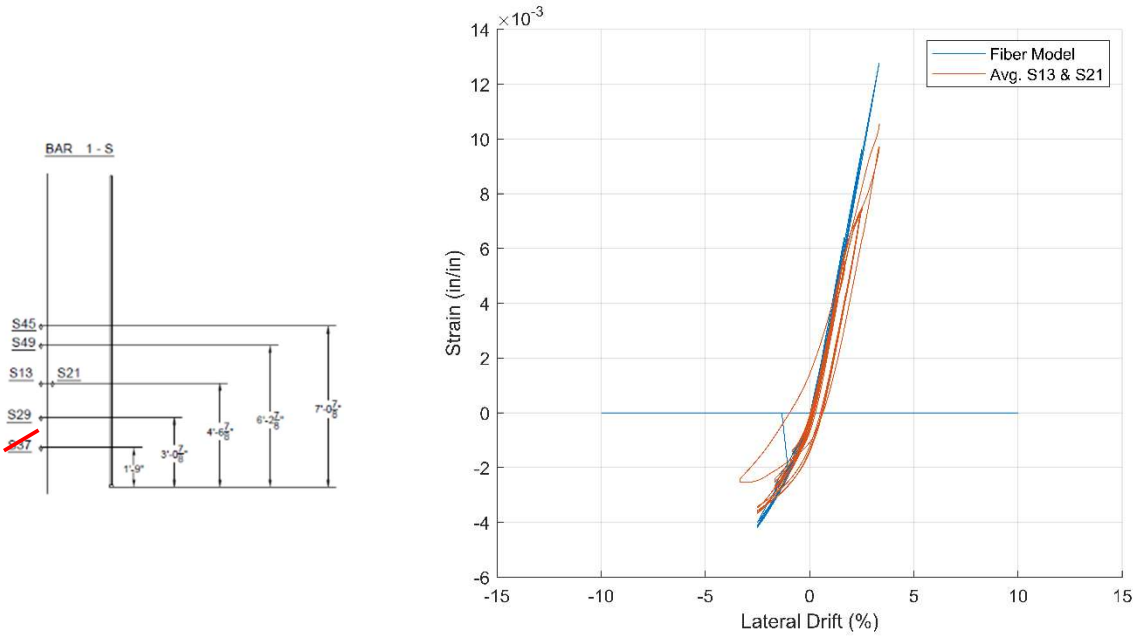

Figure 10.19: Strains in the extreme south bar of Specimen 1 from fiber model and test

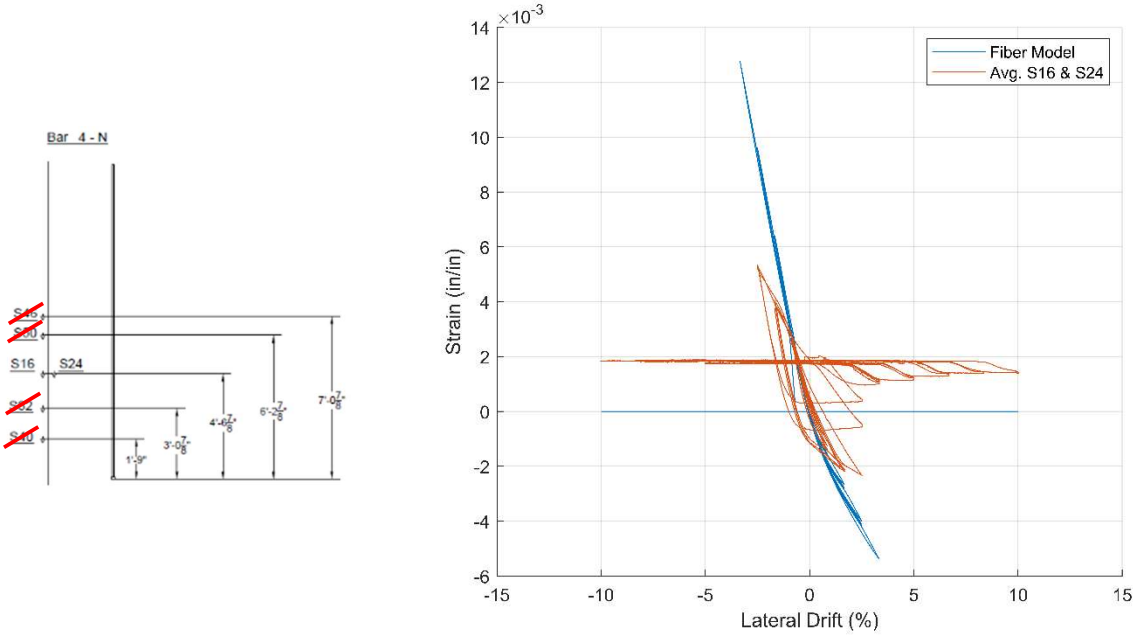

Figure 10.20: Strains in the extreme north bar of Specimen 1 from fiber model and test

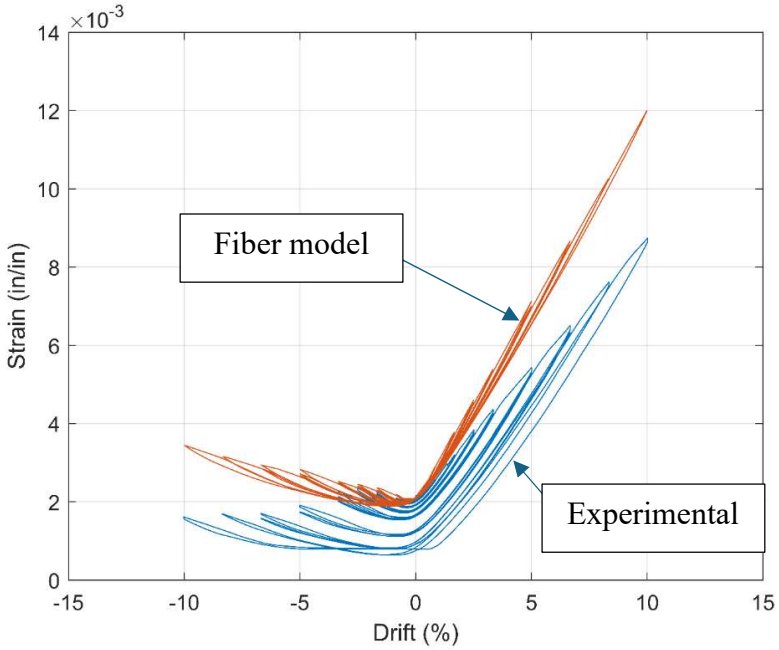

Figure 10.21: Strains in south prestressing strands of Specimen 1 from fiber model and test (strain gauge locations shown in Figure D.4)

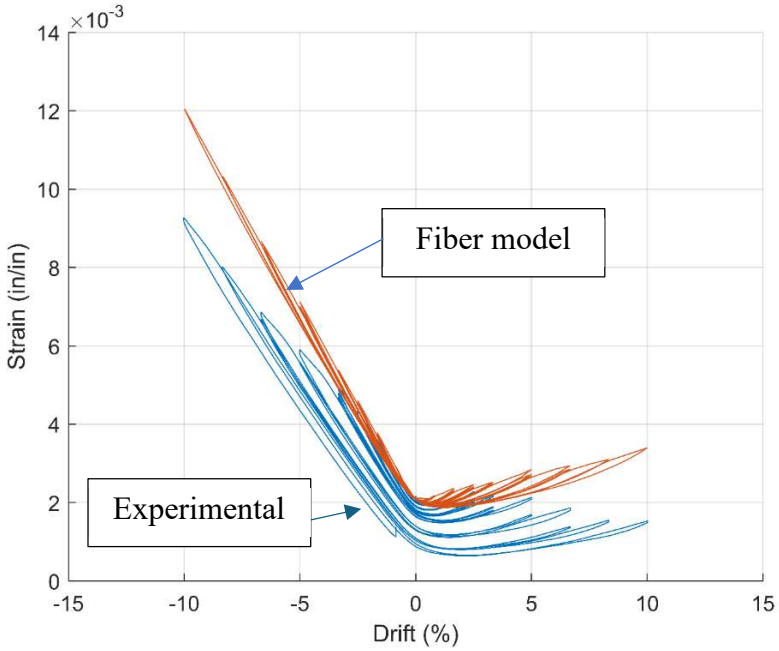

Figure 10.22: Strains in north prestressing strands of Specimen 1 from fiber model and test (strain gauge locations shown in Figure D.4)

10.6 Rebar Model for Specimen 2

The longitudinal rebars in Specimen 2 were not allowed to enter into compression. None of the rebars fractured in tension during the test. Hence, the rebar model does not need to account for low-cycle fatigue or compressive resistance. Each longitudinal rebar in the specimen consisted of a #8 bar (fuse bar) coupled with a #10 bar, which was supposed to remain elastic. It is modeled as two springs in series. For convenience, the constitutive relation for the coupled bars is formulated in terms of the bar force and bar elongation as opposed to a stress-strain relation. In the model, the tensile force-deformation relation is represented by a tri-linear curve as shown in Figure 10.23. The values of the material parameters are determined from the yield and tensile strengths, and the corresponding strain values of the #10 and #8 bars obtained from material tests, as discussed below.

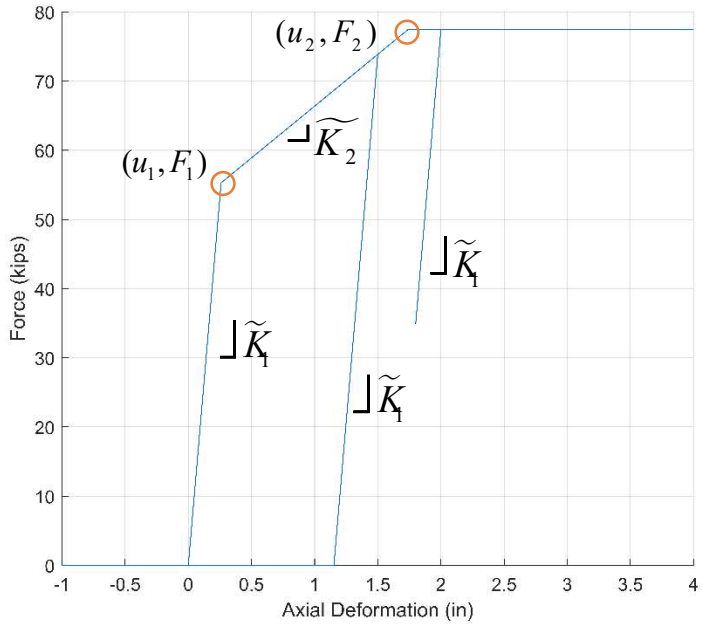

Figure 10.23: Rebar force-vs.-axial deformation relation

The axial stiffnesses of the elastic (#10) bar and the fuse (#8) bar in each longitudinal rebar are given by Equations (10.24a) and (10.24b), respectively.

$$K_e = \frac{E_s A_e}{L_{ue}} \tag{10.24a}$$

$$K_f = \frac{E_s A_f}{L_{uf}} \tag{10.24b}$$

where A_e and A_f are the cross-sectional areas of the elastic and the fuse bars, respectively, and L_{ue} and L_{uf} are the unbonded lengths of the bars. The initial stiffness, $\widetilde{K_1}$, of the rebar formed by the coupled bars is given by Equation (10.25).

$$\widetilde{K_1} = \frac{K_e K_f}{K_e + K_f} \tag{10.25}$$

Force, F_1, in the trilinear curve is the yield force of the fuse bar, which is calculated from the yield stress of 70 ksi obtained from material tests. The axial deformation of the entire rebar at yield, u_1, can be determined with Equation (10.26).

$$u_1 = \frac{F_1}{\widetilde{K_1}} \tag{10.26}$$

The ultimate force, F_2, is calculated from the tensile strength of the fuse bar, which is 98 ksi (since it is lower than the yield force of the elastic bar). The post-yield stiffness, $\widetilde{K_2}$, of the rebar can be calculated with Equation (10.27).

$$\widetilde{K_2} = \frac{\alpha_1 K_f K_e}{\alpha_1 K_f + K_e} \tag{10.27}$$

The value of α_1 is given by Equation (10.28).

$$\alpha_1 = \frac{\dfrac{F_2 - F_1}{u_{fu} - u_{fy}}}{K_f} \tag{10.28}$$

where u_{fy} is the axial deformation of the fuse bar at which its yield strength is reached and u_{fu} is the axial deformation at which the tensile strength is reached. To calculate these deformations, the yield strain of the bar is assumed to be 0.0024 and the strain at which the ultimate strength is reached is assumed to be 0.0443. It is assumed that the plastic strain is uniform along the fuse bar. The axial deformation of the rebar, u_2, at which F_2 is first reach is given by the following equation.

$$u_2 = u_1 + \frac{F_2 - F_1}{\widetilde{K_2}} \tag{10.29}$$

10.7 Modeling of Specimen 2 using the Fiber-Section Model

The response of Specimen 2 with the grouted hinge has been simulated with the fiber-section model. The behavior of the rebars is represented by the model presented in the previous section. Figure 10.24 shows the lateral force-vs- lateral drift ratio curves obtained from the fiber model and the test. As shown in the figure, the fiber model under-estimates the post-peak load degradation observed in the test. This can be attributed to two factors that are not accounted for in the fiber model. The first is the crushing of concrete underneath the heads of the rebars on the top surface of the loading block, which reduced the tension in the rebars, and the second is the slip of some strands in the anchors. However, the second factor is believed to play an insignificant role. As it will be shown later, the maximum strand strain reached in the test exceeded the yield strain,

and, as a result, the higher strain reached in the fiber model leads to only a little higher tensile stress.

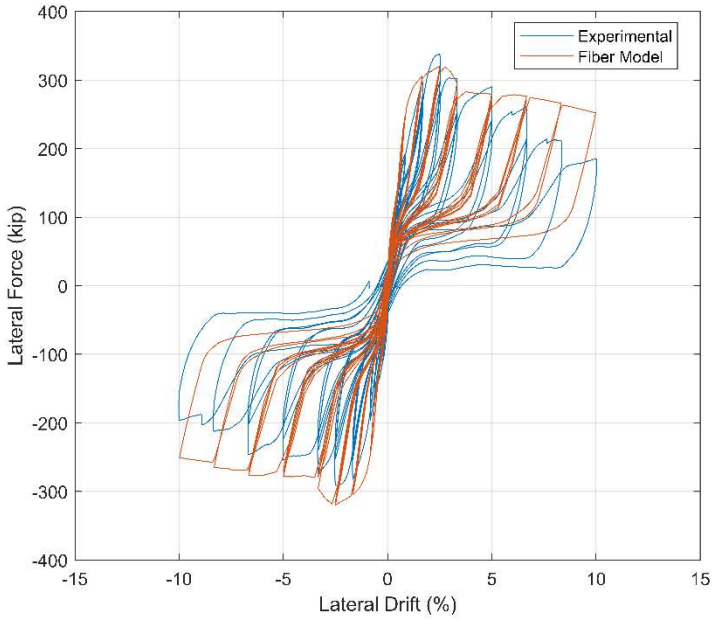

Figure 10.24: Comparison of lateral load-vs.-lateral drift curves obtained from fiber model and test of Specimen 2 with grouted hinge

Figure 10.25 compares the axial deformation of the rocking hinge from the analysis to that in the test, while Figure 10.26 compares the shift of the neutral axis of bending during rocking. Both phenomena are well captured by the model. However, the model shows a more symmetric behavior in the two drift directions than the specimen.

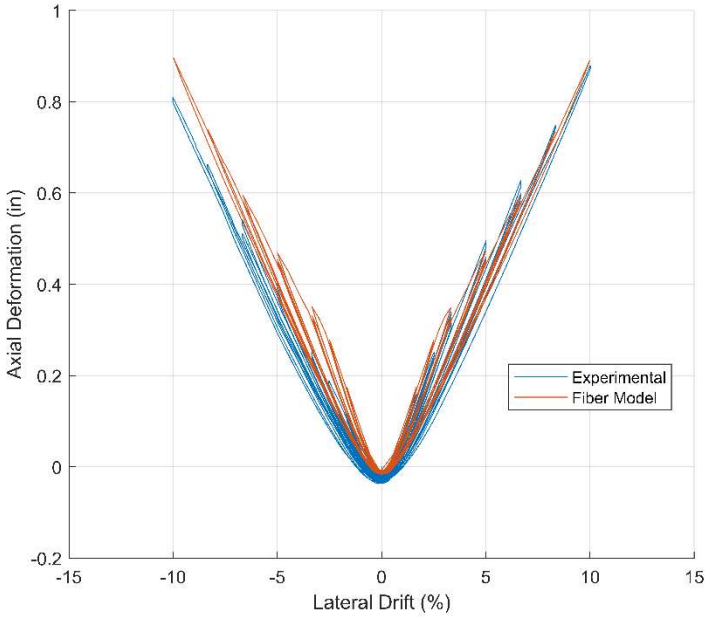

Figure 10.25: Comparison of hinge axial deformation-vs.-lateral drift curves obtained from fiber model and test of Specimen 2 with grouted hinge

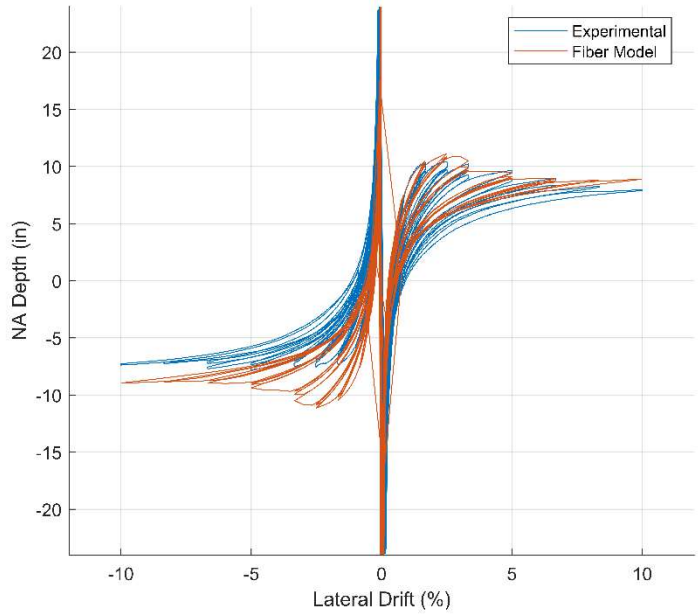

Figure 10.26: Comparison of neutral axis (NA) depth-vs.-lateral drift curves obtained from fiber model and test of Specimen 2 with grouted hinge

Each rebar in Specimen 2 had a #10 bar and a #8 bar coupled together. The #10 bar was the lower segment and the #8 bar was the upper segment. The rebar model employed in the fiber-section analysis represents the global force-displacement relation of the two bars connected in series. Hence, the strain values for the #10 and #8 bars are not directly available from the numerical results, and they have to be extracted from the force and the total deformation developed in the coupled bars. Since the model has the assumption that the #10 bar always remains linearly elastic, the strain in that bar can be determined from the force, F, developed in the rebar with the following expression.

$$\varepsilon_e = \frac{F}{E_s A_e} \tag{10.30}$$

where E_s is the modulus of elasticity, which is 29,000 ksi, and A_e is the cross-sectional area of the #10 bar. The strain in the #8 (fuse) bar can then be determined as follows.

$$\varepsilon_f = \frac{u_T - L_{ue}\varepsilon_e}{L_{uf}} \tag{10.31}$$

where u_T is the total axial deformation of the rebar, L_{ue} is the length of the #10 bar, and L_{uf} is the length of the #8 bar.

The strain-vs.-drift ratio plots for the extreme south and north rebars from the analysis and the test are compared in Figures 10.27 and 10.28, respectively. Strains in the #10 and #8 bars are plotted separately. In the fiber model, the south and north rebars show similar responses. The strains in the #10 bars level off at a value slightly below 0.001, which is way below the yield strain of 0.0025, due to the yielding of the #8 (fuse) bars. The maximum tensile strains developed in the #8 bars are slightly below 0.09. In the test, the maximum tensile strains developed in the #10 bars

were a little beyond the yield strain of 0.0025, because the bond between the bars and the concrete was not completely absent, while the #8 bars had the maximum tensile strains barely reach the yield strain. The lower strains in the #8 bars, compared to the analysis results, were partly due to the partial bonding of the #10 bars, which reduced the tensile stress transmitted to the #8 bars above. Another factor was the crushing of concrete on the top face of the loading block underneath the anchoring heads of the #8 bars, which reduced the strain demand on the bars as the column rocked.

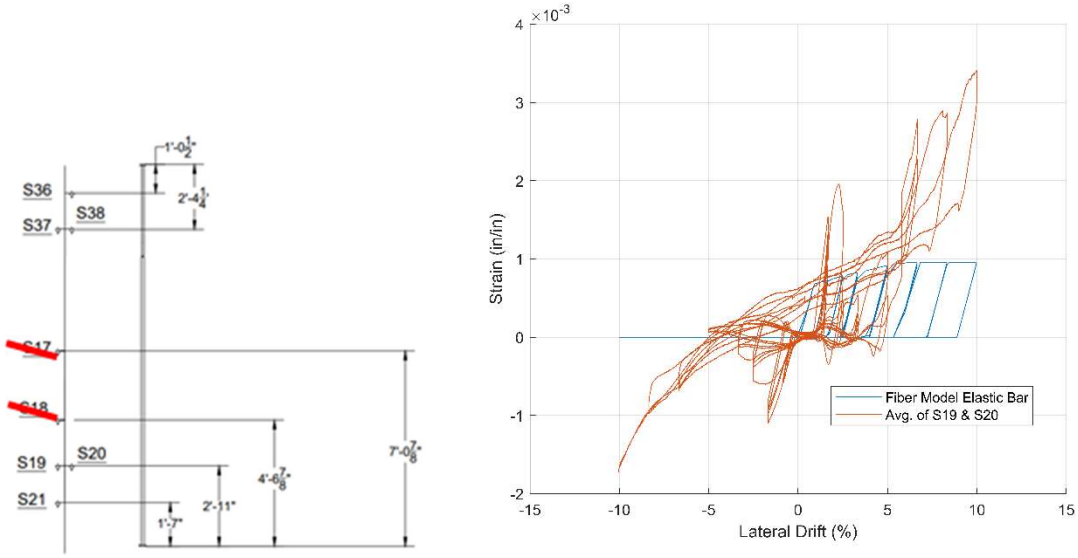

(a) No. 10 Bar (lower segment)

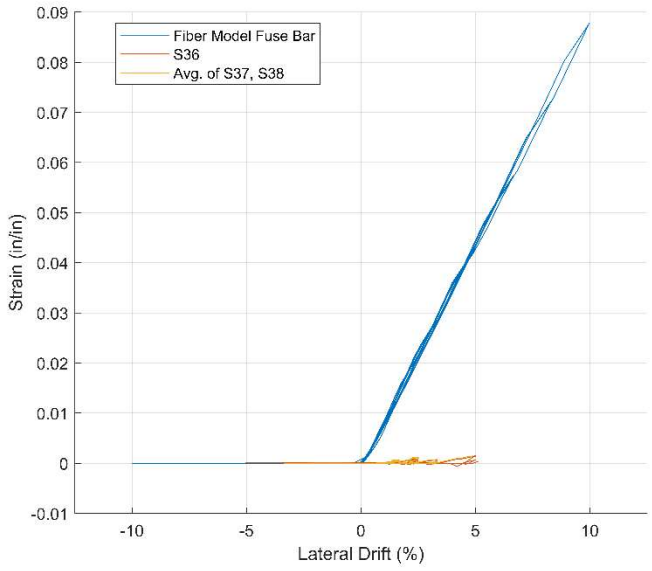

(b) No. 8 Bar (upper segment)

Figure 10.27: Strains in the extreme south bar of Specimen 2 from fiber model and test

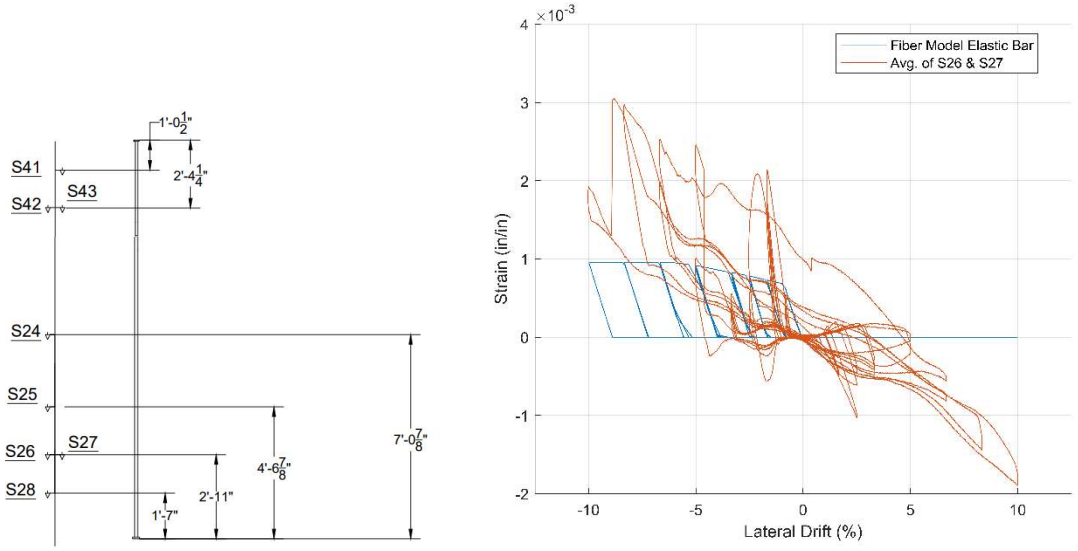

(a) No. 10 Bar (lower segment)

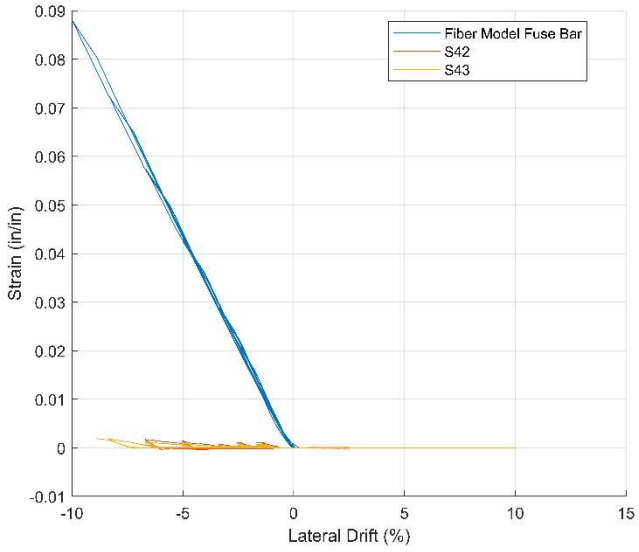

(b) No. 8 Bar (upper segment)

Figure 10.28: Strains in the extreme north bar of Specimen 2 from fiber model and test

Figures 10.29 and 10.30 show the strains in the prestressing strands on the south and north sides of the column from the analysis and the test. Similar to that observed for Specimen 1, the model shows higher strain values than the test, because the model does not account for the slip of

the strands in the anchors as well as the progressive shortening of the hinge. Since the maximum strains attained in the analysis and the test exceed the yield strain, the difference in the strain levels has little effect on the maximum tensile stress developed by the strands.

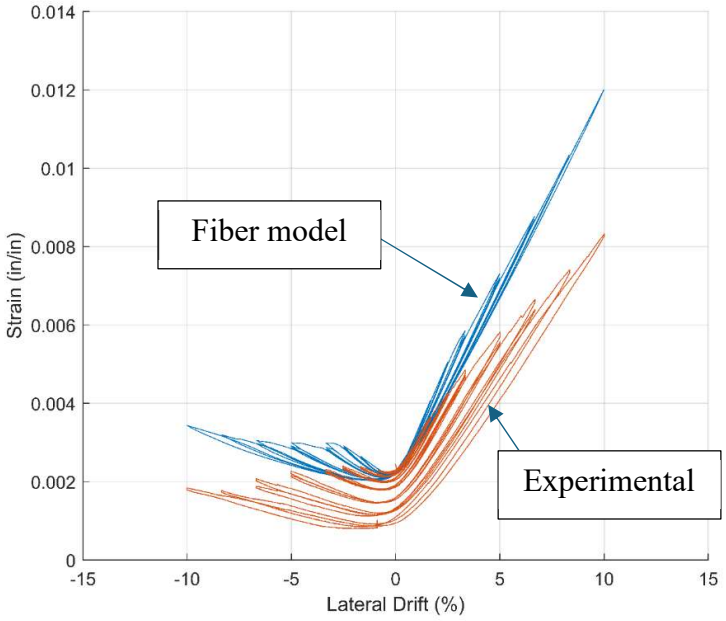

Figure 10.29: Strains in south prestressing strands of Specimen 2 from fiber model and test (strain gauge locations shown in Figure D.14)

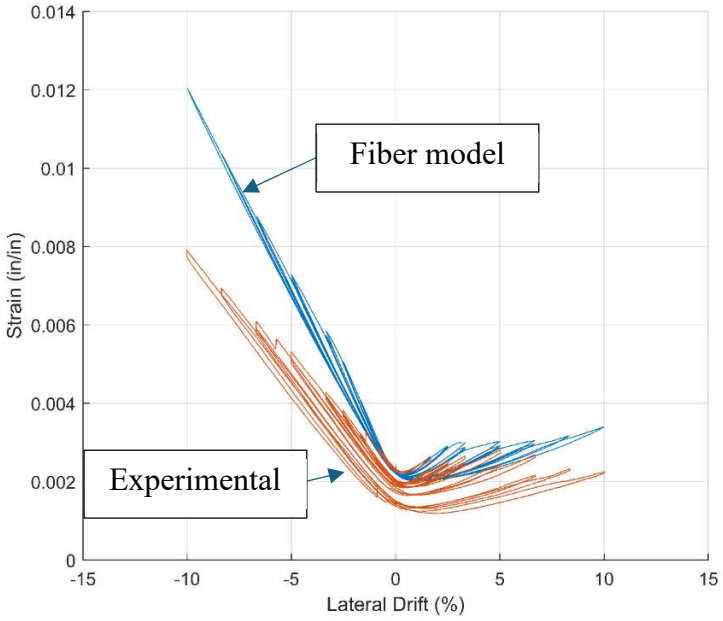

Figure 10.30: Strains in north prestressing strands of Specimen 2 from fiber model and test (strain gauge locations shown in Figure D.14)

Chapter 10 is, in part, a reprint of the material in a California Department of Transportation report entitled "Experimental Investigation of a Self-Centering RC Column Design and a Displacement-Based Design Method for Highway Bridge Applications." The authors of the report are: the author of the dissertation, Dimitrios Kalliontzis, and P. Benson Shing. Professor Dimitrios Kalliontzis worked on much of the construction of the first test specimen. The author of the dissertation provided input for the design of the second specimen, and was responsible for overseeing the construction and experimental work, post-test analysis of the two specimens, modeling and worked with Professor P. Benson Shing on the development of the displacement-based design methodology.

Chapter 11 Displacement-Based Design Method

11.1 Introduction

This chapter presents a displacement-based method for the design of self-centering columns for damage-resilient bridge structures. In the procedure proposed here, the displacement-based design framework proposed by Prestley et al. (2007) is adopted, and Rayleigh's method is used to reduce the bridge structure to a single-degree-of-freedom (SDOF) system, with the structural nonlinearity represented by an equivalent stiffness and damping. The fiber-section model presented in Chapter 10 is used as a tool to carry out the design. The formulation of the equivalent SDOF system for a bridge structure using Rayleigh's method is presented in Section 11.2, and the design procedure is described in Section 11.3. Design examples are provided in Sections 11.4 and 11.5.

11.2 Modeling of Bridge Structures with Rayleigh's Method

For displacement-based design, a displacement response spectrum is used to determine the desired effective period of the structure defined in terms of its mass and equivalent stiffness. Hence, the bridge structure has to be represented by an equivalent linearly elastic SDOF system. In the procedure proposed here, Rayleigh's method is used to derive the equivalent SDOF system, which has been studied by Turksonmez (2016) for the design of abutment shear keys in bridges. With this method, the lateral displacement response of the bridge superstructure is expressed as the product of two functions, with the longitudinal coordinate, x, and the temporal coordinate, t, as the respective variables.

$$u(x,t) = \psi(x)z(t) \tag{11.1}$$

where $z(t)$ is the generalized displacement of the equivalent SDOF system and $\psi(x)$ is the assumed shape function, which has to satisfy the boundary conditions of the bridge superstructure. Table 11.1 shows possible shape functions for three common bridge configurations. In the table, Type-1 bridge configuration represents a bridge that has continuous spans and a relatively flexible (with respect to the column stiffness) superstructure whose ends are laterally restrained by abutment shear keys; in this case, both the shear keys and the columns provide lateral resistance to the seismic forces. Type-2 has a relatively stiff superstructure, with the lateral resistance to the seismic forces provided by the bridge columns only; this can happen because the abutment shear keys are normally stiffer than the columns, and they may not be able to resist the full seismic forces transmitted by the stiff superstructure before the columns are effectively engaged in a major seismic event. Type-3 is a bridge with internal hinges in the superstructure to accommodate thermal effects; in this case, both the abutment shear keys and the columns resist the lateral seismic forces.

Table 11.1: Examples of bridge configurations

Type	Bridge Configuration	Shape Function $\psi(x)$
1	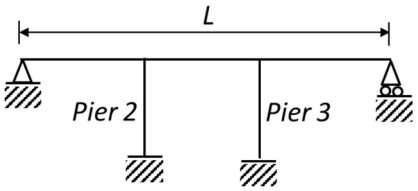	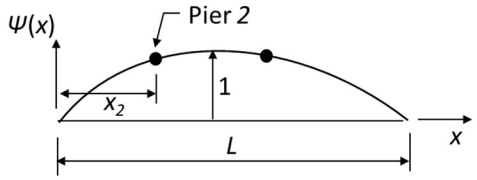
2	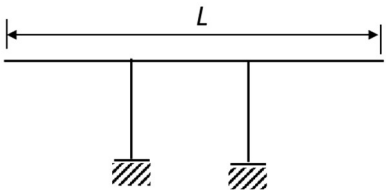	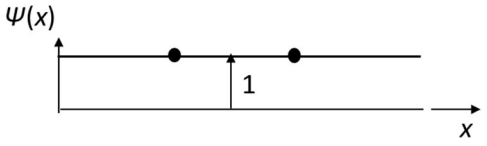
3	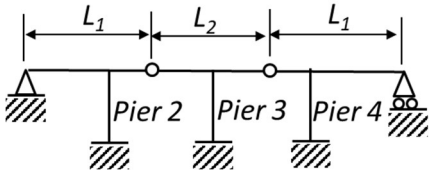	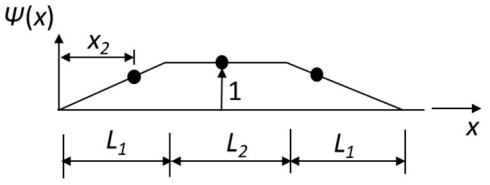

For Type-1 bridge, one can assume that

$$\psi(x) = \sin\frac{\pi x}{L} \tag{11.2}$$

where L is the total length of the bridge superstructure, as shown in Table 11.1. For Type-2, if the center of mass of the bridge superstructure coincides with the center of stiffness of the bridge, $\psi(x) = 1$; otherwise, $\psi(x)$ may assume a linear function to represent the translation and rotation of the superstructure. For the second case of Type-2, the stiffness ratios for the piers have to be estimated first, and based on the estimated stiffness ratios, a static analysis with a concentrated

force applied at the mass center can be conducted to determine the linear shape function. Since the magnitude of the shape function is not relevant, the absolute stiffness values for the piers are not required for the analysis. For Type-3, $\psi(x)$ can be a trilinear function, as shown in Table 11.1. However, if there are more than two internal hinges, it will be convenient to have the deflected shape represented by the sine function shown in Equation (11.2). For other bridge configurations, shape functions can be determined with a static analysis using appropriate load distribution and boundary conditions.

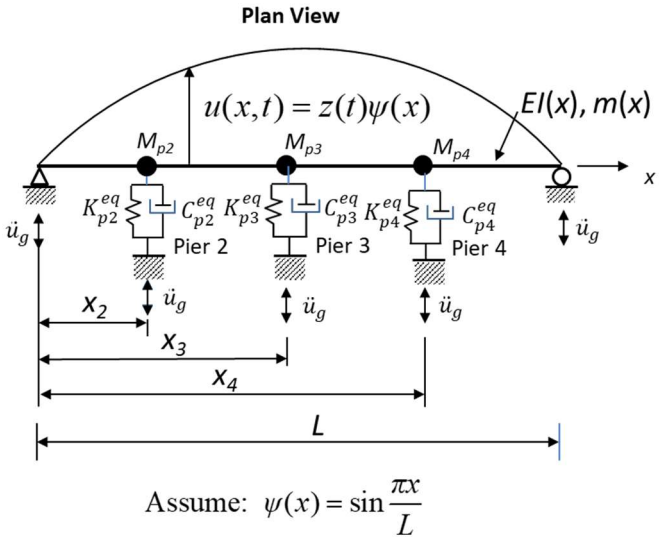

Figure 11.1: Plan view of idealized bridge model

The equivalent stiffness, K_{pi}^{eq}, is defined in Figure 11.2. It is the slope of the line passing through $\left(-u_{pi,\max}, -F_{pi,\max}\right)$ and $\left(u_{pi,\max}, F_{pi,\max}\right)$, where $F_{pi,\max}$ is the maximum lateral resistance developed by the pier in a response cycle with a displacement amplitude equal to $u_{pi,\max}$. For a pier with multiple columns, $F_{pi,\max}$ is the total resistance provided by the columns. The

displacement amplitude $u_{pi,\max}$ is the maximum displacement allowed for the pier in the displacement-based design.

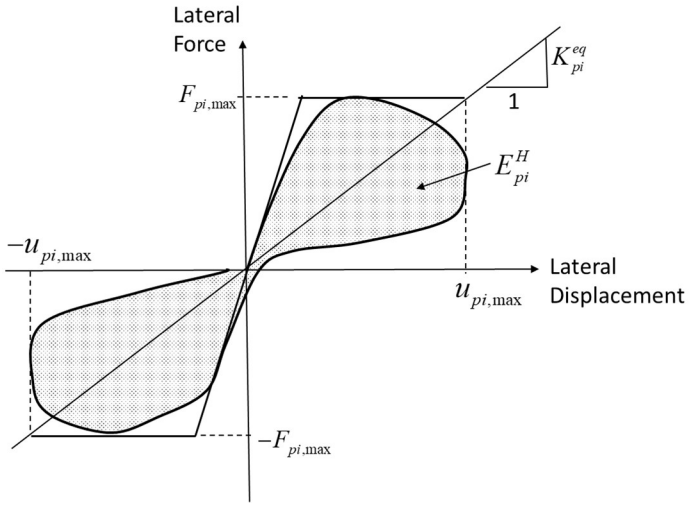

Figure 11.2: Equivalent linear-elastic properties for an inelastic pier

The value of the equivalent viscous damping coefficient for the pier is to be calculated with the following equation.

$$C_{pi}^{eq} = \frac{E_{pi}^{H}}{\pi \omega_{eq} u_{pi,\max}^{2}} = \frac{E_{pi}^{H}}{\pi \omega_{eq} z_{\max}^{2} \psi^{2}(x_i)} \tag{11.3}$$

in which E_{pi}^{H} is hysteretic energy dissipated in one cycle of displacement response with an amplitude of $\pm u_{pi,\max}$, as shown in Figure 6.2, ω_{eq} is the equivalent natural frequency of the bridge structure as will be defined later, $z_{\max}$ is the maximum displacement response of the equivalent SDOF system, and x_i is the x coordinate of the pier, as shown in Figure 11.1. The hysteretic energy E_{pi}^{H} represents the total energy dissipated by the columns in the pier.

Applying the principle of virtual displacements, with the displacement function of the bridge superstructure given by Equation (11.1), one can obtain the following equation of motion for the equivalent SDOF system.

$$M^*\ddot{z} + C^*\dot{z} + K^*z = -L^*\ddot{u}_g \quad \text{or} \quad \ddot{z} + 2\xi^*\omega\dot{z} + \omega^2 z = -\frac{L^*}{M^*}\ddot{u}_g \tag{11.4a}$$

where

$$M^* = \int_0^L m(x)\psi^2(x)dx + \sum_i M_{pi}\psi^2(x_i) \tag{11.4b}$$

$$K^* = \int_0^L EI(x)\left(\frac{d^2\psi(x)}{dx^2}\right)^2 dx + \sum_i K_{pi}^{eq}\psi^2(x_i) \tag{11.4c}$$

$$L^* = \int_0^L m(x)\psi(x)dx + \sum_i M_{pi}\psi(x_i) \tag{11.4d}$$

$$\omega_{eq} = \sqrt{K^*/M^*}\ ; \quad T_{eq} = 2\pi\sqrt{M^*/K^*} \quad \text{(equivalent natural frequency and period)} \tag{11.4e}$$

$$\xi^* = 0.05 + \frac{\sum_i C_{pi}^{eq}\psi^2(x_i)}{2M^*\omega_{eq}} = 0.05 + \frac{\sum_i E_{pi}^H}{2\pi K^* z_{\max}^2} \tag{11.4f}$$

The variables in Equation (11.4) are defined as follows:

$m(x)$ = mass per unit length of the bridge superstructure;

$EI(x)$ = bending stiffness of the superstructure;

M_{pi} = tributary seismic mass of pier *i*.

In Equation (11.4f), the value of 0.05 represents the damping ratio of the bridge structure when its response is within the elastic regime. For the bridge configurations shown in Table 11.1, with the assumption that the superstructure has a uniform stiffness and mass distribution, Equations (11.4b) – (11.4d) lead to the following expressions.

For Type-1 bridge,

$$M^* = \frac{mL}{2} + M_{p2}\sin^2\frac{\pi x_2}{L} + M_{p3}\sin^2\frac{\pi x_3}{L} \tag{11.5a}$$

$$K^* = \frac{\pi^4 EI}{2L^3} + K_{p2}^{eq}\sin^2\frac{\pi x_2}{L} + K_{p3}^{eq}\sin^2\frac{\pi x_3}{L} \tag{11.5b}$$

$$L^* = \frac{2mL}{\pi} + M_{p2}\sin\frac{\pi x_2}{L} + M_{p3}\sin\frac{\pi x_3}{L} \tag{11.5c}$$

For Type-2 bridge,

$$M^* = mL + M_{p2} + M_{p3} \tag{11.6a}$$

$$K^* = K_{p2}^{eq} + K_{p3}^{eq} \tag{11.6b}$$

$$L^* = mL + M_{p2} + M_{p3} \tag{11.6c}$$

For Type-3 bridge,

$$M^* = m\left(\frac{2}{3}L_1 + L_2\right) + M_{p2}\left(\frac{x_2}{L_1}\right)^2 + M_{p3} + M_{p4}\left(\frac{L - x_4}{L_1}\right)^2 \tag{11.7a}$$

$$K^* = K_{p2}^{eq}\left(\frac{x_2}{L_1}\right)^2 + K_{p3}^{eq} + K_{p4}^{eq}\left(\frac{L - x_4}{L_1}\right)^2 \tag{11.7b}$$

$$L^* = m(L_1 + L_2) + M_{p2}\frac{x_2}{L_1} + M_{p3} + M_{p4}\frac{L - x_4}{L_1} \tag{11.7c}$$

where L is the total length of the bridge.

11.3 Design Procedure

For displacement-based design, the site-specific displacement response spectrum representing the design earthquake has to be determined. Typically, for bridge design, it corresponds to an earthquake that has a 1,000-year return period, and a structural damping ratio of 5%. The first step in the design process is to determine the preliminary layout of the bridge structure, including the locations of internal hinges, if any, in the superstructure, the locations of the piers, the number of columns in each pier, and the height of the columns. Next, the bridge superstructure can be designed, the trial size of the columns can be selected, and the target displacement limit for each pier is to be specified.

The bridge structure is then represented by an equivalent SDOF model using Rayleigh's method as discussed in the previous section. For this purpose, an appropriate shape function $\psi(x)$ is to be selected for the superstructure, with the consideration of whether the shear keys should remain functional under the design earthquake, as discussed in the previous section. With the given response spectrum and the SDOF model, the bridge columns can be designed with the following procedure.

1. Determine the maximum allowed generalized displacement, $z_{\max}$, of the SDOF model representing the bridge structure based on the maximum displacement, $u_{pi,\lim}$, allowed for each pier *i*. It can be determined with the condition that $z_{\max}\psi(x_i) \le u_{pi,\lim}$ for all the piers, where x_i is the *x* coordinate of pier *i*.

2. Calculate the mass, $m(x)$, of the superstructure and estimate the tributary mass, M_{pi}, of each pier *i*. Calculate the values of M^* and L^* for the SDOF bridge model using Equations (11.4b) and (11.4d).

3. Select a trial value (e.g., 0.25) for the equivalent damping ratio ξ^*, which accounts for the hysteretic damping introduced by the inelastic deformations of the columns.

4. Construct a displacement response spectrum for the damping ratio equal to ξ^*. In the absence of ground motion records, one may use the following equation recommended in Eurocode 8 (Eurocodes, 1998) to obtain the spectral displacement curve from the selected site-specific spectrum, $S_d(T, \xi = 0.05)$, where T is the structural period and ξ is the damping ratio:

$$S_d(T, \xi^*) = S_d(T, \xi = 5\%)\sqrt{\frac{0.07}{0.02 + \xi^*}} \tag{11.8}$$

5. Calculate the maximum allowed spectral displacement using the expression $S_d^* = \frac{M^*}{L^*} z_{\max}$. Based on the displacement response spectrum, $S_d\left(T, \xi^*\right)$, use the value of S_d^* to determine the required equivalent structural period, T_{eq}, as illustrated in Figure 11.3.

6. Calculate the required stiffness of the equivalent SDOF model with the following equation: $K^* = 4\pi^2 M^* / T_{eq}^2$.

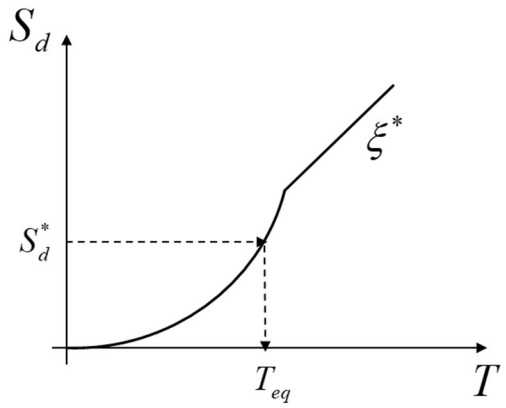

Figure 11.3: Displacement response spectrum for design

7. With the target value of K^* determined, select an adequate value for the equivalent stiffness, K_{pi}^{eq}, for each pier *i* to meet the following condition:

$$\sum_i K_{pi}^{eq}\psi^2(x_i) \geq K^* - \int_0^L EI(x)\left(\frac{d^2\psi(x)}{dx^2}\right)^2 dx \tag{11.9}$$

where EI is the elastic bending stiffness of the superstructure and x_i is the *x* coordinate of pier *i*. The values of K_{pi}^{eq} should be so selected that the resisting forces developed by the piers in different locations be as uniform as possible. Then, determine the required peak strength of each pier with the following equation (see Figure 11.2 for definitions): $F_{pi,\max} = K_{pi}^{eq} u_{pi,\max}$, where $u_{pi,\max} = \psi(x_i) z_{\max}$.

8. Design the columns so that each pier will develop the required peak strength, $F_{pi,\max}$, when the maximum pier displacement, $u_{pi,\max}$, is reached. For this purpose, the design considerations presented in Section 8.2 for the baseline column specimen can be followed and trial designs can be carried out with an analytical tool, such as the fiber-section model presented in Chapter 10.

9. Check the hysteretic energy dissipation of the designed piers and estimate the value of the equivalent damping ratio, ξ^*, for the bridge structure with the following equation:

$$\xi^* = 0.05 + \frac{\sum_i E_{pi}^H}{2\pi K^* z_{\max}^2} \tag{11.10}$$

where E_{pi}^H is the hysteretic energy dissipated by pier *i* over one cycle of response with a displacement amplitude $u_{pi,\max}$. It can be estimated with the following formula:

$$E_{pi}^H = 2\alpha F_{pi,bar} \times \left(u_{pi,\max} - u_{pi,bar\ yield}\right) \text{ but not less than 0} \tag{11.11}$$

where $F_{pi,bar}$ and $u_{pi,bar\ \text{yield}}$ are the lateral resistance and nominal yield displacement, respectively, of the pier with only the longitudinal reinforcing bars and no prestressing strands or axial load in the columns, as illustrated in Figure 11.4, and α is a reduction factor that accounts for the pinching effect introduced by residual plastic strains in the reinforcing bars developed in previous loading cycles. This equation is based on the assumption that all the hysteretic energy dissipation is contributed by the inelastic deformation of the reinforcing bars. The values of $F_{pi,bar}$ and $u_{pi,bar\ \text{yield}}$ are to be determined by a pushover analysis with the prestressing strands and axial load in the columns removed. Even though the value of the reduction factor, α, depends on the response history of the pier, it can be assumed to be equal to 0.8 based on the numerical parametric study presented in Section 11.4.2.

10. If the value of ξ^* calculated in the above step differs from the value assumed previously by more than 20%, repeat Steps 4 through 9 using the updated value of ξ^*. Use updated

values of M^* and L^* in the next iteration if the diameters of the columns previously selected have been changed. Otherwise, the column design is completed.

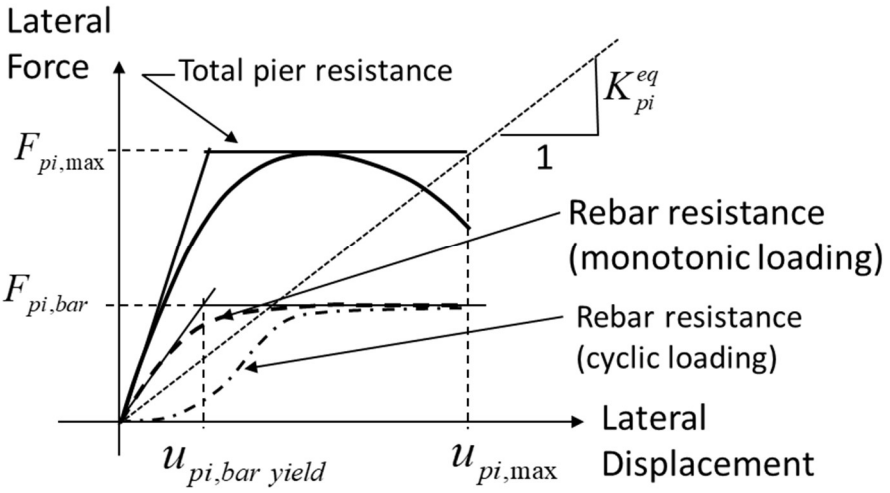

Figure 11.4: Lateral load-displacement relation of a pier

Once the columns have been designed, the abutment shear keys can be designed. The designed bridge system can be checked with nonlinear time-history analyses, in which the columns can be represented by the fiber-section model presented in Chapter 10.

11.4 Design Example 1

11.4.1 Bridge Configuration

The first design example considered is a bridge with the Type-2 configuration shown in Table 11.1. The bridge is to have self-centering columns that have similar design details as Specimen 2 tested in this study, except that each column will have identical rocking hinges at the top and the bottom, respectively. The bridge is to be designed for lateral earthquake loading perpendicular to the direction of the bridge deck. The lateral load resistance is provided by two

piers. Each pier may have multiple columns. The superstructure is stiff and the abutment shear keys are not strong enough to resist the design earthquake. The superstructure has a uniform cross-section and the two piers have identical properties. Hence, the stiffness and the mass centers are both at the midpoint of the superstructure. It is assumed that the gravity loads are carried entirely by the piers. The bridge has the following geometric properties:

$L_d = 5,400$ in.
$A_d = 10,400$ in.^{2}
$H_c = 240$ in.
$x_2 = 1,800$ in.
$x_3 = 3,600$ in.

where L_d is the length of the superstructure, A_d is the net cross-sectional area of the superstructure, H_c is the clear height of the columns, and x_2 and x_3 are the x coordinates of piers 2 and 3, respectively, measured from the left abutment.

In the analysis, the mass of each pier is assumed to be lumped at the top and bottom of the pier. The masses of the piers and the bridge deck are calculated as follows:

$$M_{p2} = M_{p3} = \frac{\gamma_c A_{g,col}}{g} \times \frac{H_c}{2} \times N_{col} \tag{11.12a}$$

$$m = \frac{\gamma_c A_d}{g} \tag{11.12b}$$

where M_{pi} is the mass of pier i lumped at the superstructure level, γ_c is the unit weight of the reinforced concrete members, which is assumed to be 150 pounds per cubic foot, m is the mass per unit length of the superstructure, $A_{g,col}$ is the cross-sectional area of a column, H_c is the clear height of a column, g is the acceleration due to gravity, and N_{col} is the number of columns per pier.

The bridge is situated in a site in Los Angeles, CA. The design pseudo-spectral acceleration spectrum with 5% damping considered is shown in Figure 11.5. It is determined according to the AASHTO LRFD Seismic Bridge Design Specifications (AASHTO 2017) with S_{DS} = 2.0g, and S_{D1} = 0.9g. The corresponding displacement spectrum with 5% damping is shown in Figure 11.6.

In this design example, the target drift limit specified for the columns is 6%, which is selected for the illustration purpose. With the 240 in. tall columns, the lateral displacement limit for each pier *i* is $u_{pi,\lim} = 0.06 \times H_c$ = 14.4 inches.

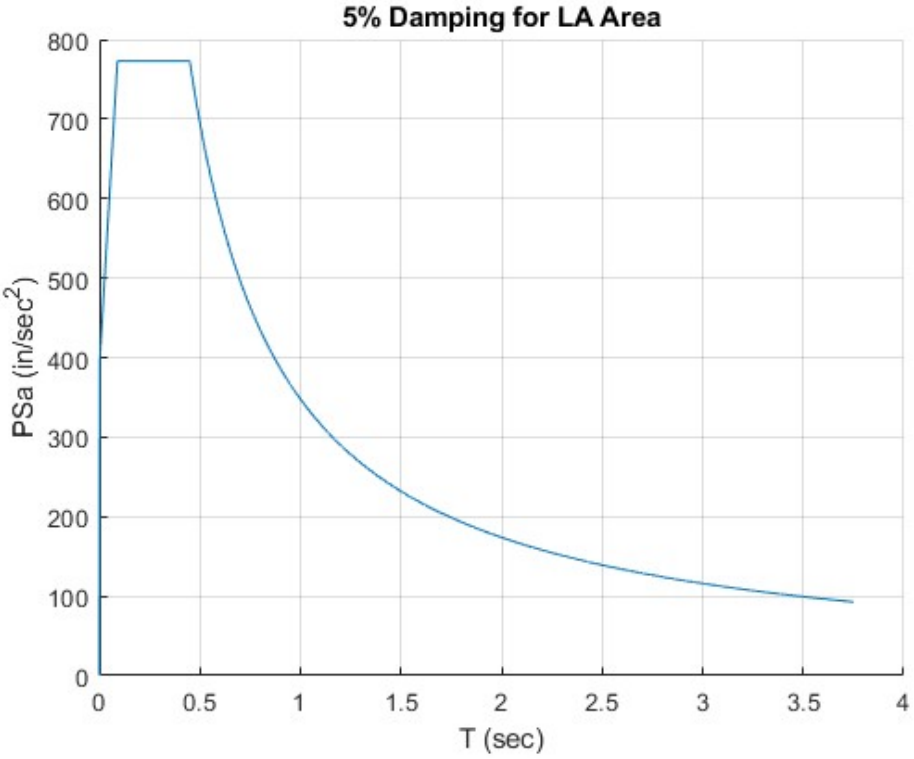

Figure 11.5: Design (pseudo-spectral acceleration) spectrum with 5% damping for the LA Site

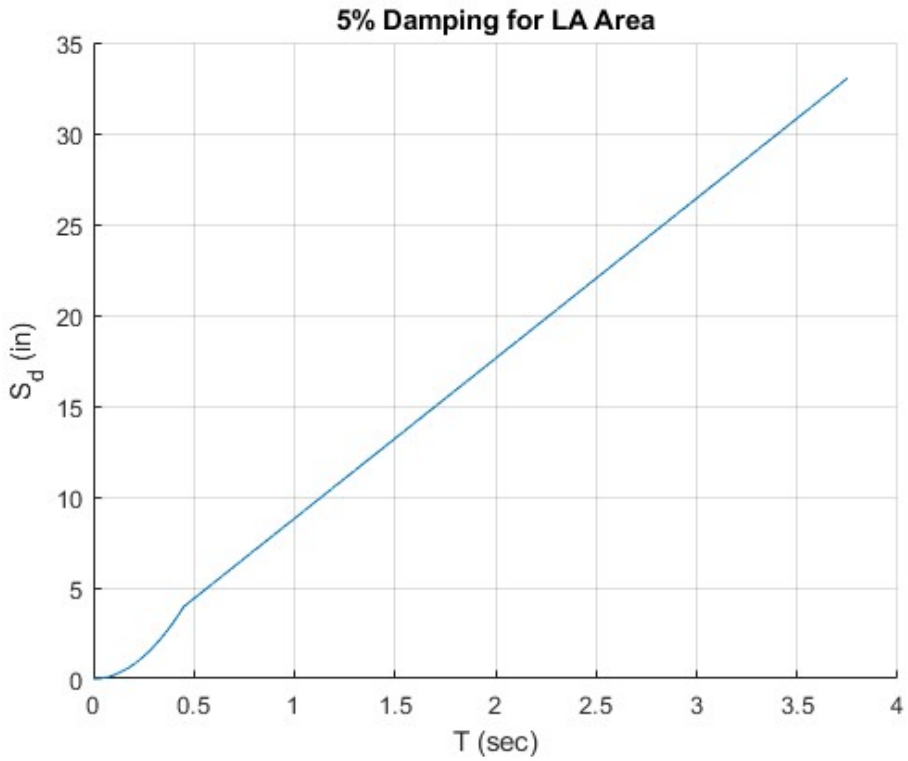

Figure 11.6: Displacement spectrum with 5% damping for the LA site

11.4.2 Estimation of Hysteretic Energy Dissipation

To estimate the equivalent damping ratio, ξ^*, introduced by hysteretic energy dissipation using Equations (11.10) and (11.11), the value of α has to be determined. To this end, a numerical parametric study has been conducted with the Type-2 bridge configuration considered here using a set of five earthquake ground motion records, which are the El Centro record from the 1940 Imperial Valley earthquake, the Rinaldi and Sylmar records from the 1940 Northridge earthquake, and the Takatori Station 0° and 90° records from the 1995 Kobe earthquake. Each pier is assumed to have two columns and each column has the same reinforcement as Specimen 2, but with two rocking hinges. The analyses have been conducted with the columns represented by the fiber-section model presented in Chapter 10. The response histories of the bridge for these ground motion records and the hysteretic response curves for the columns are obtained. The value of α

that provides a conservative estimate of the hysteretic energy dissipation obtained in the numerical results is determined. The ground acceleration time histories of these records are shown in Figure 11.7. The records have different time-history and response spectrum characteristics. The Rinaldi record has a few strong long-duration acceleration pulses, the Sylmar record has a long-duration pulse followed by a few large acceleration cycles, the El Centro record has multiple large acceleration cycles throughout the duration of the earthquake, and the Takatori records have many cycles of very long duration pulses. Their pseudo-spectral acceleration plots will be shown in later discussion (see Figure 11.2).

In the parametric study, the columns have a clear height of 240 in. and a diameter of 48 inches. As shown in Table 11.2, four column reinforcement scenarios are considered. Scenario 1 has the same reinforcement as Specimen 2. For the full-height column, each longitudinal No. 8 fuse bar has a length of 67 in. and each No. 10 elastic bar is 240 in. long. For Scenario 4, the fuse bars are shortened to 40 in. and the elastic bars are lengthened to 267 inches. Time-history analyses are conducted for each design scenario using the earthquake records. Each record is scaled to three intensity levels so that the bridge columns will reach maximum drift ratios of 3%, 6%, and 10%, respectively. The ground motion records and the maximum drift ratios considered for each design scenario are shown in Table 11.3.

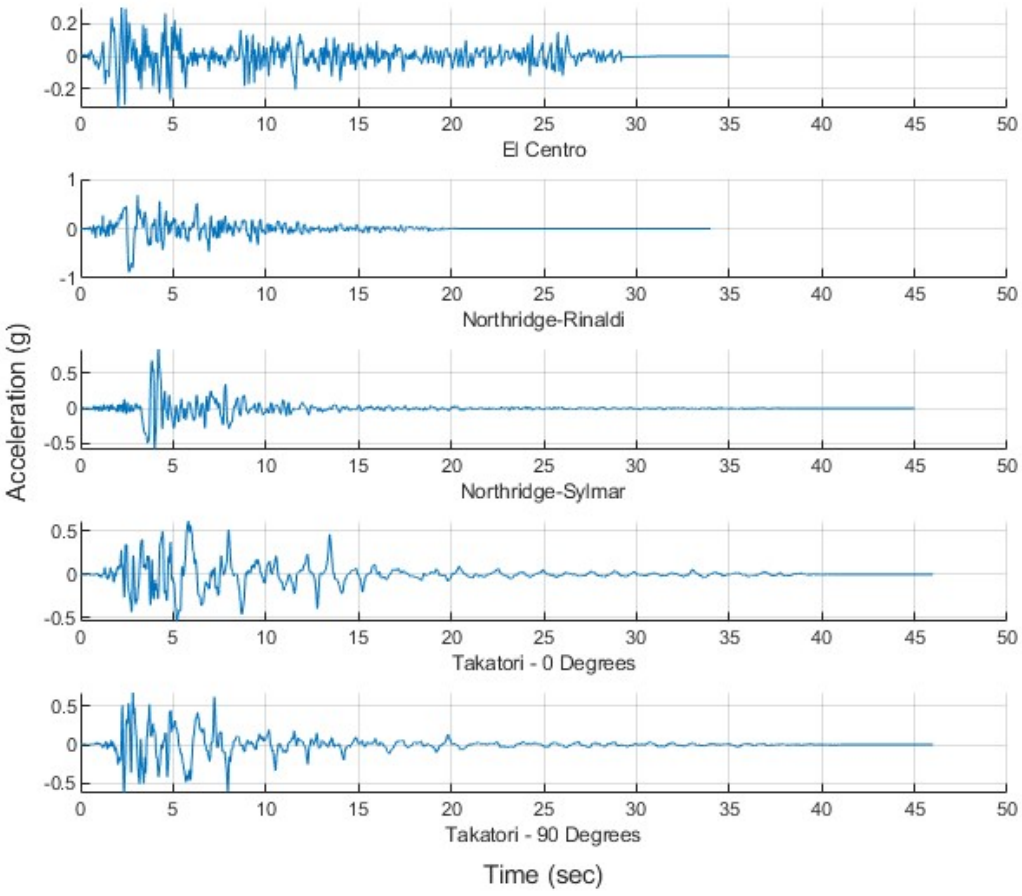

Figure 11.7: Ground acceleration records for the earthquakes used in the parametric study and for the design examples

Table 11.2: Column reinforcement scenarios

Scenario	No. of Prestressing Strands	Number of Reinforcing Bars	Elastic Bar Size	Fuse Bar Size	Fuse Bar Length (in)
1	20	16	No. 10	No. 8	67
2	24	16	No. 11	No. 8	67
3	24	16	No. 11	No. 9	67
4	24	20	No. 11	No. 9	40

Table 11.3: Ground motion records and maximum drift ratios considered for each column reinforcement scenario

Scenario	El Centro Peak Drift Ratios (%)	Rinaldi Peak Drift Ratios (%)	Sylmar Peak Drift Ratios (%)	Takatori 0° Peak Drift Ratios (%)	Takatori 90° Peak Drift Ratios (%)
1	3, 6, 10	3, 6, 10	3, 6, 10	3, 6, 10	3, 6, 10
2	6, 10	6, 10	-	6, 10	-
3	6, 10	6, 10	-	6, 10	-
4	6, 10	6, 10	-	6, 10	-

It should be noted that E_{pi}^{H} calculated with Equation (11.11) for use in Equation (11.10) to estimate the value of ξ^{*} is the energy dissipated in pier *i* in one full response cycle that has an absolute amplitude, $u_{pi,\max}$, in both displacement directions. Hence, α is calibrated with the data from each time-story analysis as follows. The half-cycle response in which the maximum absolute

displacement, $u_{pi,\max}$, occurs in the time-history analysis is identified. The hysteretic energy dissipated in one column during that half-cycle response is obtained by calculating the area within the hysteretic force-displacement curve for the column with numerical integration. The hysteretic energy, E_{pi}^{H}, is estimated to be four times the energy dissipated by one column in the half-cycle response since each pier has two identical columns. Then, a quasi-static analysis is performed on one column using the fiber-section model with the axial load and prestressing strands removed, according to Step 9 of the procedure presented in Section 11.3, to obtain a monotonic force-displacement curve up to the maximum displacement, $u_{pi,\max}$, obtained in the time-history analysis. From the quasi-static force-displacement curve, the values of $F_{pi,bar}$ and $u_{pi,bar\ \text{yield}}$ for each pier, as defined in Figure 11.4, are determined. The value of α is then determined so that it will satisfy Equation (11.11) with the values of E_{pi}^{H}, $F_{pi,bar}$, $u_{pi,bar\ \text{yield}}$, and $u_{pi,\max}$ obtained.

Figures 11.8 and 11.9 show the numerical results from two time-history analyses with the column reinforcement Scenario 4 (see Table 11.2) and the Takatori 0° record scaled to two different intensity levels.

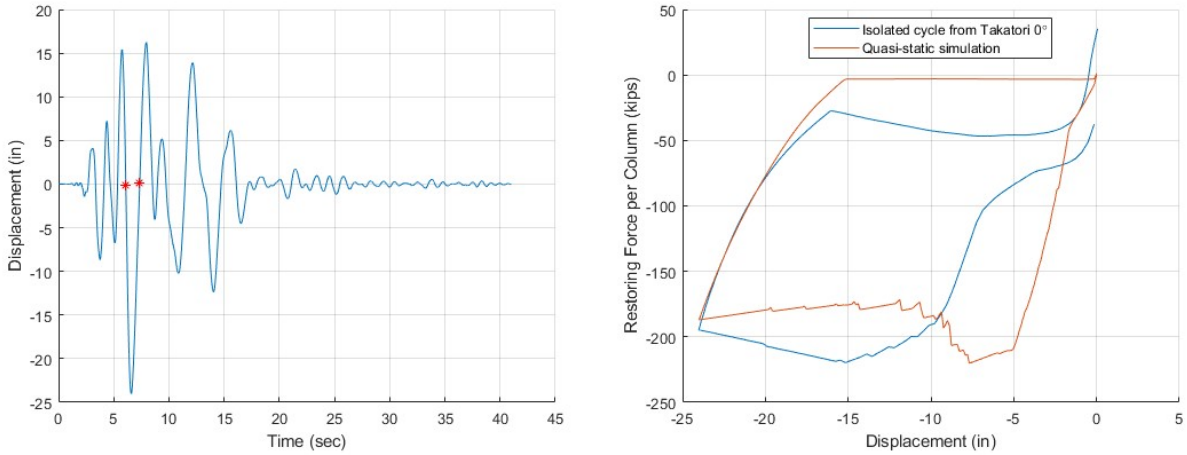

Figure 11.8: (left) Displacement response history for column reinforcement scenario 4 and Takatori 0° record scaled to achieve 10% drift; (right) comparison of force-displacement curves for one column from time-history and quasi-static analyses

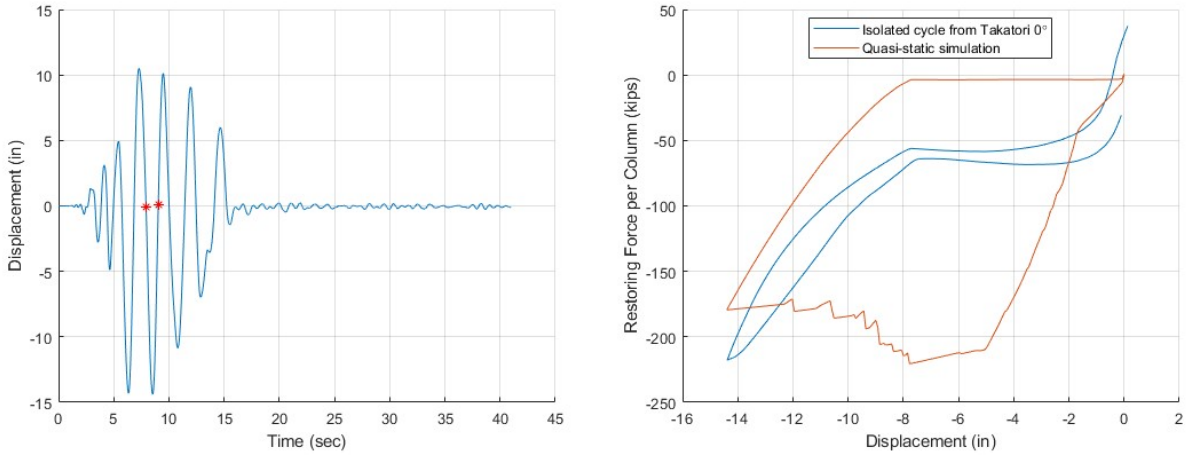

Figure 11.9: (left) Displacement time history for column reinforcement scenario 4 and Takatori 0° record scaled to achieve 6% drift; (right) comparison of force-displacement curves for one column from time-history and quasi-static analyses

In Figure 11.8, the hysteretic force-displacement curve for one column in the half-cycle that has the maximum displacement response is compared to the result from a quasi-static analysis of the same column with the same displacement amplitude. It shows that the force-displacement

hysteresis curves from the time-history and quasi-static analyses are similar to one another. This is because the maximum response attained in the time-history analysis is not preceded by any large-amplitude response, as shown in the time-history plot in Figure 11.8. However, this is not the case for the results shown in Figure 11.9, in that the hysteretic response curve from the time-history analysis is severely pinched because of the large-amplitude response cycles preceding the maximum response. The influence of the displacement history on the shape of the hysteresis curve is associated with the residual plastic elongation in the unbonded reinforcing bars. The second case will result in a much smaller value of α.

Figures 11.10 through 11.13 show the values of α obtained from all the analyses with the four column reinforcement scenarios. The displacement response histories and the column restoring force-vs.-displacement curves from these analyses are present in Appendix F. For column reinforcement scenario 1, the average value of α obtained is 1.18; for scenario 2, the average α value is 0.95; for scenario 3, the average α value is 0.94; and for scenario 4, the average α value is 0.61. The average value of α across all four scenarios is 0.90. For the Sylmar and Rinaldi records, which have one or several strong long-duration acceleration pulses followed by weaker motion, the maximum response is not preceded by any large amplitude displacements and consequently, the values of α always exceed one. Based on these results, it is recommended that the value of α to be used in the design procedure presented in Section 11.3 be equal to 0.80. This is deemed conservative as it is lower than most of the values obtained from the parametric study with the exception of a few outliers.

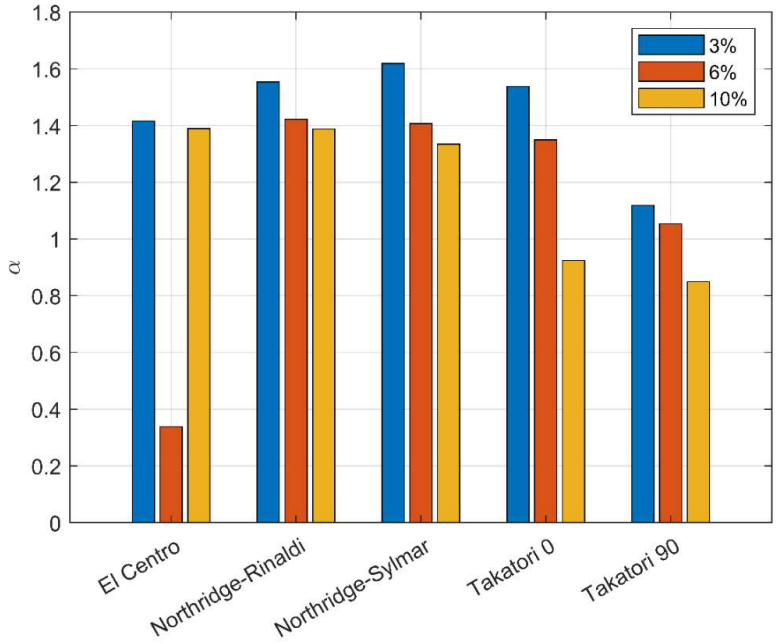

Figure 11.10: Values of α for column reinforcement scenario 1

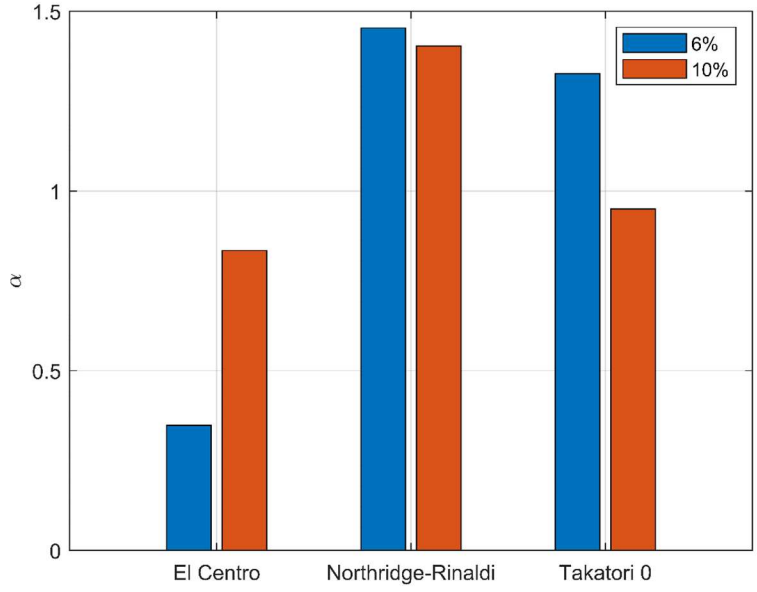

Figure 11.11: Values of α for column reinforcement scenario 2

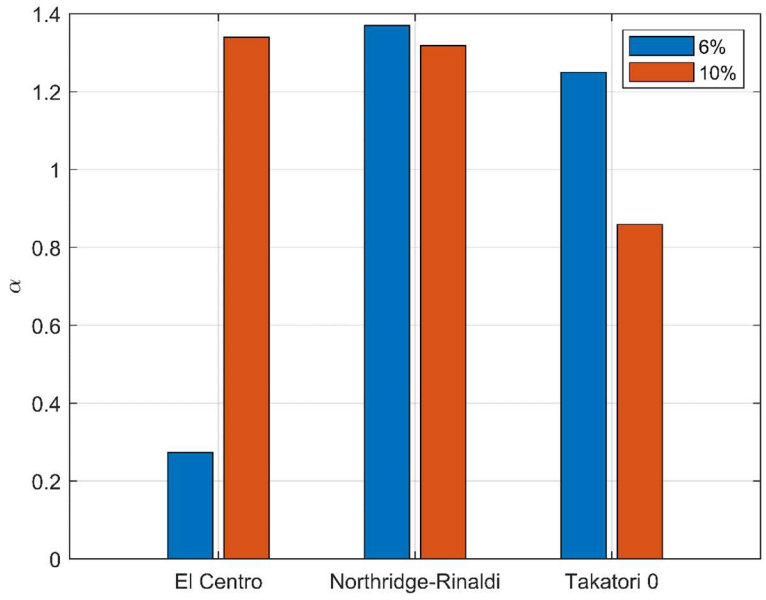

Figure 11.12: Values of α for column reinforcement scenario 3

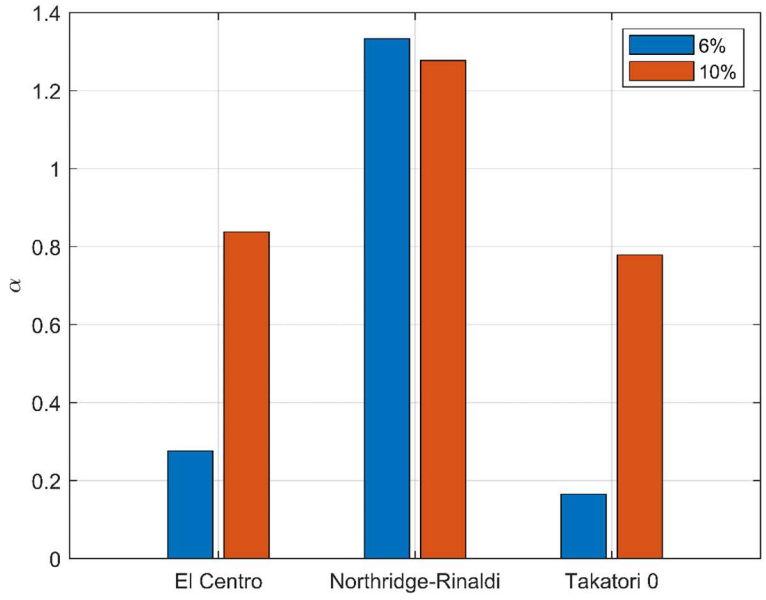

Figure 11.13: Values of α for column reinforcement scenario 4

11.4.3 Design of Self-Centering Columns in the Bridge Example

With the bridge configuration described in Section 11.4.1, the trial design starts with four columns, with two in each pier. The trial column design has a diameter of 48 in., 24-in. diameter rocking plates in each hinge, 16 lines of unbonded longitudinal reinforcing bars that have fuses, and 20 prestressing strands. The design is similar to that of the column in Specimen 2 tested in the laboratory, except that each bridge column has two rocking hinges, with one at each end, and each No. 8 fuse bar is 40 in. long and each No. 10 elastic bar is 267 inches. With the Type-2 configuration shown in Table 11.1, the bridge has three spans and two piers. With two columns per pier and the geometric properties presented in Section 11.4.1, the mass of each pier and that of the deck have been calculated with Equations (11.12a) and (11.12b), and the values of M^* and L^* for the equivalent SDOF system have been calculated with Equations (11.6a) and (11.6c), respectively, and are shown below.

$$M^* = 12.82 \ \frac{\text{kip-sec}^2}{\text{in.}}$$

$$L^* = 12.82 \ \frac{\text{kip-sec}^2}{\text{in.}}$$

Since the target drift limit for each pier is $u_{pi,\text{lim}} = 0.06 * H_c$ = 14.4 in. and the shape function $\psi(x) = 1$, the target values for $z_{\max}$ and S_d^* are:

$$z_{\max} = u_{pi,\text{lim}} = 14.4 \text{ in.}$$

$$S_d^* = \frac{M^*}{L^*} z_{\max} = 14.4 \text{ in.}$$

With an initial assumption of $\xi^* = 0.25$, the displacement response spectrum shown in Figure 11.14 is constructed with the given site-specific design spectrum using Equation (11.8).

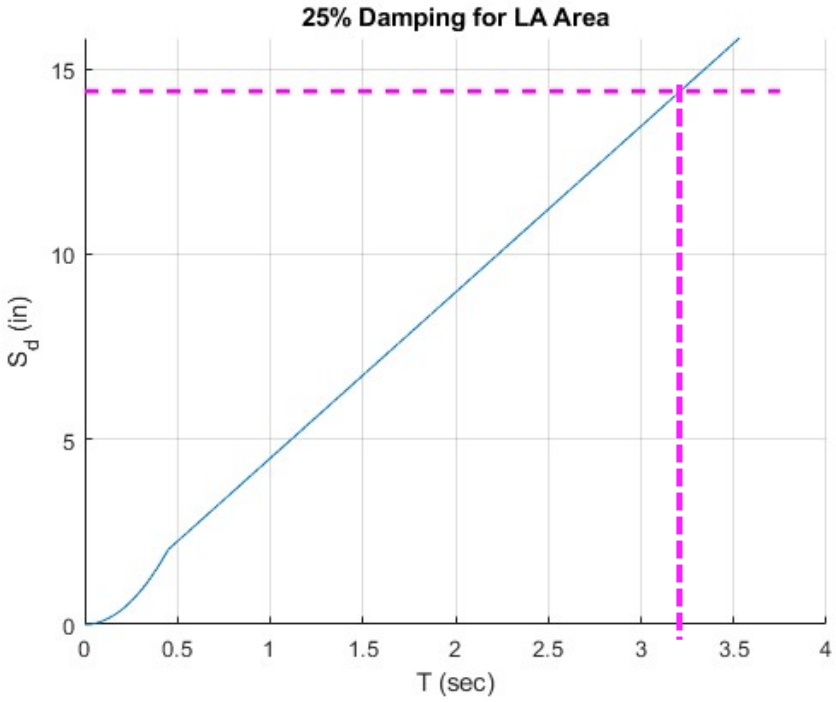

Figure 11.14: Displacement spectrum with 25% damping for LA area

With the target displacement of 14.4 in., Figure 11.14 gives the period of 3.21 sec, which is the period, T_{eq}, required for the equivalent linearly elastic structure. With this period and the calculated generalized mass, M^*, the stiffness required for the equivalent structure is calculated to be:

$$K^* = 4\pi^2 M^* / T_{eq}^2 = 49 \frac{\text{kips}}{\text{in.}}$$

Since the bridge has four identical columns (two per pier), the equivalent stiffness and maximum lateral load resistance required of each column are calculated, according to Equation (11.6b), as follows.

$$K_c^e = \frac{K^*}{4} = 12.2 \ \frac{\text{kips}}{\text{in.}}$$

$$F_c = K_c^e u_{pi,\text{lim}} = 175 \text{ kips}$$

A pushover analysis is conducted with the fiber-section model on one column, which, in the trial design, has the same reinforcement details as the column in Specimen 2 but with two rocking hinges, and an applied axial load of 1,238 kips. The column diameter is 48 in. and the rocking plate diameter is 24 inches. There are twenty 0.6-in. diameter prestressing strands and 16 longitudinal rebars. Each line of rebar consists of a No. 10 elastic bar and a No. 8 fuse bar. The lengths of the elastic bars and fuse bars are 267 and 40 in., respectively. Figure 11.15 shows the monotonic force-displacement curve for the column.

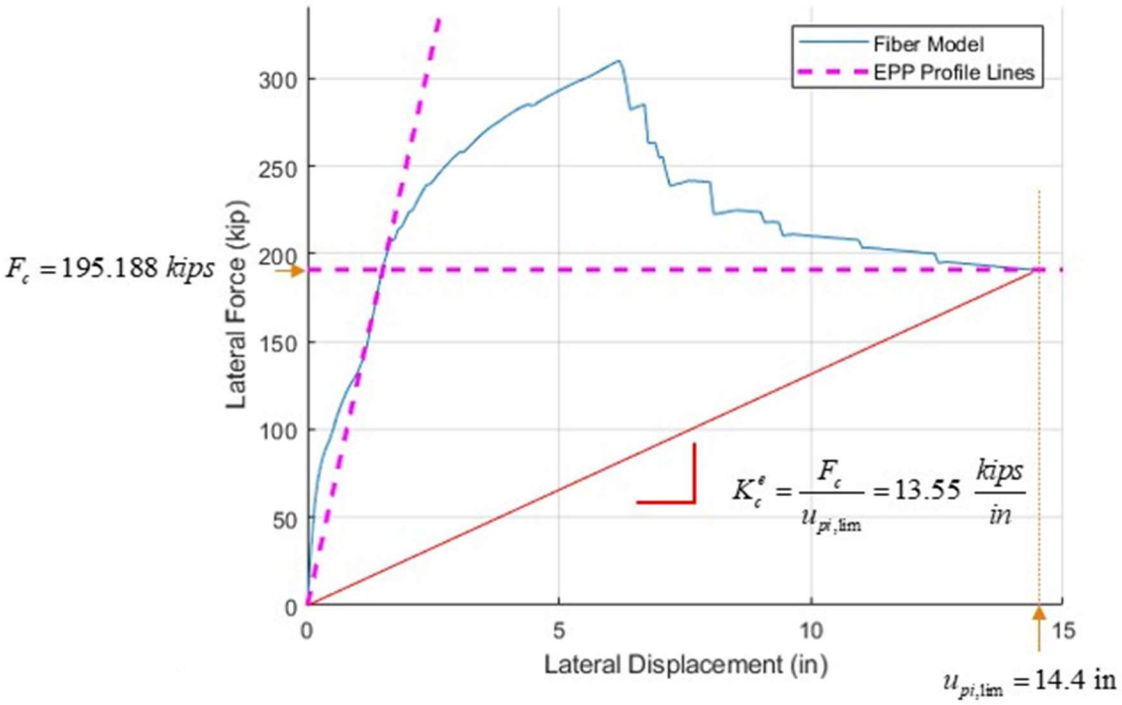

Figure 11.15: Pushover force-displacement curve for the column with the initial trial design in the Type-2 bridge

As shown in Figure 11.15, the trial design has a slightly stiffer and stronger column. This is deemed adequate. Next, the equivalent damping ratio, ξ^*, for the bridge structure based on the trial design is calculated. To this end, a pushover analysis is conducted on one column with the axial load and prestressing strands removed from the column. Figure 11.16 shows the pushover curve.

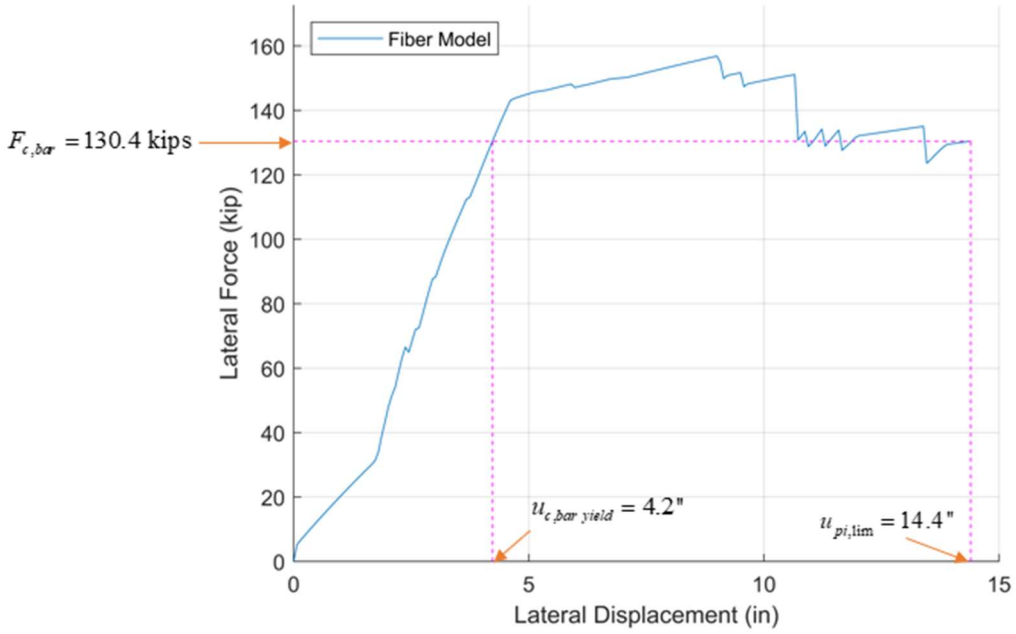

Figure 11.16: Pushover curve used to determine hysteretic energy dissipation by one column with the initial trial design for the Type-2 bridge

From Figure 11.16, the yield force of the column, $F_{c,bar}$, is determined to be 130 kips, and the displacement, $u_{c,bar\ \text{yield}}$, at which the column yields is 4.2 inches. For each pier, $F_{pi,bar}$ is $2F_{c,bar}$ and $u_{pi,bar\ yield} = u_{c,bar\ \text{yield}}$. With Equation (11.11) and α = 0.8, the hysteretic energy dissipation by one pier, E_{pi}^{H}, is calculated to be 4,256 kips-inch. With Equation (6.10), K^* equal to $4 \times 13.55 = 54.2$ kips/in. (see Figure 11.15), and $z_{\max}$ equal to 14.4 in., the equivalent damping ratio,

ξ^*, is calculated to be 0.17. Compared to the original assumption of $\xi^* = 0.25$, there is a change of 32%. Thus, the column design is revised. In the second trial, the diameter of each column is increased to 54 in., with 27-in.-diameter rocking plates in each rocking hinge and the reinforcement and prestressing remaining the same. There are twenty 0.6-in. diameter prestressing strands and 16 longitudinal lines of rebars. Each line of rebar consists of a No. 10 elastic bar and a No. 8 fuse bar. The lengths of the elastic bars and fuse bars are 267 in. and 40 in., respectively. The centroid of each prestressing strand group is 11.5 in. away from the centroid of the column section, and the rebars have a 2.375-in. clear cover. Figure 11.17 shows the displacement spectrum calculated with Equation (11.8) using $\xi^* = 0.17$.

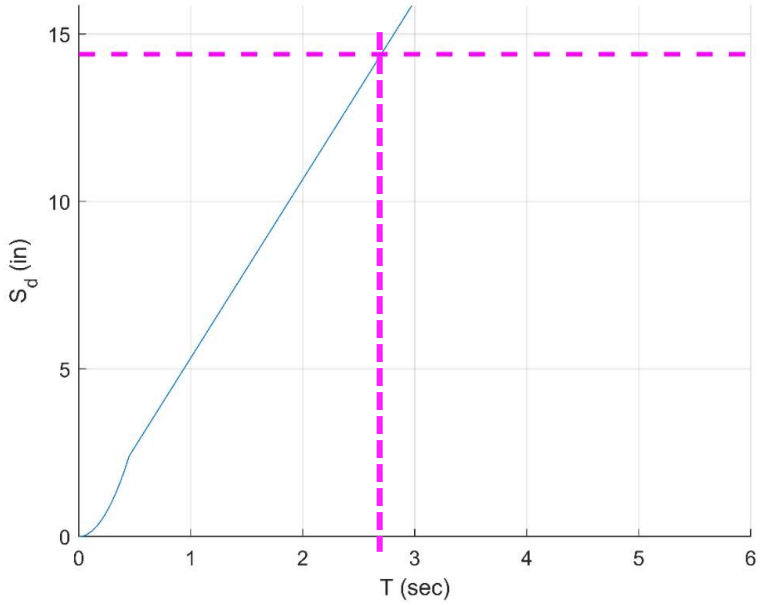

Figure 11.17: Displacement spectrum with 17% damping for LA area

With the target displacement of 14.4 in., Figure 11.17 gives the period of 2.70 sec, which is the period, T_{eq}, required for the equivalent linearly elastic structure. With this period and the

calculated generalized mass, the stiffness required for the equivalent structure is then calculated as:

$$K^* = 4\pi^2 M^* / T_{eq}^2 = 69.5 \frac{\text{kips}}{\text{in.}}$$

Since the bridge has four identical columns (two per pier), the effective stiffness and maximum lateral load resistance required for each column are calculated as follows.

$$K_c^e = \frac{K^*}{4} = 17.4 \ \frac{\text{kips}}{\text{in.}}$$
$$F_c = K_c^e u_{pi,\text{lim}} = 250.6 \text{ kips}$$

A pushover analysis is conducted on one column based on the second trial design with an applied axial load of 1,243 kips. Figure 11.18 shows the monotonic force-displacement curve for this column. As shown in Figure 11.18, the column in the second trial design is slightly stiffer and stronger than needed. This is deemed adequate. Next, the equivalent damping ratio, ξ^*, is calculated as in the previous trial. Figure 11.19 shows the pushover curve for the column without the axial load and prestressing strands.

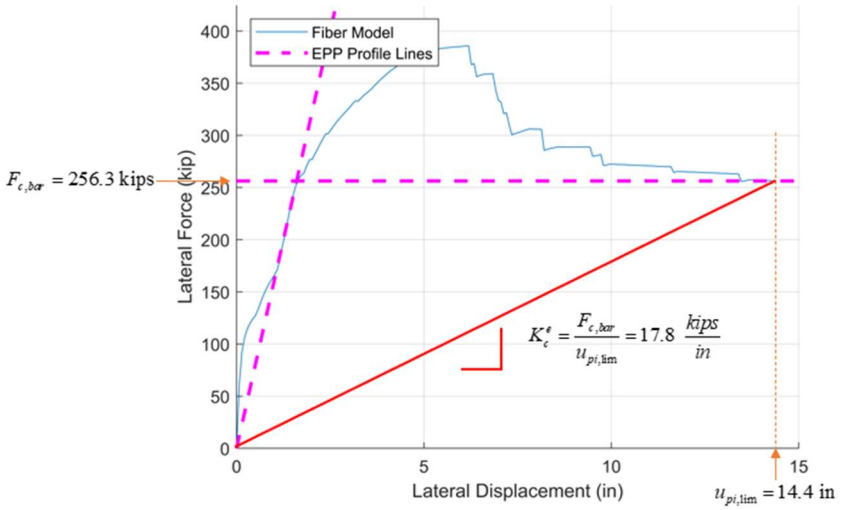

Figure 11.18: Pushover force-displacement curve for the column with the second trial design in the Type-2 bridge

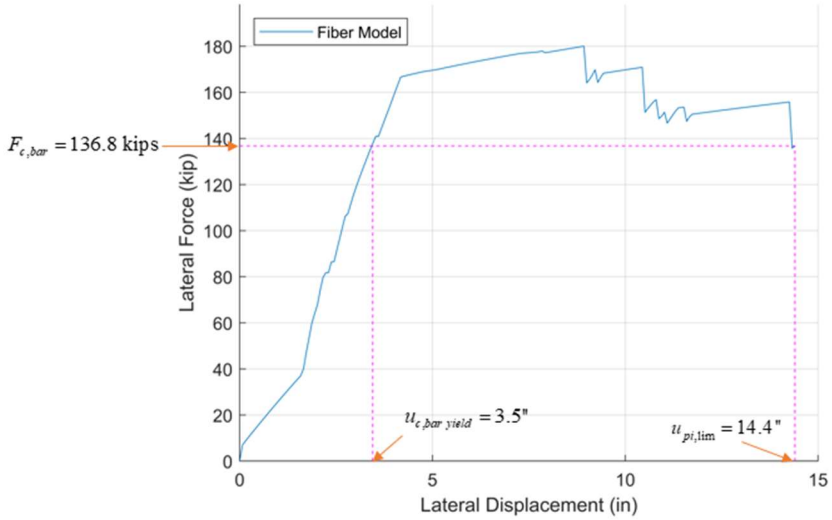

Figure 11.19: Pushover curve used to determine hysteretic energy dissipation by the column with the second trial design for the Type-2 bridge

From Figure 11.19, the yield force of the column, $F_{c,bar}$, is determined to be 137 kips, and the displacement, $u_{c,bar\ \text{yield}}$, at which the column yields is 3.5 inches. For each pier, $F_{pi,bar}$ is $2F_{c,bar}$ and $u_{pi,bar\ yield} = u_{c,bar\ \text{yield}}$. With Equation (11.11) and α = 0.8, the hysteretic energy dissipation by

one pier, E_{pi}^{H}, is calculated to be 4,772 kips-in. With Equation (11.10), K^* equal to $4 \times 17.8 = 71.2$ kips/in., and $z_{\max}$ equal to 14.4 in., the equivalent damping ratio, ξ^*, is calculated to be 0.15. Compared to the previous trial in which $\xi^* = 0.17$, there is a change of 12%. With the stiffness of the bridge, K^*, slightly higher than required, and the change in the equivalent damping ratio, ξ^*, less than 20%, the second trial is considered satisfactory. Tables 11.4 and 11.5 show a summary of the design trials.

Table 11.4: Design iterations for the columns in the Type-2 bridge

Iteration	Column Diameter (in.)	Rocking Plate Diameter (in.)	Number of Rebars	Elastic Bar Size	Fuse Bar Size	Number of PT Strands
1	48	24	16	No. 10	No. 8	20
2	54	27	16	No. 10	No. 8	20

Table 11.5: Hysteretic energy dissipations and equivalent damping ratios for the trial designs of the Type-2 bridge

Iteration	M^* $(\frac{\text{kip-sec}^2}{\text{in.}})$	K^* $(\frac{\text{kips}}{\text{in.}})$	Hysteretic Energy Dissipation Per Pier (kip-in.)	Damping Ratio ξ^*	% Change in Damping
1	12.8	54.2	4,256	0.17	-32
2	12.9	71.2	4,772	0.15	-11

To examine if the design obtained with this methodology is adequate, the five ground motions shown in Figure 11.7 are used to evaluate the response of the bridge structure. The bridge structure is a single-degree-of-freedom system with the lateral resistance provided by four columns. The nonlinear behavior of the columns is represented by the fiber-section model. Viscous damping is assumed to be 5% of the critical to account for the damping of the structure in the elastic regime. The seismic mass of the structure is 12.9 kip-sec^2/in. and the initial elastic stiffness of the structure is estimated to be 640 kips/in., which results in an initial elastic period of 0.89 sec. The initial elastic stiffness is estimated with the monotonic force-displacement curve for each column, as shown in Figure 11.18. When the bridge structure reaches the target drift ratio of 6%, the effective stiffness of the equivalent linearly elastic structure is 71.2 kips/in., as shown in Table 11.5, which results in an effective final period of 2.67 sec. The time-history analyses are performed with the explicit Newmark integration scheme that does not introduce numerical damping. The integration time step is the same as the time interval in the digitized ground motion record. For the El Centro ground motion, the integration time step is 0.01 sec; for the Rinaldi record, the integration time step is 0.002 sec; for the Sylmar record, the integration time step is 0.01 sec; and for the two Takatori ground motion records, the integration time step is 0.005 sec. The time steps are sufficiently small compared to the initial period of the bridge.

The pseudo-spectral acceleration plots for the five ground motion records with 5% damping are shown in Figure 11.20 together with the AASHTO design spectrum used for the bridge structure.

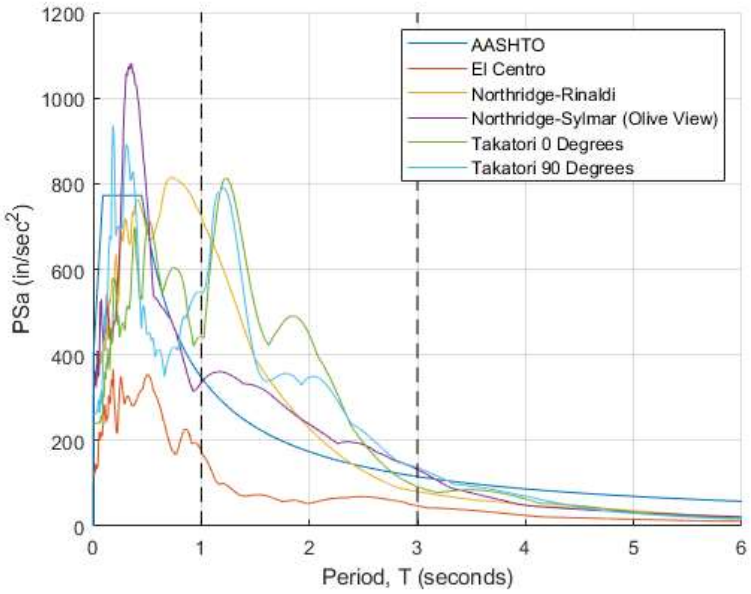

Figure 11.20: Unscaled pseudo-spectral acceleration plots for ground motions used in time-history analyses

For proper evaluation of the bridge performance, the ground motions must be scaled so that their spectral intensity matches that of the design spectrum for the period range of interest. To this end, the ground acceleration in each record is scaled so that its spectral curve matches the design spectrum for the period range between 1 and 3 sec, which covers the variation of the natural period of the bridge structure from the linearly elastic state to a highly nonlinear state (when it reaches a drift ratio of 6%). The dashed vertical lines in the above figure indicate the period range of interest. The value of the scale factor for each ground motion is so determined that the area under the pseudo-spectral acceleration curve for the ground motion is equal to the area under the design spectrum between the above period range as described in Equation (11.13).

$$F\int_{1}^{3} PSa_{gm}(T)dT = \int_{1}^{3} PSa_{AASHTO}(T)dT \tag{11.13}$$

where F is the scale factor, $PSa_{gm}(T)$ is the pseudo-spectral acceleration of the unscaled ground motion, and $PSa_{AASHTO}(T)$ is the design pseudo-spectral acceleration according to AASHTO. The scale factors determined are shown in Table 11.6.

Table 11.6: Scale factors for the ground motions used in the Type-2 bridge analyses

Ground Motion	Scale Factor
El Centro	2.6717
Northridge-Rinaldi	0.6692
Northridge-Sylmar	0.7663
Takatori 0°	0.4832
Takatori 90°	0.5268

The scaled pseudo-spectral acceleration-vs.-period curves are compared to the design spectrum in Figure 11.21.

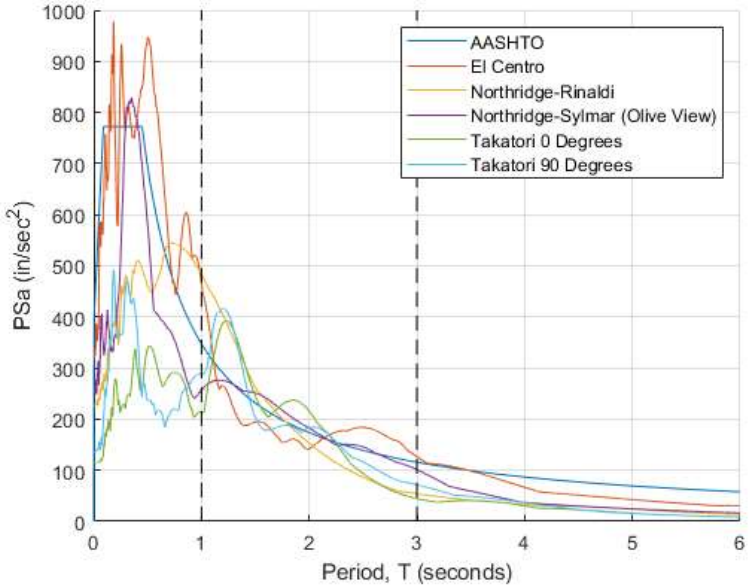

Figure 11.21: Scaled pseudo-spectral acceleration plots for ground motions used in time-history analyses

The numerical results obtained with the five ground motion records are shown in Figures 11.22 through 11.26. The peak displacement response for each ground motion is summarized in Table 11.7. The average peak displacement for the five ground motions is 13.0 in., which is a little lower than the target displacement of 14.4 inches. Two of the five cases have the peak displacements greater than the target value, with the worst case 19% greater.

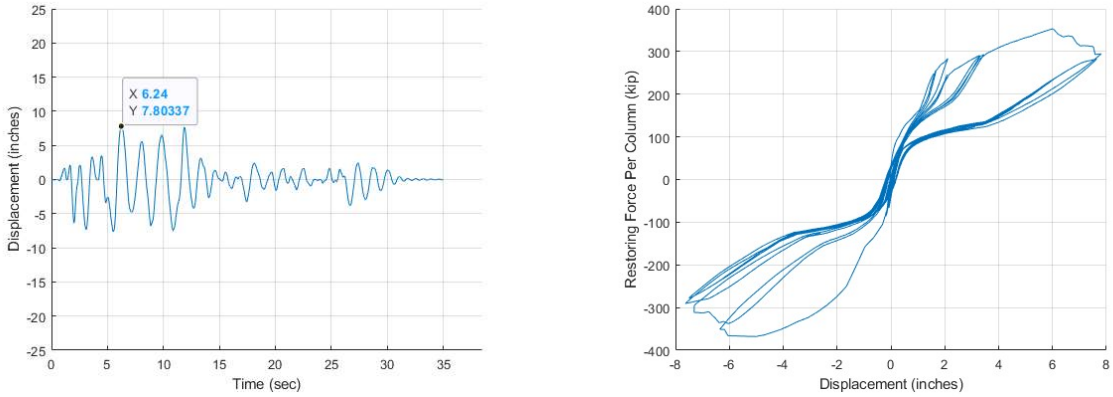

Figure 11.22: (left) Displacement time history for the Type-2 bridge subjected to scaled El Centro ground motion; (right) Force-displacement hysteresis curves for a single column

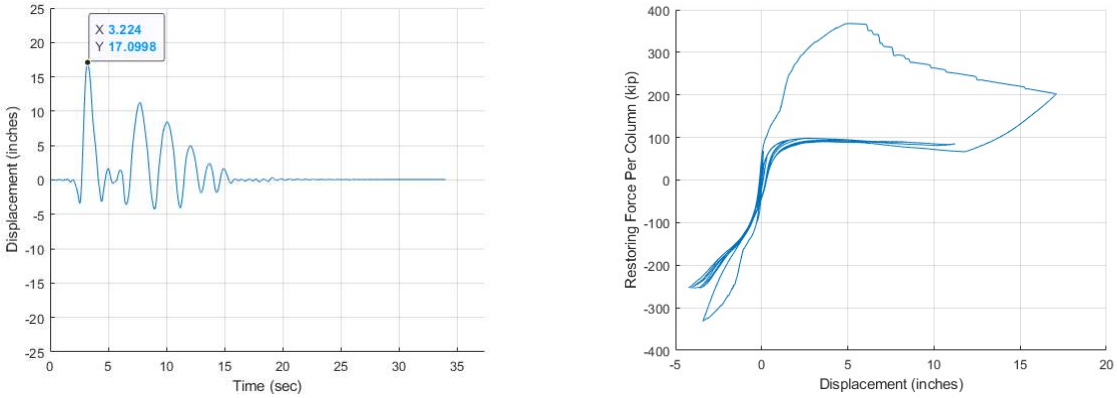

Figure 11.23: (left) Displacement time history for the Type-2 bridge subjected to scaled Rinaldi ground motion; (right) Force-displacement hysteresis curves for a single column

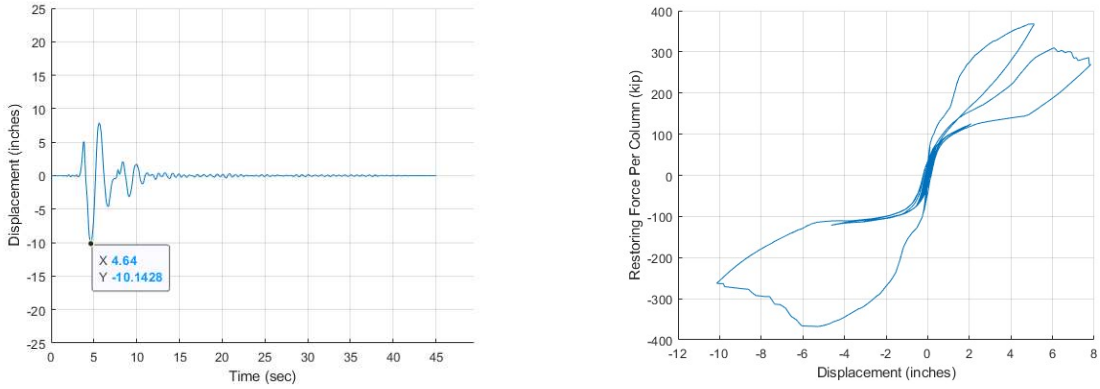

Figure 11.24: (left) Displacement time history for the Type-2 bridge subjected to scaled Sylmar ground motion; (right) Force-displacement hysteresis curves for a single column

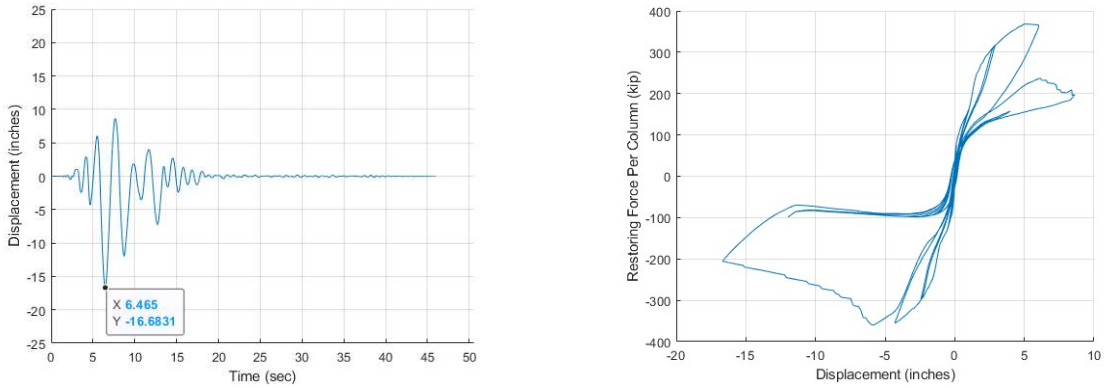

Figure 11.25: (left) Displacement time history for the Type-2 bridge subjected to scaled Takatori 0° ground motion; (right) Force-displacement hysteresis curves for a single column

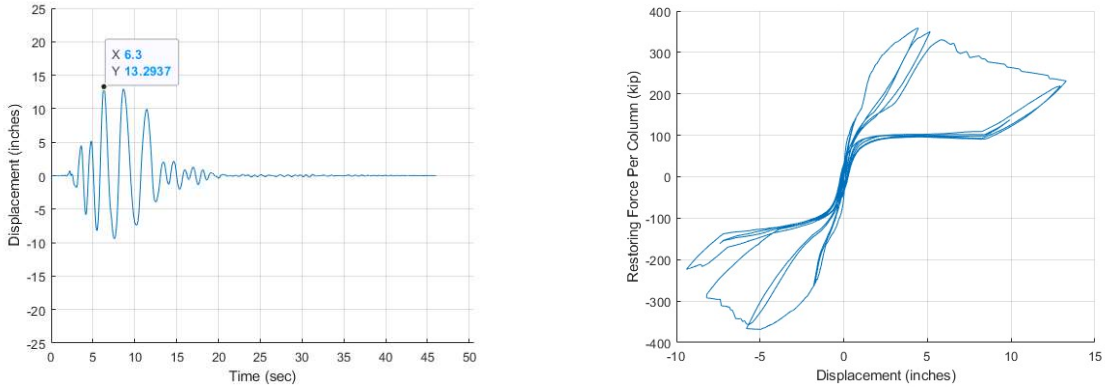

Figure 11.26: (left) Displacement time history for the Type-2 bridge subjected to scaled Takatori 90° ground motion; (right) Force-displacement hysteresis curves for a single column

Table 11.7: Peak displacements of the Type-2 bridge induced by the ground motions

	El Centro	**Rinaldi**	**Sylmar**	**Takatori 0**	**Takatori 90**
Peak Displacement	7.8 in.	17.1 in.	10.1 in.	16.8 in.	13.3 in.

11.5 Design Example 2

11.5.1 Bridge Configuration

The second design example is a bridge with the Type-3 configuration shown in Table 11.1. The bridge has four spans and three piers. The deck has two hinges as expansion joints. The lateral load resistance is mainly provided by the three piers. The abutment shear keys resist the inertia forces developed at the two ends of the bridge deck. Each pier may have multiple columns, each of which has one rocking hinge at the top and one at the bottom. The bridge has a uniform superstructure and the three piers have identical design. Hence, the bridge is symmetrical about

the center line perpendicular to the deck in term of the stiffness and mass distribution. The bridge has the following geometric properties:

$L_d = 7,200$ in.
$A_d = 10,400$ in.^{2}
$H_c = 240$ in.
$x_2 = 1,800$ in.
$x_3 = 3,600$ in.
$x_4 = 5,400$ in.

where L_d is the length of the superstructure, A_d is the net cross-sectional area of the superstructure, H_c is the clear height of the columns, and x_2, x_3 and x_4 are the *x* coordinates of piers 2, 3 and 4, respectively, measured from the left abutment.

In the analysis, the mass of each pier is assumed to be lumped at the top and bottom of the pier. The masses of the piers and the bridge deck are calculated as follows:

$$M_{p2} = M_{p3} = M_{p4} = \frac{\gamma_c A_{g,col}}{g} * \frac{H_c}{2} * N_{col} \tag{11.14a}$$

$$m = \frac{\gamma_c A_d}{g} \tag{11.14b}$$

where M_{pi} is the mass of each pier *i* lumped at the superstructure level, m is the mass per unit length of the superstructure, γ_c is the unit weight of the reinforced concrete members, which is assumed to be 150 pounds per cubic foot, $A_{g,col}$ is the cross-sectional area of a column, H_c is the clear height of a column, g is the acceleration due to gravity, and N_{col} is the number of columns per pier. The hinges in the deck are spaced uniformly at 1/3 points, and their *x* coordinates have the following values: x_{hinge1} = 2,400 in. and x_{hinge2} = 4,800 inches.

The bridge is situated in the same location as the Type-2 bridge considered in the previous example, and, thus, the same design spectrum shown in Figure 11.5 is used.

11.5.2 Design of Self-Centering Columns in the Bridge Example

In the first trial, each of the three piers has two columns. Each column is assumed to have a diameter of 40 in., two rocking hinges that have 20-in.-diameter rocking plates, 16 lines of unbonded longitudinal reinforcing bars, and 20 prestressing strands. Each longitudinal rebar consists of a No. 10 elastic bar and a No. 8 fuse bar. The lengths of the elastic bars and fuse bars are 240 in. and 67 in., respectively. The centroid of each prestressing strand group is 8 in. away from the centroid of the column section, and the rebars have a 2.375-in. clear cover.

For this bridge, the shape function is given by the following expression.

$$\psi(x) = \begin{Bmatrix} \dfrac{x}{L_1} \text{ for } x \le L_1 \\ 1.0 \text{ for } L_1 < x \le L_1 + L_2 \\ \dfrac{L_d - x}{L_1} \text{ for } L_1 + L_2 < x \le L_d \end{Bmatrix} \tag{11.15}$$

where L_1 is the distance between the left abutment and the first deck hinge, and L_2 is the distance between the two deck hinges. The values of M^* and L^* for the bridge are calculated with Equations (11.7a) and (11.7c), respectively, with the mass of each pier and the deck calculated with Equations (11.14a) and (11.14b). The following results are obtained.

$$M^* = 9.50 \ \frac{\text{kip-sec}^2}{\text{in.}}$$

$$L^* = 11.39 \ \frac{\text{kip-sec}^2}{\text{in.}}$$

The target drift limit for each pier is $u_{pi,\lim} = 0.06 * H_c = 14.4$ in. and the target drift level of the bridge, $z_{\max}$, is governed by Pier 3. Hence,

$$z_{\max} = \frac{u_{p3,\lim}}{\psi(x_3)} = 14.4 \text{ in.}$$

and the target spectral displacement for the equivalent single-of-degree structure is

$$S_d^* = \frac{M^*}{L^*} z_{\max} = 12 \text{ in.}$$

It is assumed that the equivalent damping ratio $\xi^* = 0.25$. The corresponding displacement response design spectrum constructed with Equation (11.8) is shown in Figure 11.27.

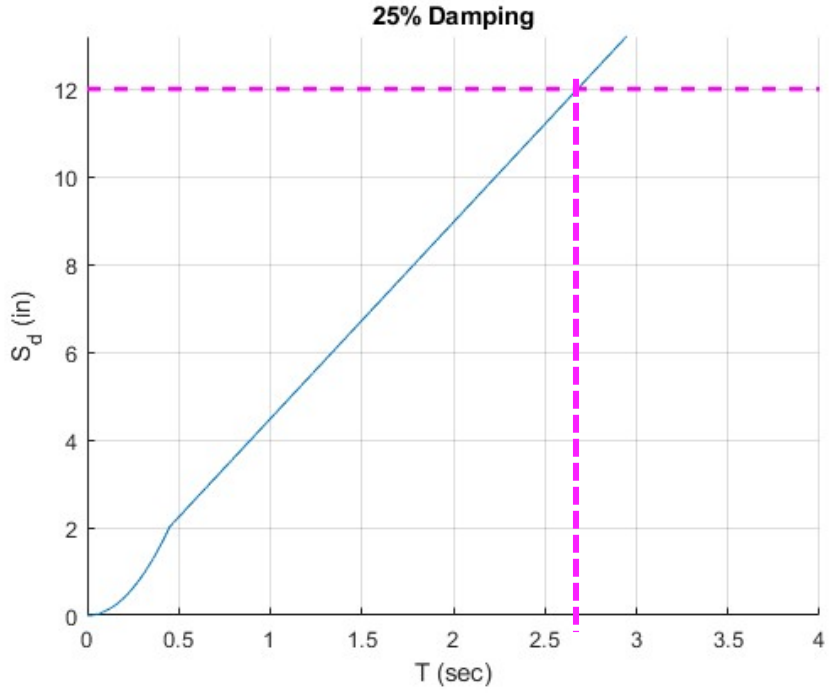

Figure 11.27: Spectral displacement with 25% damping for LA area

With the target displacement of 12 in., Figure 11.27 gives the period of 2.68 sec, which is the effective period, T_{eq}, required for the equivalent linearly elastic structure. With this period and the calculated generalized mass, M^*, the stiffness required for the equivalent structure is calculated to be:

$$K^* = 4\pi^2 M^* / T_{eq}^2 = 52 \frac{\text{kips}}{\text{in.}}$$

A pushover analysis is conducted on one column in Pier 3 (middle pier) and one column in Pier 4 (see pier locations in Table 11.1). The columns have the design described previously. Figures 11.28 and 11.29 show the monotonic pushover force-displacement curves for the two columns reaching their respective target displacements, and the equivalent column stiffnesses determined from the pushover curves.

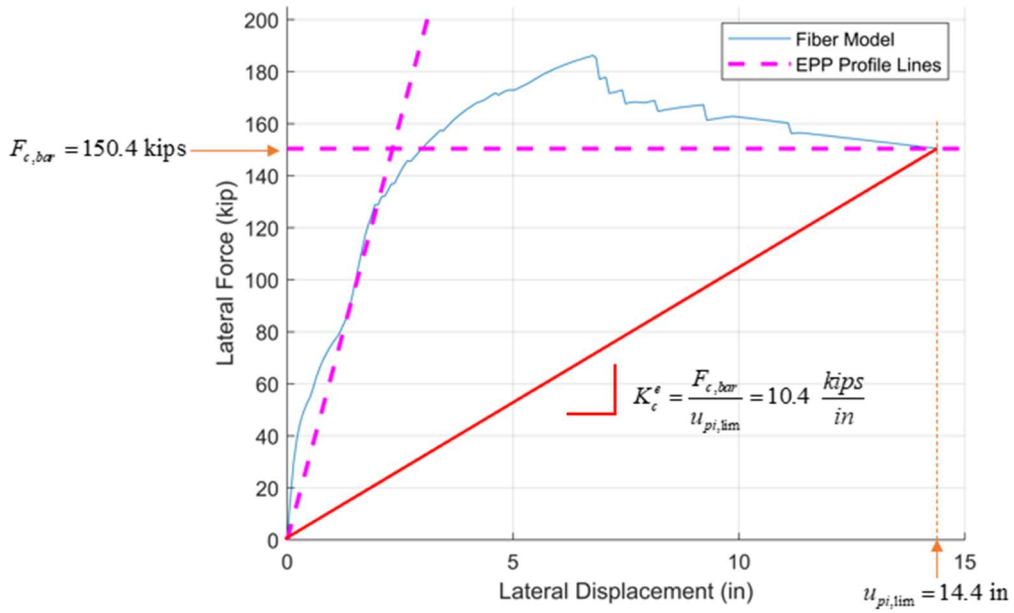

Figure 11.28: Pushover force-displacement curve for the column with the initial trial design in the middle pier (Pier 3) of the Type-3 bridge

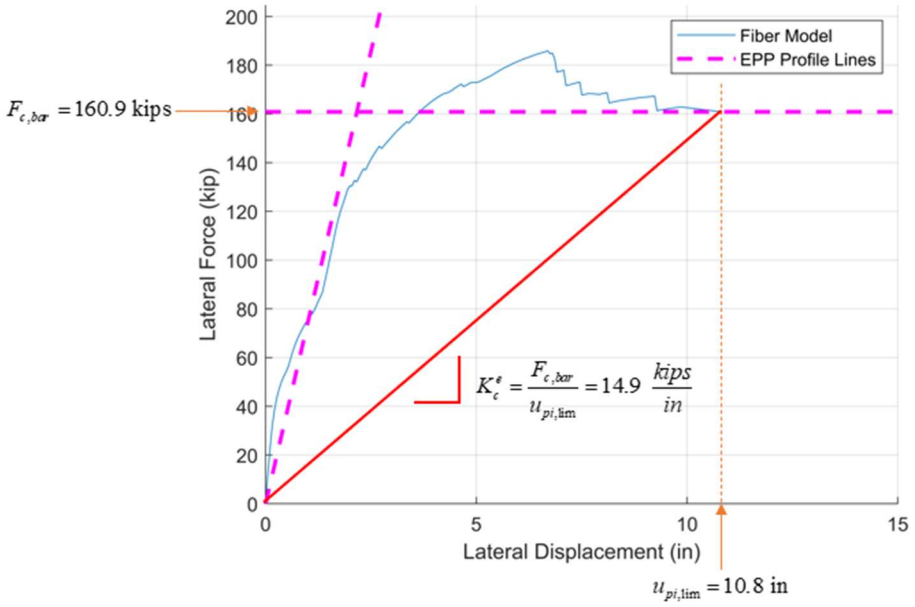

Figure 11.29: Pushover force-displacement curve for the column with the initial trial design in an exterior pier (Pier 4) of the Type-3 bridge

The calculation of the equivalent structural stiffness follows Equation (11.7b). Since each pier has two columns and the two exterior piers have the same equivalent column stiffness, Equation (11.7b) can be simplified to:

$$K^* = 2K_{c,p3}^{eq} + 4K_{c,p2}^{eq}\left(\frac{x_2}{L_1}\right)^2$$

where x_2 is the distance of Pier 2 from the left abutment as shown in Table 11.1, and $K_{c,pi}^{eq}$ is the equivalent stiffness of the column in Pier *i* identified in Figures 11.28 and 11.29. Hence,

$$K^* = 2*10.4 + 4*14.9*(\frac{1800}{2400})^2 = 54 \ \frac{\text{kips}}{\text{in.}}$$

The calculated equivalent stiffness of the trial design is slightly stiffer than required, which is 52 kips/in. This is deemed adequate. Next, the hysteretic damping property of the bridge structure is estimated. To this end, Equation (11.10) is used to calculate the hysteretic energy dissipation per cycle of response of each pier at the target drift level. Since all the piers have identical columns, a pushover analysis is conducted on one column through the target drift levels for Piers 3 and 4. The target displacement for Pier 3 is 14.4 in. and the target displacement for Pier 4 is 10.8 inches. Based on Step 9 of the procedure presented in Section 11.3, the axial load and prestressing strands are removed from the column. Figure 6.30 shows the pushover curve with the target drift levels for Piers 3 and 4 indicated.

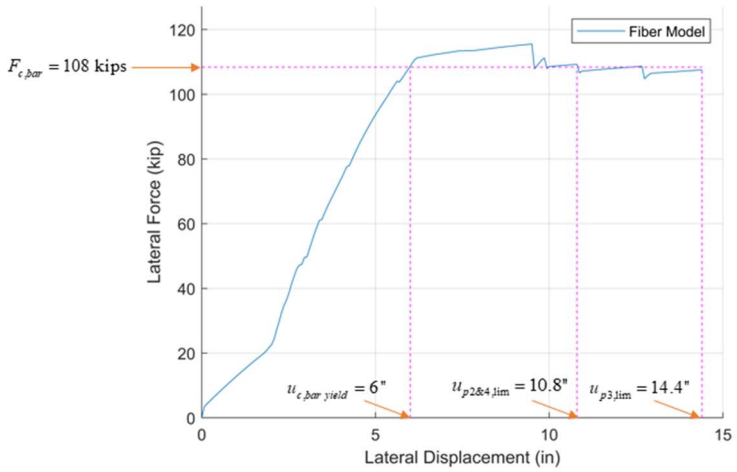

Figure 11.30: Pushover curve used to determine hysteretic energy dissipation by the column with the initial trial design for the Type-3 bridge

The yield force, $F_{c,bar}$, and yield displacement, $u_{c,bar\ \text{yield}}$, for each column are determined from Figure 11.30. As shown in the figure, $F_{c,bar}$ is the average lateral force developed in the region where the target displacements are reached, and the yield displacement, $u_{c,bar\ \text{yield}}$, is the displacement at which that the yield force is first reached. From Figure 11.30, the yield force of

the column, $F_{c,bar}$, is determined to be 108 kips, and the yield displacement, $u_{c,bar\ \text{yield}}$, is estimated to be 6.0 inches. Each pier has two columns. Hence, for each pier, $F_{pi,bar}$ is $2F_{c,bar}$ and $u_{pi,bar\ yield} = u_{c,bar\ \text{yield}}$. With Equation (11.11) and α = 0.8, the hysteretic energy dissipation of Pier 3, E_{p3}^{H}, is calculated to be 2,903 kip-in., and for each of Pier 2 and Pier 4, the energy dissipation, E_{p2}^{H} and E_{p4}^{H}, is calculated to be 1,659 kip-in. With K^* equal to $54\ \frac{\text{kips}}{\text{in.}}$ and $z_{\max}$ equal to 14.4 in., the equivalent damping ratio, ξ^*, calculated with Equation (11.10) is 0.14. Compared to the original assumption of $\xi^* = 0.25$, there is change of 44%. Thus, another iteration of the column design needs to be performed with the design spectrum that has $\xi^* = 0.14$, which is shown in Figure 11.31.

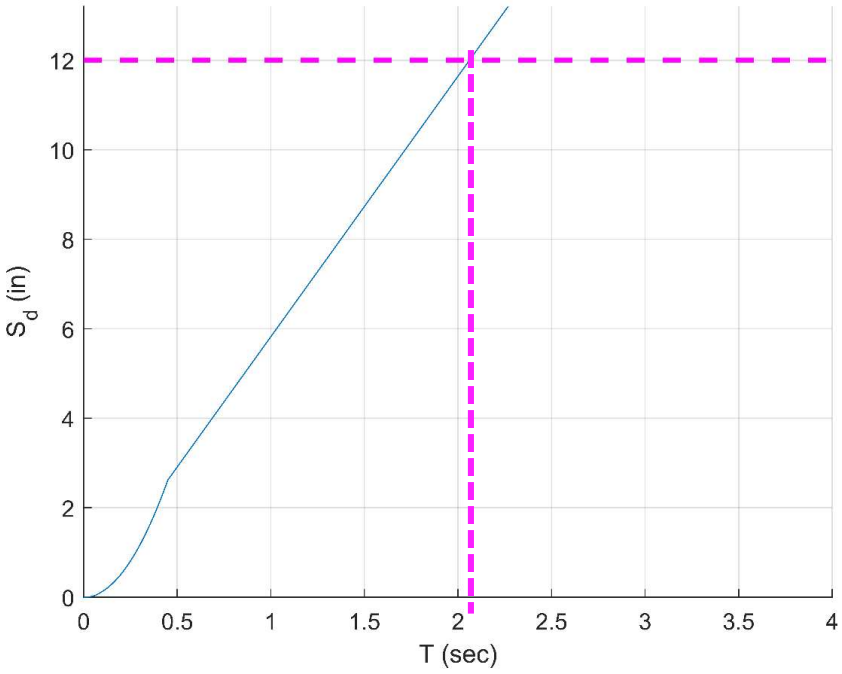

Figure 11.31: Spectral displacement with 14% damping for LA area

In the second trial, the diameter of each column is increased to 54 in. and the rocking plate diameter is increased to 27 in., with the type and amount of reinforcement remaining the same.

There are twenty 0.6-in. diameter prestressing strands, and 16 lines of longitudinal rebar. Each longitudinal rebar consists of a No. 10 elastic bar and a No. 8 fuse bar. The lengths of the elastic bars and fuse bars are 240 in. and 67 in., respectively. The centroid of each prestressing strand group is 11.5 in. away from the centroid of the column section, and the rebars have a 2.375-in. clear cover.

With the target spectral displacement of 12 in., Figure 11.31 gives the period of 2.06 sec, which is the period, T_{eq}, required for the equivalent linearly elastic structure. With this period and the calculated generalized mass, M^*, the stiffness required for the equivalent structure is calculated to be:

$$K^* = 4\pi^2 M^* / T_{eq}^2 = 89.1 \frac{\text{kips}}{\text{in.}}$$

A pushover analysis is conducted on one column in Pier 3 and one column in Pier 4 based on the second trial design with an applied axial load of 837 kips. Figures 11.32 and 11.33 show the force-displacement curves for these two columns reaching their respective target displacements.

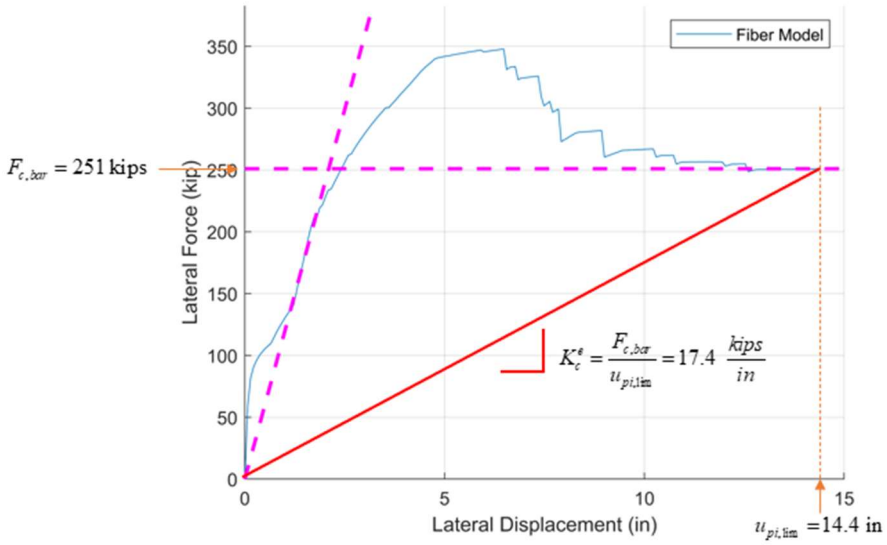

Figure 11.32: Pushover force-displacement curve for the column with the second trial design in the middle pier (Pier 3) of the Type-3 bridge

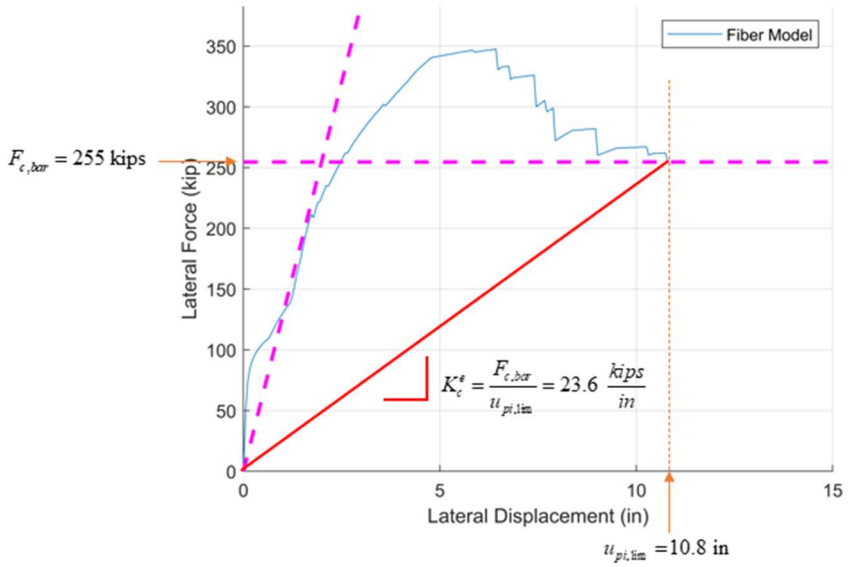

Figure 11.33: Pushover force-displacement curve for the column with the second trial design in an exterior pier (Pier 4) of the Type-3 bridge

Based on the equivalent column stiffnesses identified in Figures 11.32 and 11.33, the stiffness for the equivalent structure is calculated with Equation (11.7b) as follows:

$$K^* = 2*17.4 + 4*23.6*(\frac{1800}{2400})^2 = 88 \ \frac{kips}{in}$$

The second trial design is slightly less stiff than required, which is 89.1 kips/in. This is deemed adequate. Next, the hysteretic damping property of the bridge structure is estimated. To this end, Equation (11.10) is used to calculate the hysteretic energy dissipation per cycle of response of each pier at the target drift level. A pushover analysis is conducted on one column through the target drift levels for Piers 3 and 4. The target displacement for Pier 3 is 14.4 inches and the target displacement for Pier 4 is 10.8 inches. Based on Step 9 of the procedure presented in Section 11.3, the axial load and prestressing strands are removed from the column. Figure 11.34 shows the pushover curve.

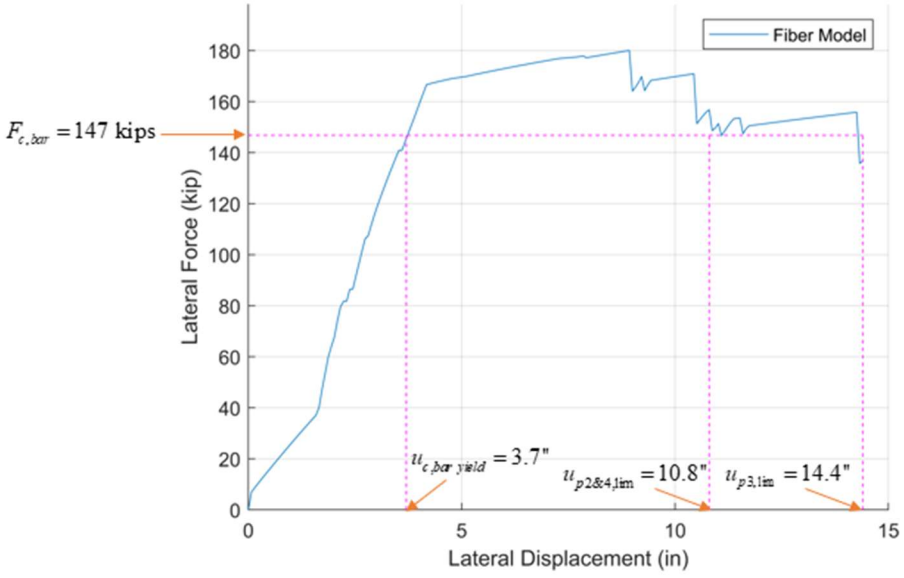

Figure 11.34: Pushover curve used to determinate hysteretic energy dissipation by the column with the second trial design for the Type-3 bridge

The yield force, $F_{c,bar}$, and yield displacement, $u_{c,bar\ \text{yield}}$, are determined for each column from Figure 11.34 in the same way as in the first iteration. From Figure 11.34, the yield force, $F_{c,bar}$, of the column is determined to be 147 kips, and the yield displacement, $u_{c,bar\ \text{yield}}$, is estimated to be 3.7 inches. These values are determined to provide a good fit for the piers that have different drift limits. For each pier, $F_{pi,bar}$ is $2F_{c,bar}$ and $u_{pi,bar\ yield} = u_{c,bar\ \text{yield}}$. With Equation (11.11) and α = 0.8, the hysteretic energy dissipation of Pier 3, E_{p3}^{H}, is calculated to be 5,033 kip-in., and for each of Pier 2 and Pier 4, the energy dissipation, E_{p2}^{H} and E_{p4}^{H}, is calculated to be 3,340 kip-in. With K^* equal to $88\ \frac{\text{kips}}{\text{in.}}$ and $z_{\max}$ equal to 14.4 in., the equivalent damping ratio, ξ^*, calculated with Equation (11.10) is 0.15. Compared to the first trial design where $\xi^* = 0.14$, there is a change of 9%. With the stiffness of the bridge, K^*, approximately equal to what is required, and the change in the equivalent damping ratio, ξ^*, less than 20%, the second trial is considered satisfactory. Tables 11.8 and 11.9 show a summary of the design trials.

Table 11.8: Design iterations for the displacement-based design of the Type-3 bridge

Iteration	Column Diameter (in)	Rocking Plate Diameter (in)	Number of Rebars	Elastic Bar Size	Fuse Bar Size	Number of PT Strands
1	40	20	16	No. 10	No. 8	20
2	54	27	16	No. 10	No. 8	20

Table 11.9: Hysteretic energy dissipations and calculated equivalent damping ratios in design iterations for the Type-3 bridge

Iteration	M^* $(\frac{\text{kip-sec}^2}{\text{in.}})$	K^* $(\frac{\text{kips}}{\text{in.}})$	Hysteretic Energy Dissipation Pier 3 (kip-in.)	Hysteretic Energy Dissipation Per Piers 2, 4 (kip-in.)	Calculated Damping Ratio	% Change
1	9.50	54	2,903	1,659	0.14	-44
2	9.62	88	5,033	3,340	0.15	9

To examine if the design obtained with this methodology is adequate, the five ground motions shown in Figure 11.7 are used to evaluate the response of the bridge structure. The bridge structure can be exactly represented by a single-degree-of-freedom system formulated according to Rayleigh's method because the shape function adopted represents the exact deflected shape of the superstructure. The effective mass is equal to 9.62 kip-sec^2/in., computed with Equation (11.7a), and the lateral resistance is equal to the total resisting force developed by the three piers, each of which has 2 columns. The resisting force contributed by each of Pier 2 and Pier 4 is equal to the actual restoring force developed by the pier multiplied by (x_2/L_1), where x_2 is the distance of Pier 2 from the left abutment and L_1 is the length of the first span of the bridge. The nonlinear behavior of the columns is represented by the fiber-section model. Viscous damping is assumed to be 5% of the critical to account for the damping of the structure in the elastic regime.

For the purpose of scaling the ground motions as in the first design example, the initial elastic stiffness of the structure is estimated to be 506 kips/in., which results in an initial elastic period of 0.9 sec. The initial elastic stiffness is calculated with Equation (11.7b), in which the

equivalent pier stiffness, K_{pi}^{eq}, is replaced by the initial elastic stiffness of each pier, which is two times the initial stiffness of each column from the pushover analysis. When the bridge structure reaches the target drift ratio of 6%, the stiffness of the equivalent linearly elastic structure is 88 kips/in., as shown in Table 11.9, which results in an effective period of 2.1 second. This period range is similar to that of the Type-2 bridge in the first design example. Hence, the same scaling factors used in Section 11.4.3 (Table 11.6) are used here.

The time-history analyses are performed with the explicit Newmark integration scheme that does not introduce numerical damping. The integration time steps are the same as those used in Section 11.4.3. Figures 11.35 through 11.49 show the time-history plots of the displacements of the piers, the restoring force-vs.-displacement hysteresis curves for one column in each pier, and the time-history plots of the abutment shear-key force for each ground motion.

The peak displacement response for each ground motion is summarized in Table 11.10. The average peak displacement with the five ground motions is 12.8 in., which is less than the target displacement of 14.4 inches.

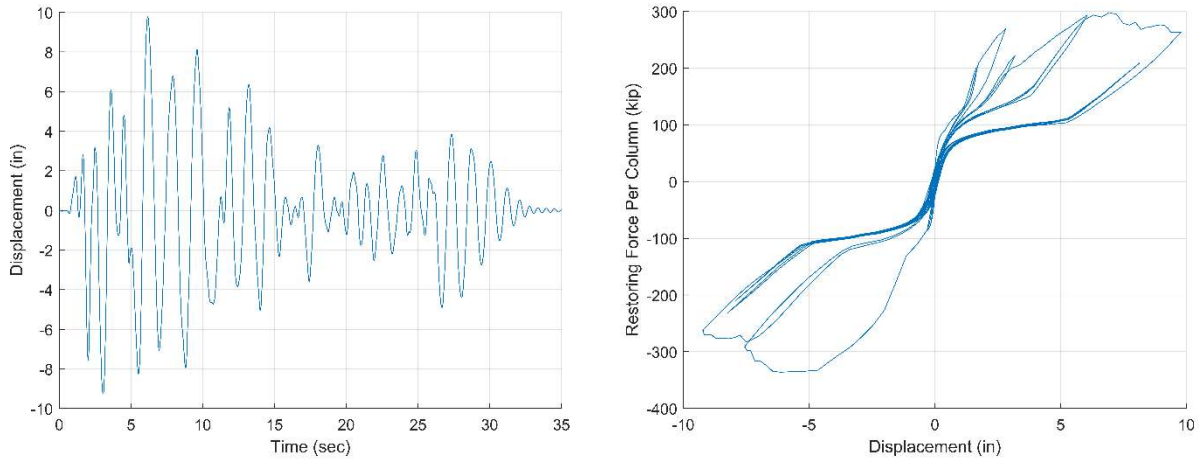

Figure 11.35: (left) Displacement time history for Pier 3 in the Type-3 bridge subjected to scaled El Centro ground motion; (right) Force-displacement hysteresis curves for a single column

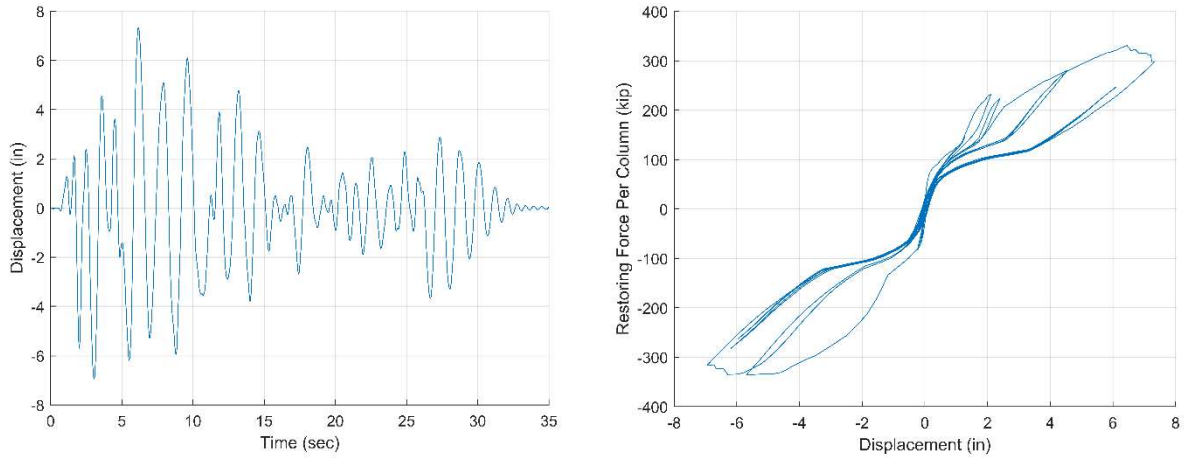

Figure 11.36: (left) Displacement time history for Piers 2 and 4 in the Type-3 bridge subjected to scaled El Centro ground motion; (right) Force-displacement hysteresis curves for a single column

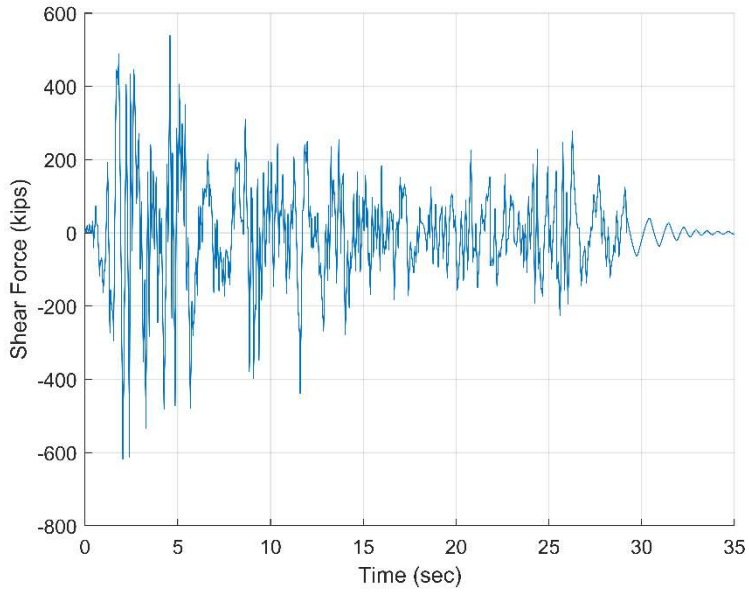

Figure 11.37: Abutment shear-key force developed in the Type-3 bridge subjected to the scaled El Centro ground motion

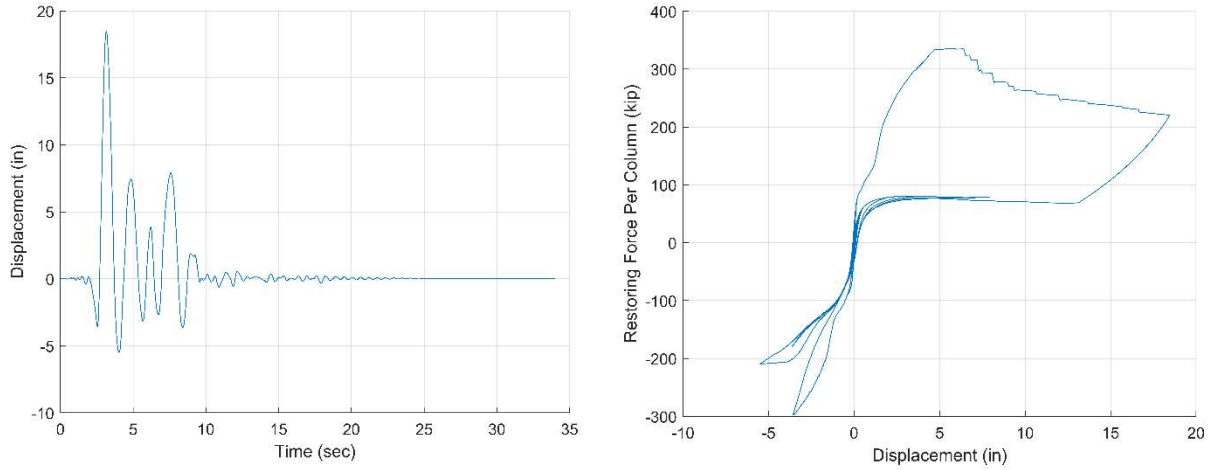

Figure 11.38: (left) Displacement time history for Pier 3 in the Type-3 bridge subjected to scaled Rinaldi ground motion; (right) Force-displacement hysteresis curves for a single column

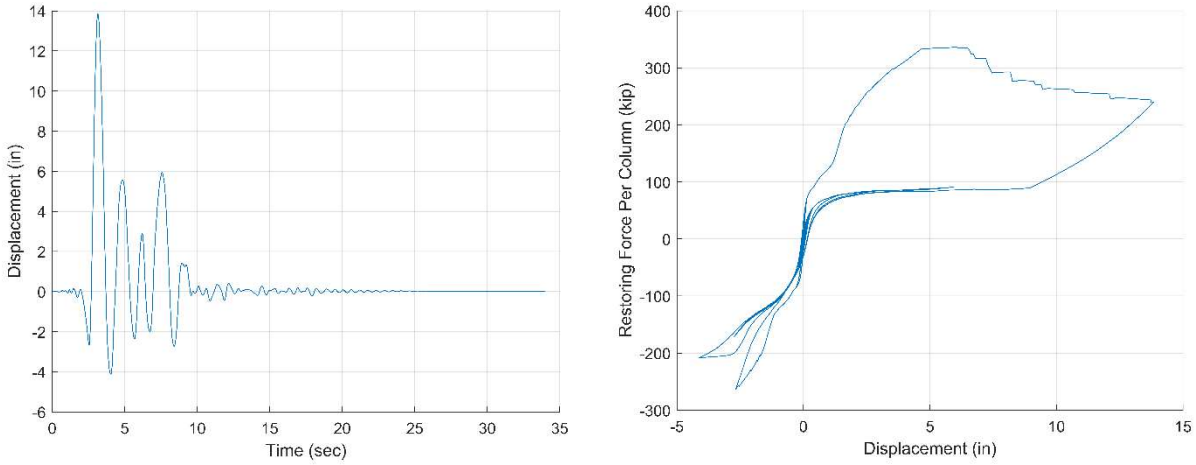

Figure 11.39: (left) Displacement time history for Piers 2 and 4 in the Type-3 bridge subjected to scaled Rinaldi ground motion; (right) Force-displacement hysteresis curves for a single column

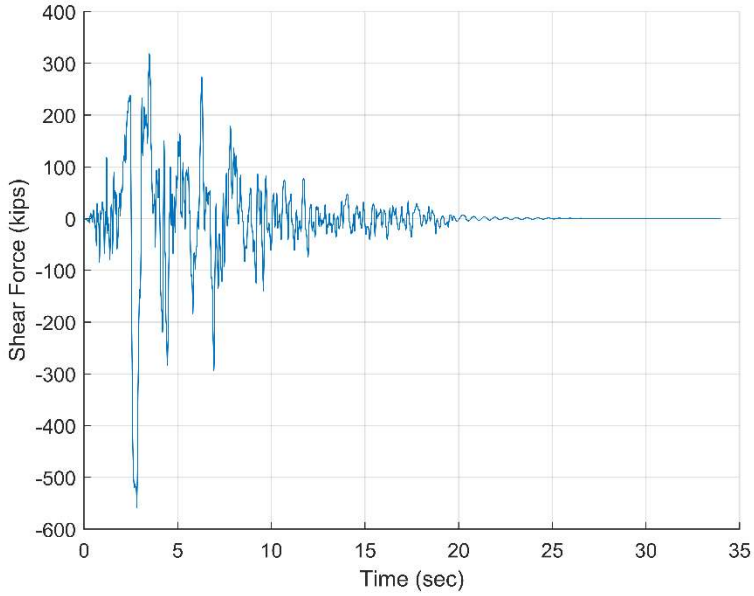

Figure 11.40: Abutment shear-key force developed in the Type-3 bridge subjected to scaled Rinaldi ground motion

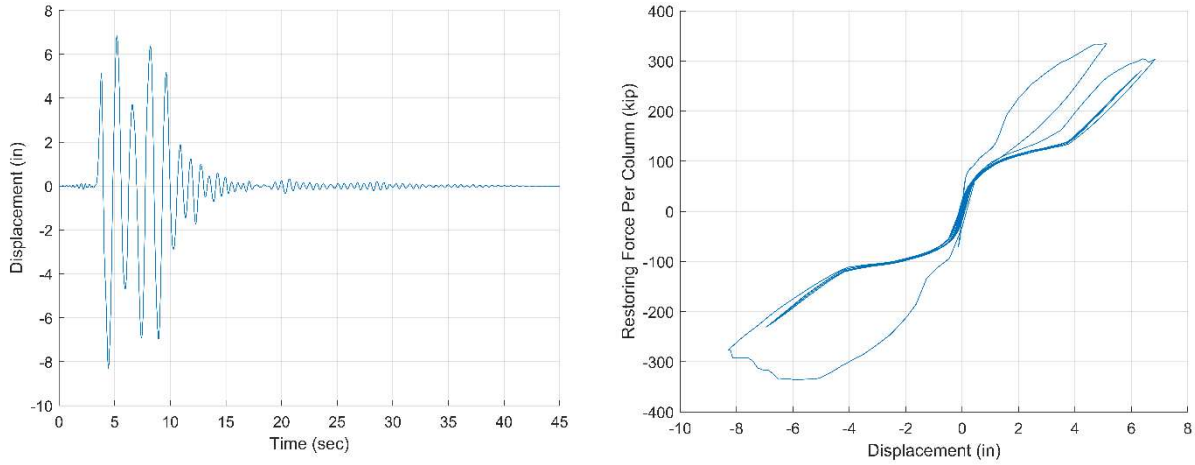

Figure 11.41: (left) Displacement time history for Pier 3 in the Type-3 bridge subjected to scaled Sylmar ground motion; (right) Force-displacement hysteresis curves for a single column

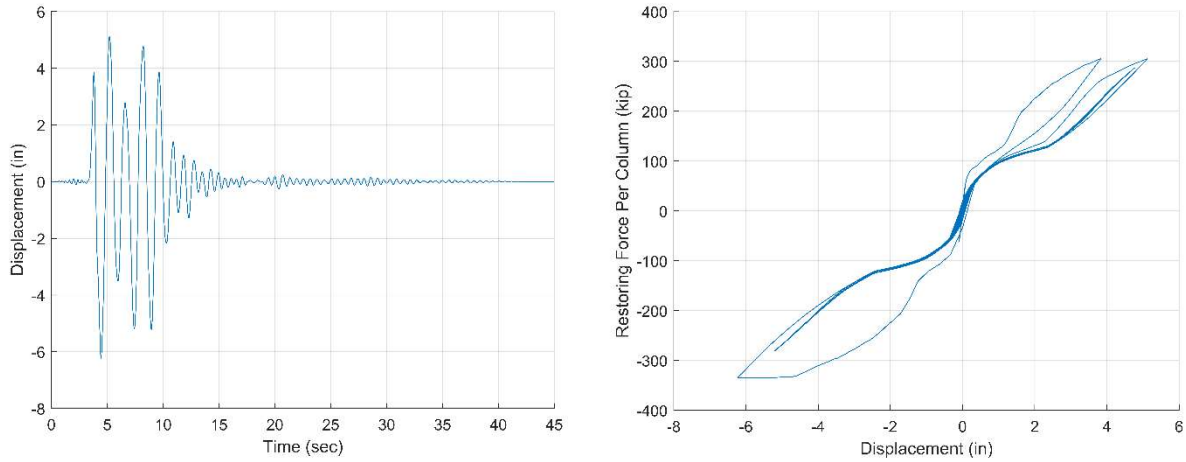

Figure 11.42: (left) Displacement time history for Piers 2 and 4 in the Type-3 bridge subjected to scaled Sylmar ground motion; (right) Force-displacement hysteresis curves for a single column

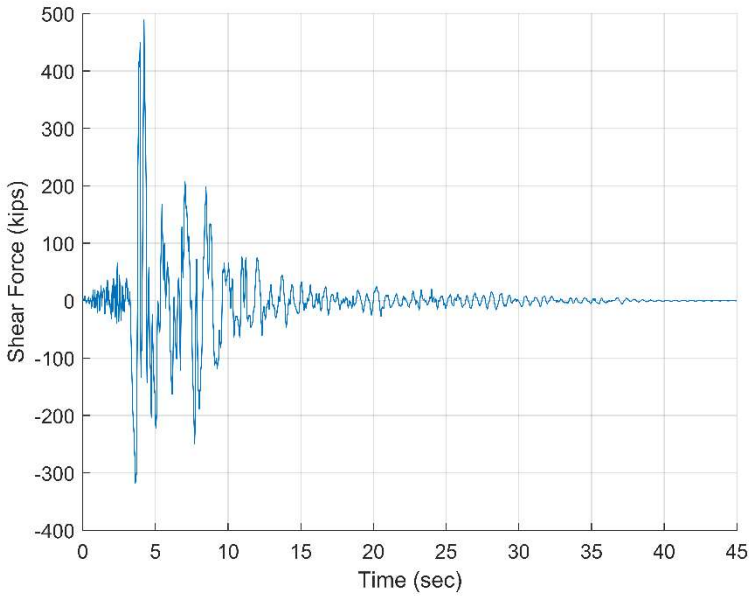

Figure 11.43: Abutment shear-key force developed in the Type-3 bridge subjected to scaled Sylmar ground motion

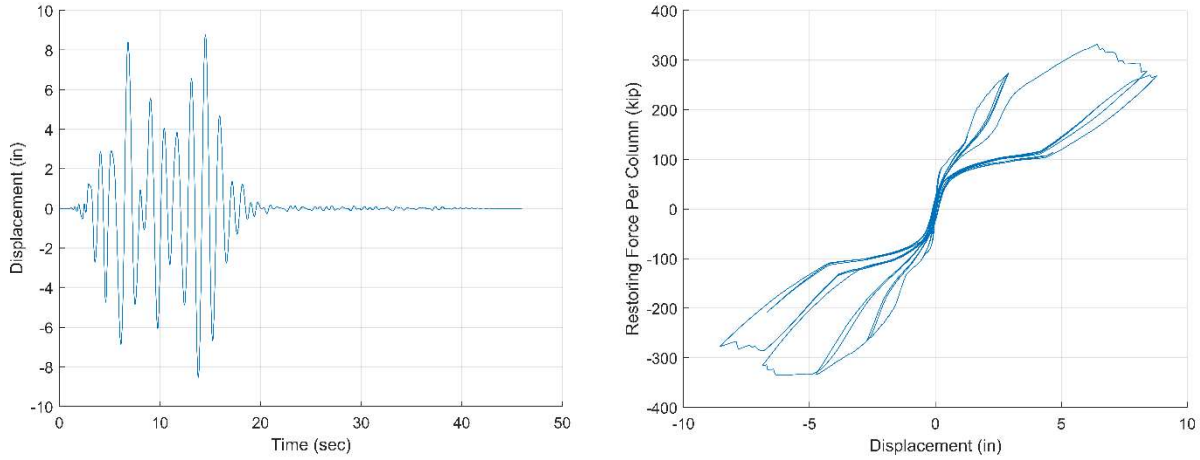

Figure 11.44: (left) Displacement time history for Pier 3 in the Type-3 bridge subjected to scaled Takatori 0° ground motion; (right) Force-displacement hysteresis curves for a single column

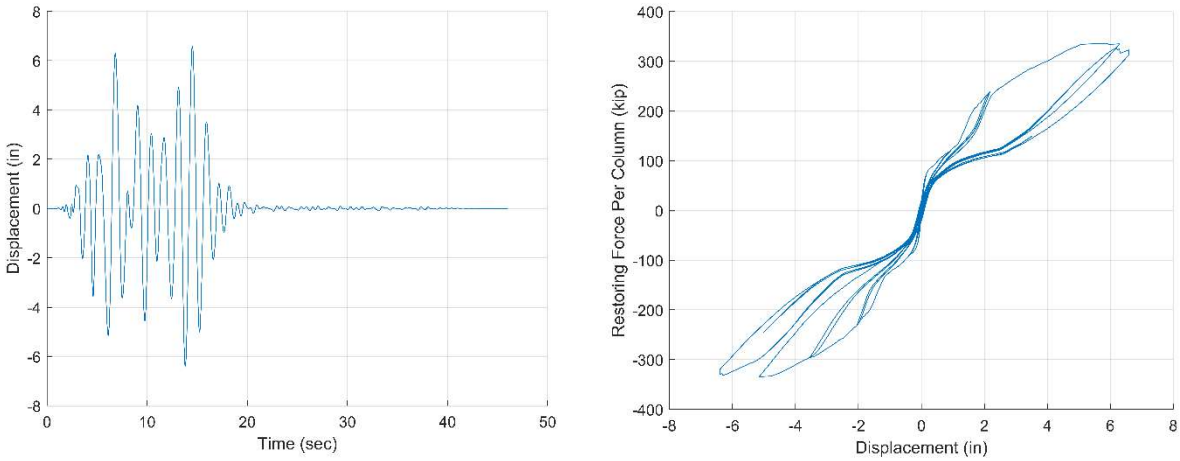

Figure 11.45: (left) Displacement time history for Piers 2 and 4 in the Type-3 bridge subjected to scaled Takatori 0° ground motion; (right) Force-displacement hysteresis curves for a single column

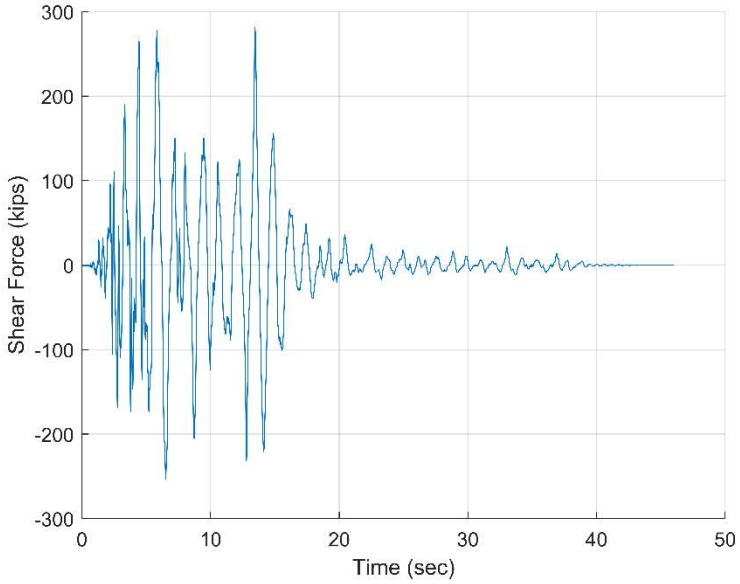

Figure 11.46: Abutment shear-key force developed in the Type-3 bridge subjected to scaled Takatori 0° ground motion

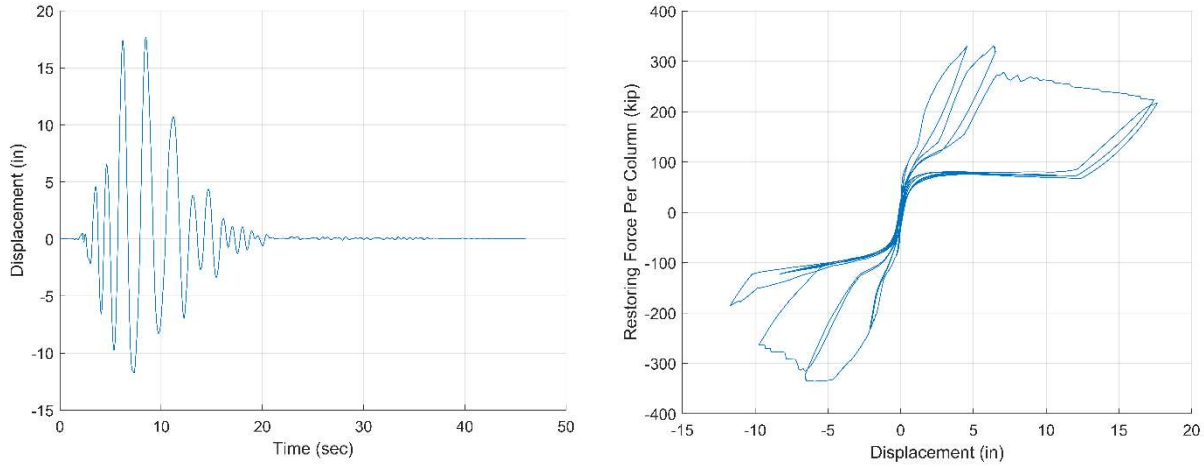

Figure 11.47: (left) Displacement time history for Pier 3 in the Type-3 bridge subjected to scaled Takatori 90° ground motion; (right) Force-displacement hysteresis curves for a single column

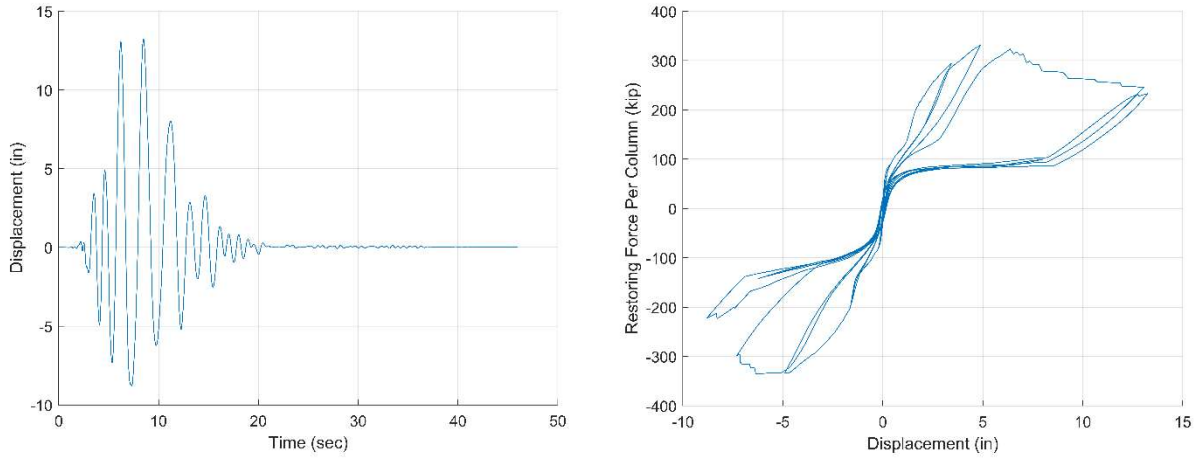

Figure 11.48: (left) Displacement time history for Piers 2 and 4 in the Type-3 bridge subjected to scaled Takatori 90° ground motion; (right) Force-displacement hysteresis curves for a single column

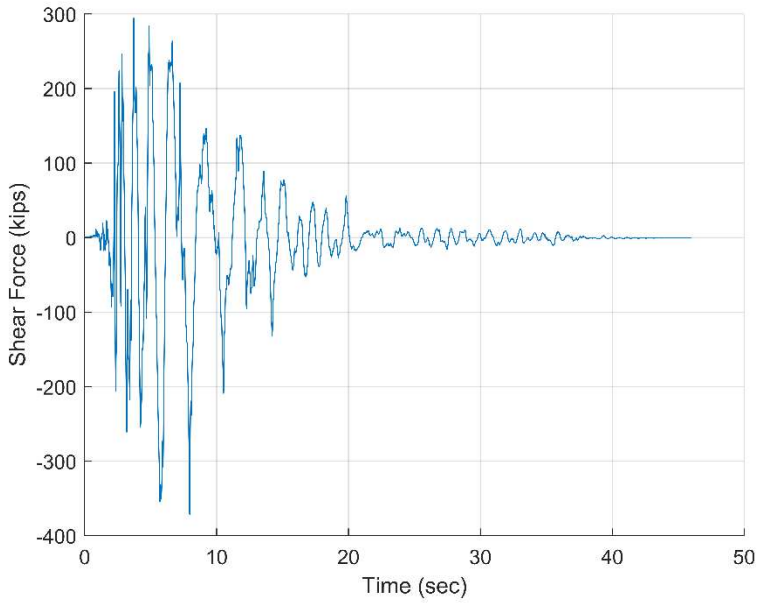

Figure 11.49: Abutment shear-key force developed in the Type-3 bridge subjected to scaled Takatori 90° ground motion

Table 11.10: Peak displacements of the Type-3 bridge induced by the ground motions

	El Centro	**Rinaldi**	**Sylmar**	**Takatori 0**	**Takatori 90**
Peak Displacement	9.78 in.	18.46 in.	8.31 in.	8.79 in.	17.65 in.

Chapter 11 is, in part, a reprint of the material in a California Department of Transportation report entitled "Experimental Investigation of a Self-Centering RC Column Design and a Displacement-Based Design Method for Highway Bridge Applications." The authors of the report are: the author of the dissertation, Dimitrios Kalliontzis, and P. Benson Shing. Professor Dimitrios Kalliontzis worked on much of the construction of the first test specimen. The author of the dissertation provided input for the design of the second specimen, and was responsible for

overseeing the construction and experimental work, post-test analysis of the two specimens, modeling and worked with Professor P. Benson Shing on the development of the displacement-based design methodology.

Chapter 12 Summary and Conclusions

12.1 Introduction

The second section of this dissertation focused on the a novel self-centering column design concept developed by Caltrans (Bromenschenkel and Mahan 2014; Yoon et al. 2015). The design was evaluated with laboratory testing. Modeling tools and a displacement-based design methodology were developed.

12.2 Summary, Main Observations and Conclusions of Study 2

12.2.1 Design and Testing of Self-Centering Bridge Columns

In this study, two cast-in-place reinforced concrete specimens were tested. The first specimen represented an initial design created by a team at Caltrans while the second specimen was a modified design aimed at reducing damage to the reinforcing bars in the vicinity of the column hinge. The designs of both specimens are shown in Chapter 8. Both column specimens were subjected to fully-reversed lateral displacement cycles without and with the rocking hinge grouted. In the ungrouted hinge tests, the columns were subjected to low lateral drift levels, whereas the tests with the grouted hinge reached maximum drifts of $\pm$10%. The first column specimen was also subjected to free-vibration testing, and a third quasi-static test to investigate the effects of radiation damping due to impact in the rocking hinge. During testing, both specimens were subjected to an applied axial compression of 900 kips to simulate loads from a bridge superstructure.

Specimen 1 experienced fracture of the longitudinal reinforcement in the vicinity of the rocking hinge during early cycles of the grouted hinge test, but there was no damage throughout the rest of the column body. The design of the second specimen was changed to achieve more

desirable behavior of the rebar. To avoid the fracture of the rebar, the bars that spanned from the pedestal to the load stub were fully debonded, and the heads of the fuse bars sat on top of the load stub in order to prevent the bars from entering into compression. The larger elastic bars were also wrapped in ½-in.-thick foam padding in the vicinity of the rocking hinge in order to minimize the effects of bending. While these changes prevented the bars from fracturing during testing, it was observed that there was crushing of the load stub concrete directly under the heads of the rebar, as well as several PT strand seats that failed. As with Specimen 1, no damage to the column body of Specimen 2 was observed.

12.2.2 Modeling of Self-Centering Bridge Columns

The experimental data from the column tests presented in Chapter 9 have shown that the behavior of the materials in these types of self-centering columns can be highly non-linear. To properly capture the global behavior of the columns, a fiber model has been developed and presented in Chapter 10. The material models employed within the fiber model are calibrated using the experimental data in order to best capture the response of the test specimens during cyclic quasi-static testing. The fiber model created is usable as a tool for the design of self-centering columns, as presented in Chapter 11. The examples presented in Chapter 11 cover a range of possibly considered design scenarios. These examples illustrate how to use the fiber model and a displacement-based design methodology to properly design a bridge with self-centering columns for seismic loading. While the modeling tools and design examples are for specific bridge configurations, they can be applied to a wide range of bridge layouts.

12.2.3 Conclusions

The testing of the self-centering bridge column specimens shown in Chapter 8 shows that these types of columns can be effective in providing lateral resistance through large lateral drifts,

with minimal damage to a bridge substructure, and nearly negligible residual drifts. The changes in the design between Specimen 1 and Specimen 2, as discussed in Chapter 8, showed notable improvement in the behavior of the column. While the comparison in Section 9.4.4 showed that Specimen 1 had higher normalized energy dissipation, the testing of Specimen 2 showed that the changes to the design achieved the desired longitudinal reinforcement behavior and prevented the rebar from fracturing in the vicinity of the rocking hinge. This is a more desirable outcome which may allow for easier rehabilitation of columns that could be damaged during major seismic events. The material models and fiber model shown in Chapter 10 provide insight into the mechanics of the behavior of the self-centering columns and the considerations that must be considered while designing this specific type of column. The displacement-based design methodology and design examples outlined in Chapter 11 provide a clear and concise procedure for the design of this type of self-centering column for use in seismically resistant bridge structures.

12.2.4 Recommendations for Future Research

The design of the self-centering columns in this dissertation could be further modified, improved, and tested. Due to the way the column specimens were designed, as presented in Chapter 8, the longitudinal reinforcement in Specimen 2 was guaranteed to not enter into compression. In a full height column, all heads of the rebar will have to be fully embedded in concrete. To account for this, the performance of self-centering columns with various design details including the amount of effective debonding, the layout of the larger elastic and smaller fuse bars, and the size of the headed bars to prevent concrete crushing should be examined. Optimizing these factors in a full height column warrants more rigorous testing. In addition, further testing can be performed to determine the effects of and methods to accommodate twisting of a self-centering column in a bridge structure.

The modeling of the self-centering columns presented in Chapter 10 provides reasonable agreement with the experimental data. The comparisons between the experimental response and the fiber model are shown in Chapter 10. Despite the general agreement with data, there are ways the model can be improved in future research. The material models employed in the fiber model are simplistic. The model employs tri-linear functions for the longitudinal reinforcement, and the steel plate materials, as well as linear-elastic unloading and reloading of the prestressing strands. Use of more refined material models may serve to further increase the accuracy of the fiber model with only minor changes in the computational efficiency. Furthermore, the fiber model can be implemented in an opensource coding language such as *Opensees* or *Python* in order to make the design methodology in Chapter 11 more widely available.

Appendix A Coronado –Instrumentation Drawings

This appendix contains a complete set of instrumentation drawings used in the testing of the pile specimens discussed in Chapter 3.

A.1 Specimen 1

The internal and external instrumentation drawings for Specimen 1 are shown below.

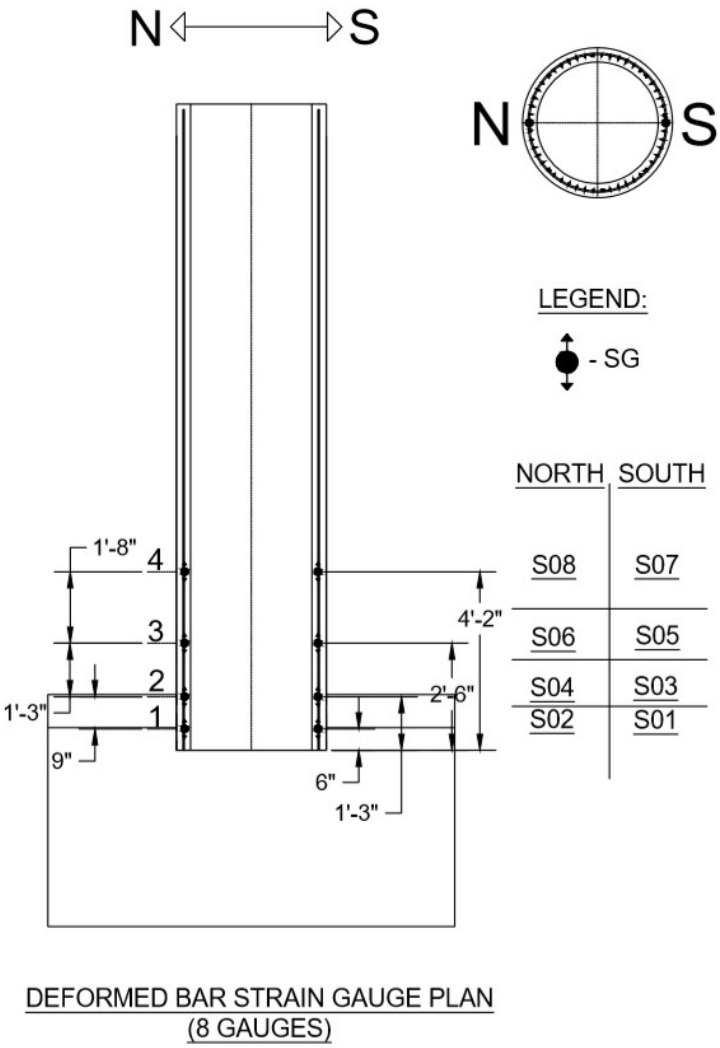

Figure A.1: Strain gauges on longitudinal reinforcing bars in the shell of Specimen 1

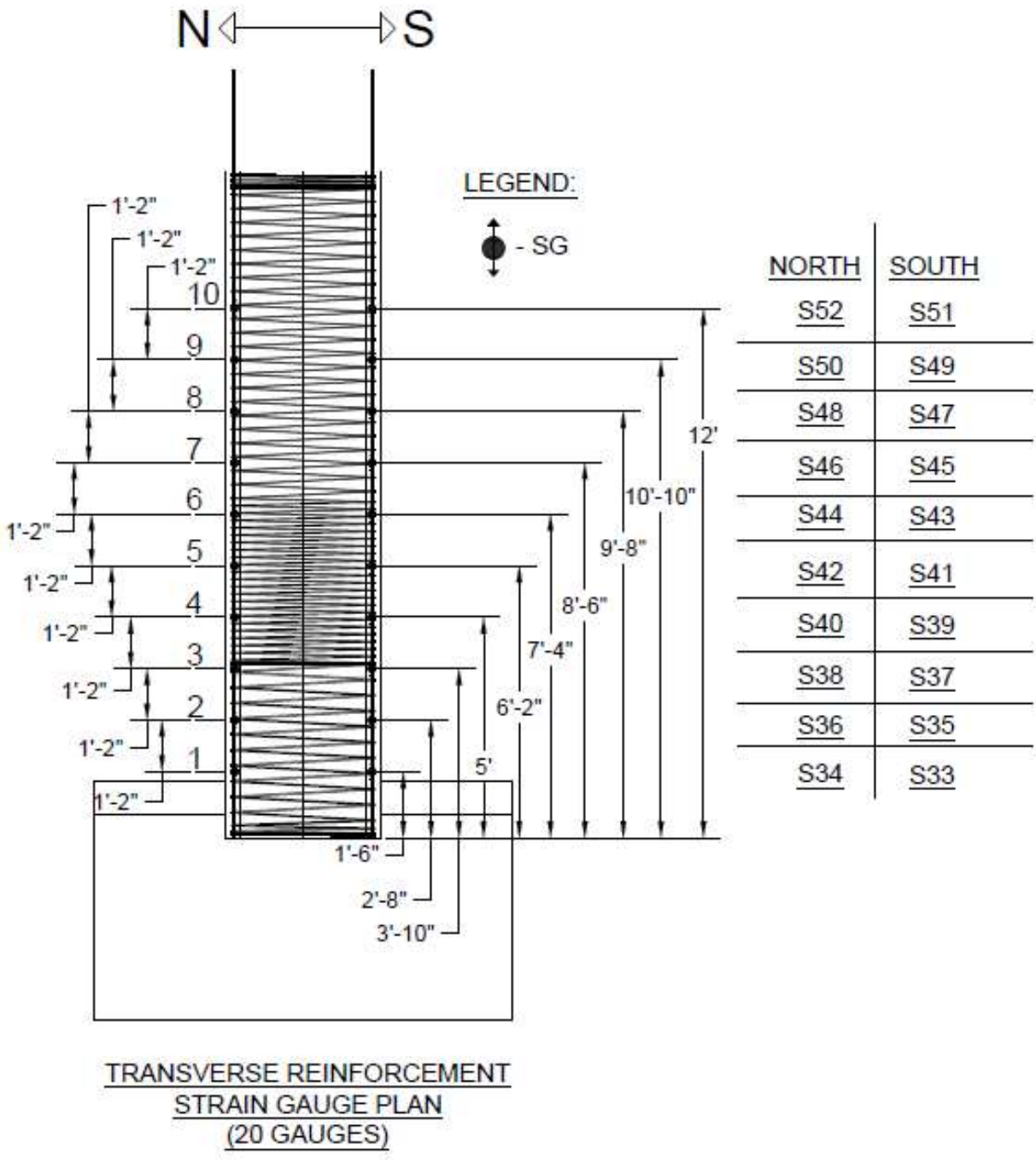

TRANSVERSE REINFORCEMENT
STRAIN GAUGE PLAN
(20 GAUGES)

Figure A.2: Strain gauges on transverse reinforcing bars in the shell of Specimen 1

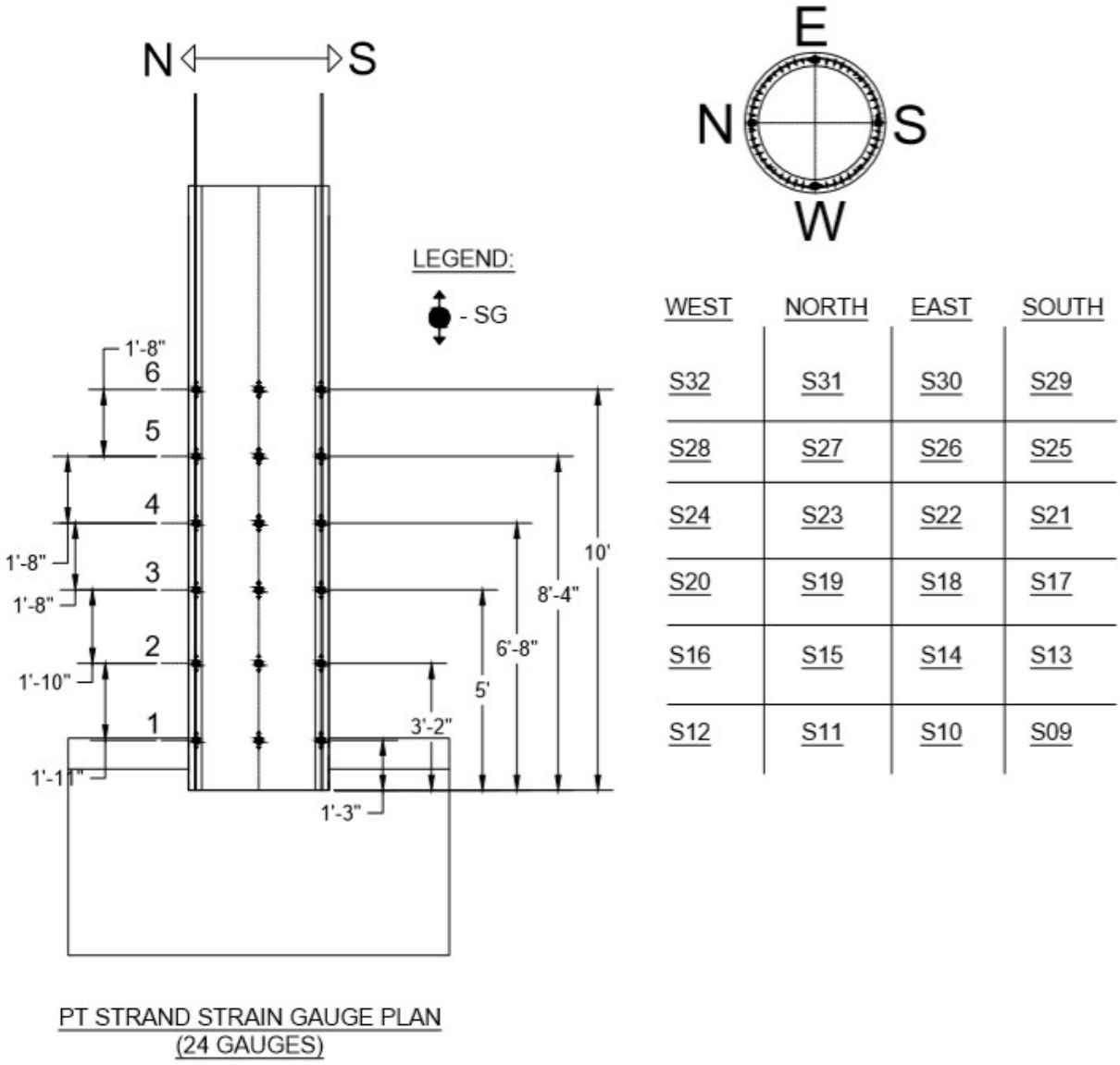

Figure A.3: Strain gauges on prestressing strands in the shell of Specimen 1

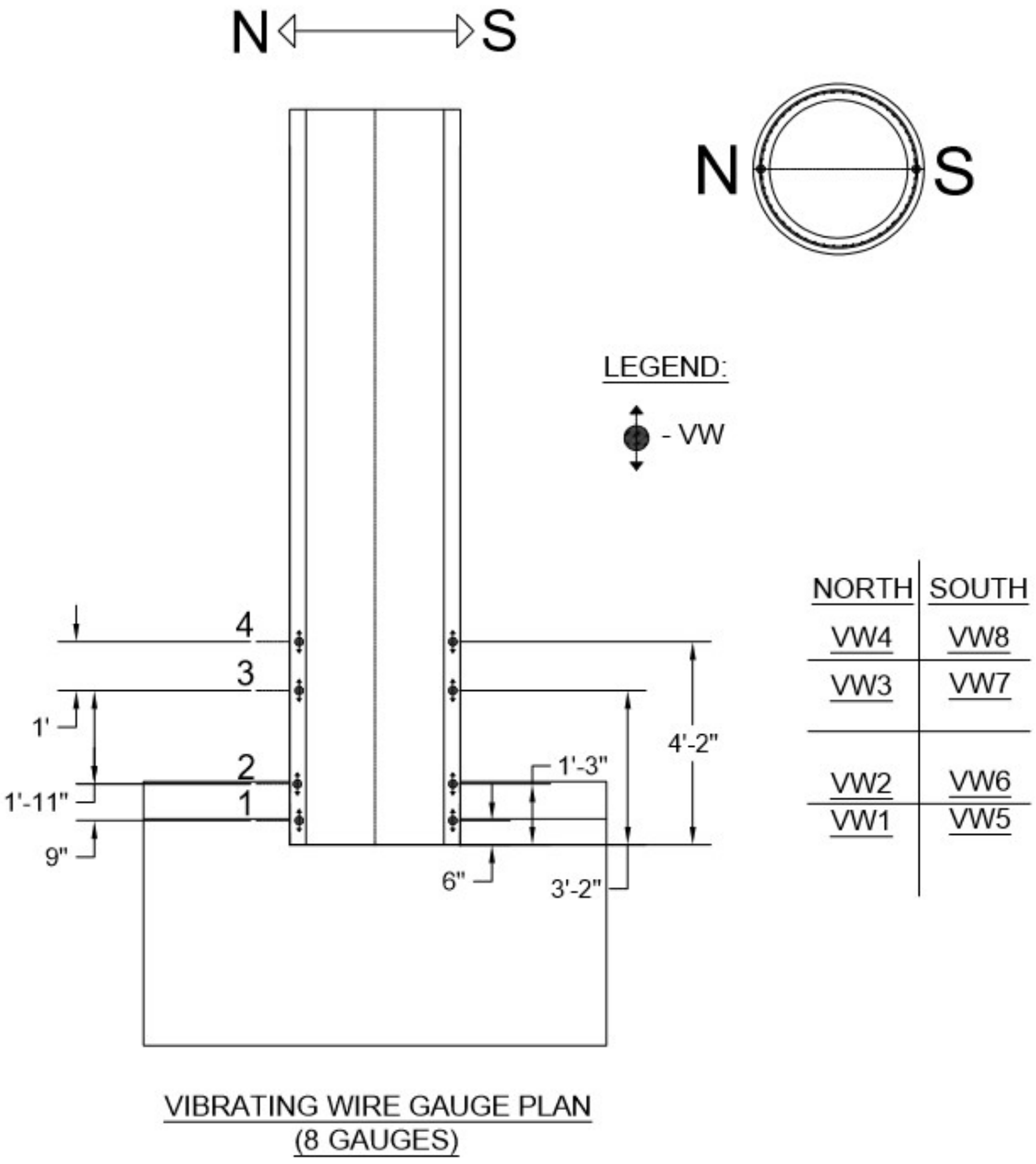

Figure A.4: Vibrating-wire gauges in the shell of Specimen 1

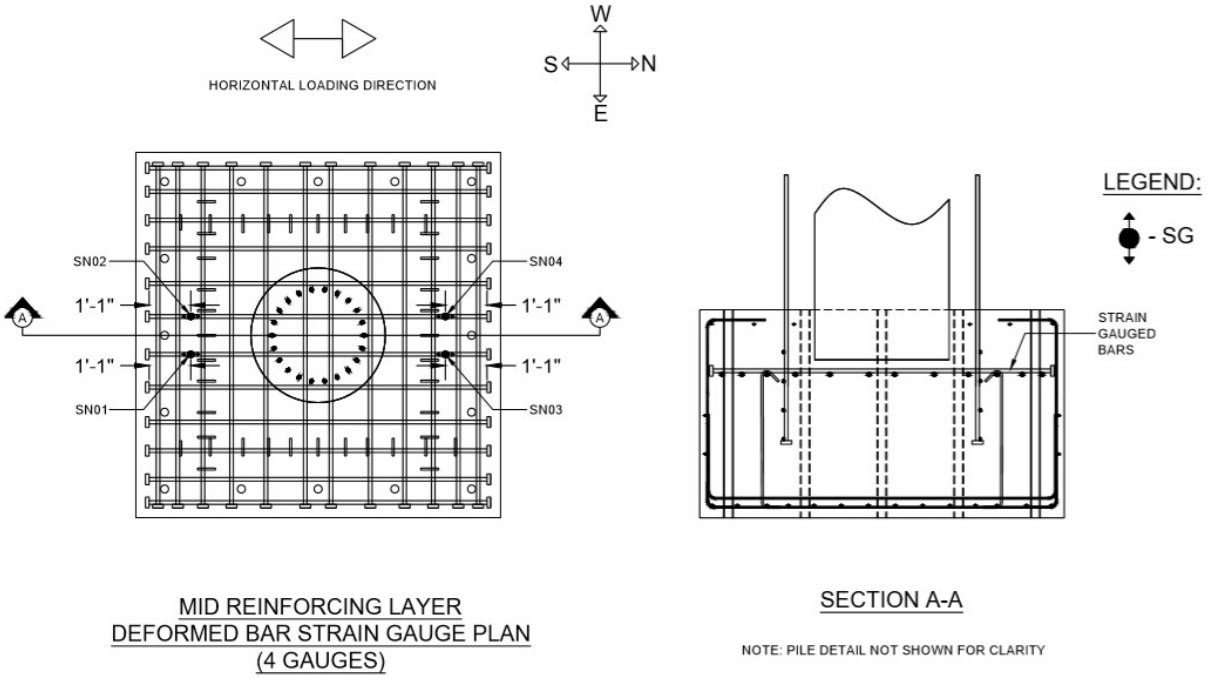

Figure A.5: Strain gauges on bars in middle reinforcement layer in the pile cap of Specimen 1

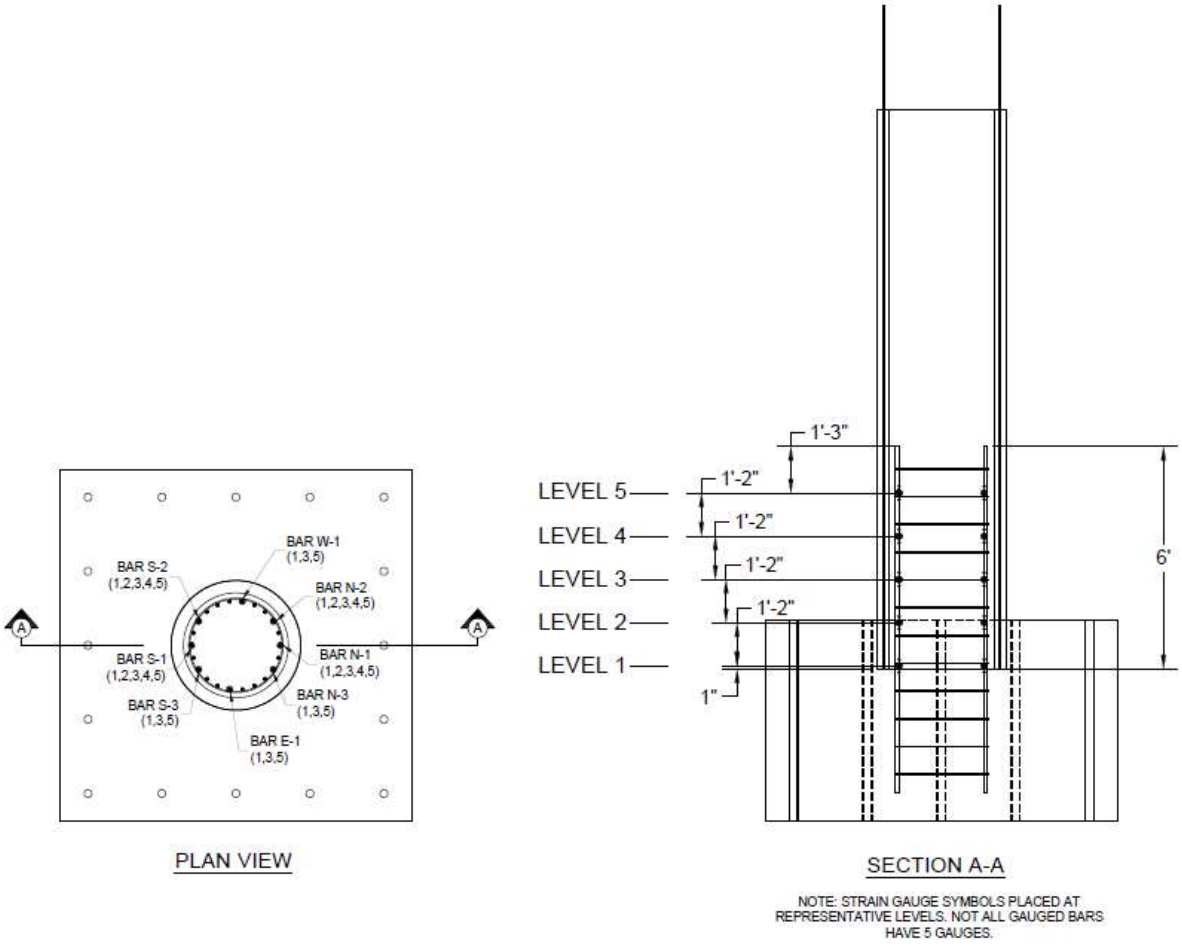

Figure A.6: Strain gauges on core reinforcing bars in Specimen 1 (numbers in parentheses below bar ID number in the plan view indicate the levels at which the gauges were located)

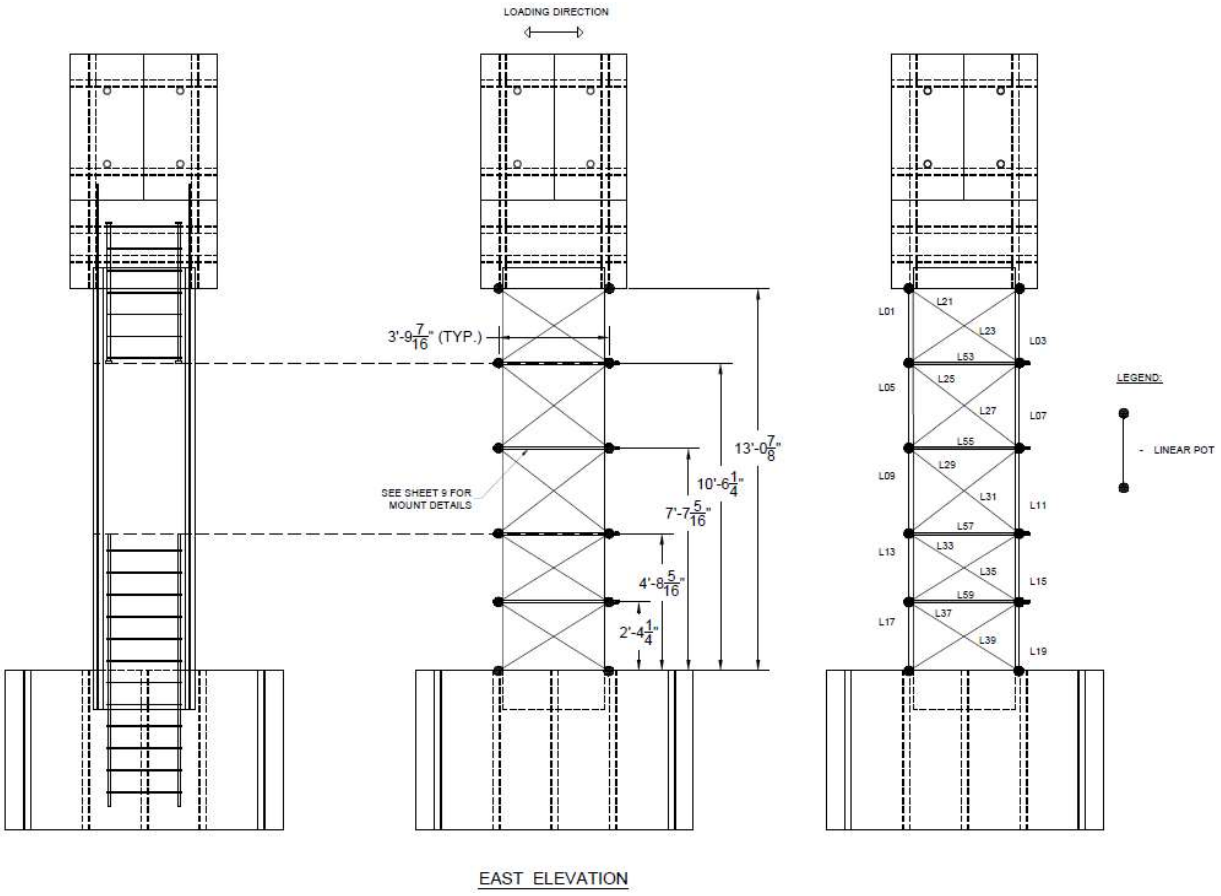

Figure A.7: Linear displacement potentiometers on east side to measure flexural and shear deformations (same for Specimens 1, 2, and 3)

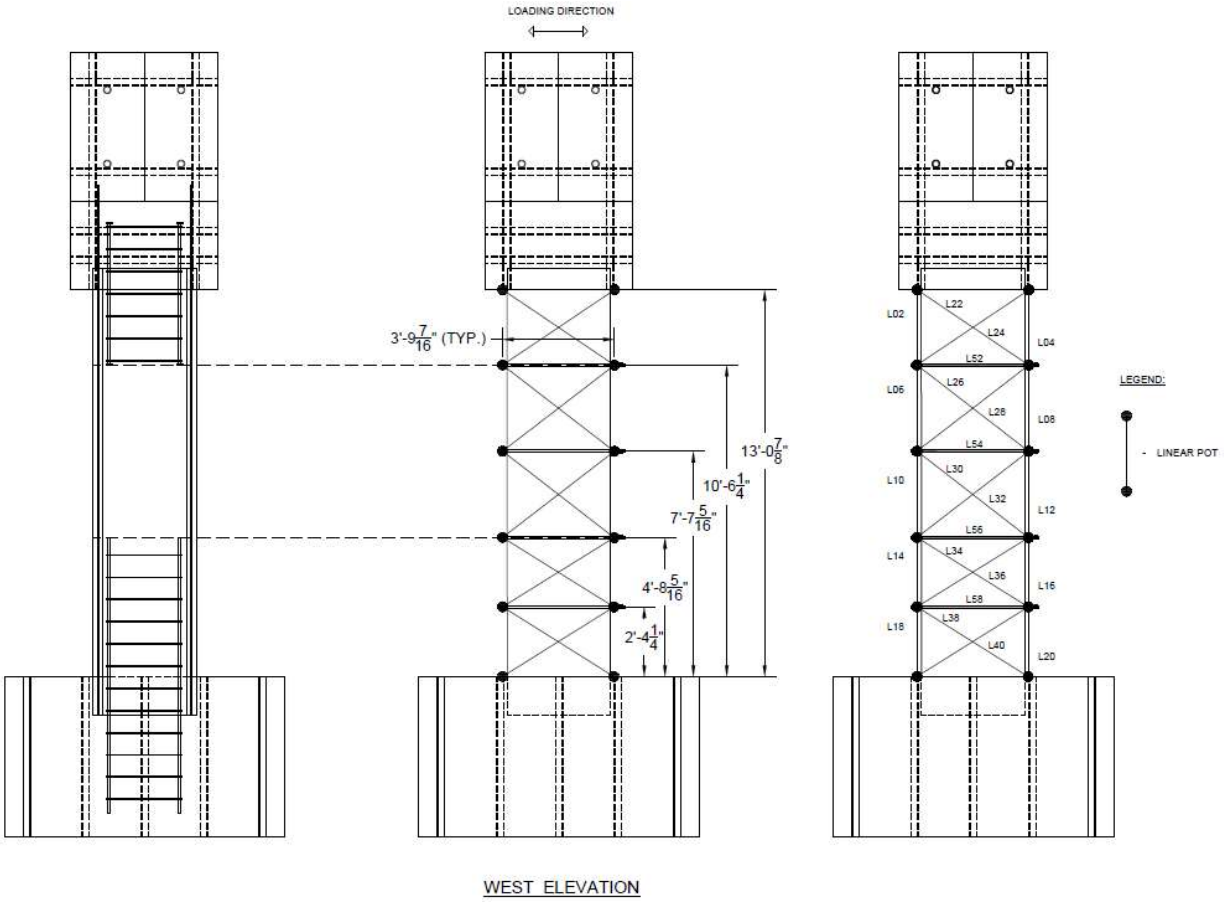

Figure A.8: Linear displacement potentiometers on west side to measure flexural and shear deformations (same for Specimens 1, 2, and 3)

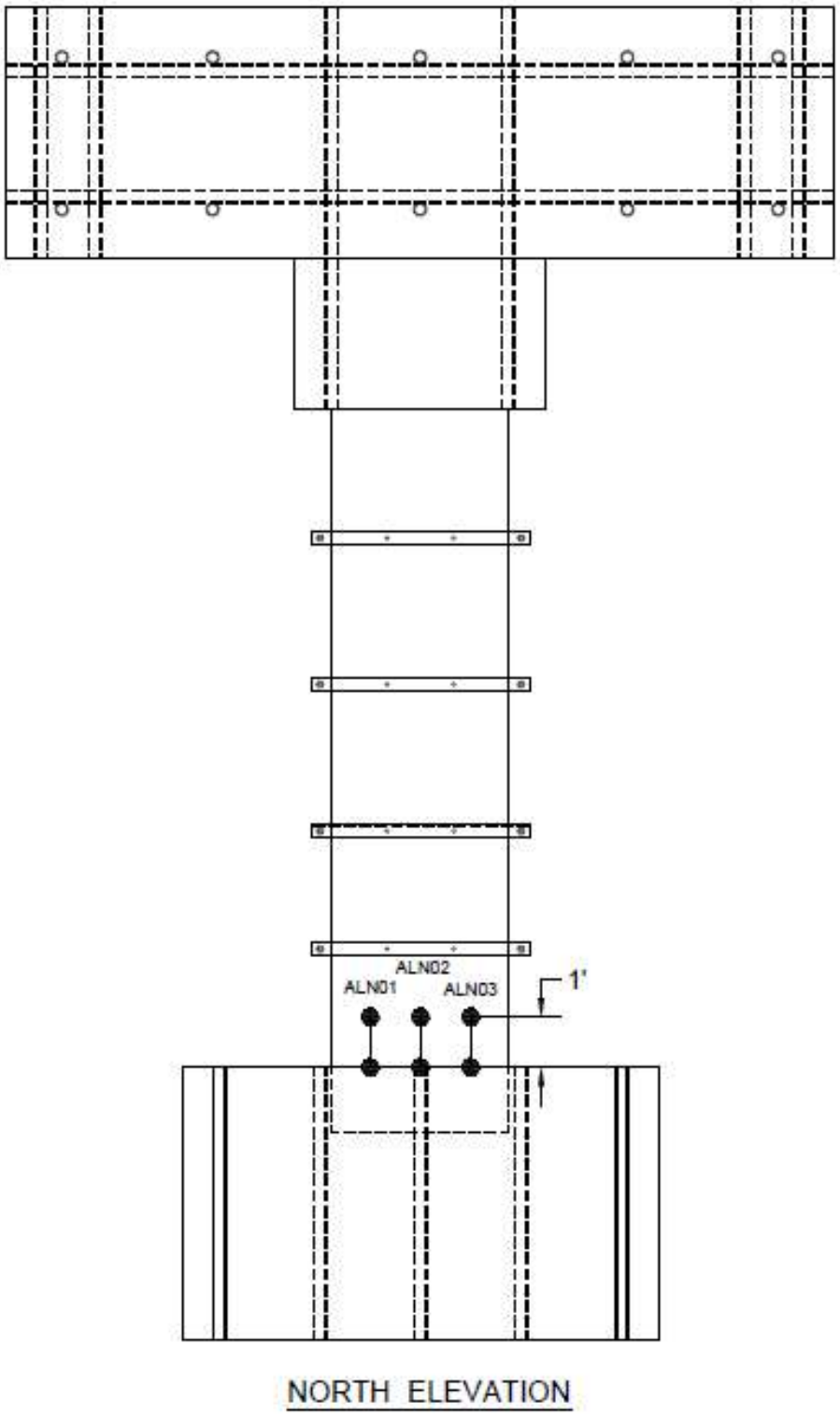

Figure A.9: Linear displacement transducers at interface between pile cap and pile on north side of Specimen 1

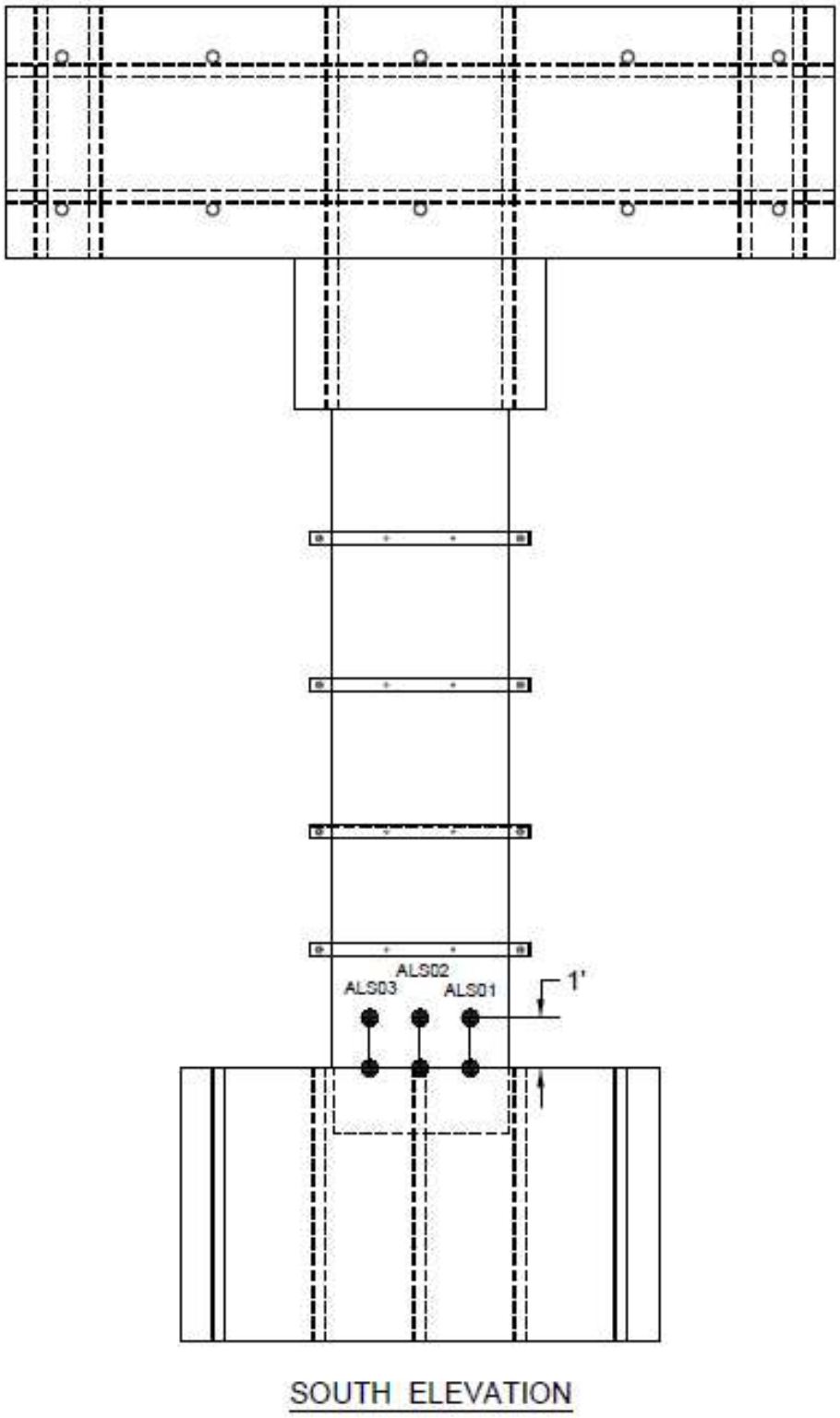

Figure A.10: Linear displacement transducers at interface between pile cap and pile on south side of Specimen 1

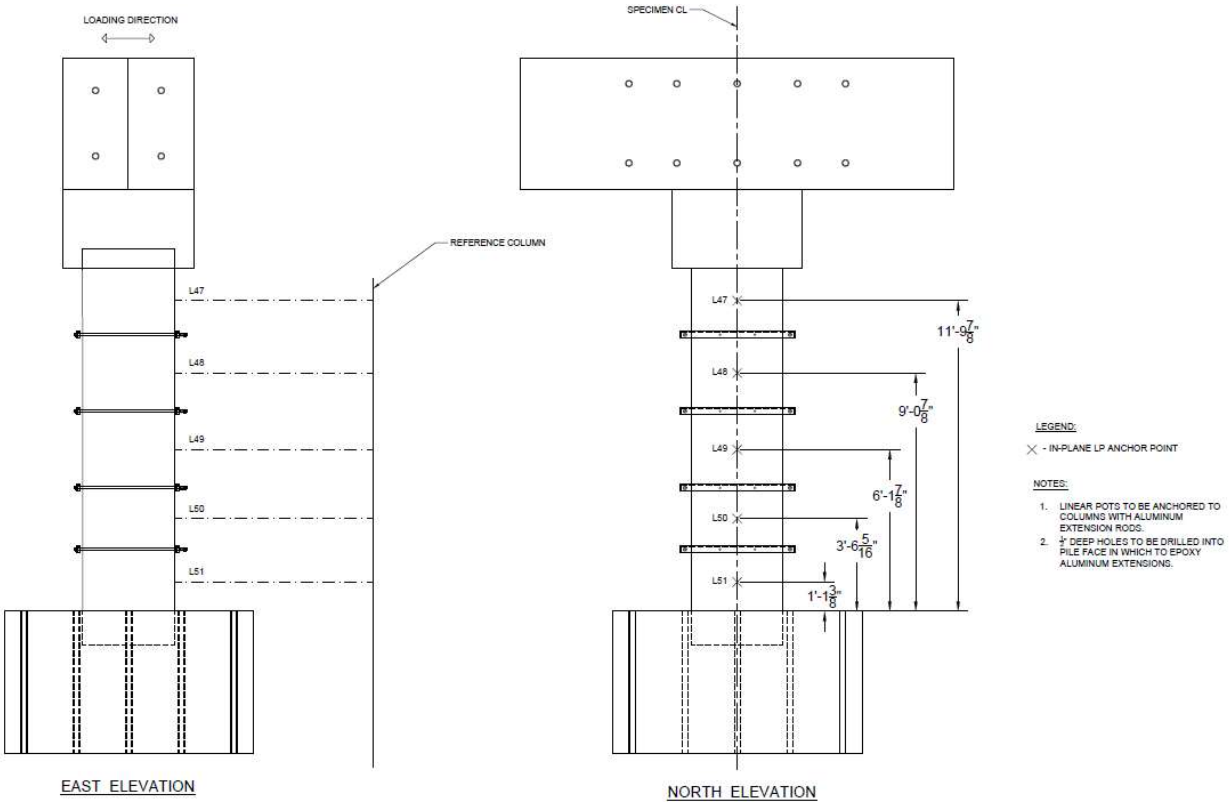

Figure A.11: Linear potentiometers to measure in-plane lateral displacements (same for Specimens 1, 2, and 3)

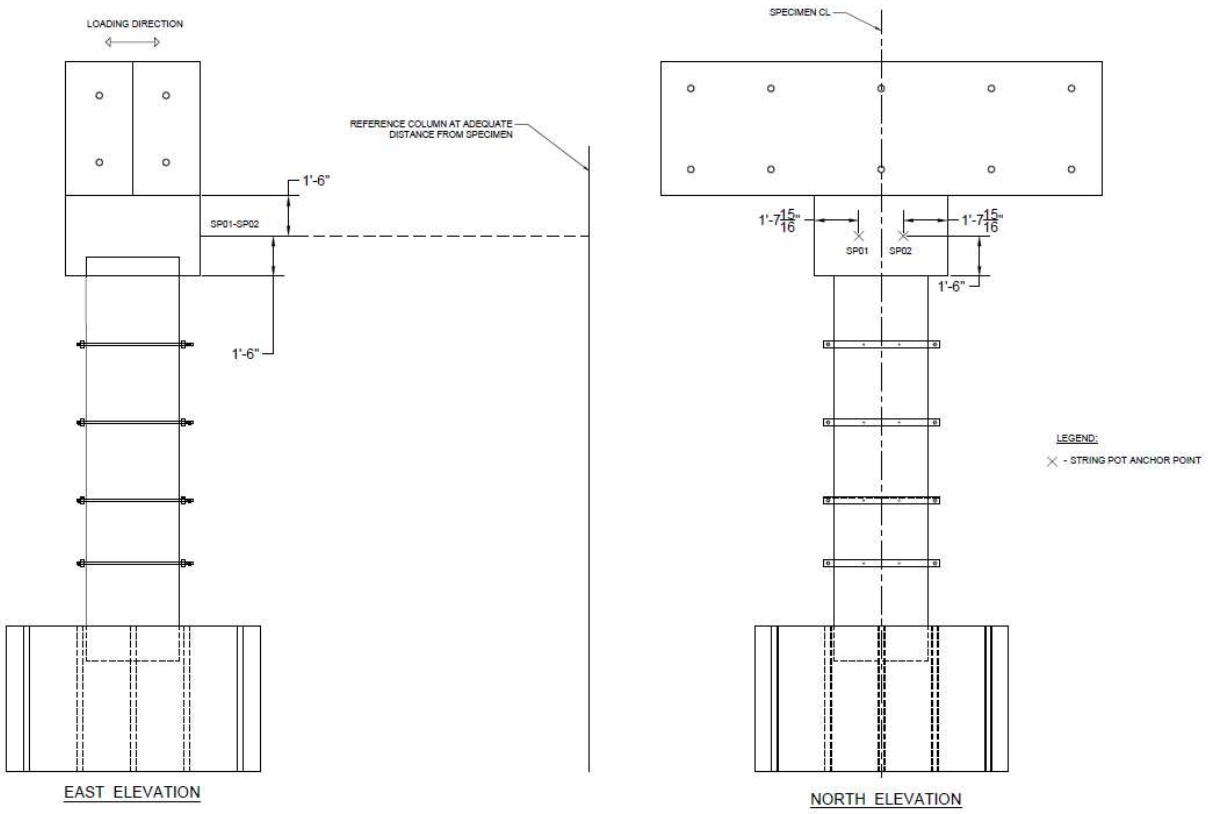

Figure A.12: String potentiometers to measure in-plane lateral displacement at the horizontal actuator level (same for Specimens 1, 2, and 3)

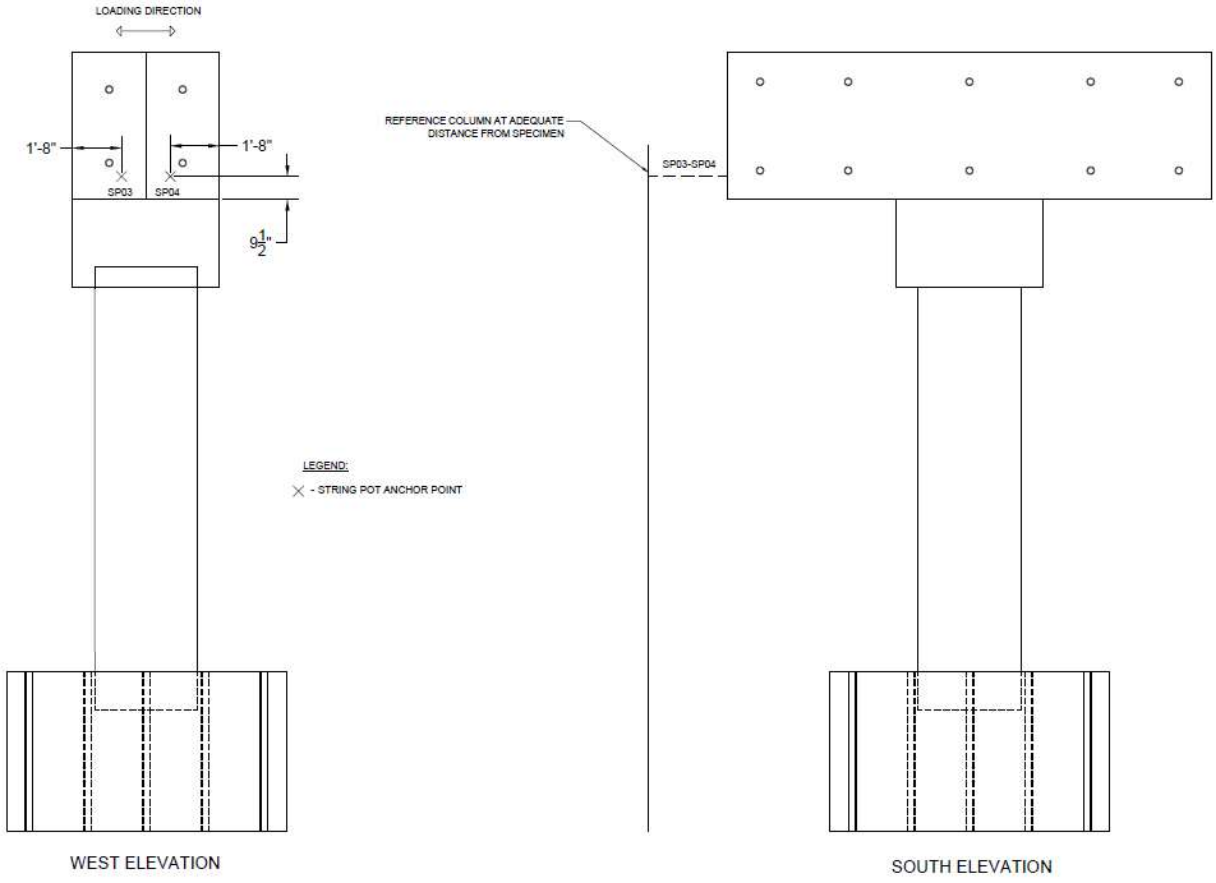

Figure A.13: String potentiometers to measure out-of-plane displacement (same for Specimens 1, 2, and 3)

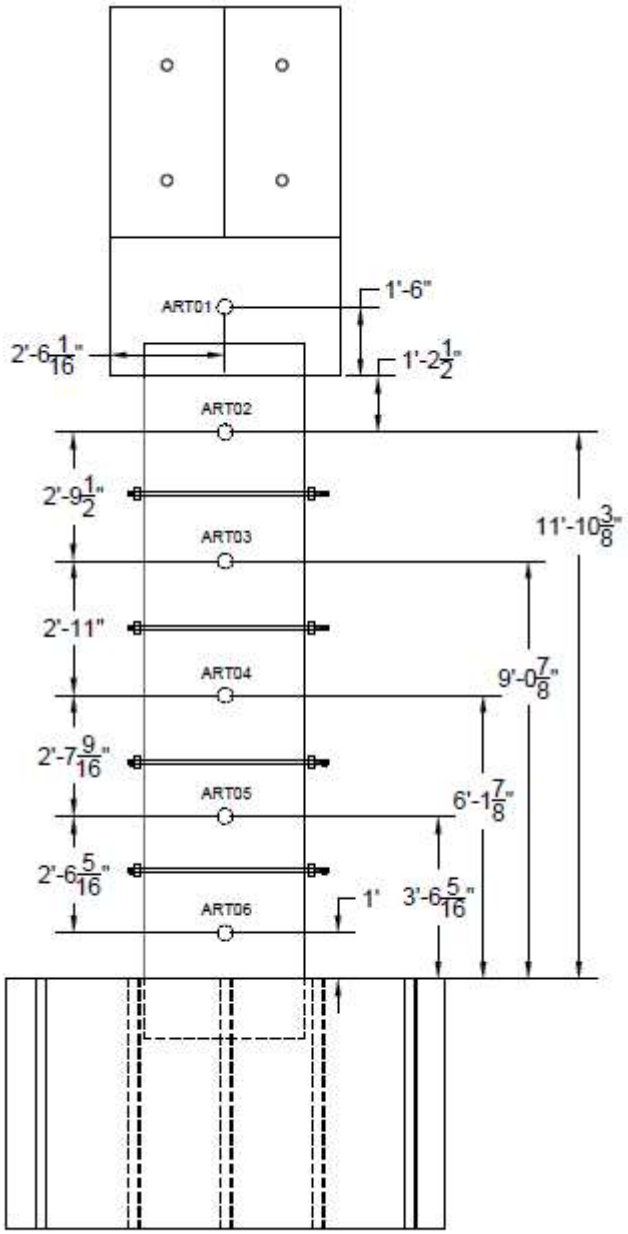

Figure A.14: Inclinometers to measure in-plane rotation (same for Specimens 1, 2, and 3)

A.2 Specimen 2

The external instrumentation drawings for Specimen 2 that are different than Specimen 1 are shown below. The internal instrumentation for Specimen 2 is also shown in this section.

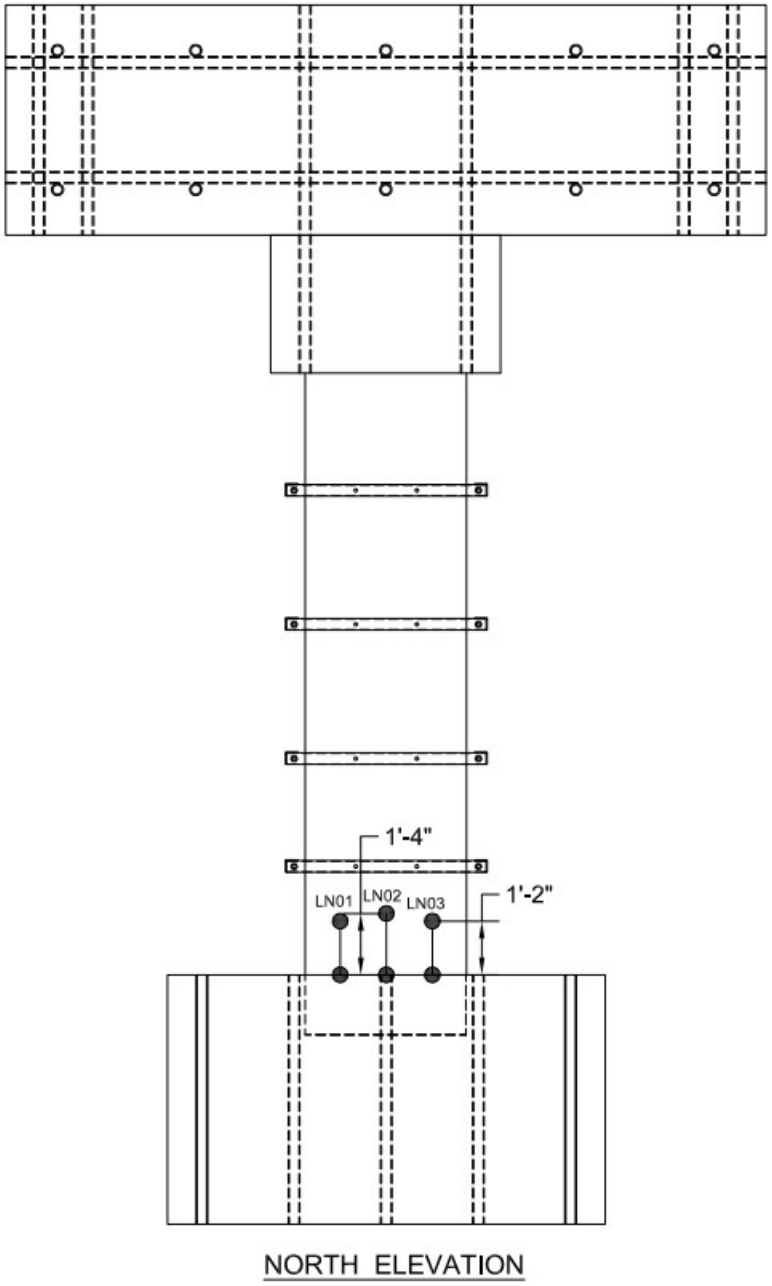

Figure A.15: Linear displacement transducers at interface between pile cap and pile on north of Specimens 2 and 3

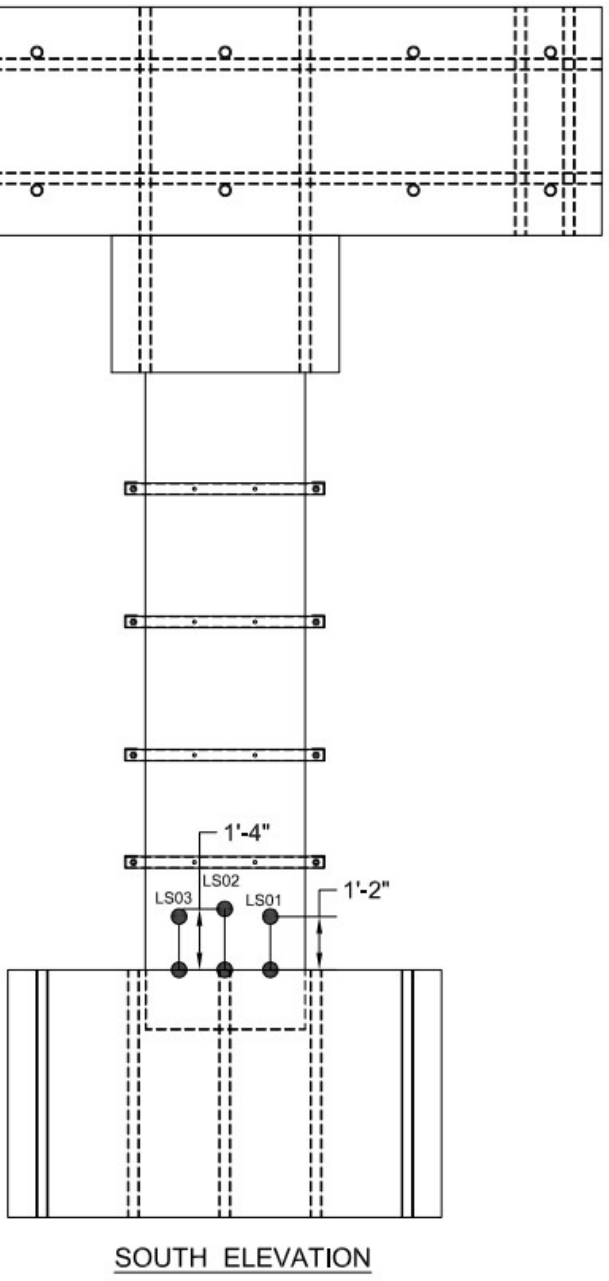

Figure A.16: Linear displacement transducers at interface between pile cap and pile on south of Specimens 2 and 3

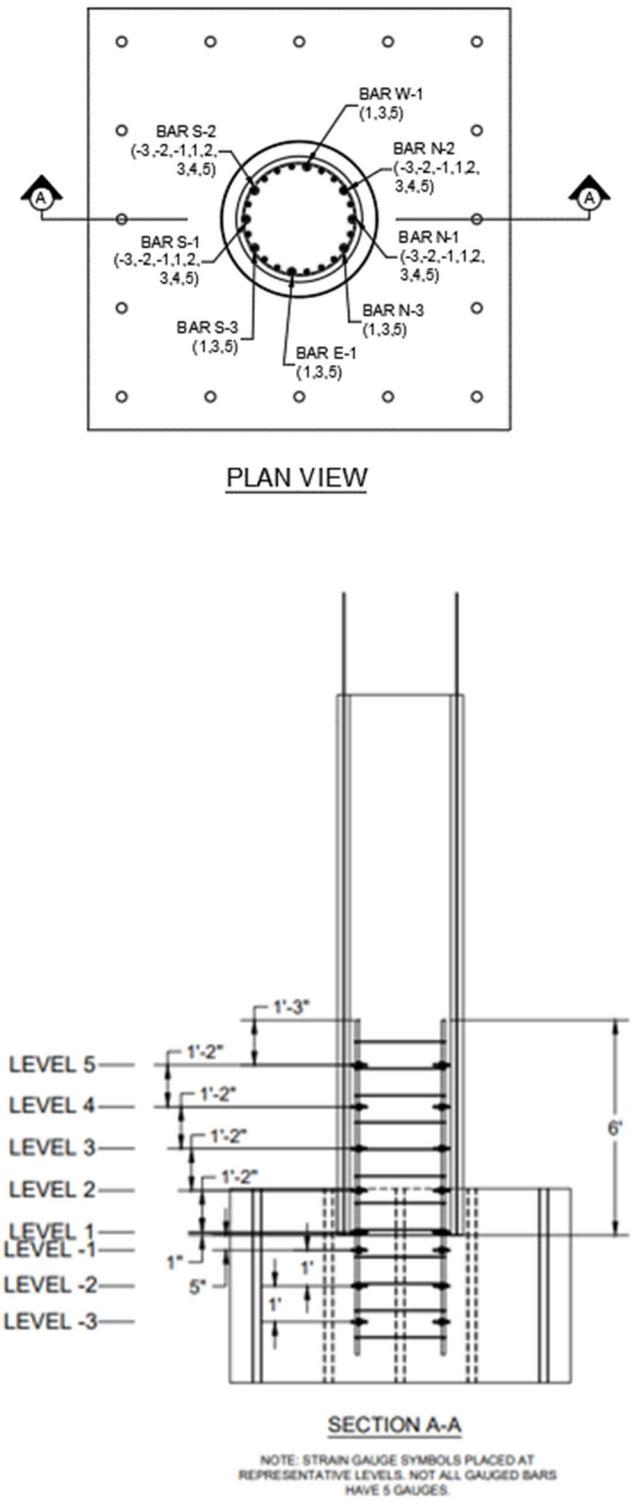

Figure A.17: Strain gauges on core reinforcing bars in Specimen 2 (numbers in parentheses below bar ID number in the plan view indicate the levels at which the gauges were located)

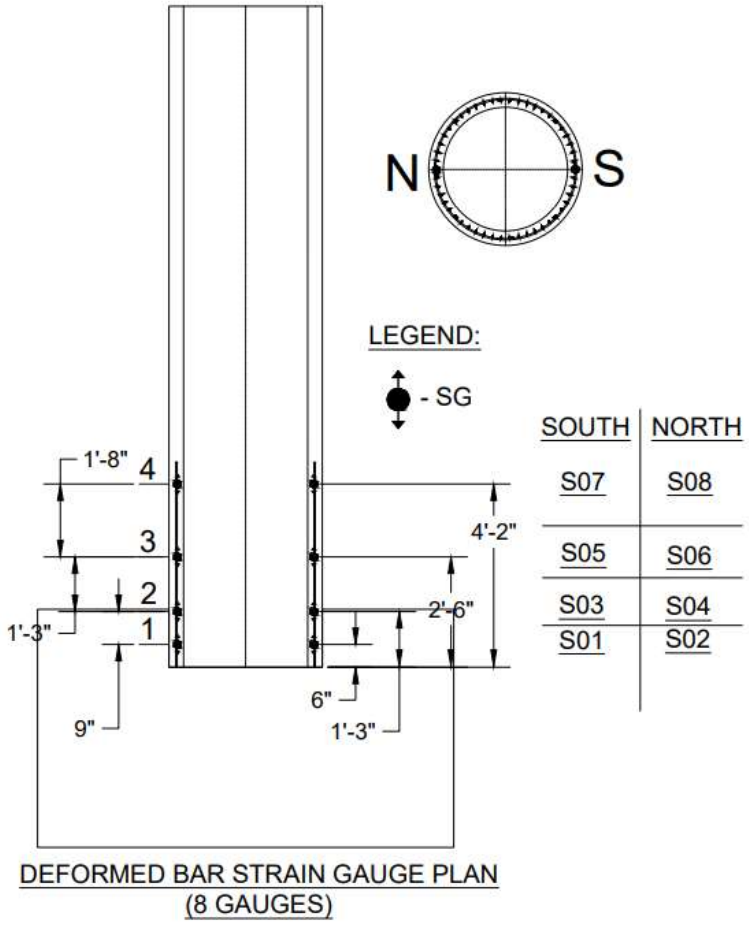

Figure A.18: Strain gauges on longitudinal reinforcing bars in the shell of Specimen 2

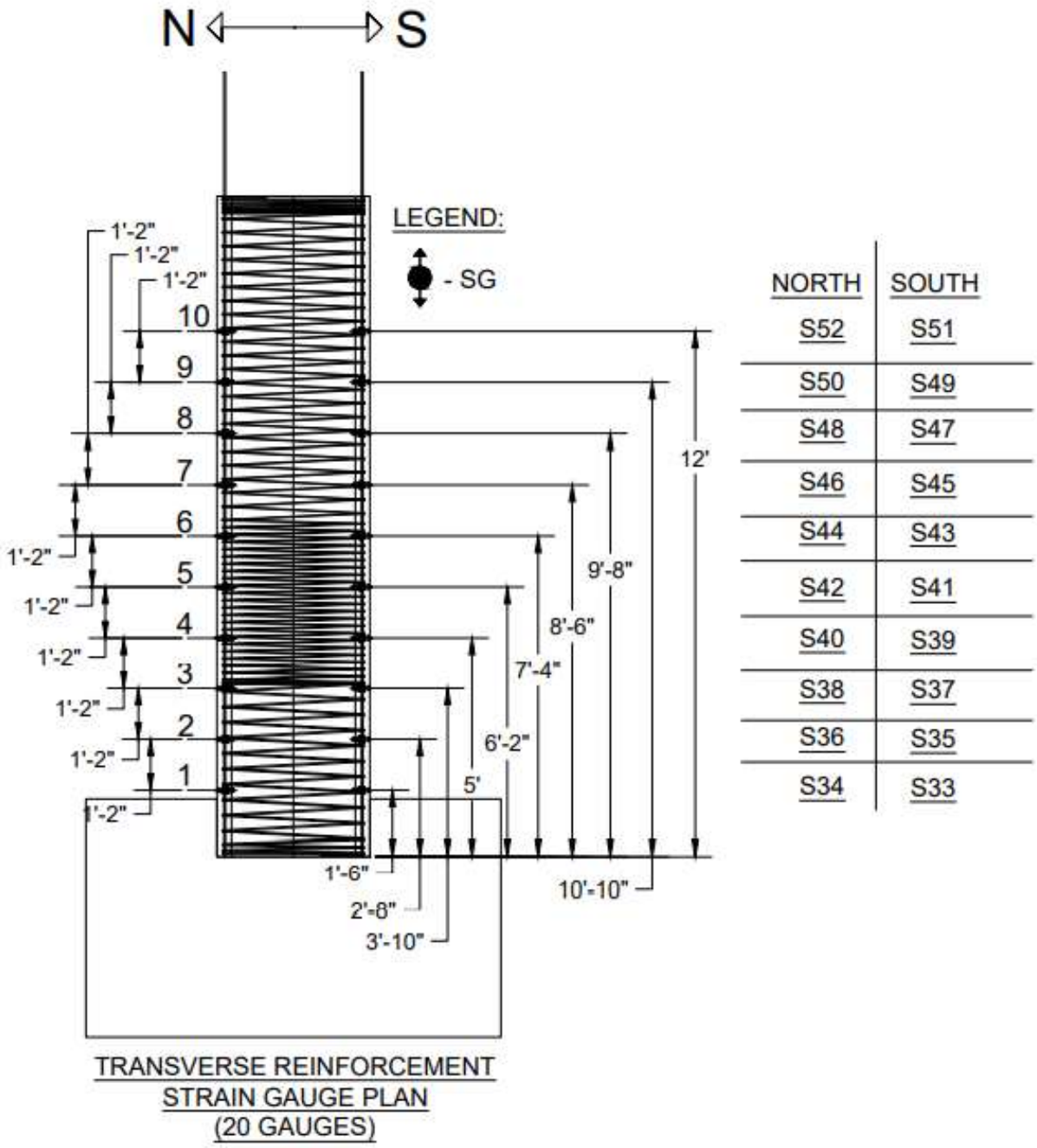

Figure A.19: Strain gauges on transverse reinforcing bars in the shell of Specimen 2

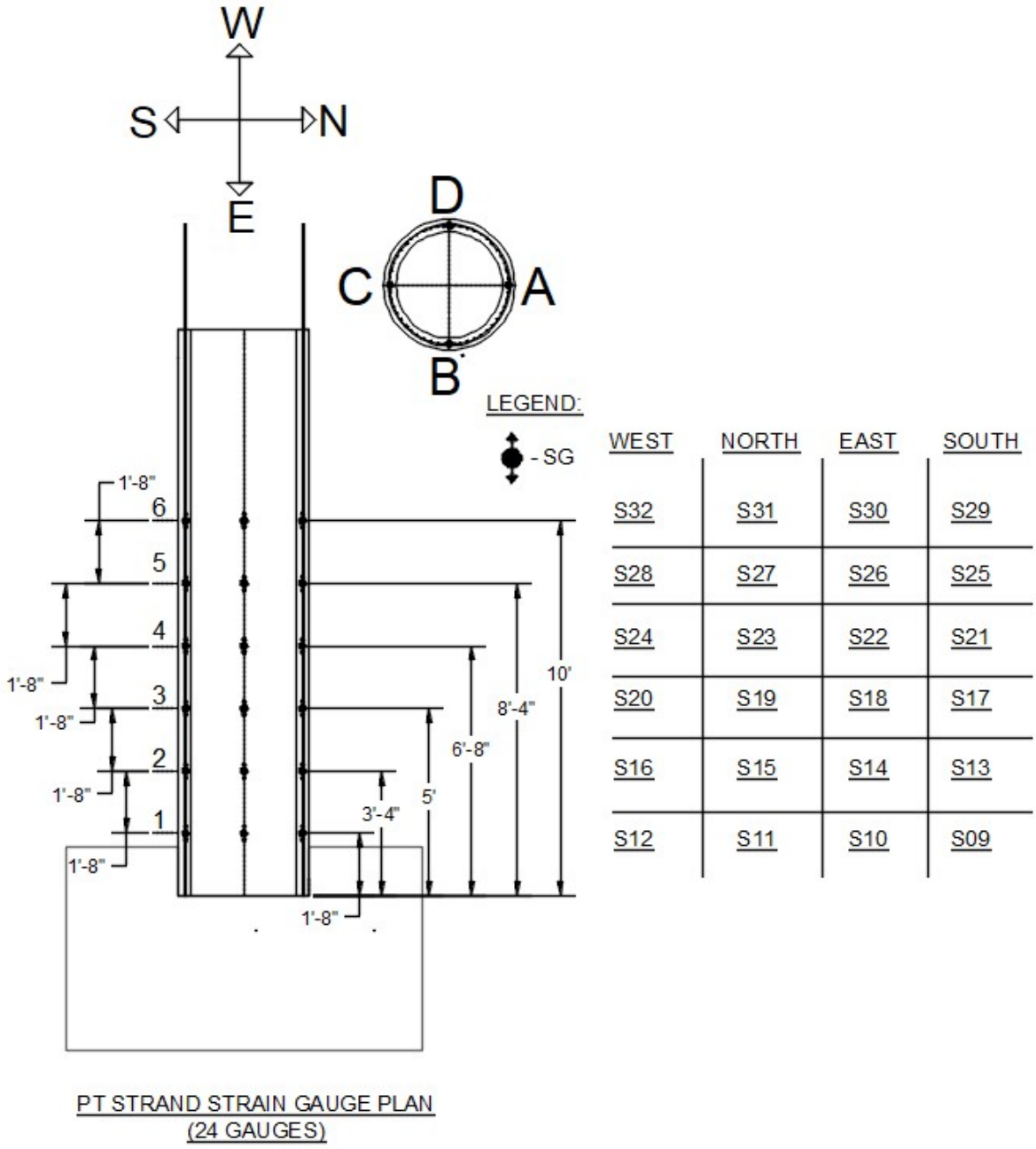

Figure A.20: Strain gauges on prestressing strands in the shell of Specimen 2

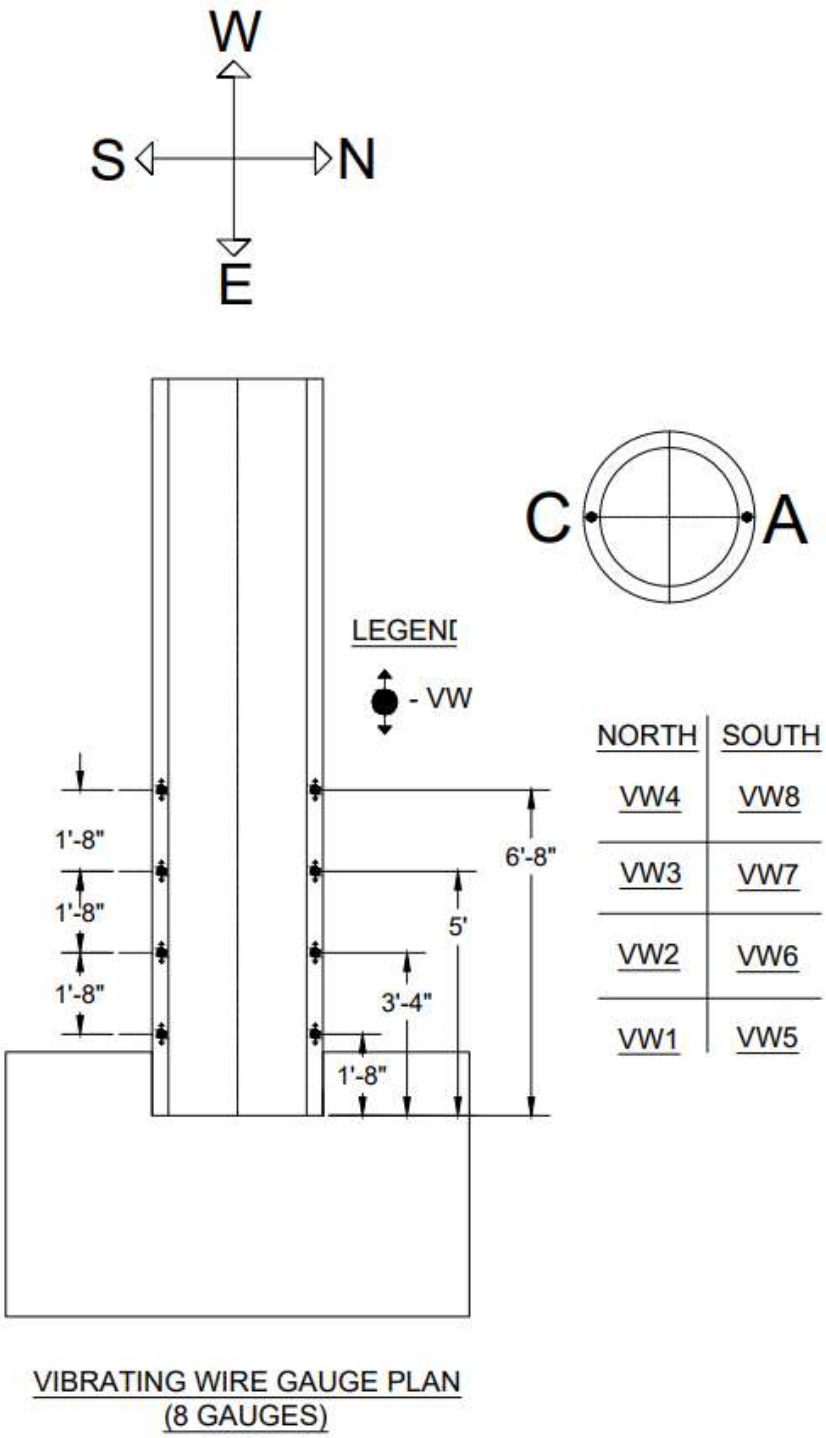

Figure A.21: Vibrating-wire gauges in the shell of Specimen 2

A.3 Specimen 3

The external instrumentation for Specimen 3 was identical to that for Specimen 2. The strain gauge plans for Specimen 3 are shown below. Some of them are identical to those for the first two specimens.

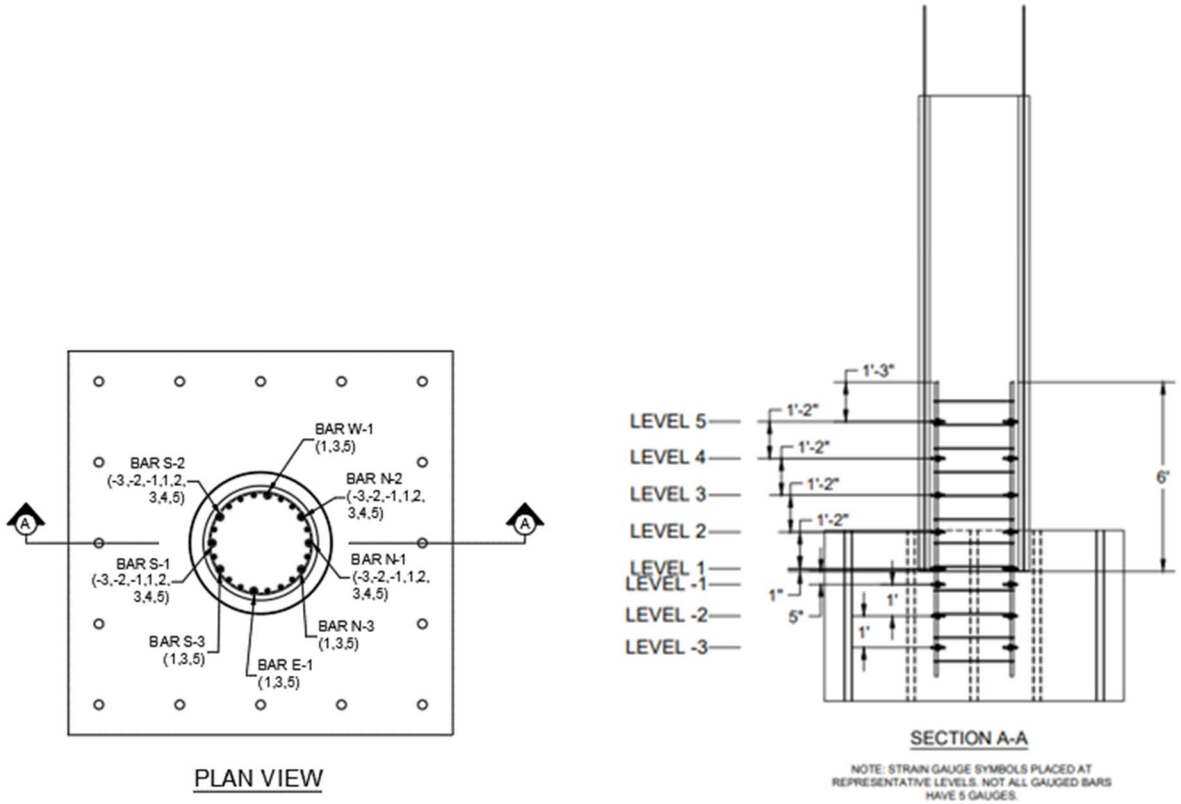

Figure A.22: Strain gauges on core reinforcing bars in Specimen 3 (numbers in parentheses below bar ID number in the plan view indicate the levels at which the gauges were located)

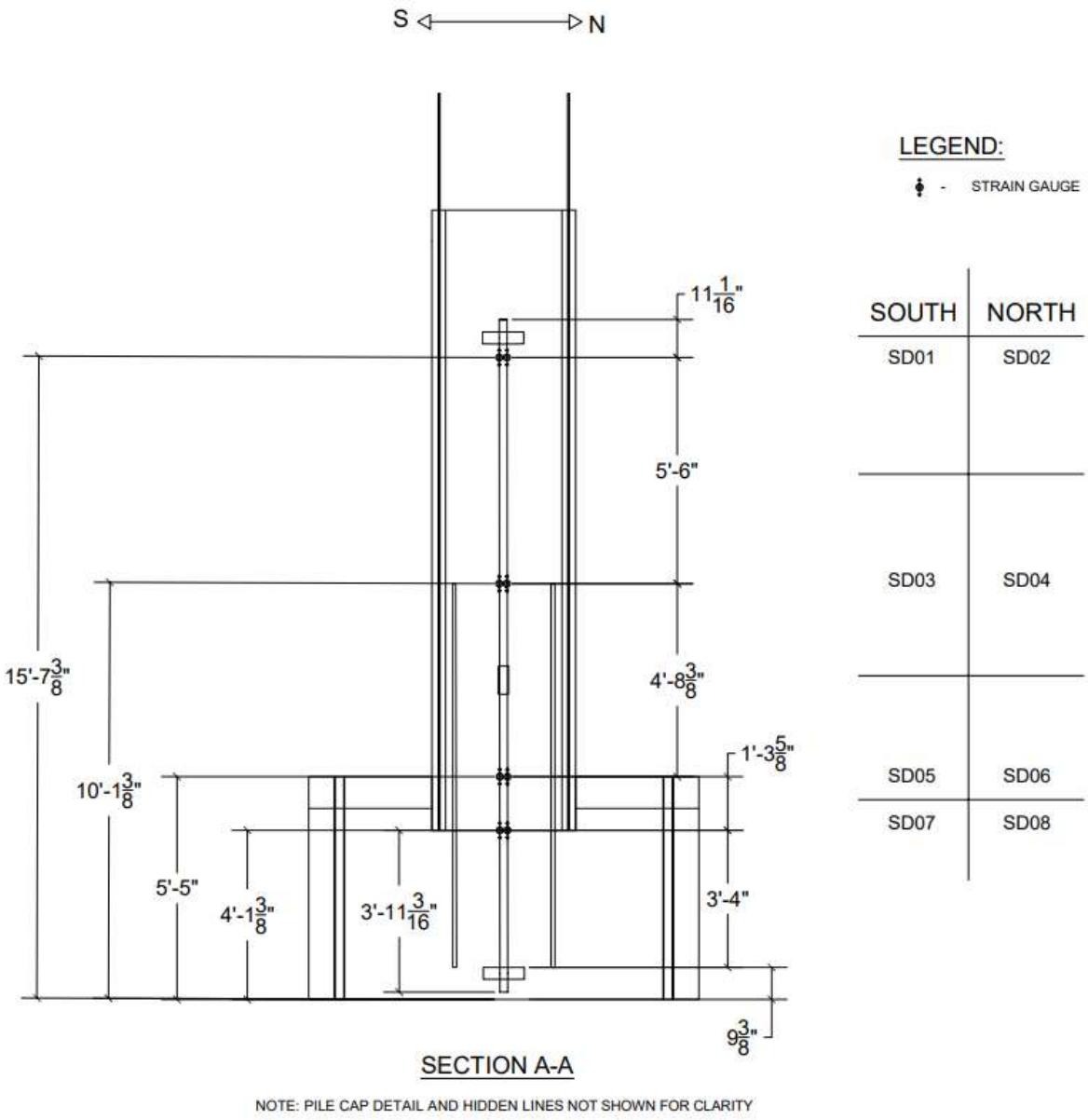

Figure A.23: Strain gauges on DYWIDAG bar in Specimen 3

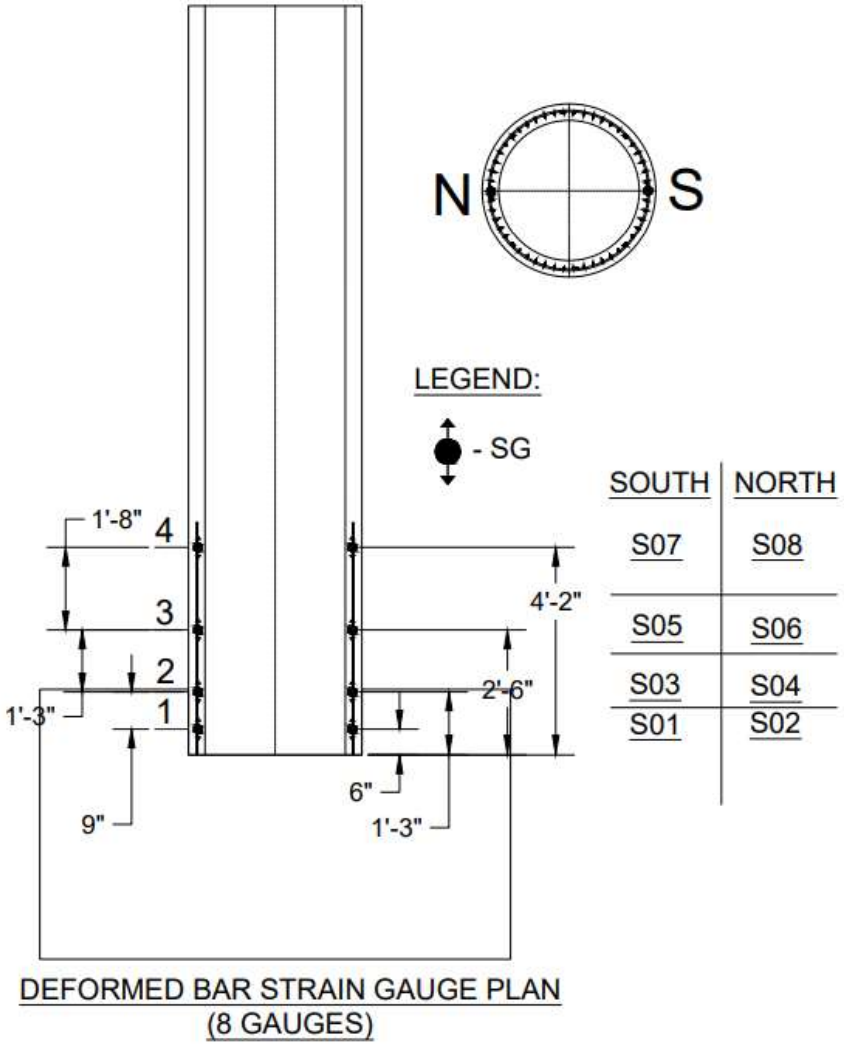

Figure A.24: Strain gauges on longitudinal reinforcing bars in the shell of Specimen 3

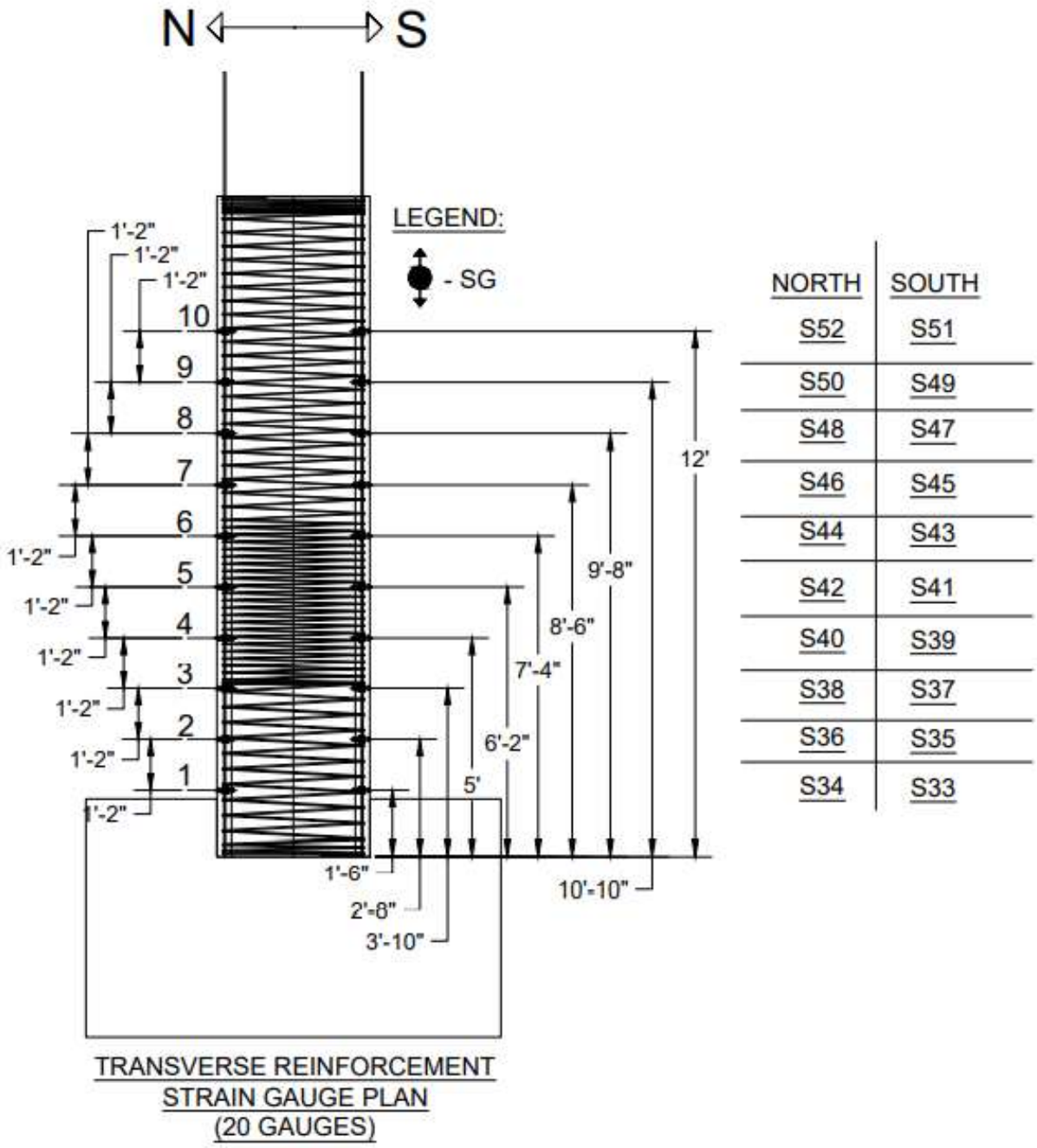

Figure A.25: Strain gauges on transverse reinforcing bars in the shell of Specimen 3

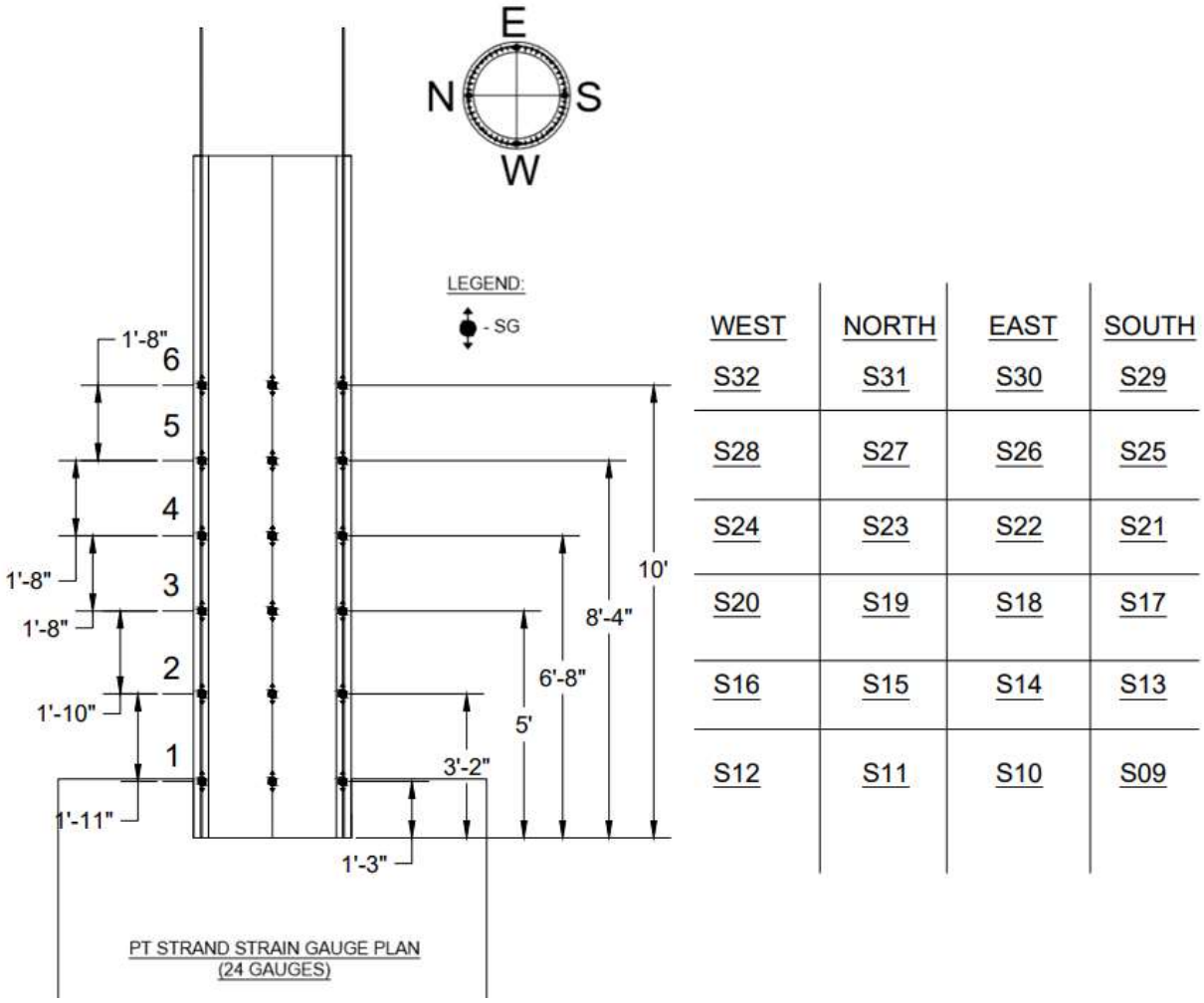

Figure A.26: Strain gauges on prestressing strands in the shell of Specimen 3

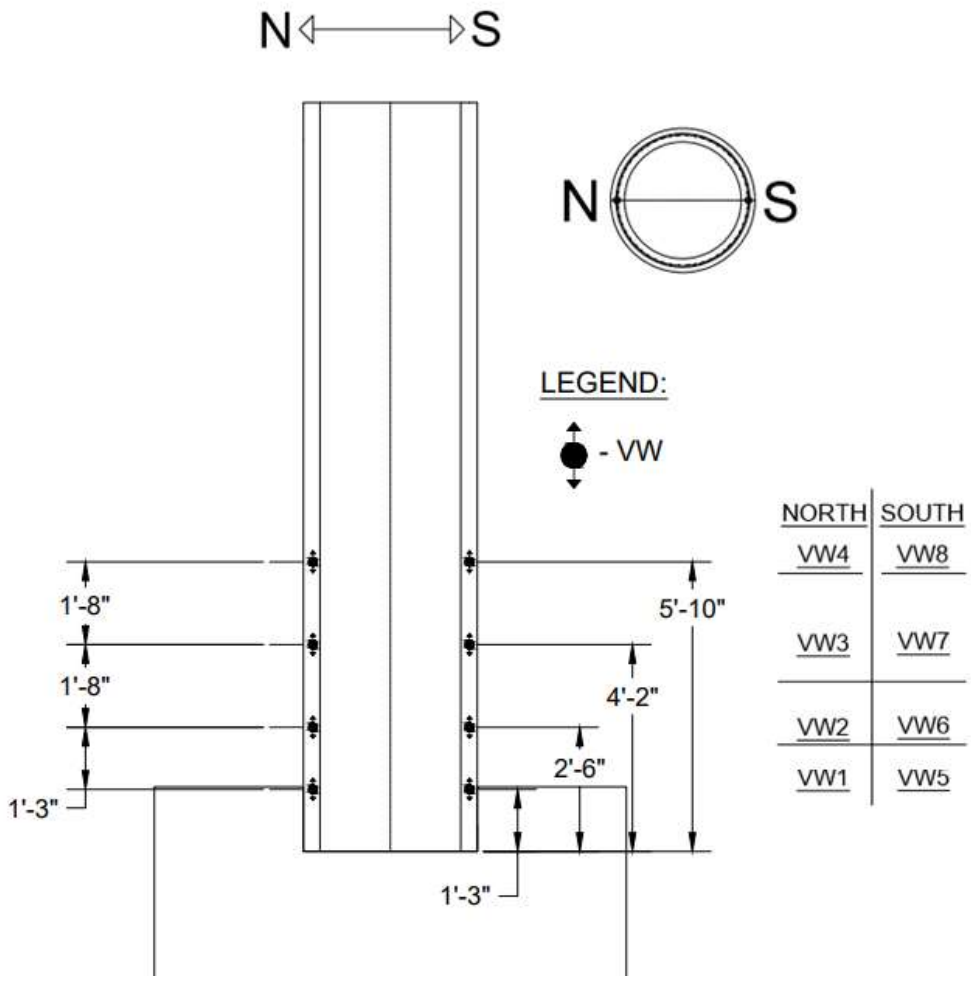

Figure A.27: Vibrating-wire gauges in the shell of Specimen 3

Appendix B Strain Measurements During Fabrication of Precast Shells

Data collected from strain gauges and vibrating-wire (VW) gauges during the fabrication of the precast shells are presented and analyzed in this appendix. Strain gauges were attached to prestressing strands, transverse reinforcement, and longitudinal rebars inside the precast shells, and VW gauges were mounted on the steel cages to measure concrete strains in the longitudinal direction of the shells. The locations of these gauges are shown in Chapter 3. Strain data were collected during the prestressing process and also during stress transfer.

The compressive strength of the concrete specified for the precast shells was 7,000 psi, and the strength at stress transfer was specified to be 4,500 psi. Each shell had a cross-sectional area (A_c) of 478 in.^{2}. There were 50 Grade-270, 3/8-in.-diameter, seven-wire strands in each shell, with the total strand cross-sectional area (A_p) equal to 4.25 in.^{2}. The jacking stress (f_{pj}) was specified to be 189 ksi, with the effective prestress at the time the specimens were tested targeted at 153 ksi. From the stress-strain curves shown in Figure 3.14, the modulus of elasticity (E_p) of the strands was measured to be 30,000 ksi. Based on the formula in ACI 318 (2019) and the concrete compressive strength of 4,500 psi, the modulus of elasticity of the concrete at stress transfer (E_{ci}) was estimated to be 3,824 ksi. The initial prestress (f_{pi}) right after stress transfer and the elastic-shortening loss can be calculated with the following formula.

$$f_{pi} = \frac{f_{pj}}{1+\alpha} \tag{B.1}$$

where

$$\alpha = \frac{E_p A_p}{E_{ci} A_c} \tag{B.2}$$

With Equations (B.1) and (B.2) and the target jacking stress of $f_{pj} = 189$ ksi, the initial prestress f_{pi} was estimated to be 177 ksi, based on the above material properties. The actual jacking stress and initial prestress attained for each shell specimen were estimated from the strain data collected during the shell fabrication as discussed in the following sections.

According to ACI 318, the stress transfer length required for the strands right after stress transfer can be calculated with the following equation.

$$l_t = \frac{f_{pi}}{3000} d_b \tag{B.3}$$

in which the effective prestress in the ACI formula is replaced by the initial prestress f_{pi} and d_b is the nominal strand diameter. The units are in pounds and inches. Hence, for $f_{pi} = 177$ ksi and $d_b = 3/8$ in., $l_t = 22$ in.

B.1 Specimen 1

The shell of Specimen 1 had 52 strain gauges and 8 VW gauges installed. However, during the pre-tensioning, 3 VW gauges and 19 of the 24 strain gauges on the strands did not work.

Figure B.1 shows strain readings from the north and east strands during the pre-tensioning and stress transfer, provided by the surviving gauges. During the pre-tensioning, the strands were tensioned in a random pattern. An initial jacking force was applied to the strands to make them taut prior to applying the full jacking force. The initial jacking force was approximately 20% of the final jacking force. Once all the strands were fully tensioned, the shell was cast and left to steam cure for one day before stress transfer. At the end of the curing period, the strands were torched to transfer the stress to the shell.

As Figure B.1 shows, the tensile strains measured at the end of the jacking process vary from 0.0057 to 0.0066, with the higher values registered by gauges closer to the shell tip that was to be connected to the pile cap. The average tensile strain is calculated to be 0.006, which corresponds to a jacking stress (f_{pj}) of 180 ksi. Figure B.1 shows that the average strain decrease during the stress transfer is about 0.00045. Some gauges registered lower strains than the others at the beginning, probably due to gauge zeroing issues. However, the strain drop during the stress transfer does not appear to depend on the distance of the gauge from the shell tip. Assuming that the strain decrease was entirely due to elastic shortening, the elastic shortening loss is estimated to be 14 ksi. Based on the above estimates, the initial prestress (f_{pi}) is calculated to be 166 ksi. With the values of f_{pj} and f_{pi} estimated from the strain data and E_p = 30,000 ksi, the value of E_{ci} calculated with Equations (B.1) and (B.2) is 3,163 ksi, which is a little lower than that estimated with the ACI 318 formula based on 4,500-psi concrete strength.

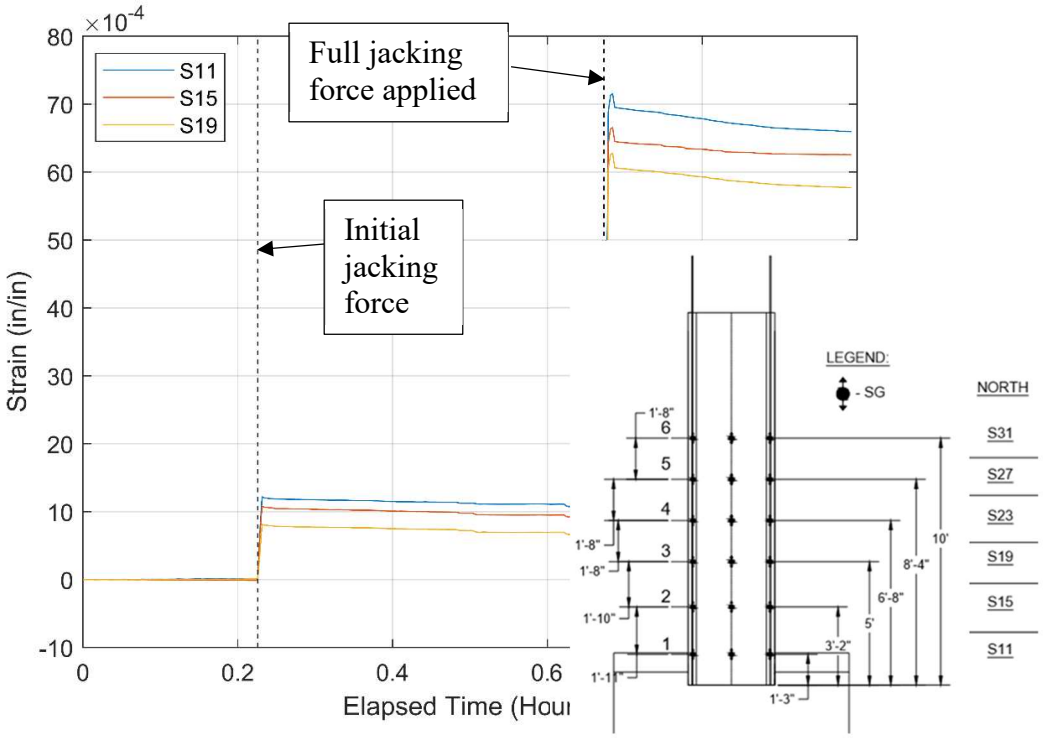

(a) North strand during pre-tensioning

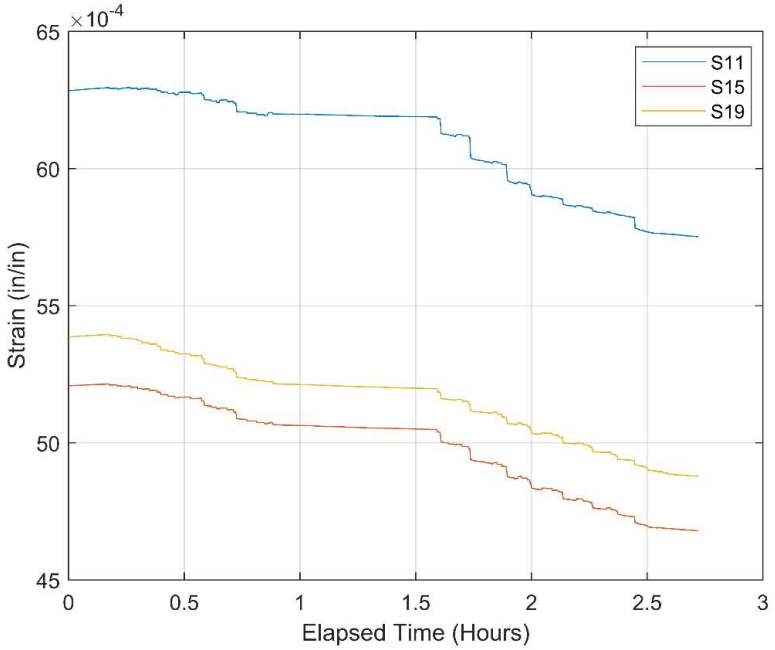

(b) North strand during stress transfer

Figure B.1: Strain data from prestressing strands for Specimen 1

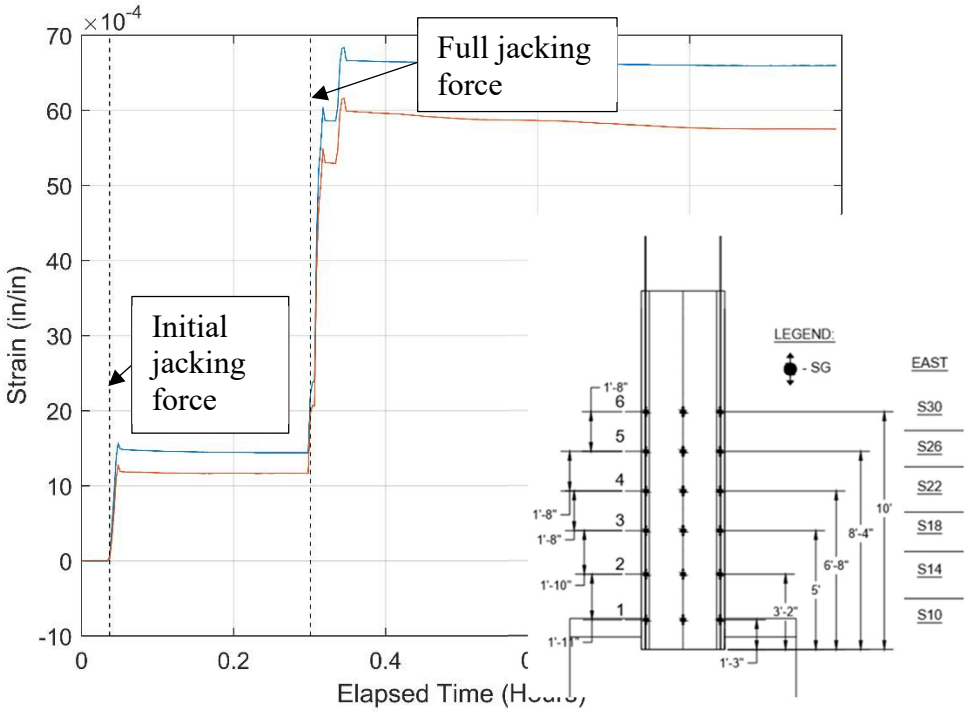

(c) East strand during pre-tensioning

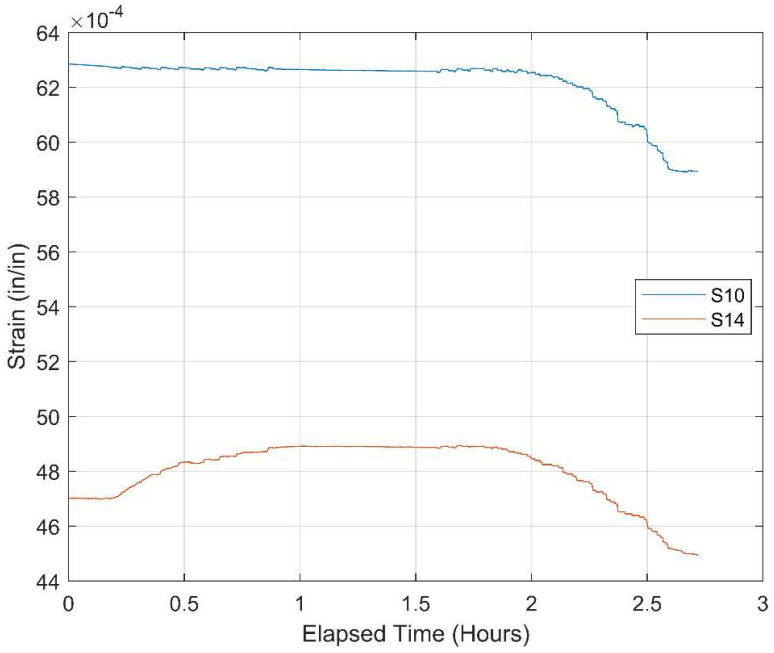

(d) East strand during stress transfer

Figure B.1 (continued): Strain data from prestressing strands for Specimen 1

Figures B.2 shows the VW strain data versus time obtained during the stress transfer. Figure B.3 shows the average strain data at each elevation. Unfortunately, because of the malfunctioning of 3 VW gauges, only readings from VW1 and VW5 can be averaged. In general, it can be observed that the compressive strains registered by the gauges farther away from the shell tip are higher than those from closer gauges, probably because the strands slipped more near the shell tip. Gauges VW1, VW5, and VW6 were within the stress transfer region of the shell, calculated with Equation (B.3). The highest compressive strain registered by VW4 at the end of the stress transfer is 0.00075, which is a bit higher than the strain decrease measured in the strands during the stress transfer.

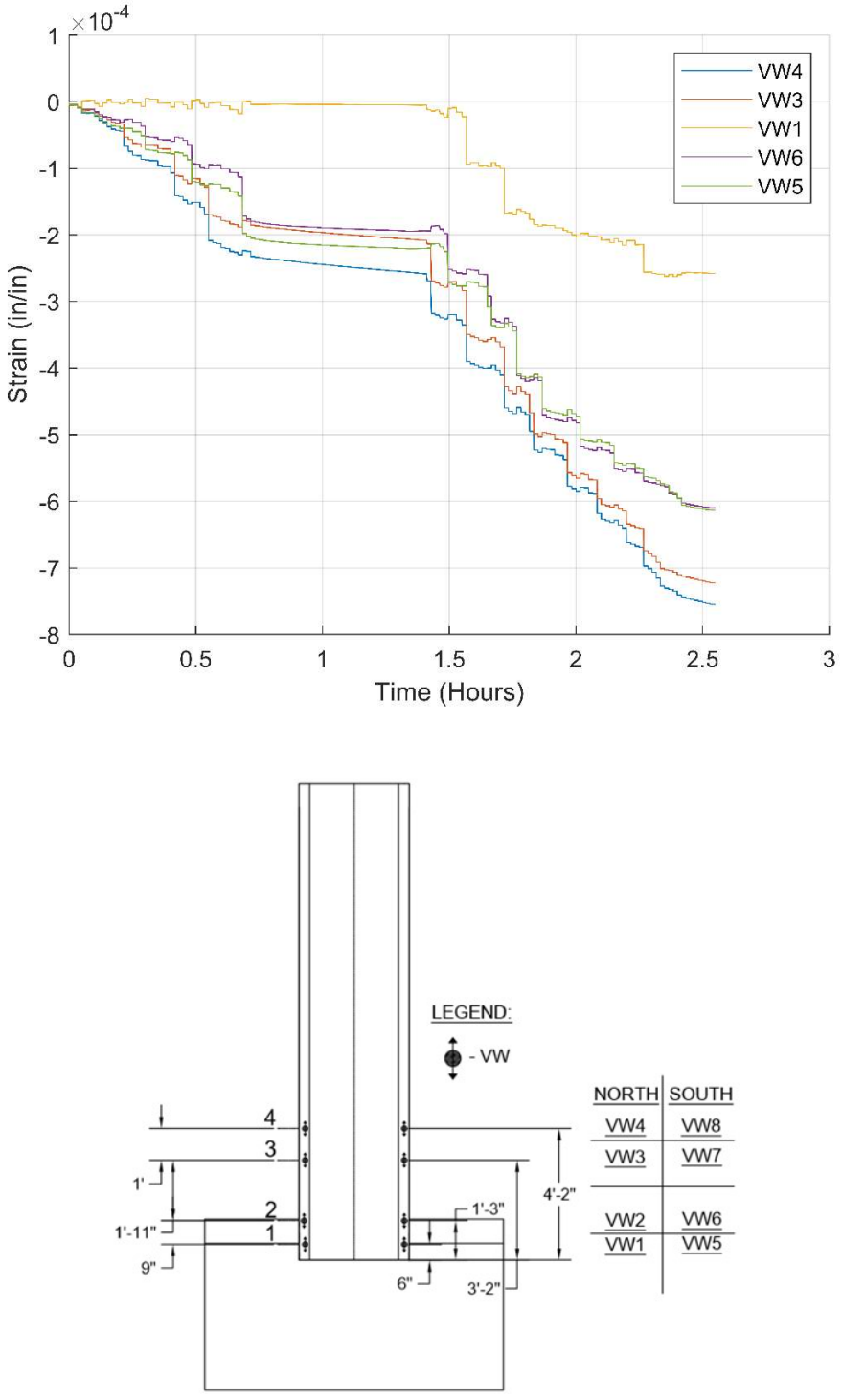

Figure B.2: VW gauge data during stress transfer for Specimen 1

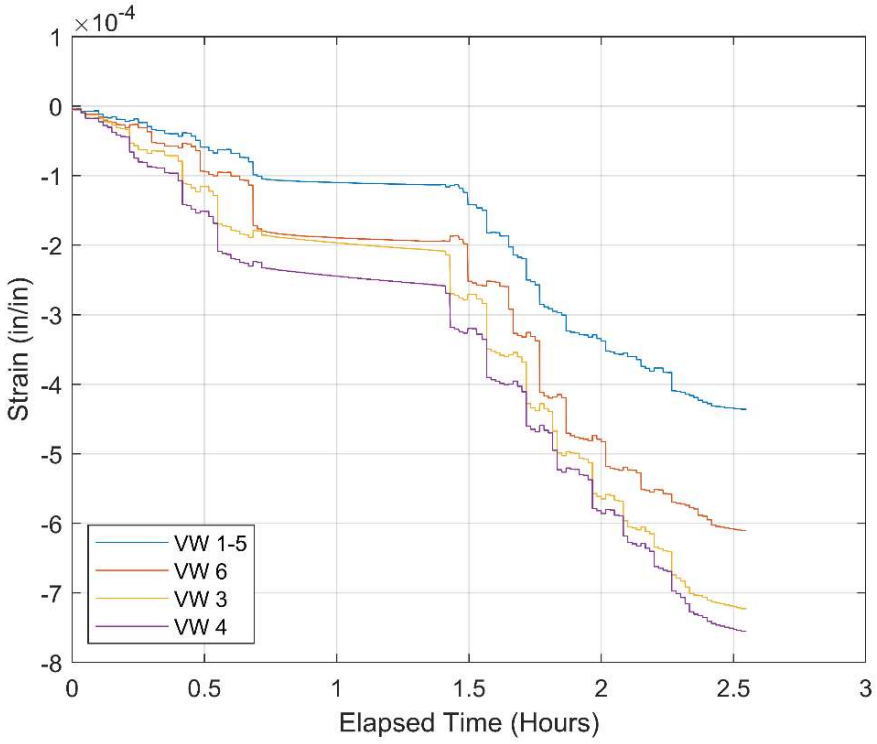

Figure B.3: Average VW gauge data at each elevation during stress transfer for Specimen 1

Figure B.4 shows the strains measured during the stress transfer by strain gauges attached to longitudinal bars in the shell. The maximum average compressive strain measured by gauges S07 and S08 at the end of the stress transfer is about 0.0006.

Figure B.5 shows the strains measured during the stress transfer by gauges attached to the transverse reinforcement. In general, the gauges registered small tensile strains, which are consistent with the Poisson effect as the concrete shell was subjected to axial compression during the stress transfer.

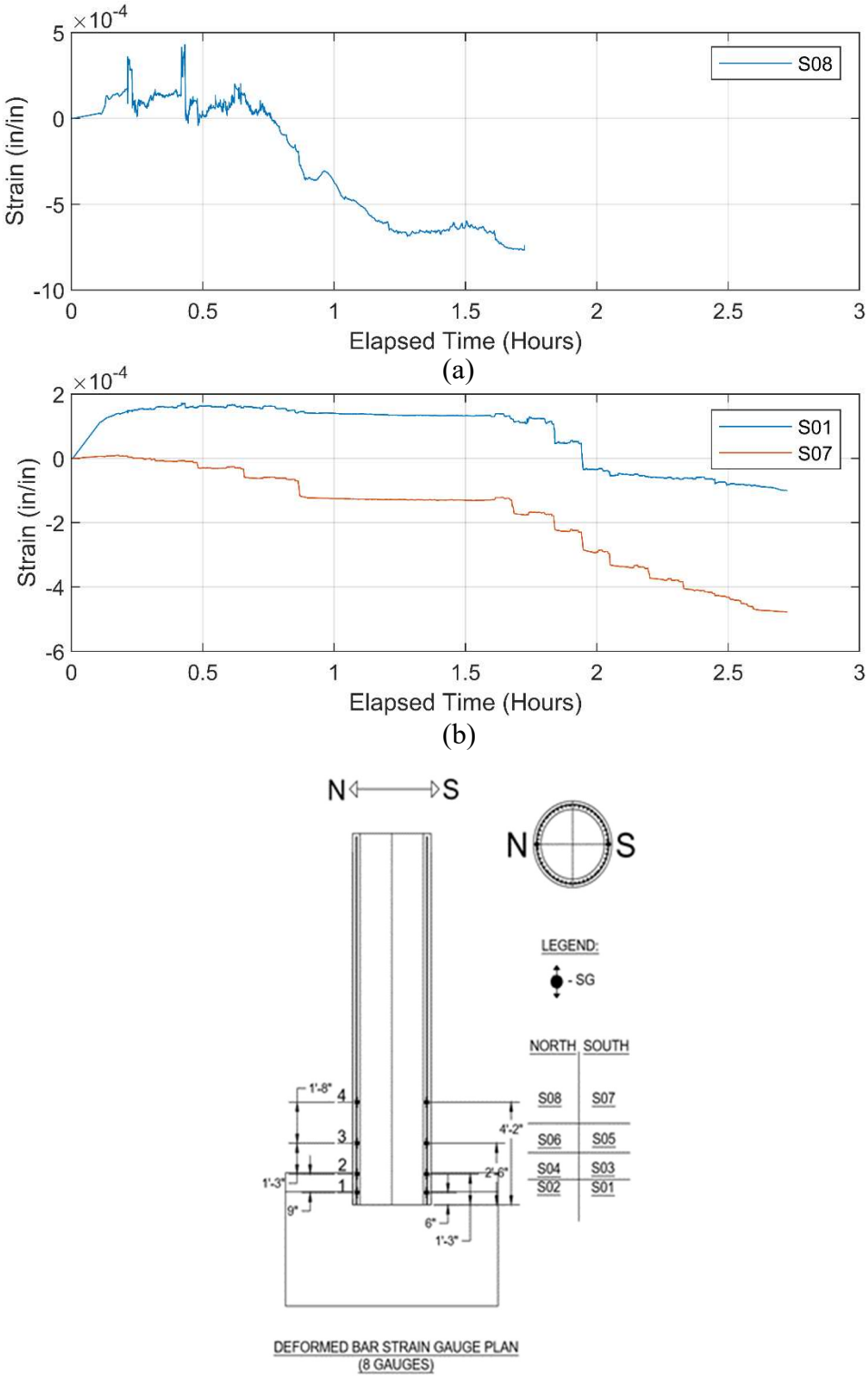

Figure B.4: Strain gauge data during stress transfer from (a) north longitudinal bar; (b) south longitudinal bar for Specimen 1

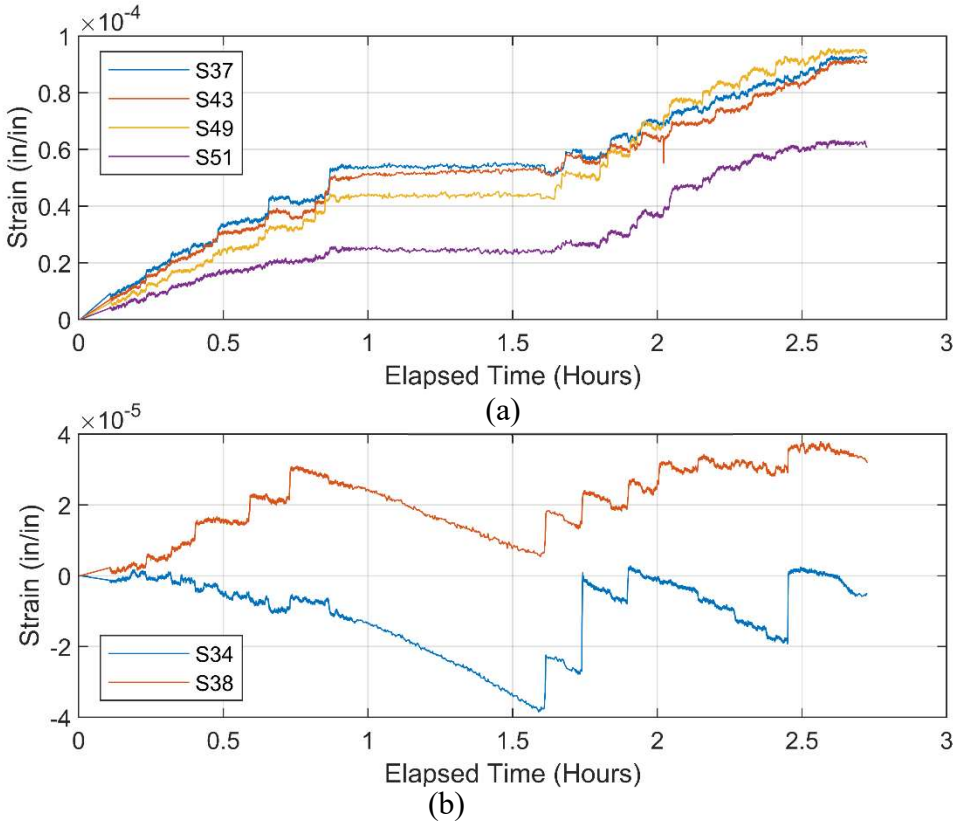

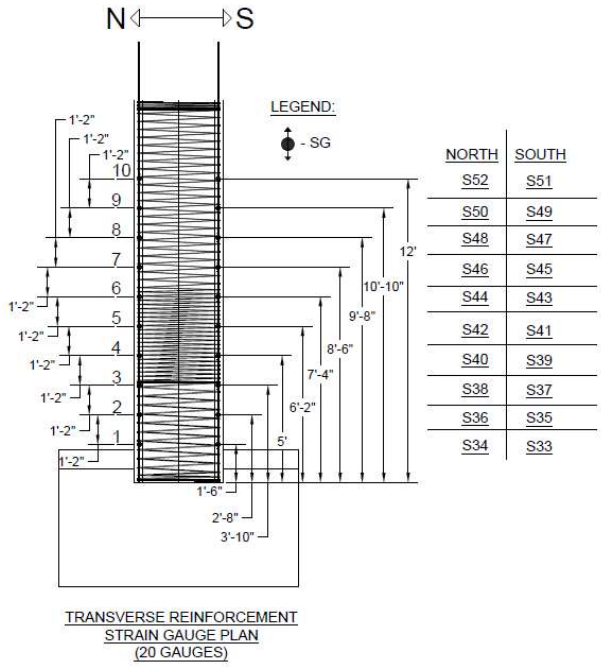

Figure B.5: Strain gauge data from transverse reinforcement during stress transfer for Specimen 1: (a) south side; (b) north side

B.2 Specimen 2

The shell of Specimen 2 had a similar instrumentation scheme as Specimen 1. All 8 VW gauges installed were working during the stress transfer, but 15 of the 24 strain gauges on the strands broke. The strands in this specimen were unbonded over a distance of 31.5 in. from the pile tip.

Figure B.6 shows strain readings from the west, north, east, and south strands during the pre-tensioning and stress transfer, provided by the surviving gauges. The average tensile strain measured at the end of the jacking process is about 0.006, which is the same as that for Specimen 1. This corresponds to a jacking stress (f_{pj}) of 180 ksi. For this specimen, the variation of the strain values with the gauge locations does not show a consistent trend. Figure B.6 shows that the average strain decrease during the stress transfer is about 0.0005. Assuming that the strain decrease was entirely due to elastic shortening, the elastic shortening loss is estimated to be 15 ksi. Based on the above estimates, the initial prestress (f_{pi}) is 165 ksi. With the values of f_{pj} and f_{pi} estimated from the strain data and E_p = 30,000 ksi, the value of E_{ci} calculated with Equations (B.1) and (B.2) is 2,934 ksi, which is a little lower than that estimated with the ACI 318 formula.

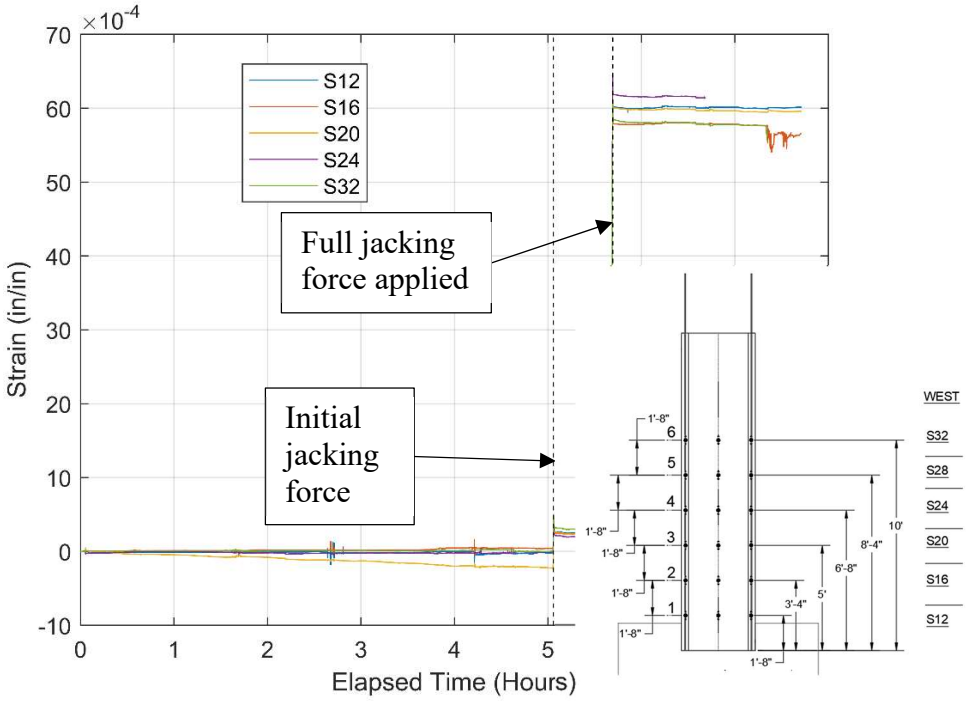

(a) West strand during pre-tensioning

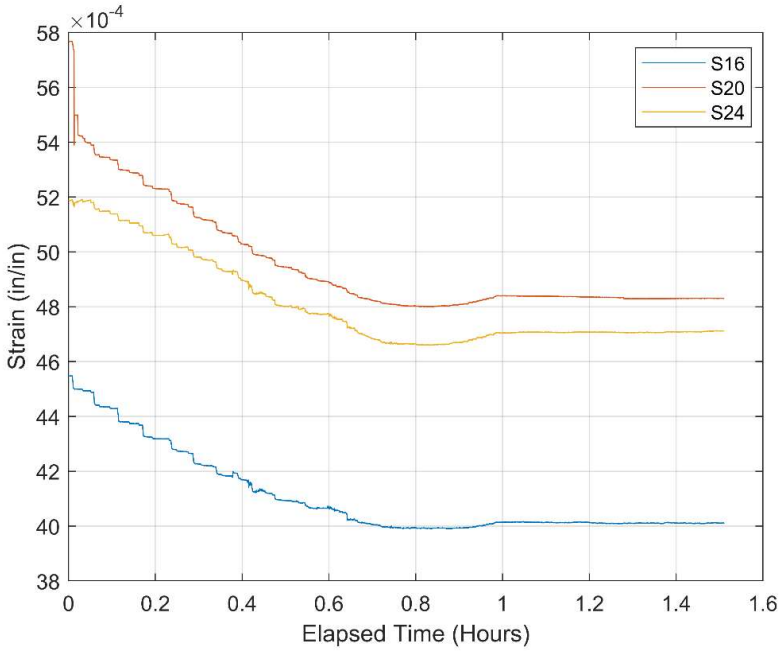

(b) West strand during stress transfer

Figure B.6: Strain data from prestressing strands for Specimen 2

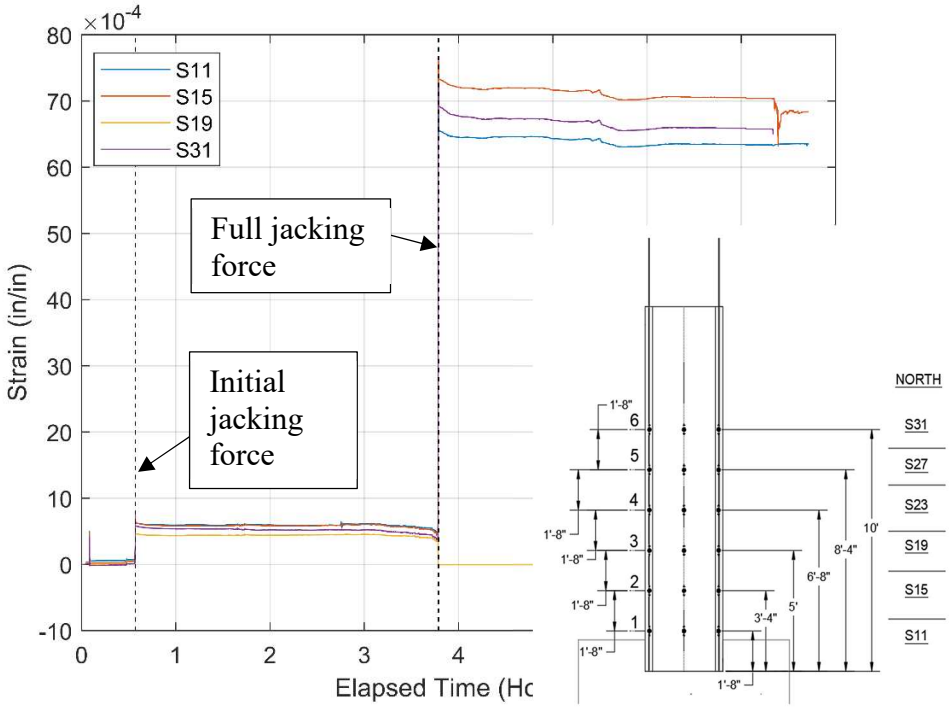

(c) North strand during pre-tensioning

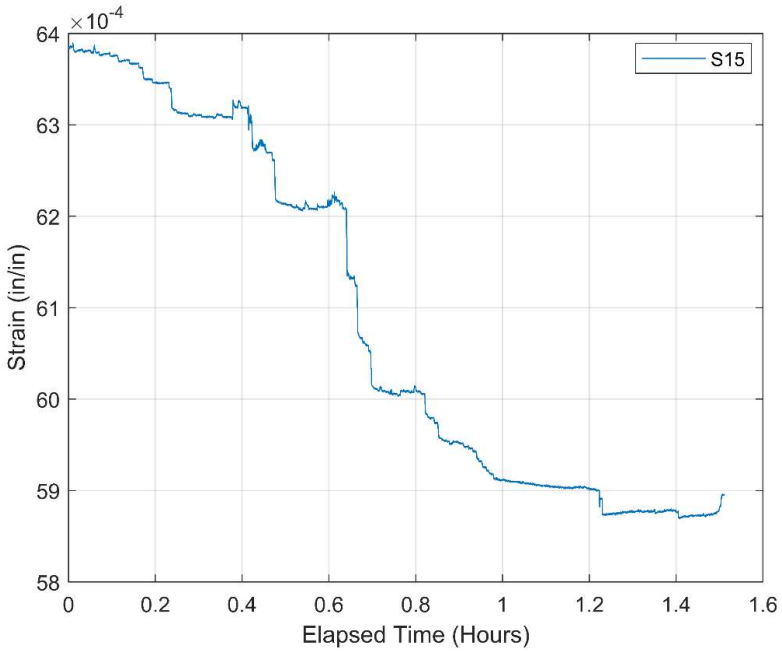

(d) North strand during stress transfer

Figure B.6 (continued): Strain data from prestressing strands for Specimen 2

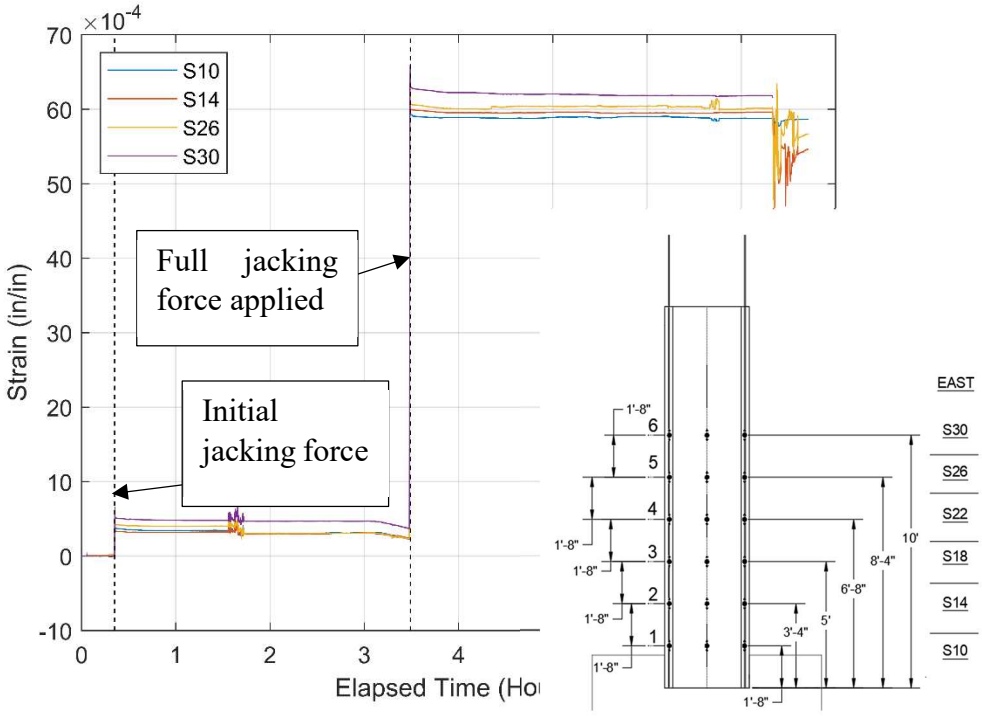

(e) East strand during pre-tensioning

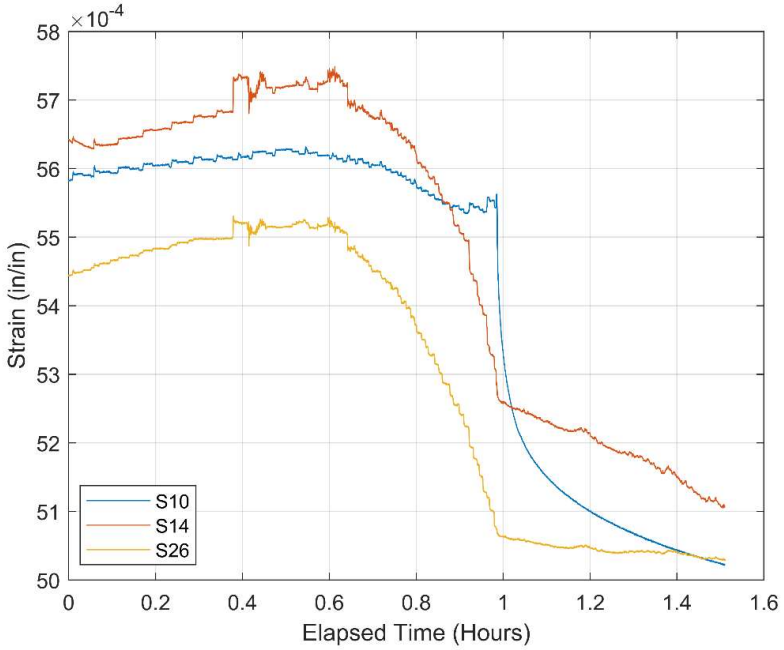

(f) East strand during stress transfer

Figure B.6 (continued): Strain data from prestressing strands for Specimen 2

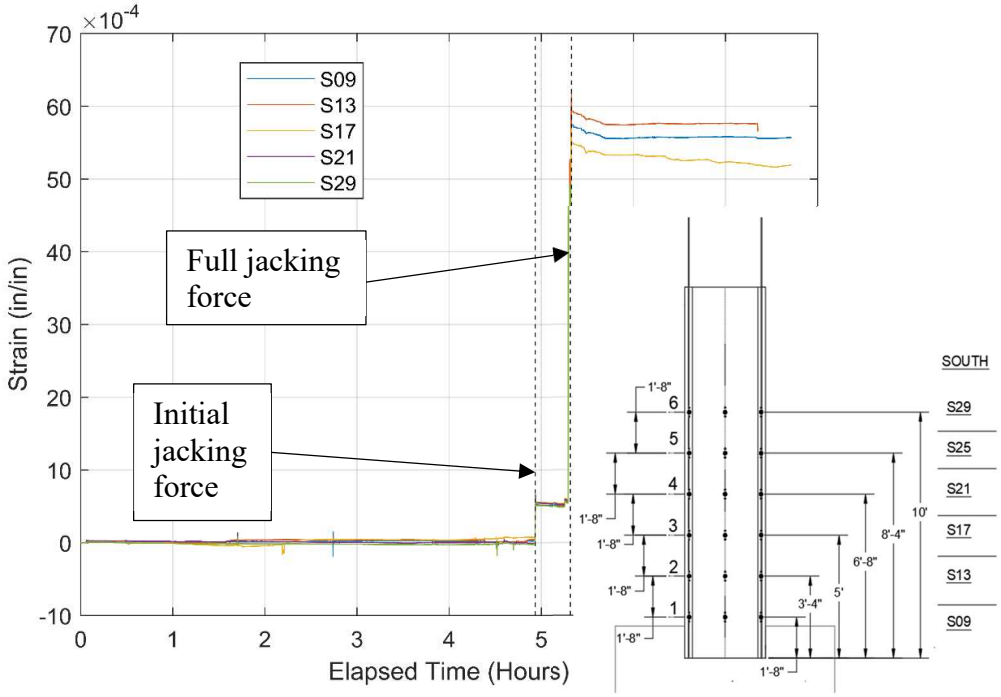

(g) South strand during pre-tensioning

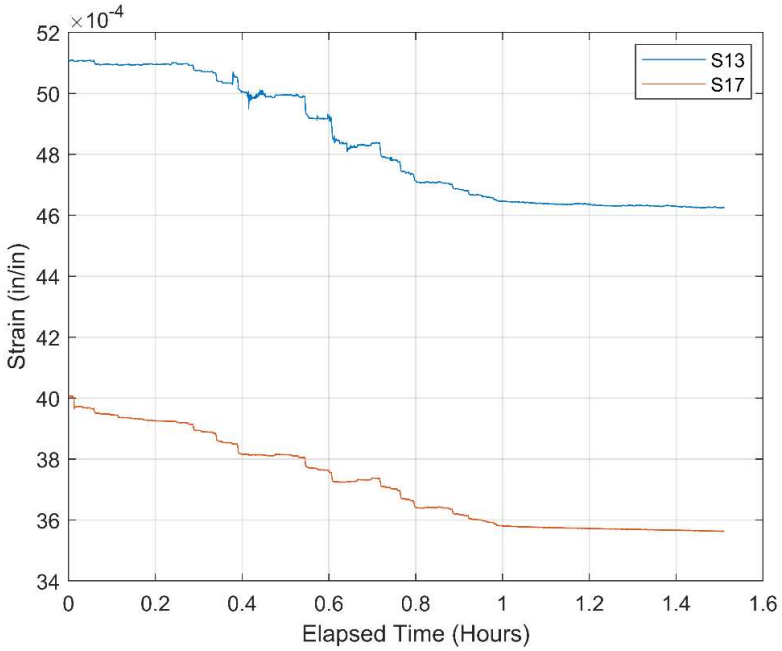

(h) South strand during stress transfer

Figure B.6 (continued): Strain data from prestressing strands for Specimen 2

Figures B.7 shows the VW strain data versus time obtained during the stress transfer for Specimen 2. Figure B.8 shows the average strain value at each elevation. It shows that the average strain from VW1 and VW5 is practically zero, which is consistent with the fact that these gauges were in the region with unbonded strands, which experienced practically no stress during the stress transfer. The average compressive strain from VW2 and VW6 is about 57% of that from VW3 and VW7, and the average compressive strain from VW3 and VW7 is close to that from VW4 and VW8, showing that the strand stress was fully developed at the location of VW3 and VW7. The distance of VW3 and VW7 from the end of the unbonded region is 28.5 in. and that of VW2 and VW6 is 8.5 in., while the required stress transfer length calculated with Equation (B.3) using f_{pi} equal to 165 ksi is 21 in. The highest average compressive strain registered by VW4 and VW8 is 0.00073, which is similar to that for Specimen 1.

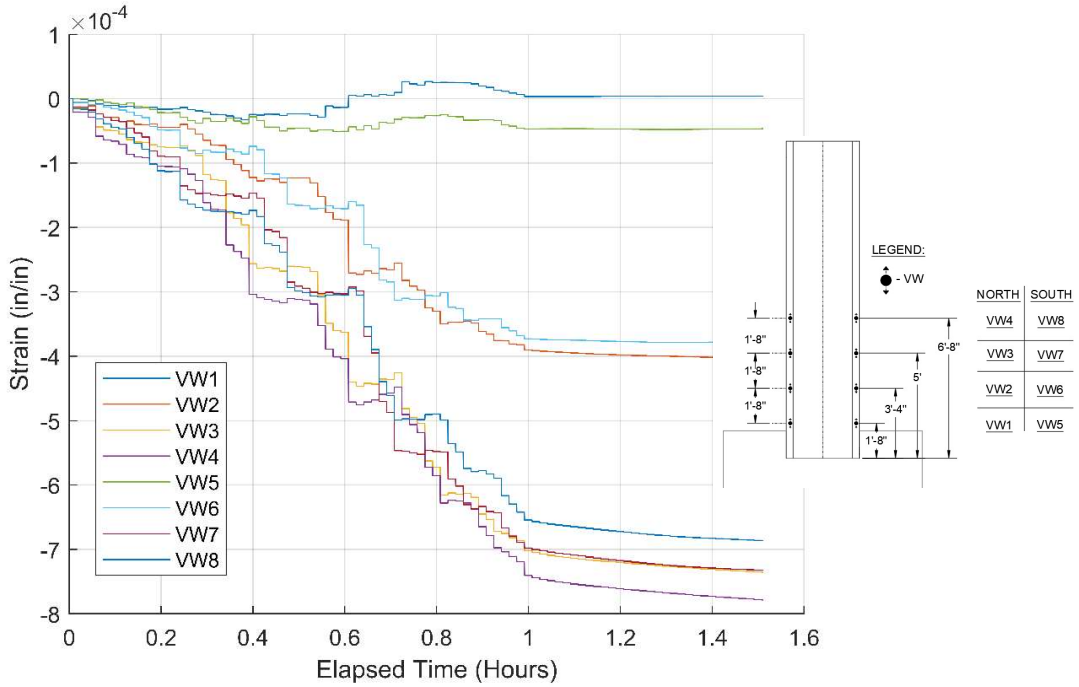

Figure B.7: VW gauge data during stress transfer for Specimen 2

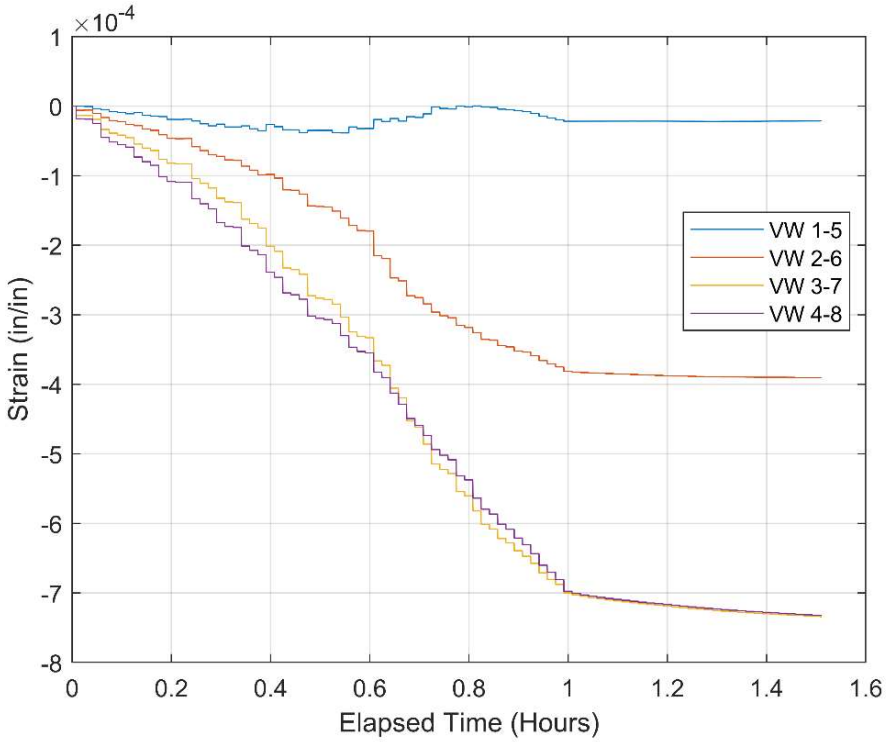

Figure B.8: Average VW gauge data at each elevation during stress transfer for Specimen 2

Figure B.9 shows the strains measured during the stress transfer by strain gauges attached to longitudinal bars in the shell. Only gauges S07 and S08 registered noticeable compressive strains. The average maximum compressive strain measured by the gauges at the end of the stress transfer is about 0.00048.

Figure B.10 shows the strains measured during the stress transfer by gauges attached to the transverse reinforcement. The gauges on the south side registered small tensile strains, which are comparable to those for Specimen 1, but those on the north side showed much higher tensile strains which are not deemed to be reasonable if the strains were due to the Poisson effect unless the shell had a splitting crack on the north side.

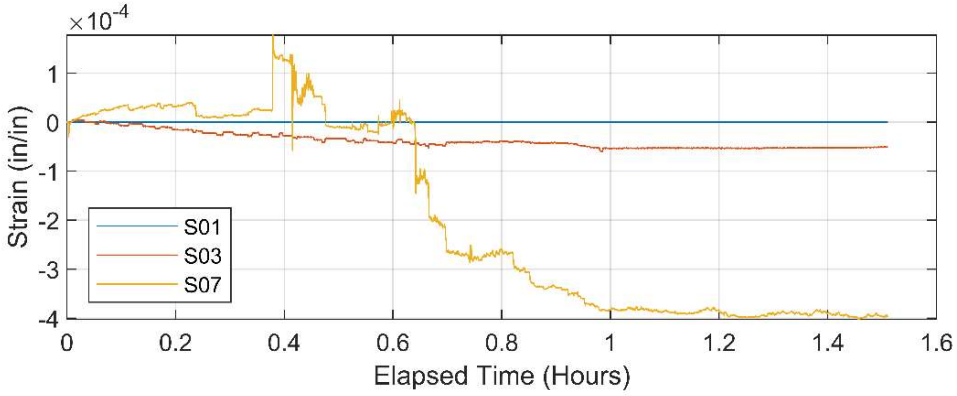

(a)

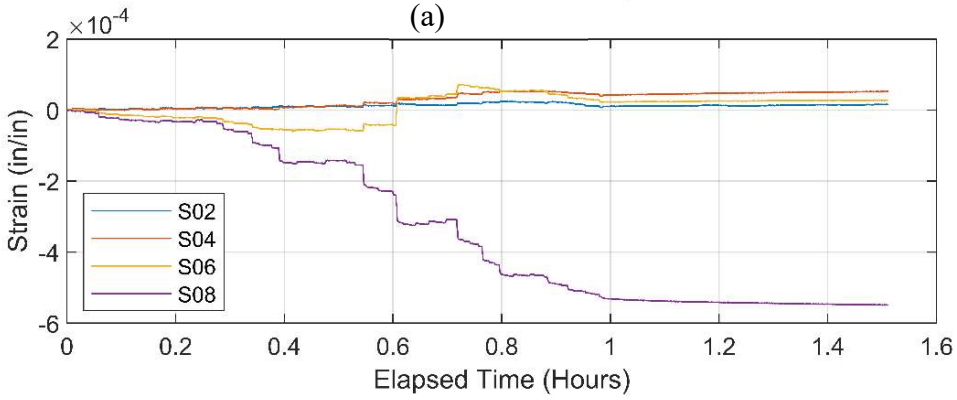

(b)

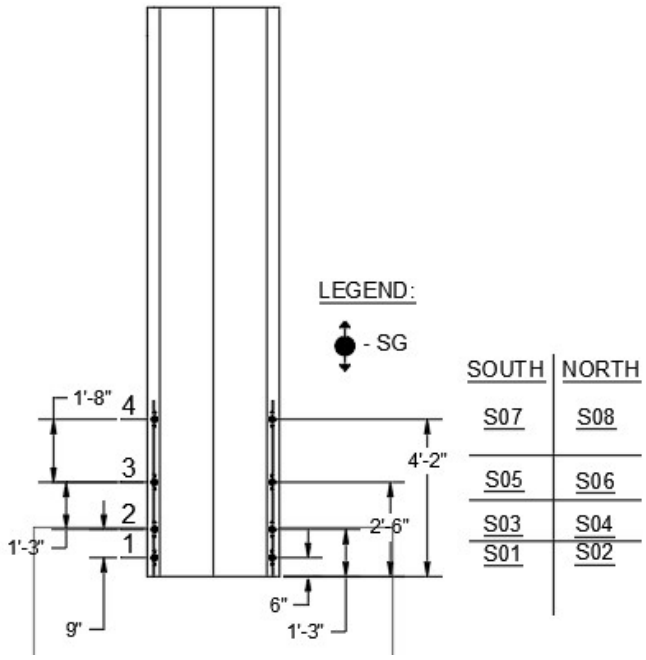

Figure B.9: Strain gauge data during stress transfer from (a) south longitudinal bar; (b) north longitudinal bar for Specimen 2

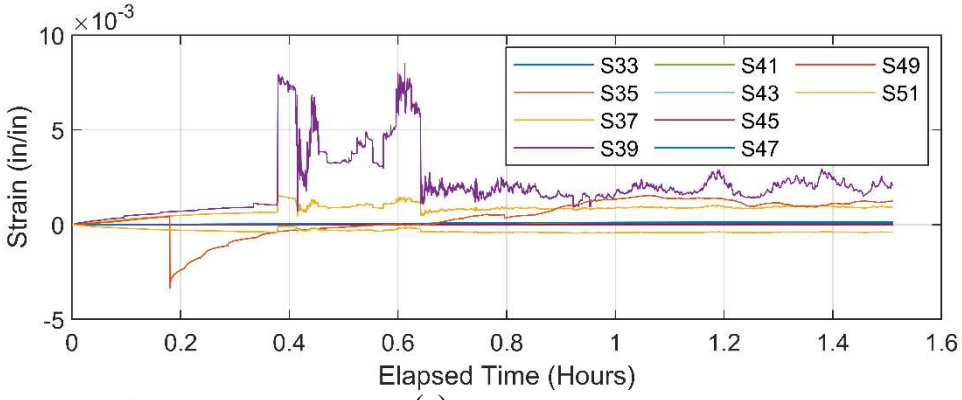

(a)

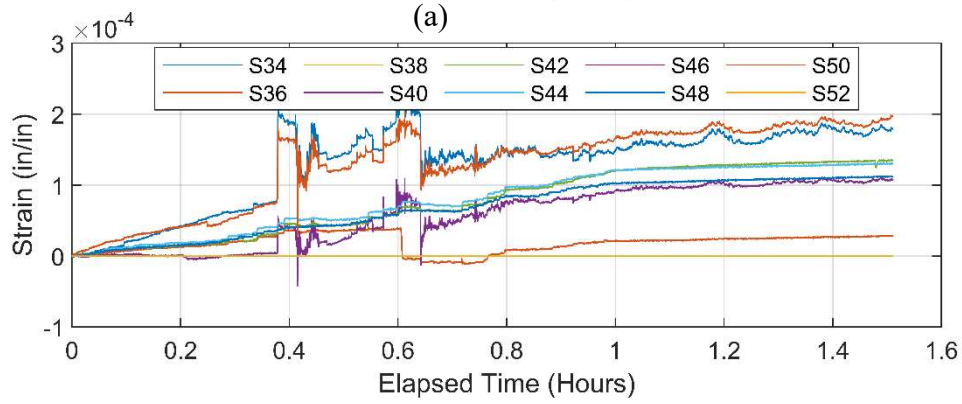

(b)

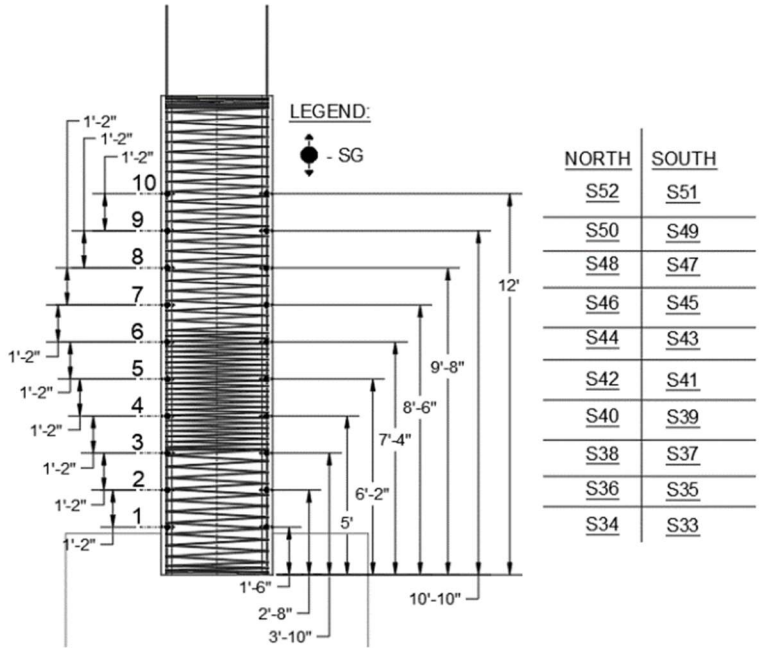

Figure B.10: Strain gauge data from transverse reinforcement during stress transfer for Specimen 2: (a) south side; (b) north side

B.3 Specimen 3

The shell of Specimen 3 had a similar instrumentation scheme as the other two specimens. All 8 VW gauges installed were working during the stress transfer, but 13 of the 24 strain gauges on the strands broke. The strands in this specimen were unbonded over a distance of 21 in. from the pile tip.

Figure B.11 shows strain readings from the west, north, east, and south strands during the pre-tensioning and stress transfer, provided by the surviving gauges. The average tensile strain measured at the end of the jacking process is about 0.0052, which is lower than that for the other two specimens. This corresponds to a jacking stress (f_{pj}) of 156 ksi. As in Specimen 2, the variation of the strain values with the gauge locations does not show a consistent trend. Figure B.11 shows that the average strain decrease during the stress transfer is about 0.00045. Assuming that the strain drop was entirely due to elastic shortening, the elastic shortening loss is estimated to be 13.5 ksi. Based on the above estimates, the initial prestress (f_{pi}) is 143 ksi. With the values of f_{pj} and f_{pi} estimated from the strain data and E_p = 30,000 ksi, the value of E_{ci} calculated with Equations (B.1) and (B.2) is 2,934 ksi, which is a little lower than that estimated with the ACI 318 formula.

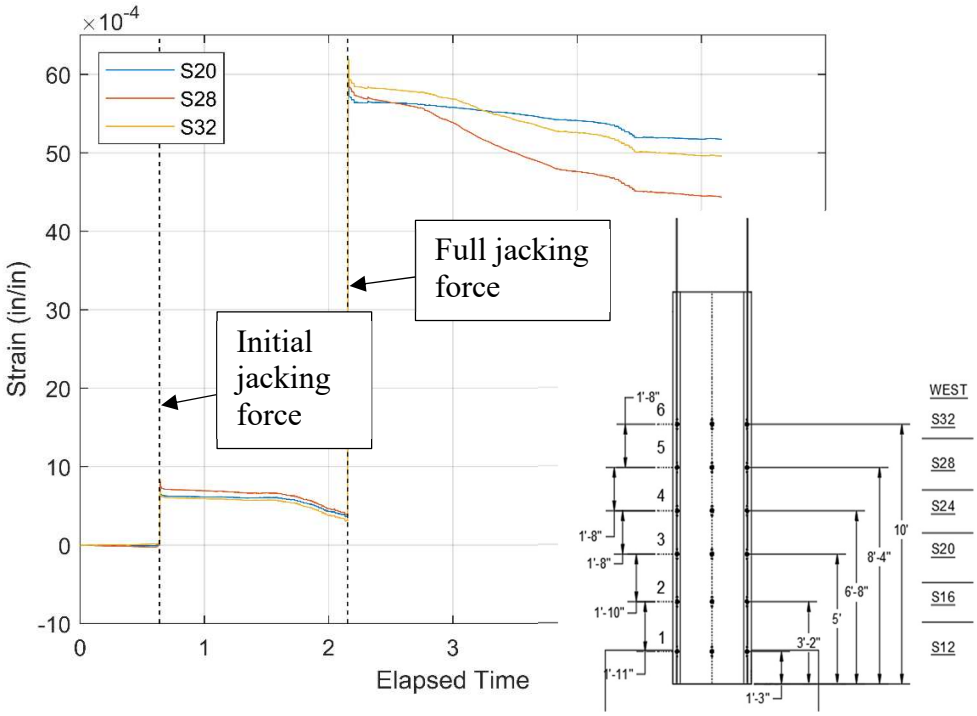

(a) West strand during pre-tensioning

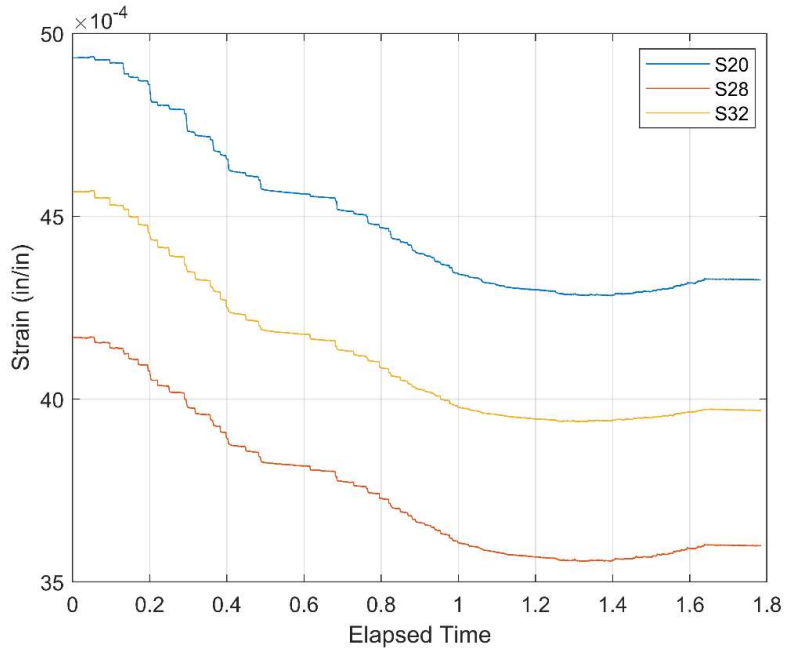

(b) West strand during stress transfer

Figure B.11: Strain data from prestressing strands for Specimen 3

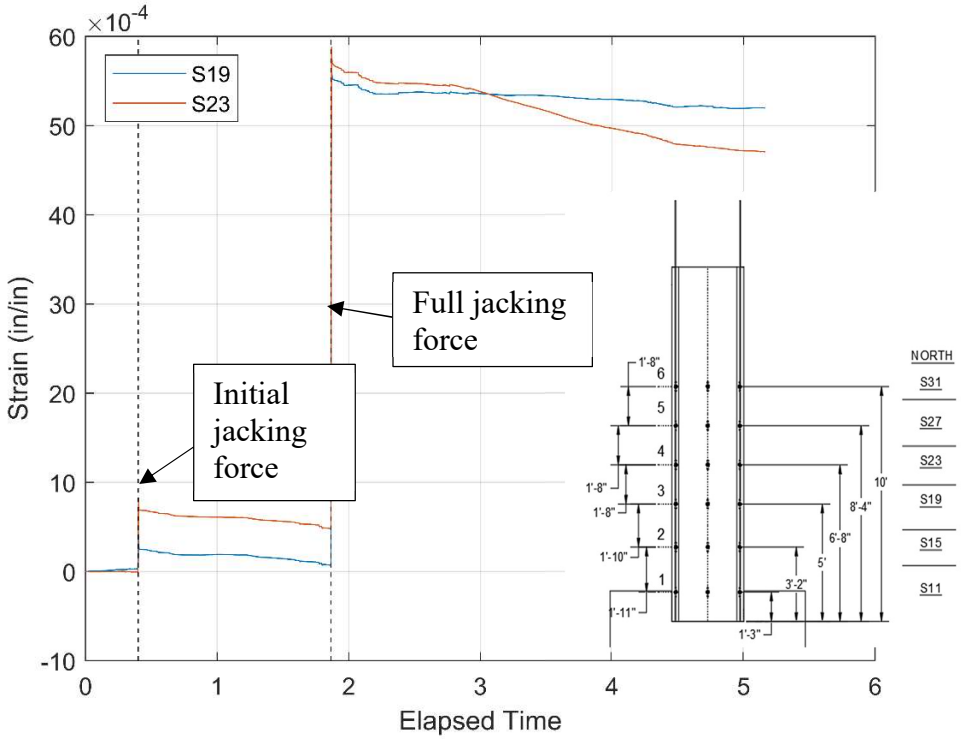

(c) North strand during pre-tensioning

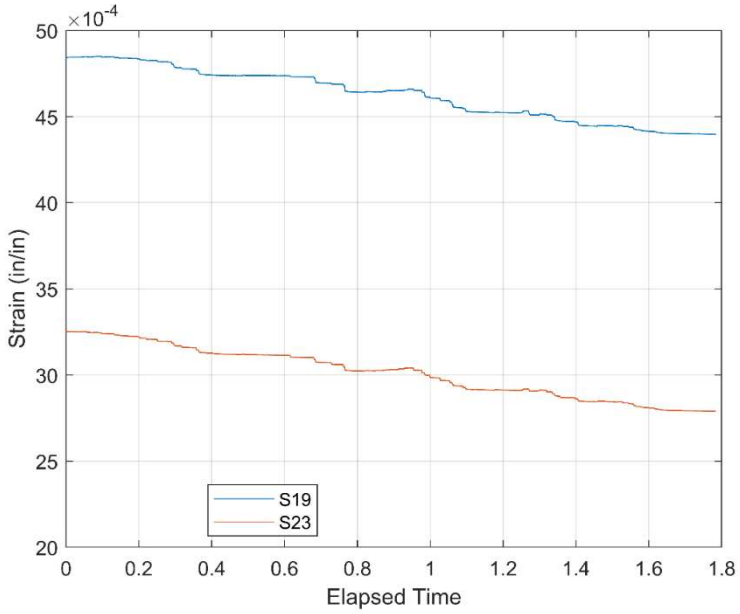

(d) North strand during stress transfer

Figure B.11 (continued): Strain data from prestressing strands for Specimen 3

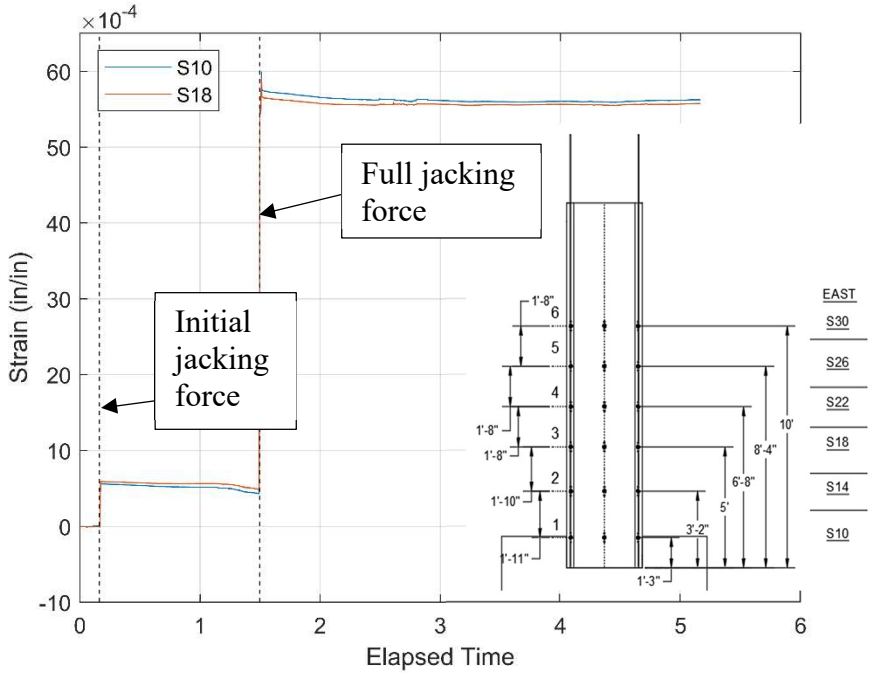

(e) East strand during pre-tensioning

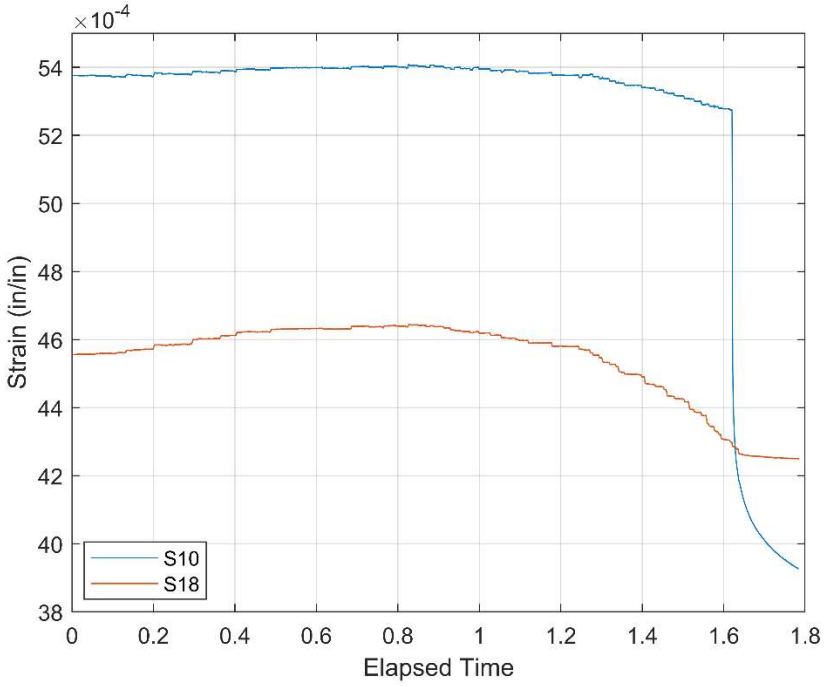

(f) East strand during stress transfer

Figure B.11 (continued): Strain data from prestressing strands for Specimen 3

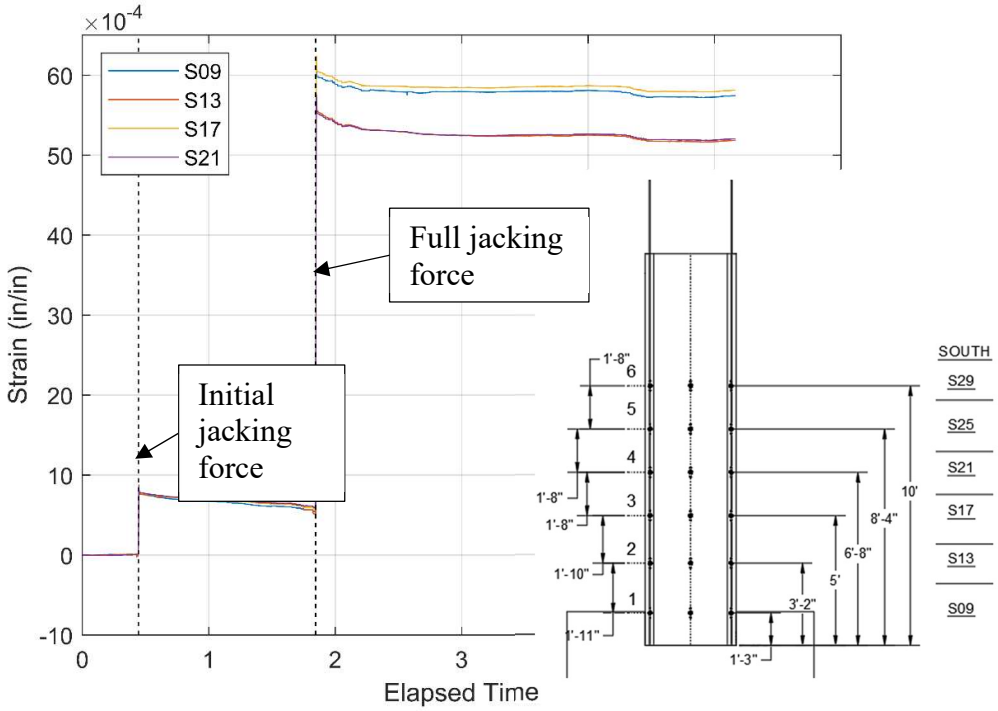

(g) South strand during pre-tensioning

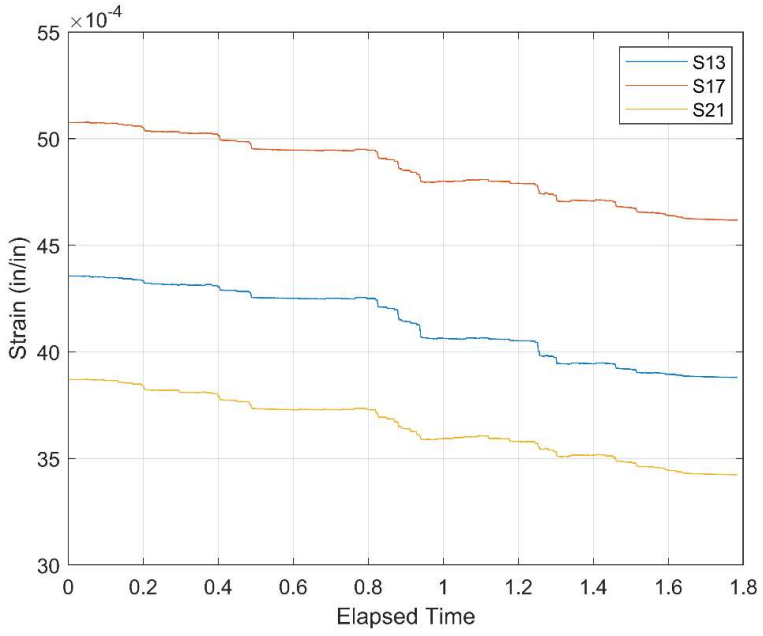

(h) South strand during stress transfer

Figure B.11 (continued): Strain data from prestressing strands for Specimen 3

Figures B.12 shows the VW strain data versus time obtained during the stress transfer. Figure B.13 shows the average strain value at each elevation. It shows that the average strain from VW1 and VW5 is practically zero, which is consistent with the fact that these gauges were in the region with unbonded strands. The average compressive strain from VW2 and VW6 is about 38% of that from VW3 and VW7, and the average compressive strain from VW3 and VW7 is close to that from VW4 and VW8, showing that the strand stress was fully developed at the location of VW3 and VW7. The distance of VW3 and VW7 from the end of the unbonded region is 29 in. and that of VW2 and VW6 is 9 in., while the required stress transfer length estimated with Equation (B.3) using f_{pi} equal to 143 ksi is 18 in. The highest average compressive strain registered at the end of stress transfer is 0.00065, which is lower than that for Specimens 1 and 2. This is consistent with the fact that this specimen had a lower jacking stress.

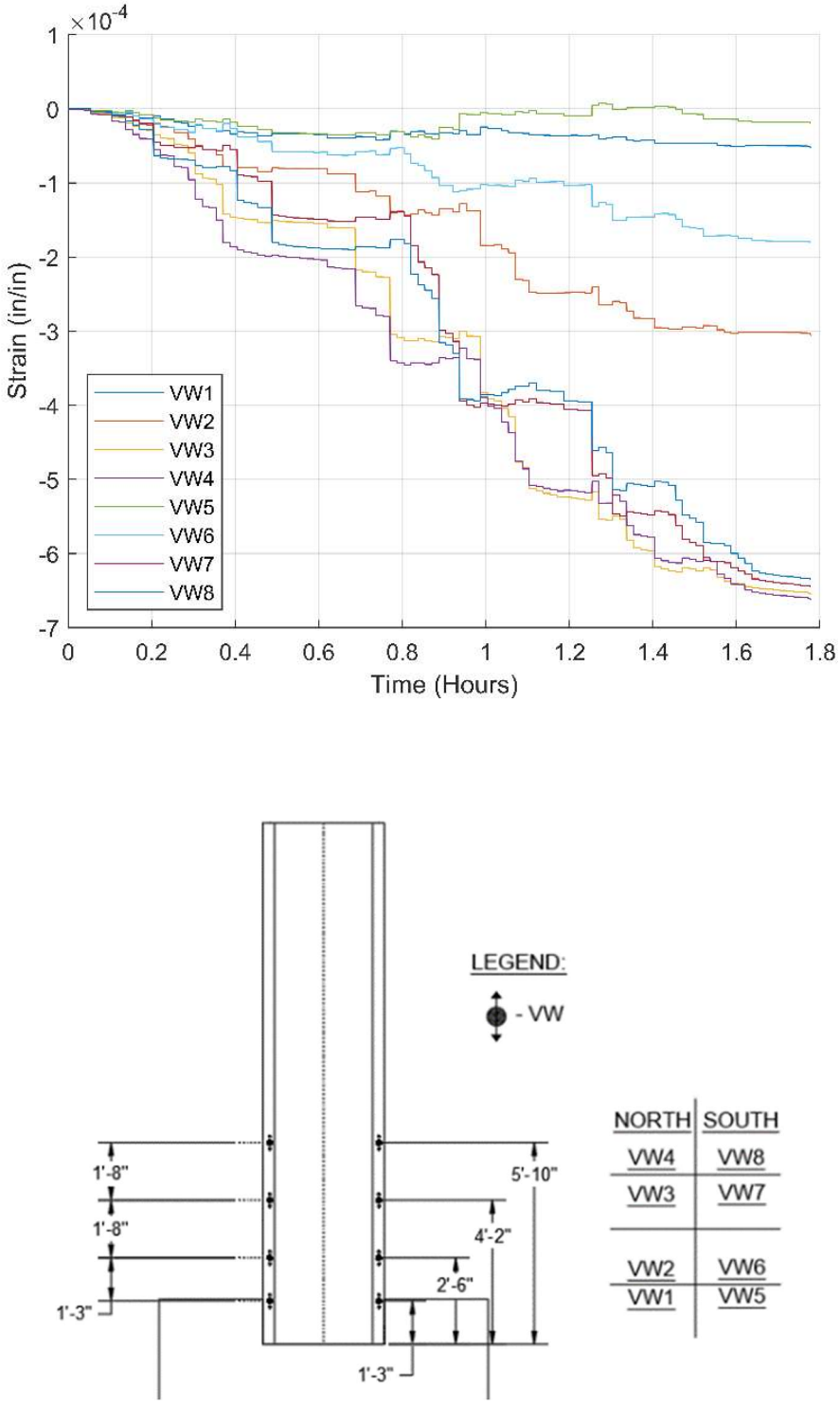

Figure B.12: VW gauge data during stress transfer for Specimen 3

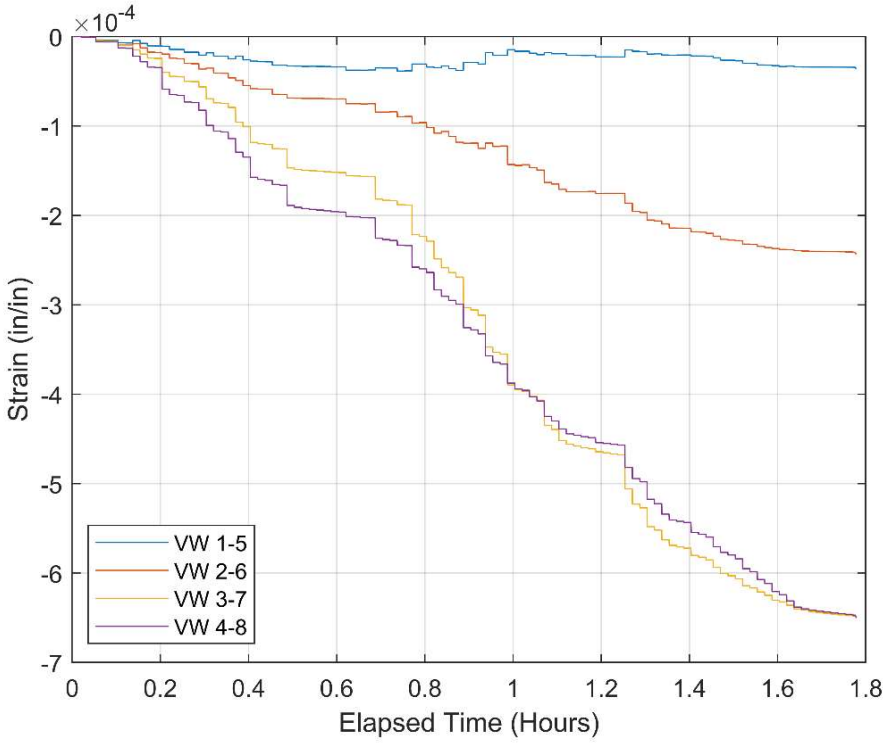

Figure B.13: Average VW gauge data at each elevation during stress transfer for Specimen 3

Figure B.14 shows the strains measured during the stress transfer by strain gauges attached to longitudinal bars in the shell. At the end of the stress transfer, the maximum compressive strain was registered by S07 and is about 0.0005, which is comparable to that for the other two specimens.

Figure B.15 shows the strains measured during the stress transfer by gauges attached to the transverse reinforcement. The maximum tensile strain measured at the end of the stress transfer is about 0.000088, which is comparable to that for Specimen 1.

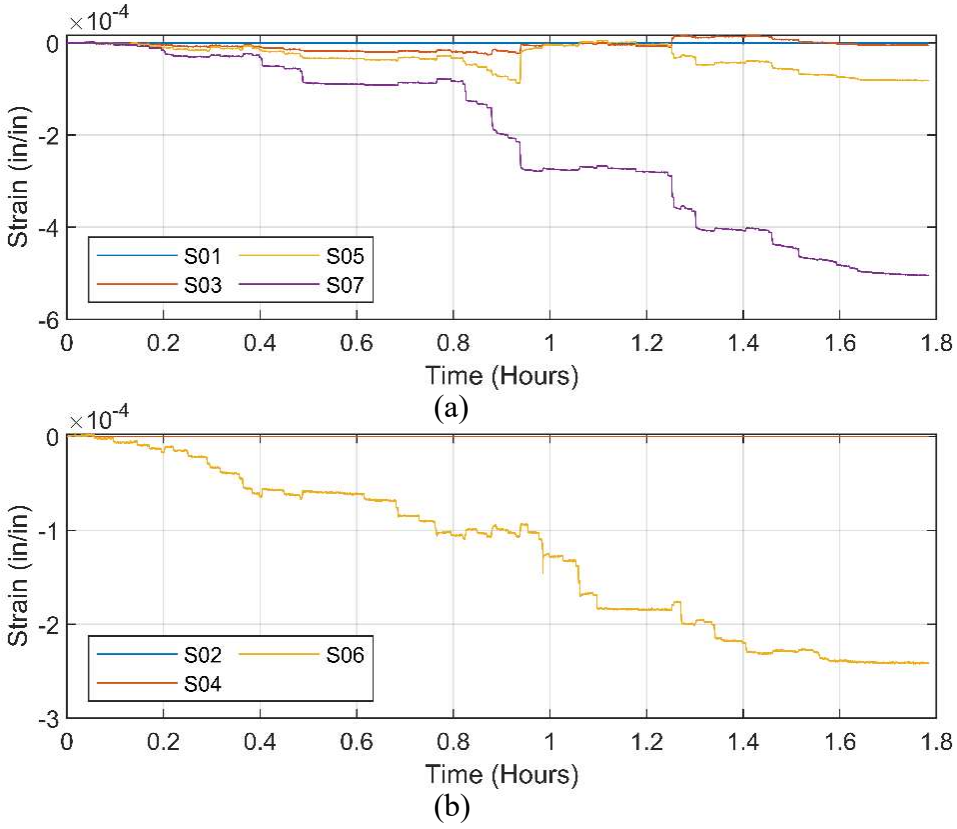

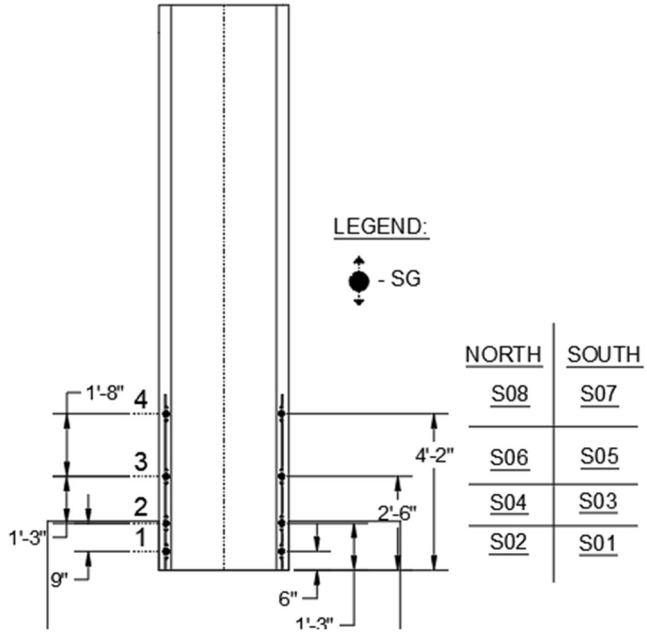

Figure B.14: Strain gauge data during stress transfer from (a) south longitudinal bar; (b) north longitudinal bar for Specimen 3

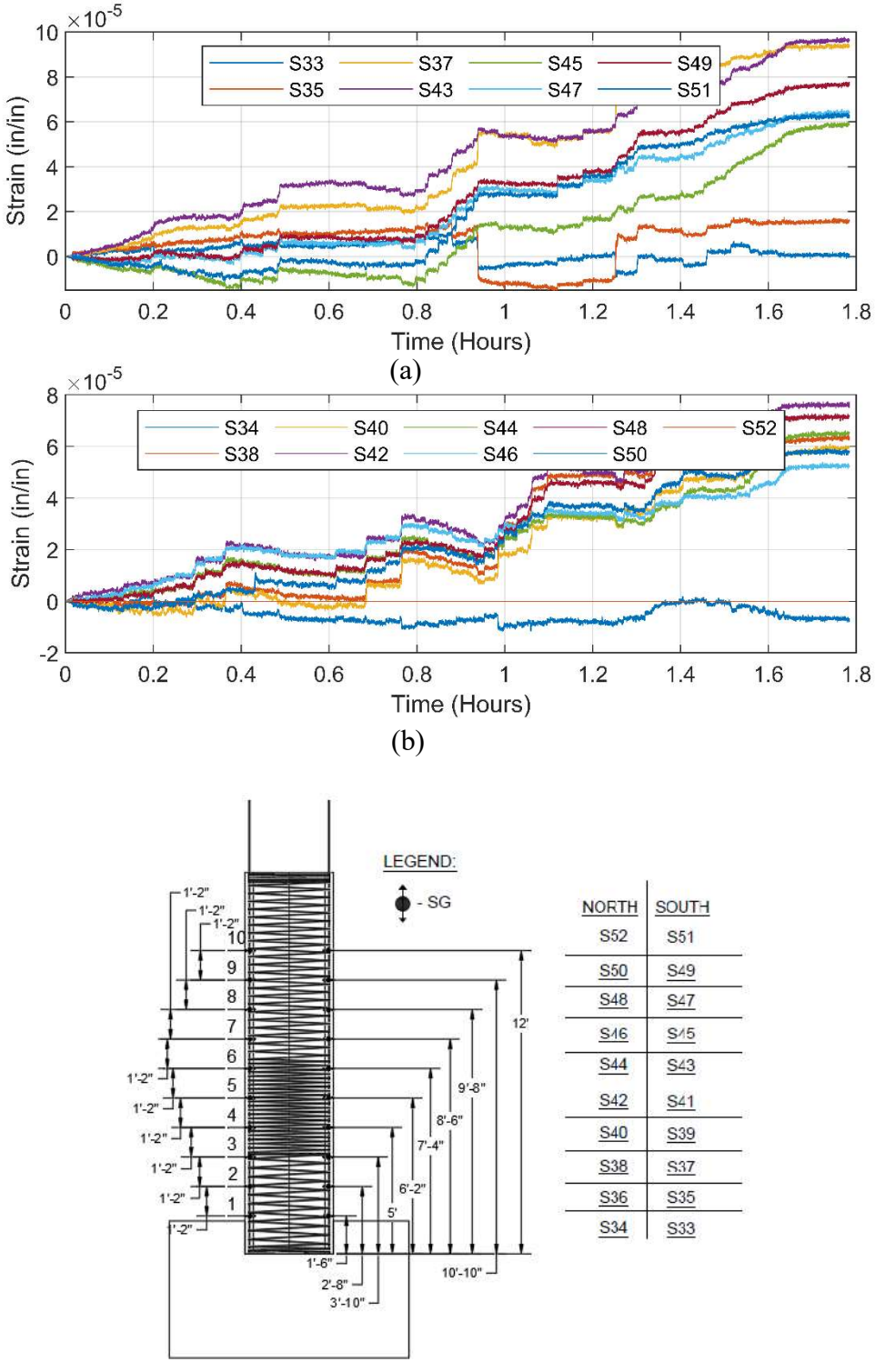

Figure B.15: Strain gauge data from transverse reinforcement during stress transfer for Specimen 3: (a) south side; (b) north side

Appendix C Creep and Shrinkage Loss Calculations

The effective prestress in the strands of each pile specimen at the beginning of the test, without considering the axial load from the load stub, load beam and the vertical actuators, is estimated by assuming that the prestress losses were entirely due to the creep and shrinkage of the concrete. Relaxation loss is ignored because of the use of low-relaxation strands. The creep and shrinkage losses are calculated according to the AASHTO LRFD Bridge Design Specifications, 8th Edition (AASHTO 2017). Since the shells of Specimens 1, 2, and 3 were cast 3, 7, and 12 months prior to the respective tests and had the core filled with concrete at a much later day (about a month prior to respective test), the core concrete is ignored in the loss calculations.

C.1 Shrinkage of Concrete

Based on AASHTO, the shrinkage strain of concrete is calculated as follows.

$$\varepsilon_{sh} = k_s k_{hs} k_f k_{td} \, 0.48 \times 10^{(-3)} \tag{C.1}$$

where k_s, k_{hs}, k_f, and k_{td} are determined with the following equations:

$$k_s = \left[\frac{t}{\frac{26e^{0.36\left(\frac{V}{S}\right)} + t}{\frac{t}{45+t}}} \right] \left[\frac{1064 - 94\left(\frac{V}{S}\right)}{923} \right] \tag{C.2}$$

$$k_{hs} = 2.00 - 0.014H \tag{C.3}$$

$$k_f = \frac{5}{1 + f'_{ci}} \tag{C.4}$$

$$k_{td} = \frac{t}{12\left(\frac{100 - 4f'_{ci}}{f'_{ci} + 20}\right) + t} \tag{C.5}$$

In the above equations, t is the age of concrete in days from the end of the curing period, $\frac{V}{S}$ is the volume-to-surface ratio, H is the humidity in %, and f'_{ci} is the compressive strength of concrete (in ksi) at stress transfer.

Here, t is the number of days between the end of the curing period (the stress transfer day) for the shell and the pile test day. Since the precast shells had the core filled at a much later time, the $\frac{V}{S}$ value is calculated with the consideration of the shell alone. The shells had an outer diameter of 42 in. and a wall thickness of 4 in. This leads to $\frac{V}{S} = 2.0\ in$. The humidity is assumed to be 60% for all three specimens, which is typical for the La Jolla, CA area. The concrete strength f'_{ci} is assumed to be 4.5 ksi, which is the specified minimum concrete strength at stress transfer.

Once the shrinkage strain is calculated, the prestress loss (Δf_{pS}) due to shrinkage is calculated with the following equation.

$$\Delta f_{pS} = E_p k_A \varepsilon_{sh} \tag{C.6}$$

where

$$k_A = \frac{A_c}{A_{c,t}} \tag{C.7a}$$

$$A_c = \pi\left(r_o^2 - r_i^2\right) \tag{C.7b}$$

$$A_{c,t} = A_c + A_s \frac{E_s}{E_{c,t}} + A_p \frac{E_p}{E_{c,t}} \tag{C.7c}$$

$$E_{c,t} = \frac{E_{ci}}{1 + 0.7\Psi} \tag{C.7d}$$

in which r_o and r_i are the outer and inner radii of the shell, A_s and E_s are the cross-sectional area and the modulus of elasticity of the longitudinal reinforcing steel, respectively, and A_p and E_p are the cross-sectional area and the modulus of elasticity of the strands. Here, E_s is assumed to be 29,000 ksi, and E_p is 30,000 ksi, as determined by the material sample tests. In the calculation of the age-adjusted modulus of elasticity of concrete, $E_{c,t}$, with Equation (C.7d), E_{ci} is the modulus of elasticity of the concrete at stress transfer, which is calculated as $E_{ci} = 47\sqrt{f'_{ci} \times 1000}$, with all stress values in ksi, and Ψ is the creep coefficient to be calculated as shown in the following section. For $f'_{ci} = 4.5\ ksi$, $E_{ci} = 3{,}824\ ksi$.

C.2 Creep of Concrete

According to AASHTO, the creep coefficient of concrete is calculated with the following formula.

$$\Psi(t, t_i) = 1.9 k_{cs} k_{hc} k_f k_{td} t_i^{-0.118} \tag{C.8}$$

in which k_f and k_{td} are defined in Equations (C.4) and (C.5), t_i is the age of concrete in days at the time of stress transfer, and k_{cs} and k_{hc} are defined in the following two equations.

$$k_{cs} = \left[\frac{t}{\frac{26e^{0.36\left(\frac{V}{S}\right)} + t}{\frac{t}{45+t}}} \right] \left[\frac{1.80 - 1.77e^{-0.54\left(\frac{V}{S}\right)}}{2.587} \right] \tag{C.9}$$

$$k_{hc} = 1.56 - 0.008H \tag{C.10}$$

For creep calculations, t is the age of concrete in days from the time of stress transfer.

The prestress loss (Δf_{pC}) due to creep is calculated as follows.

$$\Delta f_{pC} = \Psi k_A \varepsilon_0 E_P \tag{C.11}$$

where

$$\varepsilon_0 = \frac{A_p f_{pi}}{A_c E_{ci}} \tag{C.12}$$

in which k_A is defined in Equation (C.7a), and f_{pi} is the initial prestress right after stress transfer.

C.3 Effective Prestress in the Specimens at the Test Day

The effective prestress (f_{pe}) on the pile test day has been estimated for each pile specimen based on the shrinkage and creep losses calculated with the formulas presented in the previous two sections. This is the stress in the strands without considering the vertical loads from the load stub, load beam, and the vertical actuators. The results are summarized in Table C.1.

Table C.1: Effective prestress on the test day

Variable	Specimen 1	Specimen 2	Specimen 3
A_p	4.25 in.^{2}	4.25 in.^{2}	4.25 in.^{2}
A_c	478 in.^{2}	478 in.^{2}	478 in.^{2}
f'_{ci}	4.5 ksi	4.5 ksi	4.5 ksi
E_{ci}	3,824 ksi	3,824 ksi	3,824 ksi
E_s	28,000 ksi	28,000 ksi	28,000 ksi
E_p	30,000 ksi	30,000 ksi	30,000 ksi
f_{pi}	166 ksi	165 ksi	143 ksi
t_i	1 day	1 day	1 day
t	102 days	207 days	366 days
ε_{sh}	0.00033	0.00039	0.00042
Ψ	1.2	1.4	1.5
Δf_{pS}	8.6 ksi	14.0 ksi	11.0 ksi
Δf_{pC}	11.9 ksi	10.1 ksi	13.2 ksi
f_{pe}	145 ksi	140 ksi	118 ksi

Appendix D Recovery Column – Additional Specimen Design Drawings

This appendix contains a complete set of instrumentation drawings used in the testing of the column specimens discussed in Chapter 8.

D.1 Specimen 1

The instrumentation drawings for Specimen 1 are shown below.

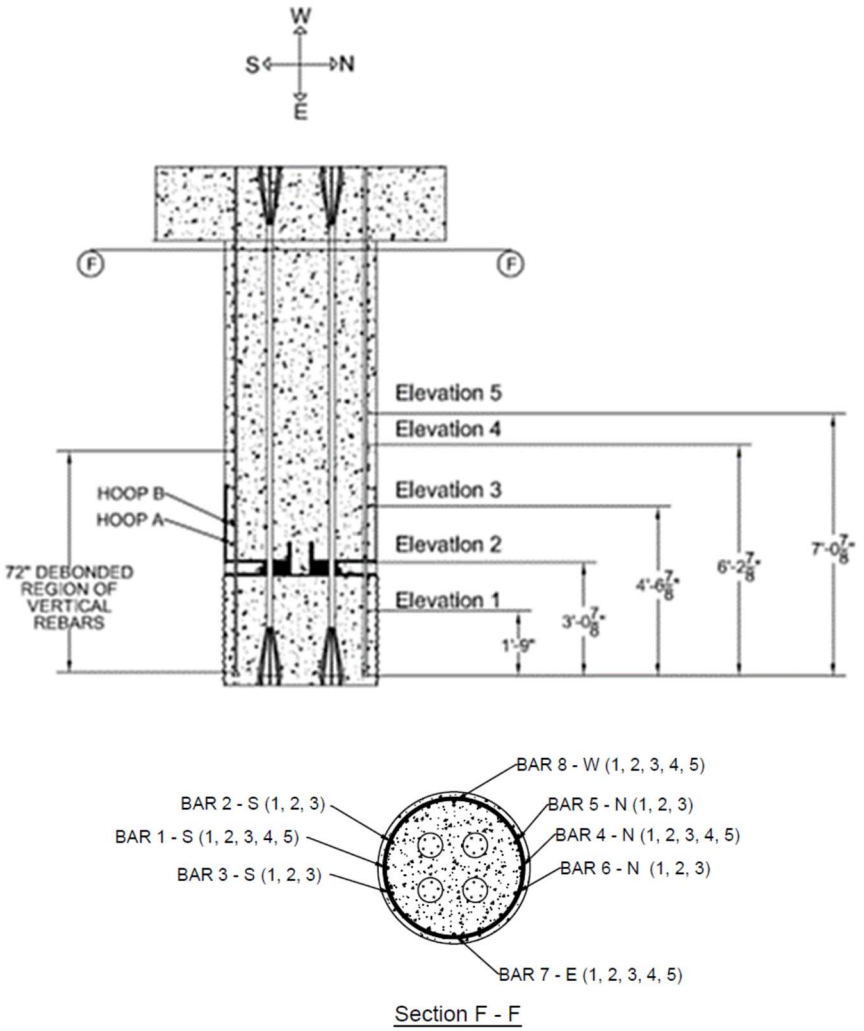

Figure D.1: Strain gauge locations on longitudinal rebars for Specimen 1 (loading along N-S direction)

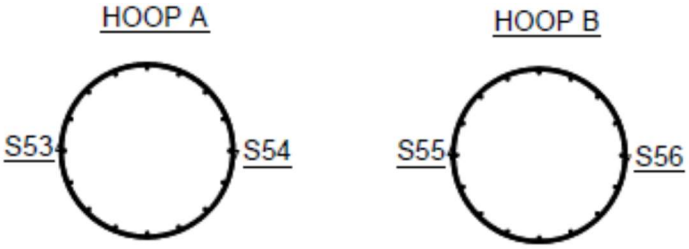

Figure D.2: Strain gauges on transverse reinforcement for Specimen 1 (locations of hoops A and B are shown in Figure D.1)

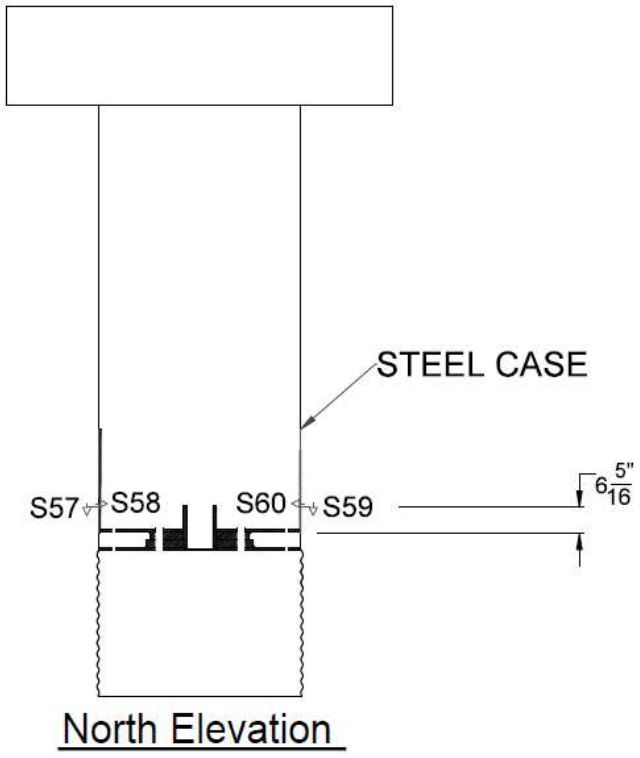

Figure D.3: Strain gauges on steel casing for Specimen 1

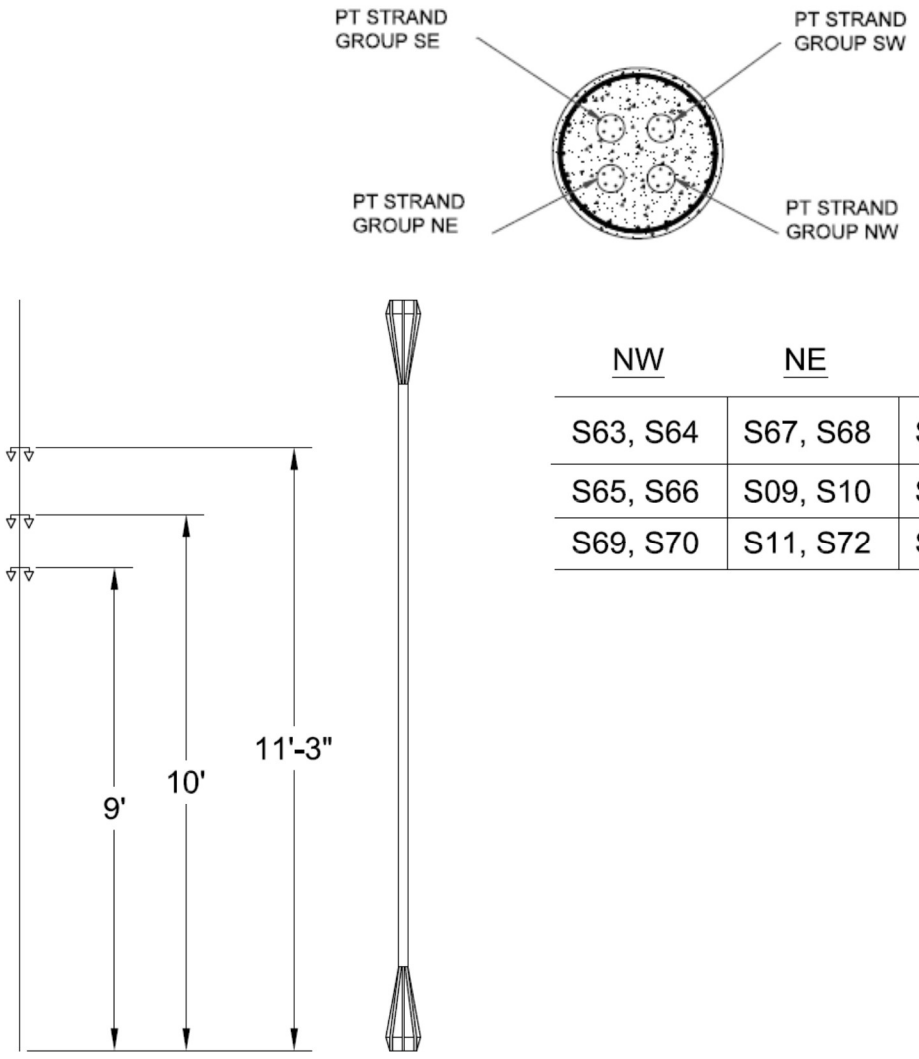

NW	NE	SW	SE
S63, S64	S67, S68	S01, S02	S07, S08
S65, S66	S09, S10	S03, S04	S61, S62
S69, S70	S11, S72	S05, S06	S71, S12

Figure D.4: Strain gauge locations on prestressing strands for Specimen 1 (loading along N-S direction)

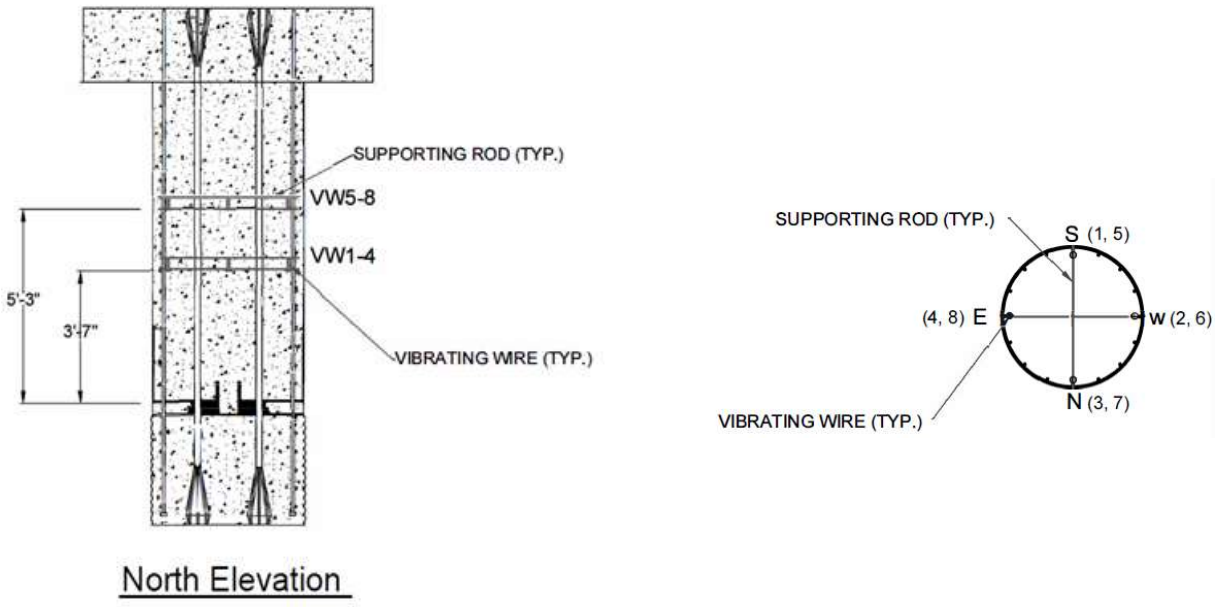

Figure D.5: Vibrating-wire gauge locations for Specimen 1

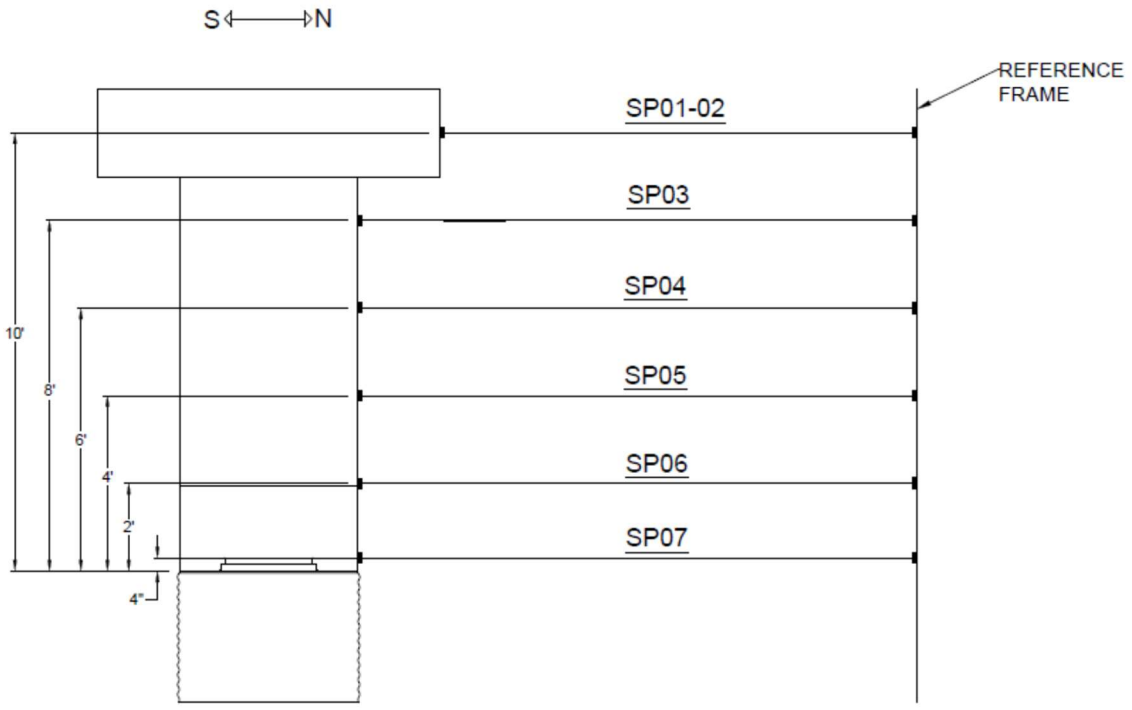

Figure D.6: String potentiometer locations for Specimen 1

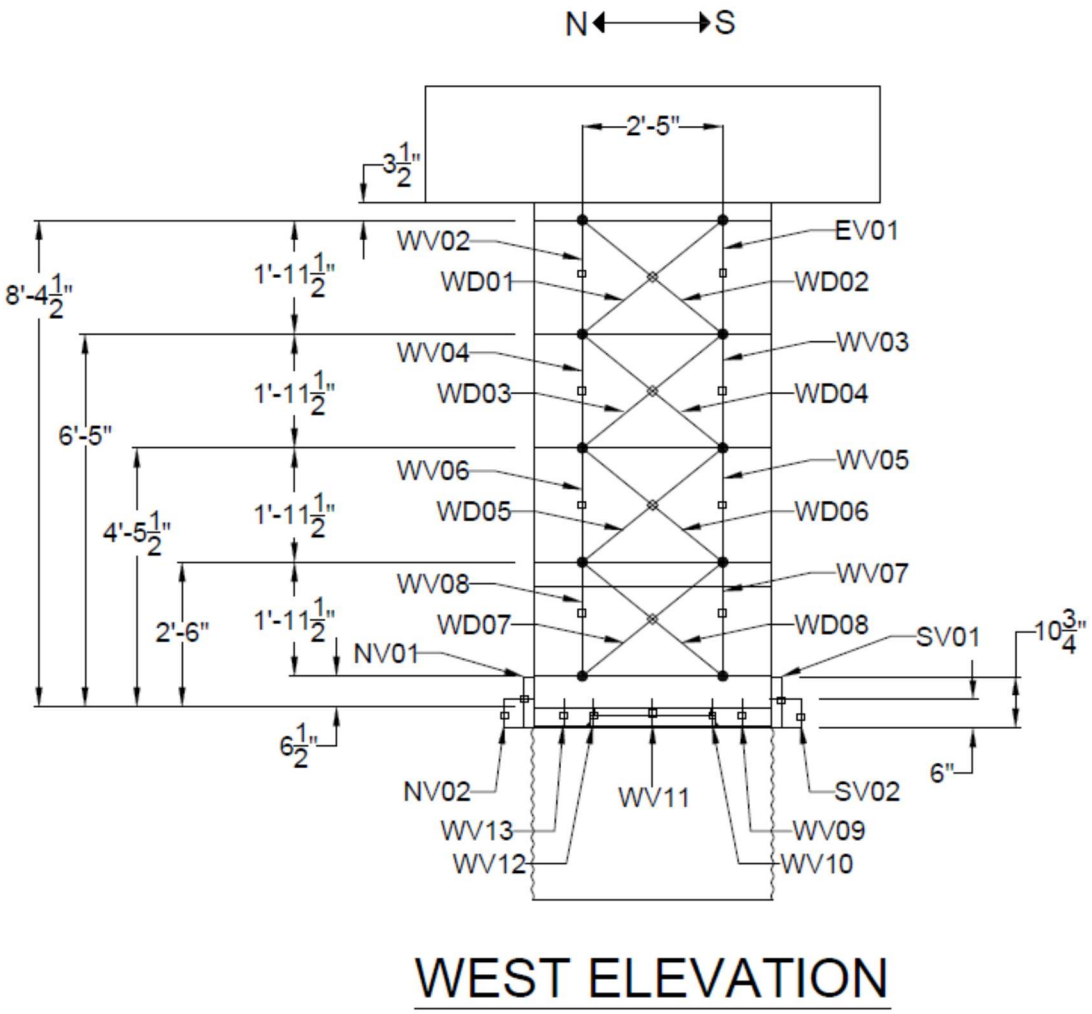

Figure D.7: Linear potentiometers locations for Specimen 1 (west elevation)

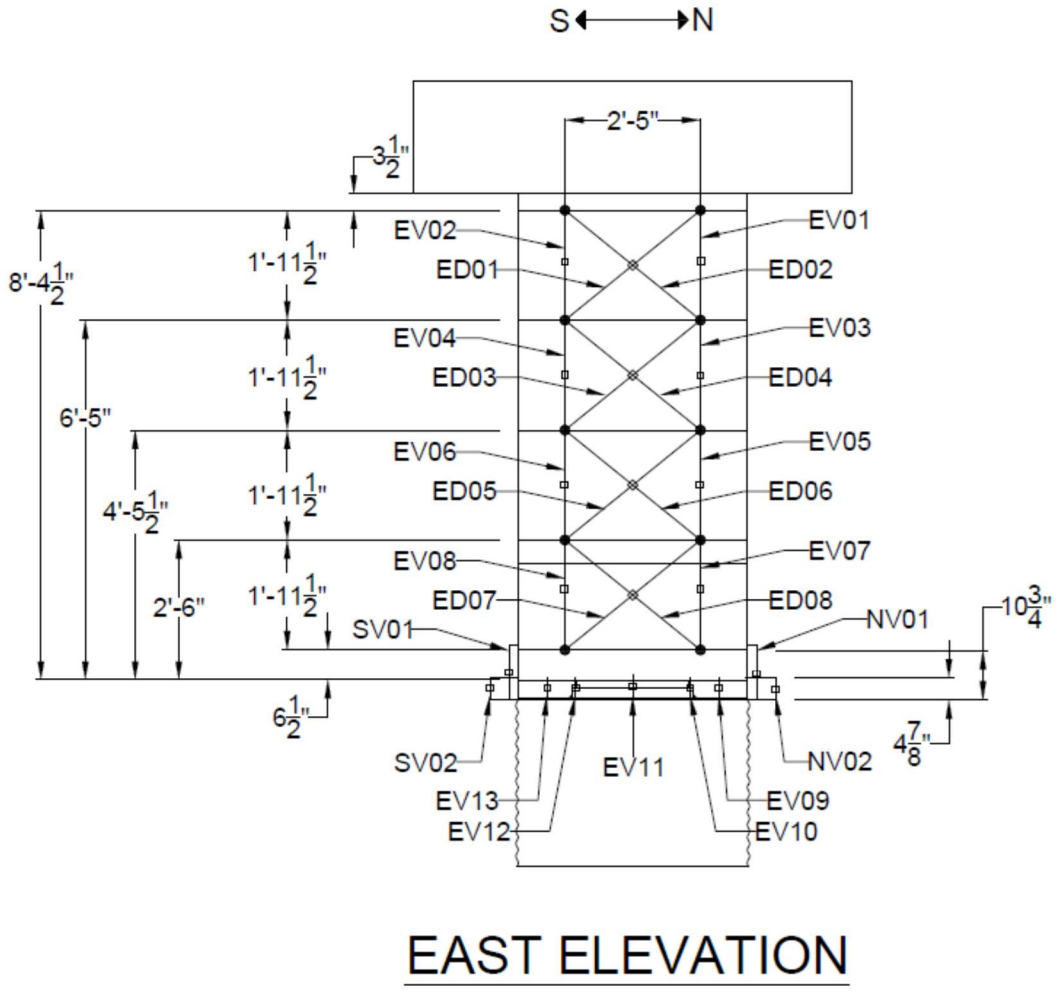

Figure D.8: Linear potentiometer locations for Specimen 1 (east elevation)

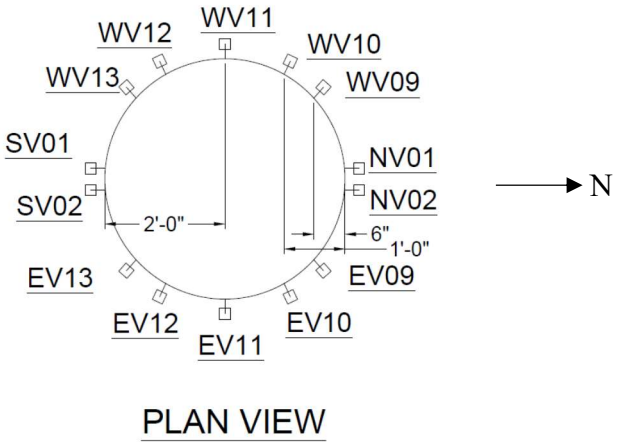

Figure D.9: Plan view of linear potentiometers locations around sacrificial zone for Specimen 1

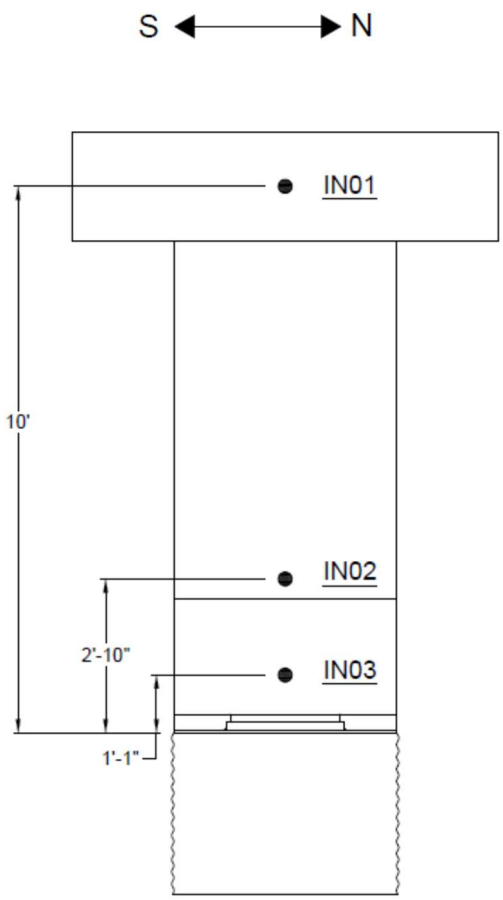

Figure D.10: Inclinometer locations for Specimen 1

D.2 Specimen 2

The instrumentation drawings for Specimen 2 are shown below.

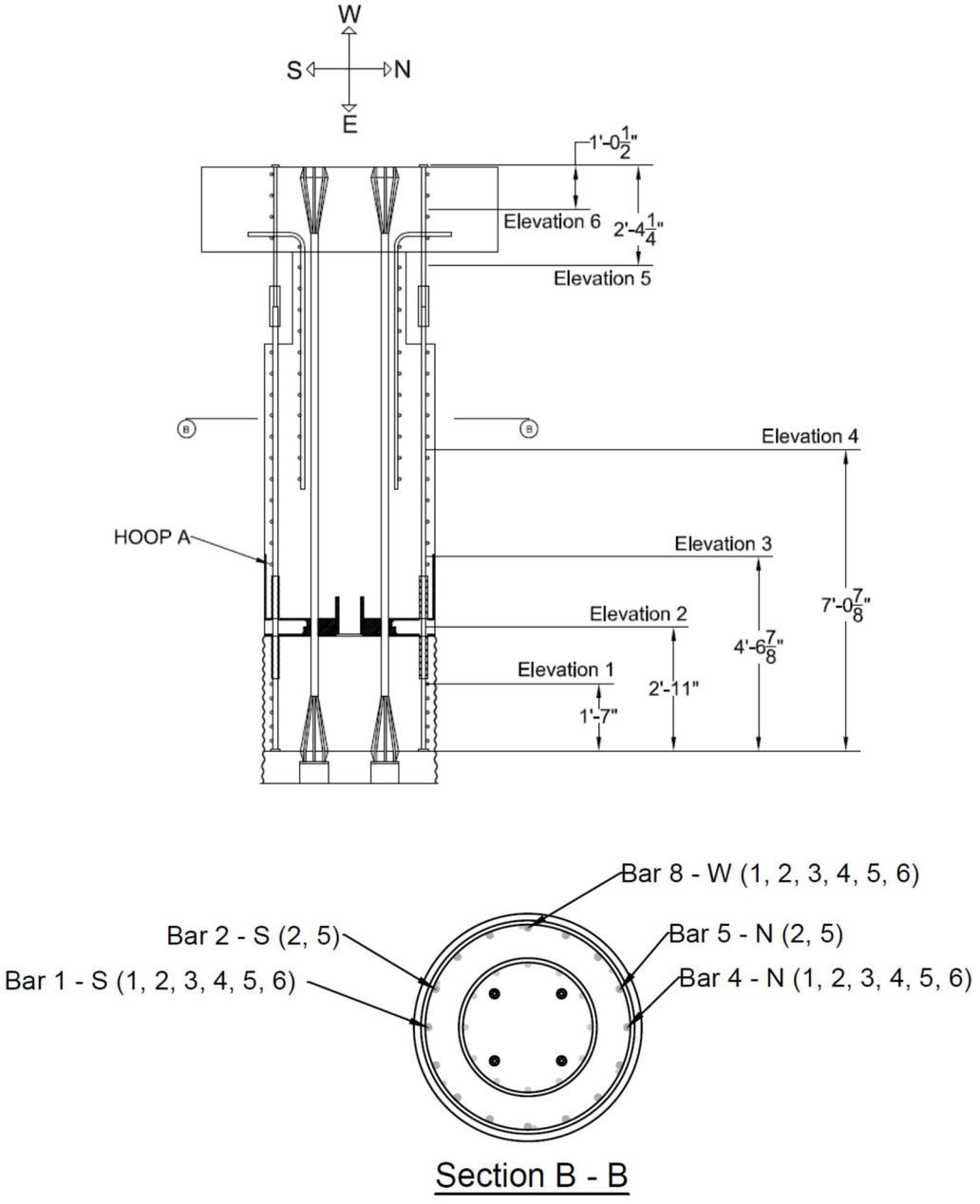

Figure D.11: Strain gauges on longitudinal rebars for Specimen 2 (loading along N-S direction)

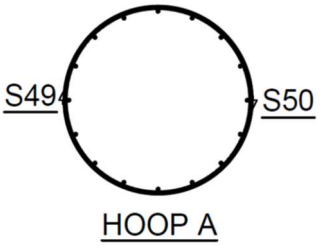

Figure D.12: Strain gauges on transverse reinforcement for Specimen 2

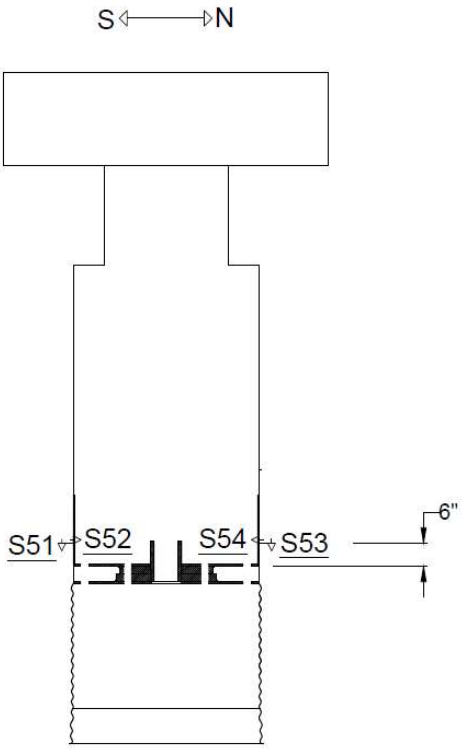

Figure D.13: Strain gauges on steel casing for Specimen 2

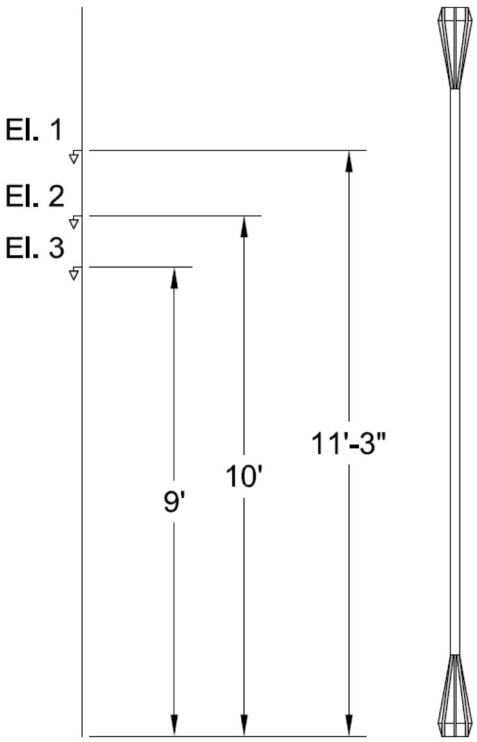

	NW 1	NE 1	SW 1	SE 1
El. 1	S13	S58	S01	S07
El. 2	S14	S59	S02	S08
El. 3	S15	S60	S03	S09

	NW 2	NE 2	SW 2	SE 2
El. 1	S55	S61	S04	S10
El. 2	S56	S62	S05	S11
El. 3	S57	S63	S06	S12

Figure D.14: Strain gauge locations on prestressing strands for Specimen 2

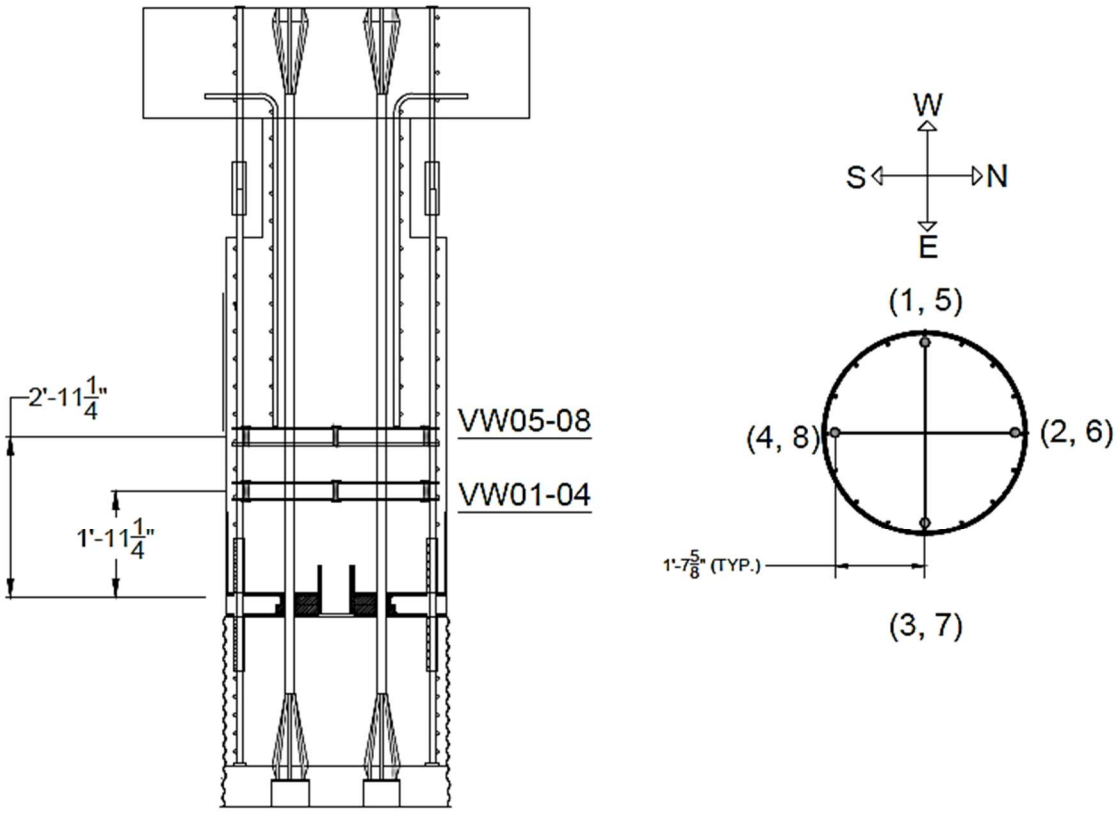

Figure D.15: Vibrating-wire gauges for Specimen 2

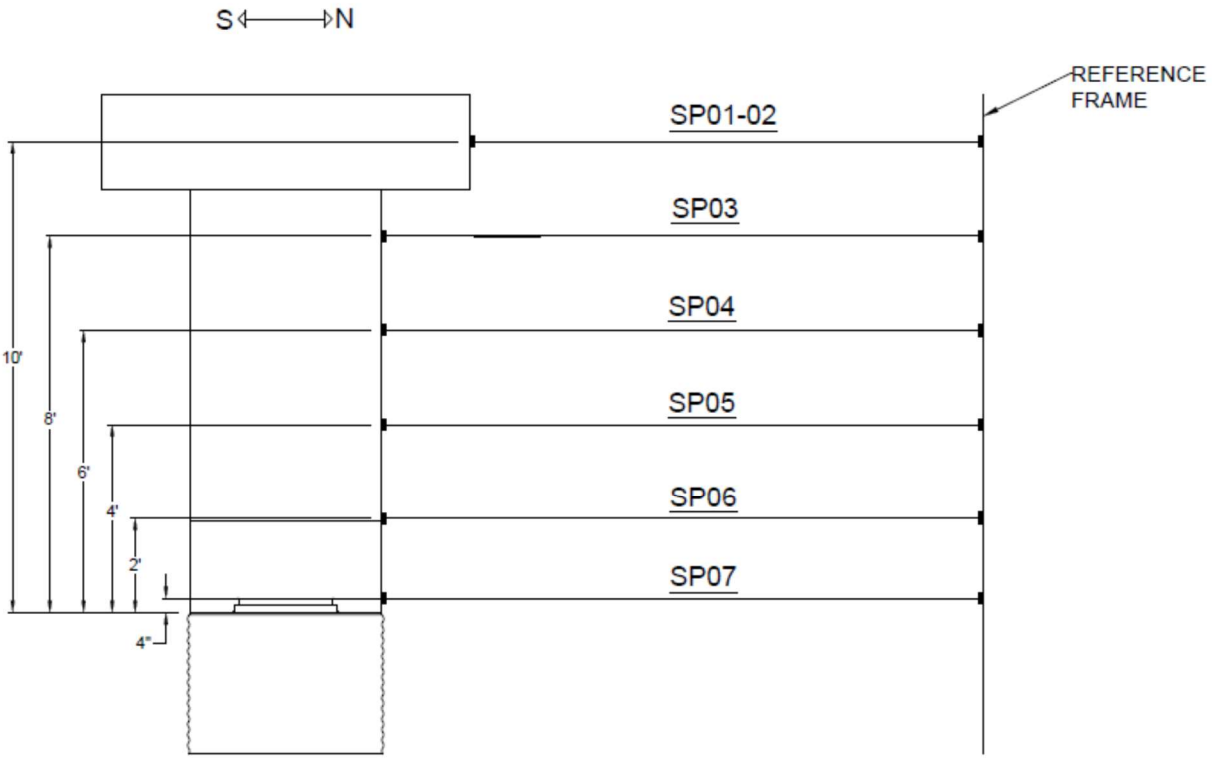

Figure D.16: String potentiometer locations for Specimen 2

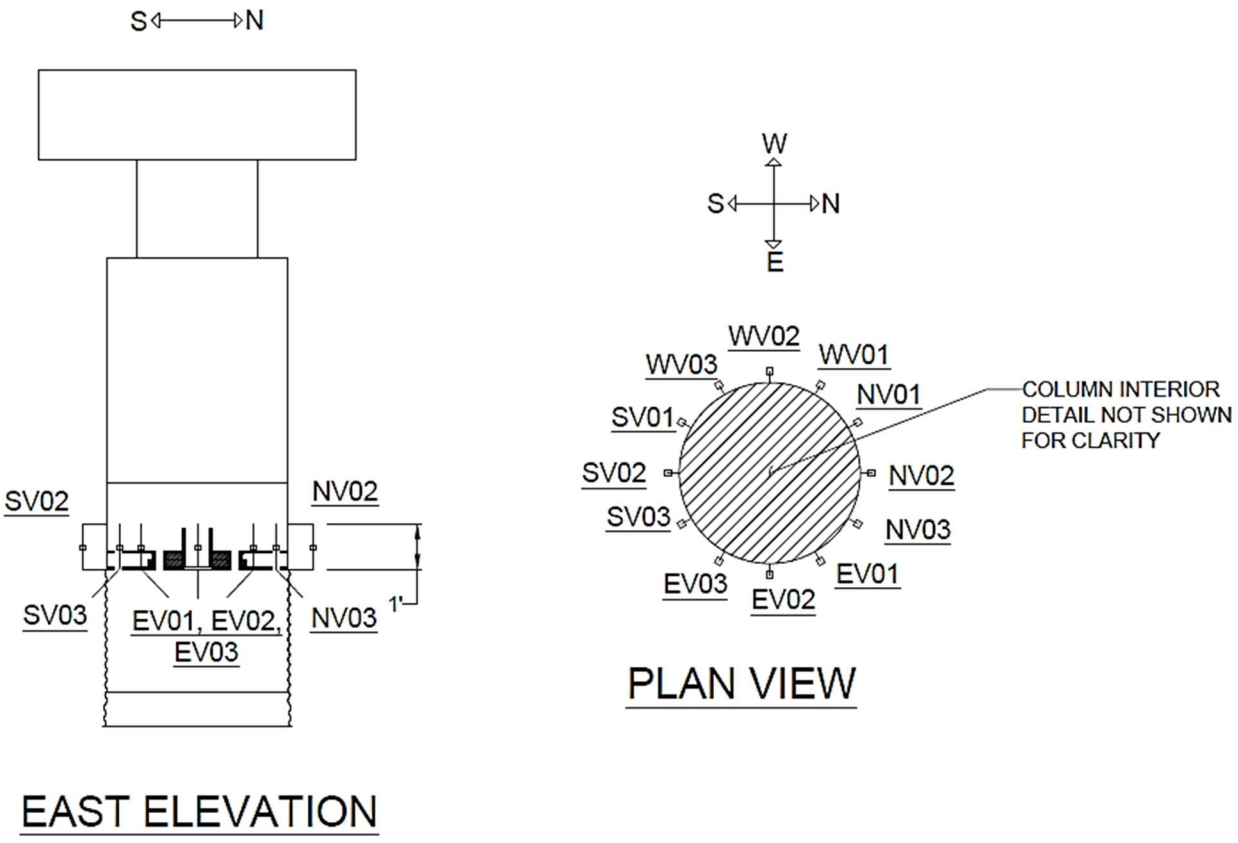

Figure D.17: Linear potentiometers around sacrificial zone for Specimen 2

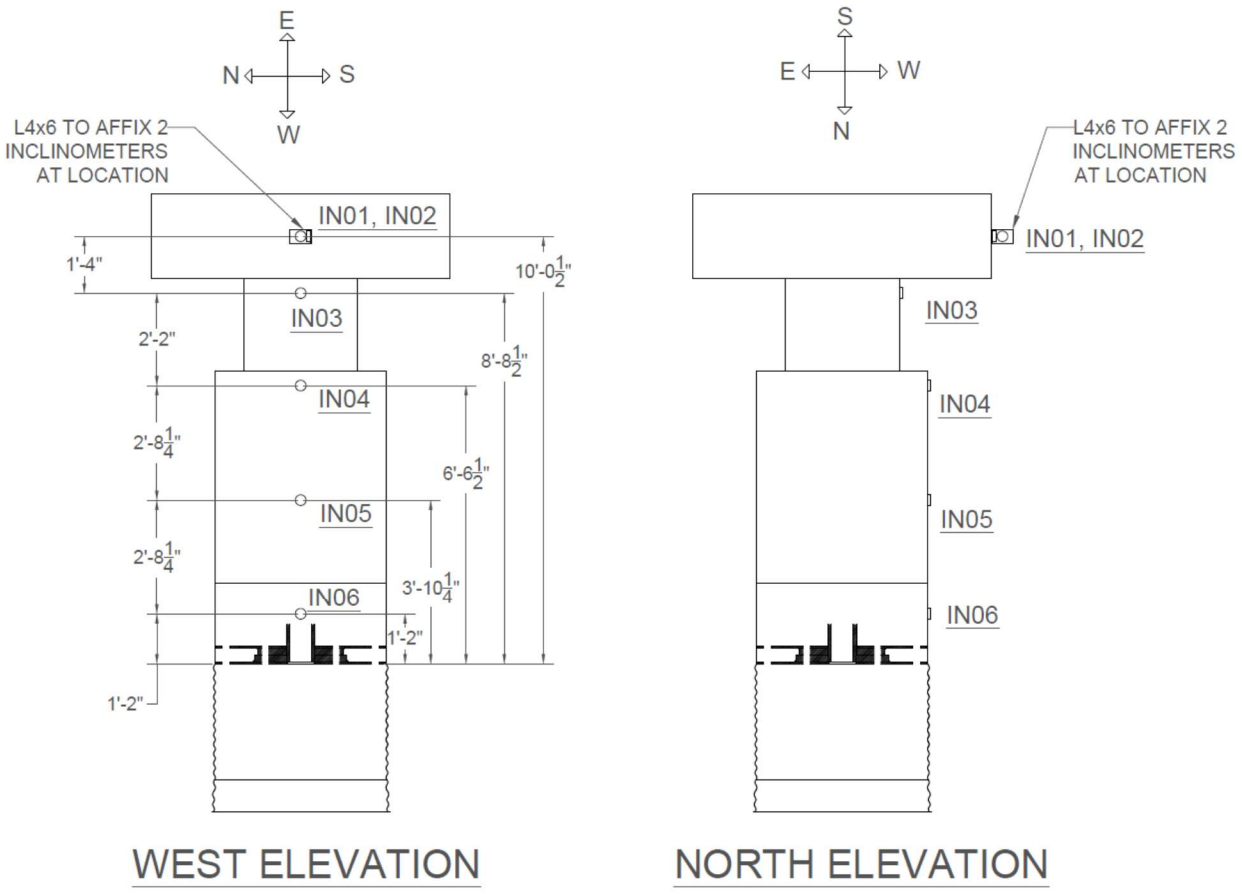

Figure D.18: Inclinometer locations for Specimen 2

Appendix E Estimation of Initial Strains in Prestressing Strands and Rebars

From the day of post-tensioning the strands, the strains in the prestressing strands and rebars were affected by the creep and shrinkage of the concrete column. Since the strain gauges on the strands and rebars were not continuously connected to the data-acquisition system and their values were zeroed at the beginning of each test, the initial strain values in the strands and rebars need to be estimated from the data collected from the vibrating-wire (VW) gauges inside the concrete column. The calculations and data for determining the initial strains in the prestressing strands and rebars during each stage of construction and testing are presented in this appendix.

E.1 Specimen 1

E.1.1 Vibrating-Wire Gauge Data

Two construction stages are considered here. One is from the day of post-tensioning to the day on which the column was secured in the foundation slab with concrete, and the other is the subsequent period till the day of the first column test, with the ungrouted rocking hinge. Figure E.1 shows the column heights and strand length considered for the calculation of the strains in the prestressing strands in different periods. In this figure, L_{ub} represents the unbonded length of the prestressing strands, $H_{c,free}$ represents the free-standing length of the column (including the pedestal) for the period between the day on which the strands were post-tensioned and the day on which the column was secured in the foundation slab with concrete, and $H_{c,fixed}$ denotes the clear height of the column after the specimen was secured in the foundation slab. The creep and shrinkage in the loading block and footing are ignored in the calculations.

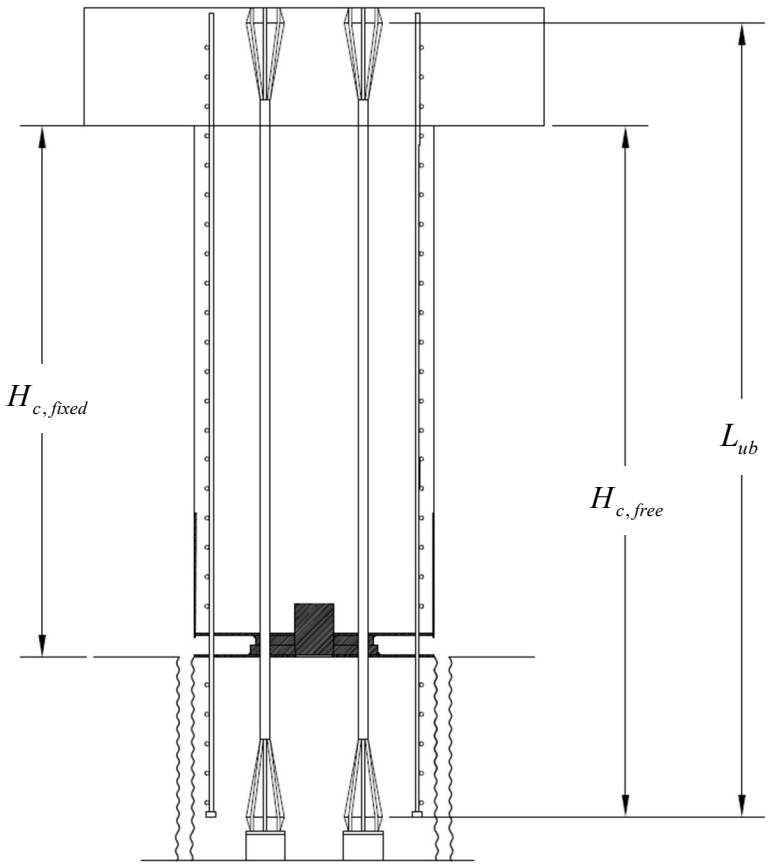

Figure E.1: Column heights and strand length considered for estimating strains in prestressing strands

Figure E.2 shows the VW gauge data from the beginning of the post-tensioning day (May 29th, 2019) through the day when Specimen 1 was set into the foundation slab (June 3rd, 2019). Figure E.3 shows the averaged VW gauge data during this period.

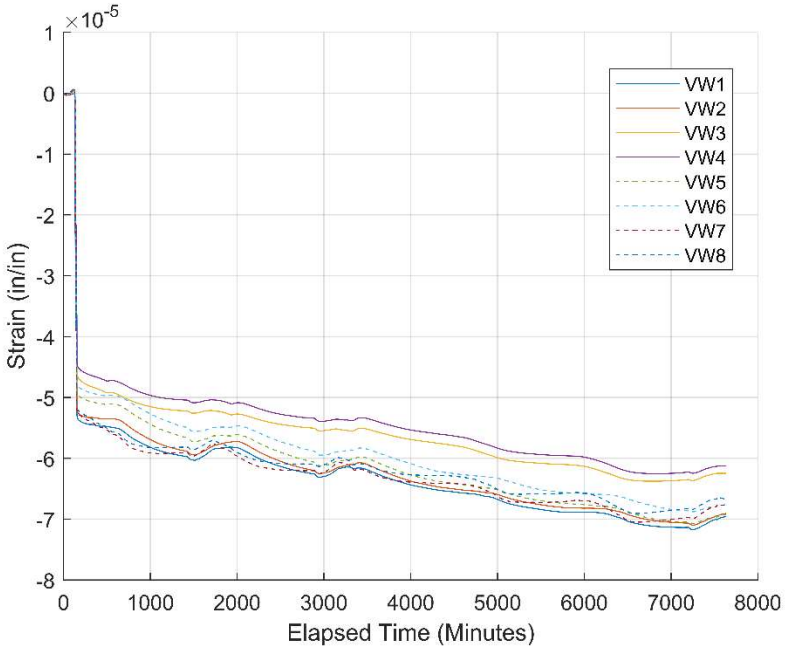

Figure E.2: Strains in concrete column from VW gauges between May 29th, 2019 and June 3rd, 2019 for Specimen 1

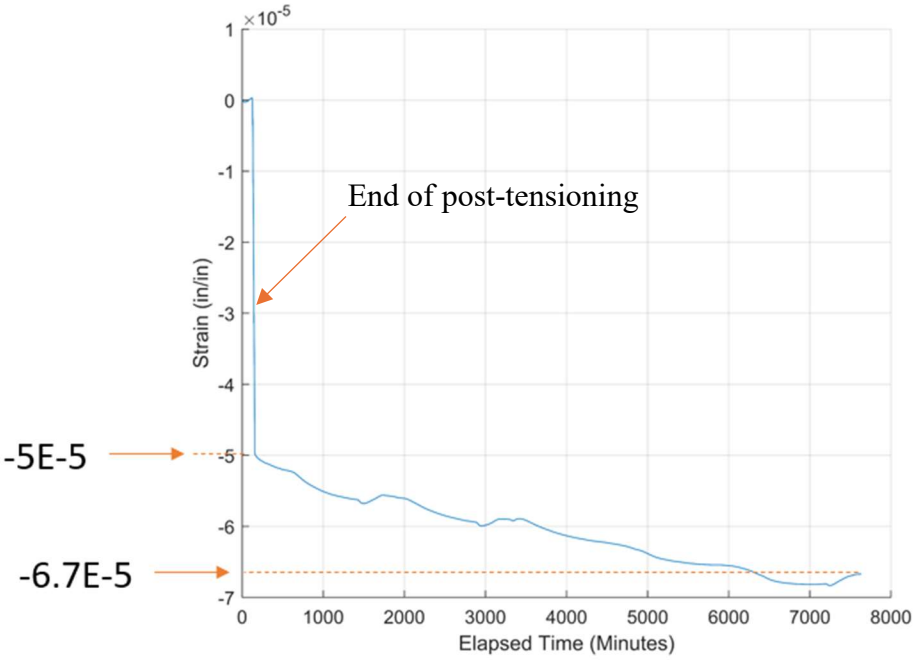

Figure E.3: Average strain in concrete column from VW gauges between May 29th, 2019 and June 3rd, 2019 for Specimen 1

Figure E.4 shows the average strain recorded by the VW gauges during the test of Specimen 1 on June 11th, 2019, with the rocking hinge ungrouted, and Figure E.5 shows the average strain recorded by the VW gauges during the test on June 14th, 2019, with the grouted rocking hinge.

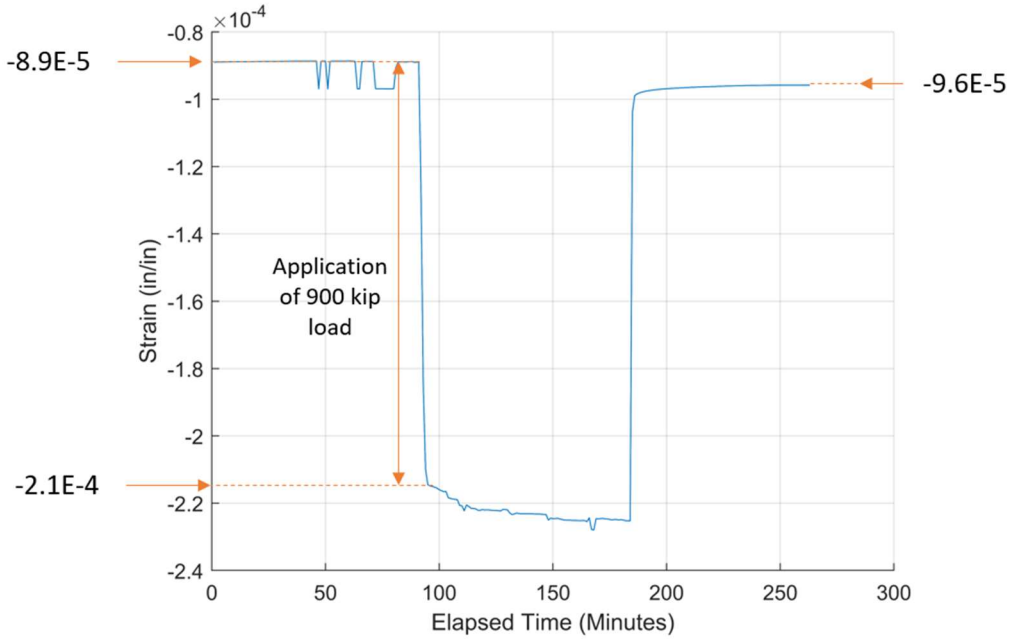

Figure E.4: Average strain from VW gauges on the test day with ungrouted rocking hinge for Specimen 1

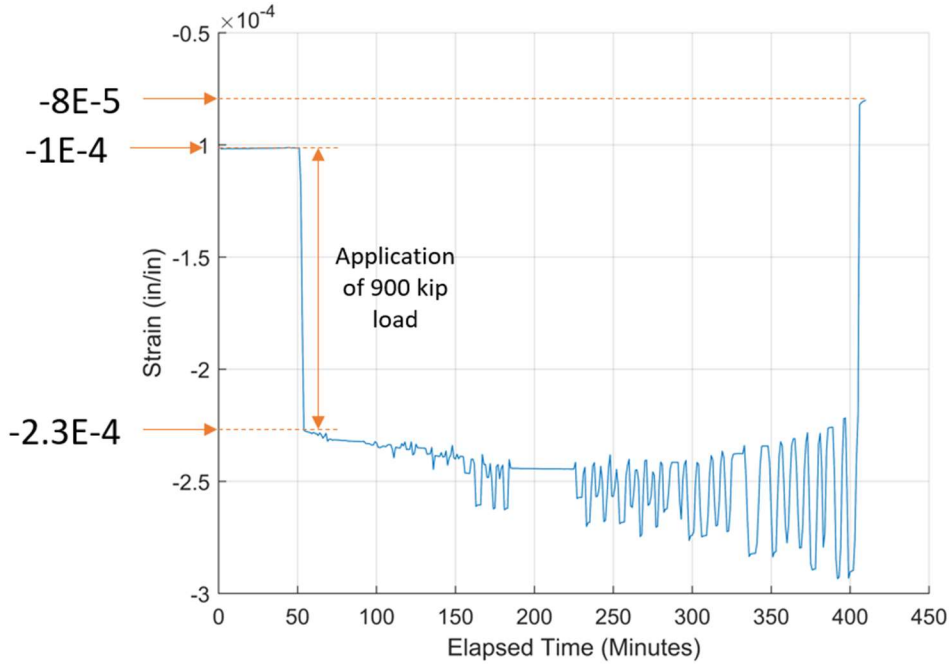

Figure E.5: Average strain in VW gauges from the test day with grouted rocking hinge for Specimen 1

The change in strain in the prestressing strands due to the creep and shrinkage of the concrete column in each stage of construction can be calculated using Equation (E.1).

$$\Delta\varepsilon_{p,sh+cr} = \Delta\varepsilon_{c,sh+cr} \frac{clear\ column\ height}{L_{ub}} \tag{E.1}$$

where $\Delta\varepsilon_{p,sh+cr}$ is the change in strain in the prestressing strands, $\Delta\varepsilon_{c,sh+cr}$ is the change in strain in the column measured by the VW gauges, the value of the clear column height depends on the specific stage of construction, and L_{ub} is the unbonded length of the prestressing strands.

To estimate the strain in the strands on the day of the test with the ungrouted hinge, the change in strains due to the creep and shrinkage of concrete during the following two periods are considered: the period between the post-tensioning day (May 29th, 2019) and the day Specimen 1

was secured in the foundation slab (June 3rd, 2019), and the subsequent period till the day of the test (June 11th, 2019).

For the first period, the clear column height is $H_{c,free}$ (shown in Figure E.1), and the total creep and shrinkage strain, $\Delta\varepsilon_{c,sh+cr}$, developed in the concrete column can be obtained from Figure E.3 as the difference in the average strain values between the end of the post-tensioning process and the last data point taken before securing Specimen 1 in the foundation slab. The loss of the tensile strain in the prestressing strands during this period is thus calculated with Equation (E.1) as follows.

$$\begin{aligned}\Delta\varepsilon_{p,sh+cr,1} &= \Delta\varepsilon_{c,sh+cr}\frac{H_{c,free}}{L_{ub}}\\ &= (0.000067-0.00005)\frac{140.9}{165}\\ &= 0.0000145\end{aligned}$$

For the second period, $\Delta\varepsilon_{c,sh+cr}$ is determined as the difference between the last average strain value from the VW gauges before securing Specimen 1 in the foundation slab and the strain value right before the test with the ungrouted hinge. The clear column height for the second stage is $H_{c,fixed}$. The loss of the tensile strain in the prestressing strands is calculated as follows.

$$\begin{aligned}\Delta\varepsilon_{p,sh+cr,2} &= \Delta\varepsilon_{c,sh+cr}\frac{H_{c,fixed}}{L_{ub}}\\ &= (0.000089-0.000067)\frac{108.4}{165}\\ &= 0.0000145\end{aligned}$$

The total strain loss experienced by the prestressing strands due to the creep and shrinkage of the concrete column, $\Delta\varepsilon_{p,sh+cr}$, at the beginning of the test with the ungrouted hinge is the sum of the losses in the aforementioned two periods.

$$\Delta\varepsilon_{p,sh+cr} = \Delta\varepsilon_{p,sh+cr,1} + \Delta\varepsilon_{p,sh+cr,2} = 0.000029$$

As discussed in Section E.1.2, the average tensile strain recorded by the strain gauges on the strands right at the end of the post-tensioning process is 0.0022. Hence, the average tensile strain in the prestressing strands at the beginning of the test with the ungrouted hinge, $\varepsilon_{p,ug}$, is then calculated as follows.

$$\varepsilon_{p,ug} = 0.0022 - \Delta\varepsilon_{p,sh+cr} = 0.00217$$

The change in strain in the strands between the beginning of the test with the ungrouted hinge and the beginning of the test with the grouted hinge, $\Delta\varepsilon_{ug}$, is calculated with Equation (E.1), where $\Delta\varepsilon_{c,sh+cr}$ is the difference in the strain values from the VW gauges between these time instants, as identified in Figures E.4 and E.5, and the clear column height is $H_{c,fixed}$.

$$\begin{aligned}\Delta\varepsilon_{ug} &= \Delta\varepsilon_{c,sh+cr}\frac{H_{c,fixed}}{L_{ub}} \\ &= (0.0001 - 0.000089)\frac{108.4}{165} \\ &= 0.0000072\end{aligned}$$

The average tensile strain in the prestressing strands at the beginning of the test with the grouted hinge, $\varepsilon_{p,gr}$, is then calculated to be

$$\begin{aligned}\varepsilon_{p,gr} &= \varepsilon_{p,ug} - \Delta\varepsilon_{ug} \\ &= 0.00217 - 0.0000072 \\ &= 0.00216\end{aligned}$$

Figure E.5 shows that when the 900-kip axial load was removed at the end of the test with the grouted hinge, the column experienced a net loss of the compressive strain compared to the beginning of the test before the application of the axial load. This indicates that the prestressing strands had experienced inelastic deformation and possible some slip in the anchors, resulting in a net loss of the prestressing force exerted on the concrete column.

E.1.2 Prestressing Strand Strain Data

Figures E.6 through E.9 show the data recorded by all the functioning strain gauges placed directly on the prestressing strands. As shown in Figure 7.18, the gauges were placed on one strand in each of the four tendon groups. Figure E.6 shows individual gauge data from the post-tensioning day, while Figure E.7 shows the averaged strain data. It can be seen from Figure E.7 that the average tensile strain in the strands right after jacking is 0.0022.

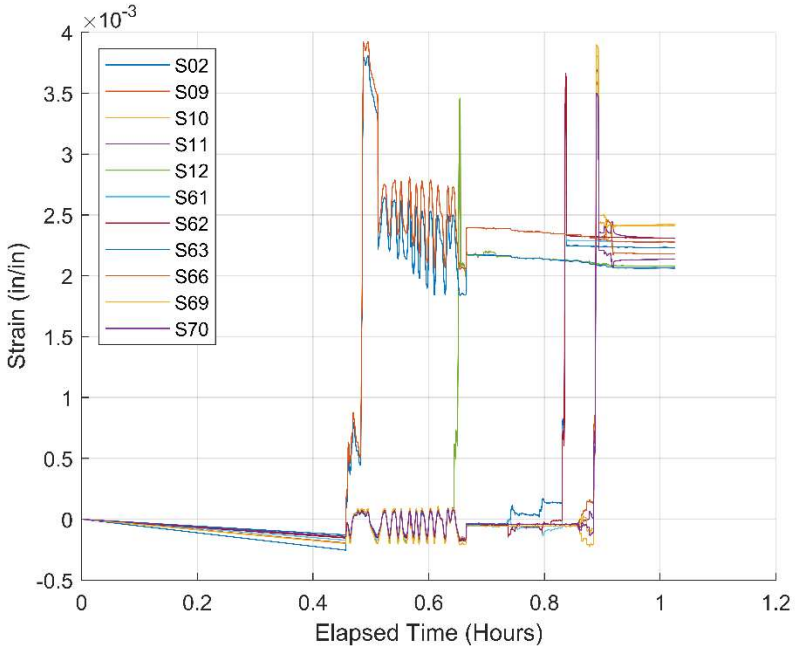

Figure E.6: Strains in prestressing strands on the day of post-tensioning for Specimen 1 (May 29th, 2019)

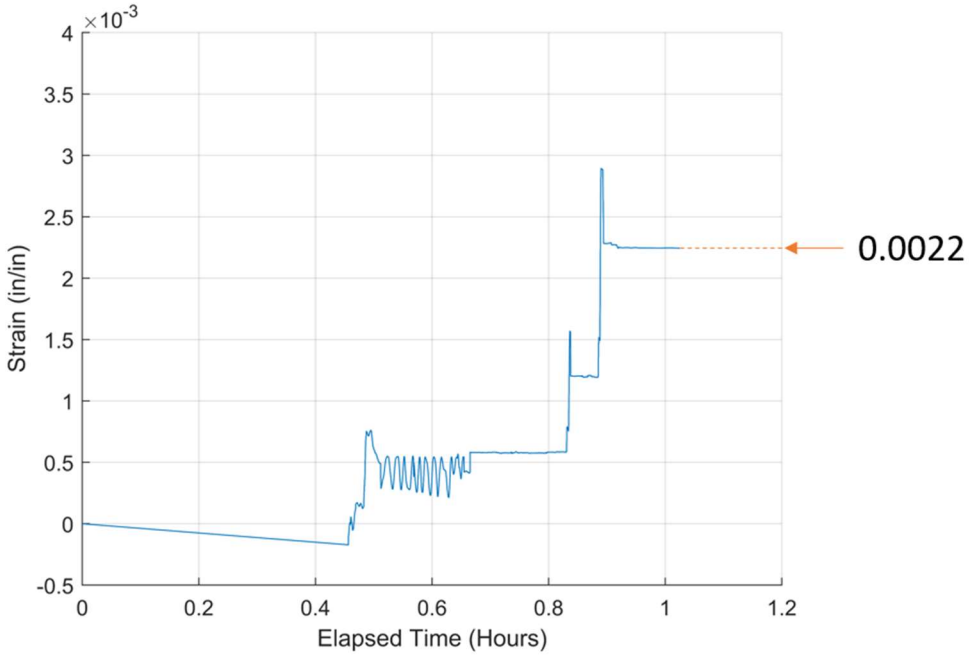

Figure E.7: Average strain in prestressing strands on the day of post-tensioning for Specimen 1 (May 29th, 2019)

Figure E.8 shows the average strain data from the test with the ungrouted rocking hinge, and Figure E.9 shows the average strain data from the test with the grouted hinge. Since the strain gauge values were zeroed at the beginning of each test, the initial strains shown in Figures E.8 and E.9 are estimated from with the VW gauge data as discussed in Section E.1.1.

Figures E.4 and E.8 show that the reduction of the tensile strain in the strands is about two times the increase of the compressive strain in the concrete column upon the application of the 900-kip axial load. Ideally, they should have a comparable change. It is believed that the VW gauge data is more reliable than the strain gauge data from the strands for this small strain change. The former gives a more reasonable estimate of the modulus of elasticity of the concrete as shown in the following section.

Figure E.9 shows that when the 900-kip axial load was removed after the end of the test, there is a net loss of the tensile strain in the prestressing strands of approximately 0.0012. This loss is likely due to the slip of the strands in the anchors during the test.

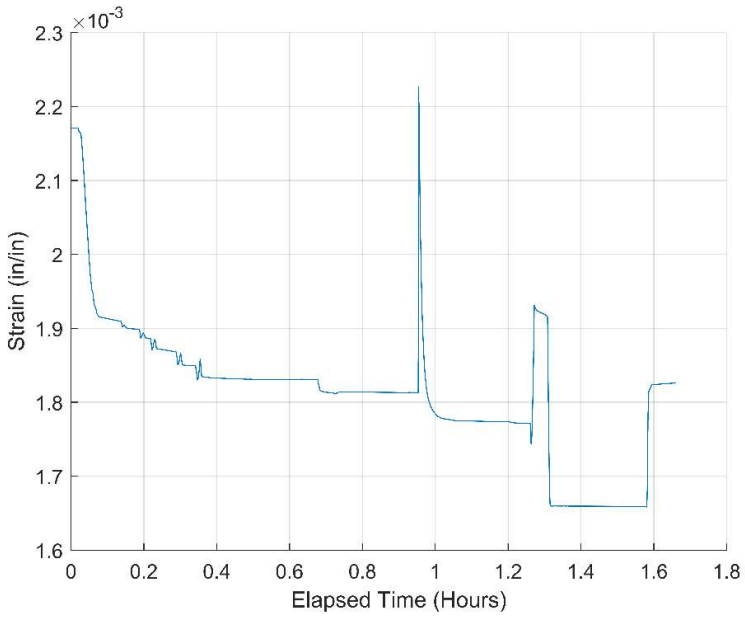

Figure E.8: Average strain in prestressing strands during the test with ungrouted rocking hinge for Specimen 1 (June 11th, 2019)

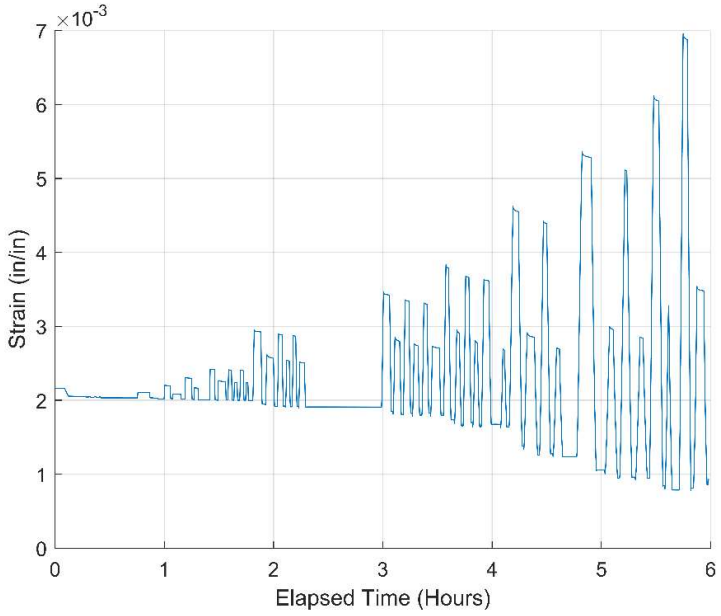

Figure E.9: Average strain in prestressing strands during the test with grouted rocking hinge for Specimen 1 (June 14th, 2019)

E.1.3 Estimation of Modulus of Elasticity of Concrete

The modulus of elasticity of the concrete for Specimen 1, E_c, can be estimated from the compressive strain increments in the column upon the application of the post-tensioning force and the 900-kip axial load as follows.

$$E_c = \frac{\Delta F}{\Delta \varepsilon_c A_n} \tag{E.2}$$

where A_n is the net cross-sectional area of the column (the gross area minus the area of the four post-tensioning ducts), ΔF is the change of the axial force exerted on the column, and $\Delta \varepsilon_c$ is the change in concrete strain recorded by the VW gauges during the load application. The net column area, A_n, is calculated to be 1,792 in.^{2}. The influence of the longitudinal reinforcing bars in the column can be neglected.

During the post-tensioning process, the column experienced an increase in compressive strain, $\Delta \varepsilon_c$, of 0.00005, as shown in Figure E.3, and the average tensile strain in the strands reached 0.0022, corresponding to a stress of 64 ksi based on the stress-strain relation for the strands as shown Figure 7.9. With 20 strands, each with a cross-sectional area of 0.217 in.^{2}, the total prestressing force is:

$$\begin{aligned} F_p &= (64 \text{ ksi})(20)(0.217 \text{ in.}^2) \\ &= 277.8 \text{ kips} \end{aligned}$$

The modulus of elasticity of the concrete can be estimated as:

$$E_c = \frac{F_p}{\Delta\varepsilon_c A_n}$$
$$= \frac{277.8 \text{ kips}}{(0.00005)(1,792 \text{ in.}^2)}$$
$$= 3{,}100 \text{ ksi}$$

At the start of the test with the ungrouted hinge, an axial load of 900 kips was applied. This applied load resulted in a change of strain, $\Delta\varepsilon_c$, of 0.00012. The net change in the axial force exerted on the column, including that from the prestressing strands, is calculated as:

$$\Delta F = 900 - \Delta\varepsilon_c \frac{H_{c,fixed}}{L_{ub}} E_p$$
$$= 900 - (0.00012)\frac{108.4}{165}(29{,}000)$$
$$= 897.7 \text{ kips}$$

The modulus of elasticity, E_c, of the concrete is estimated as:

$$E_c = \frac{\Delta F}{\Delta\varepsilon_c A_n}$$
$$= \frac{897.7 \ kips}{(0.00012)(1,792 \ in^2)}$$
$$= 4{,}175 \text{ ksi}$$

For the test with the grouted hinge, the application of the 900-kip axial load resulted in a change in the compression strain, $\Delta\varepsilon_c$, of 0.00013. The net change in the axial force is:

$$\Delta F = 900 - \Delta\varepsilon_c \frac{H_{c,fixed}}{L_{ub}} E_p$$
$$= 900 - (0.00013)\frac{108.4}{165}(29{,}000)$$
$$= 897.5 \text{ kips}$$

The modulus of elasticity, E_c, of the concrete is calculated as:

$$E_c = \frac{\Delta F}{\Delta\varepsilon_c A_n}$$
$$= \frac{897.5 \text{ kips}}{(0.00013)(1{,}792\ in^2)}$$
$$= 3{,}853 \text{ ksi}$$

The compressive strength of the concrete is 8.3 ksi. The modulus of elasticity of the concrete calculated according to the formula in ACI 318 is 5,193 ksi, which is higher than the above estimates.

E.1.4 Longitudinal Rebar Strains

The longitudinal rebars in Specimen 1 were subjected to compression by the prestressing force of the strands. However, the strain gauges on the rebars were not connected to the data-acquisition system until the beginning of the ungrouted test, and the strain gauges were zeroed at the beginning of each test. Hence, it is necessary to determine the initial compressive strain in the longitudinal rebars prior to testing. The initial compressive strain in the rebar right after post-tensioning is assumed to be 0.00005, which is the compressive strain in the concrete measured by the VW gauges as shown in Figure E.3. The additional strain increment due to the creep and shrinkage of concrete from the end of the post-tensioning process to the beginning of the test with the ungrouted hinge can be assumed to be identical to that calculated in Section E.1.1 for the prestressing strands, which is $\Delta\varepsilon_{p,sh+cr} = 0.000029$. Hence, the initial compressive strain in the

rebars right before the test with the ungrouted hinge is estimated to be 0.00008, which is negligibly small. Some of the rebars yielded during the test with the ungrouted hinge. The residual plastic strains in the rebars recorded at the end of the test are treated as the initial strains in the rebars at the beginning of the test with the grouted hinge.

E.2 Specimen 2

In Specimen 2, the VW gauges were damaged during the construction process. For this reason, the loss of the tensile strain in the strands due to the creep and shrinkage of the concrete cannot be deduced from the VW gauge data. Hence, the initial strain value in the strands for each test has to be deduced by assuming that Specimen 2 had experienced the same creep and shrinkage strains as Specimen 1.

Figure E.10 shows the strain values measured with the individual strain gauges on the strands on the post-tensioning day (January 15th, 2021), and Figure E.11 shows the averaged strain values. Figure E.12 shows the average strain in the strands on the day of the test with the ungrouted hinge (February 3rd, 2021), with the strain gauge data corrected with the aforementioned assumption. Upon removing the 900-kip axial load after the test, the final strain value in the strands is approximately 0.00218. This value is assumed to be the initial strain for the data for the test with the grouted hinge (February 9th, 2021), which is shown in Figure E.13, based on the observation that the change in strain between the two tests for Specimen 1 is negligible.

Similar to Specimen 1, Figure E.13 shows that when the 900-kip axial load was removed from Specimen 2 after the end of the test, there is a net loss of the tensile strain in the prestressing strands. However, the loss is approximately 0.00035, which is less significant than that in Specimen 1. This loss is likely due to the slip of the strands in the anchors during the test.

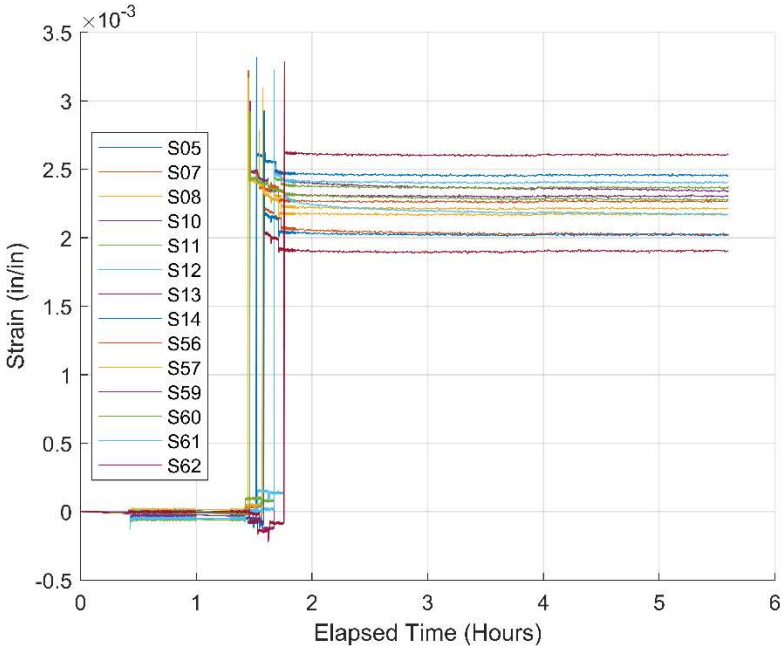

Figure E.10: Strains in prestressing strands on the day of post-tensioning for Specimen 2 (January 15th, 2021)

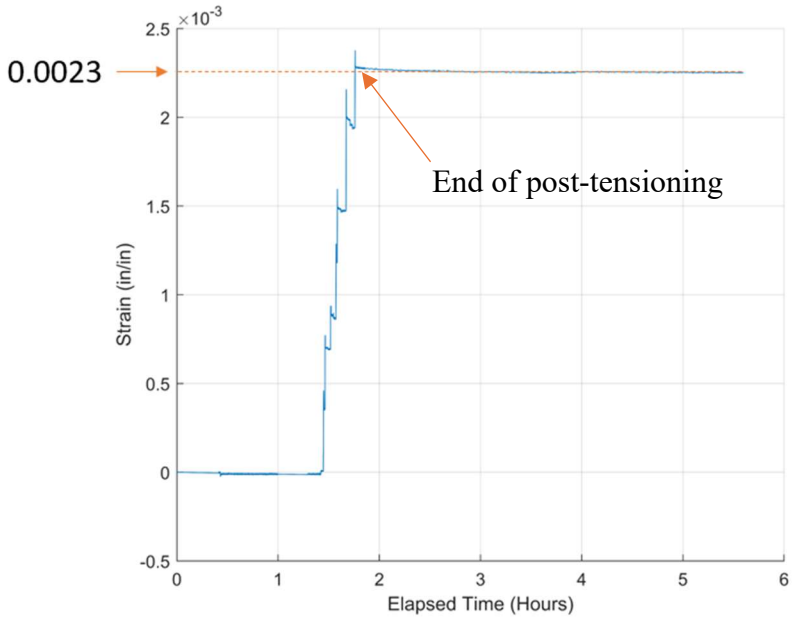

Figure E.11: Average strain in prestressing strands on the day of post-tensioning for Specimen 2 (January 15th, 2021)

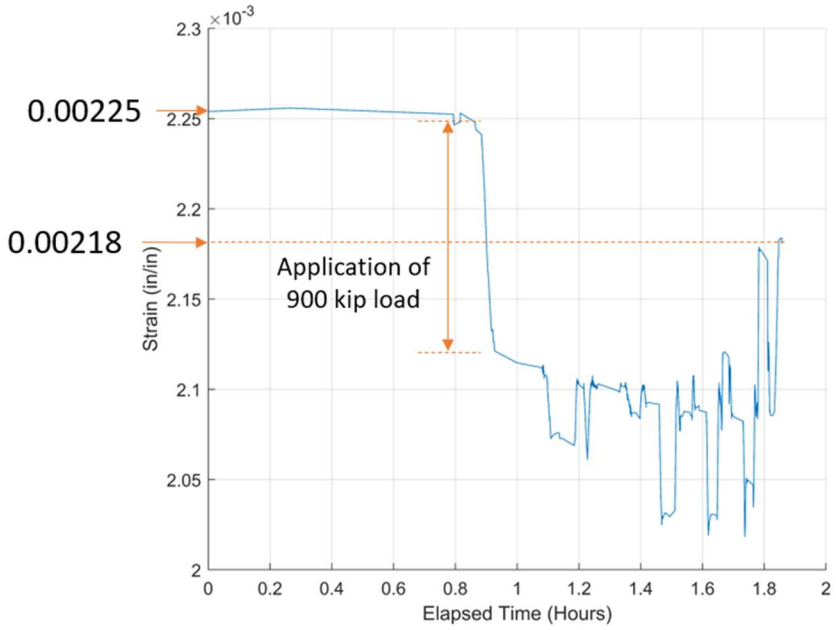

Figure E.12: Average strain in prestressing strands during the test with ungrouted rocking hinge for Specimen 2 (February 3rd, 2021)

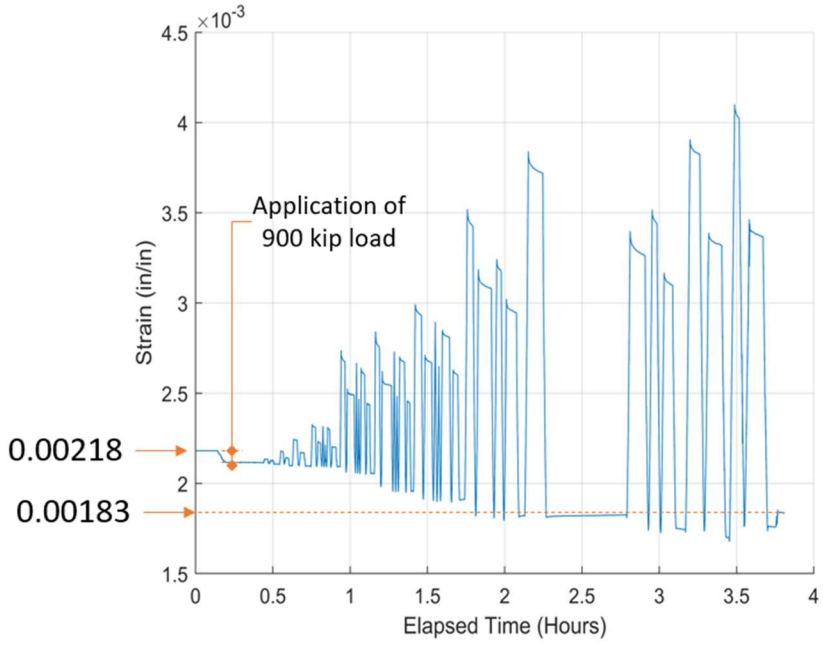

Figure E.13: Average strain in prestressing strands during the test with grouted rocking hinge for Specimen 2 (February 9th, 2021)

Appendix F Data for Calibration of Hysteretic Energy Dissipation Parameter

To calibrate the α parameter discussed in Section 10.4.2, time-history analyses are conducted on a structure that has the Type-2 bridge configuration, shown in Table 10.1, and 20 foot tall columns. The design of the columns follows that of Specimen 2 tested in this study, but with four different reinforcement scenarios. The reinforcement layout for each scenario is summarized in Table 10.2. Each design scenario is analyzed with five ground motion records, shown in Figure 10.7, each of which is scaled to different intensity levels. The results of the time-history analyses are presented in this appendix.

F.1 Scenario 1

In the first scenario, the reinforcement is identical to that to that of Specimen 2. There are 20 prestressing strands, and 16 longitudinal reinforcing bars in each column, with three columns per pier. The elastic bar and fuse bar sizes were No. 10 and No. 8 respectively, and the length of the fuse bar was 67 inches. All five ground motions shown in Figure 10.7 were scaled to achieve target column drifts of 3%, 6% and 10%, for a total of fifteen analyses. Figures F.1 through F.15 show the displacement time histories and the force-displacement curve for one column during the peak displacement half-cycle. In the displacement response time histories, the red asterisks indicate the half-cycle response that has the maximum amplitude and is used to estimate the value of α.

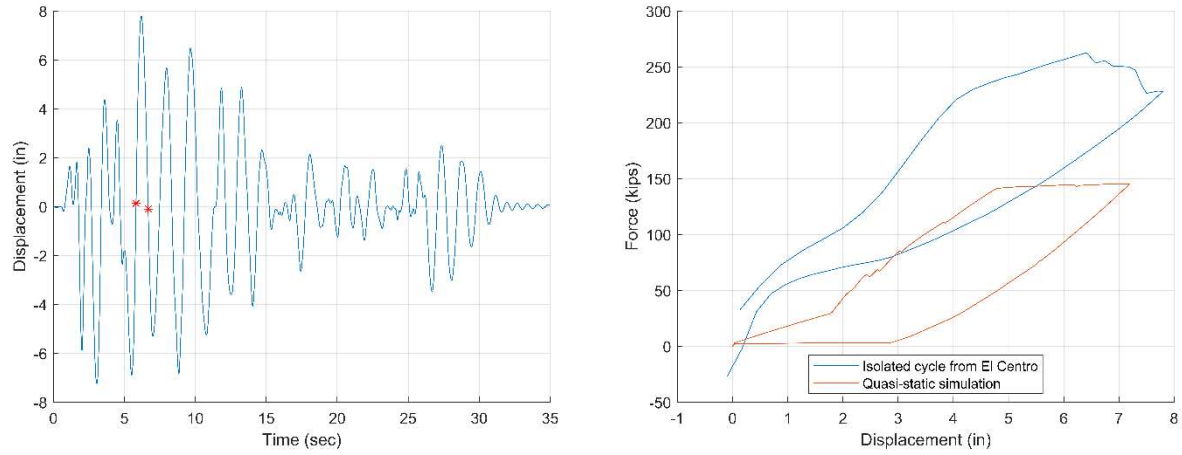

Figure F.1: (left) Displacement response time history for column reinforcement scenario 1 and El Centro record scaled to achieve 3% drift; (right) comparison of force-displacement curves for one column from time-history and quasi-static analyses

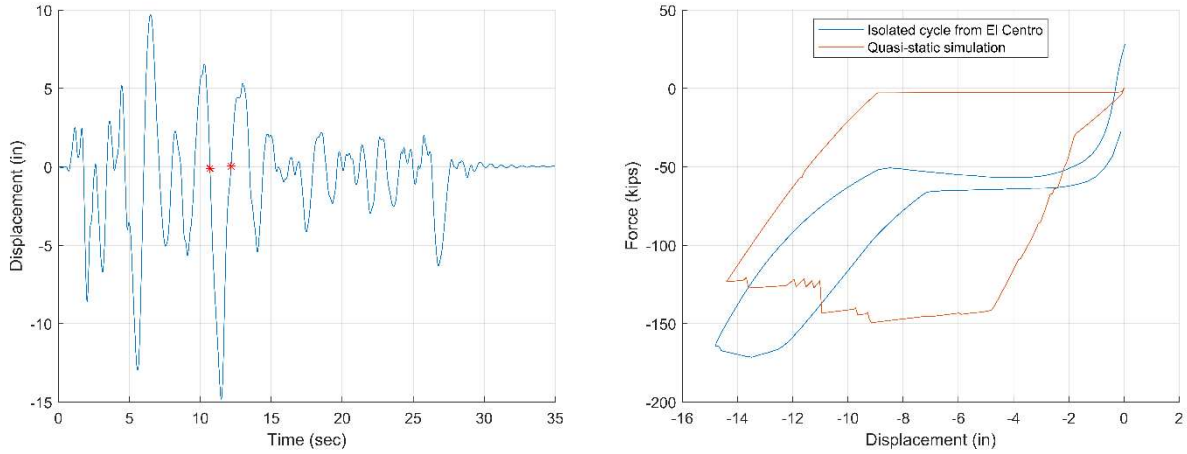

Figure F.2: (left) Displacement response time history for column reinforcement scenario 1 and El Centro record scaled to achieve 6% drift; (right) comparison of force-displacement curves for one column from time-history and quasi-static analyses

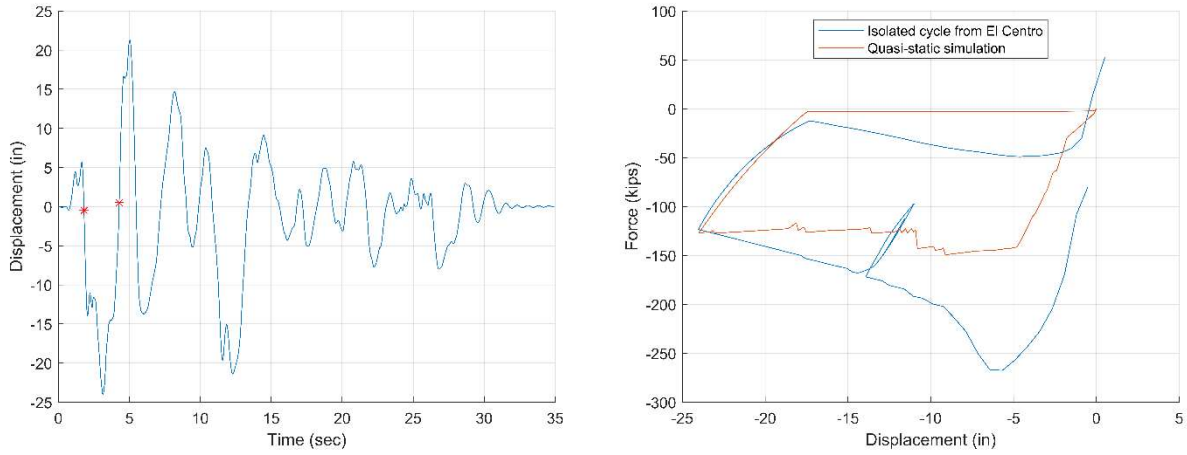

Figure F.3: (left) Displacement response time history for column reinforcement scenario 1 and El Centro record scaled to achieve 10% drift; (right) comparison of force-displacement curves for one column from time-history and quasi-static analyses

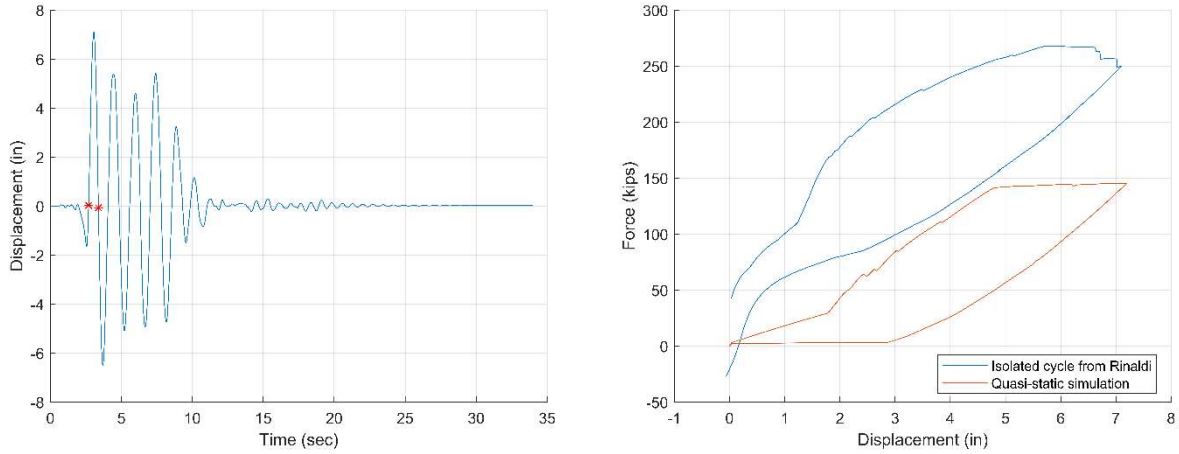

Figure F.4: (left) Displacement response time history for column reinforcement scenario 1 and Rinaldi record scaled to achieve 3% drift; (right) comparison of force-displacement curves for one column from time-history and quasi-static analyses

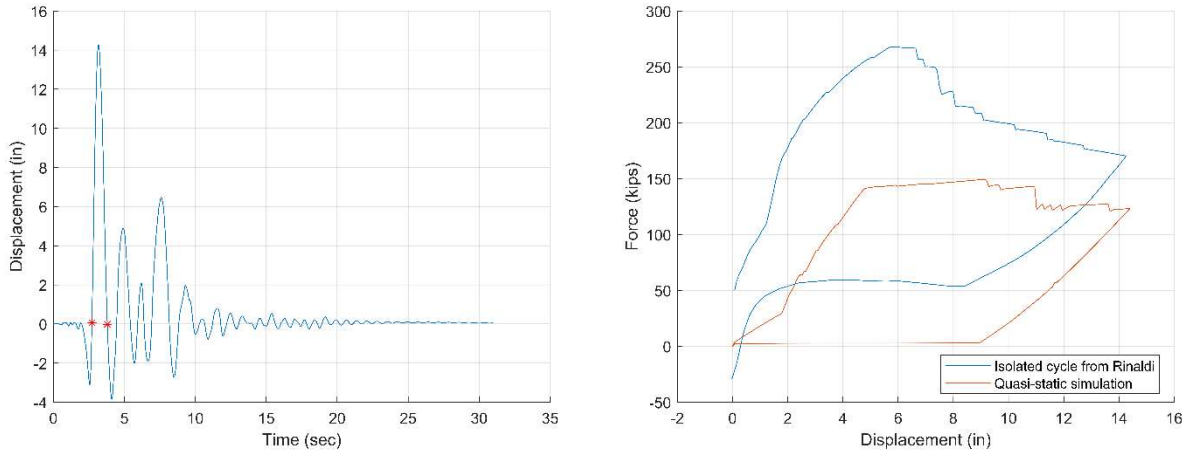

Figure F.5: (left) Displacement response time history for column reinforcement scenario 1 and Rinaldi record scaled to achieve 6% drift; (right) comparison of force-displacement curves for one column from time-history and quasi-static analyses

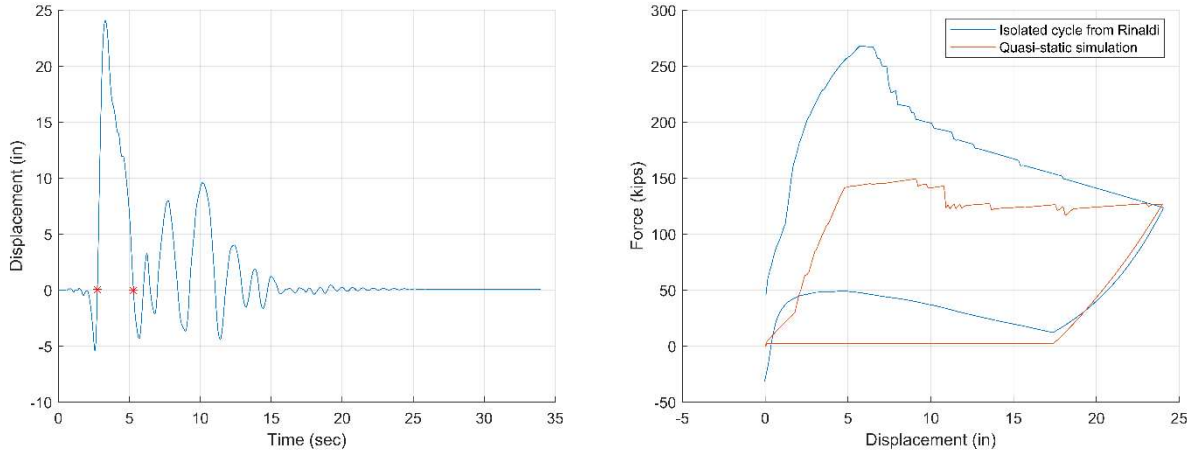

Figure F.6: (left) Displacement response time history for column reinforcement scenario 1 and Rinaldi record scaled to achieve 10% drift; (right) comparison of force-displacement curves for one column from time-history and quasi-static analyses

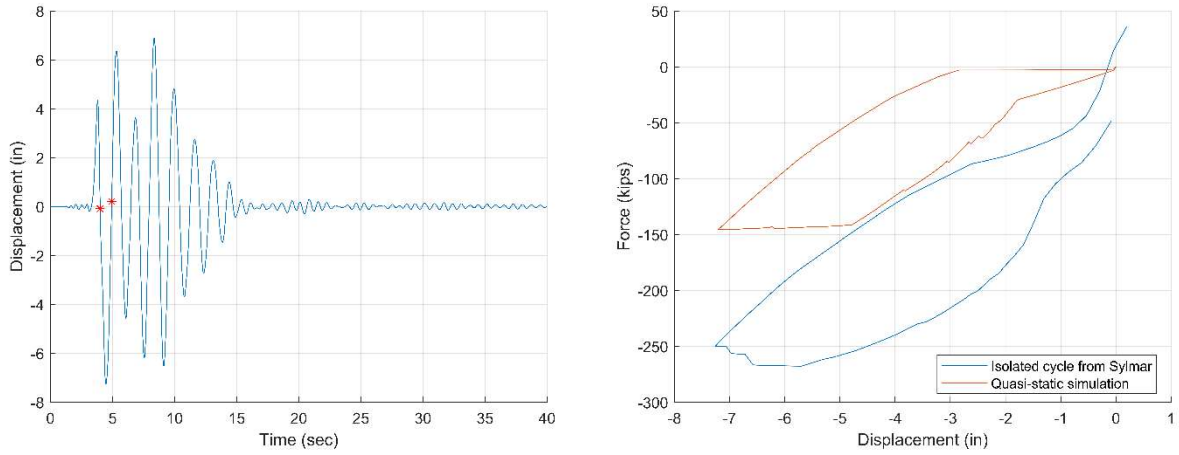

Figure F.7: (left) Displacement response time history for column reinforcement scenario 1 and Sylmar record scaled to achieve 3% drift; (right) comparison of force-displacement curves for one column from time-history and quasi-static analyses

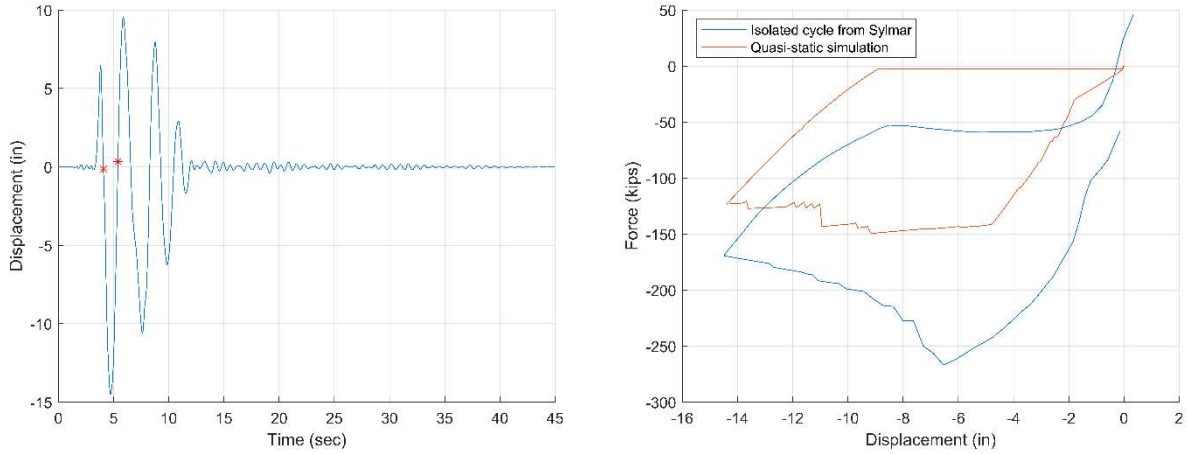

Figure F.8: (left) Displacement response time history for column reinforcement scenario 1 and Sylmar record scaled to achieve 6% drift; (right) comparison of force-displacement curves for one column from time-history and quasi-static analyses

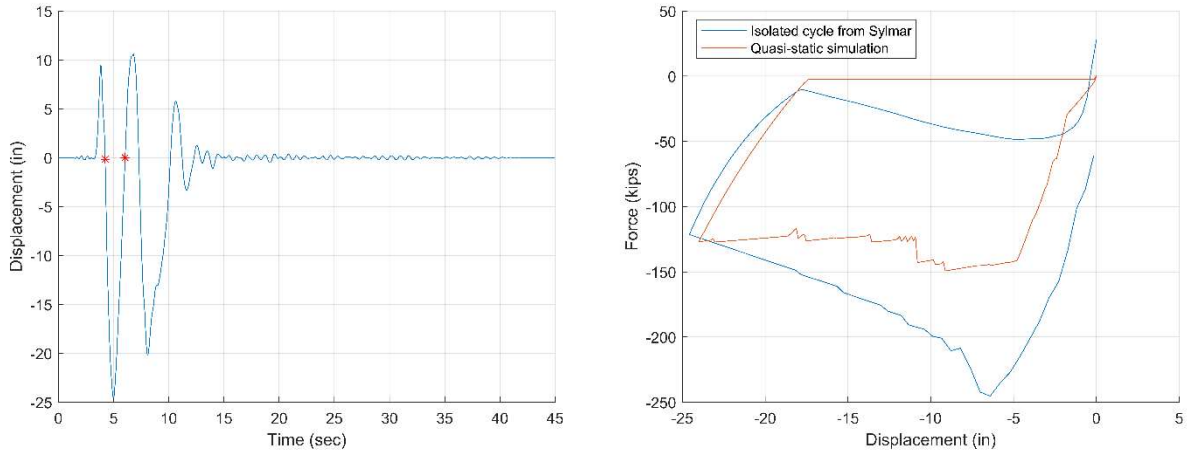

Figure F.9: (left) Displacement response time history for column reinforcement scenario 1 and Sylmar record scaled to achieve 10% drift; (right) comparison of force-displacement curves for one column from time-history and quasi-static analyses

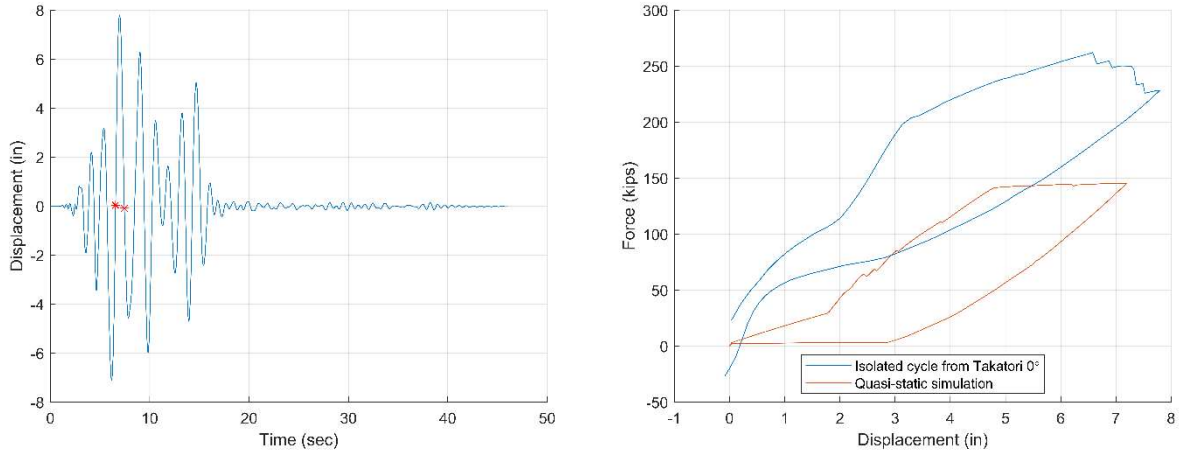

Figure F.10: (left) Displacement response time history for column reinforcement scenario 1 and Takatori 0° record scaled to achieve 3% drift; (right) comparison of force-displacement curves for one column from time-history and quasi-static analyses

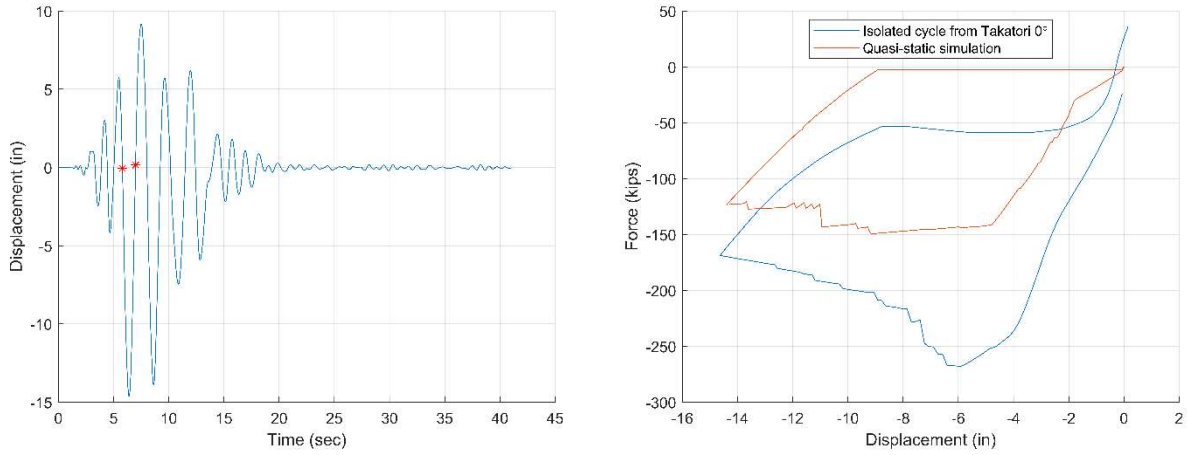

Figure F.11: (left) Displacement response time history for column reinforcement scenario 1 and Takatori 0° record scaled to achieve 6% drift; (right) comparison of force-displacement curves for one column from time-history and quasi-static analyses

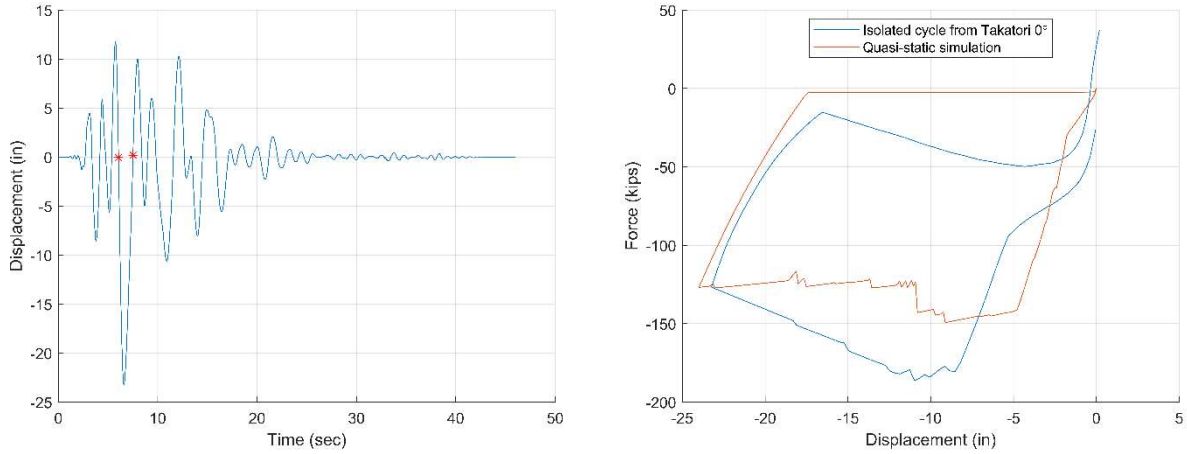

Figure F.12: (left) Displacement response time history for column reinforcement scenario 1 and Takatori 0° record scaled to achieve 10% drift; (right) comparison of force-displacement curves for one column from time-history and quasi-static analyses

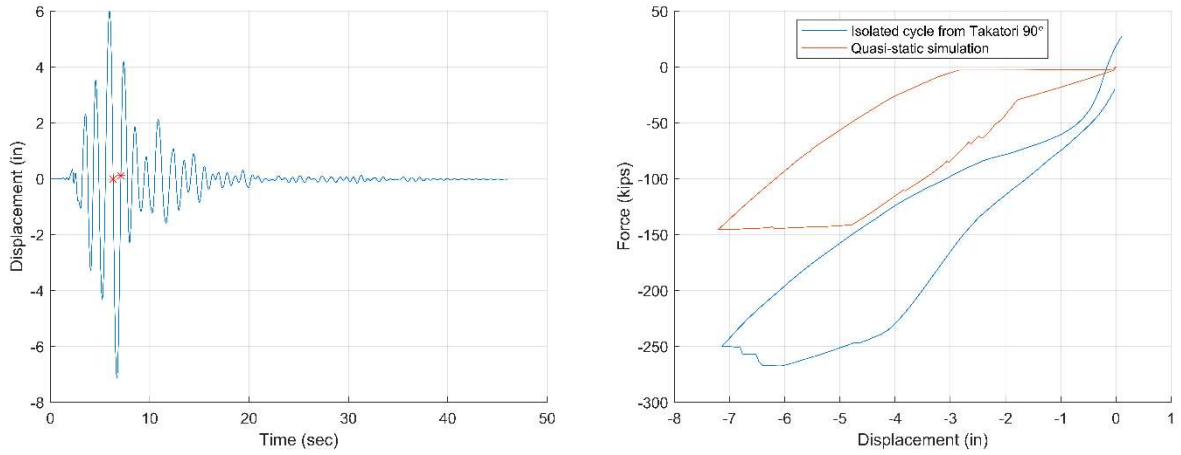

Figure F.13: (left) Displacement response time history for column reinforcement scenario 1 and Takatori 90° record scaled to achieve 3% drift; (right) comparison of force-displacement curves for one column from time-history and quasi-static analyses

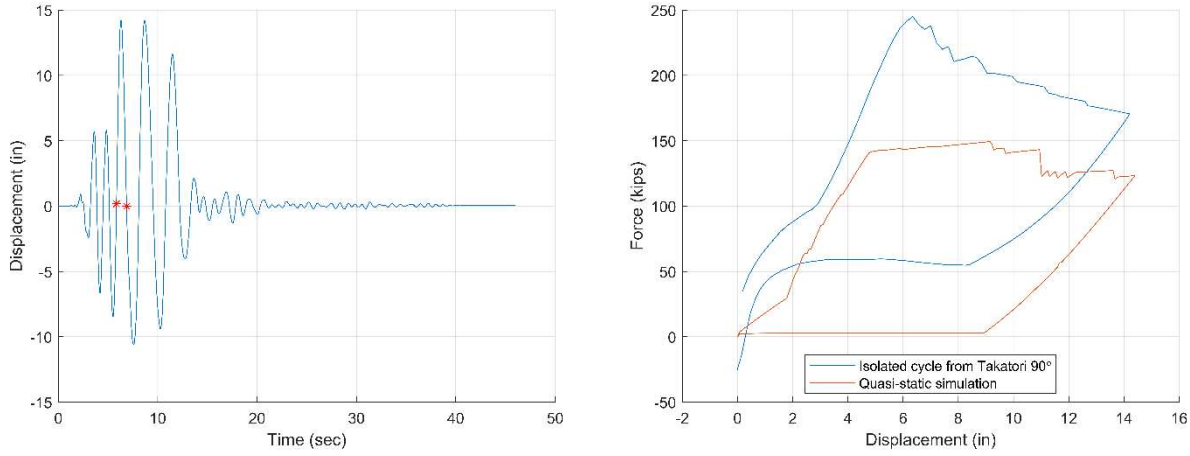

Figure F.14: (left) Displacement response time history for column reinforcement scenario 1 and Takatori 90° record scaled to achieve 6% drift; (right) comparison of force-displacement curves for one column from time-history and quasi-static analyses

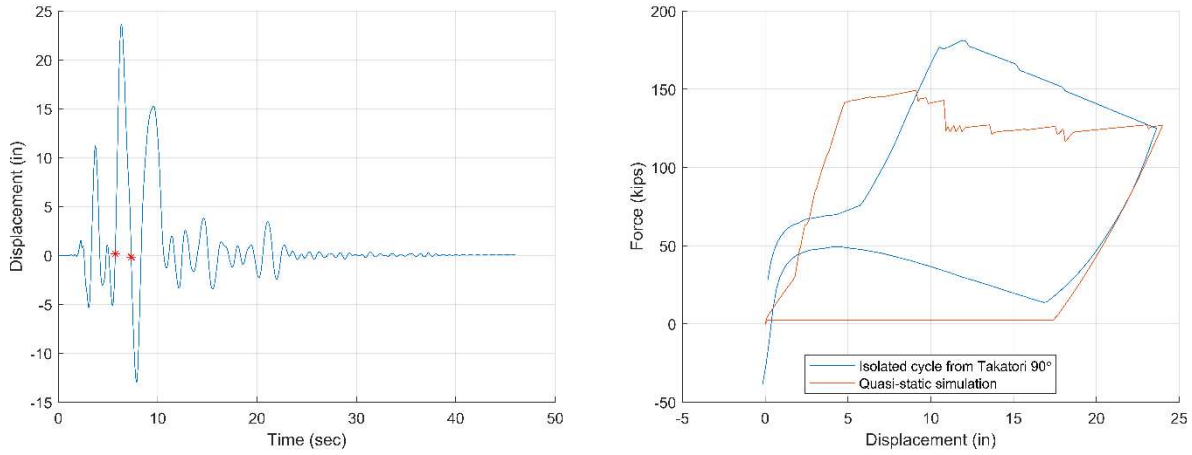

Figure F.15: (left) Displacement response time history for column reinforcement scenario 1 and Takatori 90° record scaled to achieve 10% drift; (right) comparison of force-displacement curves for one column from time-history and quasi-static analyses

F.2 Scenario 2

In the second scenario, there were 24 prestressing strands, and 16 reinforcing bars in each column, with three columns per pier. The elastic bar and fuse bar sizes were No. 11 and No. 8 respectively, and the length of the fuse bar was 67 inches. The El Centro, Rinaldi and Takatori 0° ground motions were scaled to achieve target column drifts of 6% and 10%, for a total of six analyses. Figures F.16 through F.21 show the displacement time histories and the force-displacement curve for one column during the peak displacement half-cycle.

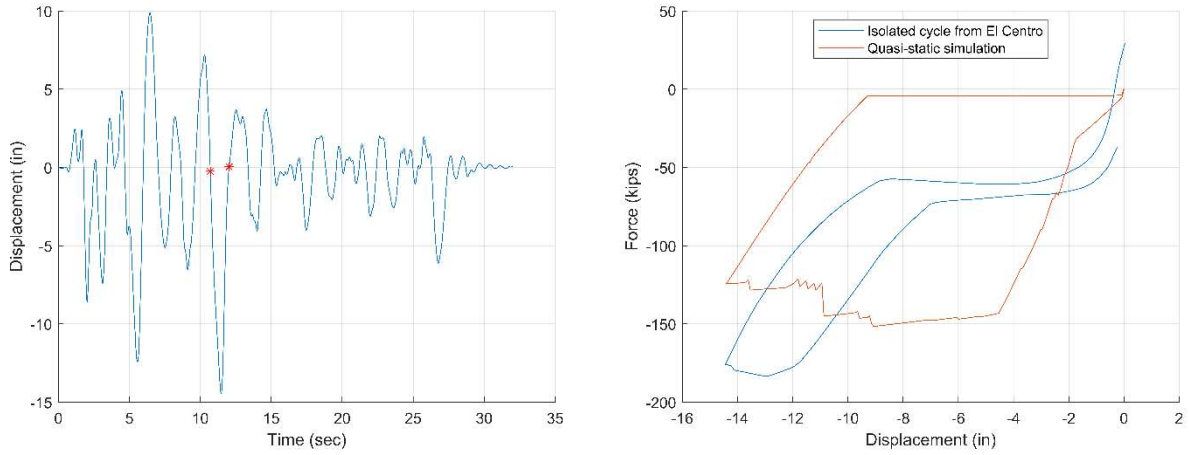

Figure F.16: (left) Displacement response time history for column reinforcement scenario 2 and El Centro record scaled to achieve 6% drift; (right) comparison of force-displacement curves for one column from time-history and quasi-static analyses

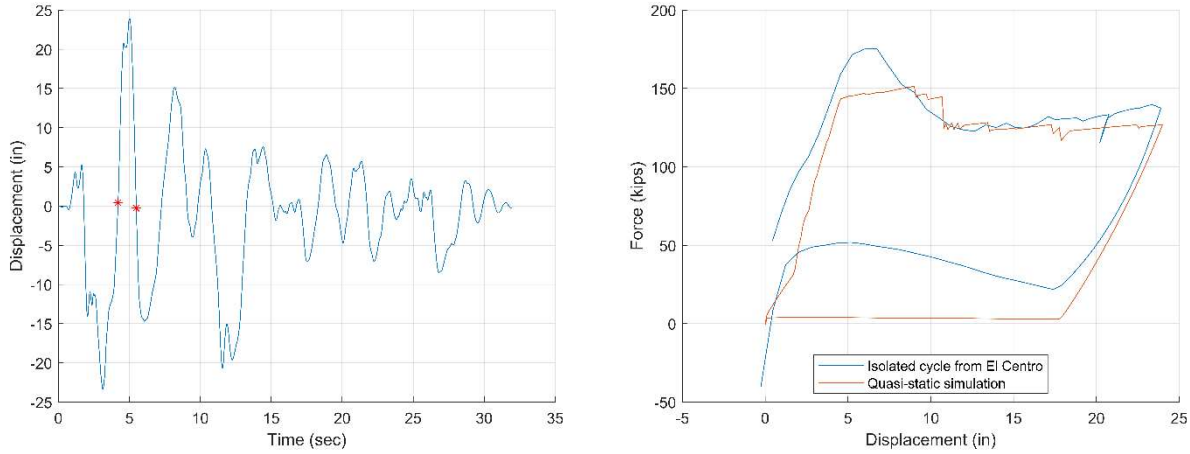

Figure F.17: (left) Displacement response time history for column reinforcement scenario 2 and El Centro record scaled to achieve 10% drift; (right) comparison of force-displacement curves for one column from time-history and quasi-static analyses

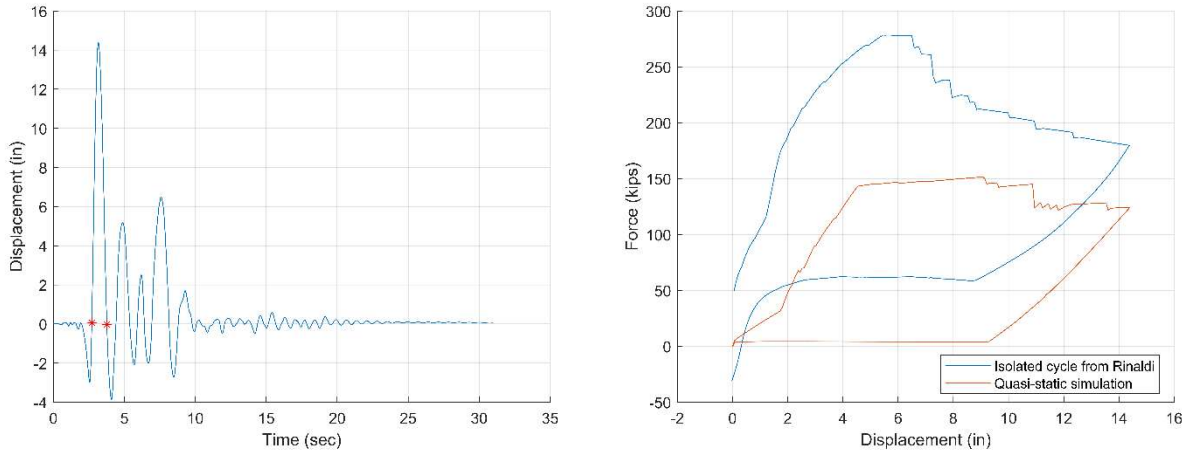

Figure F.18: (left) Displacement response time history for column reinforcement scenario 2 and Rinaldi record scaled to achieve 6% drift; (right) comparison of force-displacement curves for one column from time-history and quasi-static analyses

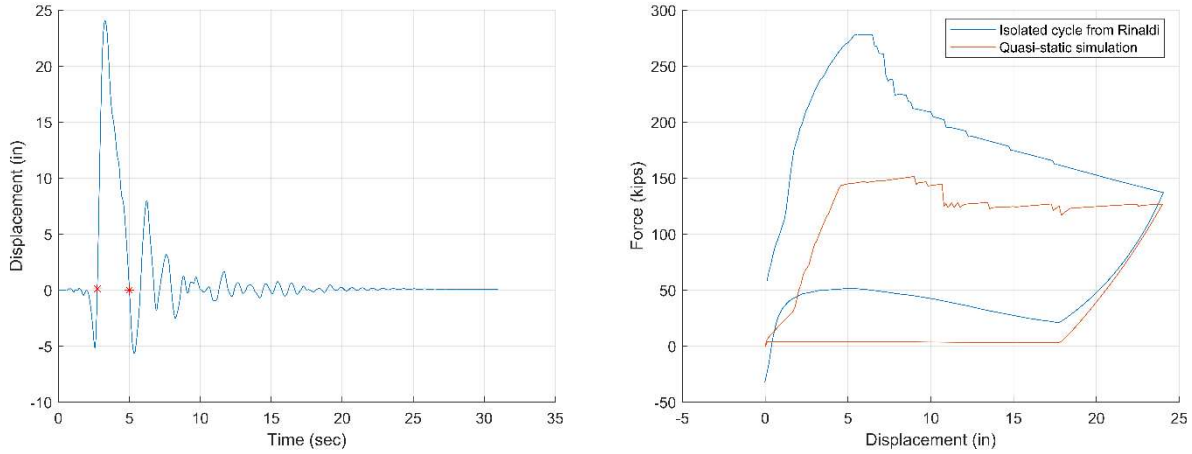

Figure F.19: (left) Displacement response time history for column reinforcement scenario 2 and Rinaldi record scaled to achieve 10% drift; (right) comparison of force-displacement curves for one column from time-history and quasi-static analyses

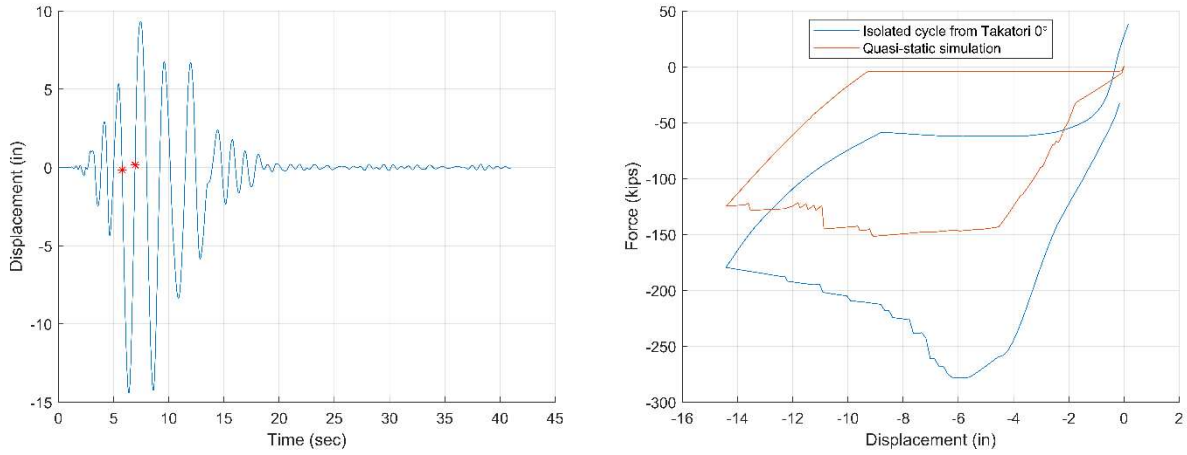

Figure F.20: (left) Displacement response time history for column reinforcement scenario 2 and Takatori 0° record scaled to achieve 6% drift; (right) comparison of force-displacement curves for one column from time-history and quasi-static analyses

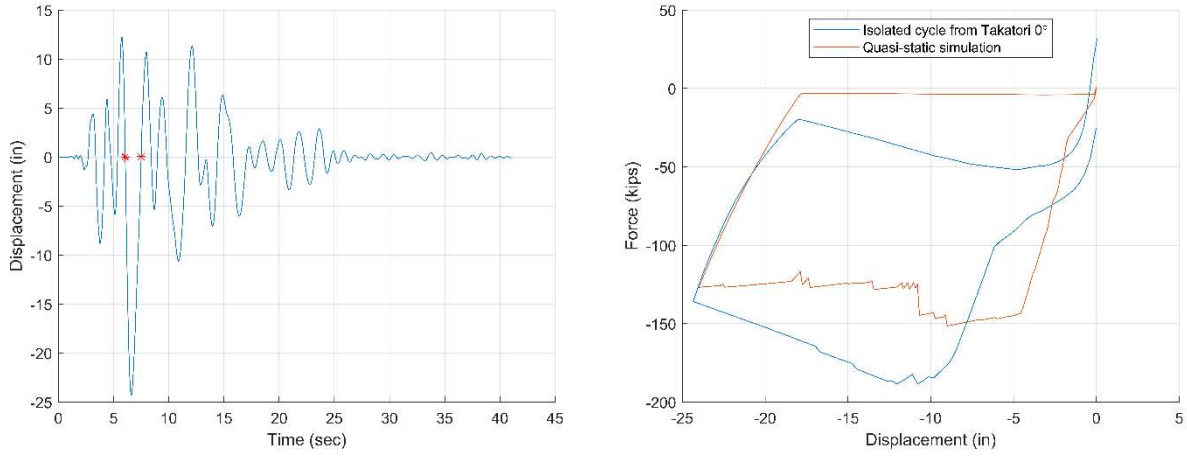

Figure F.21: (left) Displacement response time history for column reinforcement scenario 2 and Takatori 0° record scaled to achieve 10% drift; (right) comparison of force-displacement curves for one column from time-history and quasi-static analyses

F.3 Scenario 3

In the third scenario, there were 24 prestressing strands, and 16 reinforcing bars in each column with 2 columns per pier. The elastic bar and fuse bar sizes were No. 11 and No. 9

respectively, and the length of the fuse bar was 67 inches. The El Centro, Rinaldi and Takatori 0° ground motions were scaled to achieve target column drifts of 6% and 10%, for a total of six analyses. Figures F.22 through F.27 show the displacement time histories and the force-displacement curve for one column during the peak displacement half-cycle.

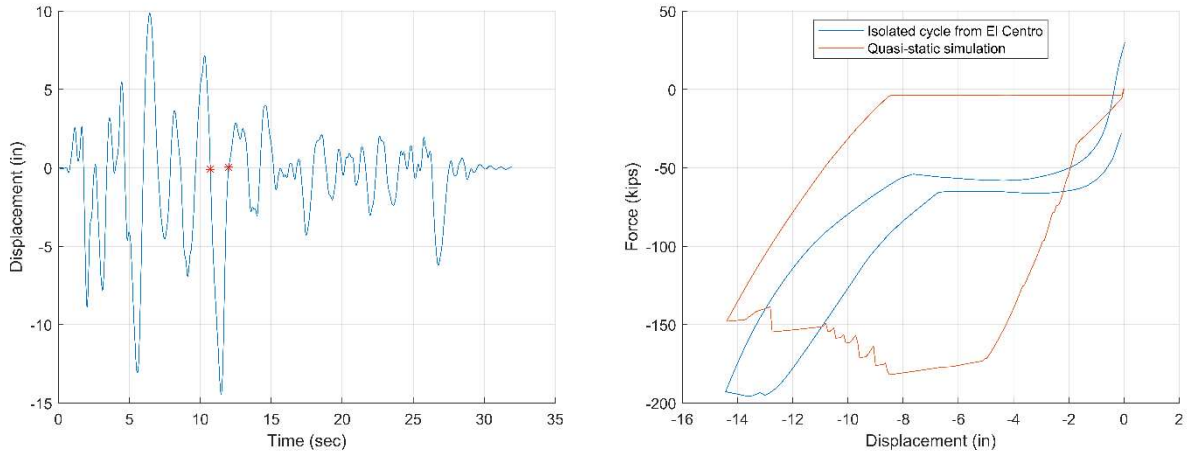

Figure F.22: (left) Displacement response time history for column reinforcement scenario 3 and El Centro record scaled to achieve 6% drift; (right) comparison of force-displacement curves for one column from time-history and quasi-static analyses

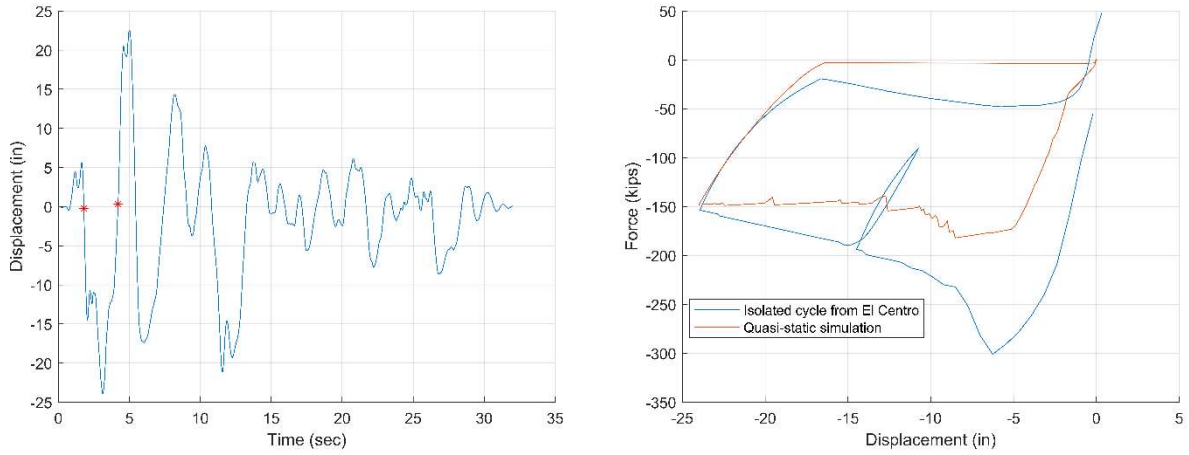

Figure F.23: (left) Displacement response time history for column reinforcement scenario 3 and El Centro record scaled to achieve 10% drift; (right) comparison of force-displacement curves for one column from time-history and quasi-static analyses

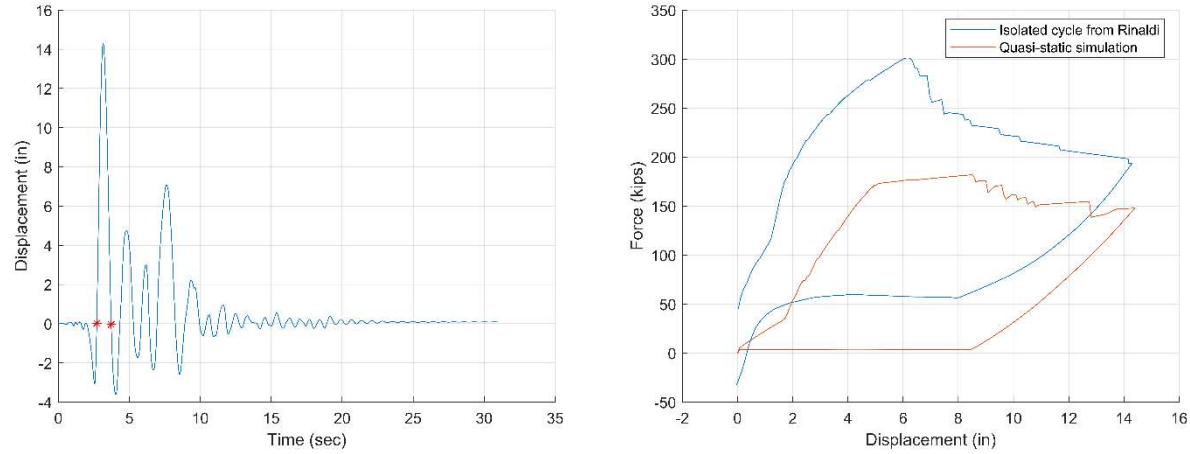

Figure F.24: (left) Displacement response time history for column reinforcement scenario 3 and Rinaldi record scaled to achieve 6% drift; (right) comparison of force-displacement curves for one column from time-history and quasi-static analyses

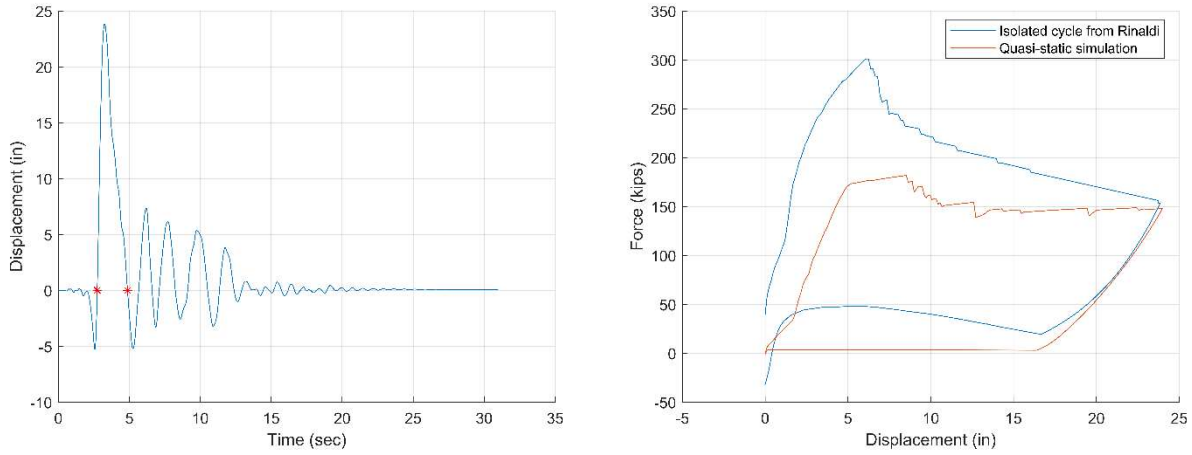

Figure F.25: (left) Displacement response time history for column reinforcement scenario 3 and Rinaldi record scaled to achieve 10% drift; (right) comparison of force-displacement curves for one column from time-history and quasi-static analyses

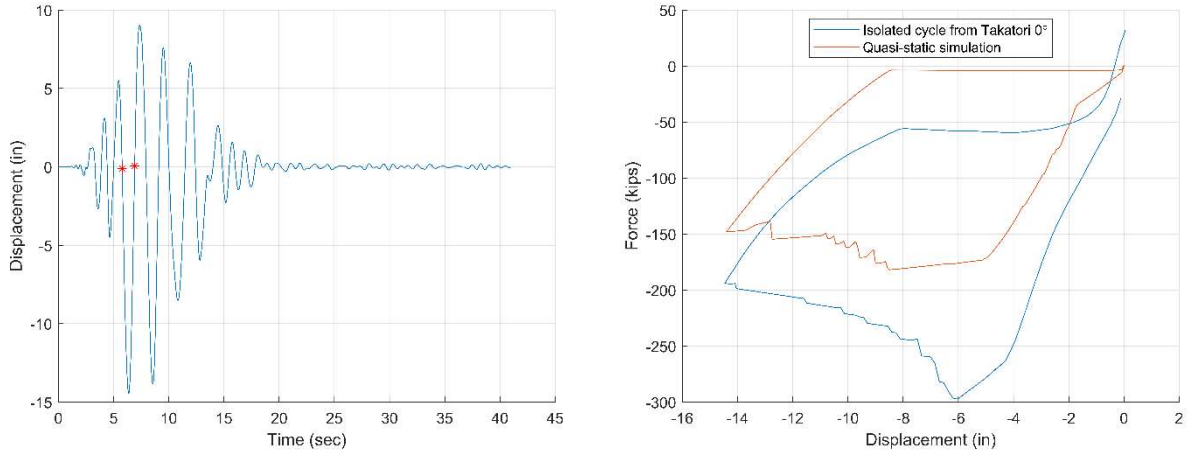

Figure F.26: (left) Displacement response time history for column reinforcement scenario 3 and Takatori 0° record scaled to achieve 6% drift; (right) comparison of force-displacement curves for one column from time-history and quasi-static analyses

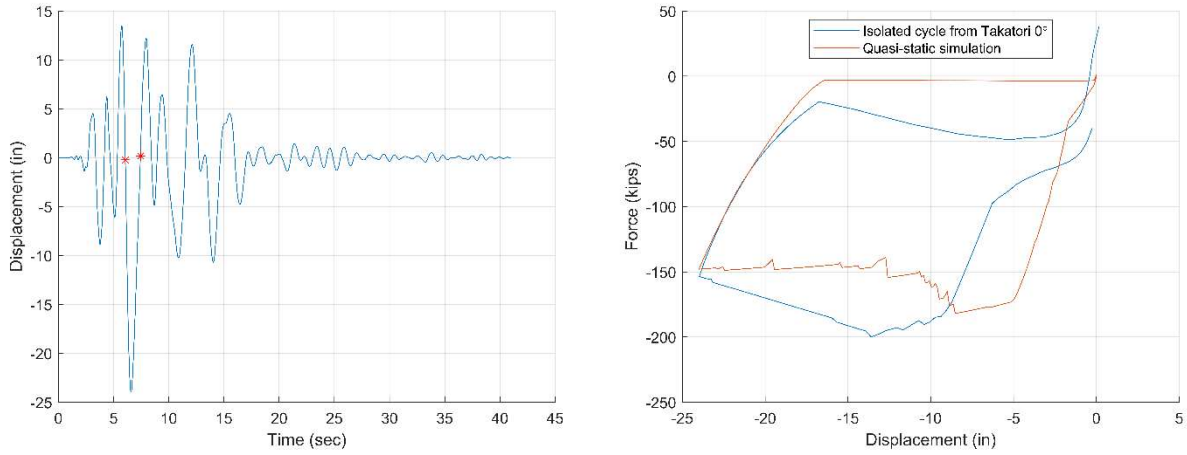

Figure F.27: (left) Displacement response time history for column reinforcement scenario 3 and Takatori 0° record scaled to achieve 10% drift; (right) comparison of force-displacement curves for one column from time-history and quasi-static analyses

F.4 Scenario 4

In the fourth scenario, there were 24 prestressing strands, and 20 reinforcing bars in each column, with 3 columns per pier. The elastic bar and fuse bar sizes were No. 11 and No. 9 respectively, and the length of the fuse bar was 40 inches. The El Centro, Rinaldi and Takatori 0° ground motions were scaled to achieve target column drifts of 6% and 10%, for a total of six analyses. Figures F.28 through F.33 show the displacement time histories and the force-displacement curve for one column during the peak displacement half-cycle.

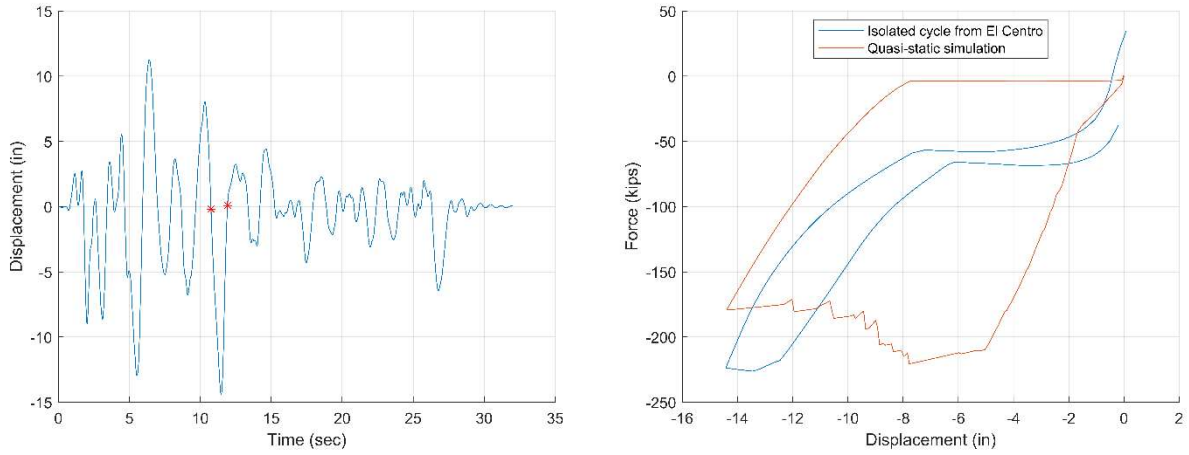

Figure F.28: (left) Displacement response time history for column reinforcement scenario 4 and El Centro record scaled to achieve 6% drift; (right) comparison of force-displacement curves for one column from time-history and quasi-static analyses

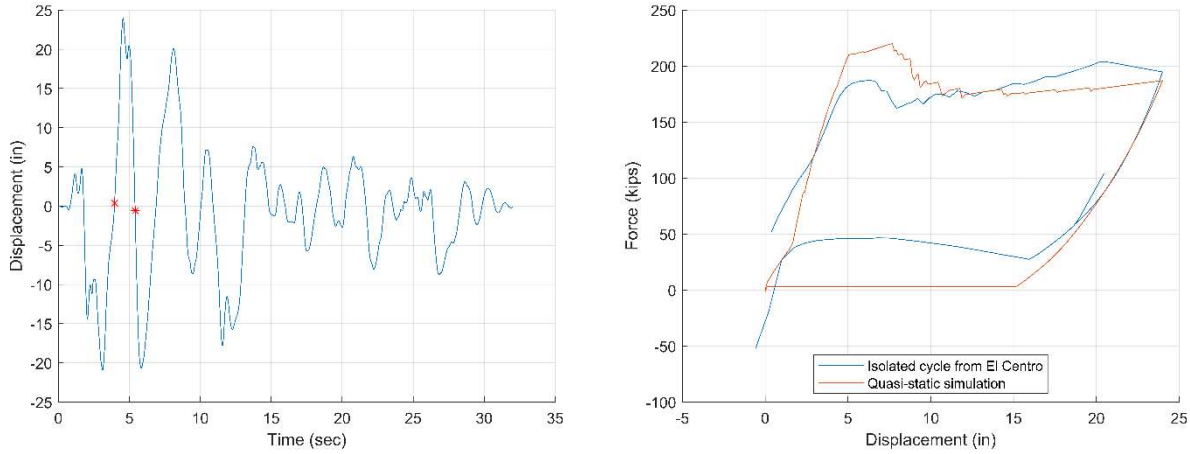

Figure F.29: (left) Displacement response time history for column reinforcement scenario 4 and El Centro record scaled to achieve 10% drift; (right) comparison of force-displacement curves for one column from time-history and quasi-static analyses

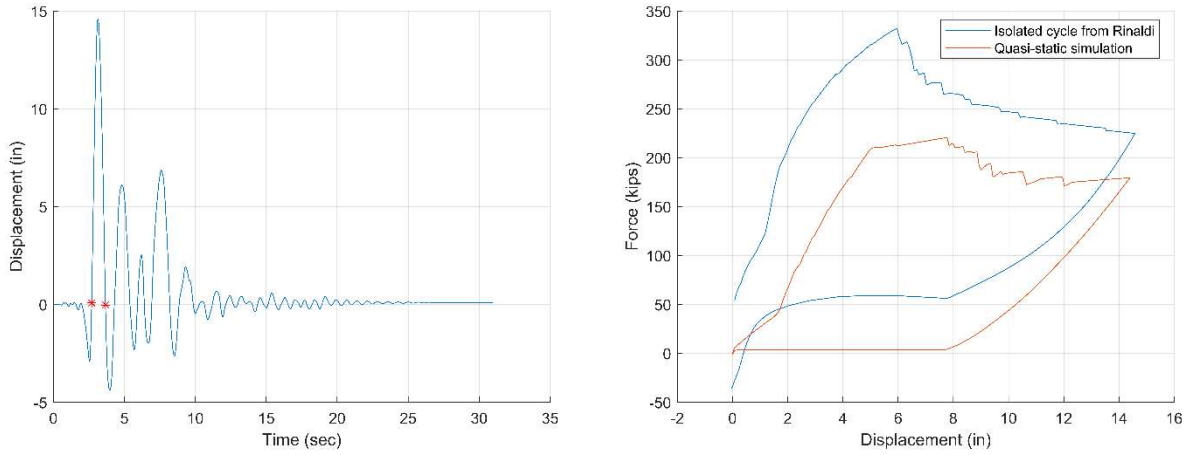

Figure F.30: (left) Displacement response time history for column reinforcement scenario 4 and Rinaldi record scaled to achieve 6% drift; (right) comparison of force-displacement curves for one column from time-history and quasi-static analyses

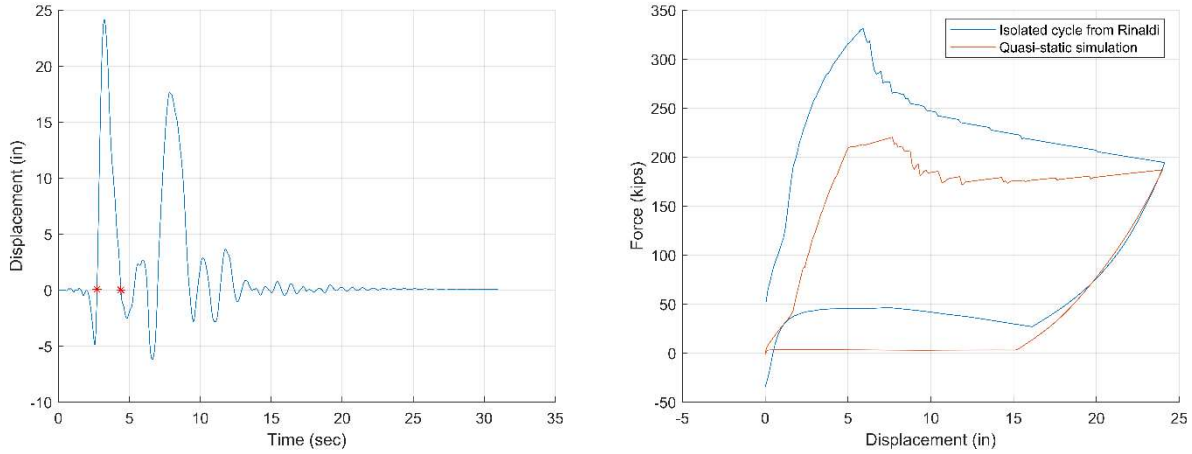

Figure F.31: (left) Displacement response time history for column reinforcement scenario 4 and Rinaldi record scaled to achieve 10% drift; (right) comparison of force-displacement curves for one column from time-history and quasi-static analyses

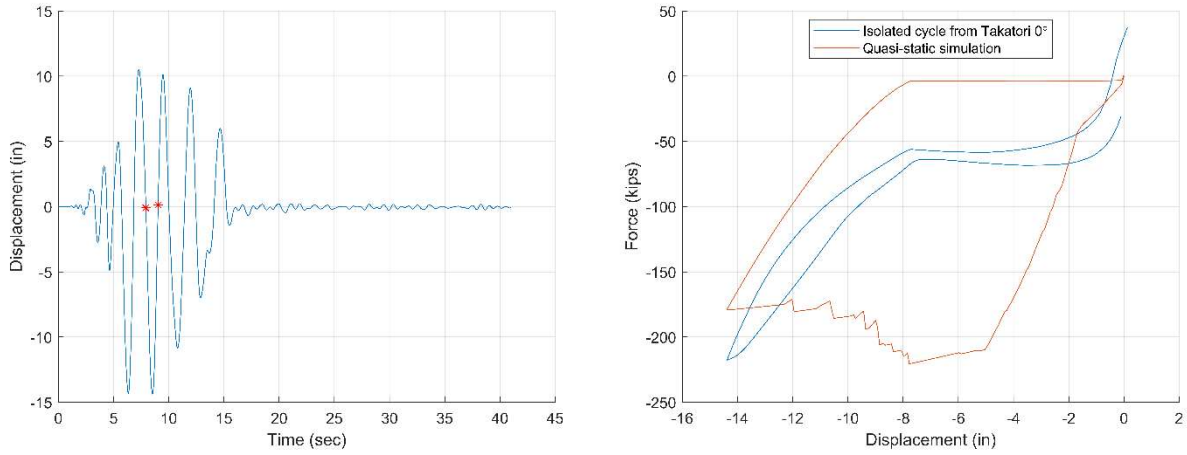

Figure F.32: (left) Displacement response time history for column reinforcement scenario 4 and Takatori 0° record scaled to achieve 6% drift; (right) comparison of force-displacement curves for one column from time-history and quasi-static analyses

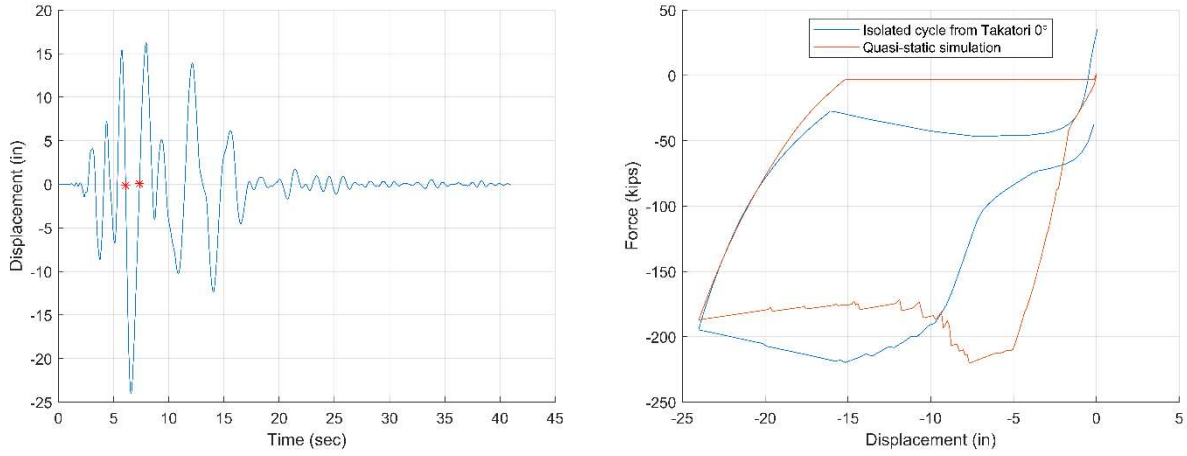

Figure F.33: (left) Displacement response time history for column reinforcement scenario 4 and Takatori 0° record scaled to achieve 10% drift; (right) comparison of force-displacement curves for one column from time-history and quasi-static analyses

REFERENCES

AASHTO. 2017. AASHTO LRFD bridge design specifications, 8th Edition, American Association of State Highway and Transportation Officials

ACI 318-19. 2019. Building code requirements for structural concrete. American Concrete Institute.

Anderson N S, J E Brewe, A O Humphreys, and C M Slavin. 2017. Development of a new generation high-strength P/T anchorage bar (experimental program). Final Report, Simpson Gumpertz & Heger.

ASTM International. (2020). ASTM A572/A572M-20 - Standard Specification for High-Strength Low-Alloy Columbium-Vanadium Structural Steel (Standard designation). Retrieved from https://www.astm.org/

ASTM International. (2020). Standard Specification for Low-Relaxation, Seven-Wire Steel Strand for Prestressed Concrete (Standard No. ASTM A416-20). ASTM International.

ASTM International. (2022). Standard Specification for Deformed and Plain Carbon-Steel Bars for Concrete Reinforcement (ASTM A615). Retrieved from https://www.astm.org/Standards/A615.htm

Belleri, A., Schoettler, M. J., Restrepo, J. I., & Fleischman, R. B. (2014). Dynamic Behavior of Rocking and Hybrid Cantilever Walls in a Precast Concrete Building. *ACI Structural Journal*, 111(3).

Bromenschenkel, R. and Mahan, M. (2014). “Recovery ERS – Vol. 1.” Caltrans Internal Report.

California Department of Transportation. (2021, October 18). *Assessment of Seismic Performance of Coronado Bay Bridge Piles with and without Simulated Damage and the Effectiveness of a Retrofit Method* (P. B. Shing, D. Kalliontzis, & L. Deyglun, Authors; Research Report No. UCSD/SSRP-21/02).

California Department of Transportation. (n.d.). *Experimental Investigation of a Self-Centering RC Column Design and a Displacement-Based Design Method for Highway Bridge Applications* (L. Deyglun, D. Kalliontzis, & P. B. Shing, Authors; Research Report No. SSRP-24-01).

Cheng, C. T. (2007). Energy dissipation in rocking bridge piers under free vibration tests. *Earthquake engineering & structural dynamics*, 36(4), 503-518.

Cheng, C. T. (2008). Shaking table tests of a self-centering designed bridge substructure. *Engineering Structures*, 30(12), 3426-3433.

Chopra, A. K. (2017). Dynamics of Structures (5th ed.). Pearson.

Chouw, N. "Low-Damage Design Philosophy for Future Earthquake-Resistant Structures." Proceedings of the ASME 2017 Pressure Vessels and Piping Conference. Volume 8: Seismic Engineering. Waikoloa, Hawaii, USA. July 16–20, 2017. V008T08A034. ASME. https://doi.org/10.1115/PVP2017-65273

Coffin, L. F., Jr., (1954), "A Study of the Effects of Cyclic Thermal Stresses in a Ductile Metal", ASME Transactions, Vol. 16, pp. 931-950.

Cohagen, L. S., Pang, J. B., Stanton, J. F., & Eberhard, M. O. (2008). *A precast concrete bridge bent designed to re-center after an earthquake* (No. WA-RD 684.3). Seattle, WA: TransNow.

Davis, P. M., Janes, T. M., Eberhard, M. O., and Stanton J. F. (2012). "Unbonded Pre-tensioned Columns for Bridges in Seismic Regions." PEER Report No. 2012/04, Pacific Earthquake Engineering Research Center, University of California, Berkeley, CA.

Devalapura, R K, and M K Maher K. Tadros. 1992. "Stress-strain modeling of 270 ksi low-relaxation prestressing strands." PCI Journal, Vol. 37 (2): 100-106.

European Committee for Standardization. (1998). Eurocode 8: Design of structures for earthquake resistance - Part 1: General rules, seismic actions and rules for buildings (EN 1998-1:1998).

Gebman, M J, S A Ashford, and J I Restrepo. 2006. Axial force transfer mechanisms within cast-in-steel-shell piles. Report No. SSRP-06/16, Department of Structural Engineering, University of California, San Diego.

Guerrini, G., Restrepo, J.I., Massari, M., and Vervelidis, A. (2015). "Seismic Behavior of Posttensioned Self-Centering Precast Concrete Dual-Shell Steel Columns." Journal of Structural Engineering, 141(4).

Hiraishi, H. (1984). Evaluation of shear and flexural deformations of flexural type shear walls. *Bulletin of the New Zealand Society for Earthquake Engineering*, 17(2), 135-144.

Housner, G. W. (1963). The behavior of inverted pendulum structures during earthquakes. *Bulletin of the seismological society of America*, 53(2), 403-417.

Junhua Wang, Hua Zhao, "High Performance Damage-Resistant Seismic Resistant Structural Systems for Sustainable and Resilient City: A Review", *Shock and Vibration*, vol. 2018, Article ID 8703697, 32 pages, 2018. https://doi.org/10.1155/2018/8703697

Kalliontzis, D., Morrison, M., Liu, Q., Nazari, M., & Kotzamanis, V. (2022). Improving recovery of hybrid rocking walls through locally heat-treated replaceable bars for hysteretic energy dissipation. *Engineering Structures*, 267, 114621.

Kurama, Y. C. (2005). Seismic design of partially post-tensioned precast concrete walls. *PCI journal*, 50(4), 100.

Ladjinovic, D., & Folic, R. (2004). Application of improved damage index for designing of earthquake resistant structures. *13th WCEE, Paper*, (2135), 1-15.

Lee, W., Jeong, H., Billington, S., Mahin, S. A., & Sakai, J. (2007). Post-tensioned structural concrete bridge piers with self-centering characteristics. In *Structural Engineering Research Frontiers* (pp. 1-15).

Makris, N., & Vassiliou, M. F. (2013). Planar rocking response and stability analysis of an array of free-standing columns capped with a freely supported rigid beam. *Earthquake Engineering & Structural Dynamics*, 42(3), 431-449.

Makris, N., & Vassiliou, M. F. (2015). Dynamics of the rocking frame with vertical restrainers. *Journal of Structural Engineering*, 141(10), 04014245.

Mander, J B, M J N Priestley, and R Park. 1988. "Theoretical stress-strain model for confined concrete." Journal of Structural Engineering, Vol. 114 (8): 1804-1826.

Manson, S. S. (1953). *Behavior of materials under conditions of thermal stress* (Vol. 2933). National Advisory Committee for Aeronautics.

Mantawy, I. M., Thonstad, T., Sanders, D. H., Stanton, J. F., & Eberhard, M. O. (2016). Seismic performance of precast, pretensioned, and cast-in-place bridges: Shake table test comparison. *Journal of Bridge Engineering*, 21(10), 04016071.

Miner, M. A. (1945), "Cumulative Damage in Fatigue", Journal of Applied Mechanics, Vol. 12, No. 3, pp.159-164.

Nema, A. and Restrepo, J.I. (2020). "Low Seismic Damage Columns for Accelerated Bridge Construction." PEER Report No. 2020/10, Pacific Earthquake Engineering Research Center, University of California, Berkeley, CA.

OEEAR. 2018. San Diego-Coronado Bay Bridge (Bridge 57-0857)-foundation refurbishment analysis. Office of Earthquake Engineering Analysis and Research, California Department of Transportation.

Papadopoulos, V, and P B Shing. 2015. Influence of the spacing of longitudinal reinforcement on the performance of laterally loaded CIDH piles - Analytical investigation. Report no. CA15-2173, Department of Structural Engineering, San Diego: University of California San Diego.

Priestley, M. J. N., Calvi, G. M., & Kowalsky, M. J. (2007, March). Direct displacement-based seismic design of structures. In *NZSEE conference* (pp. 1-23).

Priestley, M. N., & MacRae, G. A. (1996). Seismic tests of precast beam-to-column joint subassemblages with unbonded tendons. *PCI journal*, 41(1), 64-81.

Priestley, M. N., & Tao, J. R. (1993). Seismic response of precast prestressed concrete frames with partially debonded tendons. *PCI journal*, 38(1), 58-69.

Schaefer, J., Kennedy, B., Stanton, J. F., and Eberhard, M. O. (2013). "Unbonded Pretensioned Bridge Columns with Rocking Detail." PEER Report No. 2014/08, Pacific Earthquake Engineering Research Center, University of California, Berkeley, CA.

Silva, P, F Seible, and N Priestley. 1997. Response of the Coronado Bay Bridge pile-to-pile cap connections under simulated seismic loads. Report No. SSRP-97/11, Division of Structural Engineering, University of California, San Diego.

Sritharan, S., Aaleti, S., Henry, R. S., Liu, K. Y., & Tsai, K. C. (2015). Precast concrete wall with end columns (PreWEC) for earthquake resistant design. *Earthquake Engineering & Structural Dynamics*, 44(12), 2075-2092.

Thonstad, T., Mantawy, I. M., Stanton, J. F., Eberhard, M. O., & Sanders, D. H. (2016). Shaking table performance of a new bridge system with pretensioned rocking columns. *Journal of Bridge Engineering*, 21(4), 04015079.

Trono1, W., Jen, G., Panagiotou, M., Schoettler, M., and Ostertag, C.P. (2015). "Seismic Response of a Damage-Resistant Recentering Posttensioned-HYFRC Bridge Column." Journal of Bridge Engineering, 20(7).

Turksonmez, B. (2016). "Simplified Analysis of Bridge Structures for Abutment Shear Key Design." Internal Research Report supervised by P.B. Shing, Department of Structural Engineering, University of California, San Diego, CA.

Wang, J., & Zhao, H. (2018). High performance damage-resistant seismic resistant structural systems for sustainable and resilient city: A review. *Shock and Vibration*, *2018*.

Yashinsky, M., Ostrom, T., Alameddine, F., & Zokaie, T. (2022). Caltrans Seismic Retrofit Program after the 1971 San Fernando Earthquake. *Lifelines*, 48-60. https://doi.org/10.1061/9780784484432.005

Yoon, Y., Mahan, M., and Bromenschenkel, R. (2014). "Recovery ERS – Vol. 2." Caltrans Internal Report.